

UC Berkeley

UC Berkeley Electronic Theses and Dissertations

Title

3D Block Erodibility: Dynamics of Rock-Water Interaction in Rock Scour

Permalink

<https://escholarship.org/uc/item/61q7798m>

Author

George, Michael Freeman

Publication Date

2015

Peer reviewed|Thesis/dissertation

3D BLOCK ERODIBILITY: DYNAMICS OF ROCK-WATER INTERACTION
IN ROCK SCOUR

by

Michael Freeman George

A dissertation submitted in partial satisfaction of the

requirements for the degree of

Doctor of Philosophy

in

Engineering – Civil & Environmental Engineering

in the

GRADUATE DIVISION

of the

UNIVERSITY OF CALIFORNIA at BERKELEY

Committee in charge:

Professor Nicholas Sitar, Chair
Professor Steven D. Glaser
Professor William Dietrich

Fall 2015

Blank Page

Abstract

3D BLOCK ERODIBILITY: DYNAMICS OF ROCK-WATER INTERACTION
IN ROCK SCOUR

by

Michael Freeman George

Doctor of Philosophy in Engineering – Civil & Environmental Engineering

UNIVERSITY OF CALIFORNIA at BERKELEY

Professor Nicholas Sitar, Chair

Erosion of rock by flowing water is an integral process in the evolution of natural landscapes as well as a critical hazard for key infrastructure such as dams, spillways, bridges and tunnels. The removal of individual blocks of rock is one of the primary mechanisms by which rock scour can occur. This research examined the influence of 3D geologic structure on erodibility of rock blocks with the aim to understand the basic mechanics of the process as well as to develop a predictive framework for block erodibility. To do this, a multifaceted research program was established. Field investigation of a prototype site in the Sierra Nevada Mountains in northern California was used as a basis for the development of an extensive series of hydraulic model experiments, which were complemented by theoretical deterministic and stochastic analyses based on 3D block theory.

Past experimental studies have been limited to simplified cubic or rectangular block geometries in laboratory settings, with very little data regarding hydrodynamic pressures surrounding 3D blocks and subsequent block response to hydrodynamic loading. For more complex block shapes (as often found in nature), such simplifications in geometry can be problematic as the 3D orientation of discontinuities within the rock mass largely influence block removability, kinematics and stability. Accordingly, a major focus of this research was to obtain a high resolution experimental data set from both field and laboratory settings for hydraulic and rock mass parameters pertaining to 3D non-cubic block geometries.

Field work was carried out in a prototype setting at an actively eroding unlined rock spillway at a dam site in northern California. High resolution rock mass data was obtained using light detection and ranging (LiDAR) scanning which permitted statistical characterization of rock mass parameter variability for use in a probabilistic scour prediction model. Two instrumented artificial rock block were cast in existing block molds to capture hydrodynamic pressures and block displacements during spill events. Climatic conditions in northern California, however, prevented reservoir discharges on the blocks such that no data to date have been collected.

A scaled physical hydraulic model, loosely representing conditions at the above field site was also performed. The advantage of the laboratory model was the ability to investigate a broad range of variables and flow conditions not readily achievable in a field setting. For the model, an instrumented 3D block mold was constructed that could be rotated with respect to the flow

direction to study the influence of discontinuity orientation on block erodibility. As would be expected, the block erodibility threshold was found to be highly dependent on the flow direction. This can be attributed to changes in kinematic constraints associated with the block mold geometry in the downstream direction as well as the relative profile of block protrusion above the channel bottom. Three separate block response types were observed which are closely associated with block kinematic resistance. Pressure values, represented by the dimensionless average dynamic pressure coefficient, C_p , were determined as a function of the block mold orientation, turbulence intensity, block protrusion height, and flow velocity. Overall, the average hydrodynamic pressures on block faces were found to be adequate in the evaluation model block stability. Accordingly, the data presented herein may be applied to a variety of flow conditions.

A reliability-based, block theory framework was also developed for evaluation of 3D block erodibility given parameter uncertainty associated with the inherent variability within the rock scour process. Block theory provides a rigorous analytical methodology to identify removable blocks, determine potential failure modes, and assess 3D block stability. Block stability is evaluated in a pseudo-static manner using block theory limit equilibrium and kinematic constraint equations. Theoretical predictions for block erodibility threshold compare well with those obtained from hydraulic model testing for both high and low turbulence flows. Improved prediction was observed for some cases when a mobilized joint friction angle was used.

Applicability of the reliability-based, block theory methodology was demonstrated through two example analyses for the field site in northern California. Removable blocks from the spillway channel were identified and analyzed deterministically to determine their erodibility threshold. Variability in rock mass parameters was included based on statistical analysis of the LiDAR data set to calculate the failure probability of the block with the lowest erodibility threshold. FORM analysis for parameter importance indicates block protrusion height, followed by rock joint orientations and flow velocity, are the most influential variables on block stability, while joint friction angle is relatively insignificant.

From a design standpoint, the benefit of the proposed methodology is that 3D, site-specific geologic structure information can be incorporated into evaluation of rock mass erodibility. Variability in site parameters can be addressed in a probabilistic manner to classify locations most susceptible to erosion as well as identify the most influential variables affecting rock block stability. This can lead to more efficient scour remediation designs as well as more focused field and laboratory efforts to investigate parameters with the most impact on the system. Furthermore, reliability data can be useful for designers and infrastructure owners in decision making and management of risk at a specific site.

*To my family, your support and contribution to this endeavor is immeasurable.
I am forever grateful.*

Acknowledgements

The undertaking of a doctoral degree can, at times, seem monumental. It is not, by any means, a task that can be completed without the help and support of an entire community. I would like to acknowledge those individuals most influential in this study.

First and foremost, I am most grateful to my advisor, Professor Nicholas Sitar. Nick supported my efforts to approach this problem as I saw fit, really allowing me to develop as a researcher. At the same time, he always had an open door for discussion and has an incredible ability to see directly to the root of any matter. I especially appreciated his drive for simplicity, particularly to perform meaningful experiments. From the very first day that I came to Berkeley, I felt that he always looked out for my best interests, affording me the confidence to plunge head first into graduate work. I will definitely miss our Friday afternoons mapping on Grizzly Peak with the engineering geology students.

I would also like to thank Dr. George Annandale. George introduced me to the topic of rock scour when I started working at his consulting company after my undergraduate degree. It was a wonderful experience to work alongside the person who literally wrote the book on rock scour. George is true professional in every sense of the word and not to mention a great colleague and mentor. He engaged me to tackle complex scour problems that really set fire to my interest in pursuing this topic further. His enthusiasm towards the subject was extremely contagious.

Another individual I would like to recognize is Professor Richard E. Goodman. As one of the co-developers of block theory, Dick was instrumental in initiating this study. It was truly a pleasure to be able to interact with and work alongside someone of such creative and technical talent. His support and interest in my research was exceptionally gratifying.

It is a pleasure to also thank Professor Armen Der Kiureghian. His class on reliability really opened my eyes to engineering with variable systems and he was particularly insightful in developing the rock scour reliability approach presented in Chapter 6. I would also like to thank Professors Steve Glaser and Bill Dietrich for their perceptive review of this dissertation.

Additionally, I would like to acknowledge Bob McManus, Willie Whittlesey and Emily Steen of PG&E for their cooperation and support in using their Spaulding Dam site for my field investigations. Andy Snyder, Avery Clifton and Dan Brown, also of PG&E, I am enormously appreciative for always being available to assist in my excursions to the site as well as helping carry a bag of concrete or two. Someday we'll get that data!

I would also like to recognize Bob Wright of AMEC and Chin Man Mok of GSI Environmental (formerly of AMEC) for their collaboration and use of their LiDAR data set at the Spaulding Dam site.

At the Richmond Field Station, I would like to thank Professor Leonard Sklar of San Francisco State University and Dr. Christian Braudrick of UC-Santa Cruz for their expert advice on hydraulic modeling and conversations on the scouring process. I am also indebted to Stuart Foster at the RFS. He was instrumental in problem solving during construction and operation of the flume experiment.

I am deeply grateful for my colleagues at Berkeley. Particularly, I would like to thank Julien Waeber and Dr. Josh Zupan not only for their assistance in my field studies at Spaulding but also for their willingness to spend a night "on the edge of America", Dr. Roozbeh Geraili Mikola for many good conversations about rock mechanics over a fine Budweiser lager, Dr. Justin Hollenback for his astounding statistical advice, Michael Gardner for collaboration in the numerical modeling of my flume experiments, Uri Shelby for help in construction of my

physical hydraulic model, and Carly Schaeffer for her assistance in the statistical analysis of the LiDAR data set. I would also like to acknowledge my office mate, Maggie Parks, who among many other things, never faltered in her desire to make the trek with me all the way to the south side of campus to enjoy our weekly burrito lunch as well as Robert Lanzafame for the spectacular tours around the Bay in his sailboat. For Matt Over, thank you for keeping me to my Midwestern roots with a friendly game of washers.

This study was principally funded by the National Science Foundation under Grant No. CMMI-1363354, with additional support provided by the University of California Cahill Chair, the Hydro Research Foundation, and the United States Society on Dams. These sources are hereby cordially acknowledged.

Finally, I would like to acknowledge my family. For my mom, dad and brother who have been so loving and supportive. They provided the foundation in my life to make this work possible. An additional thanks to my dad who, “for fun”, took some of Gen-hua Shi’s original block theory computer codes in BASIC and converted them to EXCEL. These programs were used in creating the limit equilibrium stereonet presented in this dissertation. For my beautiful wife, Liane, who single handedly kept our family afloat throughout the entirety of this degree (while working a full-time engineering job too). The added weight she pulled so I could focus on research was Herculean. She even used vacation days to help do field work! For her unwavering support in this endeavor, I am forever grateful. Last but not least, I would like to thank our baby daughter, Violet. Her smile is such a bright light in the world that provides daily motivation. Hopefully, by the time she is able to read this, she isn’t too disappointed that her “old man” is just a geological engineer who bangs rocks together for a living.

Table of Contents

Acknowledgements.....	ii
Table of Contents	iv
List of Symbols	vi
Chapter 1. Introduction	1
1.1 Overview	1
1.2 Research objectives	5
1.3 Research outline	6
Chapter 2. Current scour evaluation methods	8
2.1 Scour mechanisms.....	8
2.2 Engineering scour models	11
2.3 Landscape evolution models	19
2.4 Limitations of current scour technology	21
Chapter 3. Field investigations.....	23
3.1 Overview	23
3.1.1 Field Site	24
3.2 Methodology	30
3.2.1 Artificial rock blocks	30
3.2.2 Rock mass discontinuity characterization.....	39
3.3 Results	43
3.3.1 Artificial rock blocks	43
3.3.2 Rock mass discontinuity characterization.....	44
3.4 Summary	51
3.4.1 Artificial rock blocks	52
3.4.2 Rock mass discontinuity characterization.....	52
Chapter 4. Hydraulic model experiment.....	53
4.1 Overview	53
4.2 Methodology	54
4.2.1 Model development.....	54
4.2.2 Model instrumentation & data acquisition.....	60
4.2.3 Model testing strategy	63
4.3 Results	64
4.3.1 Flow characterization.....	65
4.3.2 Block erodibility threshold.....	76
4.3.3 Block removal mechanics	80
4.3.4 Block pressure statistics	106
4.4 Summary	124
4.4.1 Flow characterization.....	124
4.4.2 Block erodibility threshold.....	125

	4.4.3	Block removal mechanics	126
	4.4.4	Block pressure statistics	128
Chapter 5.	Block theory framework.....		130
	5.1	Overview	130
	5.2	Block theory basics	131
	5.2.1	Assumptions.....	131
	5.2.2	Block removability.....	131
	5.2.3	Block kinematics.....	133
	5.2.4	Block stability	135
	5.3	Rock scour application.....	138
	5.3.1	Pseudo-static analysis	138
	5.3.2	Active resultant force vector	140
	5.3.3	Application to hydraulic model experiments	140
	5.4	Example Analysis.....	145
	5.4.1	Removability	145
	5.4.2	Block erodibility threshold.....	148
	5.5	Summary	151
Chapter 6.	Reliability analysis: General system formulation		152
	6.1	Overview	152
	6.2	Model Formulation.....	153
	6.3	System failure probability	157
	6.4	Parameter importance.....	158
	6.5	Numerical implementation.....	159
	6.6	Example analysis.....	159
	6.6.1	Variable distributions and correlation.....	160
	6.6.2	Block failure probability and parameter importance	163
	6.7	Summary	166
Chapter 7.	Conclusions		168
	7.1	Block response to hydraulic loading	169
	7.2	Reliability-based, block theory framework for block erodibility.....	170
	7.3	Recommendations for future study	171
References			172
Appendix A – Statistical distributions			181
Appendix B – Hydraulic model experiment: Model development.....			182
Appendix C – Hydraulic model experiment: Flow characterization.....			183
Appendix D – Hydraulic model experiment: Block erodibility threshold			200
Appendix E – Hydraulic model experiment: Block removal mechanics.....			203
Appendix F – Hydraulic model experiment: Block pressure statistics			379
Appendix G – Block theory analysis			436

List of Symbols

Bold font = vector/matrix quantity

A	Block face area	(m ²)
a, b	Fit parameters for C_1 and C_3	(-)
C_1, C_2, C_3	Correction coefficients for C_p	(-)
C_p	Average dynamic pressure coefficient	(-)
C'_p	Fluctuating dynamic pressure coefficient	(-)
C_p^+	Maximum instantaneous dynamic pressure coefficient	(-)
C_p^-	Minimum instantaneous dynamic pressure coefficient	(-)
C_k	Cut-set	(-)
d	Flow depth	(m)
\mathbf{D}'	Diagonal standard deviation matrix of equivalent normal random variables evaluated at the design point	
EP	Excavation pyramid	(-)
f	Block free face	(-)
f_{char}	Characteristic frequency of pressure fluctuations	(Hz)
F	Magnitude of required stabilizing force applied in direction of block movement	(N)
\mathbf{F}	Required stabilizing force vector applied in direction of block movement	(N)
F_a	Magnitude of applied force	(N)
F_{a_min}	Minimum applied force required to rotate \mathbf{r} to block yield condition	(N)
\mathbf{F}_a	Applied force vector	(N)
\mathbf{F}_{a_min}	Minimum applied force vector required to rotate \mathbf{r} to block yield condition	(N)
Fr	Froude number	(-)
F_r	Ratio of prototype to model force scales	(-)
F_x	Marginal cumulative density function of random variable x (Chap. 6 only)	
g	Gravitational constant	(m/s ²)
g	Component limit state function (Chap. 6 only)	
\mathbf{g}	Gravitational acceleration vector (0, 0, g)	(m/s ²)
\mathbf{g}^*	Non-dimensional gravitational acceleration vector	(-)
h	Block protrusion height	(m)
\mathbf{i}	Intersection unit vector of two joints	(-)
i_ϕ	discontinuity dilation angle	(deg.)
I	Boolean indicator function for Monte Carlo simulation	(-)
J	Discontinuity (joint) set	(-)
$\mathbf{J}_{\mathbf{x},\mathbf{u}}$	Jacobian matrix for transformation from \mathbf{x} to \mathbf{u} space evaluated at the design point	
JP	Joint pyramid	(-)
l_b	Length (trace) of block face at the surface (free face)	(m)
L	Characteristic length scale	
\mathbf{L}_0	Choleski decomposition of correlation matrix \mathbf{R}_0	
L_r	Ratio of prototype to model length scales	(-)
M_r	Ratio of prototype to model mass scales	(-)
\mathbf{n}	Discontinuity normal unit vector	(-)
\mathbf{n}_{avg}	Average discontinuity normal unit vector	(-)

N	Number of Monte Carlo simulations	(-)
N_0	Maximum number of Monte Carlo trials	(-)
N_{cs}	Number of cut-sets	(-)
N_g	Number of system components defined by a limit state function	(-)
N_t	Number of mesh triangles	(-)
p_1, p_2, p_3, p_4	Statistical distribution parameters (beta, normal, log normal)	
P	Pressure	(Pa)
P^*	Non-dimensional pressure	(-)
P	Root mean square (RMS) of pressure fluctuations	(Pa)
P_{avg}	Average pressure	(Pa)
P_{char}	Characteristic dynamic pressure	(Pa)
$P_{f,s}$	System failure probability	(-)
$P_{f,MC}$	System failure probability determined by Monte Carlo simulation	(-)
P_{max}	Maximum instantaneous pressure	(Pa)
P_{min}	Minimum instantaneous pressure	(Pa)
P_r	Ratio of prototype to model pressure scales	(-)
P_s	Pseudo-static pressure	(Pa)
P_{static}	Static pressure	(Pa)
Q	Discharge	(m ³ /s)
Q_r	Ratio of prototype to model discharge scales	(-)
\mathbf{r}	Active resultant force vector	(N)
\mathbf{r}_0	Initial active resultant force vector	(N)
\mathbf{r}_{avg}	Average active resultant force vector	(N)
\mathbf{R}_0	Correlation matrix	(-)
Re	Reynolds number	(-)
\mathbf{s}	Block movement unit vector	(-)
s_f	Energy grade line slope	(-)
SP	Space pyramid	(-)
S	Water force applied to block face	(N)
S_{xx}	Power spectral density	((·) ² /Hz)
t	Time	(s)
t^*	Non-dimensional time	(-)
T_r	Ratio of prototype to model time scales	(-)
T_u	Turbulence intensity	(-)
u_x	Horizontal (stream-wise) velocity component	(m/s)
u'_x	Root mean square (RMS) of horizontal (stream-wise) velocity fluctuations	(m/s)
u_x^+	Maximum instantaneous horizontal (stream-wise) velocity fluctuations	(m/s)
u_y	Lateral velocity component	(m/s)
u'_y	Root mean square (RMS) of lateral velocity fluctuations	(m/s)
u_y^+	Maximum instantaneous lateral velocity fluctuations	(m/s)
u_z	Vertical (transverse) velocity component	(m/s)
u'_z	Root mean square (RMS) of vertical (transverse) velocity fluctuations	(m/s)
u_z^+	Maximum instantaneous vertical velocity fluctuations	(m/s)
U	Characteristic velocity scale	(m/s)
U_r	Ratio of prototype to model velocity scales	(-)
\mathbf{u}	Velocity vector (u_x, u_y, u_z)	(m/s)

\mathbf{u}	Vector of random variables in std. normal domain $\mathbf{u} = [u_1 \dots u_n]$ (Chap. 6 only)	
\mathbf{u}^*	Non-dimensional velocity vector	(-)
\mathbf{u}^*	Design point in std. normal system domain (Chap. 6 only)	
\mathbf{v}	Block-side unit normal vector	(-)
V_b	Block volume	(m ³)
\mathbf{W}_b	Block weight vector	(N)
We	Weber number	(-)
x	Length/coordinate	(m)
x^*	Dimensionless length/coordinate	(-)
\mathbf{x}	Vector of random variables = $[x_1 \dots x_n]$ (Chap. 6 only)	
\mathbf{x}^*	Design point in system domain (Chap. 6 only)	
y	Length/coordinate	(m)
y^*	Dimensionless length/coordinate	(-)
z	Length/coordinate	(m)
z^*	Dimensionless length/coordinate	(-)

Greek symbols

α	Importance vector for statistically independent variables	
β	Reliability index	(-)
δ	Rock joint dip angle	(deg.)
δ_0	Tolerance for δ_{Pf} during Monte Carlo simulation	(-)
δ_{Pf}	Coefficient of variation of failure probability	(-)
γ	Importance vector for dependent random variables	
γ_w	Unit weight of water	(N/m ³)
μ	Sample mean	
ν_w	Kinematic viscosity of water	(m ² /s)
∇	Nabla operator ($\partial/\partial x, \partial/\partial y, \partial/\partial z$)	
$\Omega(\mathbf{x})$	System domain for variables \mathbf{x} (Chap. 6 only)	
$\varphi(\mathbf{u})$	Standard normal system domain for transformed variables \mathbf{u} (Chap. 6 only)	
Φ	Univariate standard normal cumulative density function	
ϕ	Discontinuity (joint) friction angle	(deg.)
ψ	Block mold rotation angle	(deg.)
$\psi_{\mathbf{r}}$	Azimuth of active resultant force vector	(deg.)
ρ	Correlation coefficient between variables	(-)
ρ_b	Density of rock	(kg/m ³)
ρ_r	Ratio of prototype to model density scales	(-)
ρ_w	Density of water	(kg/m ³)
σ	Sample standard deviation	
σ_w	Water surface tension	(N/m)
τ	Bed shear stress	(Pa)
θ	Rock joint dip direction	(deg.)
θ_{F_a}	Required angle of \mathbf{F}_a to rotate \mathbf{r} to block yield condition	(deg.)
$\theta_{\mathbf{r}}$	Required angle of rotation of \mathbf{r} from vertical to reach block yield condition	(deg.)
ζ	Angle of block protrusion with respect to flow direction	(deg.)

Chapter 1. Introduction

1.1 Overview

Erosion of rock channels by flowing water is a process that has defined the natural landscape, but is also a critical issue for important elements of the world's key infrastructure such as dams, bridges and tunnels (Figure 1-1). Excessive scour of the foundation, spillway, or even the structure itself can compromise stability leading to high remediation costs and even the loss of life should catastrophic failure occur. For dams, specifically, this has led to increased safety concerns arising from the continued development of communities directly downstream from these structures, particularly in dense urban environments where land space is limited.

In the United States, the application of more stringent requirements for managing the probable maximum flood (PMF), coupled with improved hydrologic methods and more robust climate data sets, has generally resulted in significantly greater estimated magnitudes of the design floods (Achterberg et al. 1998). Accordingly, the risk of foundation or spillway erosion is increased, particularly at existing structures that may now be inadequate to safely pass the revised design flow. Therefore, reliable prediction of scour for new and retrofit projects alike is vitally important.

Scour of rock is a complex process involving rock, water and air interaction. As such, making reliable spatial and temporal estimates for scour requires an intimate understanding of the fundamental mechanics governing the process, which has proven to be a challenging hurdle. Much of the early pioneering work on rock scour was hydraulically driven and focused on a few key average hydraulic parameters, such as discharge, flow velocity, and energy potential, e.g. Schoklitsch (1932) or Veronese (1937), with little consideration given to rock mass variables. These relationships were generally empirically derived from laboratory data and, therefore,

limited in applicability to their tested range. Additionally, limited insight regarding the scouring process is gained through their application.

As understanding of turbulence and rock mechanics evolved, so did the awareness of the complexity of the scour problem. Research in the last 30 years or so has provided significant insight into break-up of a rock mass by hydraulic forces. One of most prominent mechanisms by which scour can occur is the removal of individual blocks of rock (also referred to as plucking or quarrying). This occurs predominantly in natural bedrock channels, unlined spillways/water conveyance tunnels, plunge pools and dam abutments (Figure 1-2). Numerous investigations from both engineering and geomorphologic perspectives have examined the erosion of rock blocks subject to a variety of flow conditions including open-channels (Reinius 1986, Coleman et al. 2003, Frizell 2007, Dubinski 2009, Chatanantavet & Parker 2009), hydraulic jumps (Fiorotto & Rinaldo 1992, Fiorotto & Salandin 2000), knick-points (Lamb & Dietrich 2009), and plunging jets/plunge pools (Yuditskii 1967, Annandale 1995, 2006, Liu et al. 1998, Robinson & Kadavy 2001, Bollaert 2002, Manso 2006, Melo et al. 2006, Federspiel et al. 2011, Duarte 2014). A common focus has been the evaluation of the role of discontinuities bounding the block in transmitting hydraulic pressures to the underside of the block promoting ejection from the surrounding rock mass.

In nearly all studies, simplified rectangular or cubic block geometries with vertical and horizontal discontinuities are considered and lesser emphasis has been given to more complex 3D geologic structures typically encountered in nature. Such simplifications can be problematic, particularly for block analysis, where the 3D orientation of discontinuities within the rock mass largely influence block removability, kinematics and stability (Goodman & Shi 1985).



Figure 1-1. Erosion of Grand Canyon (left) by Colorado River over geologic time – $O(10^7)$ years) (National Park Service 2015) and slot canyon (right) at Spaulding Dam in Northern California by reservoir spills over human time – $O(10^1-10^2)$ years).



Figure 1-2. Removal of large rock blocks from unlined spillway at Wivenhoe Dam in Australia (Stratford et al. 2013). For scale, spillway width is approximately 90 m.

The role of geologic structure on rock mass erodibility can be significant, as shown for the well-known case of Ricobayo Dam in Spain. The dam had a 400 m long unlined rock spillway with a capacity of $4,650 \text{ m}^3/\text{s}$ designed to discharge over a granite cliff. Within two years of operation, multiple flood events (with discharges well below the design flow) caused significant deterioration of the spillway raising concern for the safety of the dam (Figure 1-3).

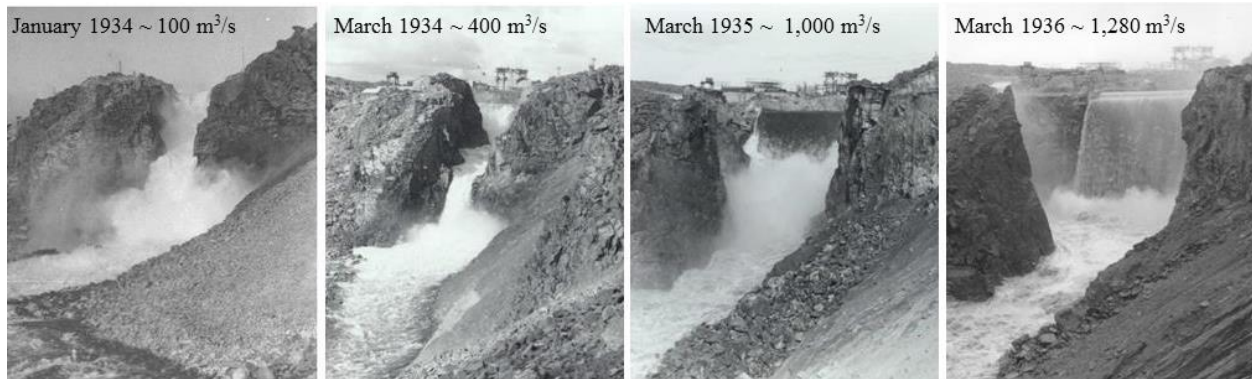


Figure 1-3. Scour evolution at Ricobayo Dam (Annandale 2006).

Progression of scour through the spillway was greatly influenced by the 3D nature of discontinuities within the rock mass. A key geologic feature was an anticline-like structure orthogonally bisecting the spillway (Figure 1-4). On the downstream side (Zone 1) of this structure, jointing of one of the prominent discontinuity sets dips in the direction of flow, while upstream (Zone 2) this same joint set dips against the direction of flow. For the downstream section, this kinematically enabled the sliding failure of larger size rock blocks in the spillway when subjected to relatively small amounts of discharge. Accordingly, scour progression for the first three events occurred rapidly back towards the dam in a nearly horizontal direction. As scour proceeded upstream past the anticline axis, progression slowed in the horizontal direction but advanced vertically downwards forming a large plunge pool. Rock joints dipping against the flow direction in the upstream section made it kinematically more difficult to remove larger size blocks even at higher flow rates of later events. As such, only smaller size blocks could be

plucked from the rock mass, which significantly limited further horizontal scour migration. While the dam stability was not immediately threatened, significant cost was expended to contain and eventually remediate the scour (Figure 1-5).

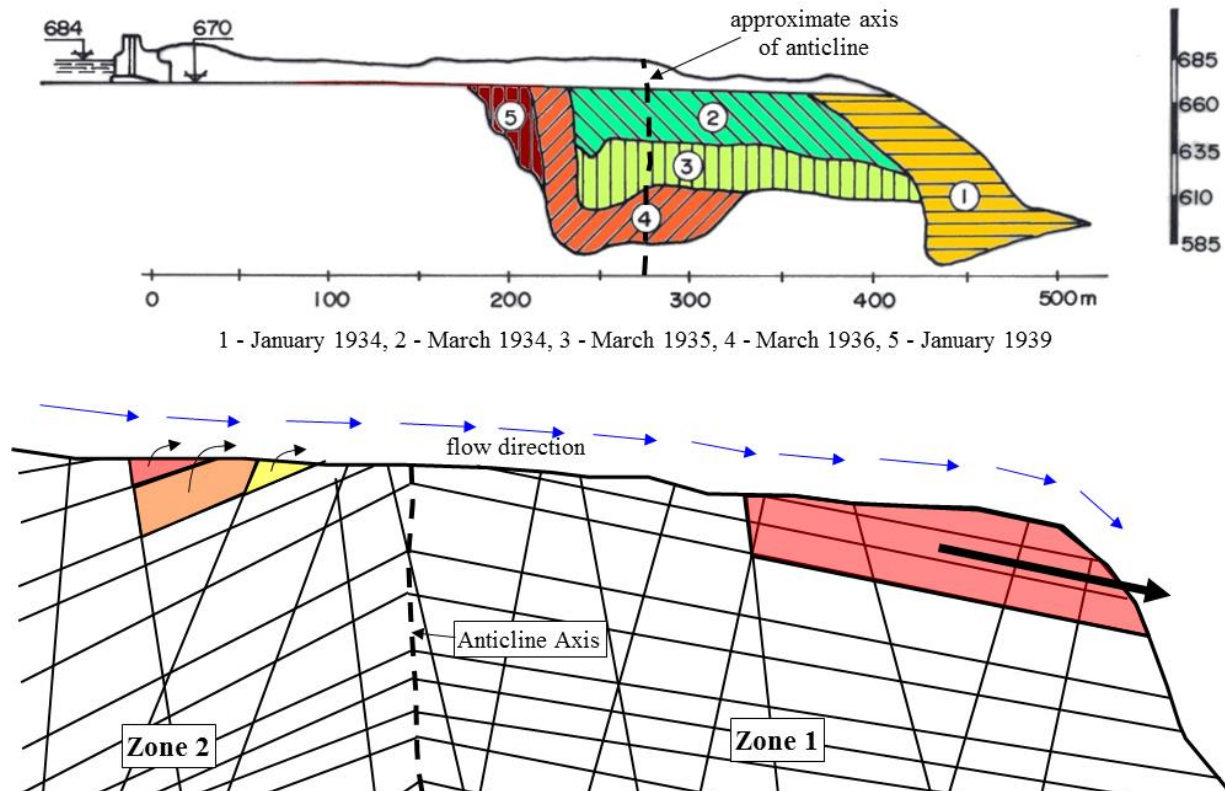


Figure 1-4. Cross-section of Ricobayo spillway showing scour from early flood events (top) and block removal kinematics associated with anticline-like structure (bottom) (Annandale 2006).

The Ricobayo example highlights a real need to understand and quantify the influence of 3D geologic structure on rock mass erodibility. To do so, however, requires a significant amount of detailed data regarding not only rock mass parameters but also flow hydraulics and forces applied to and around these blocks, which has historically been a substantial obstacle to overcome. For field (prototype) cases, such as those discussed above, this type of data is non-existent and can be very difficult to obtain, particularly information regarding hydrodynamic pressures in-side actual rock joints. Often in these scenarios, a researcher or designer has available only a crude topographic map showing the pre- and post-scour geometry and, if one is lucky, some discharge data that may have been recorded near the timeframe when the flood event(s) occurred! Additionally, capturing a scour event can be tricky as the timing of spills is often controlled by natural rainfall episodes.



Figure 1-5. Scour remediation at Ricobayo (note extensive excavation and concrete work in the plunge pool region in addition to flow splitters on the spillway lip to dissipate hydraulic energy) (photo source unknown).

1.2 Research objectives

The removal of individual blocks of rock is one of the primary mechanisms by which rock scour can occur and strongly depends on the 3D orientations of discontinuities defining the block. Despite this, idealized rectangular or cubic block geometries have been used for investigations of block erodibility and typically only simple 1D lifting or 1D sliding failure modes are considered. For more complex 3D block geometries, as are often found in nature, a number of block failure modes exist. It is not well understood, however, how this geometry affects block erodibility. This research aimed to close this gap in knowledge with the following key objectives:

- Investigate influence of 3D geologic structure on the erodibility of blocks from rock masses.
- Collect high-resolution experimental data for hydraulic and rock mass parameters from both field and laboratory settings to help bridge the gap between idealized model and actual prototype conditions.

- Identify dominant modes/mechanisms for removal of 3D rock blocks subject to hydraulic loading.
- Address uncertainty in the scour process associated with natural variability in rock mass and flow parameters.
- Develop a framework to incorporate 3D geologic structure and natural variability into predictive analysis of block erodibility.

1.3 Research outline

A multifaceted approach focusing on theoretical and experimental investigations was adopted to examine the influence of 3D geologic structure on erodibility of rock blocks. The dual-nature of this subject required equal founding on the basic underlying principles of rock mechanics and hydraulics. The individual elements of the research program and the findings are presented as follows:

A background discussion on the current state of scour technology is presented in Chapter 2. The physical mechanisms leading to the break-up of a rock mass by hydraulic forces are addressed and prominent scour prediction models are outlined. Focus is on research on the erodibility of individual blocks and/or multi-block systems. Limitations of existing rock scour technologies are highlighted to provide a basis for the research program described herein.

An overview of field investigations and results is presented in Chapter 3. Field work was carried out to obtain measurements for hydrodynamic pressures and block displacements in a prototype setting in an unlined spillway at a dam site in northern California as well as high resolution rock mass data using light detection and ranging (LiDAR) scanning. For the former, prototype data of this nature has previously never been collected. Statistical characterization of natural variability of rock mass parameters from LiDAR data is presented herein for use in the probabilistic scour model presented in Chapter 6.

A synthesis of experimental results for a scaled physical hydraulic model, loosely representing conditions at the above field site, is presented in Chapter 4. An instrumented 3D block mold was constructed that could be rotated with respect to the flow direction to study the influence of discontinuity orientation on block erodibility over a range of flow conditions. Each flow condition is characterized according to the mean stream-wise and transverse velocity, fluctuating stream-wise and transverse velocity, flow depth, turbulence intensity and power spectral density. The critical (threshold) mean flow velocity resulting in removal of the 3D block is determined for each flow condition. For model runs resulting in block removal, real-time analysis of hydrodynamic pressures around the block and of block displacements is performed to determine block failure mechanics. For runs not resulting in block removal, a statistical description of hydrodynamic pressures around the block is made.

A conceptual approach for addressing 3D geologic structure within the scouring process is outlined in Chapter 5. A block theory framework is utilized for 3D characterization of the rock mass structure. Block theory provides a rigorous analytical methodology to identify removable blocks, determine potential failure modes, and assess 3D block stability. This section provides an overview of block theory concepts as well as applicability to the rock scour process. Results from the physical hydraulic model are examined within the block theory framework and a predictive model for block erodibility threshold is presented. An example analysis for an

actively eroding unlined rock spillway at a dam site in northern California is presented to demonstrate application of the results and methodologies developed herein.

A theoretical means for addressing variability associated with the rock scour process is explored in Chapter 6. Variability in rock mass and flow conditions is dealt with through development of a general system reliability approach for stability of 3D rock blocks within the block theory framework. Monte Carlo sampling is used to determine block failure probability under hydraulic loading, while first-order reliability method (FORM) provides a convenient means to estimate importance of system parameters and their overall influence on block erodibility. The example analysis in Chapter 5 is extended to show application of the reliability methods developed for scour evaluation to address variability at the dam site in northern California.

The major findings of this research are then summarized and ideas for future studies and/or modifications to the existing study are discussed in Chapter 7.

Chapter 2. Current scour evaluation methods

Numerous methods are available for prediction of scour for many types of flow conditions. This section is not meant to provide a review of every method, but rather focus on those more commonly used or those which focus on the removal of rock blocks. First, however, a discussion of the physical mechanisms leading to the break-up of a rock mass subject to hydraulic loads is presented.

2.1 Scour mechanisms

The break-up of a rock mass can occur by three main mechanisms:

- Abrasion
- Fracture of intact rock
- Removal of individual rock blocks

Abrasion refers to the gradual grinding away or wearing of a rock surface due to repeated impacts from particles (e.g., sand, cobbles, etc.) carried by flowing water. The incision rate is dependent on the size distribution of saltating particles and is sensitive to the sediment transport capacity of the flow in the sense that an upper limit to the rate exists due to reduced impact frequency associated with coverage of the bed with sediment (Sklar & Dietrich 2004). Typically, the timescale for significant scour to occur by abrasion is generally very long (i.e., on a

geomorphological timescale) and, therefore, abrasion is more notably considered in landscape evolution modeling. For engineering structures, such as dams, spillways and tunnels, while flows generally contain significantly more energy (with higher sediment transport capacity) they are often sediment starved (containing few to no particles to impact the rock mass, thus limiting the abrasion rate). This is particularly the case for dam overtopping and spillway discharges where the reservoir causes deposition of incoming coarse sediment and spills are generally “clear” or have a very fine suspended fraction. Accordingly, abrasion is typically not the dominant mechanism for flows at engineering structures.

Fracture of intact rock refers to the propagation (growth) of close-ended fissures when subject to hydraulic loads (Figure 2-1). The fissure opening allows transmission of hydrodynamic pressures to the fissure tip. This mechanism has been shown to be prominent for high energy flows at certain depths in plunge pools where conditions are such that resonance can lead to amplification of pressure within the fissure. This can result in propagation of existing fissures causing break-up of the rock mass (Bollaert 2002). Depending on the magnitude of the applied pressure, rock may fail nearly instantaneously by brittle fracture or over time by fatigue.

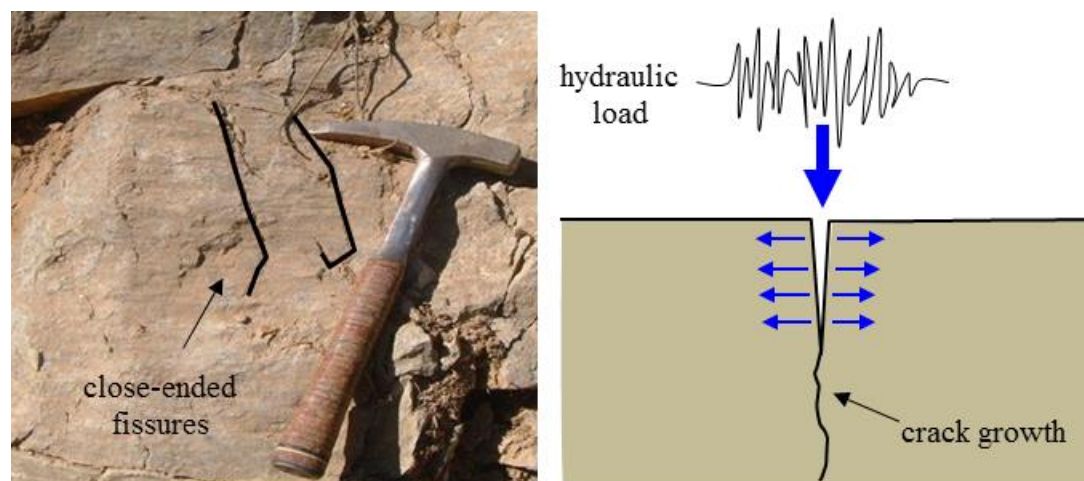


Figure 2-1. Close-ended fissures in rock mass (left) and schematic for fracture of intact rock due to transmission of hydraulic pressures into fissure (right).

Block removal is the most predominant physical mechanism for rock scour and refers to the “plucking” or “quarrying” of rock blocks from the surrounding rock mass due to forces induced by flowing water and gravity (Figure 2-2). Discontinuities bounding the blocks (such as joint planes, foliation, faults, contacts between geologic units or those created through brittle fracture / fatigue) allow for transmission of hydrodynamic pressures to the underside of the block resulting in removal.

The removal of individual blocks from a rock mass is highly dependent on the 3D orientation of the discontinuities bounding the block, and subsequently, a number of kinematic failure modes exist (Figure 2-3). These include: 1) pure translational modes, such as lifting and sliding (1-plane or 2-plane), 2) pure rotational modes, such as rotation about an edge or a corner, or 3) some combination of translation and rotation, such as slumping or torsional sliding. For pure translational modes, the resultant vector of all the forces applied to the rock block passes through the block centroid causing a zero moment about the centroid. For pure rotational modes, the

resultant vector only acts along the axis of rotation. Finally, flutter (not shown) may also occur when a block is subjected to a dynamic load such that small plastic displacements are realized over time and the block “walks” or “flutters” out of its mold. A block mold refers to the space in the rock mass from which a block was removed.

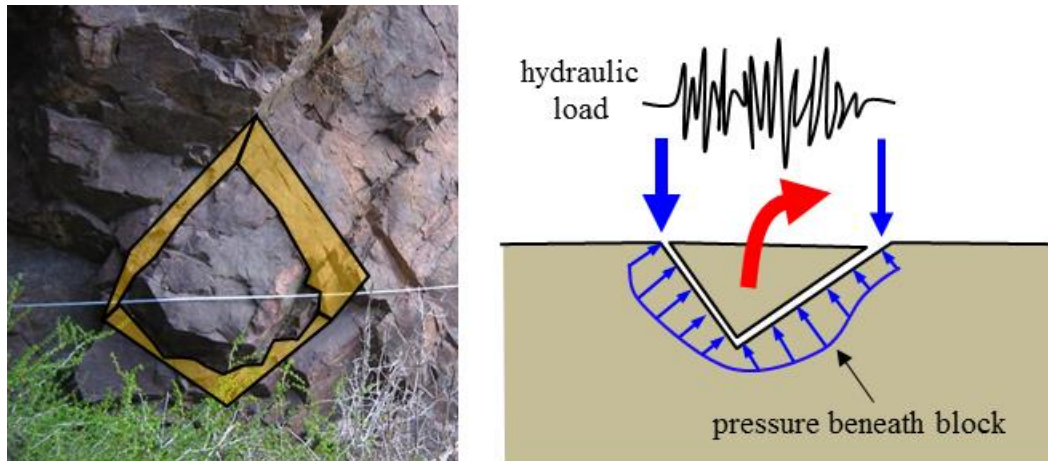


Figure 2-2. Rock block as defined by surrounding discontinuities (left) and schematic for block removal due to transmission of hydraulic pressures beneath block (right).

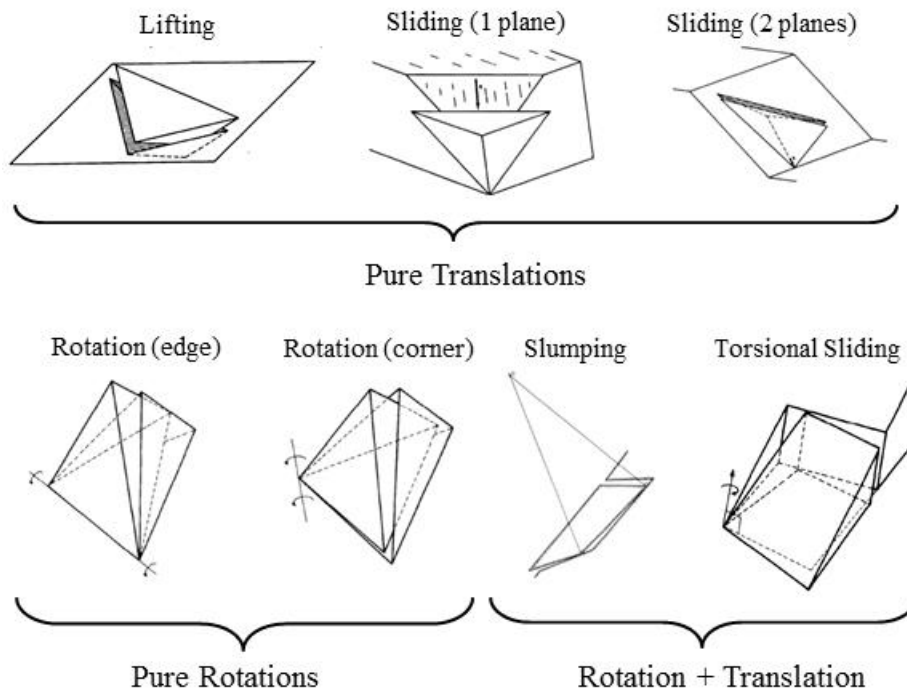


Figure 2-3. Kinematic block failure modes (Goodman 1995).

For the above failure modes, blocks are assumed to be rigid. Block compressibility can be important for situations of combined rotation and translation where a significant moment about the block centroid exists (Tonon 2007, Asadollahi 2009).

Documentation of the dominant 3D block failure modes in actual scour applications is absent from literature, however, given the variety of flow conditions typically encountered in unlined channels, on dam abutments or in plunge pools, the potential for block removal in any of the above manners is likely high. Subsequently, methodologies for analyzing scour of rock blocks should consider these failure modes.

2.2 Engineering scour models

The engineering approach for scour modeling is typically performed for localized flow conditions at the structure of interest (e.g., plunge pools, bridge piers, etc.). One of the most prominent methodologies for predicting rock scour is the Erodibility Index Method (EIM) (Annandale 1995, 2006). The EIM is a semi-empirical, geo-mechanical index that can be used to calculate the erosion resistance of any earth material. The Erodibility Index, K (dimensionless), for rock is defined by:

$$K = M_s \cdot K_b \cdot K_d \cdot J_s \quad (2-1)$$

where M_s = mass strength number (based on rock unconfined compressive strength (UCS)), K_b = block size number (based on rock quality designation (RQD) and number of discontinuity sets), K_d = discontinuity shear strength number (based on joint roughness and alteration), and J_s = relative ground structure number (based on dip direction and dip angle of discontinuities relative the flow direction).

Rock erodibility is based on a rippability index developed by Kirsten (1982, 1988) to evaluate the machine power required to excavate various earth materials. The index was modified from Barton's Q-system used to classify rock masses for tunnel support (Barton et al. 1974, Barton 1988).

To determine scour potential, rock erodibility is compared to the erosive capacity of water quantified using unit stream power, P_{sp} (expressed in W/m^2). In general form, this may be expressed as:

$$P_{sp} = \frac{\gamma_w \cdot Q \cdot \Delta E}{A} \quad (2-2)$$

where γ_w = unit weight of water (N/m^3), Q = the flow rate (m^3/s), A = flow area (m^2), and ΔE = energy dissipated over the flow area, expressed in terms of hydraulic head (m).

Annandale (1995, 2006) provides modifications of the above equation to determine the erosive capacity for a variety of flow conditions including open channels, knick-points, hydraulic jumps, head-cuts and plunge pools. Based on 137 case studies and near-prototype hydraulic testing, Annandale developed a threshold relationship between flow erosive capacity and earth material erodibility (Figure 2-4). When the unit stream power of the water and the rock erodibility index plot above the threshold line, scour is likely to occur.

The simplicity and wide applicability to various flow conditions makes the EIM particularly attractive for use in practice. The method, however, is not without limitation. As its name implies, the method incorporates an empirical index to characterize the rock. Subsequently, the EIM does not delineate between different scour mechanisms (i.e., brittle fracture, fatigue failure, or block removal). This results in a more generalized assessment of scour. Although weaker

rock units or weathered zones can be identified and their erosion resistance quantified, the identification of individual key rock blocks is not possible. Also rock geometry is simplified into 2D and although some account for the discontinuity structure with respect to the flow direction is given, the complete 3D nature of the joint orientations is not addressed

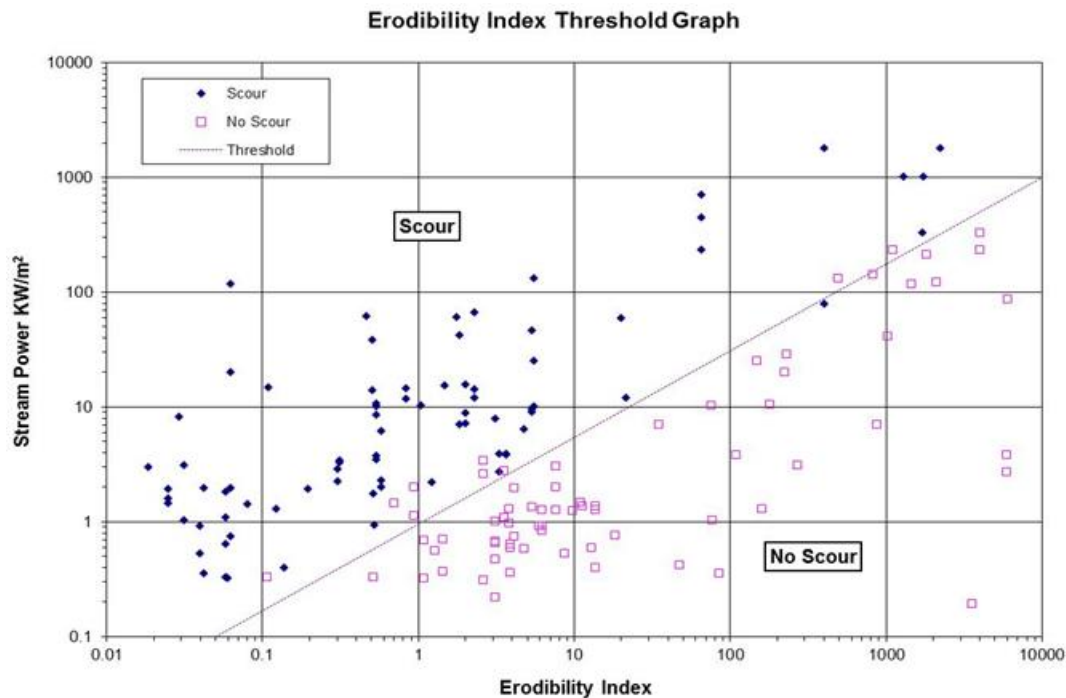


Figure 2-4. Annandale Erodibility Index graph.

The other prominent engineering model for rock scour prediction is the Comprehensive Scour Model (CSM) by Bollaert (2002). Based on several near-prototype scale laboratory tests Bollaert examined the behavior of turbulent hydrodynamic pressures on plunge pool floors and in simplified rock joint geometries subject to an impinging water jet. The CSM is significant in that it attempts to represent the physics of the scour process and analyze the various scour mechanisms (brittle fracture, fatigue failure and block removal). The key components of Bollaert's CSM are outlined in Figure 2-5.

Using fracture mechanics theory from Atkinson (1987) and testing results from Paris et al. (1961) on metals, Bollaert developed relationships to evaluate the potential for intact rock to fail by brittle fracture or fatigue, respectively. He also examined the potential for lifting of individual block when subjected to dynamic pressure impulses from a jet impinging into a plunge pool. He found that transient pressures can develop beneath individual blocks via open joints surrounding the block, resulting in uplift (dynamic impulsion).

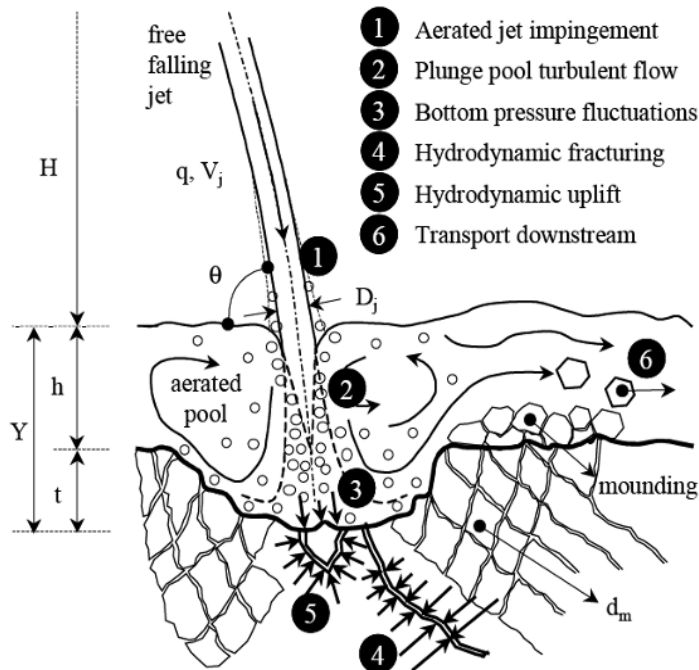


Figure 2-5. Key components of the CSM (Bollaert 2002).

Block geometry, however, is simplified to rectangular blocks and no account is made for other joint orientations (Figure 2-6), such that lifting is the only mode of failure considered. Based on case study data, Bollaert & Schleiss (2005) calculated the block may be considered removed from the matrix when the uplift caused by a single pressure pulse (Δz) is greater than about 20% of the vertical block dimension (z_b) (i.e., $\Delta z/z_b > 0.20$).

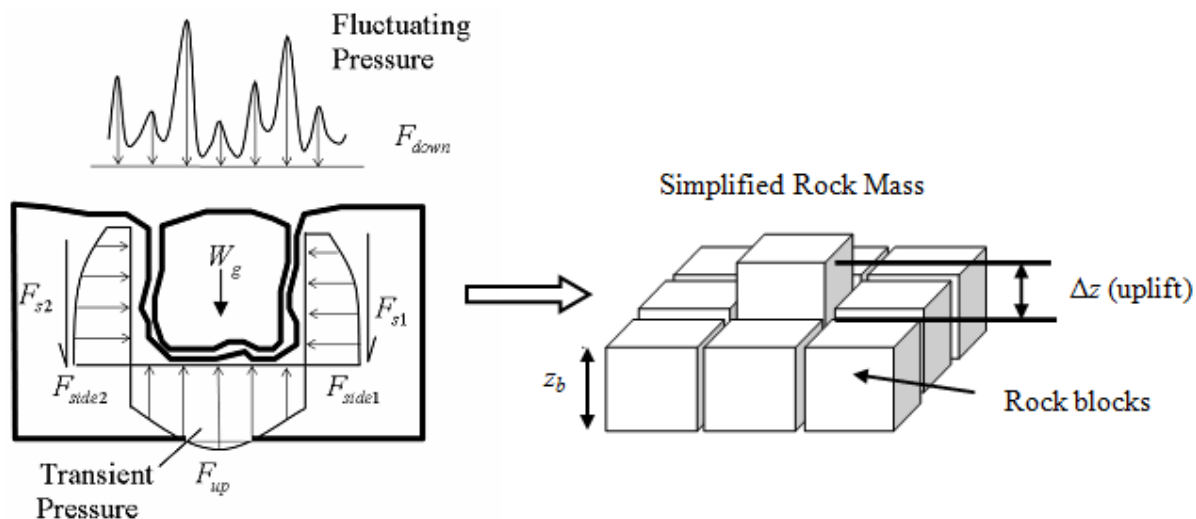


Figure 2-6. Bollaert block removal model.

Hydrodynamic pressures within the plunge pool are highly dependent on a number of factors including jet air entrainment, jet thickness, plunge pool depth, plunge pool geometry and air concentration in rock fissures and has been studied by many researchers, e.g. Ervine & Falvey

(1987), Ervine et al. (1997), Castillo et al. (2007), Bollaert (2002), Manso (2006). The resulting dynamic pressure associated with the impinging jet can be quantified using the general equation below (from Bollaert 2002):

$$P = \gamma_w \cdot (C_p + \Gamma \cdot C'_p) \cdot \varphi \cdot \frac{v_j^2}{2 \cdot g} \quad (2-3)$$

where C_p = average dynamic pressure coefficient (dimensionless), C'_p = fluctuating dynamic pressure coefficient (dimensionless), Γ = amplification factor to account for resonance in close-ended rock fissures (dimensionless), φ = energy coefficient (usually assumed = 1) (dimensionless), v_j = impact velocity of the jet, and g = acceleration of gravity.

Evaluating the potential for intact rock fracture and block removal as a function of plunge pool depth provides the maximum scour depth achievable under a certain set of flow conditions as well as gives insight into the dominant scour mechanism occurring at various elevations in the plunge pool.

Federspiel et al. (2009) have extended the work of Bollaert to analyze the response of 3D cubic block due to vertical water jet impact in a plunge pool (previous measurements by Bollaert were for 2D block geometry). Analysis of power spectral density curves for a vertical jet impacting the top center of a block indicated block response (displacement) was primarily influenced by pressure fluctuations with low frequencies below approximately 10 Hz. These frequencies correspond to larger-scale structures (eddies) within the plunge pool. More recent analysis for vertical jets impacting the top edge of a block has shown two additional peaks in the power spectral density curves at frequencies between approximately 20 Hz to 100 Hz and 100 Hz to 300 Hz, which the researchers suggest is likely related to the fundamental resonant frequency of the pressure waves around the rock block Federspiel et al. (2011). Further work by Duarte (2014), using the same experimental set-up as Federspiel et al. (2009,2011), confirmed similar peaks in pressure signals associated with resonance (Figure 2-7a,b). Block response to resonance was more pronounced for scenarios when the block position was fixed in the mold. In these scenarios a peak in the power spectral density curves for block displacement corresponding to the peak in pressure is witnessed (Figure 2-7a,c). For scenarios when the block was free (i.e., detached from the mold), similar peaks in displacement are not evident although the authors mention a small response is observed (Figure 2-7b,d). In both scenarios (fixed and free) high frequency vibrations (400 Hz to 500 Hz) are noted resulting from small rotations of the block within its mold. In all scenarios, from both of Federspiel et al. (2009, 2011) and Duarte (2014), the amount of observe uplift of the block appears to be relatively small (approximately 1% of the vertical block dimension) and potentially shows the limitation of using a cubic block geometry where lifting is the only block failure mechanism.

Asadollahi (2009) used a modified version of the numerical Block Stability in 3D (BS3D) code (developed by Tonon (2007)) to determine the dynamic uplift of the cubic block tested by Federspiel et al. (2009, 2011). BS3D considers all general failure modes of rock blocks subject to generic forces. Using BS3D, Asadollahi found reasonable agreement between modeled and observed uplift when using actual pressure measurements around the block as input model parameters. Additionally, using data from Martins (1973) of physical model tests on cubic blocks in a riverbed and two case studies at the Picote Dam in Portugal and the Kondopoga Dam in Russia, Asadollahi used BS3D to slightly refine Bollaert's criteria, indicating a value of $\Delta z/z_b > 0.25$ might be more representative of block removal.

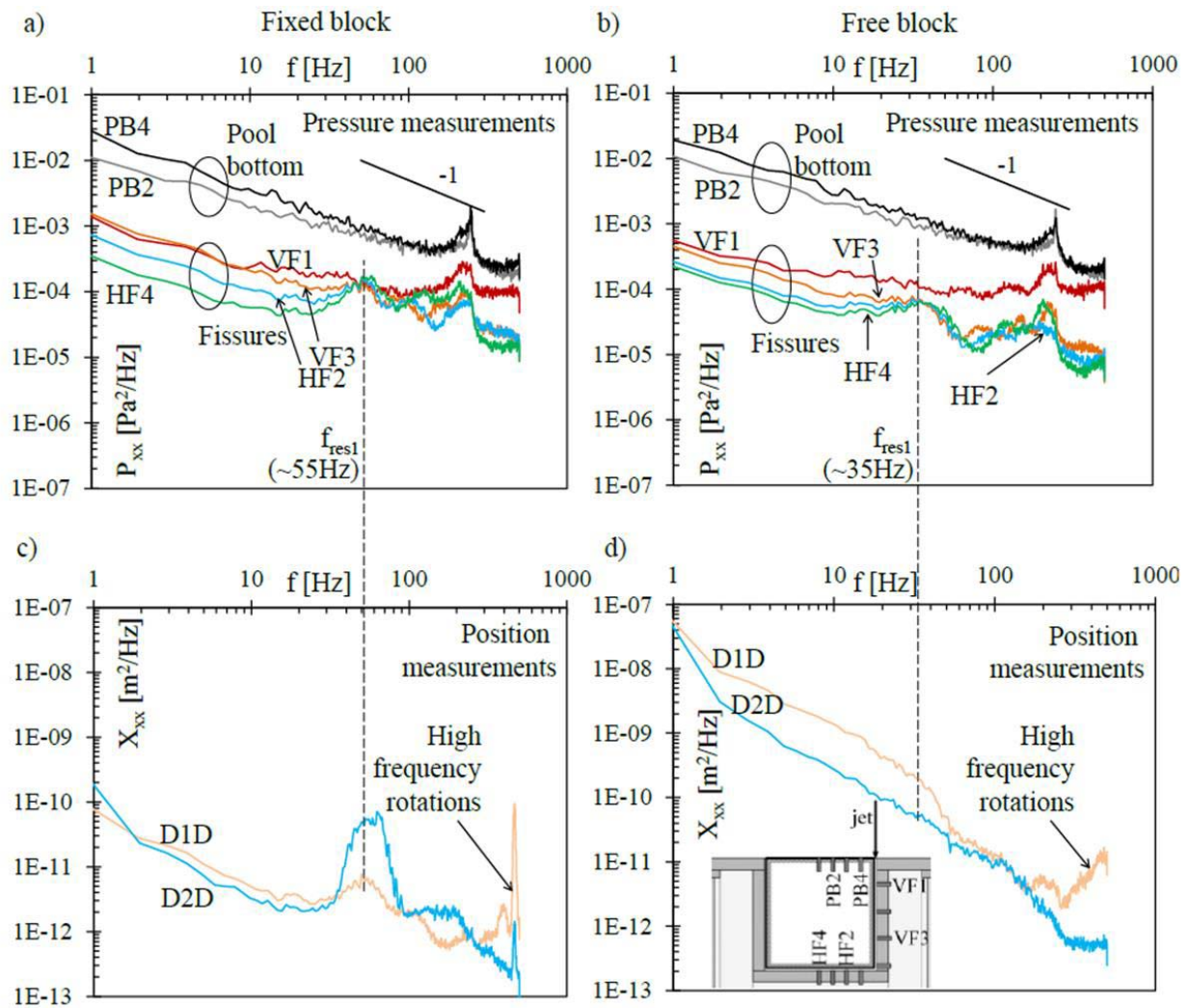


Figure 2-7. Power spectral density vs. frequency curves for vertical jet impact onto top of block edge for a) pressure signal, fixed block, b) pressure signal, free block, c) displacement signal, fixed block, and d) displacement signal, free block (Duarte 2014).

George & Annandale (2006) modified Bollaert's CSM to evaluate the stability of abutment rock blocks subject to hydrodynamic forces from overtopping jet impact (Figure 2-8). Joint structure in 2D was analyzed and a relationship for the required rock bolt force to prevent dynamic impulsion was developed.

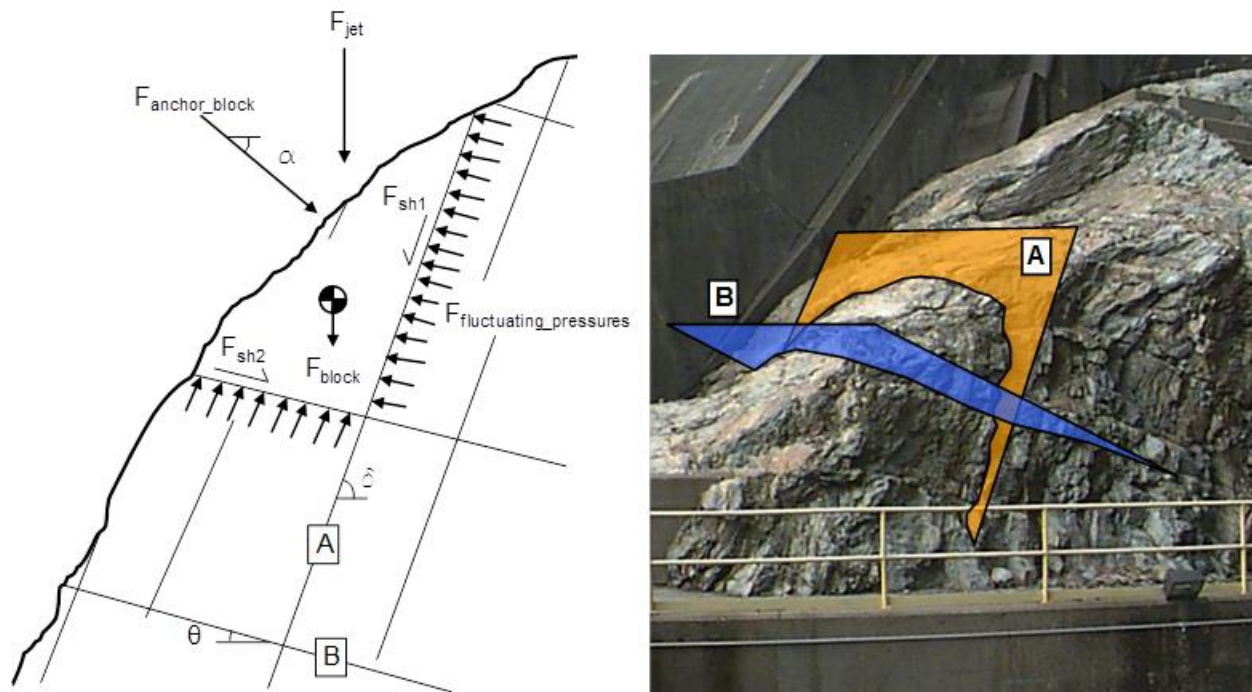


Figure 2-8. Analysis of abutment block due to overtopping jet impact (George & Annandale 2006).

Goodman & Hatzor (1991), in what may be the first 3D block scour analysis, performed an extensive examination of abutment stability using block theory for the Kendrick Dam Project in Wyoming. Large key blocks were identified based on joint orientations and a 3D block stability analysis was conducted. Only the static water pressure on the joint planes was considered for the overtopping jet and the role of the hydrodynamic pressures was unexamined. Similar analyses were presented by Goodman & Powell (2003) for other dam sites.

Reinius (1986) evaluated the removability of rectangular rock blocks subject to horizontal channel flows. He related the initial amount of protrusion of the block above the channel bottom to a critical flow velocity resulting in ejection. Frizell (2007) performed a similar study looking at the hydraulic jacking of concrete slabs in lined spillway channels. They related the average stagnation pressure that develops underneath a slab (a function of the flow velocity) to the shape, offset and discontinuity aperture (gap) between two adjacent slabs (Figure 2-9).

Independently, Bollaert (2010) extending the work of Reinius, and George et al. (2010) using the work of Frizell, incorporated the influence of turbulent pressure fluctuations on the hydraulic jacking of rectangular blocks in channel bottoms. Based on research by Emmerling (1973) and Hinze (1975), summarized Annandale (2006), the magnitude of the pressure fluctuations, P' , were quantified using:

$$P' = (3 \text{ to } 18) \cdot \tau \quad (2-4)$$

where τ is the turbulent boundary layer shear stress.

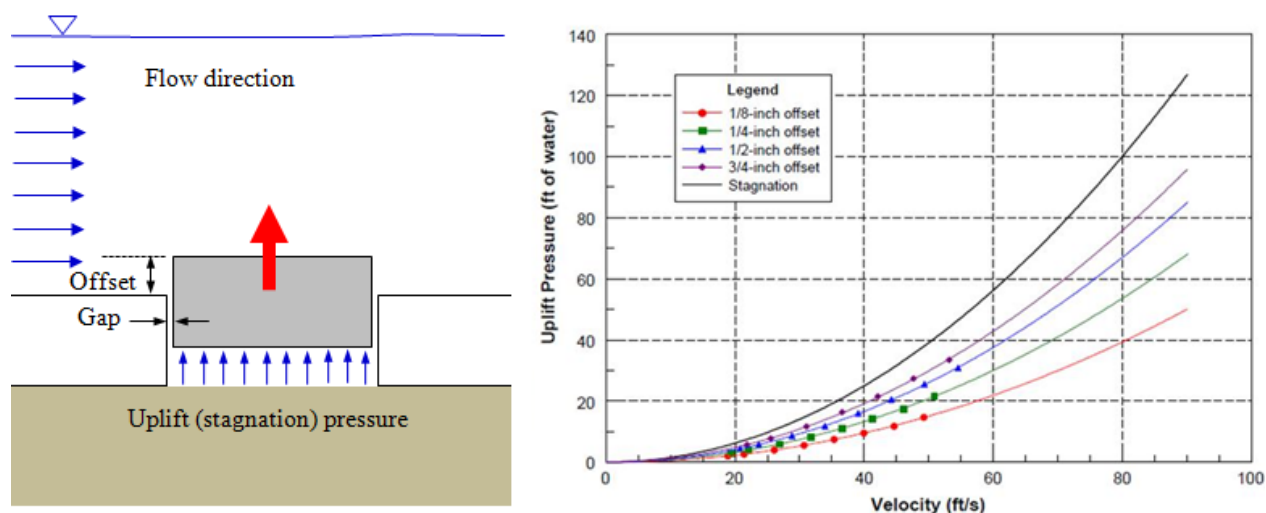


Figure 2-9. Hydraulic jacking of concrete spillway slabs (Frizell 2007).

Accordingly, the total lift applied to a protruding block is a function of the block buoyancy, quasi-steady (or pseudo-static) uplift resulting from build-up of stagnation pressure beneath the block, and the turbulent uplift resulting from pressure fluctuations (Figure 2-10) (Bollaert 2010). As implied, buoyancy and stagnation pressure are considered in a static manner, while the pressure fluctuations are analyzed in a dynamic sense. For a protruding block, and depending on the flow conditions, stagnation pressure or turbulent pressure fluctuations may be more dominant in causing uplift. However, for smaller block protrusions the stagnation pressure diminishes such that a block that is flush with the ground surface may only be removed by turbulent pressure fluctuations.

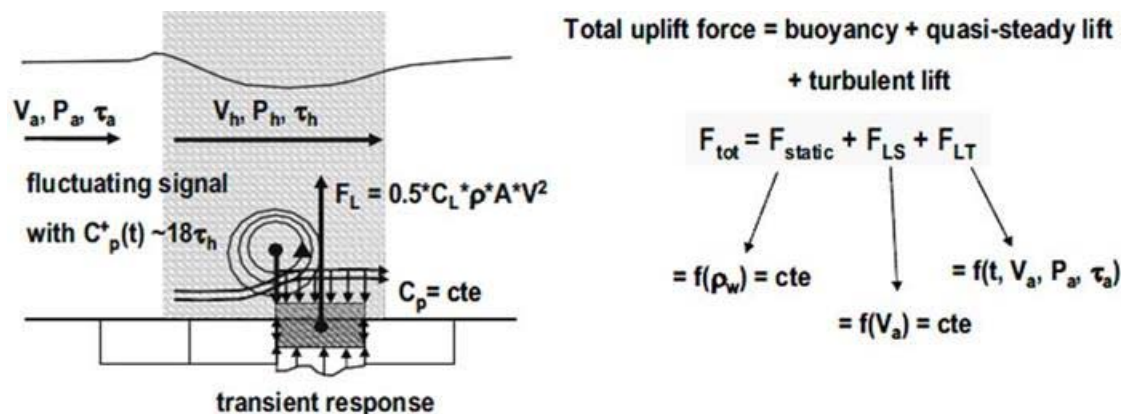


Figure 2-10. Block uplift at bridge pier (Bollaert 2010).

When considering turbulent uplift, Bollaert concluded that the critical flow velocity causing removal can be significantly decreased. For the flow scenarios analyzed by George, however, the influence of pressure fluctuations on uplift was found to be negligible. This suggests that some scenarios may be adequately analyzed in a pseudo-static manner, while for others a more dynamic representation is needed.

The majority of the above methods examine a single representative block subject to a characteristic hydraulic load dependent on the flow conditions and geometry. In the case of

plunge pools, for example, if the representative block is removable at a certain elevation in the pool, scour will occur. The block is then analyzed again in a similar fashion at lower and lower elevations in the pool (corresponding to different hydraulic conditions) until the block is stable at which point scour is thought to cease. A few researchers, however, have begun analyzing multi-block systems through numerical analysis.

Multi-block analyses are significant in that the spatial estimates of scour may be obtained (opposed to simply determining scour initiation or maximum scour depth). Additionally, multiple block shapes and geometries may be considered. Lin & Wibowo (2008) applied key block theory from Goodman & Shi (1985) to find removable blocks exposed by an excavation for unlined rock spillways (Figure 2-11). Stability analyses were conducted for key blocks under flow conditions, however, it appears only 2D blocks were considered.

A similar attempt by Li & Liu (2010) was made, but for impinging jets into plunge pools. Removable 2D blocks were identified based on joint structure and corresponding plunge pool geometry was determined. Block stability was determined using empirical relationships for pressure distribution within the rock mass. Their simulated results yielded reasonable agreement with observed scour at the Xi Luo Du hydro-electric power plant in China.

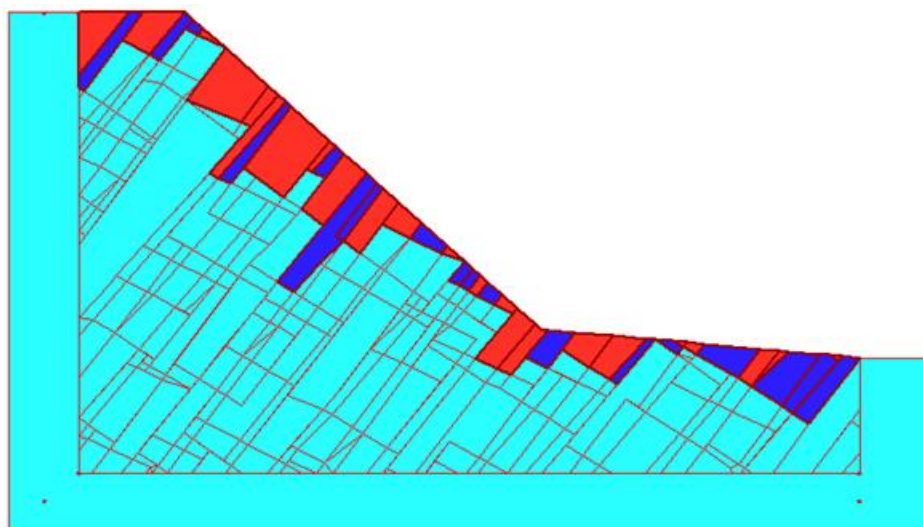


Figure 2-11. 2D removable blocks in unlined spillway (Lin & Wibowo 2008).

More recently, Dasgupta et al. (2011) performed numerical simulations to estimate plunge pool scour formation at Kariba Dam in Zimbabwe. They used 3D computational fluid dynamics software (ANSYS FLUENT) to determine erosive capacities along with the 2D universal distinct element code (UDEC) to model the rock mass. Dynamic pressures at the bottom of the plunge pool were determined over a time interval and then input into UDEC to evaluate block removal and brittle fracture independently. Results from the block analysis and fracture analysis were superimposed to get an idea of the final scour hole shape, which showed reasonable agreement with that observed at Kariba Dam (Figure 2-12).

Interestingly, they found that blocks first to fail were just outside of the impingement region, which shows the importance of analyzing multiple block systems instead of a single representative block. Although the rock mass was modeled in 2D, their approach gives promise

to the use of numerical methods to incorporate the 3D geometry of a rock mass along with complex flow conditions.

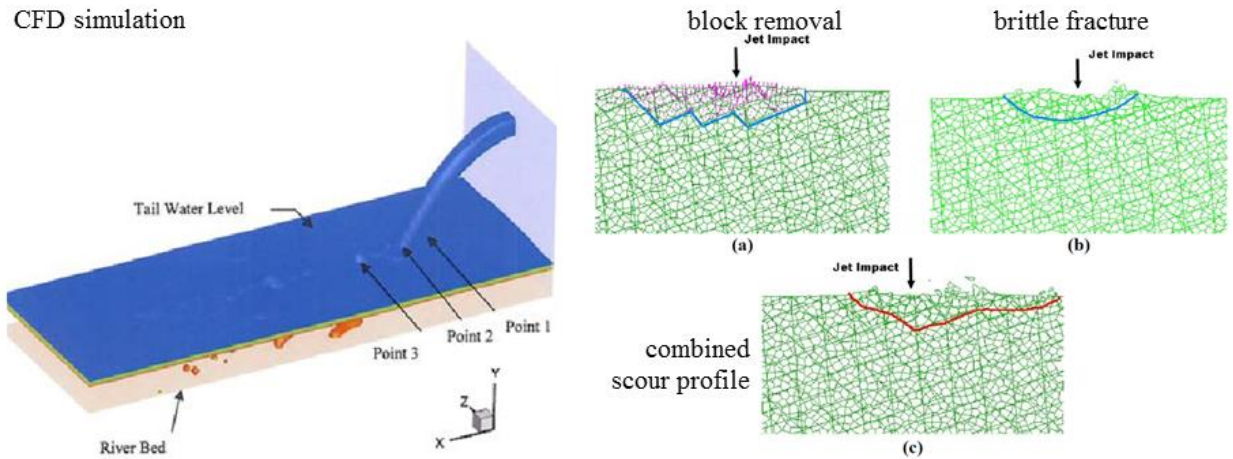


Figure 2-12. Numerical simulation of plunge pool scour (Dasgupta et al. 2011).

2.3 Landscape evolution models

Geomorphologists approach the rock scour problem from a landscape evolution perspective, since stream erosion and the upstream migration of knick points in bedrock channels are key mechanisms of landscape evolution in mountainous terrain, and there has been extensive amount of research and publication in this area. Excellent reviews of the full range of processes under consideration can be found in Hancock et al. (1998), Whipple et al. (2000), and Lamb et al. (2015) for example. While some of the models treat bedrock as a homogenous mass, void of any discontinuities (e.g., Howard et al. (1994), Lague (2014)) and apply a power function with empirically derived parameters, such as drainage area and channel gradient, to evaluate the erosion rate by scour, bedrock plucking has been well recognized as an important aspect of the process (Miller 1991, Hancock et al. 1998, Whipple et al. 2000).

Dubinski (2009) conducted detailed physical hydraulic model experiments using cubic blocks to evaluate the mechanics of knick-point migration in bedrock channels (Figure 2-13). He found that, typically, blocks were eroded a few at a time or in larger masses. In the latter case, the mass movements were often preceded by erosion of single blocks, which he termed key blocks similar to Goodman & Shi (1985), as their removal made it possible for others to be readily removed.

Chatanantavet & Parker (2009) developed a physically based model that considers both abrasion and plucking of rectangular rock blocks. They applied it with success to measured erosion rate along a channel reach that has been subjected to long term monitoring (Chatanantavet & Parker 2011).

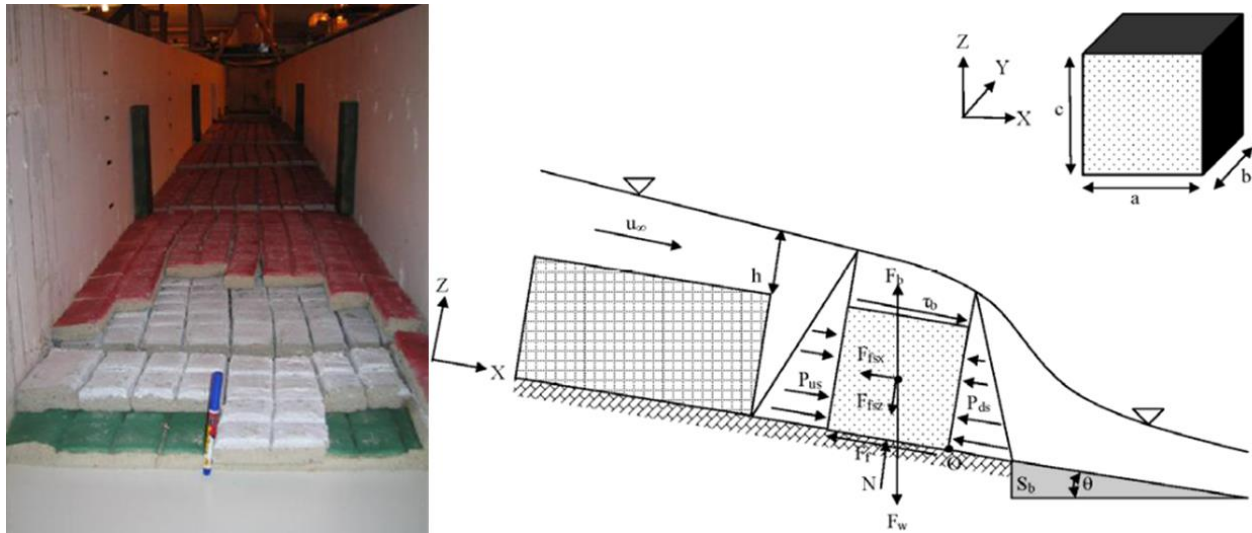


Figure 2-13. Simulated jointed bedrock in the flume (left) and idealized schematic for block stability at a knick-point (right) (Dubinski 2009).

Lamb & Dietrich (2009) also conducted physical hydraulic model experiments on elongated rectangular blocks to simulate waterfall action over columnar basalt bedrock. For their particular rock mass geometry, they found failure by block toppling could explain knick-point migration in the absence of undercutting (i.e., erosion of softer underlying layers, resulting in failure of the harder overlying rock), which is most commonly associated with the phenomenon. They pointed out the significance of bedrock fracture geometry in determining knick-point morphology and retreat rate.

More recent work by Lamb et al. (2015) as well as work by Coleman et al. (2003) and Melville et al. (2006) casts incipient block motion within a critical Shields stress framework (Shields 1936) for idealized rectangular block geometries subject to vertical entrainment (lifting), sliding, and toppling (rotation) (Figure 2-14). The Shields parameter, τ_{pc}^* , is likely the most widely used indicator for threshold motion (transport) of cohesionless sediment and is relatively constant for high Reynolds number flows ($\tau_{pc}^* \sim 0.045$). Theoretical values from Lamb et al. (2015) show good agreement with those determined experimentally by others for the case of vertical block entrainment (Coleman et al. 2003) and sliding (Carling et al. 2002, Dubinski & Wohl 2013). Results indicate a strong dependence of block incipient motion on the relative protrusion height (P) of the block with respect to the horizontal block dimension (L). When the ratio of $P/L < \sim 0.5$, block removal becomes exponentially more difficult for rough channel beds. For smooth channel beds, this ratio is much lower as channel velocities are higher closer to the bed. There is no influence of the vertical block dimension (H) when compared to L except for the case of toppling. Intuitively, as the ratio H/L increases, toppling becomes the most dominant failure mode. Finally, the effect of block wall stresses, τ_w^* , are negligible when block sides are relatively smooth, such as is the case for most idealized laboratory experiments. This was noted by both Dubinski (2009) and Coleman et al. (2003). As wall stresses increase (associated with greater block wall roughness, more typical of field/prototype settings) the critical block threshold also increases.

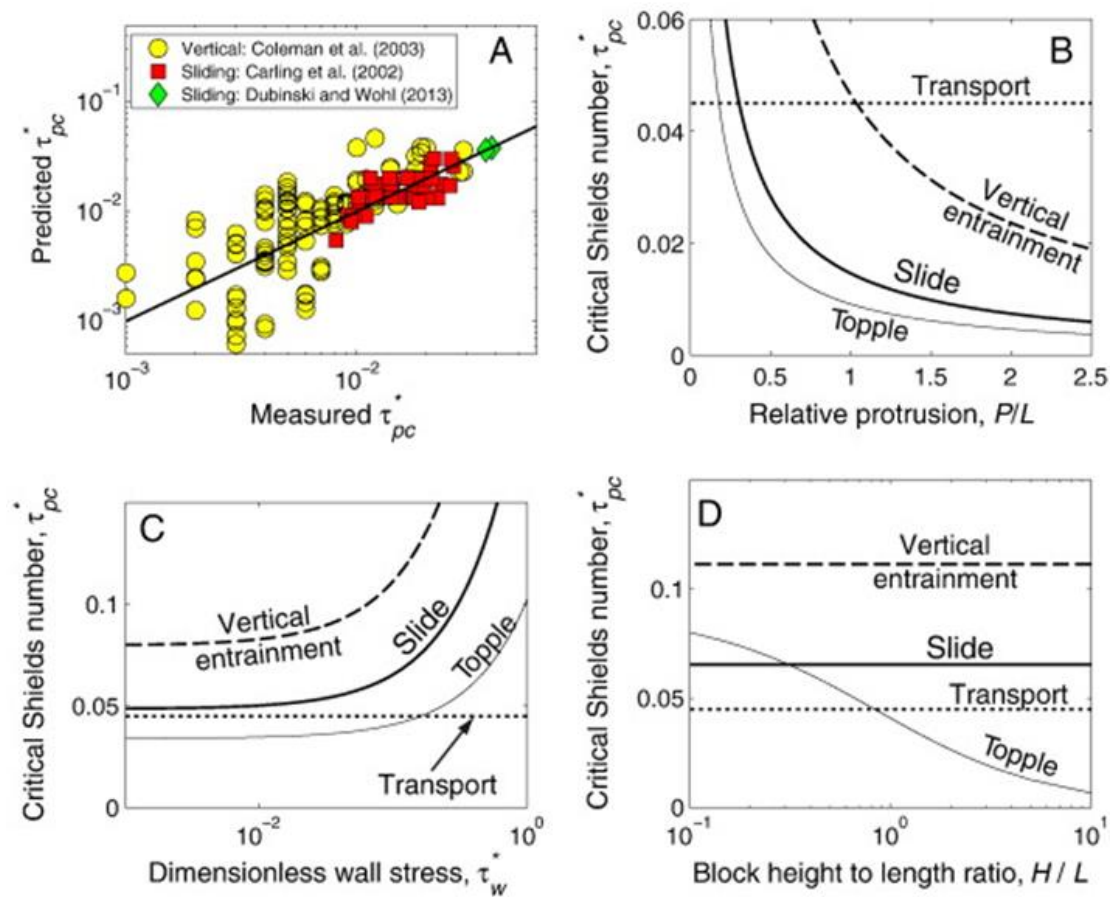


Figure 2-14. Theoretical critical Shields parameter, τ_{pc}^* , versus A) experimental, B) relative block protrusion ratio (P/L), C) dimensionless wall stress, and D) block height to length ratio (H/L) (Lamb et al. 2015).

2.4 Limitations of current scour technology

Some models, such as Annandale (1995, 2006), Howard et al. (1994) or Lague (2014), are limited due to their inability to represent the physics of the scour process in that the mechanisms causing scour (abrasion, block removal, fracture of intact rock) are not modeled. Additionally, limited or no insight is gained regarding the dominant mechanisms for a particular location/system. This can be an artifact of the intended application for which a specific model was developed. For landscape evolution purposes, the area of interest is often very large and that specific level of detail may not be required or desired. From an engineering standpoint, often concerned with more localized scour behavior, not knowing the driving mechanism can be particularly problematic when trying to determine what type of remedial measure may best suited for a specific application (e.g., rock bolting, concrete lining, etc.).

Block models that incorporate simplified 2D rectangular or cubic block geometries are limited when orientations of the discontinuities are not orthogonal, such is commonly the case in actual rock masses, as block kinematics are not properly addressed. For these idealized blocks with one free face (e.g., Figure 2-6 or Figure 2-10), the kinematic failure mode is limited to 1D uplift (e.g.,

Bollaert (2002, 2010), Coleman et al. (2003), Frizell (2007), Federspiel et al. (2009, 2011), Duarte (2014)). In instances where the actual geologic structure is more complex, restricting evaluation to block uplift in a simplified geometry could *over*-predict the block erodibility threshold as more applied force is generally required to lift the block upwards under the entirety of its weight than, for example, to slide it upwards at an angle (should sliding be a potential failure mode). This would result in rock mass erosion at lower than anticipated erosive capacities.

For 2D rectangular or cubic blocks with an additional free face on the downstream side, such as at knickpoints (Figure 2-13), two additional failure modes are applicable: 1D sliding in the downstream direction and rotation about the downstream block edge (e.g., Chatanantavet & Parker (2009, 2011), Dubinski (2009), Lamb & Dietrich (2009), Lamb et al. (2015)). While these models highlight the variability of block erodibility threshold for blocks multiple potential kinematic failure modes, their extension to fully 3D block systems is significantly limited.

Similarly, 2D blocks that are not rectangular (such as those witnessed in the multi-block simulations above, e.g., Lin & Wibowo (2008), Li & Liu (2010), Dasgupta et al. (2011)) are still restricted in their ability to represent a rock mass and a process that is inherently 3D.

The stark influence of kinematic constraints on block stability that arise from 3D block geometry is undeniable. Block geometry is governed by geologic structure within the rock mass, which is inherently site-specific. The limitations of the above scour models ultimately take away from the site-specific nature of the analysis being performed and accordingly may yield unreliable results. An ideal local scour model would represent an entire 3D rock mass comprised of multiple blocks while also evaluating 3D flow conditions that responded to changes in geometry due to scour progression over time. At this time, the effort required to develop such a model in any meaningful manner is great and demands complex numerical codes. As such, the focus of this research is to develop a framework to incorporate the 3D geologic structure of a site to analyze scour potential of single 3D rock blocks. This is done with the intention to gain improved understanding of the block removal process that may be applied later to more complex 3D multi-block systems.

Chapter 3. Field investigations

A robust field effort was desired for this research to develop new data and understanding of the scouring process, which has predominantly been derived from laboratory studies. Accordingly, field efforts were carried out to obtain measurements for hydrodynamic pressures and block displacements in a prototype setting in an unlined spillway at dam site in northern California as well as high resolution rock mass data using light detection and ranging (LiDAR) scanning. Statistical characterization of natural variability of rock mass parameters from LiDAR data is presented herein for use in the probabilistic scour model presented in Chapter 6.

3.1 Overview

The main objectives for field investigations were to 1) obtain measurements for hydrodynamic pressures and block displacements in a prototype setting, and 2) perform high resolution characterization of site-specific rock mass parameters. Historically, scour investigations have been confined to laboratory settings under idealized conditions due, in part, to the uncertainty associated in working with natural systems. This is related to the ability to locate readily accessible sites where scour is actively occurring, the unpredictability of occurrence of natural discharges, as well as the difficulty to install, power and maintain sensors to withstand a range of environmental conditions. As such, detailed field data, particularly related to hydrodynamic pressures within rock joints during flood events, does not exist. Accordingly, there is significant benefit to capture data of this nature to supplement experimental laboratory work and was a high priority for this research effort.

3.1.1 Field Site

Location

Field investigations were carried out at the Spaulding Dam site, which is owned and operated by Pacific Gas & Electric (PG&E). The site contains an actively eroding rock spillway where discharges are made on a relatively consistent basis. Spaulding Dam is located in the Sierra Mountains in northern California just north of Interstate 80 (Figure 3-1). The main dam (Spaulding Dam No. 1) is a concrete arch dam constructed in 1913 and was raised to the current crest height of approximately 84 m in the 1920's. The dam is situated on the South Fork of the Yuba River and serves several important purposes including water supply, power generation, flood control and recreational boating/camping. The dam has a main spillway (Spaulding Dam No. 2) and an auxiliary spillway (Spaulding Dam No. 3) to handle flows from the reservoir during flood events and discharges into Jordan Creek, a tributary to the South Fork of the Yuba River (Figure 3-2).

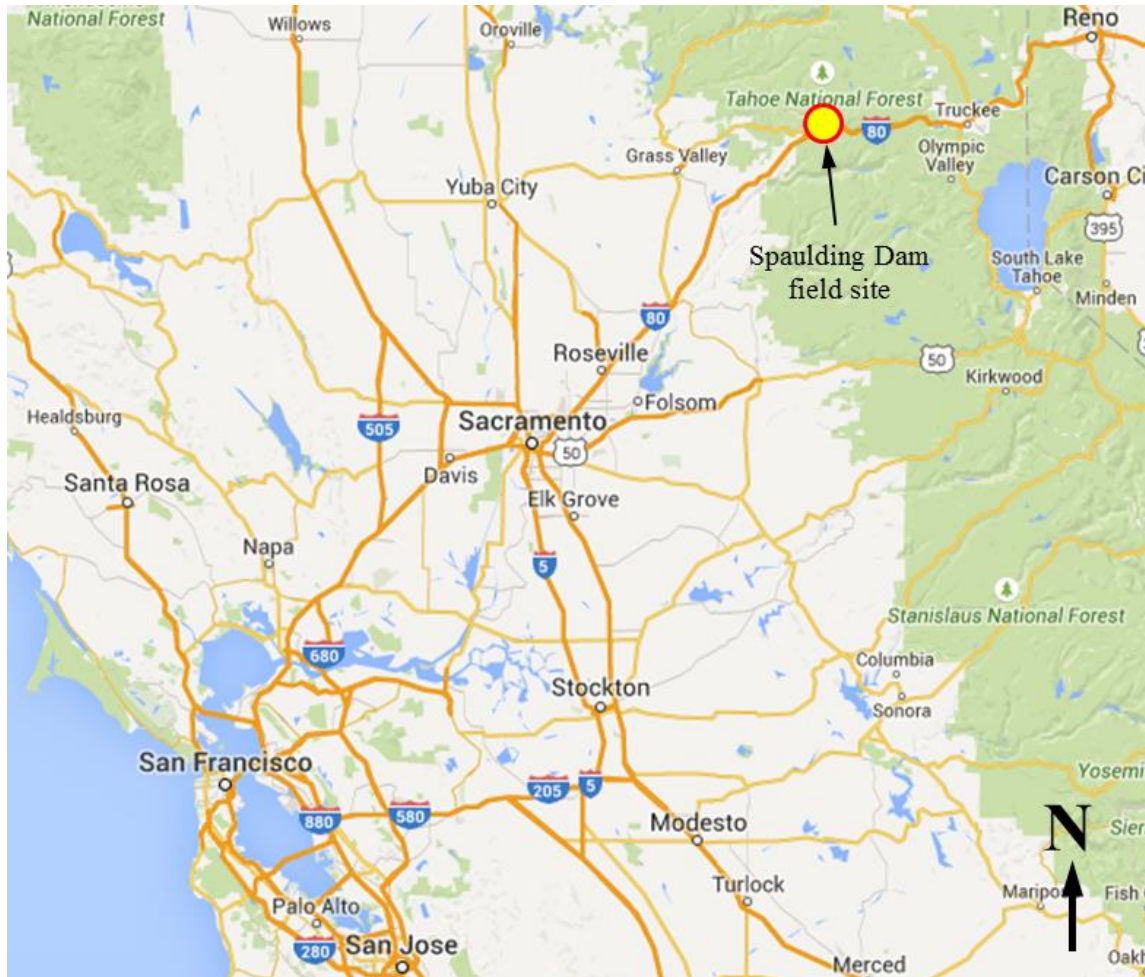


Figure 3-1. Regional map showing field site location (accessed from Google Maps, 2015).

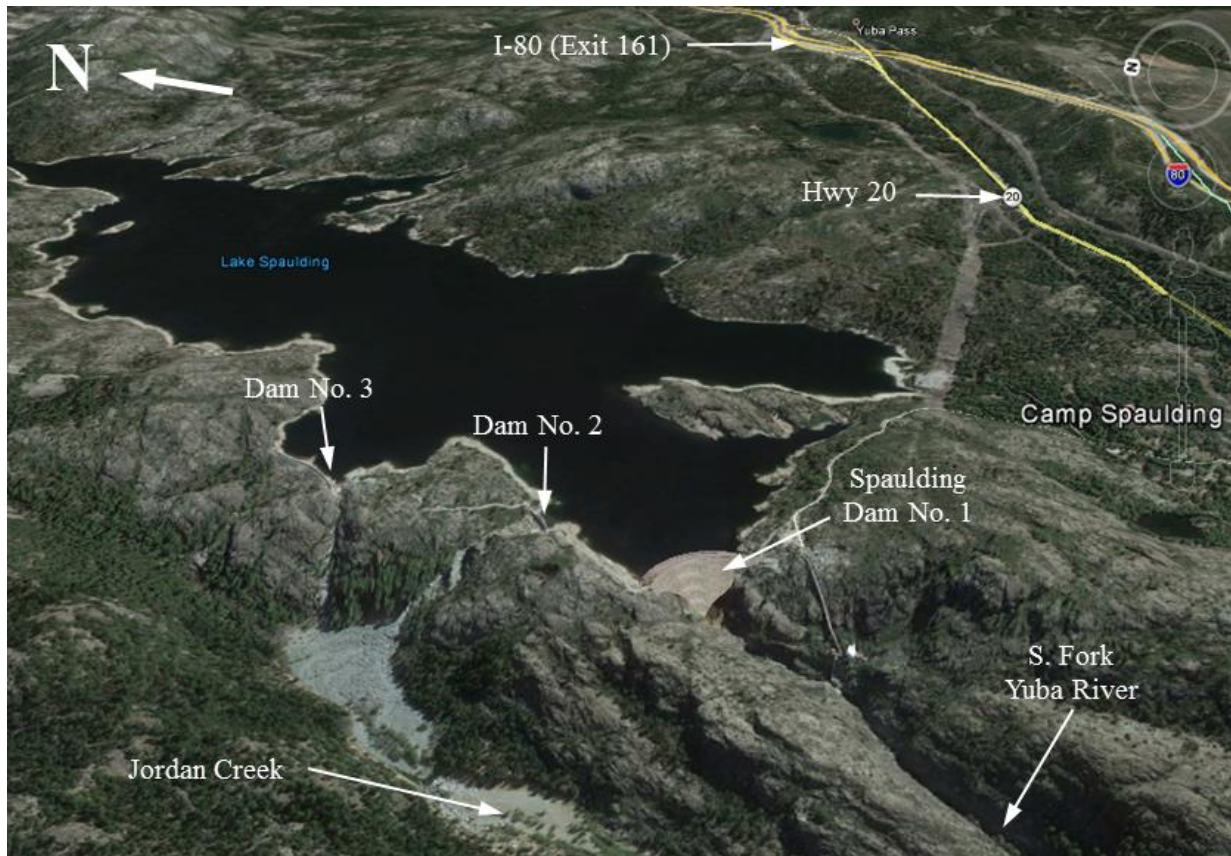


Figure 3-2. Overview of Spaulding Dam site. For scale, crest length of the main dam is 245 m. Aerial image accessed from Google Earth (2015).

Flood Events, Erodibility & Remediation

Field efforts focused on the unlined spillway channel at Spaulding Dam No. 2 which is situated in hard, moderately jointed, granodioritic rock of the Sierra Nevada Batholith. Over the nearly 100 year lifetime of the structure significant scour has occurred as evidenced by the 185,000 m³ of material comprising the extensive alluvial fan where the spillway channel enters Jordan Creek (Figure 3-3).

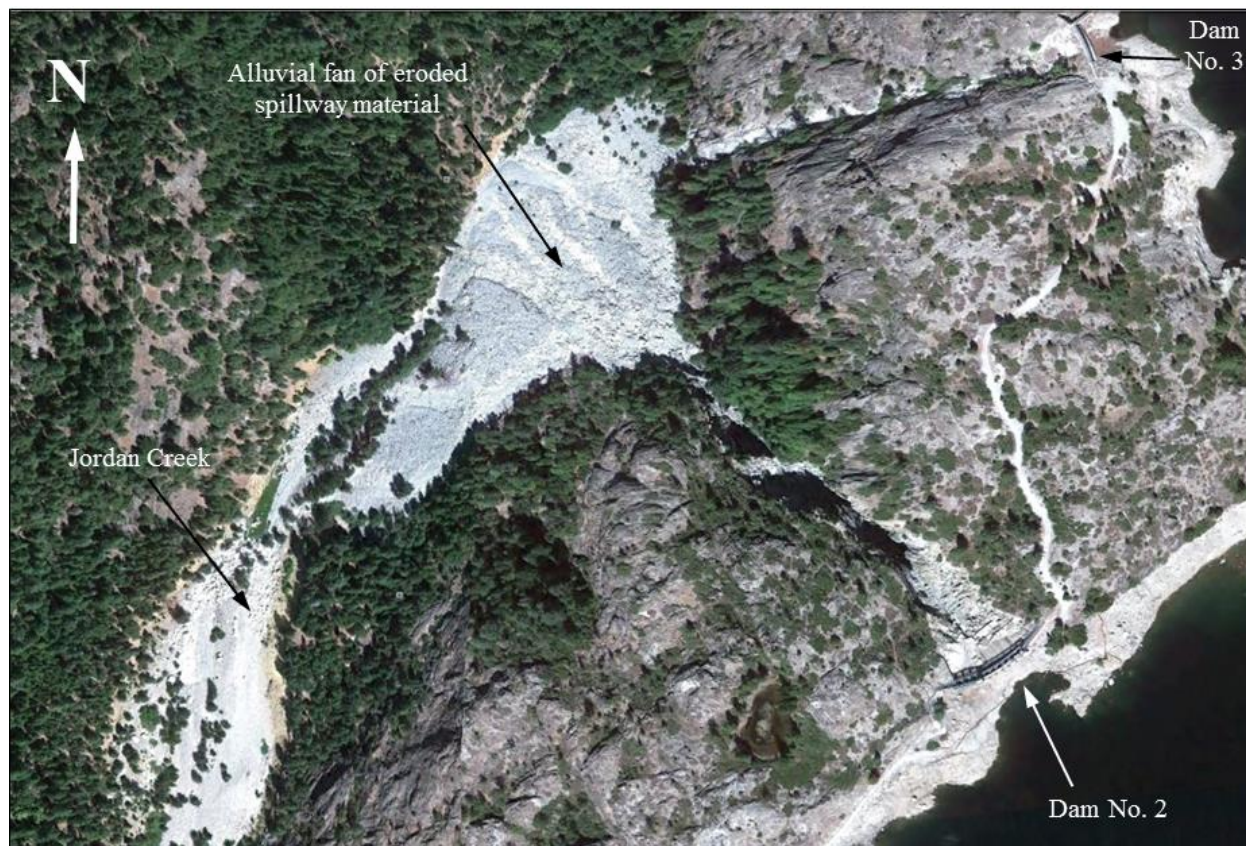


Figure 3-3. Alluvial fan of eroded rock from Dam No. 2 spillway (approximately 185,000 m³). For scale, crest length of the Dam No. 2 is 91 m. Aerial photo accessed from Google Earth (2012).

Spaulding Dam No. 2 has been modified over the years to allow improved control of discharges from the reservoir. Figure 3-4 shows the original pre-1919 geometry, which consisted an overflow ogee crest topped with removable wood stoplogs. In 1939, seven 4.27 m wide by 4.57 m high radial gates were cut into the crest (Gates 1 to 7) (Figure 3-4), followed by installation of three additional lower level 4.27 m wide by 6.10 m high radial gates in 1974 (Gates 8 to 10), which is the present configuration (Figure 3-5).

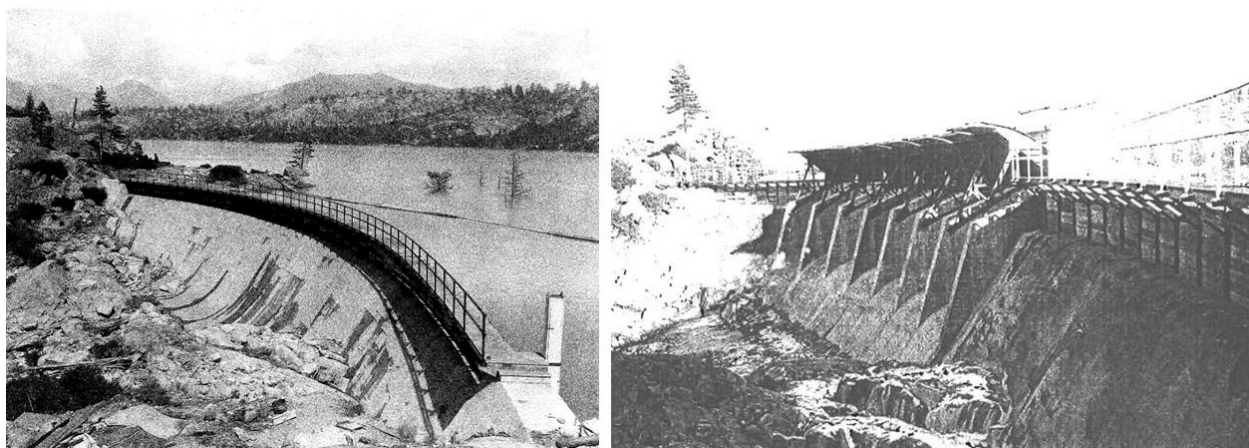


Figure 3-4. Dam No. 2 original pre-1919 geometry (left, photo source unknown) and 1939 geometry after installation of seven radial gates (right, photo from W.A. Perkins inspection on 11/27/39, provided by GEI Consultants Inc. (2003)).



Figure 3-5. Dam No. 2 current geometry (left, December 2012 spill event approximately 14 m^3/s) and May 1996 spill event (right, 716 m^3/s , photo from Mattson (1996)).

The current spillway capacity of Spaulding Dam No. 2 is 1,161 m^3/s which, to date, has not been exceeded. Several large flood events, however, have occurred and include: December 1964 (934 m^3/s), January 1980 (558 m^3/s), May 1996 (716 m^3/s , Figure 3-5) and January 1997 (968 m^3/s , a portion of which, $\sim 140 \text{ m}^3/\text{s}$, was passed through Dam No. 3). No single flood event has resulted in catastrophic erosion of the spillway, but rather scour has occurred more gradually over time. One of the first documented instances of scour of the Dam No. 2 spillway was in 1944 (later summarized in a memorandum from I.S. Nao on May 7, 1968) which noted “some erosion of blocks of bedrock on downstream end [of Dam No. 2].” A concrete apron at the toe of the radial gates was constructed in 1952-1953 to help mitigate this erosion (Figure 3-6).

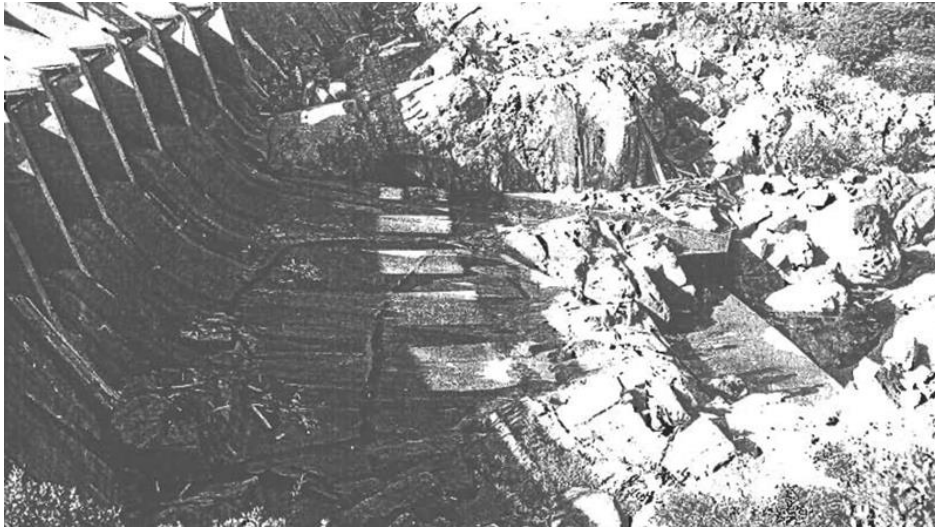


Figure 3-6. Addition of concrete spillway apron below original seven radial gates (photo taken 9/25/53, provided by GEI Consultants Inc. (2003)).

Installation of the three lower radial gates in 1974 lead to significantly increased scour in the spillway channel and the formation of a large slot canyon (Figure 3-7). This was predominately related to the presence of multiple shear zones directly downstream of the lower spillway gates (Figure 3-8). These zones contain weak, highly fractured rock that act as catalysts for scour. The removal of material from these shear zones made it possible for much larger blocks of rock to be eroded (Figure 3-9 - top).



Figure 3-7. Upper reach of eroded slot canyon viewed from middle of spillway (left) and lower reach of slot canyon viewed from Jordan Creek with alluvial fan of scoured material in the foreground (right).

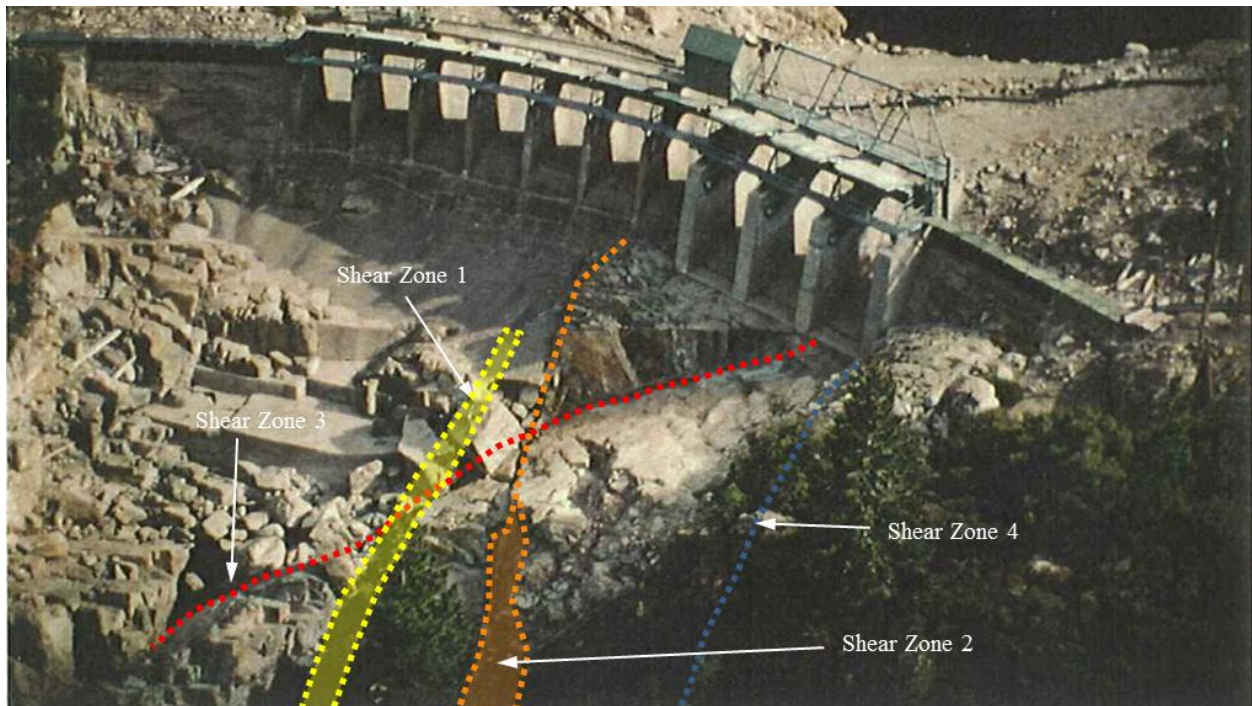


Figure 3-8. Aerial view of Spaulding Dam No. 2 showing approximate shear zone locations (base photo from GEI Consultants Inc. & Pacific Gas & Electric (1998)).

Spills during the 1985-1986, 1994-1995 and 1996-1997 winter/spring seasons resulted in erosion that migrated to the Dam No. 2 toe, ultimately raising concerns regarding the stability of the structure and the potential for an uncontrolled release from the reservoir. An extensive shotcrete and rock bolting endeavor was undertaken in 1997 along with placement of dental concrete within the eroded shear zones (Figure 3-9 - bottom). A more robust concrete apron was installed downstream of the three lower radial gates post-1998 and has performed reasonably well to date.



Figure 3-9. Scour (top) and remediation (bottom) downstream of three lower radial gates (Page 1997, 1998). Note person for scale.

3.2 Methodology

3.2.1 Artificial rock blocks

To capture prototype measurements for hydrodynamic pressures and block displacements during actual flood events, two instrumented artificial rock blocks were installed in the spillway channel at Spaulding Dam No. 2. These blocks were fabricated into existing block molds (i.e., locations where blocks had previously existed but had since been scoured away). Blocks were instrumented with pressure and displacement sensors to record hydrodynamic pressures inside rock joints surrounding the block as well as monitor block movements during spill events.

Block locations

Locations for artificial blocks in the spillway are shown in Figure 3-10. Block 1 was installed downstream of the upper level Gates 4 and 5, while Block 2 was installed downstream of the lower level Gates 8 to 10. Blocks were strategically positioned to capture potential discharges resulting from the bimodal operation of the radial spillway gates. From Spring to early Fall (approximately April to October), all radial gates are closed to capture spring snowmelt and maximize water storage in the reservoir. Any discharges during these months are typically made through the upper level gates (Gates 1 to 7). From late Fall to early Spring (approximately October to April), all gates are open such that any discharge would initially pass through the lower level gates (Gates 8 to 10). In the event of a large discharge all gates are used, no matter the season, to prevent overtopping of the main dam.

Blocks were positioned close to the spillway gates where flow conditions could still be characterized as 2D channel flow. This was done to facilitate comparison of results obtained from the idealized physical hydraulic model with near-similar flow conditions presented in Chapter 4.



Figure 3-10. Location of artificial rock blocks. Left photo accessed from Google Earth (2015).

Block construction

Artificial rock blocks were cast in existing block molds, which represent locations previously occupied by blocks that have since been vacated due to erosion (Figure 3-11). Specifically, tetrahedral block molds were used (i.e., blocks with three bounding joint planes and one free block face). Block 1 was cast in November 2012, while Block 2 was cast in November 2013.



Figure 3-11. Tetrahedral molds for artificial rock blocks at Spaulding Dam No. 2. Note concrete added to Block 2 mold to provide continuity of the free face when the block is installed.

For block construction, a wire frame to hold sensors flush on the block faces was first fitted to the general mold shape. Additionally, for Block 2, stainless steel targets were epoxied to each of the block mold walls opposite each of the displacement sensors. Plastic lining was temporarily installed on the inside of the molds such that concrete could be poured without adhering to the actual mold surface (Figure 3-12). Sensor wires were placed inside waterproof conduit exiting the block molds which were later connected to the datalogger. A high strength concrete mix was then added to the molds and allowed to dry to form the blocks. Although concrete density is approximately 10% to 15% less than the surrounding granodiorite rock, it was deemed adequate for the purposes of the investigation. After the blocks cured, blocks were lifted from their molds and the plastic lining was removed (Figure 3-13). Finally the blocks were reset into their molds and sensor wires were connected to the datalogger (Figure 3-14).

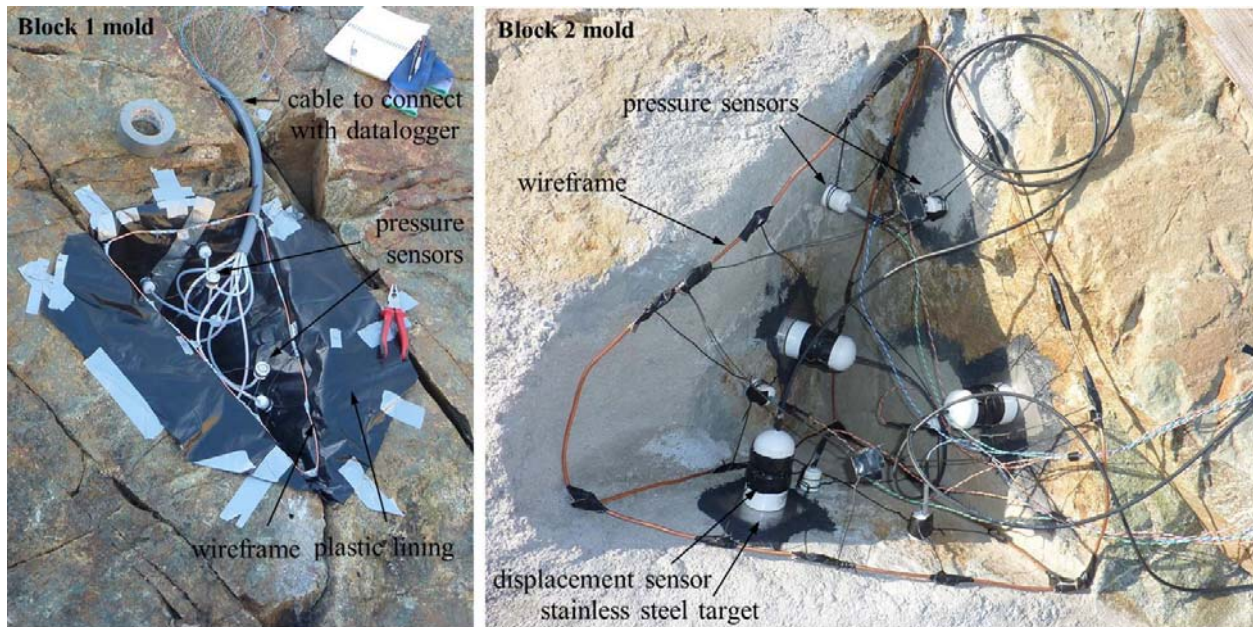


Figure 3-12. Wireframe support for block sensors. Note Block 2 (right) has three additional sensors to monitor block displacements.

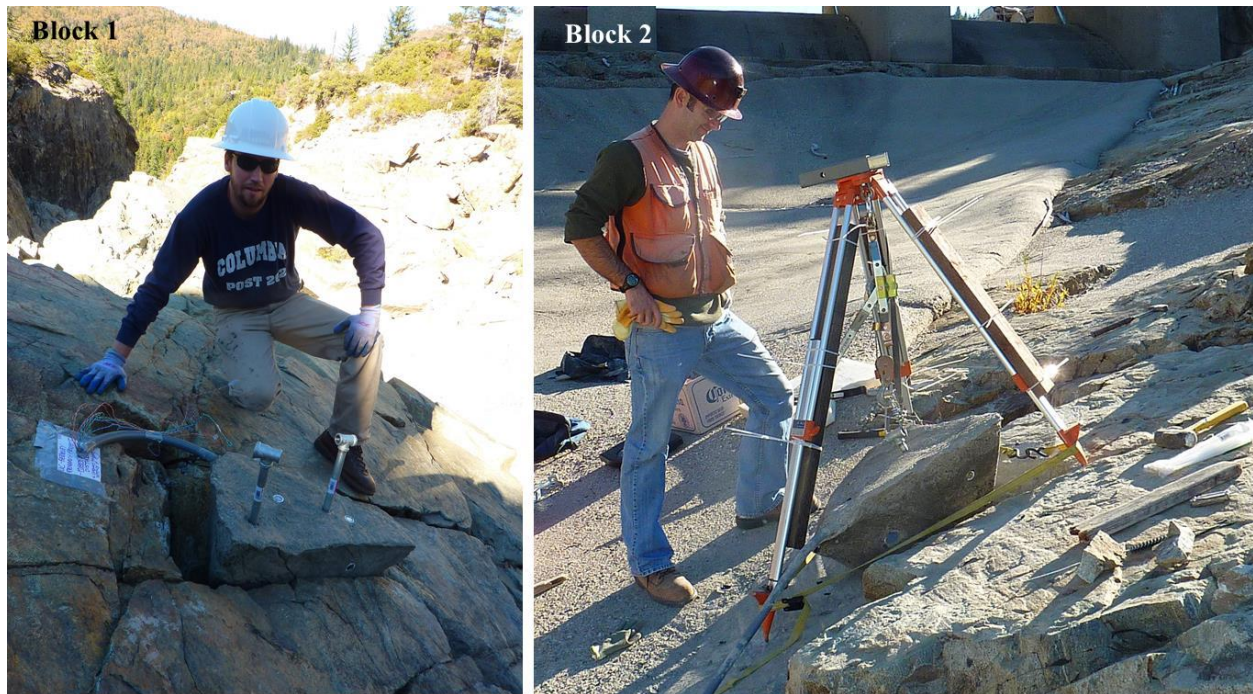


Figure 3-13. Lifting of artificial blocks from mold to remove plastic lining. Block 1 was lifted using removable handles while Block 2 required the assistance of a come-along-winch and tripod.

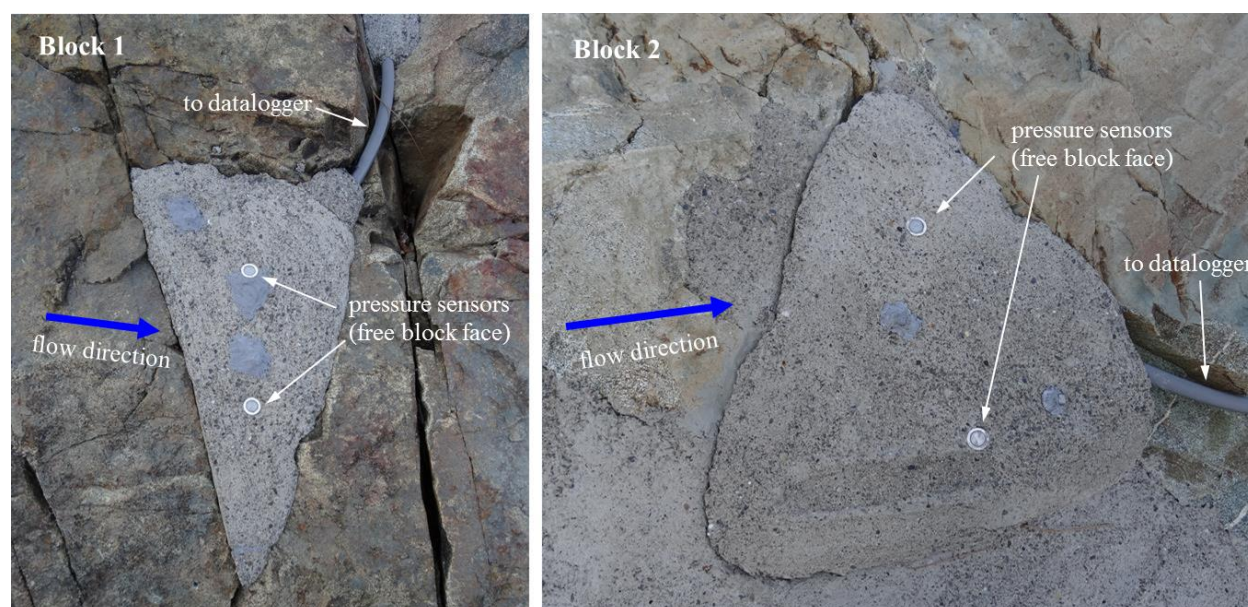


Figure 3-14. Artificial rock blocks, as constructed.

Block instrumentation & data acquisition

Block 1 was instrumented with eight pressure transmitters (two per block face), while Block 2 was instrumented with eight pressure transmitters (two per block face) and three displacement sensor (one per block face, excluding the free block face). For displacement sensors, stainless steel targets (one per sensor) were installed on the block mold walls, opposite each sensor (Figure 3-12). Distance measured by the sensor is from the sensor tip (block face) to the target (block mold). All sensors (pressure and displacement) were installed flush with block faces. Prior to installation, sensors were checked to ensure operation as specified by the manufacturer. Table 3-1 provides relevant technical specifications for each sensor type.

Table 3-1. Artificial block sensor technical specifications.

Specification	Pressure	Displacement
Make	Keller	SICK
Model	PA-9LY	IMA30-40NE1ZCOK
Type	Flush diaphragm	Inductive analog
Range	0 - 6 bar (absolute)	0 - 40 mm
Power	8 - 32 V DC	15 - 30 V DC
Output	4 - 20 mA	4 - 20 mA
Accuracy	± 0.015 bar	± 0.1 mm
Sampling freq.	100 Hz	100 Hz
No. of sensors	18 total (8/block, 2/block face, 2 to measure atm. pressure)	3 total (Block 2 only - 1/block face, excluding free face)

Sensor wires from the block were enclosed in waterproof conduit and ran to dataloggers, housed in a utility shed above Gate 7 on the Spaulding No. 2 Dam (Figure 3-10). Two additional pressure transmitters were installed at the utility shed to measure atmospheric pressure for reference to sensors installed on the blocks.

Two Campbell Scientific CR3000 dataloggers were used for data acquisition (one per block). For current output (4 – 20 mA) sensors, 100 Ohm shunt resistors were fabricated to connect sensor wires to datalogger input terminals. A sampling rate of 100 Hz was used for each sensor, with the exception of one pressure transmitter measuring atmospheric pressure which was sampled at a rate of 0.2 Hz and averaged hourly. Data were written to 16 GB CompactFlash (CF) storage cards in two hour increments. CF cards were connected to the datalogger via Campbell Scientific CFM100 adapters. Stored data were manually downloaded using a Toshiba Portege R705 laptop PC. Figure 3-15 shows the data acquisition system for Block 1.

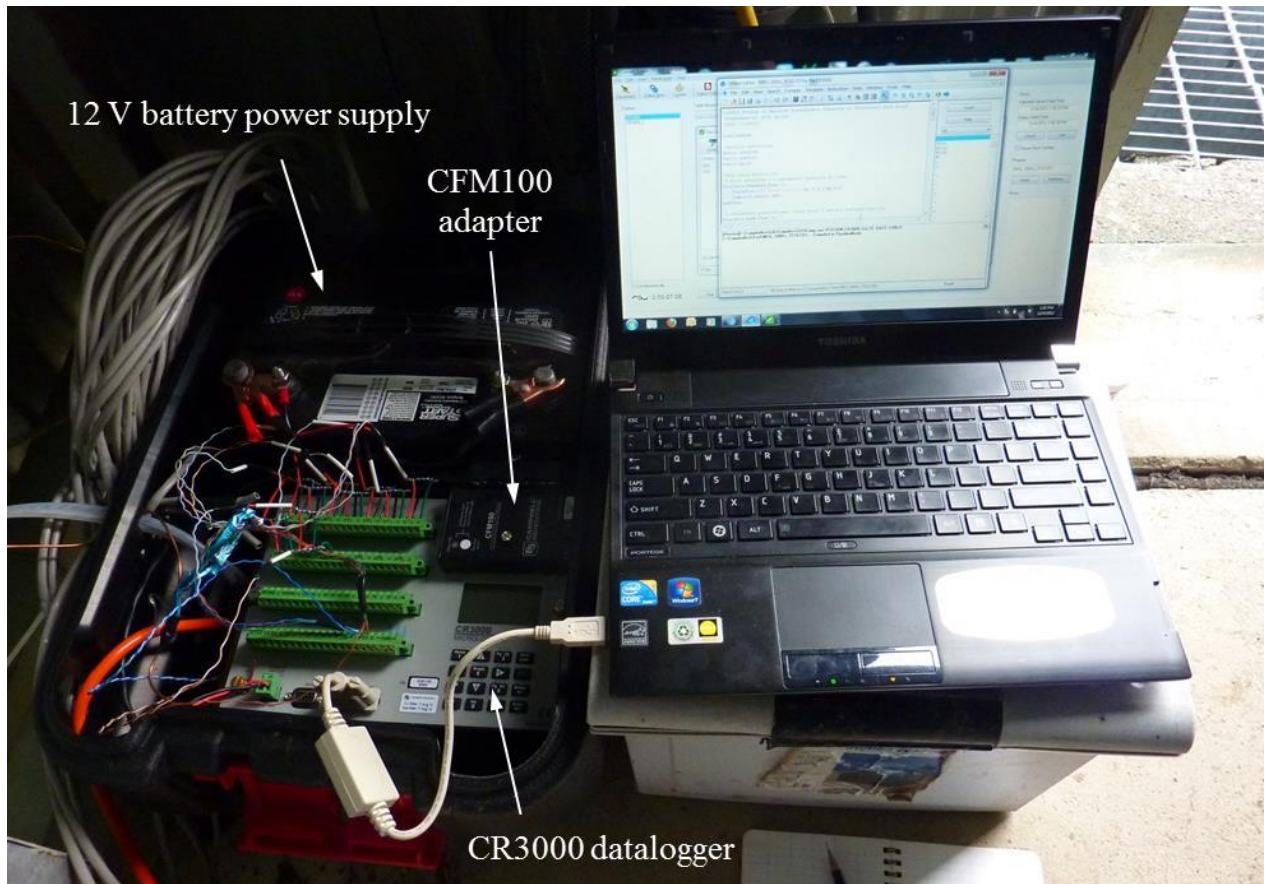


Figure 3-15. Data acquisition system for Block 1 (system for Block 2 is identical, with one additional 12 V battery connected in series to power displacement sensors).

Program code for the CR3000 datalogger, used for data acquisition from Block 1 and Block 2, was developed using CRBasic Editor which is part of the Campbell Scientific's LoggerNet software package.

Block geometry & specifications

Relevant parameters for the two artificial rock blocks are presented in Table 3-2. Parameters were determined from field measurements and from 3D reconstructions of the blocks using digital photographs and PhotoScan photogrammetry software (AgiSoft 2015) (Figure 3-16).

Table 3-2. Artificial block specifications.

Specification	Block 1	Block 2
Weight (N) ^a	502	917
Volume (cm ³) ^b	21300	38900
Density (kg/m ³) ^c	2400	2400
Protrusion, h (mm)	see Figure 3-18	see Figure 3-19
Edge type	Rounded	Rounded
Orientation face 1 (deg.) ^d	116/46	295/52
Orientation face 2 (deg.) ^d	110/88	151/65
Orientation face 3 (deg.) ^d	051/84	224/87
Orientation face 4 – free face (deg.) ^d	042/26	074/20
Dimensions (m)	see Figure 3-17	see Figure 3-17
Flow direction (deg.) ^e	325	000

Notes:

^a Calculated. Block 1 measured weight = 569 N after curing 48 hrs. Still likely had considerable moisture so used assumed density to calculate weight. Block 2 could not be weighed in the field.

^b Measured from 3D solid mesh constructed using photogrammetric methods.

^c Assumed.

^d Orientation given as dip direction (θ)/dip angle (δ).

^e Flow direction is approximate and depends on flow rate. Given as azimuth from North.

Both blocks are tetrahedral in shape defined by three joint planes and one free face. Orientations of block faces, given as dip direction (θ , deg.) and dip angle (δ , deg.) (see Figure 3-20), are 116/46, 110/88, 051/84, and 042/26 (free face) for Block 1, and 295/52, 151/65, 224/87, 074/20 (free face) for Block 2. Orientations were obtained using a Brunton geologic compass. The azimuth of flow direction in the vicinity of the blocks is approximately 325 deg. and 000 deg., for Block 1 and Block 2, respectively. For Block 1, this value is fairly constant for all flow rates, however, for Block 2 this value will tend to rotate northwest (towards the value for Block 1) with increasing flow rate.

Block volumes were determined using PhotoScan photogrammetry software (AgiSoft 2015). To do this, a scaled 3D mesh of each block was reconstructed from digital photographs taken of the blocks and block molds (Figure 3-17). Block dimensions and approximate sensor locations are also shown for each of the block faces. Block 1 was weighed in the field two days after the concrete was poured, but likely still had a significant amount of water weight. Accordingly, a concrete density of 2400 kg/m³ was assumed to calculate a more representative value of the block weight. A similar procedure was done for Block 2 as the weight in the field could not be obtained due to its large size.

The protrusion height of each block above the surrounding rock mass is shown in Figure 3-18 and Figure 3-19. The 3D mesh of each block was imported into SketchUp (Trimble Navigation 2015) where cross-section profiles of the block free face were made in the approximate direction of flow at 10 cm increments. For Block 1, protrusion of the upstream face ranges from approximately 0.6 cm to 1.2 cm. A portion of the block is slightly recessed below the surrounding rock mass as indicated by sections A-A' and B-B'. Block 2 is more variable with an

equal number of sections above and below the surrounding rock mass with the amount of protrusion/recession being less than 0.5 cm in either case.

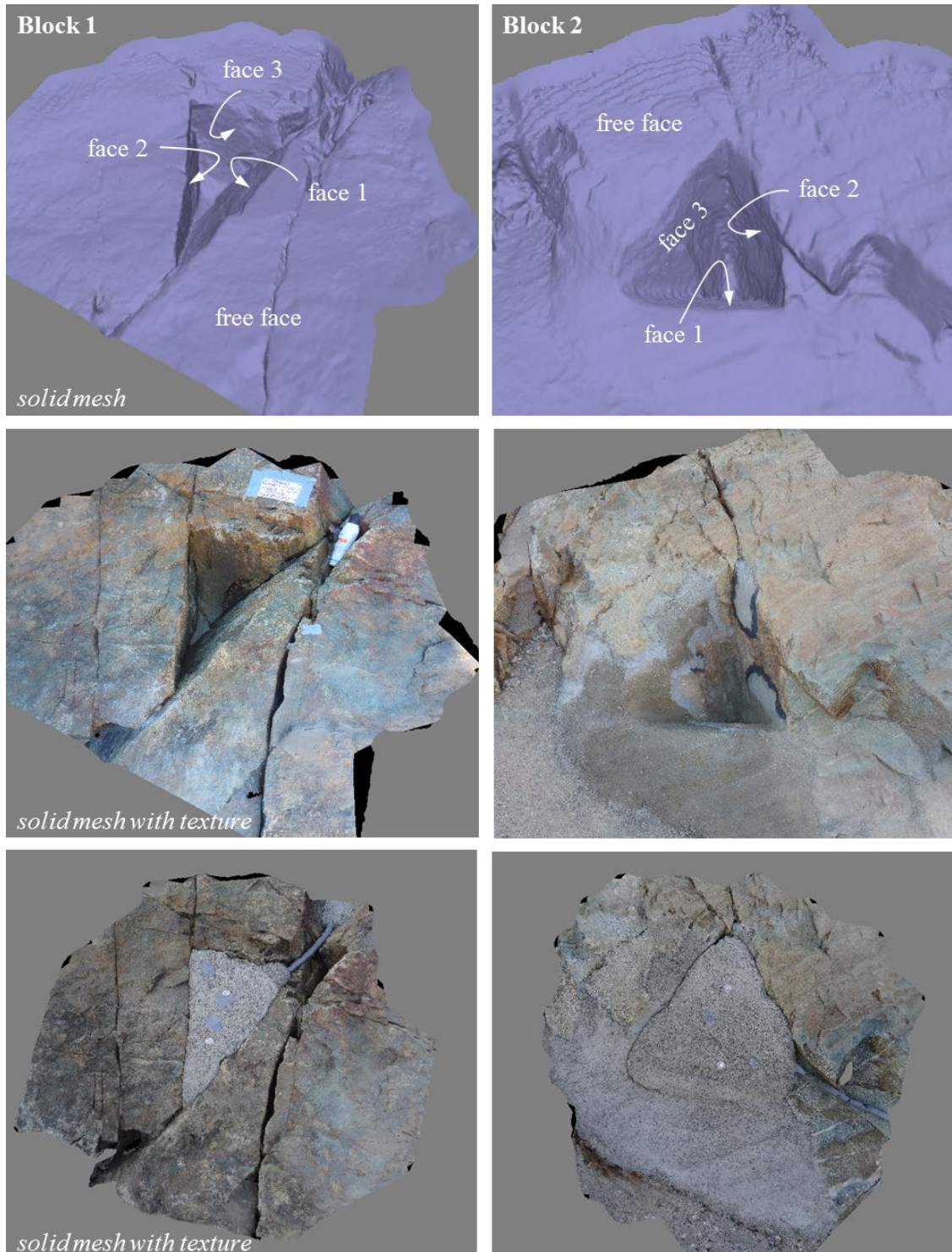


Figure 3-16. 3D reconstruction of artificial rock block geometry using photogrammetric methods (Block 1 – left, Block 2 – right).

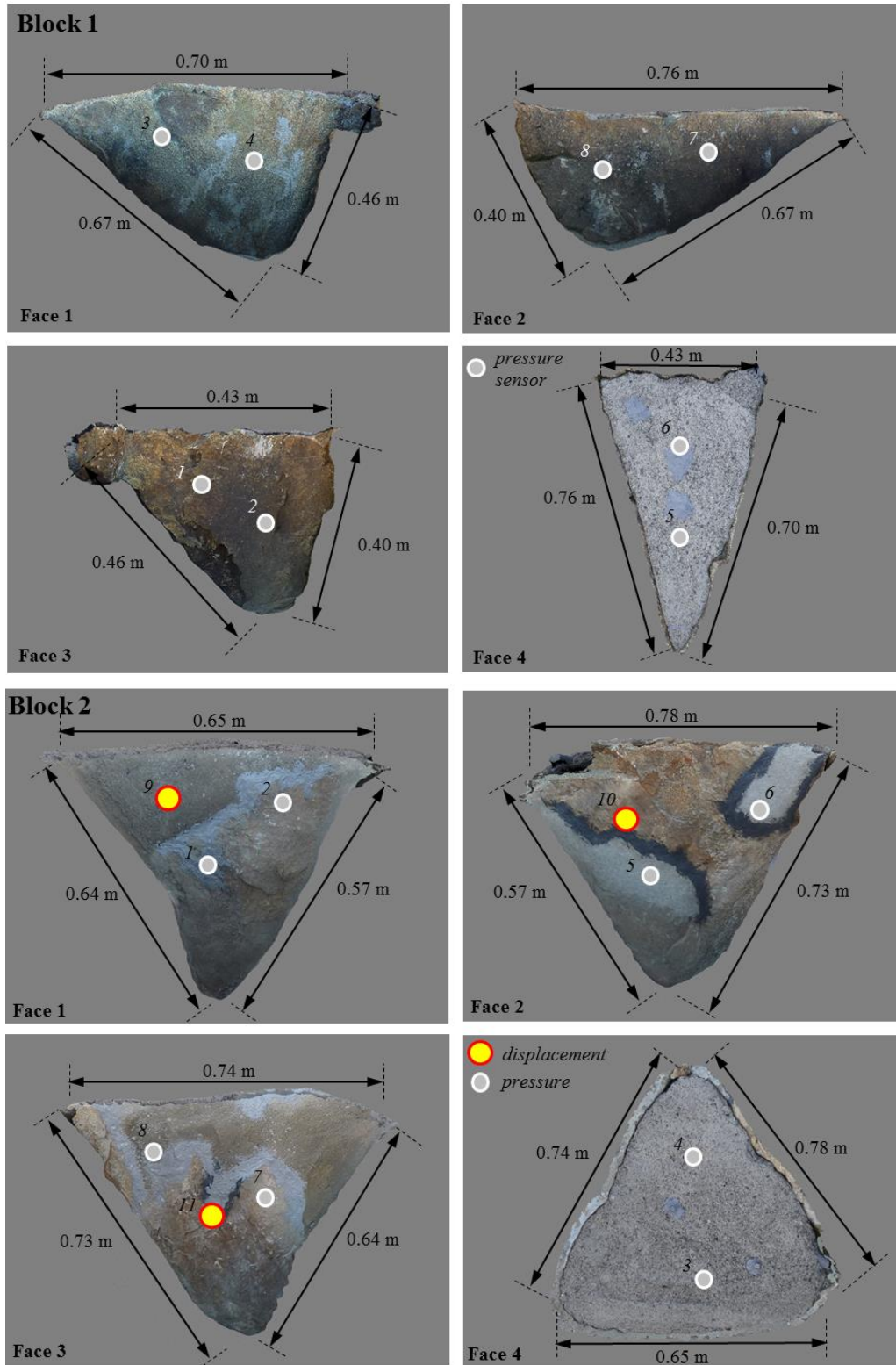


Figure 3-17. 3D mesh with photo texture of Block 1 (top) and Block 2 (bottom). Note sensor locations are approximate. Not to scale.

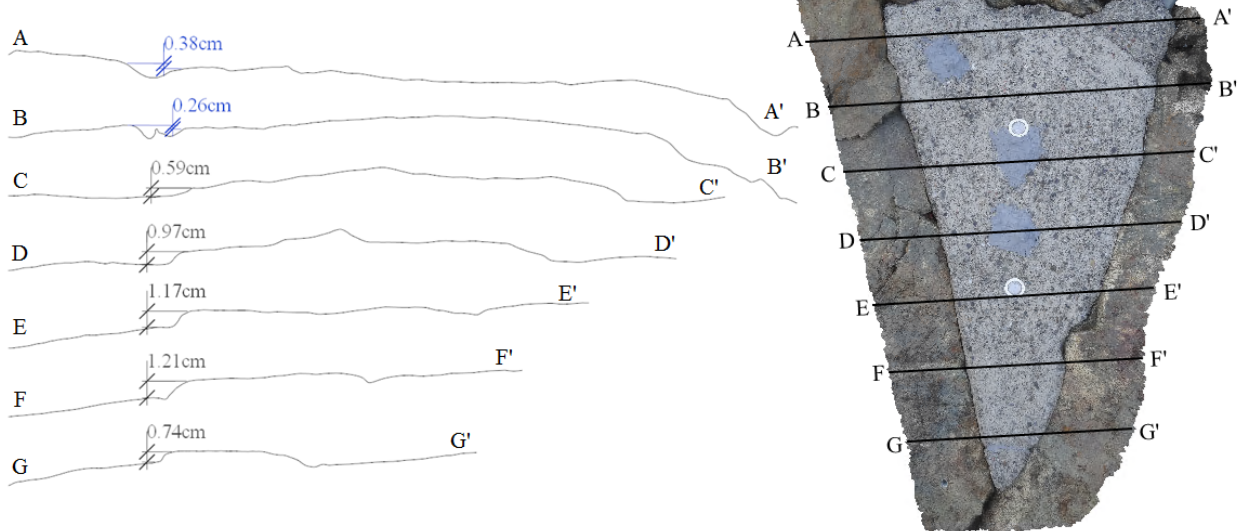
Block 1 protrusion profiles*blue value* = negative protrusion

Figure 3-18. Protrusion profiles for Block 1.

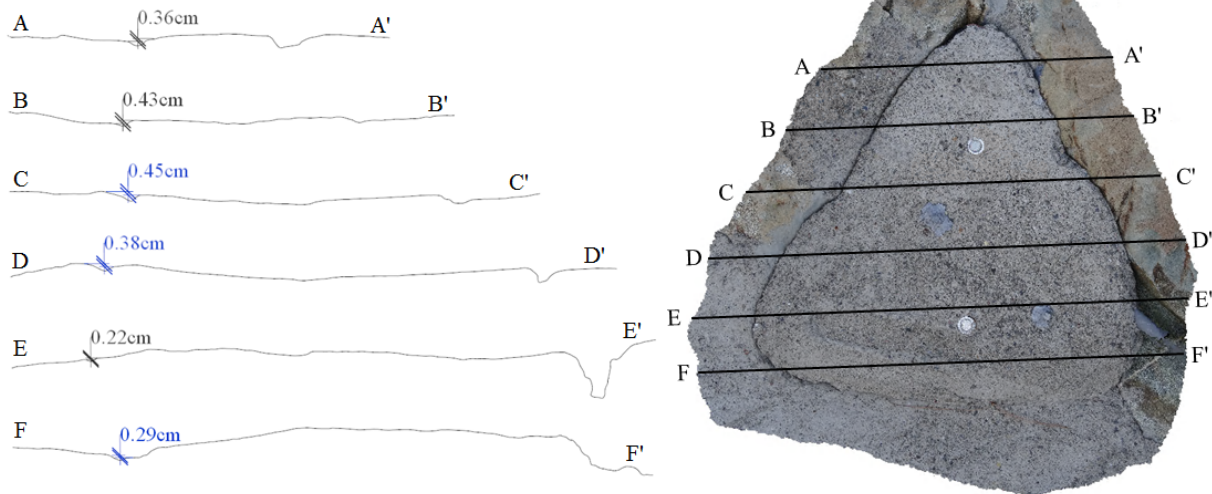
Block 2 protrusion profiles*blue value* = negative protrusion

Figure 3-19. Protrusion profiles for Block 2

3.2.2 Rock mass discontinuity characterization

Terrestrial LiDAR scanning was performed at the Spaulding Dam No. 2 site to collect high resolution data for rock discontinuity orientations (which can be represented by the dip angle (δ) and dip direction (θ), or the discontinuity normal vector (\mathbf{n}), discontinuity dilation angle (i_ϕ), and site topography. Note **bold** font represents a vector/matrix quantity. For completeness, δ refers to the angle of a planar feature with respect to a horizontal plane (from 0 to 90 deg.), while

θ is the azimuth referenced from North to the direction of the dip (from 0 to 360 deg.). The discontinuity normal vector is a unit vector perpendicular to the rock face. The dilation angle refers to the angle of asperities on a discontinuity surface that must be overcome for sliding of a block on that surface (Figure 3-20). The use of LiDAR data for rock mass classification is beneficial due to the large quantities of measurements that can be readily obtained in a relatively short period of time. This is particularly convenient for regions with difficult access to make physical measurements using a traditional geologic compass.

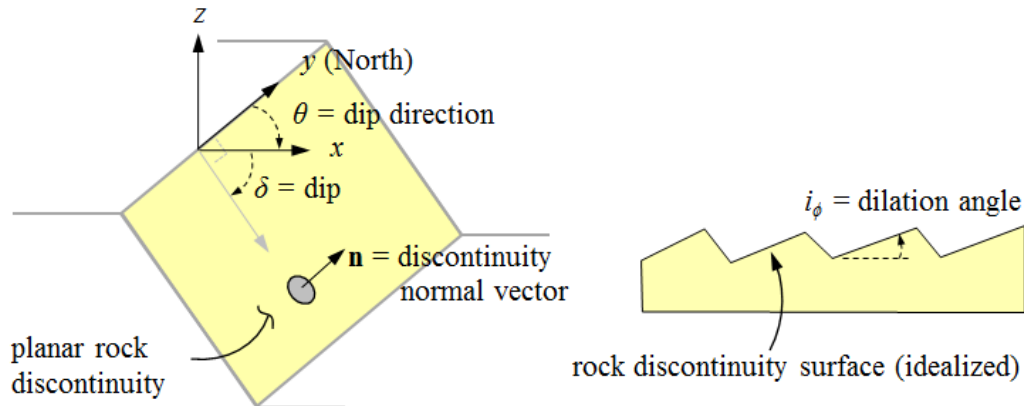


Figure 3-20. Schematic for dip/dip direction (left) as well as dilation angle (right) definitions.

Scanning campaigns

Two terrestrial LiDAR scanning campaigns were completed at Spaulding Dam No. 2. The first was performed in July 2012 by AMEC (with assistance from the author) using a Leica ScanStation HDS8810. Five scanner locations were used that referenced four surveyed control points previously installed in the spillway channel by AMEC (Figure 3-21). Coordinates for the control points are listed in Table 3-3. A second scan was completed the following year in October 2013 using the University of California – Berkeley’s Maptek I-Site 4400 scanner. The four survey control points installed by AMEC were referenced and used for scanner locations in the second scan.



Figure 3-21. Spaulding Dam No. 2 survey control points (provided by AMEC).

Table 3-3. Survey control points^a for Spaulding Dam No. 2 (provided by AMEC).

Control point	Northing	Easting	Elevation
HDS1	2248927.49	6945653.48	4990.29
HDS2	2248953.94	6945770.48	4987.2
HDS3	2249020.06	6945687.9	4980.61
HDS4	2249079.87	6945613.36	4976.04

Notes:

^a State Plane coordinate system, California Zone 2, NAD83 (units = feet)

Post-processing

The general workflow for processing and analysis of LiDAR data is shown in Figure 3-22. Initially, raw data were collected with the scanner. Individual scans were registered and oriented to a common coordinate system using survey control points to form a single 3D point cloud of all raw data (this was done using proprietary software associated with each of the scanners, i.e., Cyclone (Leica Geosystems 2015) and I-Site Studio (Maptek 2015)). For this analysis, point clouds referenced the NAD83 State Plane Coordinate System, California Zone 2. Non-essential and noisy points were removed prior to exporting data as a single point cloud in .xyz file format. Registered point cloud data was then input into SplitFX rock mass characterization software (Split Engineering 2015). Using SplitFX, discontinuity orientations and dilation angles were obtained from the point cloud. Finally, discontinuity information was input into Matlab for statistical analysis of rock mass parameters.

Workflow for LiDAR point cloud processing

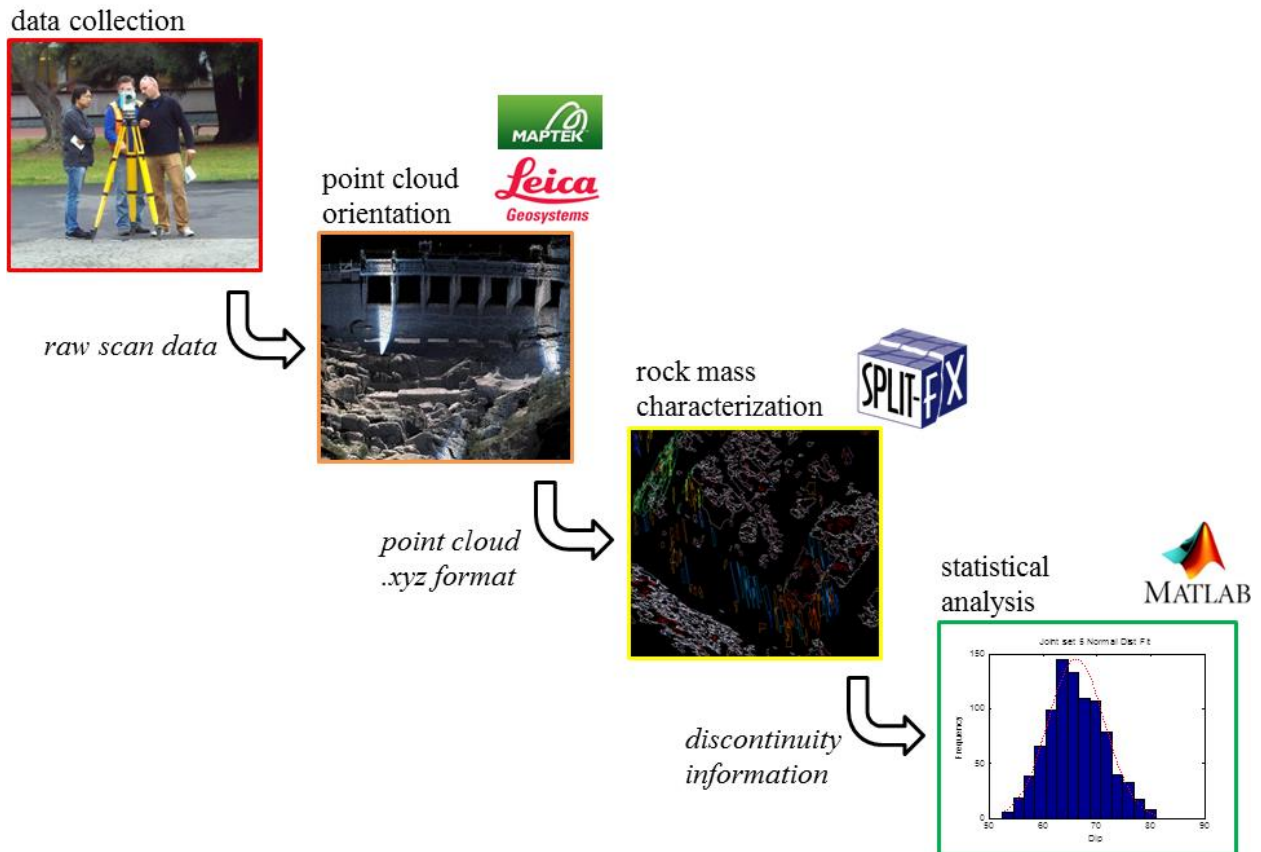


Figure 3-22. Workflow for processing LiDAR point cloud data.

To determine rock mass discontinuity orientations, the 3D point cloud of the site was processed using the SplitFX software. The program automatically detects discontinuity surfaces through identification of “patches” that define joint plane segments. To do this, a 3D triangulated mesh is fitted to the point cloud. Each individual mesh triangle is a plane represented by a normal vector (\mathbf{n}). Neighboring normal vectors are compared to determine if mesh triangles are of similar orientation. Similarly oriented mesh triangles are combined to form “patches” that represent joint plane surfaces (Figure 3-23).

Key inputs for the automated discontinuity detection algorithm are 1) the mesh triangle density (i.e., the number of triangles per meter), 2) the maximum neighbor angle (i.e., the tolerance limit to compare neighboring normal vector orientations), and 3) the minimum patch size (i.e., the number of mesh triangles required to form a patch). Based on trial and error, values of 1) 12 triangles/meter, 2) 4 deg., and 3) ≥ 5 triangles/patch for the above inputs, respectively, were determined to yield reasonable results. Based on the above parameters the minimum patch size is approximately 0.2 m by 0.2 m.

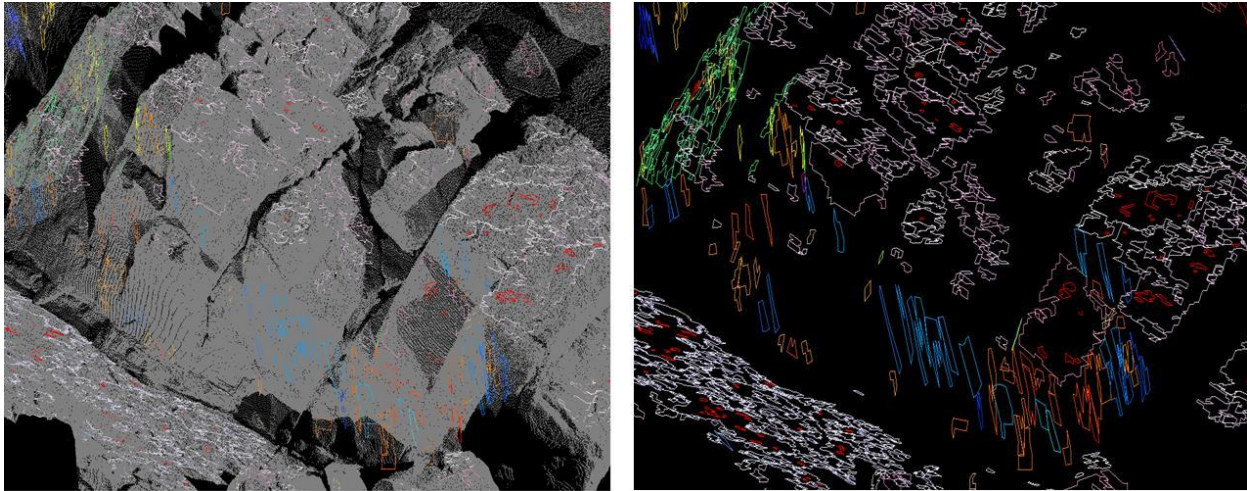


Figure 3-23. Close up of 3D point cloud for rock outcrop at Spaulding Dam No. 2 spillway (left) and patches detected for the same outcrop using SplitFX (right). Note different patch colors represent different joint sets.

Calculation of the discontinuity dilation angle is also performed automatically for each patch using SplitFX. This is accomplished by calculation of the average angle between the mean normal vector for the patch (\mathbf{n}_{avg}), and the normal vector of each mesh triangle in the patch (\mathbf{n}) (Mansfield & Kemeny 2009):

$$i_{\phi} = \frac{1}{N_t} \sum_{j=1}^{N_t} \cos^{-1} \left(\frac{\mathbf{n}_{avg} \cdot \mathbf{n}_j}{|\mathbf{n}_{avg}| \cdot |\mathbf{n}_j|} \right) \quad (3-1)$$

where N_t is the number of mesh triangles in the patch.

3.3 Results

3.3.1 Artificial rock blocks

Since installation of Block 1 (November 2012) and Block 2 (November 2013), climatic conditions in California have been extremely dry. Accordingly, only three small spill events have occurred at Spaulding Dam No. 2, none of which significantly impacted the installed blocks. Events occurred in December 2012, April 2014 and February 2015, and were less than 14 m³/s (Figure 3-24). To date, no meaningful data have been collected, however, instrumentation is still in operation at the site.

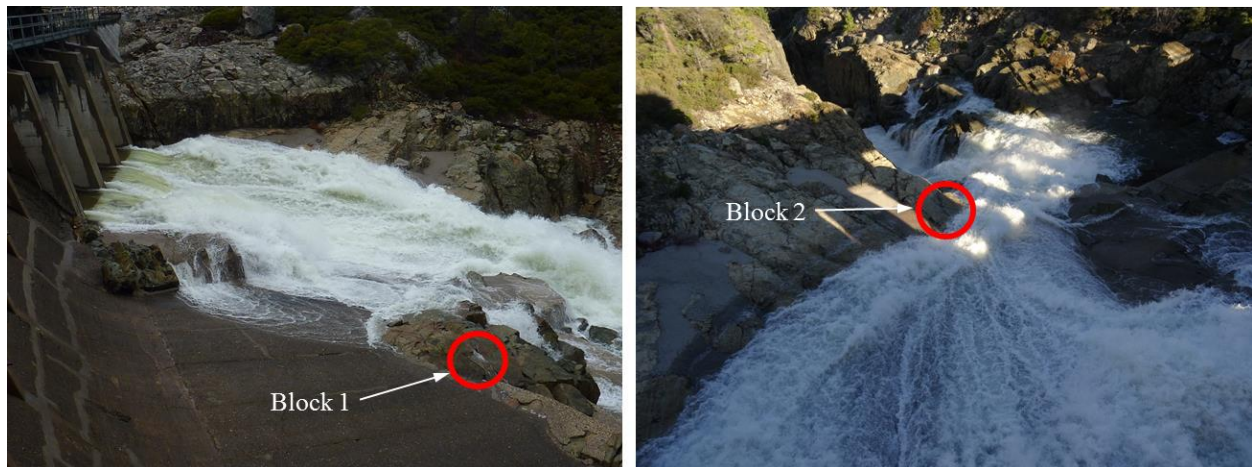


Figure 3-24. Spills at Spaulding Dam No. 2 on 12/4/12 (left) prior to installation of Block 2, and on 2/10/15 (right) barely missing edge of Block 2.

3.3.2 Rock mass discontinuity characterization

Five regions within the Spaulding No. 2 Dam spillway were used for rock mass classification from the LiDAR 3D point cloud data (Figure 3-25). These regions provided good exposure of the rock mass that appeared to have minimal vegetation and loose rocks that could yield noisy data. For the analysis, the point cloud obtained in July 2012 from AMEC's Leica scanner was used due to higher resolution / point density capabilities associated with the instrument. Each region was cropped from the main site point cloud and individually analyzed using the SplitFX rock mass characterization software.

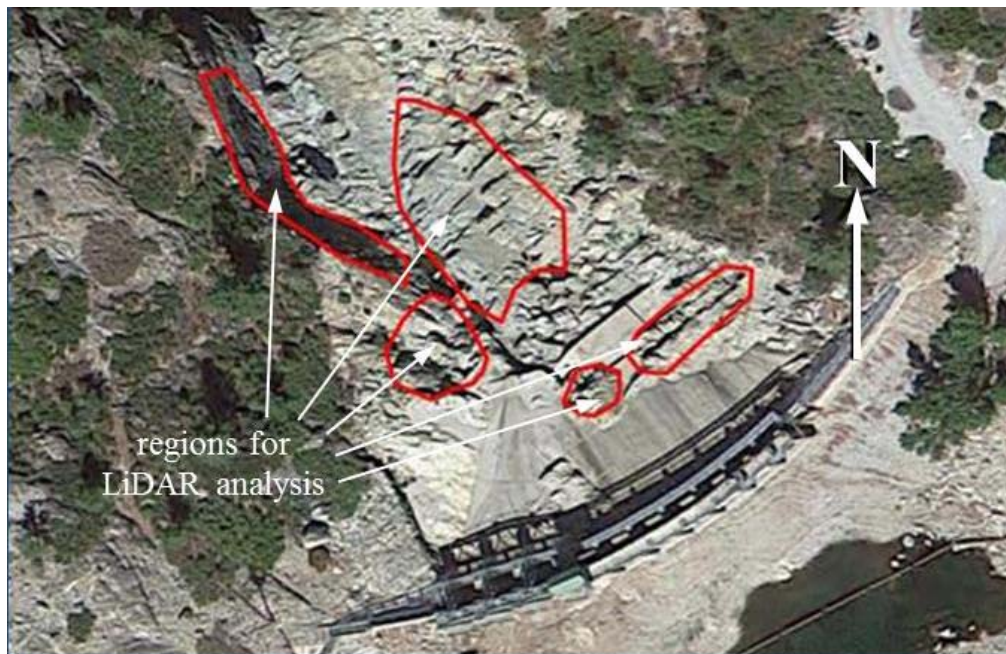


Figure 3-25. Regions in Spaulding Dam No. 2 spillway used in LiDAR analysis for rock mass characterization.

For the Spaulding site, four dominant discontinuity sets (J_1 , J_2 , J_3 , J_{4a} , and J_{4b}) were identified with mean orientations of 060/25, 132/30, 315/67, 045/73 and 225/85, respectively (Table 3-4). The fourth set was separated into two sub-sets, J_{4a} , and J_{4b} , due to the near-vertical dipping nature of the discontinuity. Joints dipping to the Northeast were grouped with set J_{4a} while those dipping to the Southwest were grouped with J_{4b} . This was done to accommodate the probabilistic block theory model discussed in Chapter 6. A stereonet plot showing normal vectors (poles) for all the discontinuity patches identified by SplitFX is shown in Figure 3-26. Despite efforts to remove unwanted data, a considerable amount of noise is observed. A contour plot of the pole density allows easier identification of the dominant discontinuity orientations. For statistical characterization, noisy data were manually removed by filtering regions with low density. Stereonet plots for the remaining poles and corresponding pole density are shown in Figure 3-27.

Table 3-4. Statistical parameters for rock mass discontinuity sets.

Parameters	Joint set 1	Joint set 2	Joint set 3	Joint set 4a	Joint set 4b
θ – distribution	Beta	Beta	Beta	Beta	Beta
mean (deg.)	060	132	315	045	225
p_1^a	3.333	2.745	2.577	2.284	1.412
p_2^a	2.679	3.388	3.146	2.534	1.522
p_3 (deg.) ^b	023	101	304	029	214
p_4 (deg.) ^b	090	170	328	063	237
δ – distribution	Beta	Beta	Beta	Beta	Beta
mean (deg.)	25	30	67	73	85
p_1^a	5.903	6.476	3.469	1.587	1.923
p_2^a	5.271	5.029	3.681	1.463	0.943
p_3 (deg.) ^b	10	5	53	54	76
p_4 (deg.) ^b	38	50	81	90	90
i_ϕ – distribution	Beta	Beta	Beta	Beta	Beta
mean (deg.)	2.3	2.3	2.7	2.2	2.2
p_1^a	5.816	7.084	3.926	5.962	4.456
p_2^a	8.137	21.422	17.927	9.702	4.285
p_3 (deg.) ^b	0	0	0	0	0
p_4 (deg.) ^b	5.6	9.4	14.8	5.8	4.3
Correlation coef., ρ (θ and δ)	-0.123	0.303	0.164	-0.070	0.135

Notes:

^a Distribution parameters controlling Beta distribution shape

^b Lower and upper bounds for Beta distribution

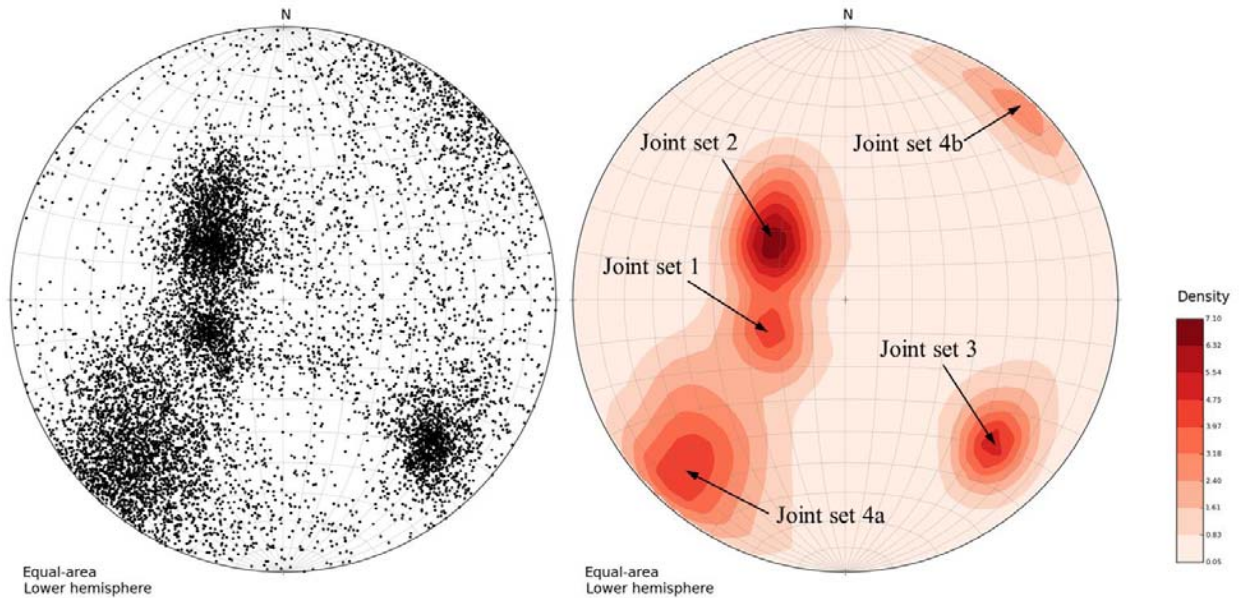


Figure 3-26. Lower hemisphere stereonet showing discontinuity poles (normal vectors, \mathbf{n}) (left) and discontinuity pole density contours (right) for all LiDAR data. Plotted using OpenStereo (Grohmann & Campanha 2010).

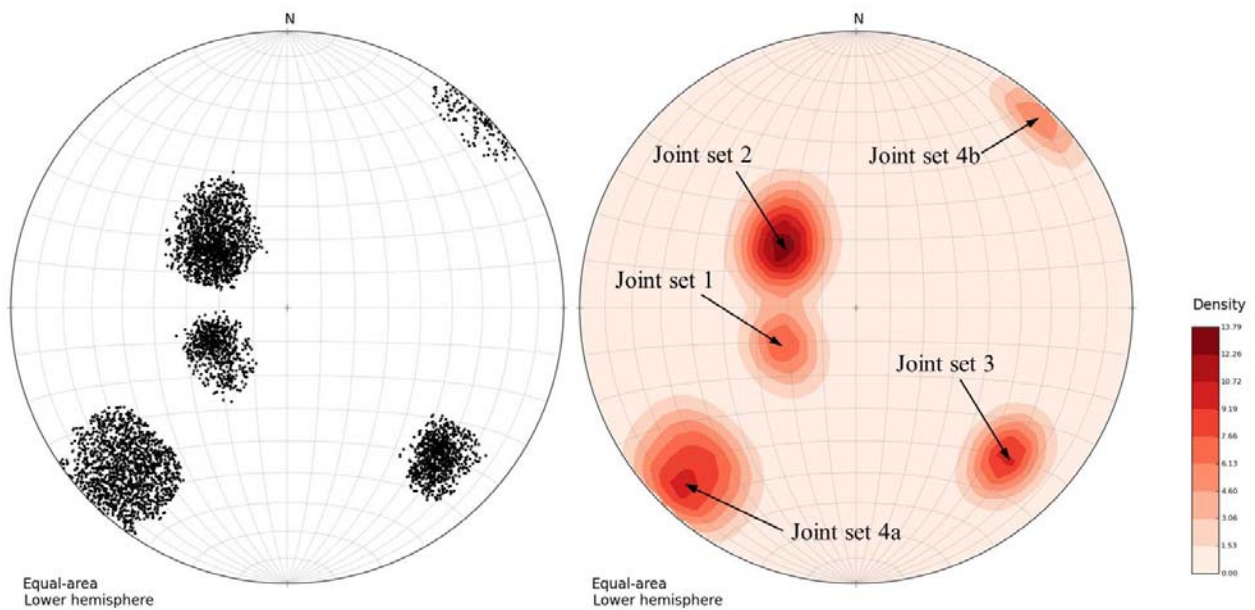


Figure 3-27. Lower hemisphere stereonet showing discontinuity poles (normal vectors, \mathbf{n}) (left) and discontinuity pole density contours (right) for filtered LiDAR data. Plotted using OpenStereo (Grohmann & Campanha 2010)

Nearly 5,000 filtered measurements of discontinuity orientation and dilation angle were obtained from the LiDAR point cloud using SplitFX rockmass characterization software.

Statistical distributions for θ , δ and i_ϕ were fitted for each discontinuity set. Commonly for rock mass discontinuity orientations, a Fisher distribution is implemented to characterize the degree of dispersion of the discontinuity normal vector about the mean vector orientation in 3D spherical space (Fisher 1953). However, this can be problematic if the density distribution of poles around the mean is not symmetric. Accordingly, a Beta distribution was used to characterize both θ and δ to capture anisotropy in the orientation of the discontinuity sets. The Beta distribution is versatile due to the variety of distribution shapes that can be achieved through alteration of the distribution parameters. Additionally, the Beta distribution is bounded over a specified interval. This is beneficial for variables that must exist within a certain range, such as θ (0 to 360 deg.) or δ (0 to 90 deg.). Definitions for statistical distributions and associated parameters can be found in Appendix A.

Figure 3-28 and Figure 3-29 show fitted Beta distributions alongside histograms of measured orientation data delineated into 2 deg. wide bins for θ and δ , respectively. Distribution parameters for each discontinuity set are provided in Table 3-4. In general, most distributions for θ and δ show some degree of asymmetry. For θ , discontinuity sets are slightly negatively skewed with the exception of set J_1 . Conversely, for δ , discontinuity sets are symmetric or positively skewed.

Correlation between θ and δ for each discontinuity set is shown in Figure 3-30. Correlation coefficients, ρ , were determined from linear regression of the orientation data (Table 3-4). In general, correlation was low between θ and δ ($\rho \sim \pm 0.1$). Set J_2 , however, showed a much stronger positive correlation between values ($\rho = 0.303$), nearly two to four times the magnitude of the other discontinuity sets.

Finally, Figure 3-31 shows fitted distributions alongside histograms of measured data for i_ϕ for each discontinuity set. Similarly, a Beta distribution was utilized to provide logical bounds on the datasets. In all cases, a lower bound $i_\phi = 0$ deg. was used corresponding to a completely smooth rock discontinuity surface. The upper bound was determined as the maximum value of i_ϕ measured for each discontinuity set using SplitFX, which ranged between 4 to 15 deg. (Table 3-4). The mean value of i_ϕ is approximately 2 to 3 deg. for all discontinuity sets (Table 3-4) and indicates rock discontinuities are relatively smooth and planar, which is consistent with field observations.

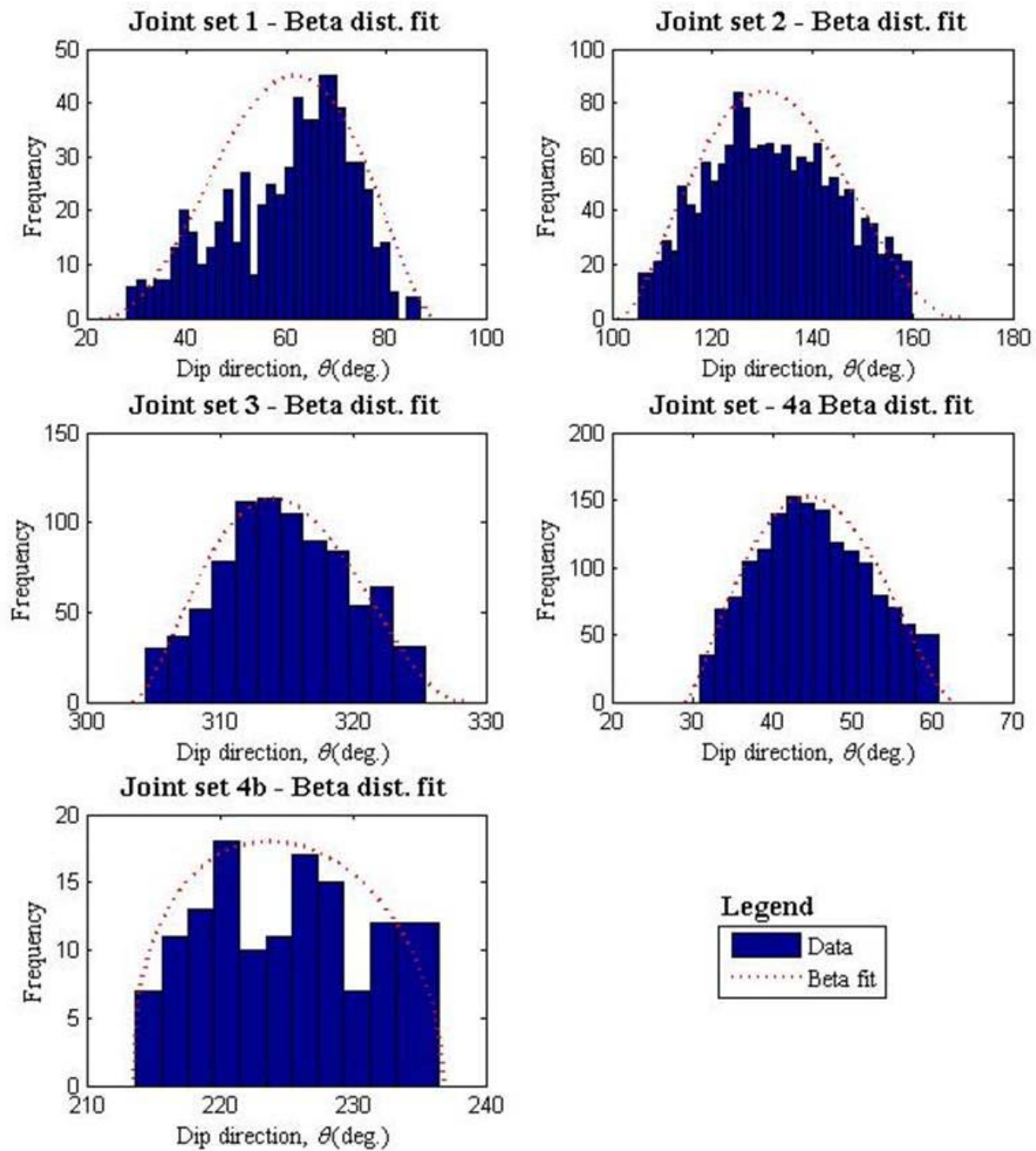


Figure 3-28. Histograms of measured dip direction (θ) showing Beta distribution fit.

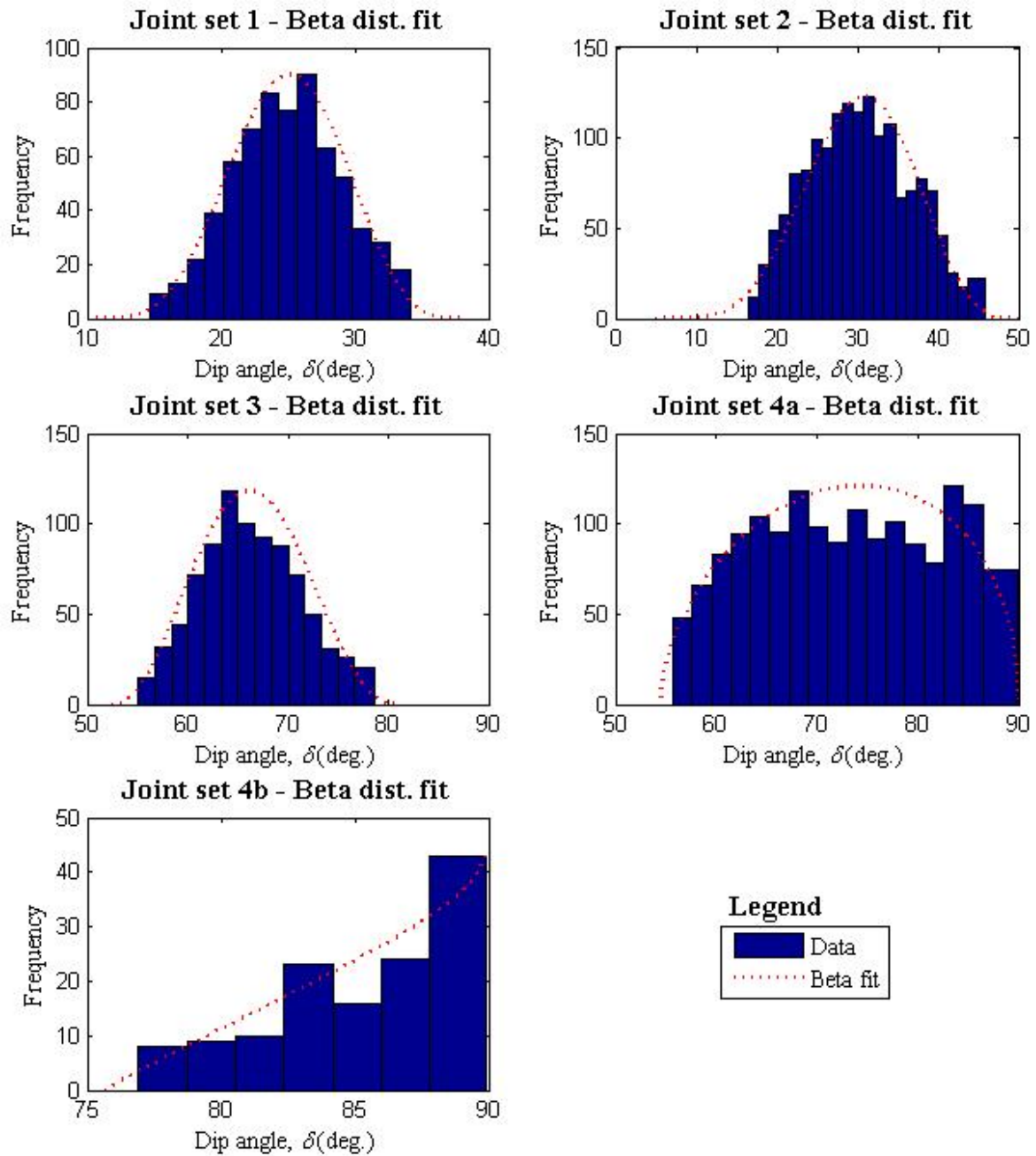


Figure 3-29. Histograms of measured dip angle (δ) showing Beta distribution fit.

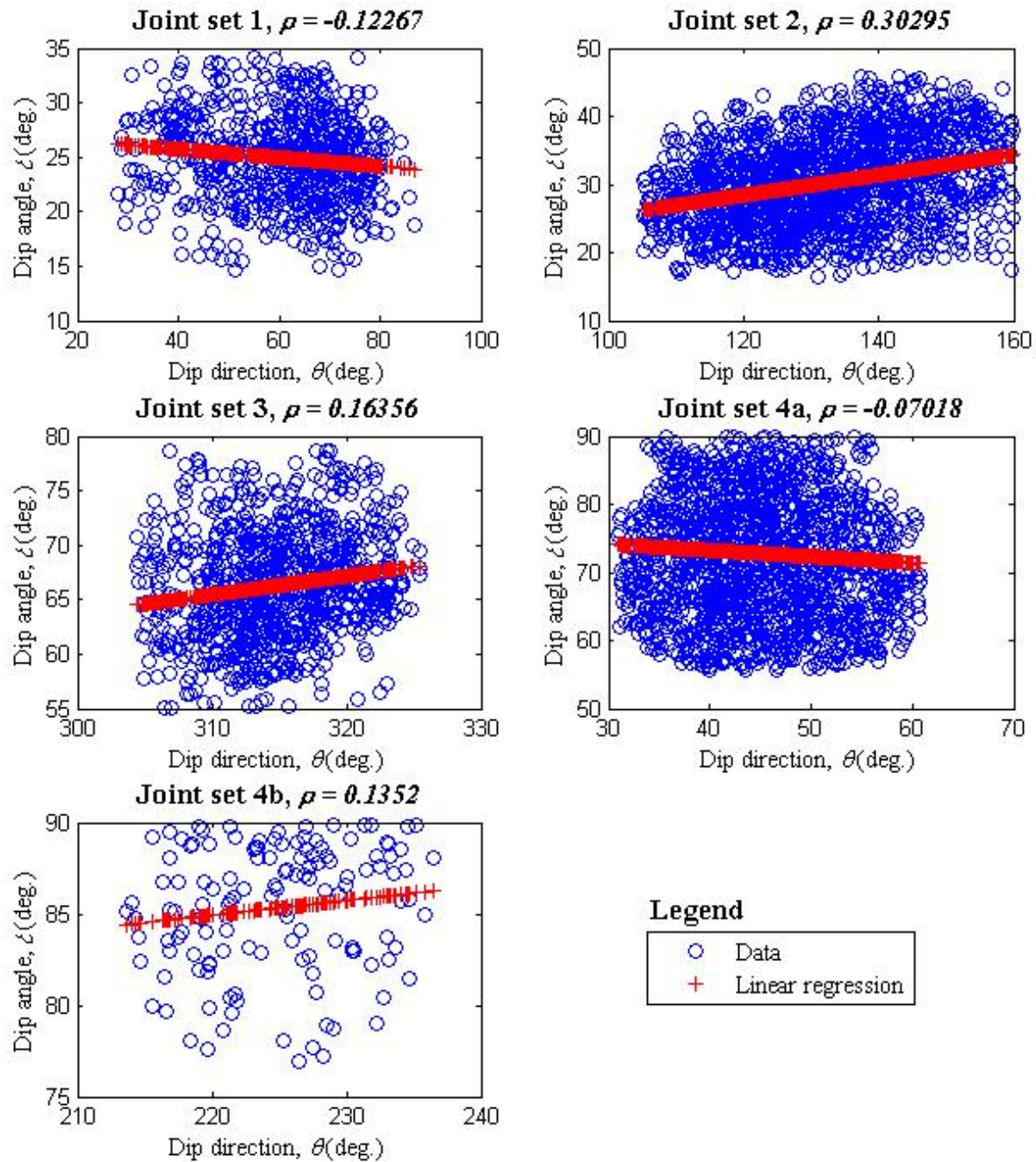


Figure 3-30. Correlation between dip direction (θ) and dip angle (δ).

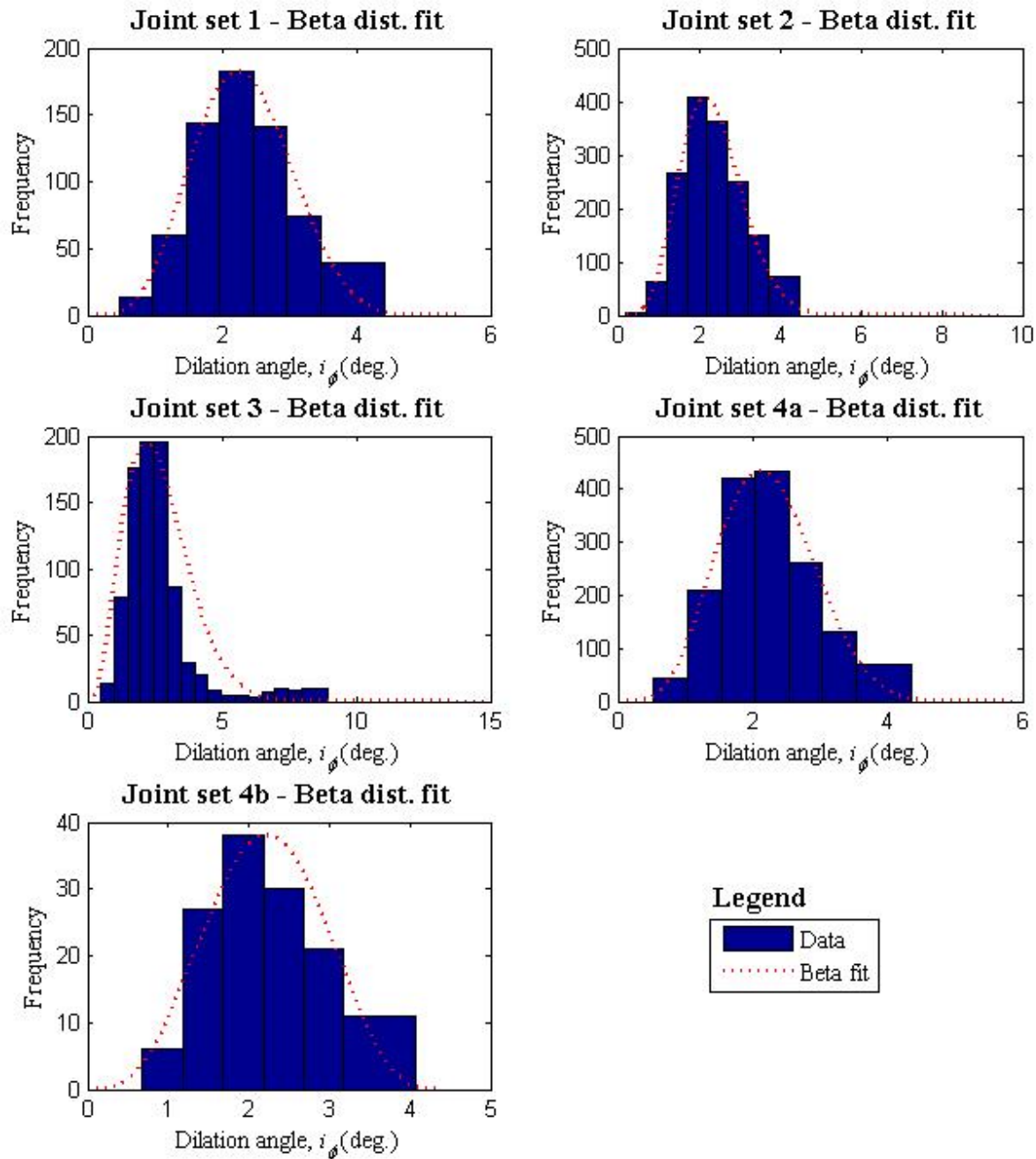


Figure 3-31. Histograms of measured dilation angle (i_ϕ) showing Beta distribution fit.

3.4 Summary

An extensive field investigation was carried out at the Spaulding Dam site in northern California. The purpose was to obtain prototype measurements of hydrodynamic pressures and displacements of 3D rock blocks within an actively eroding unlined spillway channel as well as high resolution rock mass data for statistical characterization of site variability. The former was

investigated through construction of two instrumented artificial rock blocks within existing block molds (i.e., locations where blocks once resided but have since been eroded), while the latter was achieved using terrestrial LiDAR scanning. Key points from the field investigations for block erodibility are summarized below.

3.4.1 Artificial rock blocks

- Two artificial rock blocks (Figure 3-14) were constructed into existing block molds (Figure 3-11) and instrumented with pressure and displacement sensors (Figure 3-12) to capture prototype data in an actively eroding spillway channel, which had previously never been attempted. Unfortunately, excessively dry climatic conditions in northern California for the past three years have resulted in minimal spills from the reservoir (Figure 3-24) yielding no meaningful data to date. The installations, however, show successful proof of concept and continue to operate should a future spill event occur.
- Before and after 3D surfaces of the artificial rock blocks were constructed using photogrammetric methods (Figure 3-16) and provided a convenient means to visualize block geometry (Figure 3-17) as well as perform measurements of block parameters, such as protrusion height (Figure 3-18 and Figure 3-19).

3.4.2 Rock mass discontinuity characterization

- High resolution terrestrial LiDAR scanning was performed at the Spaulding Dam No. 2 spillway to provide detailed, site-specific information for 3D rock structure and geometry in a relatively short period of time. SplitFX rock mass characterization software was utilized to extract nearly 5,000 measurements for rock discontinuity orientation (θ and δ) (Figure 3-27) as well as discontinuity dilation angle (i_ϕ). The large quantity of data allowed for statistical analysis of site rock mass parameters.
- Statistical analysis was performed to characterize the natural variability of rock mass parameters at the Spaulding site. Statistical parameters for the site are summarized in Table 3-4. Four dominant discontinuity sets (J_1 , J_2 , J_3 , J_{4a} , and J_{4b}) were identified with mean orientations of 060/25, 132/30, 315/66, 045/73 and 225/85, respectively. The near-vertical dipping fourth set was separated into two sub-sets, J_{4a} , and J_{4b} , to accommodate probabilistic block theory analysis presented in Chapter 6. Beta distributions were fitted to rock mass parameters θ , δ , and i_ϕ (Figure 3-28, Figure 3-29, and Figure 3-31) for each discontinuity set. Correlation coefficients (ρ) for θ and δ (Figure 3-30) were also determined for each discontinuity set. Statistical data was used to perform site-specific probabilistic analysis of 3D block erodibility using the methodology developed and applied in Chapter 6 to the Spaulding site.

Chapter 4. Hydraulic model experiment

A scaled physical hydraulic model was built to evaluate 3D block erodibility under controlled laboratory conditions. The experiments were performed in an open channel flume at the University of California's Richmond Field Station (RFS). An instrumented 3D block mold was constructed that could be rotated with respect to the flow direction to study the influence of discontinuity orientation on block erodibility over a range of flow scenarios. This section provides an overview of the experimental model and methodology as well as the results in terms of flow characteristics, block erodibility threshold, block removal mechanics and block hydrodynamic pressure statistics.

4.1 Overview

Evaluation of 3D block erodibility requires detailed knowledge regarding hydraulic loads applied to the block in both a spatial and temporal sense. Data of this nature, however, is extremely limited in current literature (e.g., Reinius (1986), Bollaert (2002), Frizell (2007), Federspiel et al. (2011), Duarte (2014)) and non-existent for non-cubic 3D rock blocks. Therefore, a key objective of this research was to develop a comprehensive, high resolution dataset that could offer improved understanding of the 3D block scour process. To this end, a scaled hydraulic model study was performed in an open channel flume at the University of California's RFS. An idealized model was constructed to produce 2D channel flow conditions that also loosely represented conditions at the Spaulding Dam No. 2 field site, an actively eroding spillway channel (Chapter 3). This was done, in part, to facilitate comparison of model data with prototype data collected from two instrumented artificial rock blocks installed in the

spillway channel. The advantage of the laboratory model is the ability to investigate a broad range of variables and flow scenarios not readily achievable in a field setting.

Major influences on 3D block stability are the orientations of discontinuities defining the block as well as the flow direction with respect to the block orientation. Accordingly, an instrumented 3D block mold was constructed that could be rotated with respect to the flow direction to study the influence of discontinuity orientation on block erodibility over a range of flow conditions. Each flow condition is characterized according to mean stream-wise (horizontal) and transverse (vertical) velocity components, turbulence intensity (representing the fluctuating flow velocity component), flow depth, flow rate, and velocity spectral density. The critical (threshold) mean flow velocity resulting in removal of the 3D block is determined for each flow condition. For experiments resulting in block removal, real-time analysis of hydrodynamic pressures around the block and of block displacements is performed to determine block failure mechanics. For experiments not resulting in block removal, a statistical description of hydrodynamic pressures around the block is made.

4.2 Methodology

4.2.1 Model development

Scaling

The Navier-Stokes equations provide a complete mathematical description of flow for incompressible Newtonian fluids and, accordingly, any scaled model should dimensionally abide by its governing equations. The conservation of momentum equations (top) and conservation of mass equation (bottom) comprise the Navier-Stokes equations and are expressed in vector format as:

$$\frac{\partial \mathbf{u}}{\partial t} + (\mathbf{u} \cdot \nabla) \mathbf{u} = -\frac{1}{\rho_w} \nabla P + \nu_w \nabla^2 \mathbf{u} + \mathbf{g} \quad (4-1)$$

$$\nabla \cdot \mathbf{u} = 0$$

where \mathbf{u} = velocity vector (u_x, u_y, u_z), t = time, P = pressure, ρ_w = density of water, ν_w = kinematic viscosity of water, \mathbf{g} = gravitational acceleration vector (0, 0, g), and ∇ = nabla operator ($\partial/\partial x, \partial/\partial y, \partial/\partial z$). The momentum equation is of particular interest as it provides a description of motion for a fluid parcel where the left side of the equation represents the fluid displacement terms for the parcel, while the right side of the equation represents the forces acting on the parcel. Non-dimensionalization of the momentum equation leads to identification of dimensionless parameters that can be used to guide scaling of hydraulic models. This is expressed as:

$$\frac{\partial \mathbf{u}^*}{\partial t^*} + (\mathbf{u}^* \cdot \nabla) \mathbf{u}^* = -\nabla P^* + \frac{\nu_w}{U \cdot L} \nabla^2 \mathbf{u}^* + \frac{\mathbf{g} \cdot L}{U^2} \mathbf{g}^* \quad (4-2)$$

where \mathbf{u}^* = non-dimensional velocity vector = \mathbf{u}/U , t^* = non-dimensional time = $t/(L/U)$, P^* = non-dimensional pressure = $P/(\rho_w U^2)$, \mathbf{g}^* = non-dimensional gravitational acceleration vector = \mathbf{g}/g , ∇ = nabla operator ($\partial/\partial x^*, \partial/\partial y^*, \partial/\partial z^*$) with non-dimensional lengths = $x^*, y^*, z^* = x/L, y/L,$

z/L . For these non-dimensional expressions, U and L are characteristic velocity and length scales, respectively, that can take on a variety of values, but typically equal the mean flow velocity and flow depth. Equation 4-2 may be recast in terms of the two dimensionless quantities, Reynolds number (Re) and Froude number (Fr), each of which is defined below:

$$Re = \frac{U \cdot L}{\nu_w} \quad (4-3)$$

$$Fr = \frac{U}{\sqrt{g \cdot L}} \quad (4-4)$$

The Reynolds number represents the ratio of inertial to viscous forces in the flow, while the Froude number represents the ratio of inertial to gravitational forces. Accordingly, the non-dimensional form of the momentum equation becomes:

$$\frac{\partial \mathbf{u}^*}{\partial t^*} + (\mathbf{u}^* \cdot \nabla) \mathbf{u}^* = -\nabla P^* + \frac{1}{Re} \nabla^2 \mathbf{u}^* + \frac{1}{Fr^2} \mathbf{g}^* \quad (4-5)$$

A scaled model should ideally ensure similarity between both Re and Fr numbers to reproduce prototype conditions. This is impossible, however, when like fluids are used (as is commonly done for physical hydraulic models using water) as a decrease in the length scale (L) to create a scaled model results in a decrease in Re , but an increase in Fr . Some processes, however, exhibit asymptotic behavior with increasing Re such that the condition of Re similarity can be relaxed. This is the case for form drag applied to particles. As long as the particle $Re > 1000$ (where the characteristic length scale (L) is related to a dominant length of the particle, e.g., particle diameter or particle protrusion) the forces applied to the particle will show proper similitude between model and prototype (Henderson 1966). Therefore, for the physical hydraulic model at the RFS, a Fr scale model was developed with sufficiently high Re values.

A Fr scale model is a practical choice for free surface flows as gravity is a main driver of flow conditions. For Fr scale models, secondary scale ratios that result are provided in Table 4-1.

Table 4-1. Prototype/model scale ratios for Fr scale model (after Henderson (1966)).

Mass	M_r	$= \rho_r \cdot L_r^3$
Length	L_r	$= L_r$
Velocity	U_r	$= L_r^{1/2}$
Time	$T_r = L_r \cdot U_r^{-1}$	$= L_r^{1/2}$
Discharge	$Q_r = U_r \cdot L_r^2$	$= L_r^{5/2}$
Force	$F_r = M_r \cdot L_r \cdot T_r^{-2}$	$= \rho_r \cdot L_r^3$
Pressure	$P_r = F_r \cdot L_r^{-2}$	$= \rho_r \cdot L_r$

Notes:

Subscript r indicates ratio of prototype (p) to model (m) (i.e., $L_r = L_p/L_m$).

The maximum flow velocity in the flume at RFS was $u_x \sim 3.0$ m/s which was achievable through construction of a locally steepened ramp within the flume channel (discussed in the following section). A prototype/model length scale ratio of $L_r = 10$ was chosen to allow

comparison with prototype conditions up to $u_x \sim 10$ m/s which is in the range of flow velocities anticipated at the Spaulding Dam No. 2 site.

Sizing of the 3D blocks was controlled by space requirements for sensors installed on the block mold. Accordingly, the blocks for the physical hydraulic model were approximately 5 to 10 times greater in volume when scaled to prototype size in comparison with the two artificial field blocks at the Spaulding site (Figure 3-14). This is not necessarily problematic, as much larger blocks have been eroded previously in the spillway (Figure 3-9). Block protrusion heights of, $h = 1.7$ mm and 4.5 mm above the channel bottom correspond to prototype protrusion heights 1.7 cm and 4.5 cm which are reasonable for rough unlined rock spillway channels. Additionally, using protrusion height as the characteristic length scale, allowed for particle Re numbers in the flume to be well over 1000, indicating drag forces on the blocks would be properly represented.

Although flow in the channel is predominantly gravity driven, flow through the narrow discontinuities bounding the 3D block is more analogous to pipe flow dominated by inertial and viscous forces. To minimize scale effects due to viscous forces in the model, it is required to maintain Re for the discontinuity as high as possible (where the characteristic length scale (L) is defined by the width of the discontinuity opening). This can be done by keeping L_r as small as possible (i.e., close to prototype scale), while also increasing the width of the discontinuity in the model by a factor of $L_r^{1/2}$ (to achieve Re similarity at the discontinuity opening). Typical discontinuity widths in the field are approximately 0.5 to 1 mm. Subsequently, a discontinuity width of approximately 2 mm was used in the model.

Despite minimizing L_r , prototype Re values in the channel (where the characteristic length scale (L) is defined by the flow depth) are still more than 30 times greater than those obtained in the model (i.e., $Re_r = L_r^{3/2} = 10^{3/2} = 32$). Accordingly, model flows tend to dampen high frequency (small length scale) turbulent eddies more so than in prototype settings due to the increased influence of viscosity. These eddies influence the amount of air entrained at the free surface boundary, which can explain the lack of air present in the experiments. This is only problematic in the sense that resonance phenomena attributed to high frequency pressure fluctuations and air entrainment in the rock discontinuities cannot be adequately represented in this model. This specific process was, however, beyond the scope of this research.

A final consideration for model development was to limit surface tension effects. This can be problematic in model flows with shallow flow depths. The Weber number (We) defines the ratio of inertial forces to surface tension and can be expressed as:

$$We = \frac{U^2 \cdot \rho_w \cdot L}{\sigma_w} \quad (4-6)$$

where σ_w = water surface tension. For values of $We > 12$ to 120, the influence of surface tension is negligible (Peakall & Warburton 1996). This was of concern for scenarios with lower flow rates where model flow depth, $d = 1$ to 3 cm (Table 4-9). However, due to the relatively large mean flow velocities, We values were sufficiently high in all cases.

Flume geometry

Experiments were conducted in a 30.5 m long by 0.86 m wide by 0.91 m deep flume with an overall slope = 0.01 (Figure 4-1). A wooden ramp was constructed within the flume to locally steepen the channel slope at the downstream end and increase flow velocity (Figure 4-2). The ramp contains three sections: 1) an upstream (approach) section, 2) a middle (transition) section,

and 3) a steep downstream section. The approach section has an upward slope with a relatively sharp transition to the middle section which has a mild slope = 0.02 (overall slope = 0.03 when accounting for the background flume slope = 0.01). The end of the middle section is curved to smoothly transition to the downstream section of the ramp. The downstream section of the ramp contains a rotatable block mold that housed a removable 3D tetrahedral rock block. The downstream channel slope = 0.21, making an overall slope = 0.22 at the block location. This slope was constant for all experiments and is comparable to the two instrumented blocks at the Spaulding Dam field site. Two rows of evenly spaced wooden baffle blocks were installed above the block mold (at the downstream end of the middle section) to increase the degree of turbulence at the block location. This also slightly reduced the mean flow velocity in the channel in the block vicinity. Baffles were removed for experiments where a lower degree of turbulence was desired. Figure 4-3 shows a 3D rendering of the as-built flume and ramp geometry with pertinent dimensions.

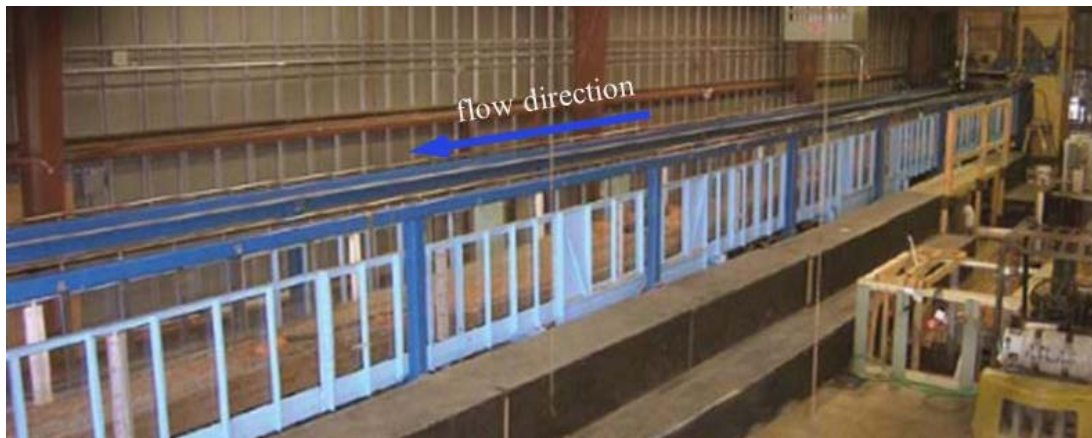


Figure 4-1. Flume at RFS (pre-ramp construction).



Figure 4-2. Ramp constructed inside flume at RFS.



Figure 4-4. 3D printed block mold with acrylic face (top left), installed in ramp (top right) and rotated at angles of 0, 60, 120, and 180 deg. (bottom left to right).

Table 4-2. Orientation^a of block/mold faces vs. mold rotation angle.

Rotation angle ψ (deg.)	Face 1 J_1 (deg.)	Face 2 J_2 (deg.)	Face 3 J_3 (deg.)	Face 4 f (deg.)
0	116/72	244/72	000/58	180/12
15	130/74	258/69	017/58	180/12
30	144/76	273/66	033/60	180/12
45	158/78	288/62	049/62	180/12
60	173/79	303/60	064/64	180/12
75	187/79	319/57	080/67	180/12
90	201/78	335/56	094/70	180/12
105	215/76	352/55	109/74	180/12
120	229/74	009/55	123/76	180/12
135	243/72	026/56	137/79	180/12
150	257/69	042/57	152/80	180/12
165	272/66	058/60	166/82	180/12
180	287/63	073/63	180/82	180/12

Notes:

^a Orientation given as dip direction (θ) / dip angle (δ).

Three tetrahedral shaped blocks were made with varying amount of protrusion height above the channel bottom (Table 4-3). Blocks were constructed from concrete and reinforced with fiberglass strands for added strength near block corners. Small, approximately 3 cm by 3 cm, stainless steel plates were added to the block faces directly opposite each proximity sensor for use as targets to determine discontinuity opening/block displacement. Edges of the block protruding from the mold were rounded with a sander to more closely resemble a natural block edge in the field.

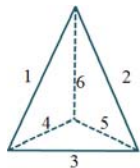
Table 4-3. Model block specifications.

Specification	Block 1	Block 2	Block 3
Weight (N)	5.358	4.956	4.674
Volume (cm ³)	232	224	209
Density (g/cm ³)	2.36	2.26	2.28
Protrusion, h (mm)	4.5	1.7	Flush
Edge type	Rounded	Rounded	Rounded
Orientation face 1 (deg.) ^{a, d}	see Table 4-3	see Table 4-3	see Table 4-3
Orientation face 2 (deg.) ^{a, d}	see Table 4-3	see Table 4-3	see Table 4-3
Orientation face 3 (deg.) ^{a, d}	see Table 4-3	see Table 4-3	see Table 4-3
Orientation face 4 – free face (deg.) ^{a, d}	180/12	180/12	180/12
Dimension 1 (mm) ^b	140.3	138.7	136.3
Dimension 2 (mm) ^b	140.2	138.9	136.7
Dimension 3 (mm) ^b	106.6	103.7	104.6
Dimension 4 (mm) ^b	106.7	104.4	103.3
Dimension 5 (mm) ^b	107.5	104.0	104.2
Dimension 6 (mm) ^b	131.2	130.0	127.0
Flow direction (deg) ^c	180	180	180

Notes:

^a Orientation given as dip direction (θ) / dip angle (δ).

^b Schematic for block dimensions:



^c Flow direction given as azimuth from North.

^d Face 1 defined by edges 1, 4, 6, face 2 defined by edges 2, 5, 6, face 3 defined by edges 3, 4, 5, and face 4 defined by edges 1, 2, 3.

4.2.2 Model instrumentation & data acquisition

The flume channel and block mold were instrumented with sensors to characterize flow conditions in the vicinity of the block as well as to record block displacements and measure dynamic pressures within the discontinuities bounding the block (Figure 4-5). The technical specifications for each sensor are provided in Table 4-4.

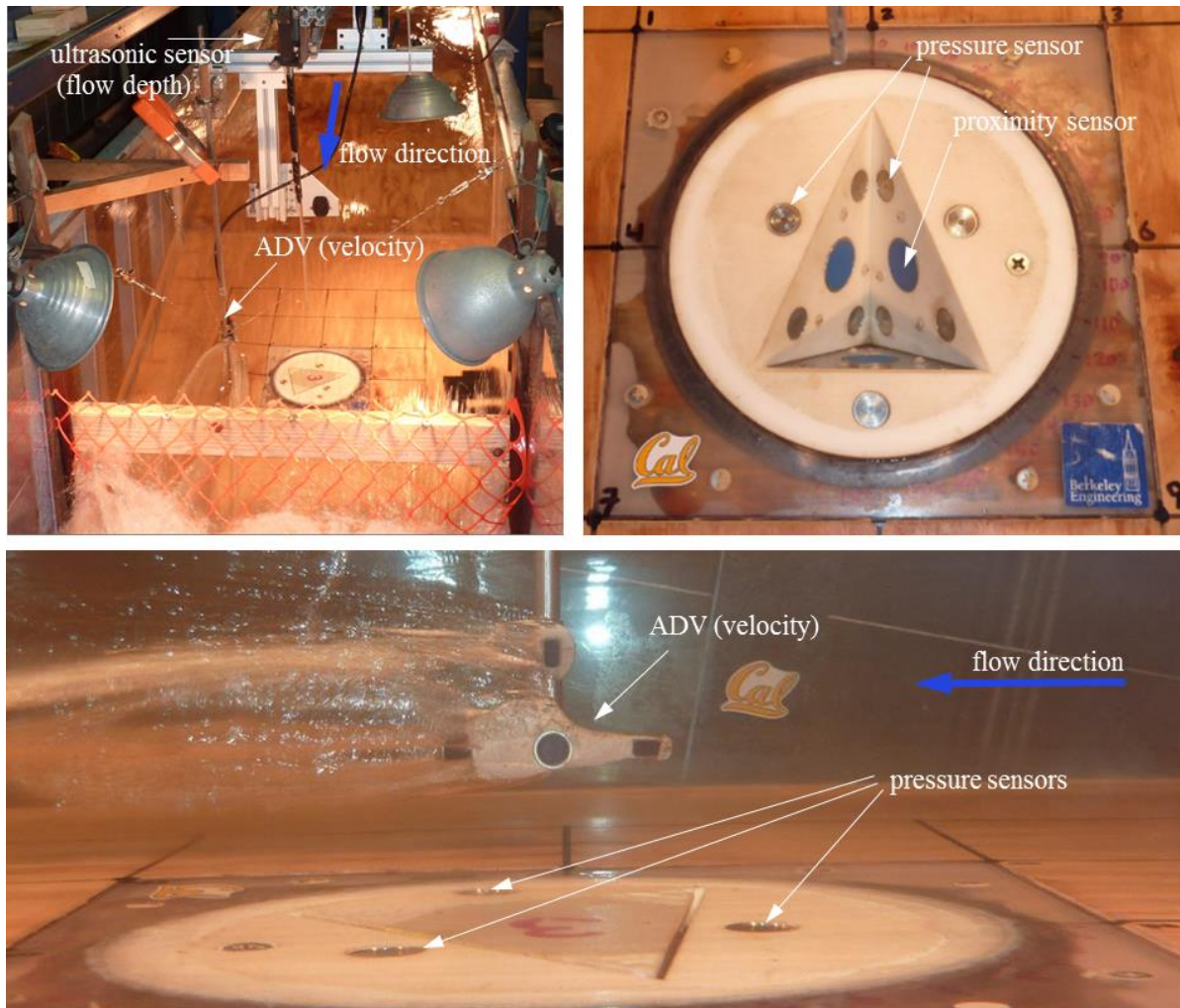


Figure 4-5. Instrumentation for flume and block mold.

For the block mold, 12 pressure transmitters (3 per block face) and 3 displacement (proximity) sensors (1 per block face, excluding the free face) were installed (Figure 4-5 – top right). Pressure sensors on the top face of the mold (i.e., on the channel bottom) were located near the center of each discontinuity opening. Sensor locations are shown in Figure 4-6. Both pressure and displacement sensors were calibrated to check their operational range. Displacement sensors compared well with manufacturer specifications, while pressure sensors showed some deviation, likely due to in-situ stresses in the block mold resulting from epoxying sensors into place. Revised coefficients to convert measured voltage to pressure were determined and are provided in Appendix B.

Schematic showing block mold sensor locations

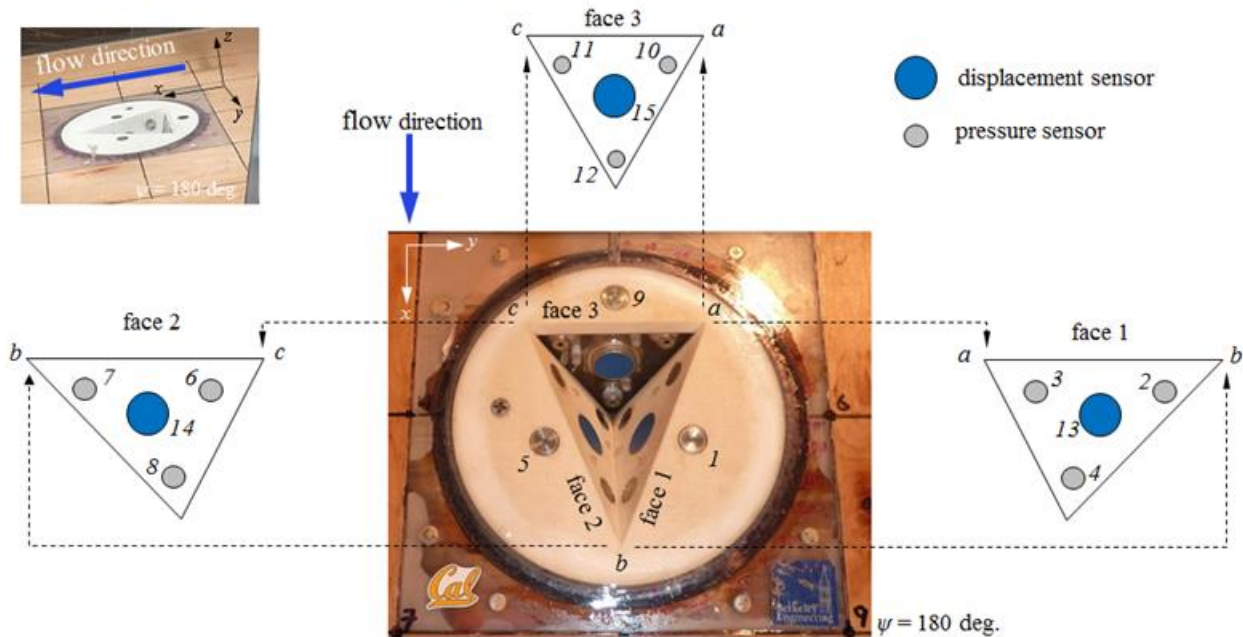


Figure 4-6. Location of pressure and displacement sensors on block mold.

The three component flow velocity vector in the channel was measured using an acoustic doppler velocimeter (ADV) (Figure 4-5 – bottom). A side-facing model was used to allow for a relatively close sensor position to the channel bed. Molding clay was added to streamline the ADV body and prevent formation of air pockets around sensor faces that could cause erroneous measurements. Additionally, a 0.3175 cm outside diameter (OD) acrylic pitot tube was installed to measure the average stream-wise velocity component at the channel bed.

Flow depth in the channel was measured using a conical beam, ultrasonic sensor. The sensor was installed directly above the block, perpendicular to the channel slope (Figure 4-5 – top left).

Data were acquired via a Campbell Scientific CR-3000 datalogger for pressure and displacement measurements, while a Toshiba Portege R705 laptop PC was used for ADV and flow depth measurements. ADV data were synchronized with pressure and displacement measurements using a pulse trigger mechanism from the CR-3000. Sampling occurred at a frequency = 100 Hz during experiments with pressure and displacement measurements and 200 Hz during experiments for flow characterization (i.e., ADV only). Program code for the CR3000 datalogger, used for data acquisition was developed using CRBasic Editor which is part of the Campbell Scientific's LoggerNet software package.

Table 4-4. Sensor technical specifications for physical hydraulic model.

Specification	Pressure	Displacement	Flow depth	Flow velocity
Make	Keller	SICK	Massa	Nortek
Model	PR-9FLY & PR-23Y ^a	IMA30-20BE1ZCOK	M-5000	Vectrino ^d
Type	Flush diaphragm	Inductive analog	Sonic (8 deg. conical beam)	Acoustic doppler velocimeter
Range	0 – 0.5 bar (gauge)	0 – 20 mm	0.1 – 1.0 m	≤ 4 m/s
Power	8 – 32 V DC	15 – 30 V DC	12 – 28 V DC	12 – 48 V DC
Output	0 – 5 V DC	4 – 20 mA	4 – 20 mA	0 – 5 V DC
Accuracy	± 0.0025 bar	± 0.1 mm	± 0.25% of meas. value	± 0.5% of meas. value
Sampling freq.	100 Hz	100 Hz	50 Hz ^c	100 & 200 Hz ^e
No. of sensors	12 (3/face)	3 (1/face) ^b	1	1

Notes:

^a PR-9FLY sensors installed on faces 1 and 2, while smaller PR-23Y sensors installed on face 3 due to space limitations.

^b Not installed on free block face.

^c Boxcar averaged every 100 samples.

^d Sensor operated with Plus firmware upgrade

^e Sampling frequency = 100 Hz during runs with pressure and displacement measurements and 200 Hz during runs for flow characterization.

4.2.3 Model testing strategy

Several test configurations were used to characterize the block response to channel flows (Table 4-5). Four main variables were monitored within the realm of this study. These included:

- *Block orientation, ψ* – Block orientation with respect to flow direction was varied by rotating the block mold in 15 deg. increments between $\psi = 0$ to 180 deg. It was not necessary to do a full 360 deg. rotation due to block symmetry.
- *Turbulence intensity, T_u* – High and low turbulence conditions were studied. Turbulence was generated with the addition of seven staggered baffles upstream of the block. Degree of turbulence was quantified using turbulence intensity which relates the root mean square (RMS) of the vertical velocity component (u'_z) to the mean horizontal (stream-wise) flow velocity component (u_x).
- *Block protrusion, h* – Three block protrusion heights of $h = 0.0$ mm (flush), 1.7 mm and 4.5 mm were examined (model scale).
- *Flow velocity, \mathbf{u} (u_x, u_y, u_z)* – Nine flow velocities, corresponding to nine different flow rates, Q_1 to Q_9 , were used. To generate the different flow rates, three pumps were used with a maximum capacity of 0.3 m³/s (0.1 m³/s each). A variable speed controller was

used with one of the pumps such that any flow rate between 0 to 0.3 m³/s could be achieved (model scale).

In general, two types of experiments were conducted. One was to determine the block erodibility threshold. For these experiments, the discharge was increased incrementally (from Q_1 to Q_9) for periods of approximately 5 minutes until the block failed. If block displacements appeared to be continually increasing, the run length was extended. The other type was to determine statistical distributions of the dynamic pressures on the block faces. For these tests, only four flow rates (Q_1 , Q_3 , Q_6 and Q_9) were tested. If a block had previously failed at a lower flow rate, a rod was placed on top of the block to hold the block in place such that high flow rates could be realized.

Table 4-5. Physical hydraulic model testing matrix.

Rotation angle	Turb. intensity	Block protrusion ^a	Flow rate
0 deg.	High	Flush	$Q_1 - Q_9$
		1.7 mm	$Q_1 - Q_9$
		4.5 mm	$Q_1 - Q_9$
	Low	Flush	$Q_1 - Q_9$
		1.7 mm	$Q_1 - Q_9$
		4.5 mm	$Q_1 - Q_9$
15 deg.	High	Flush	$Q_1 - Q_9$
		1.7 mm	$Q_1 - Q_9$
		4.5 mm	$Q_1 - Q_9$
	Low	Flush	$Q_1 - Q_9$
		1.7 mm	$Q_1 - Q_9$
		4.5 mm	$Q_1 - Q_9$
.	.	.	.
.	.	.	.
.	.	.	.
180 deg.	High	Flush	$Q_1 - Q_9$
		1.7 mm	$Q_1 - Q_9$
		4.5 mm	$Q_1 - Q_9$
	Low	Flush	$Q_1 - Q_9$
		1.7 mm	$Q_1 - Q_9$
		4.5 mm	$Q_1 - Q_9$

Notes:

^a Values provided in model scale.

4.3 Results

Results from the physical hydraulic model are presented as follows:

- *Flow characterization* – Determination of key flow parameters used to provide a description of flow conditions in the vicinity of the block and in the channel.

- *Block erodibility threshold* – Examination of critical flow condition(s) resulting in block removal.
- *Block removal mechanics* – Qualitative and quantitative description of block removal modes and characteristics due to hydraulic loading from channel flows.
- *Block hydrodynamic pressure statistics* – Statistical characterization of pressure measurements recorded on block faces.

4.3.1 Flow characterization

Flow characteristics for the nine flow rates were examined for both high and low turbulence cases. The following parameters were determined to provide a general description of flow in the vicinity of the block and in the channel:

- Flow velocity (\mathbf{u}), flow depth (d), and flow rate (Q)
- Turbulence intensity (T_u)
- Froude number (Fr)
- Reynolds number (Re)
- Velocity power spectral density (S_{xx})

A 2D grid was laid out on the downstream section of the ramp around the block mold (Figure 4-7). Measurements and analysis were performed at multiple locations along the channel centerline and adjacent to the block mold. Model experiments for flow characterization were done without the block mold, which was replaced by an acrylic insert that was flush with the channel bottom. Specifically, measurements were made at locations 0, 2, 4, 5, 8, A, B and C. Locations 2, 5, 8, A, B, and C are along with channel centerline with location 5 representing the location of the block. Location 4 is adjacent to location 5 and was used as the primary ADV location during experiments with the block so as not to interfere with flow around the block. Location C (not shown in Figure 4-7) is on the upstream end of the ramp, 17.0 m from start of the flume (Figure 4-3) to provide flow conditions in the approach section. Location 0 was used as a reference location where a 0.3125 cm outer diameter pitot tube was installed during both flow characterization and block erodibility model tests.

Flow profiles over the entire ramp for flow rate Q_9 for both low (no baffle blocks) and high (with baffle blocks) turbulence cases are shown in Figure 4-8. Photos of flow profiles for all discharges are shown in Appendix C. The presence of the ramp, in all cases, created a backwater effect upstream of the ramp, forcing a transition from subcritical to supercritical flow where the approach section meets the middle section. For low turbulence conditions, flow remained supercritical past the block location. The presence of the baffles in the high turbulence flows created a similar backwater effect in the transition section for lower discharges resulting in the formation of a hydraulic jump, shifting flow back to a subcritical regime (see flow rates Q_1 to Q_3 in Appendix C). Beyond the baffles, flow again returned to supercritical conditions due to the steep downstream slope. For the larger discharges (Q_4 to Q_9), flow contained enough energy in the transition section to remain supercritical over the baffles.

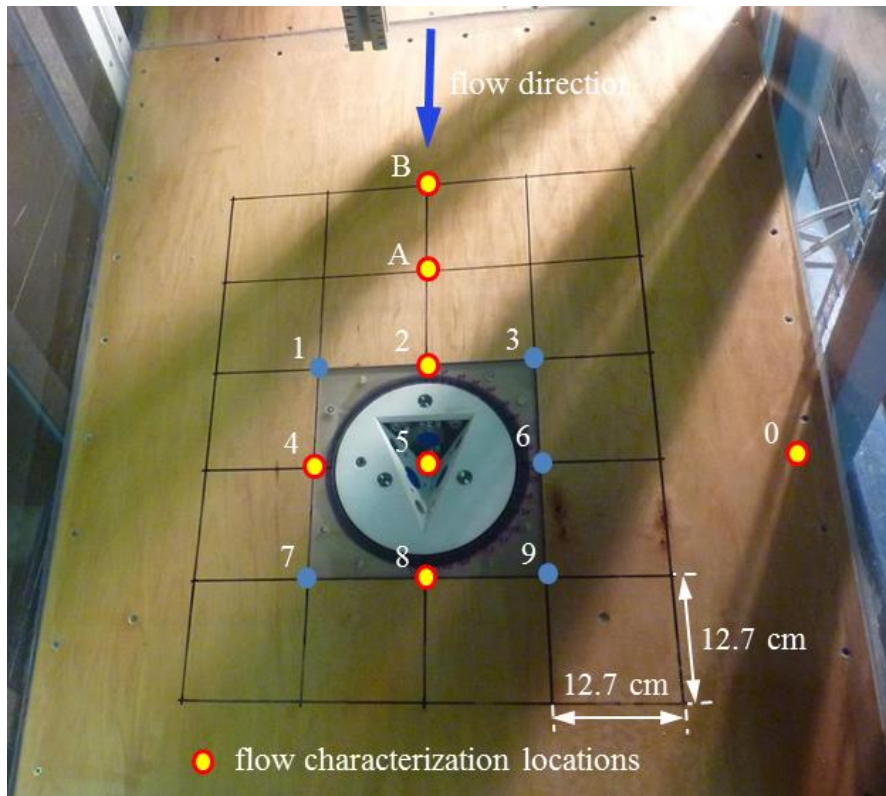


Figure 4-7. 2D grid showing locations for flow characterization (location C not shown).

Figure 4-8 also shows closer detail of flow conditions in the vicinity of the block for Q_9 . The location of the block is denoted by a piece of black tape on the flume wall just left of the sign indicating the run name. Other photos showing a close-up view of flow conditions in the block region can be found in Appendix C for all discharges. In low turbulence flows, the water surface profile appeared relatively smooth and constant. In high turbulence flows, however, the water surface profile is higher and considerably more variable (as anticipated).

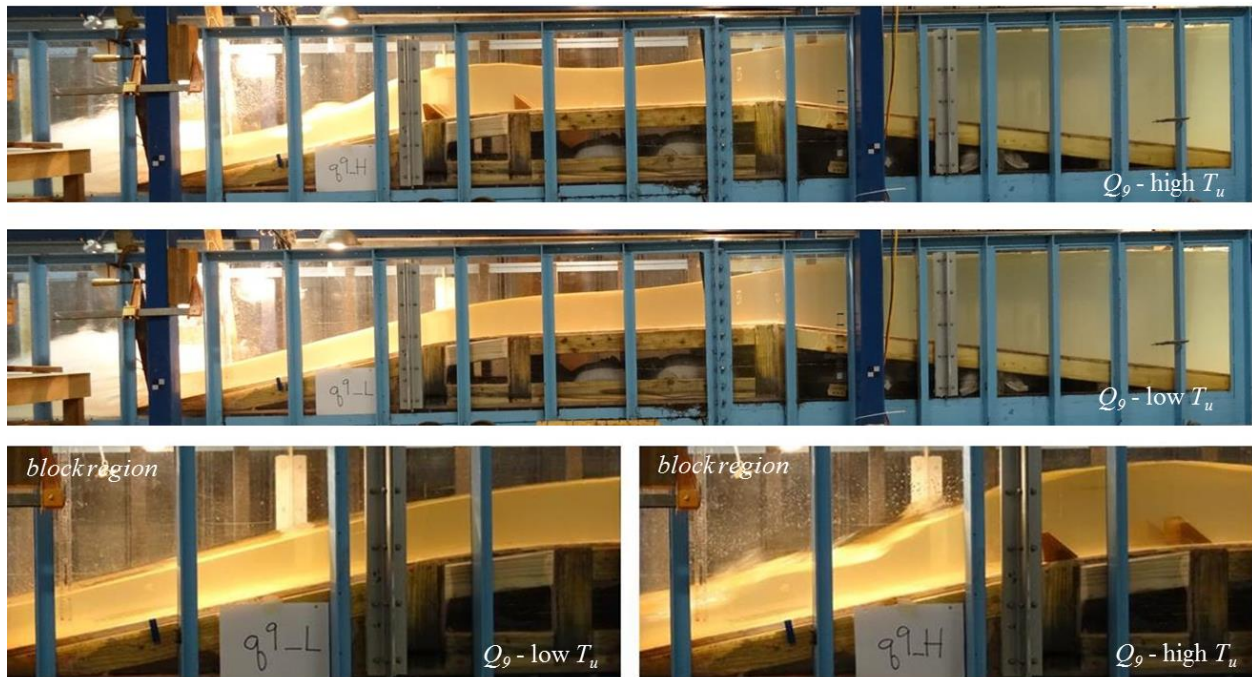


Figure 4-8. Flow profiles for high (top) and low (middle) turbulence cases for flow rate Q_9 . Close-ups of flow profiles in block region are also shown for low (bottom left) and high (bottom right) turbulence cases.

Flow velocity, flow depth, and flow rate

Flow velocity measurements for flow characterization were made using a Nortek Vectrino ADV with a sampling frequency of 200 Hz. Data were collected for the 3D components of the velocity vector, $\mathbf{u} = (u_x, u_y, u_z)$ at each location (except C) from three different ADV heights = 1.1 cm, 2.6 cm and 5.6 cm (Figure 4-9) (model scale). Additionally, a 0.3175 cm outer diameter (OD) acrylic pitot tube was placed at the channel bottom to determine the horizontal velocity (u_x) at the bed.

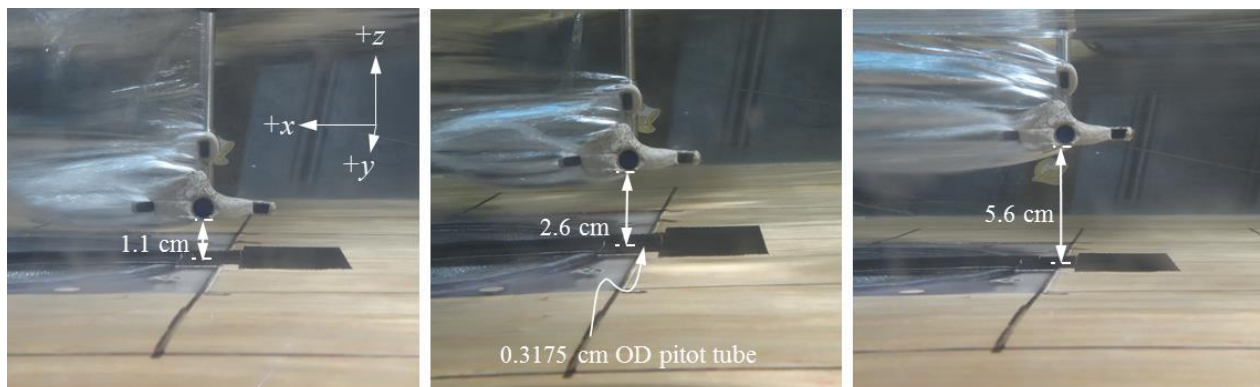


Figure 4-9. Measurement of flow velocity using ADV at location 2 at heights of 1.1 cm (left), 2.6 cm (center), and 5.6 cm (right) (model scale). Also note pitot tube on channel bottom.

ADV time series data was filtered using a phase-space despiking algorithm developed by Goring & Nikora (2002), modified by Wahl (2003) and included as part of the WinADV processing software (Wahl 2000). Filtered data was subsequently processed to determine mean, fluctuating (root mean square (RMS)), and maximum instantaneous velocity components.

Of principal interest are velocity components in the horizontal (x) and vertical (z) directions as conditions in the flume are predominantly 2D channel flow. Accordingly, Table 4-6 presents mean velocity components (u_x and u_z) for each flow scenario. Values provided for each flow condition are an average of ADV measurements taken at the three height positions. Results are provided at the block location only (location 5), however, results for the other locations (2, 4, 8, A, B, and C) can be found in Appendix C. Values for the RMS and maximum instantaneous velocity components are provided in Table 4-7 and Table 4-8, respectively.

Mean horizontal flow velocities at the block location (location 5) ranged from $u_x = 6.59$ m/s to 8.57 m/s for the high turbulence cases, while those for the low turbulence cases were approximately 10% higher with $u_x = 7.38$ m/s to 9.35 m/s (scaled prototype values). For Q_1 , the flow depth was too shallow for ADV operation and only pitot tube data were collected. Accordingly, u_x values were calculated from correlations made using pitot tube measurements and ADV measurements for discharges greater than Q_1 . For each discharge, a correlation factor was determined by dividing the flow velocity measured with the pitot tube (on the channel bottom) by the mean velocity determined by the ADV. Factors were relatively constant between discharges and were averaged to determine a correlation factor for Q_1 (Appendix C). Velocity values for Q_1 measured from the pitot tube were divided by the correlation factors for Q_1 to provide an estimate of the mean horizontal velocity away from the channel bottom boundary.

Mean vertical flow velocities at the block location ranged from $u_z = -0.54$ m/s to -1.00 m/s for high turbulence cases, while those for low turbulence cases were nearly the same with $u_z = -0.65$ m/s to -0.92 m/s (scaled prototype values). Flow depths for Q_1 to Q_3 were too shallow to facilitate accurate ADV measurements. All values for u_z are negative indicating the resultant velocity vector is orientated slightly downward towards the channel bed, which is consistent with flow acceleration in the downstream direction (i.e., gradually varied, non-uniform flow conditions). This is supported by increasing mean horizontal velocity observed between location B (most upstream) and location 8 (most downstream) along the channel centerline (Appendix C).

Table 4-6. Mean horizontal (u_x) and vertical (u_z) velocity components at block location.

Par.	Loc.	Turb.	Flow velocity (m/s) ^a								
			Q_1	Q_2	Q_3	Q_4	Q_5	Q_6	Q_7	Q_8	Q_9
u_x	5	High	2.08 ^b	2.10	2.22	2.38	2.55	2.59	2.67	2.70	2.71
			<i>6.59</i>	<i>6.65</i>	<i>7.00</i>	<i>7.52</i>	<i>8.07</i>	<i>8.19</i>	<i>8.45</i>	<i>8.54</i>	<i>8.57</i>
		Low	2.33 ^b	2.44	2.51	2.64	2.71	2.76	2.84	2.92	2.96
			<i>7.38</i>	<i>7.70</i>	<i>7.93</i>	<i>8.35</i>	<i>8.58</i>	<i>8.72</i>	<i>8.97</i>	<i>9.23</i>	<i>9.35</i>
u_z	5	High	-	-	-	-0.17	-0.21	-0.24	-0.29	-0.31	-0.31
			<i>-0.54</i>	<i>-0.68</i>	<i>-0.77</i>	<i>-0.90</i>	<i>-0.98</i>	<i>-1.00</i>			
		Low	-	-	-	-0.21	-0.22	-0.23	-0.25	-0.28	-0.29
			<i>-0.65</i>	<i>-0.69</i>	<i>-0.73</i>	<i>-0.80</i>	<i>-0.89</i>	<i>-0.92</i>			

Notes:

^a Scaled prototype values in *italics*.

^b Calculated from correlation factors.

Table 4-7. RMS horizontal (u'_x) and vertical (u'_z) velocity components at block location.

Par.	Loc.	Turb.	Fluctuating flow velocity (m/s) ^a								
			Q_1	Q_2	Q_3	Q_4	Q_5	Q_6	Q_7	Q_8	Q_9
u'_x	5	High	-	0.11 <i>0.34</i>	0.16 <i>0.51</i>	0.14 <i>0.45</i>	0.13 <i>0.42</i>	0.14 <i>0.46</i>	0.15 <i>0.47</i>	0.17 <i>0.54</i>	0.18 <i>0.58</i>
		Low	-	0.05 <i>0.14</i>	0.05 <i>0.16</i>	0.05 <i>0.15</i>	0.04 <i>0.13</i>	0.04 <i>0.14</i>	0.04 <i>0.13</i>	0.04 <i>0.13</i>	0.05 <i>0.14</i>
u'_z	5	High	-	-	-	0.16 <i>0.50</i>	0.15 <i>0.48</i>	0.16 <i>0.51</i>	0.16 <i>0.52</i>	0.19 <i>0.59</i>	0.20 <i>0.63</i>
		Low	-	-	-	0.07 <i>0.23</i>	0.07 <i>0.21</i>	0.07 <i>0.21</i>	0.06 <i>0.20</i>	0.06 <i>0.20</i>	0.06 <i>0.20</i>

Notes:

^a Scaled prototype values in *italics*.Table 4-8. Maximum instantaneous horizontal (u^+_x) and vertical (u^+_z) velocity components at block location.

Par.	Loc.	Turb.	Maximum flow velocity (m/s) ^{a,b}								
			Q_1	Q_2	Q_3	Q_4	Q_5	Q_6	Q_7	Q_8	Q_9
u^+_x	5	High	-	2.62 <i>8.30</i>	2.95 <i>9.33</i>	2.86 <i>9.05</i>	2.99 <i>9.44</i>	3.16 <i>9.99</i>	3.19 <i>10.08</i>	3.40 <i>10.74</i>	3.39 <i>10.72</i>
		Low	-	2.62 <i>8.29</i>	2.71 <i>8.57</i>	2.82 <i>8.90</i>	2.89 <i>9.13</i>	2.92 <i>9.23</i>	3.03 <i>9.57</i>	3.10 <i>9.80</i>	3.14 <i>9.94</i>
u^+_z	5	High	-	-	-	0.51 <i>1.61</i>	0.44 <i>1.39</i>	0.45 <i>1.42</i>	0.52 <i>1.64</i>	0.61 <i>1.93</i>	0.69 <i>2.19</i>
		Low	-	-	-	0.08 <i>0.26</i>	0.09 <i>0.29</i>	0.08 <i>0.25</i>	0.06 <i>0.19</i>	0.02 <i>0.06</i>	0.03 <i>0.09</i>

Notes:

^a Scaled prototype values in *italics*.^b Measured at ADV height = 1.1 cm (lowest height, closest to block)

Flow depths for each flow condition are presented in Table 4-9. Flow depth was measured using a Massa M-5000 ultrasonic sensor positioned above the channel perpendicular to the channel bed, except for at location C where a ruler was used to manually record measurements. Results are provided at the block location only (location 5), however, results for the other locations (2, 4, 8, A, B, and C) can be found in Appendix C. Values ranged from $d = 10$ cm to 1.22 m (scaled prototype values) for high turbulence cases. For low turbulence scenarios, flow depths were slightly less, $d = 10$ cm to 1.1 m, resulting from higher flow velocities due to the absence of the baffle blocks. Along the channel centerline, from location B to location 8, flow depth decreased with increased distance due to flow acceleration over the downstream ramp section (Appendix C).

Table 4-9. Mean flow depth (d) at block location

Par.	Loc.	Turb.	Flow depth (cm) ^a								
			Q_1	Q_2	Q_3	Q_4	Q_5	Q_6	Q_7	Q_8	Q_9
d	5	High	1.0	2.8	4.3	6.7	7.3	8.1	9.4	11.2	12.2
			<i>10</i>	<i>28</i>	<i>43</i>	<i>67</i>	<i>73</i>	<i>81</i>	<i>94</i>	<i>112</i>	<i>122</i>
		Low	1.0	2.2	3.0	5.4	6.7	7.3	8.7	10.3	11.0
			<i>10</i>	<i>22</i>	<i>30</i>	<i>54</i>	<i>67</i>	<i>73</i>	<i>87</i>	<i>103</i>	<i>110</i>

Notes:

^a Scaled prototype values in *italics*.

Flow rates for each flow condition are presented in Table 4-10. Three pumps with a maximum theoretical capacity of 0.3 m³/s (0.1 m³/s each) were used to generate the different flows. A variable frequency controller was used with one of the pumps such that any flow rate between 0 to 0.3 m³/s could be achieved. For the variable frequency pump, a frequency setting of 20 Hz corresponds to the initial condition just before flow begins (i.e., 0 m³/s), while a setting of 40 Hz represents full pump capacity (i.e., 0.1 m³/s).

Table 4-10. Mean flow rate (Q) and pump frequency for RFS flume.

	Flow scenario								
	Q_1	Q_2	Q_3	Q_4	Q_5	Q_6	Q_7	Q_8	Q_9
Flow rate (m ³ /s) ^a	0.021	0.050	0.074	0.128	0.156	0.179	0.216	0.262	0.284
	<i>6.6</i>	<i>15.9</i>	<i>23.5</i>	<i>40.5</i>	<i>49.5</i>	<i>56.7</i>	<i>68.4</i>	<i>82.7</i>	<i>89.8</i>
Total pump frequency (Hz) ^b	25	32	40	65	72	80	105	112	120

Notes:

^a Scaled prototype values in *italics*.^b Pump 1 = 40 Hz, pump 2 = 40 Hz, pump 3 = 20 to 40 Hz. Q_1 to Q_3 (pump 3 only), Q_4 to Q_6 (pump 1 + pump 3), Q_7 to Q_9 (pump 1 + pump 2 + pump 3).

Discharge values are calculated from mean stream-wise flow velocity (u_x) and average flow depth (d) values for locations 2, 4, 5, 8, A, and B using both high and low turbulence conditions. As indicated in Figure 4-10, the calculated values are slightly lower than the theoretical capacity of the pumps, but are in agreement with those determined from previous researchers using the flume.

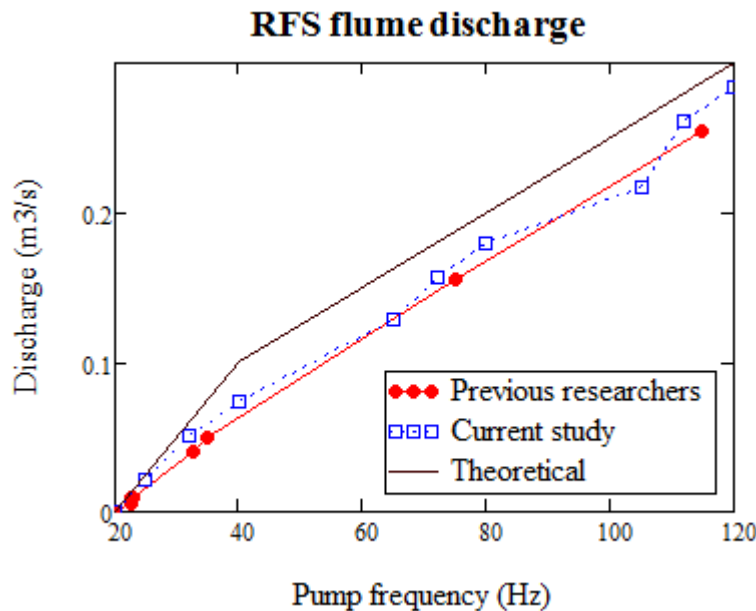


Figure 4-10. Flow rate through flume at RFS as a function of pump frequency (model scale).

Turbulence intensity

The level of turbulence in the channel was quantified using turbulence intensity (T_u), which represents the relative presence of the fluctuating component of the flow velocity. For this study, high and low turbulence conditions were examined. Turbulence intensity relates the root mean square (RMS) of the vertical velocity component (u'_z) to the mean horizontal (stream-wise) flow velocity component (u_x) and is calculated as:

$$T_u = \frac{u'_z}{u_x} \quad (4-7)$$

Results for T_u are presented in Table 4-11 for the block location (location 5). Additional results for the other locations (2, 4, 8, A, B, and C) can be found in Appendix C. Values provided for each flow are calculated using an average of ADV measurements for u_x and u'_z taken at the three height positions. For low turbulence flow, values were relatively small and ranged from 2.2 % to 2.8 %. In these cases, increased flow rate resulted in lower T_u values as the relative influence of the bed roughness diminished with higher flow depths. The addition of the baffle blocks to the channel for high turbulence cases significantly increased T_u as values ranged from 6.0 % to 7.4 %. Comparison of high and low turbulence profiles can be seen in Figure 4-8, Figure 4-11 and Appendix C.

Note that T_u values for discharges Q_1 to Q_3 could not be determined as the entire ADV was not submerged at these flows and the vertical velocity component could not be reliably measured. It is anticipated, however, T_u values for these low flows would likely become similar between the high and low turbulence cases as the flow rate decreased. As indicated in Table 4-11 for the low turbulence case, $T_u = 2.2$ % at Q_9 , but increased gradually to $T_u = 2.8$ % at Q_4 . This is likely a result of increased presence from roughness in the channel bottom boundary as the flow depth decreased. Accordingly, it is anticipated T_u values for the low turbulence case would be slightly higher for discharges Q_1 to Q_3 . A similar trend is not observed for high

turbulence flows. It is anticipated, however, T_u values may slightly decrease, as the distance from the baffles to the block location is relatively longer (compared to the flow depth) as the flow rate decreases. Over this distance, flow accelerates and turbulent eddies are “stretched” which acts to dampen the turbulent nature of the flow, thus decreasing T_u .

Table 4-11. Turbulence intensity (T_u) at block location.

Par.	Loc.	Turb.	Turbulence intensity ^a (%)								
			Q_1	Q_2	Q_3	Q_4	Q_5	Q_6	Q_7	Q_8	Q_9
T_u	5	High	-	-	-	6.6%	6.0%	6.2%	6.1%	6.9%	7.4%
		Low	-	-	-	2.8%	2.5%	2.5%	2.2%	2.2%	2.2%

Notes:

^a T_u values provide for vertical fluctuating velocity component (u'_z), however values corresponding to u'_x and u'_y can be found in Appendix C.



Figure 4-11. Low ($T_u = 2.2\%$, left) and high ($T_u = 7.4\%$, right) turbulence conditions for Q_9 looking upstream from downstream end of steep ramp section.

Froude number

Table 4-12 presents values of the Froude number at the block location (location 5). Values were calculated using the mean stream-wise velocity (u_x) from Table 4-6 and the mean flow depth (d) from Table 4-9. For low turbulence conditions, $Fr = 2.8$ to 7.4 . Values for high turbulence conditions were approximately 10 % lower due to the decrease in channel flow velocity associated with the installation of the baffle blocks. In both cases, highest Fr values were witnessed for lower flow rates (Q_1 to Q_3) due to the relatively shallow flow depths associated with these model runs. All values of Fr at the block location were significantly greater than unity (i.e., $Fr > 1$) indicating flows were supercritical for all discharges and

dominated by inertial forces and are comparable to Fr values directly downstream of the Spaulding Dam No. 2 spillway crest. This is similar to the other locations (2, 4, 8, A, and B) which also indicate flow was supercritical in the downstream section of the ramp (Appendix C).

Values of Fr upstream of ramp at location C are also provided in Table 4-12. Contrary to the block location, values of Fr in the ramp approach section were significantly less than unity (i.e., $Fr < 1$) indicating flow was subcritical and therefore must transition to supercritical further downstream, in the middle section of the ramp.

Table 4-12. Froude number (Fr) at block location and upstream of ramp.

Par.	Loc.	Turb.	Froude number (dimensionless)								
			Q_1	Q_2	Q_3	Q_4	Q_5	Q_6	Q_7	Q_8	Q_9
Fr	5	High	6.6	4.0	3.4	2.9	3.0	2.9	2.8	2.6	2.5
		Low	7.4	5.3	4.6	3.6	3.4	3.3	3.1	2.9	2.8
	C	High/ Low	0.04	0.1	0.1	0.2	0.2	0.2	0.2	0.2	0.3

Reynolds number

Table 4-13 presents values of Re in the channel at the block location (location 5). Values were calculated using the mean stream-wise velocity (u_x) from Table 4-6 and the mean flow depth (d) from Table 4-9 as the characteristic length scale. In both high and low turbulence cases, Re values ranged from approximately $2.0 \cdot 10^4$ to $3.0 \cdot 10^5$. Of additional interest is the particle Re number where the characteristic length scale is defined by the block protrusion height (h). Based on the criteria from Henderson (1966), particle $Re > 1,000$ is required to ensure form drag forces on the block are consistent between model and prototype. As indicated in Table 4-13, all values of particle Re at the block location were sufficiently large to represent the form drag on the block. Additional values for Re at the other locations (2, 4, 8, A, B, and C) can be found in Appendix C.

Table 4-13. Reynolds number (Re) at block location.

Par.	Loc.	Turb.	Reynolds number $\cdot 10^4$ (dimensionless)								
			Q_1	Q_2	Q_3	Q_4	Q_5	Q_6	Q_7	Q_8	Q_9
Re	5	High	2.0	5.6	9.0	15.0	17.7	19.9	23.9	28.7	31.3
		Low	2.2	5.0	7.1	13.5	17.1	19.0	23.3	28.5	30.9

Table 4-14. Particle Reynolds number (Re) at block location.

Par.	Loc.	Turb.	Particle Reynolds number $\cdot 10^4$ (dimensionless)								
			Q_1	Q_2	Q_3	Q_4	Q_5	Q_6	Q_7	Q_8	Q_9
Re (Block 1)	5	High	0.79	0.80	0.84	0.90	0.97	0.98	1.01	1.02	1.03
		Low	0.89	0.92	0.95	1.00	1.03	1.05	1.08	1.11	1.12
Re (Block 2)	5	High	0.30	0.30	0.32	0.34	0.36	0.37	0.38	0.38	0.39
		Low	0.33	0.35	0.36	0.38	0.39	0.39	0.40	0.42	0.42

Velocity power spectral density

Power spectral density (S_{xx}) plots for velocity fluctuations measured with the ADV at the block location (location 5) at a height of 1.1 cm (model scale) are provided in Figure 4-12 and Figure 4-13 for both high and low turbulence scenarios, respectively. Velocity values represent the magnitude of the horizontal (u_x) and vertical (u_z) velocity components minus the mean value and thus correspond to the fluctuating component of the velocity field. For Q_1 , no ADV data was collected, while for Q_2 and Q_3 , only the horizontal component of flow velocity was used. ADV velocity time series data (sampled at 200 Hz) were filtered using a Butterworth low pass filter with a cutoff frequency of 100 Hz. The number of samples used for each scenario was 108,000 (corresponding to a 9 minute run length), which were discretized into blocks of 1024 samples. A Hamming window function was applied to each block with an overlap of 50% between adjacent blocks. Power spectral density values were averaged over all sample blocks, and normalized by the square of the standard deviation (i.e., the variance, σ^2) of the velocity data for each flow scenario.

The power spectral density shows the relative strength of velocity fluctuations distributed over a frequency domain. The frequency of velocity fluctuations is inversely related to the size of turbulent eddies in the flow field. As indicated in Figure 4-12, flows with a high degree of turbulence show a prominent spike in S_{xx} between approximately 2 to 4 Hz (0.6 to 1.3 Hz scaled prototype values) which results from the presence of the baffles in the channel. This peak is less notable at the lower flow rates (Q_3 , and particularly Q_2) which supports the hypothesis presented in the turbulence intensity section above that the turbulent nature of these flows may be more closely related to runs performed in the low T_u flow condition. Common turbulent spectrum power law values are also shown for reference. High frequency spectra exhibit a -5/3 slope (particularly for flows Q_4 to Q_9) which is the well known Kolmogorov power law for the inertial subrange (Kolmogorov 1941). A -1 power law is also presented which has been shown by some to represent the energy production subrange (e.g., Kader & Yaglom (1991), Katul et al. (1995), Singh et al. (2010)).

For the low T_u flows (Figure 4-13), a large amount of energy is contained in the low frequency range with no significant peaks in spectral density to indicate the presence of a predominant fluctuating component of the velocity field. The non-conformance to the -5/3 Kolmogorov power law in higher frequency spectra potentially indicates an inefficient transfer of energy from the inertial subrange to smaller length scale eddies. This could be associated with a lack of eddies in the viscous subrange, that serve to dissipate energy from larger structures in the flow field, due to low T_u conditions.

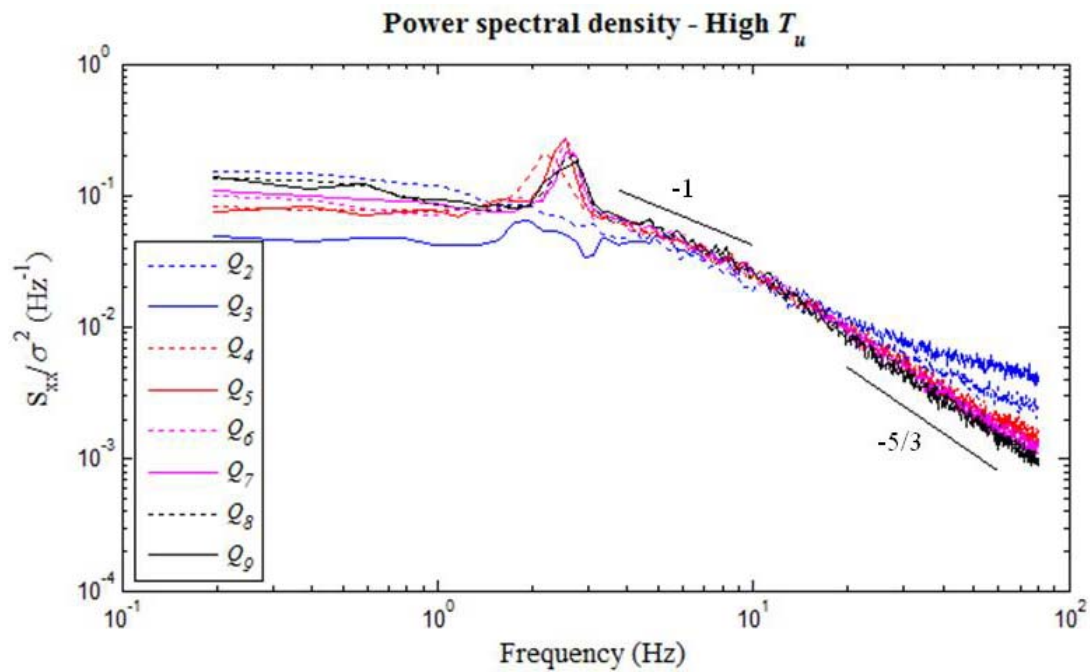


Figure 4-12. Normalized power spectral density of velocity fluctuations for high turbulence flow conditions (model scale).

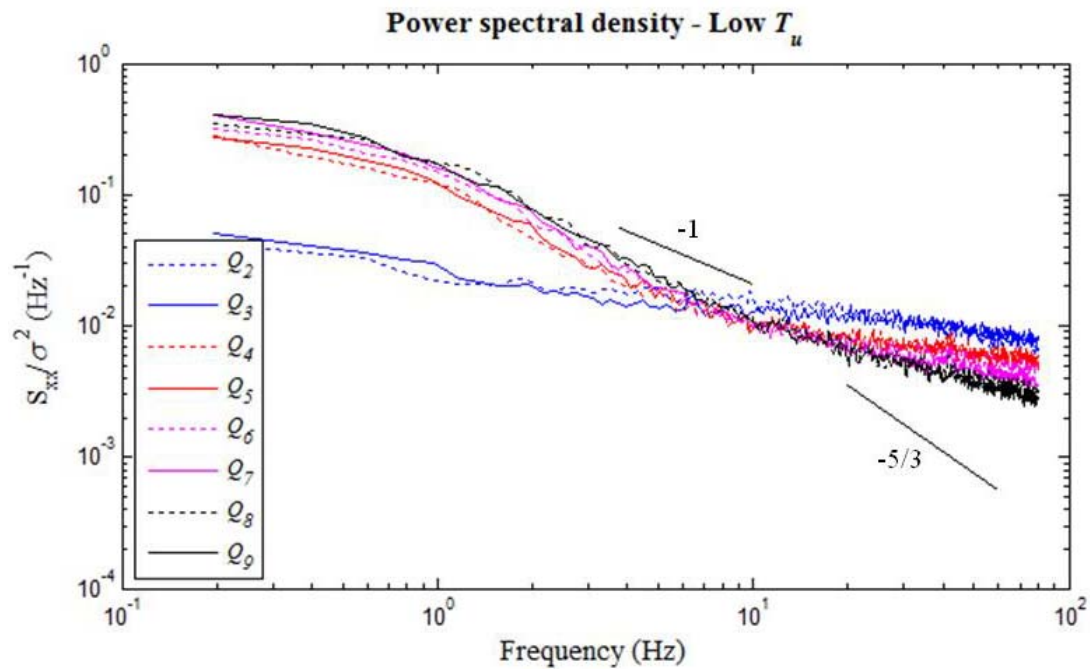


Figure 4-13. Normalized power spectral density of velocity fluctuations for low turbulence flow conditions (model scale).

4.3.2 Block erodibility threshold

The influence of 3D discontinuity orientation on block erodibility was examined over a range of flow conditions. The critical conditions resulting in block removal (i.e., block erodibility threshold) are provided as a function of:

- Block mold rotation angle (ψ)
- Mean stream-wise flow velocity (u_x)
- Turbulence intensity (T_u)
- Block protrusion height (h)

Results regarding each of these variables are discussed below. Numerical results for the block erodibility threshold are available in Appendix D.

Block mold rotation angle & mean flow velocity

The observed block erodibility thresholds for Block 1 and Block 2 are presented in Figure 4-14 and Figure 4-15, respectively, for both the high and low T_u cases. Note that Block 3 (flush) did not fail under any tested conditions and therefore no individual figure was generated. To determine the block erodibility threshold for each case, the discharge was increased incrementally (from Q_1 to Q_9) for periods of approximately 5 minutes until the block failed. If block displacements appeared to be continually increasing, the run length was extended until the block failed or displacements leveled off (and the flow rate could be increased). Occasionally, the block failed between two flow rates (i.e., while flow was ramping up from previous to next discharge). For those cases, a range values are provided (indicated by a line connecting two bounding data points).

The threshold flow velocity values are provided in prototype scale and correspond to mean stream-wise flow velocity presented in Table 4-6 at location 5 for each flow rate (Q_1 to Q_9). Some blocks failed prior to establishment of full Q_1 discharge in which case an estimate for u_x was made using pitot tube measurements taken at the reference location (location 0, Figure 4-7) during the run. This was accomplished using correlation factors between pitot tube measurements taken simultaneously at location 0 and location 5 during the flow characterization runs (Appendix C). For equal comparison with ADV data used to determine u_x at higher flow rates, a second correlation factor was applied based on pitot tube and ADV measurements also taken simultaneously at location 5 during flow characterization runs.

As indicated in Figure 4-14 and Figure 4-15, the threshold condition for incipient motion of both blocks is highly dependent on the orientation of the block with respect to the flow direction. Both blocks display a maximum resistance to scouring when $\psi = 0$ deg. and a minimum when $\psi = 75$ deg. In the low T_u case, Block 2 could not be eroded under any discharge when $\psi = 0$ and 15 deg. This configuration corresponds to a geometry where the downstream face of the block mold is fairly steep making removal of the block kinematically more difficult. Additionally, the block profile protruding into flow is narrow resulting in a minimal drag force applied to the block. This is opposed to a block with a very wide profile perpendicular to the flow direction, corresponding to $\psi = 75$ deg., where the drag force is maximum. At this rotation, the intersection of the two downstream block mold faces provides a shallower sliding path for the

block, making it kinematically easier to remove. As such, the block erodibility threshold in this location is a minimum.

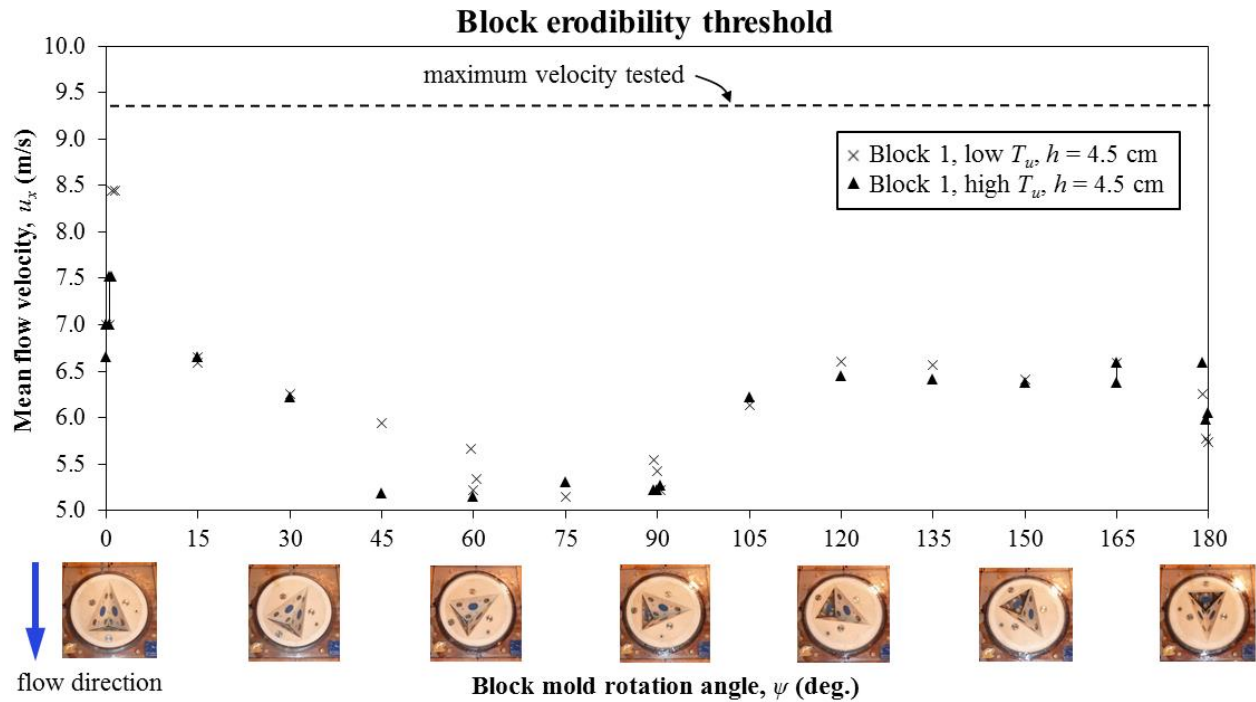


Figure 4-14. Block 1 erodibility threshold as a function of block orientation with respect to flow direction, ψ , for high and low T_u flow conditions.

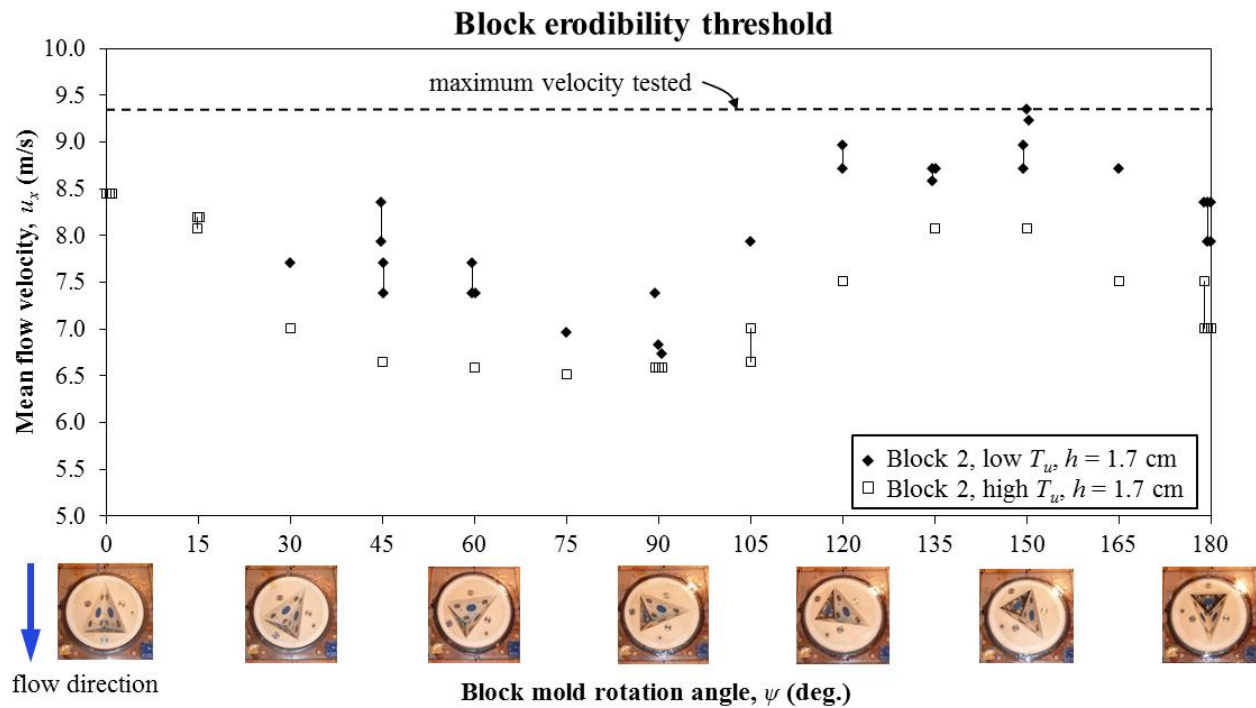


Figure 4-15. Block 2 erodibility threshold as a function of block orientation with respect to flow direction, ψ , for high and low T_u flow conditions.

Turbulence intensity

Results for high and low T_u conditions are also presented in Figure 4-14 and Figure 4-15 for Block 1 and Block 2, respectively. For reference, T_u values for the low turbulence case were approximately 2.5 %, while for the high turbulence case they were approximately 7.0 % (Table 4-11). For Block 1, increased turbulence appears to have a minimal effect on block erodibility threshold with the exception of when the mold rotation angle, $\psi = 0$ deg. At $\psi = 0$ deg., a reduction in the critical u_x value of over 10 % is observed between the peak threshold when the turbulence level is increased through the addition of the baffle blocks. Other block orientations, however, tend to yield similar threshold conditions for both the high and low T_u cases.

For Block 2, the block erodibility threshold decreased relatively evenly across the range of block orientations for high T_u flow conditions. In general, the reduction in critical u_x was approximately 10 % which was consistent with $\psi = 0$ deg. for Block 1. For block rotations $\psi = 75$ deg. and 90 deg., the reduction in block erodibility threshold between turbulence levels was not as evident.

The relative lack of response in block erodibility threshold to T_u for Block 1, as well as for the rotations of $\psi = 75$ deg. and 90 deg. for Block 2, can potentially be related to the low flow rate at which failure occurred for these runs. For these runs (with the exception of, $\psi = 0$ deg. for Block 1), failure occurred at Q_2 or less. Accordingly, T_u values for high and low turbulence cases were likely similar for these runs (as discussed in the Flow characterization results section above), which would suggest similar block threshold values. The evaluation of increased turbulence on block erodibility threshold was therefore limited to higher discharge runs (i.e., Q_3 to Q_9), which were predominantly obtained from Block 2. As mentioned above, the reduction in the critical mean flow velocity to remove Block 2 was approximately 10 % when the turbulence intensity was increased from approximately 2.5 % to 7.0% for these cases. This is a particularly important result as it suggests that velocity alone is poor indicator of incipient motion.

Block protrusion

Results for block erodibility threshold as a function of block protrusion height (h) are presented in Figure 4-16 and Figure 4-17 for the low and high turbulence scenarios, respectively. Three separate blocks were tested with $h = 4.5$ cm (Block 1), 1.7 cm (Block 2) and 0.0 cm (Block 3 – flush) (scaled prototype values) as a function of block mold rotation angle.

For both the high and low T_u flow conditions, a higher block protrusion height results in a lower block erodibility threshold. The reduction was slightly more pronounced for the low T_u case (~ 25 %) versus the high T_u case (~ 15 %) between Blocks 1 and 2. This outcome was anticipated due to the increased drag force associated with Block 1 being more exposed in the flow field. This agrees with other testing performed by Frizell (2007) for hydraulic jacking of concrete slabs in spillway channels. Similar to the case for increased turbulence intensity, increased block protrusion appears to result in a nearly uniform reduction in critical mean velocity across the range of block orientations.

For a block flush with the surrounding channel bottom (Block 3) with similar joint openings to the other two blocks, no removal occurred under any tested flow conditions.

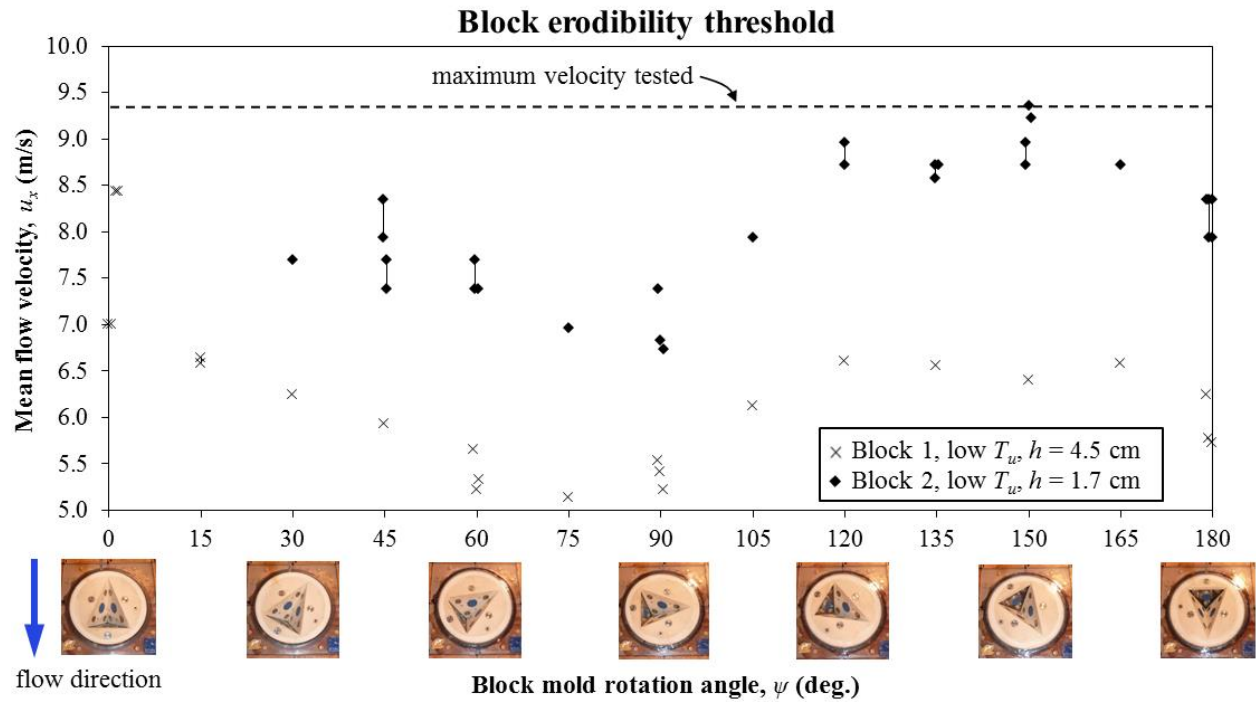


Figure 4-16. Block erodibility threshold as a function of block orientation with respect to flow direction (ψ) for varying block protrusion height, low T_u flow condition.

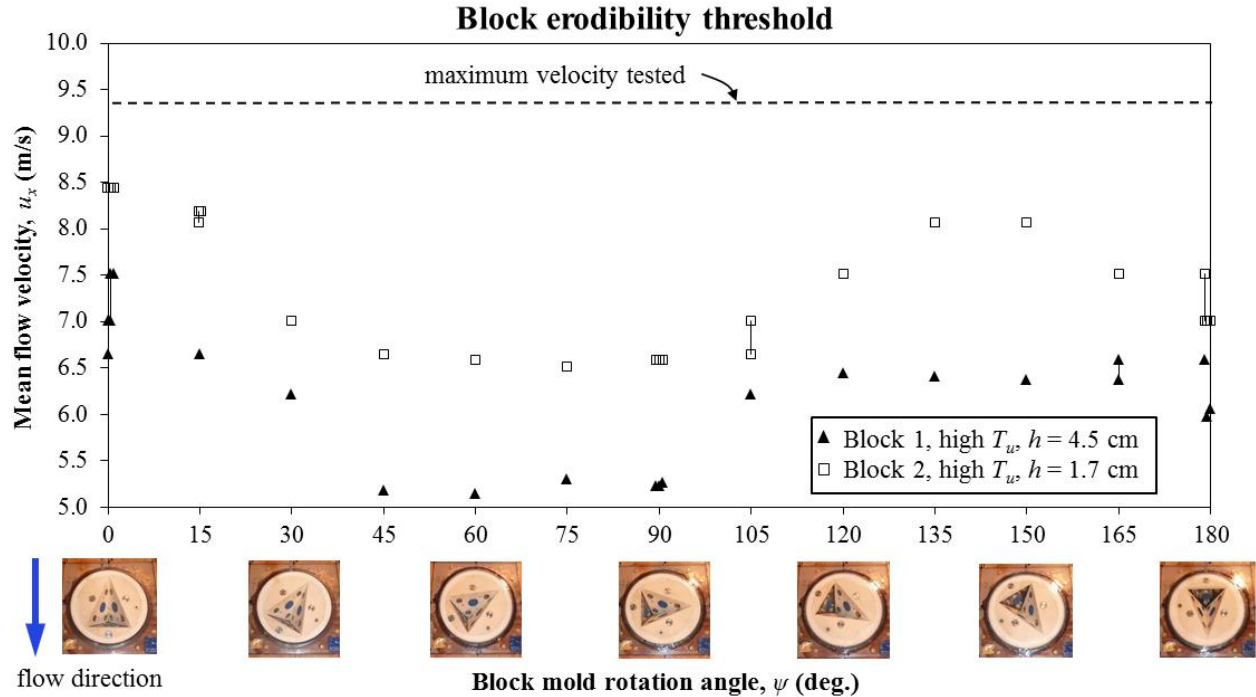


Figure 4-17. Block erodibility threshold as a function of block orientation with respect to flow direction (ψ) for varying block protrusion height, high T_u flow condition.

4.3.3 Block removal mechanics

Real-time data from experiments resulting in block removal were analyzed to both quantitatively and qualitatively examine block removal modes and flow characteristics leading to erosion due to hydraulic loading. In all, 76 runs were conducted that resulted in block removal, 34 of which occurred under steady-state conditions. Blocks eroded during unsteady flow conditions (i.e., during periods where flow was ramping up between discharges) were not analyzed due to uncertainty regarding flow parameters at the time of block removal. In general, three distinctive block behaviors were observed:

- Block response 1 – Gradual block displacement with consistent direction
- Block response 2 – Gradual block displacement with variable direction
- Block response 3 – Dynamic block displacement with variable direction

Block response was a function of kinematic constraints associated with the orientation of the block mold as well as flow conditions around the block. Typical experiments highlighting each block response are presented below. A summary table and figures for all tests analyzed are provided in Appendix E. Unless otherwise noted, *values are presented in prototype scale*.

Block response 1 – Gradual block displacement with consistent direction

Block orientations with a relatively low kinematic resistance to block movement in the general downstream direction largely resulted in gradual displacement response in a consistent direction until removal, for both high and low T_u flow conditions. A “low” kinematic resistance refers to a block with a shallow dipping downstream face or shallow plunging line of intersection between two block faces such that the block can easily slide in the downstream direction (further discussion regarding block kinematics is presented in Chapter 5).

Figure 4-18 shows total displacement time-series for Block 2 from its original starting position under low T_u conditions for Q_4 discharge for $\psi = 180$ deg. As indicated, the migration of the block from its original position occurs very gradually over a period of nearly 300 s with individual displacements occurring at a very small scale, $O(\sim 0.001 \text{ mm})$. As the block was further exposed above the channel bottom, the rate of displacement increased until finally the block was removed. Spatial distribution of block position can be seen in Figure 4-19. Initial block position was at the origin but, over the length of the run, moved directly downstream along the line of intersection between faces 1 and 2.

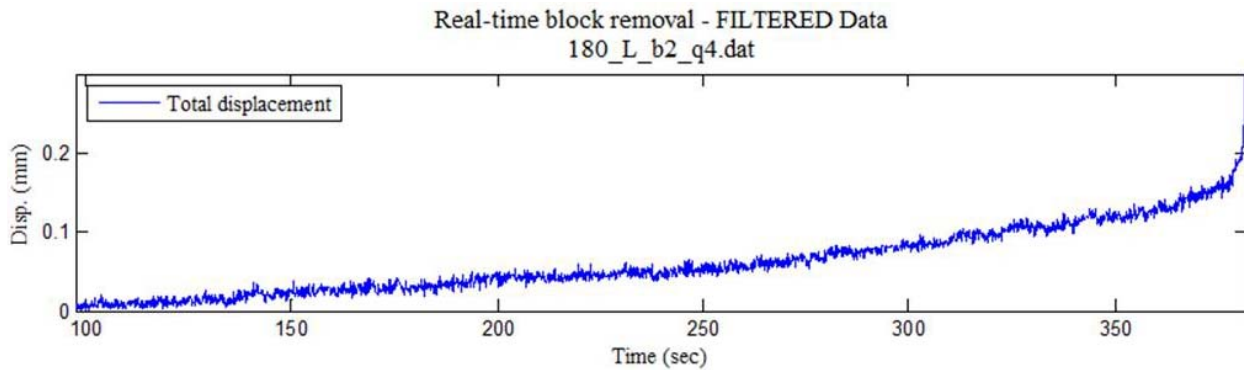


Figure 4-18. Response 1 – block displacement time-series showing gradual increase in total displacement magnitude until removal for $\psi = 180$ deg., low T_u , and Q_4 .

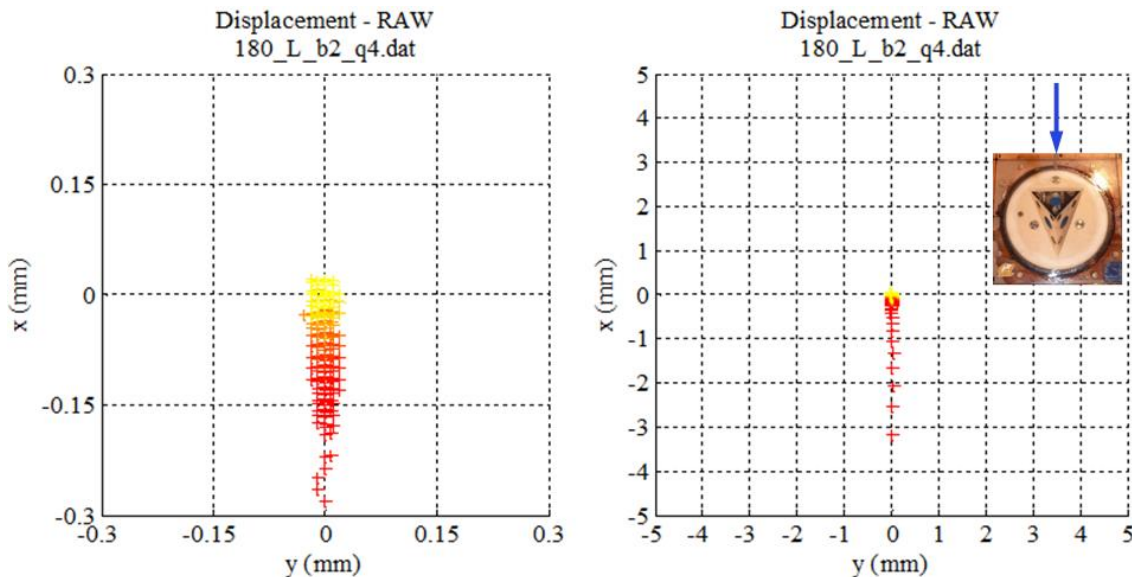


Figure 4-19. Response 1 – spatial distribution of instantaneous block position for $\psi = 180$ deg., low T_u , and Q_4 (close-up view on left). Markers colored yellow to red with increasing time. Block movement along the line of intersection (\mathbf{i}_{12}) of face 1 and face 2. Plot axes are swapped to correspond to flume coordinates.

A stereonet showing great circles corresponding to faces 1, 2 and 3 of the block as well as the orientation of the instantaneous displacement vector (i.e., the vector from the initial to current block position) is presented in Figure 4-20. Early displacement orientations (yellow markers) tended to be more variable, while subsequent orientations (red markers) became more focused at the upward intersection of block faces 1 and 2, denoted as \mathbf{i}_{12} . This indicates the kinematic mode of failure for Block 2 was 2-plane sliding on faces 1 and 2.

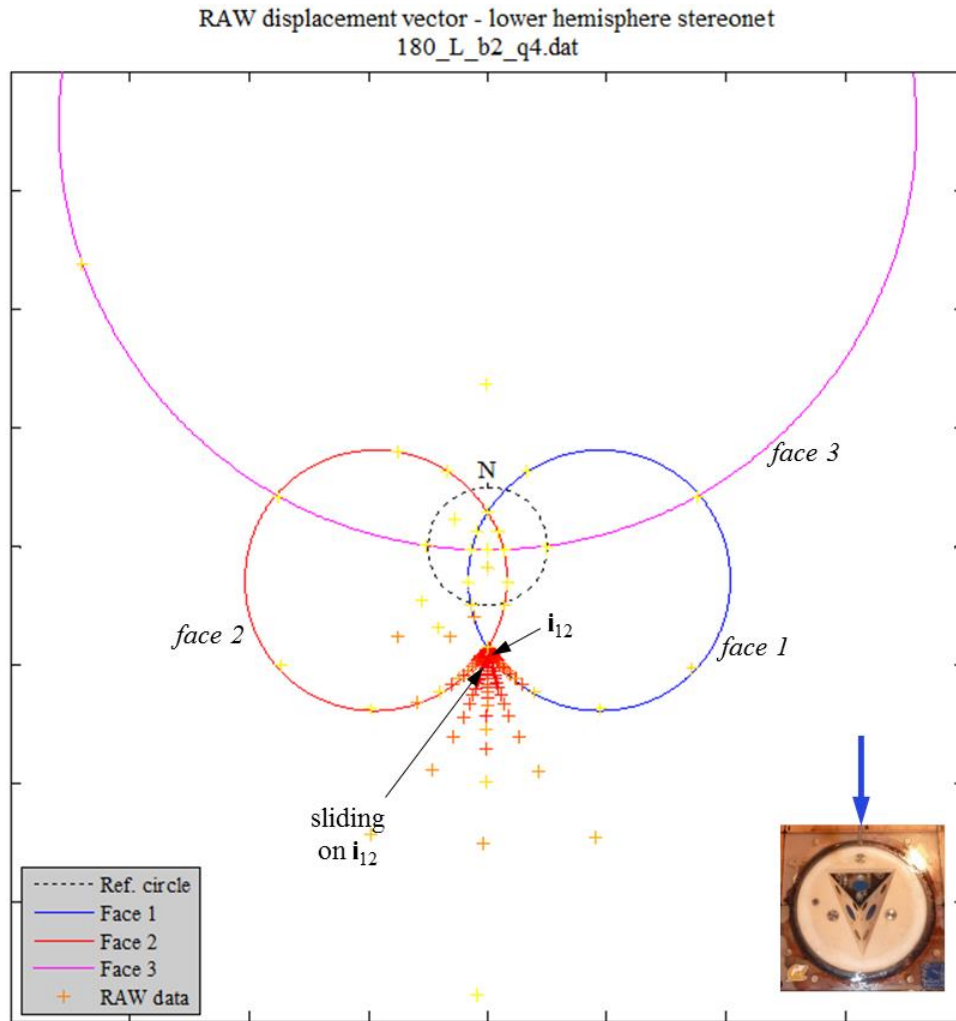


Figure 4-20. Response 1 – orientation of instantaneous vector from initial to current block position for $\psi = 180$ deg., low T_u , and Q_4 . Markers colored yellow to red with increasing time. Predominant vector orientation at intersection of faces 1 and 2.

Instantaneous values for displacement, dynamic pressure head, and stream-wise flow velocity approximately six seconds prior to block removal are presented in Figure 4-21 (sensor locations on the block mold are shown in Figure 4-6). As indicated, pressure values on all block faces remain fairly constant leading up to removal, with no obvious impulses applied to any of the block faces. This observation, coupled with the gradual displacements of the block along \mathbf{i}_{12} , suggests a pseudo-static treatment of the dynamic forces applied to the block may be appropriate for describing the overall stability of the block in these cases.

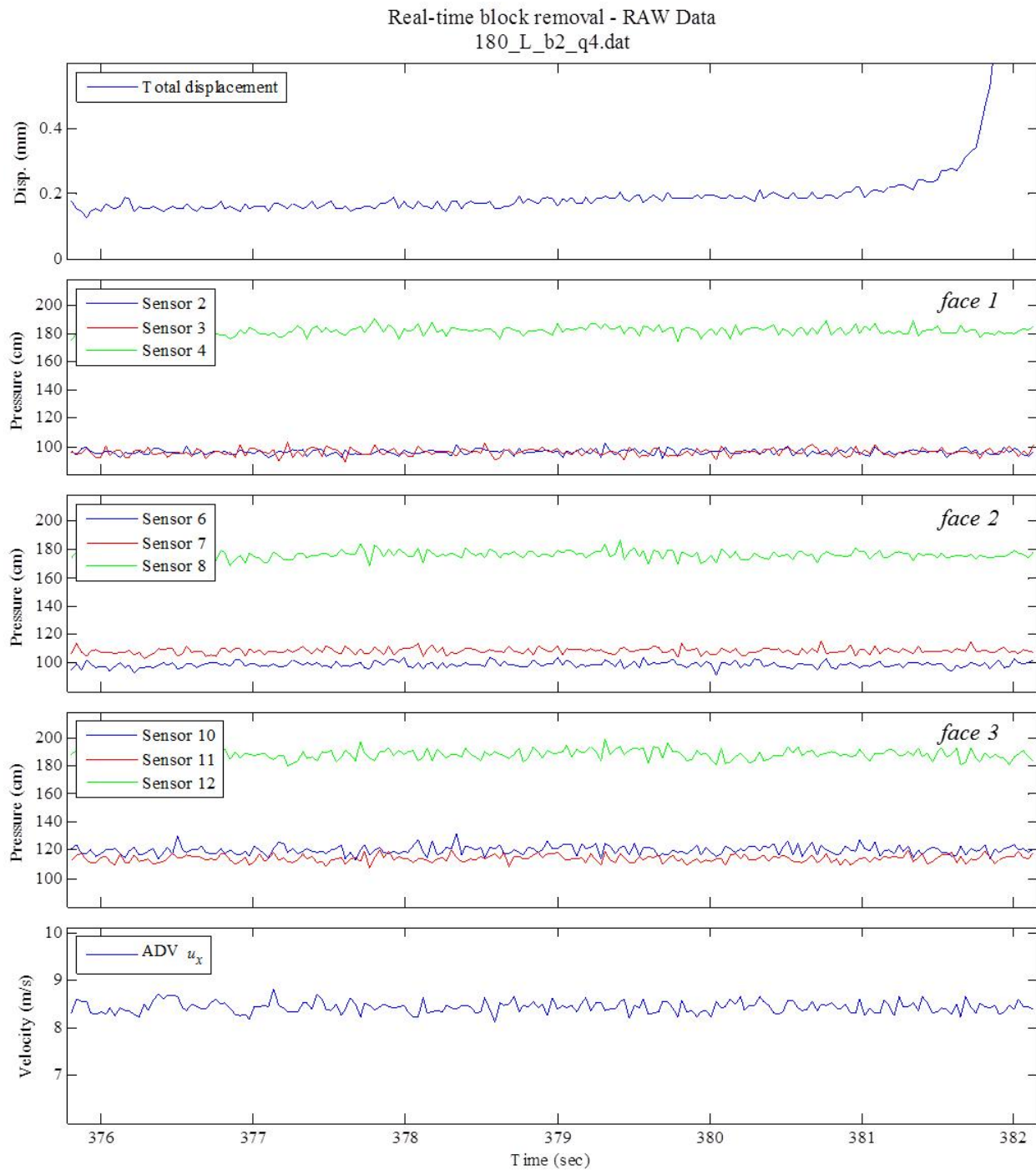


Figure 4-21. Response 1 – instantaneous values for displacement (top), dynamic pressure head (middle), and stream-wise flow velocity (bottom) approximately six seconds prior to block removal for $\psi = 180$ deg., low T_u , and Q_4 .

A graphical solution for the limit equilibrium stability of the 3D block is shown on the stereonet in Figure 4-22 (see Chapter 5 for details regarding limit equilibrium stereonets). The stereonet is divided into separate regions differentiating the kinematic failure modes for the

block (labeled by number, e.g., 1 = 1-plane sliding on face 1, 23 = 2-plane sliding on faces 2 and 3, etc.). The dashed contours are the required friction angle (ϕ) on the block faces for the block to remain stable and therefore represent the block face sliding resistance. The red highlighted contour corresponds to $\phi = 16$ deg. This was an average value determined for all model blocks through a series of tests where the block mold was inclined from near horizontal to sub-vertical until the block slide out. This was performed for all block rotation angles under dry and wet conditions, which are summarized in Appendix E. Accordingly, this contour represents the block yield condition. The orientation of the instantaneous active resultant force vector (\mathbf{r} , Chapter 5 - Equation 5-16), is also plotted in Figure 4-22. This vector represents all applied forces on the block, which for this study, are the water forces and block weight. When \mathbf{r} plots inside one of the kinematic mode regions, the block will behave according to that particular mode. As shown in Figure 4-22, values for \mathbf{r} plot within region 12, which indicates that 2-plane sliding on faces 1 and 2 was the kinematic mode by which the block was removed, which is consistent with the previous observations presented in Figure 4-19 and Figure 4-20.

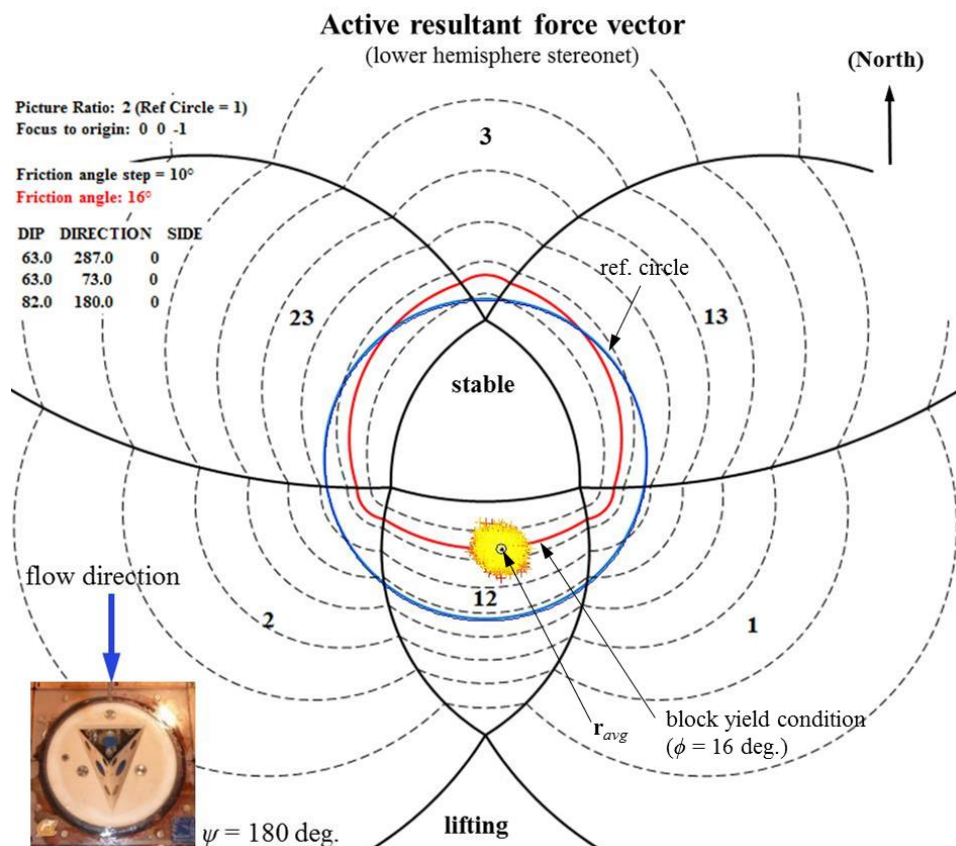


Figure 4-22. Response 1 – block limit equilibrium stereonet showing orientation of active resultant force vector (\mathbf{r}) for $\psi = 180$ deg., low T_u , and Q_4 . Markers colored yellow to red with increasing time. Kinematic mode indicated as 2-plane sliding on face 1 and face 2.

It was not possible to measure pressure on face 4 (free face) of the block during the experiments. Therefore, the force on the free face was calibrated such that the mean active resultant force vector (\mathbf{r}_{avg}) coincided with the block yield condition ($\phi = 16$ deg.), indicating the

block was in a state of equilibrium at the threshold of erosion. In actuality, the erodibility threshold was slightly exceeded as the block was removed, however, for all practical purposes an equilibrium condition can be assumed. Additional details regarding the calibration of forces on the free face are discussed in the following section on block pressure statistics.

An estimate of the shear stress (τ) applied to the face 4, included in the determination of \mathbf{r} , was calculated by:

$$\tau = \rho_w \cdot g \cdot d \cdot s_f \quad (4-8)$$

where ρ_w = density of water, g = gravitational acceleration constant, d = mean flow depth at location 5, and s_f = the slope of the energy grade line taken between location 2 and 8. It should be noted that the magnitude of the shear stress was relatively small in comparison to the pressure applied to the block due to form drag and had a negligible effect on the resultant orientation.

Figure 4-23 shows block displacement time-series response for mold rotation angle $\psi = 150$ deg., where the line of intersection between faces 1 and 2 (\mathbf{i}_{12}) is not oriented directly downstream. Similar to Figure 4-18, a gradual climb for the block from its original position until removal is observed, even though data presented in Figure 4-23 were collected under high T_u flow conditions. Spatial distribution of the block position (Figure 4-24) and orientation of the block displacement vector (Figure 4-25) indicate block movement was to the southeast along \mathbf{i}_{12} .

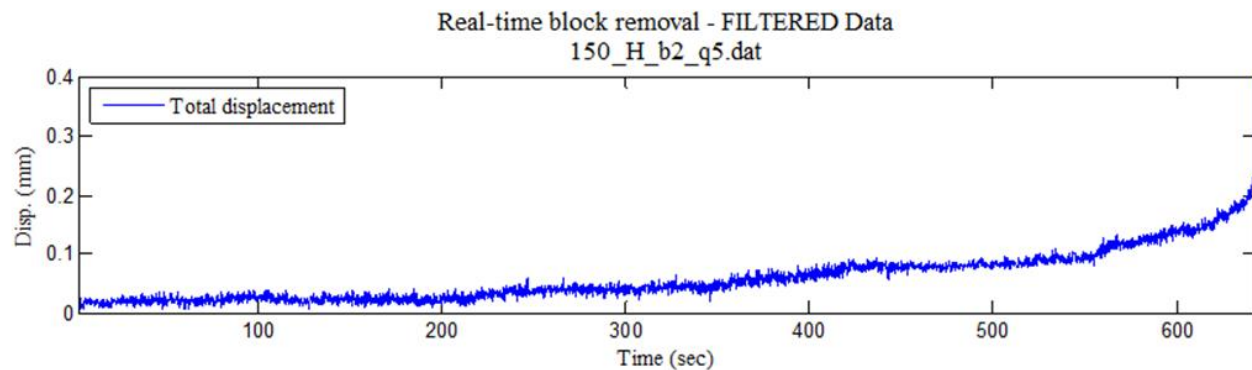


Figure 4-23. Response 1 – block displacement time-series showing gradual increase in total displacement magnitude until removal for $\psi = 150$ deg., high T_u , and Q_5 .

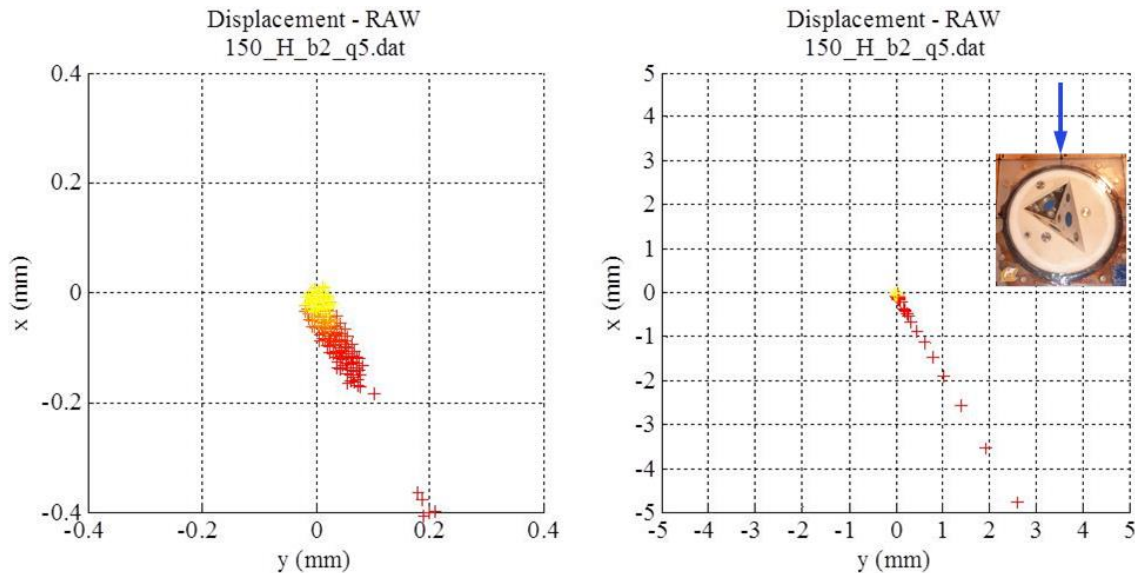


Figure 4-24. Response 1 – spatial distribution of instantaneous block position for $\psi = 150$ deg., high T_u , and Q_5 (close-up view on left). Markers colored yellow to red with increasing time. Block movement along the line of intersection (\mathbf{i}_{12}) of face 1 and face 2. Plot axes are swapped to correspond to flume coordinates.

Instantaneous values for displacement, dynamic pressure head, and stream-wise flow velocity approximately six seconds prior to block removal are presented in Figure 4-26. Due to high T_u flow conditions, pressure fluctuations are larger (in comparison with Figure 4-21), however, on average appear to remain fairly constant leading up to removal, with no large impulses applied to any of the block faces. Similar to above, this observation coupled with the gradual displacements of the block along \mathbf{i}_{12} , suggests a pseudo-static treatment of the dynamic forces applied to the block may be appropriate for describing the overall stability of the block in these scenarios. Accordingly, the orientation of the mean active resultant force vector (\mathbf{r}_{avg}) was calibrated (by adjusting the hydraulic force applied to face 4) to coincide with the block yield condition in the limit equilibrium stereonet (Figure 4-27). Variability of instantaneous \mathbf{r} orientations is significantly greater in comparison with Figure 4-22 due to high T_u flow conditions, however, the kinematic mode still remained 2-plane sliding on faces 1 and 2.

Plots for displacement time-series, block position, displacement orientation, instantaneous displacement/pressure/velocity and limit equilibrium stereonets for other block response 1 experiments can be found in Appendix E.

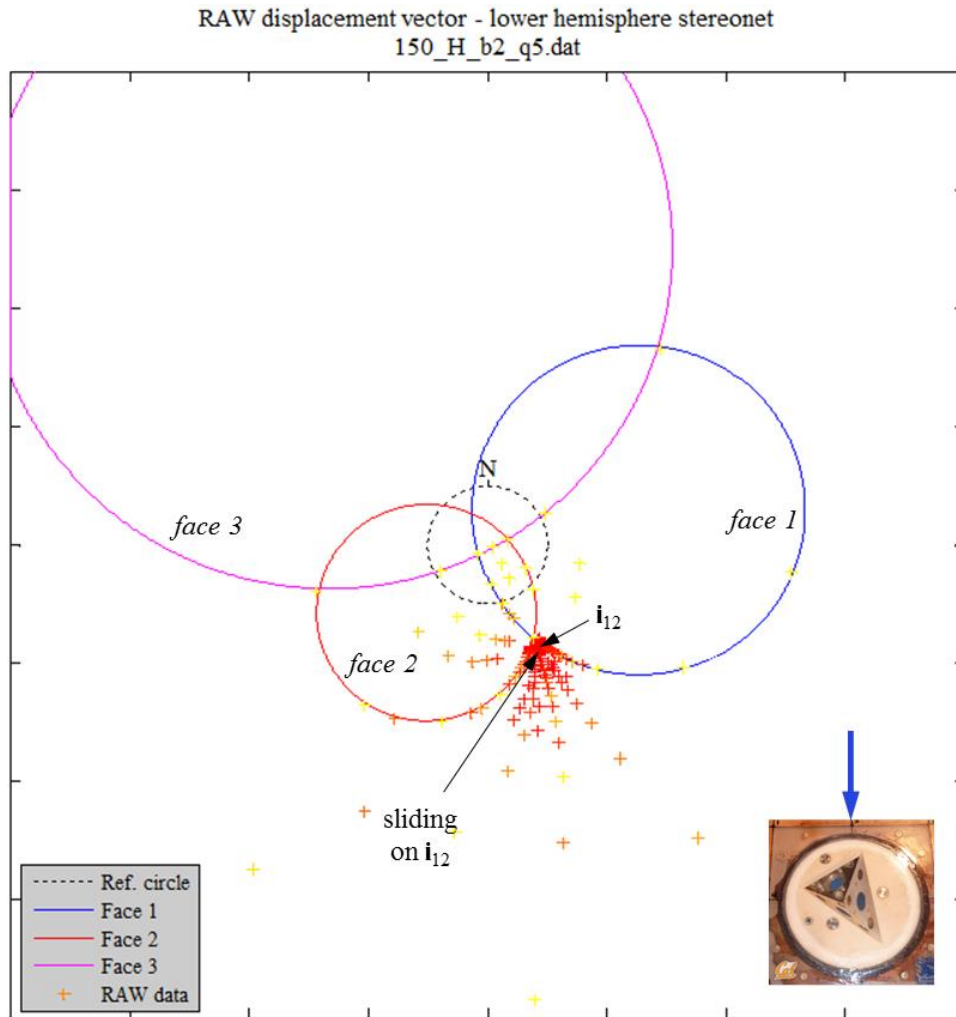


Figure 4-25. Response 1 – orientation of instantaneous vector from initial to current block position for $\psi = 150$ deg., high T_u , and Q_5 . Markers colored yellow to red with increasing time. Predominant vector orientation at intersection of face 1 and face 2 (i_{12}).

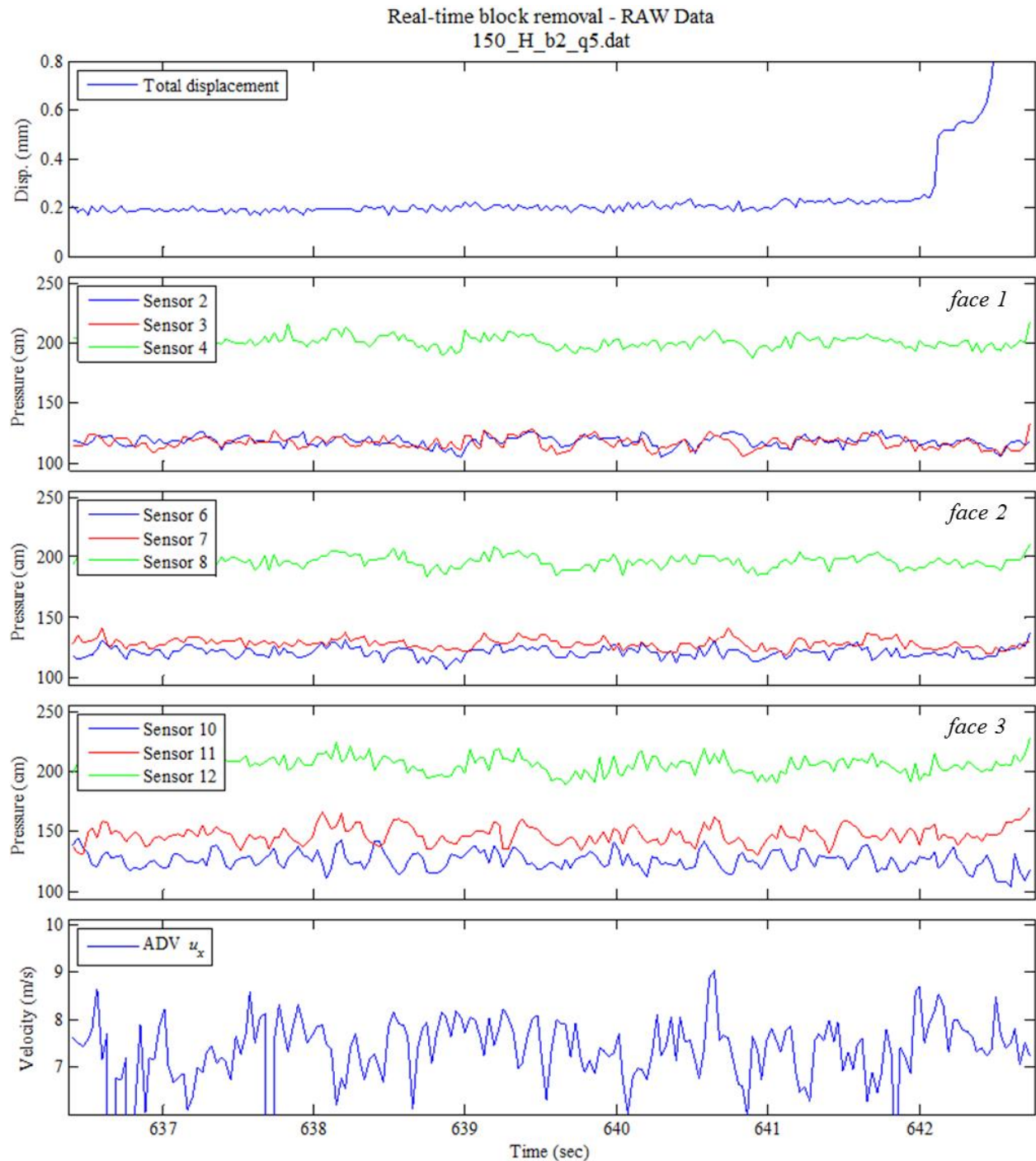


Figure 4-26. Response 1 – instantaneous values for displacement (top), dynamic pressure head (middle), and stream-wise flow velocity (bottom) approximately six seconds prior to block removal for $\psi = 150$ deg., high T_u , and Q_5 .

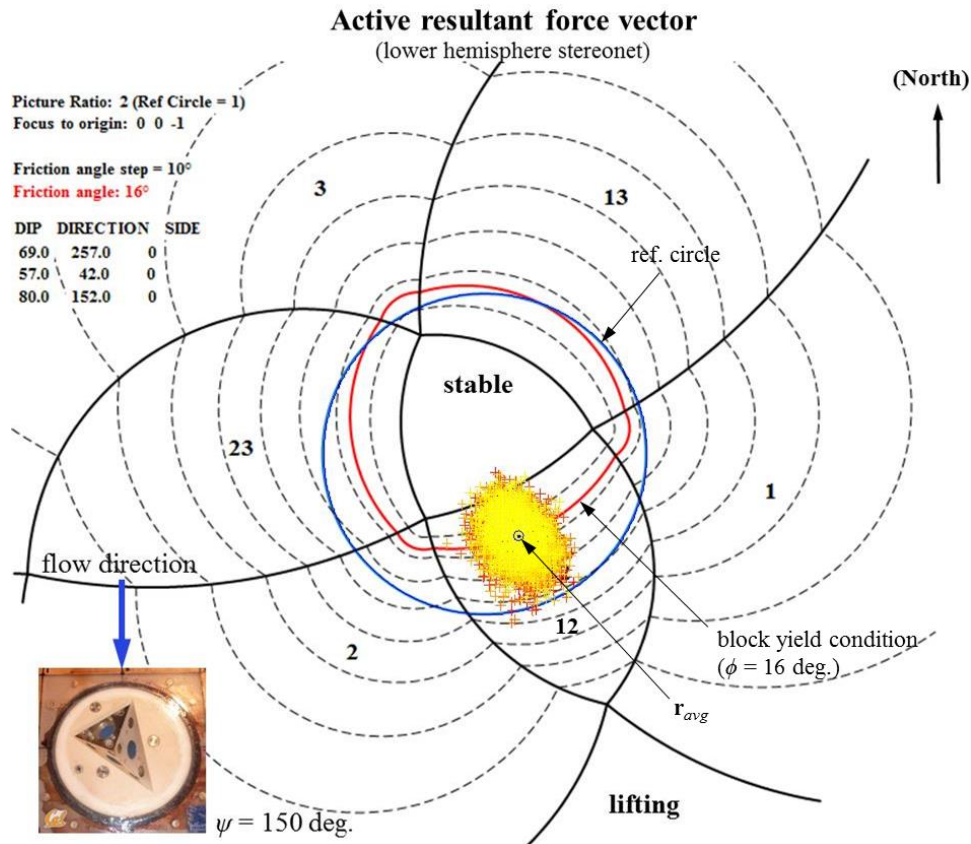


Figure 4-27. Response 1 - block limit equilibrium stereonet showing orientation of active resultant force vector, \mathbf{r} , for $\psi = 150$ deg., high T_u , and Q_5 . Markers colored yellow to red with increasing time. Kinematic mode indicated as 2-plane sliding on face 1 and face 2.

Block response 2 – Gradual block displacement with variable direction

In orientations where block mold geometry yielded a higher kinematic resistance to erosion, block displacement response was also gradual until removal (similar to response 1 above), however orientations of block displacements were considerably more variable.

Figure 4-28 shows the magnitude of block displacement time-series for the case when $\psi = 30$ deg. Similar to Figure 4-18 and Figure 4-23 above, a gradual increase in block position away from its initial location was observed over a relatively long period of time (approximately 180 s). As the block was further exposed above the channel bottom, the rate of displacement increased until finally the block was removed. Individual block displacements were small as no large impulse-like movements were witnessed. Examination of the spatial position of the block (Figure 4-29 – left) indicates movement of the block to actually be slightly west-northwest in the upstream direction into/along face 1. This is opposed to moving downstream along the intersection of face 2 and 3 (\mathbf{i}_{23}) in a similar fashion to the case above where $\psi = 150$ deg. (Figure 4-24) and sliding occurred along \mathbf{i}_{12} . The angle of intersection \mathbf{i}_{23} is oriented 44 deg. above horizontal compared to \mathbf{i}_{12} (for the case of $\psi = 150$ deg.) which is oriented 30 deg. above horizontal. The steeper incline appears to provide enough added kinematic resistance to prevent the block from easily moving along \mathbf{i}_{23} . Accordingly, block displacements were more variable in direction as indicated by the orientation of the vector from the initial to current (instantaneous)

block location (Figure 4-30). The majority of the movement appears to have occurred into or along face 1, but was highly variable in orientation. Near the end of the run (noted by the red markers) displacements shifted toward the downstream direction as the block migrated further out of the mold. The kinematic mode changed rapidly and consisted of lifting from face 1, momentarily sliding on face 3, and finally lifting in the southeast direction along the azimuth of \mathbf{i}_{23} . Re-routing of the block direction back to the southeast is also shown in Figure 4-29 (right).

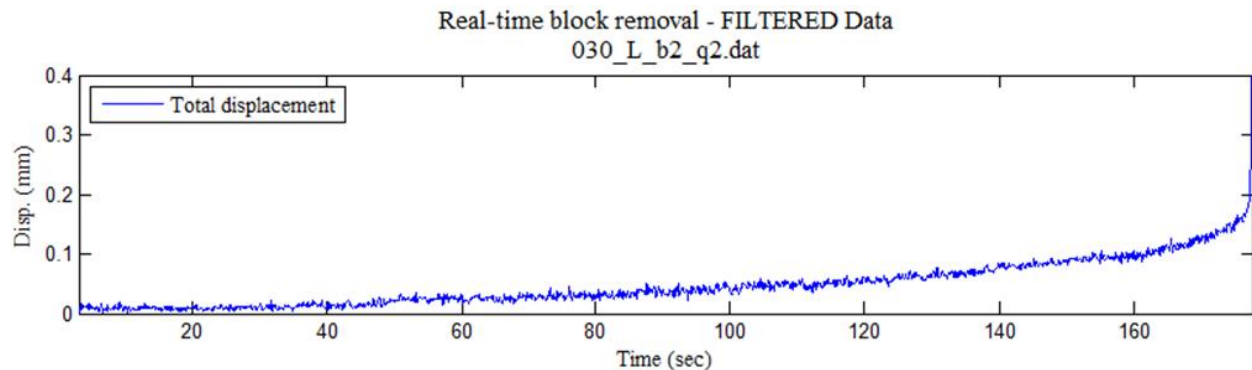


Figure 4-28. Response 2 – block displacement time-series showing gradual increase in total displacement magnitude until removal for $\psi = 30$ deg., low T_u , and Q_2 .

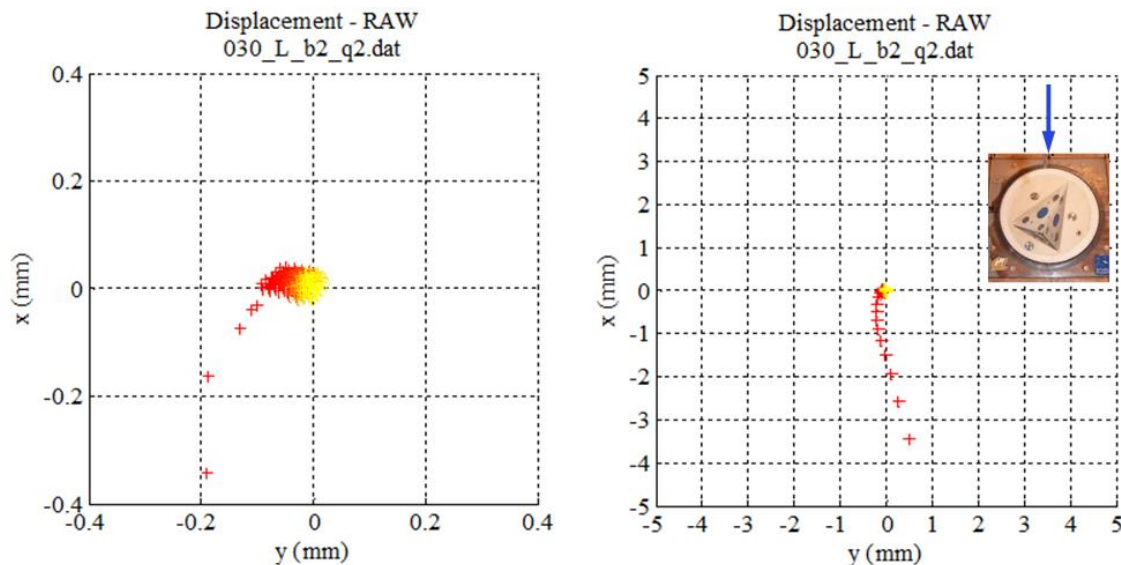


Figure 4-29. Response 2 – spatial distribution of instantaneous block position for $\psi = 30$ deg., low T_u , and Q_2 (close-up view on left). Markers colored yellow to red with increasing time. Note migration of block upstream to west-northwest prior to removal in southeast direction. Plot axes are swapped to correspond to flume coordinates.

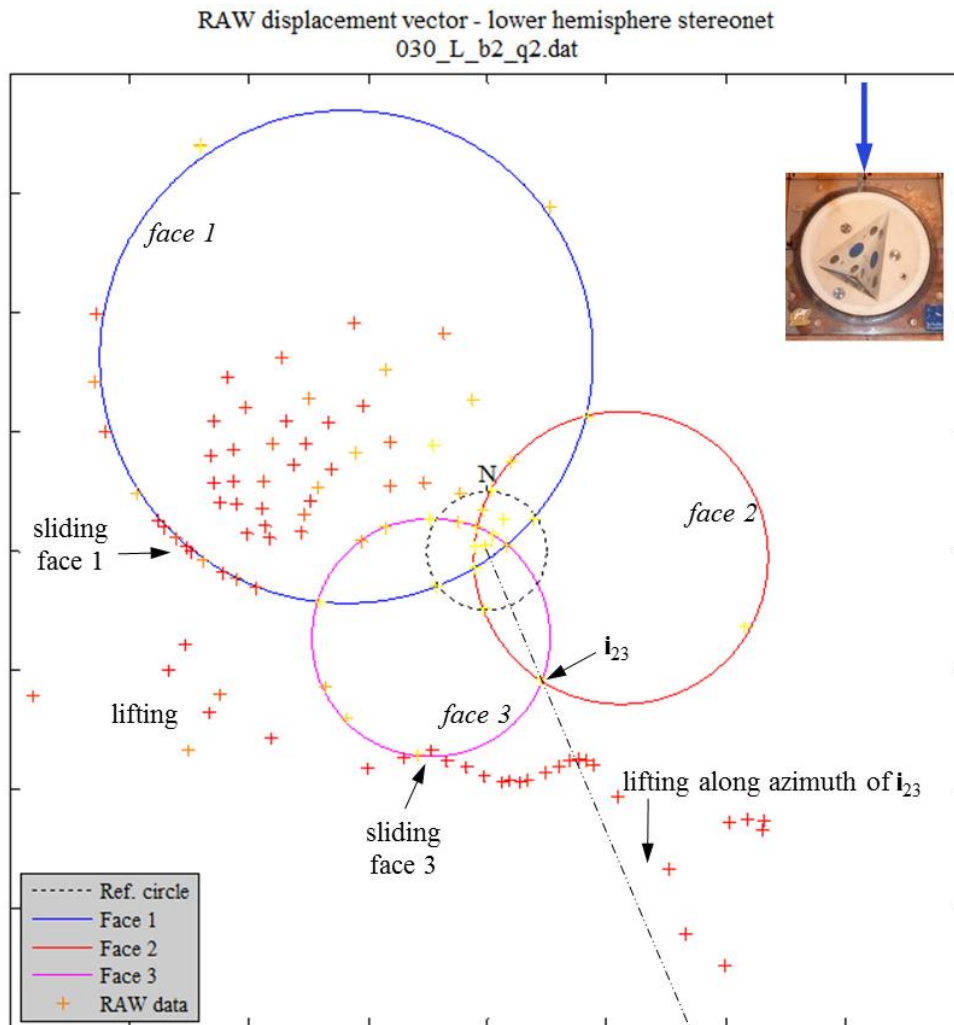


Figure 4-30. Response 2 – orientation of instantaneous vector from initial to current block position for $\psi = 30$ deg., low T_u , and Q_2 . Markers colored yellow to red with increasing time. Note high variability in vector orientation.

Instantaneous values for displacement and dynamic pressure head approximately six seconds prior to block removal are presented in Figure 4-31. Similar to experiments with block response 1, pressure values on all block faces remain fairly constant leading up to removal, with no obvious impulses applied to any of the block faces. This suggests a pseudo-static treatment of the dynamic forces applied to the block may be appropriate for describing the overall stability of the block in these scenarios.

The orientation of the mean active resultant force vector (\mathbf{r}_{avg}) was calibrated (by adjusting the hydraulic force applied to face 4) to coincide with the block yield condition in the limit equilibrium stereonet (Figure 4-32). Based on resultant force vector orientations, 2-plane sliding on faces 2 and 3 is identified as the kinematic failure mode, which is not supported by the displacement data presented in Figure 4-29 and Figure 4-31. Interestingly, block movement near the end of the run indicated the block was being lifted along the azimuth of \mathbf{i}_{23} , suggesting the block was ultimately directed along that pathway.

Plots for displacement time-series, block position, displacement orientation, instantaneous displacement/pressure/velocity and limit equilibrium stereonets for other block response 2 experiments can be found in Appendix E.

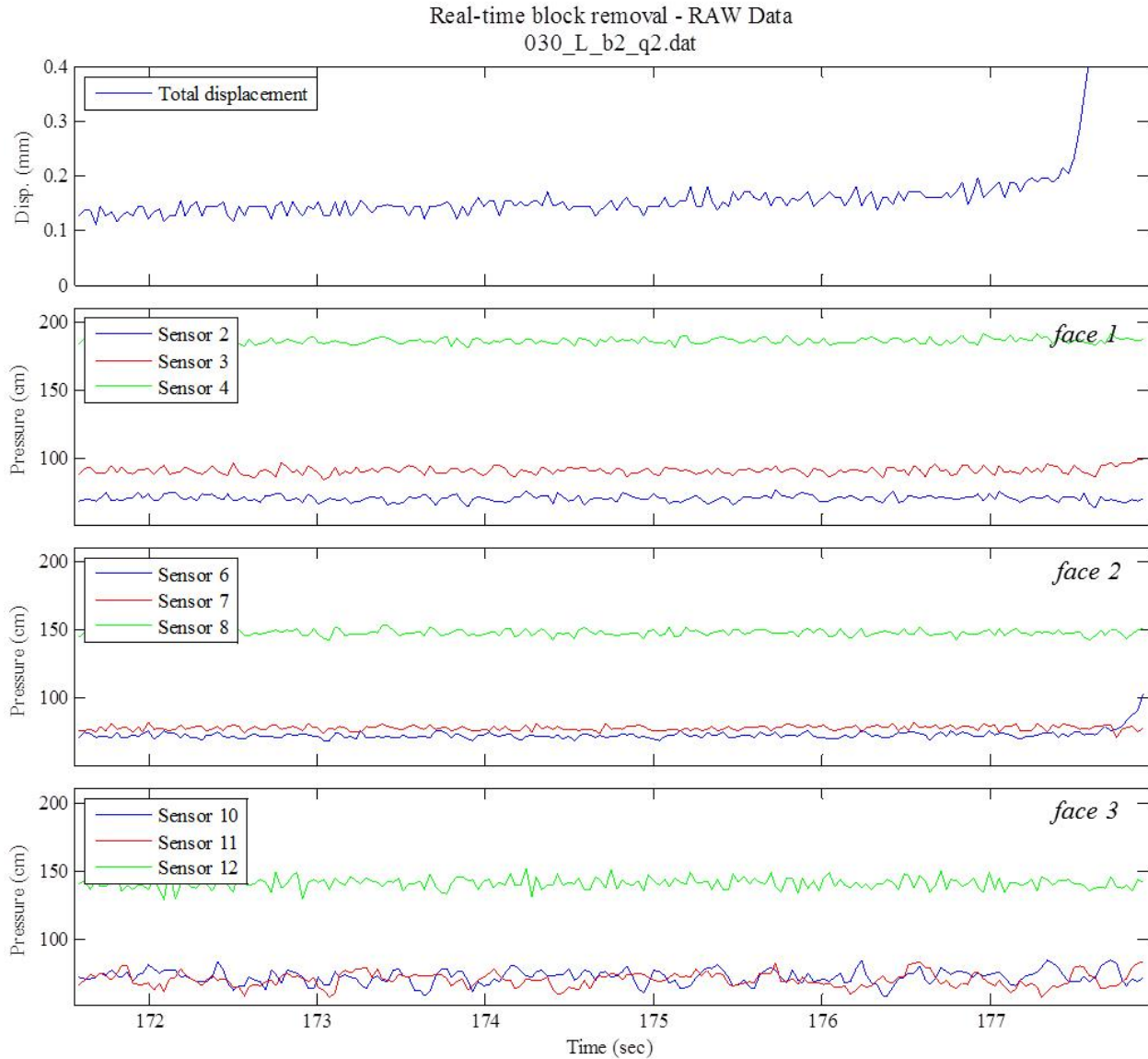


Figure 4-31. Response 2 – instantaneous values for displacement (top), and dynamic pressure head (bottom three plots), approximately six seconds prior to block removal for $\psi = 30$ deg., low T_u , and Q_2 . No instantaneous ADV data available due to low flow depth.

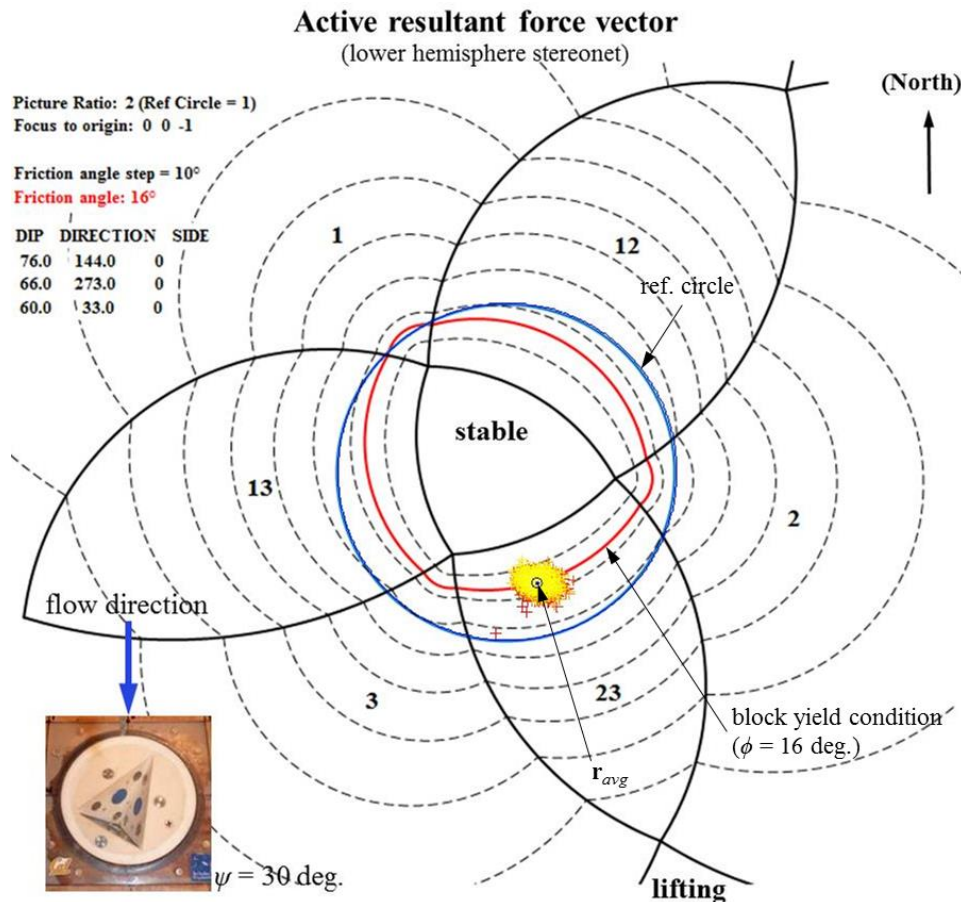


Figure 4-32. Response 2 – block limit equilibrium stereonet showing orientation of active resultant force vector, \mathbf{r} , for $\psi = 30 \text{ deg.}$, low T_u , and Q_2 . Markers colored yellow to red with increasing time. Kinematic mode indicated as 2-plane sliding on face 2 and face 3.

Block response 3 – Dynamic block displacement with variable direction

For high T_u flow conditions and orientations where block mold geometry yielded higher kinematic resistance to erosion, block displacement response was significantly more dynamic in comparison with the previous two response types. Figure 4-33 shows the magnitude of block displacement time-series for the case when $\psi = 135 \text{ deg.}$ Unlike previous examples (Figure 4-18, Figure 4-23, and Figure 4-28), block movement occurred less frequently but with larger displacements. Four impulse events are identified, with the final impulse resulting in removal of the block. The magnitude of displacement from each event prior to removal was approximately 0.2 mm, while the duration for each event was rapid lasting approximately 1 s. Flow conditions for this run (high T_u , Q_5) were identical to those for data presented in Figure 4-23 ($\psi = 150 \text{ deg.}$), interestingly however, block response differed significantly. This highlights the influence of block kinematics on block response where a relatively small 15 deg. rotation of the block mold (from $\psi = 135$ to 150 deg.) altered the displacement behavior of the block.

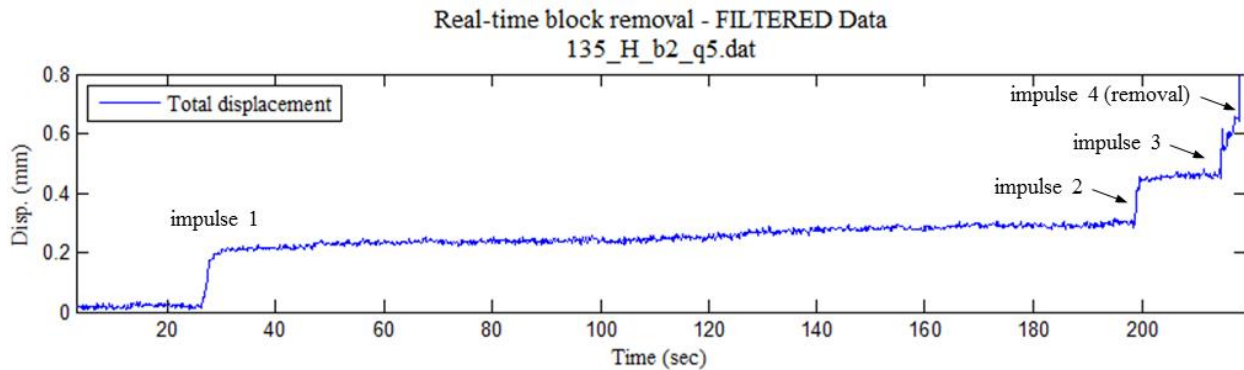


Figure 4-33. Response 3 – block displacement time-series showing larger displacements resulting from hydraulic impulses applied to the block for $\psi = 135$ deg., high T_u , and Q_5 .

Figure 4-34 shows another block displacement time-series for the case when $\psi = 0$ deg. Similar to Figure 4-33, block displacement occurs in response to impulses applied to the block from turbulent structures in the flow field. Four larger events are identified which yielded displacements of approximately 0.2 mm to 0.6 mm, with the last impulse resulting in removal of the block. The duration of each event was approximately 0.1 s to 0.2 s. Note that block movement does not significantly occur during non-impulse periods (e.g., from approximately 45 s to 60 s, and 80 s to 130 s), which suggests the mean velocity field alone could not displace the block.

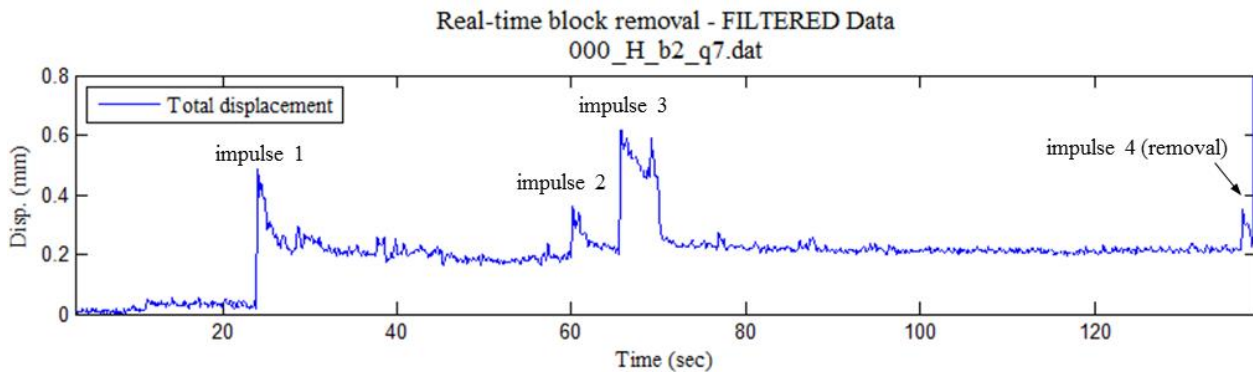


Figure 4-34. Response 3 – block displacement time-series showing larger displacements resulting from hydraulic impulses applied to the block for $\psi = 0$ deg., high T_u , and Q_7 .

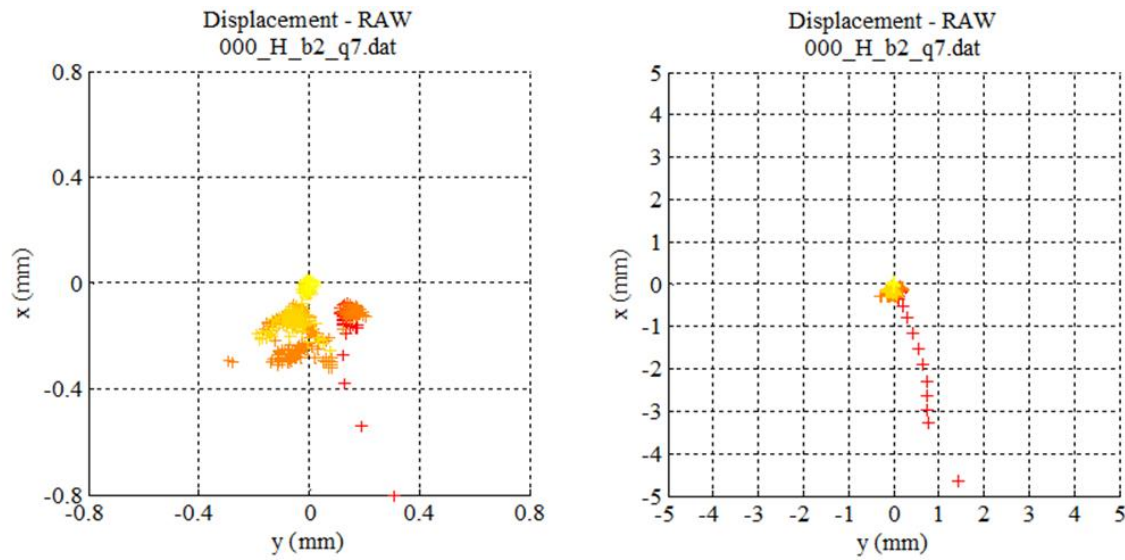


Figure 4-35. Response 3 – spatial distribution of instantaneous block position for $\psi = 0$ deg., high T_u , and Q_7 (close-up view on left). Markers colored yellow to red with increasing time. Note highly erratic block position. Plot axes are swapped to correspond to flume coordinates.

The instantaneous block position is presented in Figure 4-35. Over the entirety of the run, the block position was erratic. As indicated in Figure 4-36, block movements predominantly occurred along the downstream face of the block mold (face 3), but were highly variable in orientation. This can likely be attributed to the steep dip of face 3 on the block mold which prevented easy sliding of the block from its initial location in the downstream direction. Examination of the spatial block position during the four impulse events (Figure 4-37), however, indicated block movements were relatively consistent, all moving in the southeast direction. Similarly, displacement orientations for the impulse events were consistent with a kinematic mode of 1-plane sliding on face 3 (Figure 4-38). A comparable observation was made for other runs that showed block response 3 behavior.

Figure 4-39 shows instantaneous values for displacement, pressure and stream-wise flow velocity approximately six seconds prior to impulse 4 that resulted in removal of the block. As indicated, pressure and velocity data show considerable fluctuation leading up to failure with a significant decrease in both occurring just prior to failure. Adapting a simplistic model from Hoffmans (2012), pressure and velocity measurements in the near-bed region were related to structure of turbulent eddies within the flow field (Figure 4-40). Two (or more) oppositely rotating eddies, transported downstream at mean flow velocity, result in alternating high and low pressure zones near the channel bottom with localized areas of flow acceleration and deceleration. Mapping these regions alongside instantaneous velocity and displacement data (Figure 4-41) indicates a large zone of flow deceleration occurred prior to failure, which greatly decreased pressure in the vicinity of the block. The low pressure zone in the block region allowed flow from the next upstream eddy to accelerate towards the block, increasing pressure around the faces, causing the block to slide out from its mold. It is anticipated the low pressure zone on the channel bottom (face 4) may have been influential initiating removal by initially “sucking” the block from the mold (similar to how flow is “sucked” toward the block region). Without pressure measurement on face 4, however, it is difficult to determine with certainty.

The period of the eddy just prior to block removal was approximately 0.65 s, corresponding to a frequency of 1.5 Hz (4.9 Hz model scale). This is in near agreement with the dominant frequency observed from spectral analysis of high T_u velocity data (Figure 4-12), which ranged from approximately 0.6 to 1.3 Hz (2 to 4 Hz model scale) due to the presence of the baffles.

Plots for displacement time-series, block position, displacement orientation, instantaneous displacement/pressure/velocity and limit equilibrium stereonet for other block response 3 experiments can be found in Appendix E.

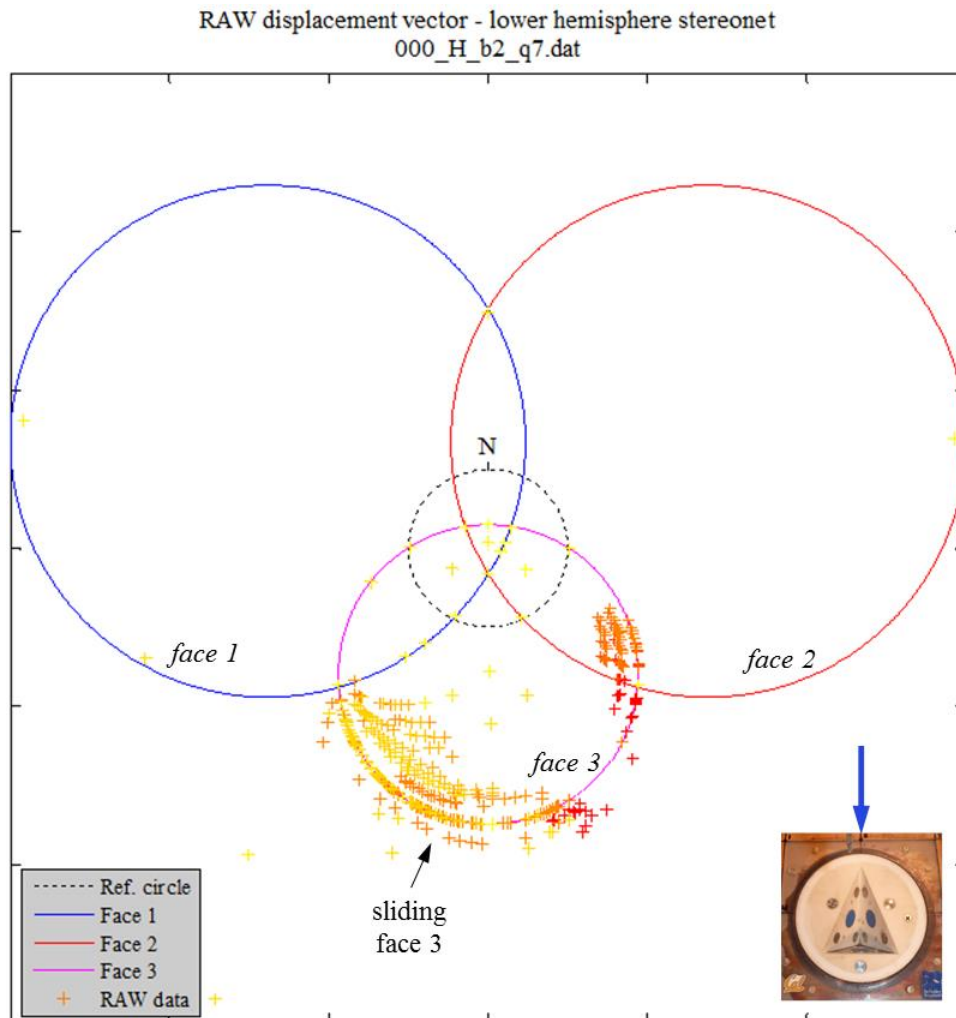


Figure 4-36. Response 3 – orientation of instantaneous vector from initial to current block position for $\psi = 0$ deg., high T_u , and Q_7 . Markers colored yellow to red with increasing time. Predominant movement occurring along face 3.

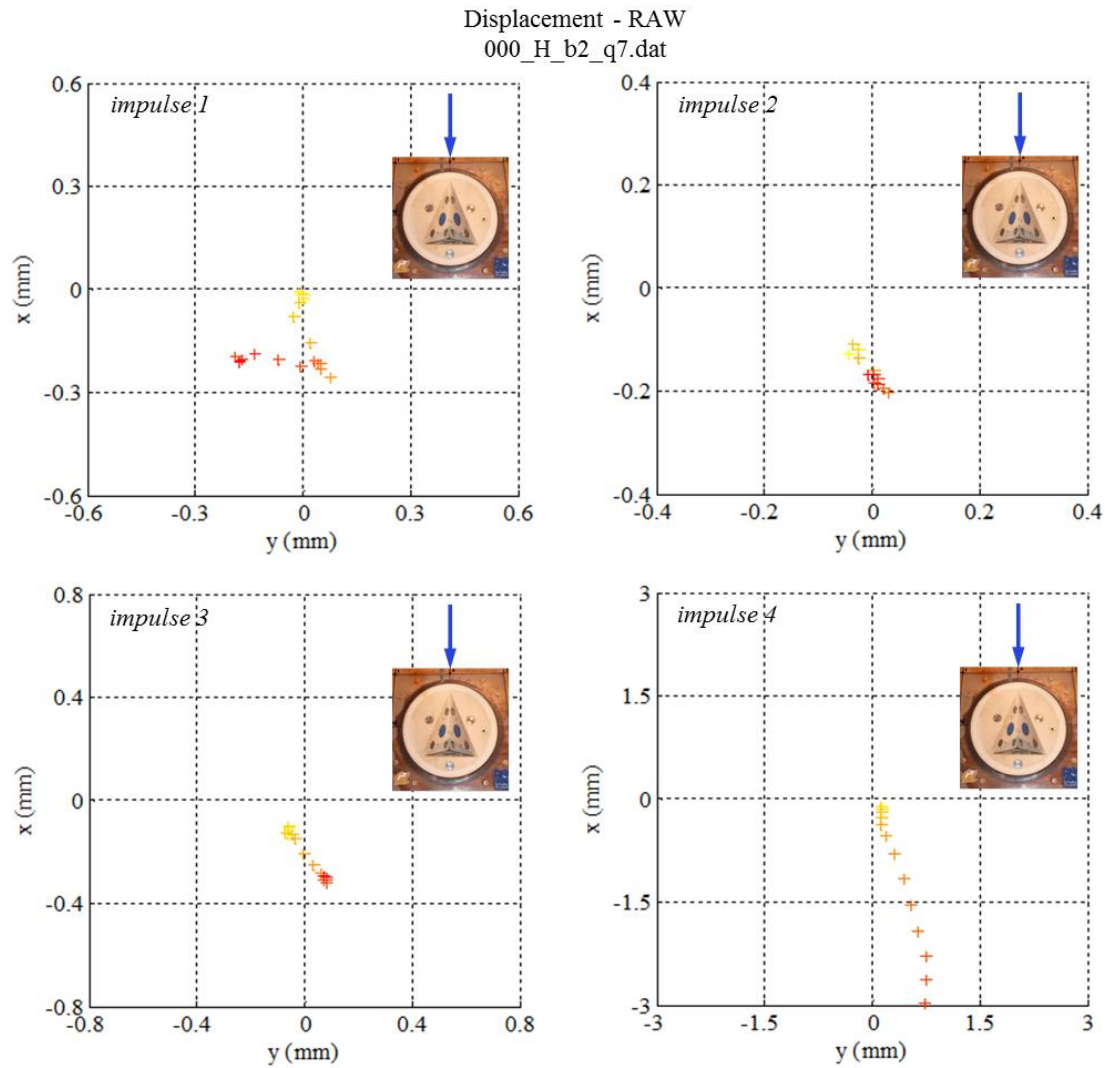


Figure 4-37. Response 3 – spatial distribution of instantaneous block position during individual impulses applied to the block for $\psi = 0$ deg., high T_u , and Q_7 . Note block displacement direction is relatively consistent (to the southeast) for each impulse.

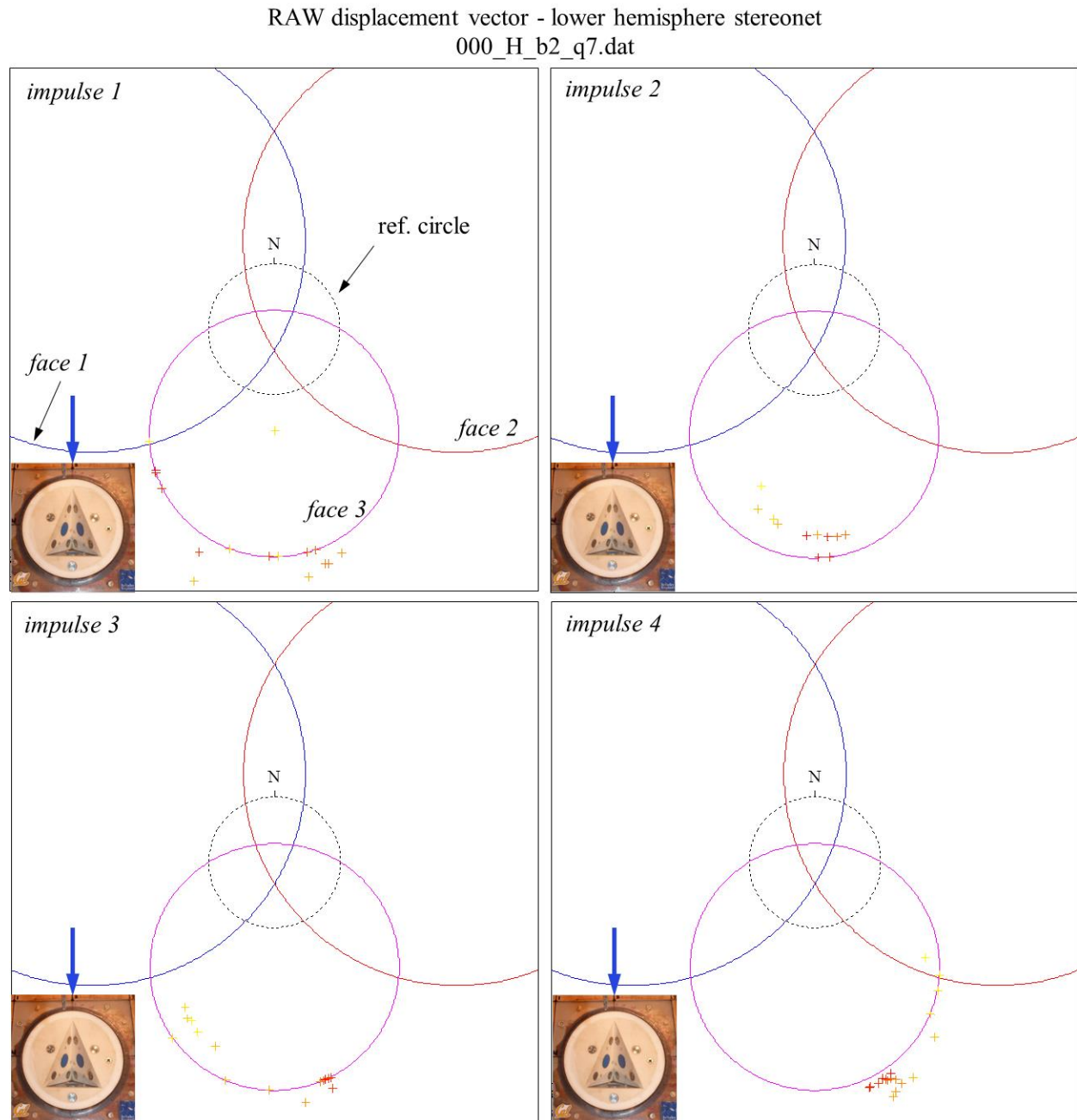


Figure 4-38. Response 3 – orientation of instantaneous vector from initial to current block position during individual impulses applied to the block for $\psi = 0$ deg., high T_u , and Q_7 . Markers colored yellow to red with increasing time. Block movement is relatively consistent for each impulse predominantly occurring along face 3.

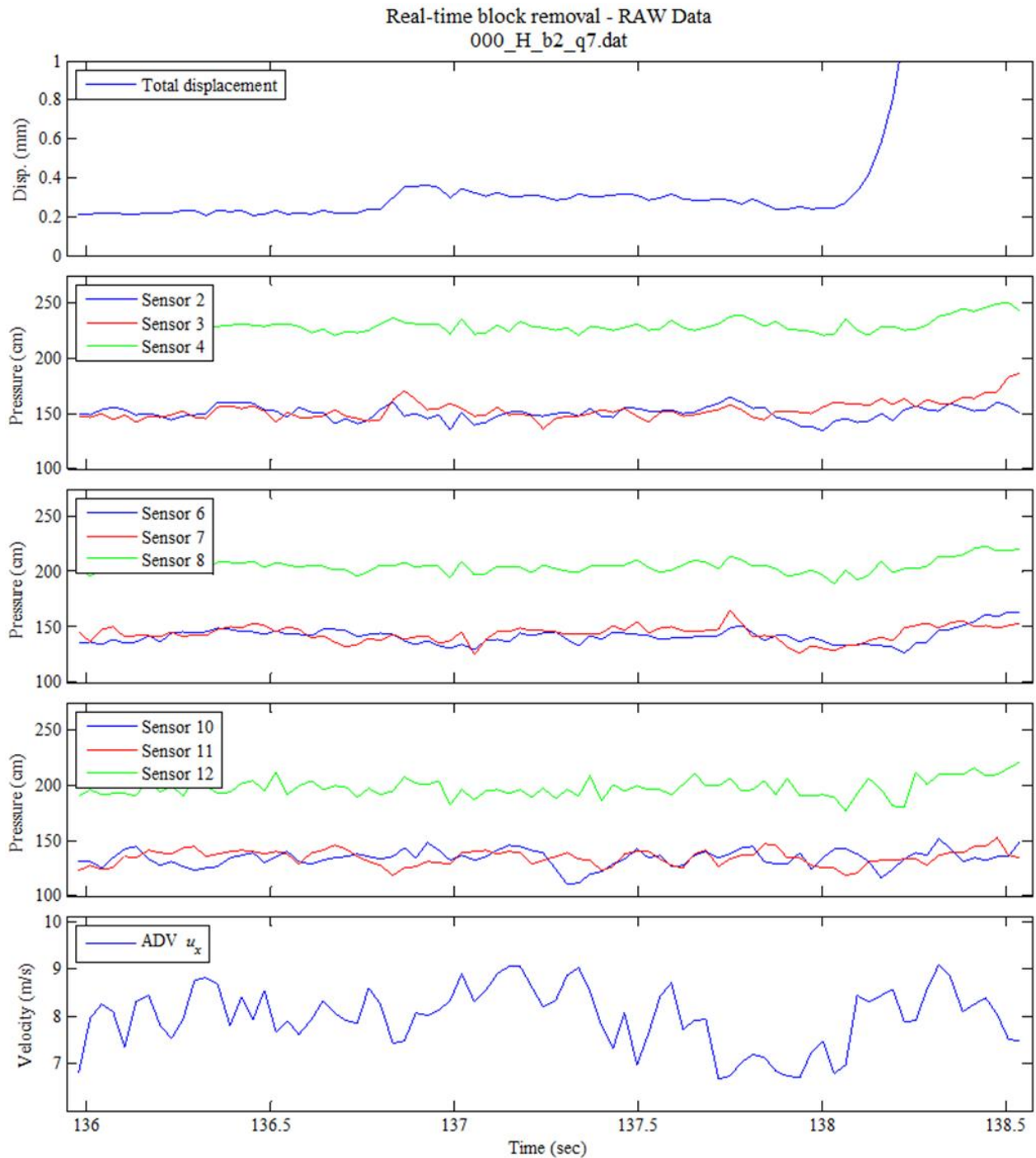


Figure 4-39. Response 3 – instantaneous values for displacement (top), dynamic pressure head (middle), and stream-wise flow velocity (bottom) for impulse 4 (Figure 4-34) for $\psi = 0$ deg., high T_u , and Q_7 .

Schematic for turbulent eddy velocity and pressure in near-bed region

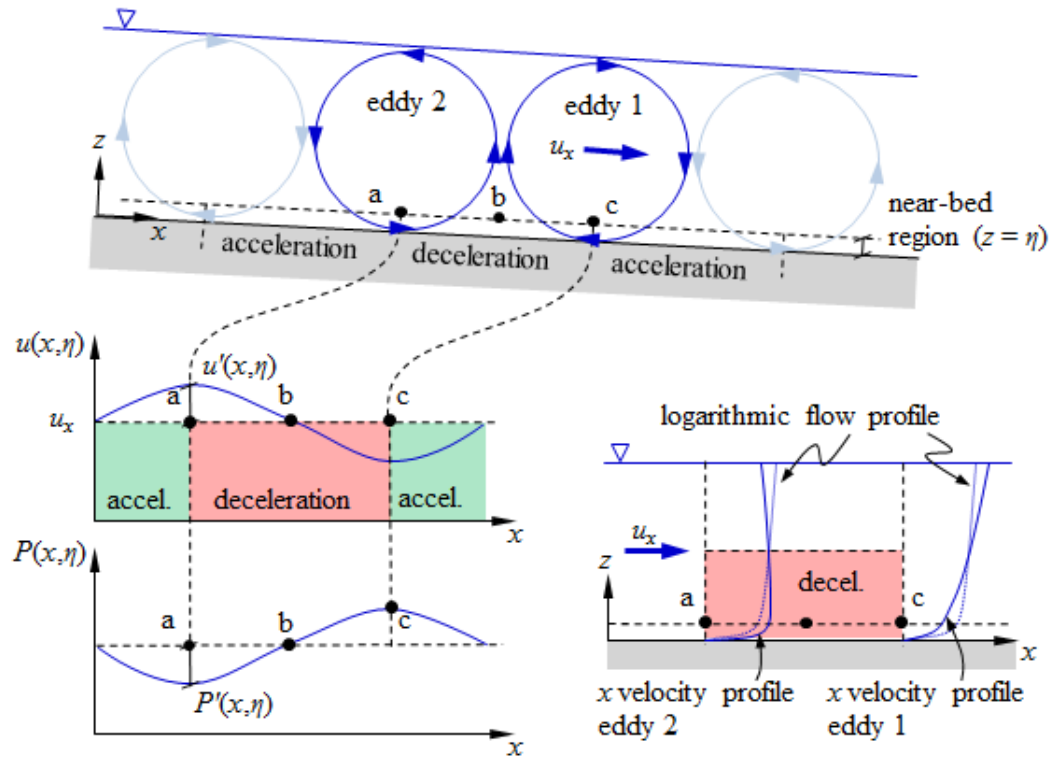


Figure 4-40. Pressure and horizontal flow velocity in the near-bed region associated with two turbulent eddies. Modified from Hoffmans (2012).

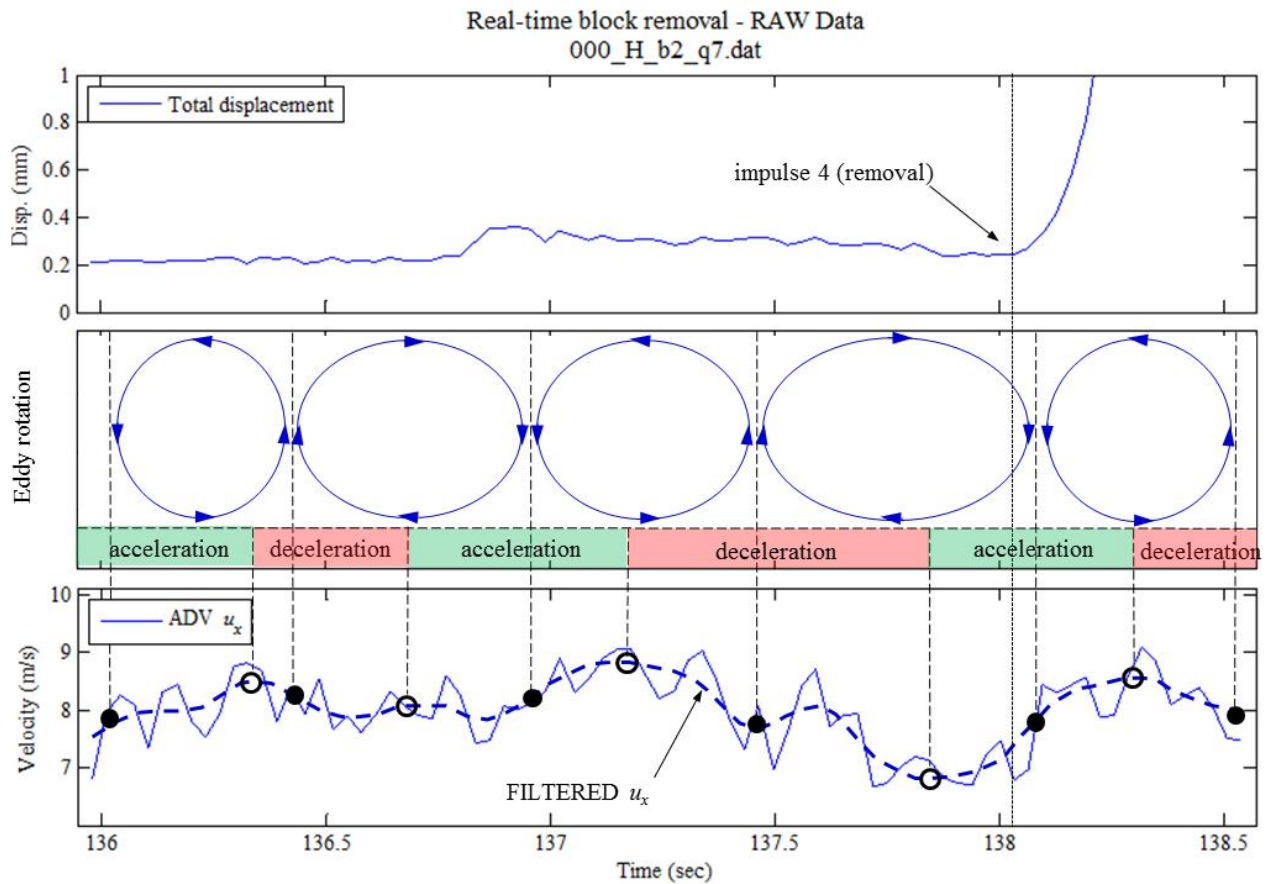


Figure 4-41. Response 3 – turbulent eddy structure associated with instantaneous values for displacement (top) and stream-wise flow velocity (bottom) for impulse 4 (Figure 4-34) for $\psi = 0$ deg., high T_u , and Q_7 . ADV time series data using a Butterworth low pass filter with cutoff frequency of 10 Hz is also shown.

Pressure and displacement power spectral density.

Power spectral density (S_{xx}) plots for pressure and displacement fluctuations were developed for experiments that resulted in block removal. This was done to identify dominant frequencies of hydrodynamic pressures within the discontinuities surrounding the block and for block movements. The power spectral density shows the relative strength of fluctuations distributed over a frequency domain. The frequency of pressure fluctuations is inversely related to the size turbulent eddies in the flow field. For this analysis, time series data (sampled at 100 Hz) were filtered using a Butterworth low pass filter with a cutoff frequency of 50 Hz (model scale). The number of samples used was variable between scenarios as the length of the run was dependent on when removal occurred. Data were discretized into blocks of 512 samples. A Hamming window function was applied to each block with an overlap of 50% between adjacent blocks. Power spectral density values were averaged over all sample blocks for each run.

In general, frequency response between different runs was variable due to changes in block rotation angle, discharge, turbulence intensity, etc. However, dominant frequencies in both pressure and displacement data were typically present in one or more of three main regions: 1) 2 to 3 Hz (0.6 to 0.9 Hz, prototype scale) – associated with the presence of baffles in high T_u flows,

2) 5 to 20 Hz (1.6 to 6.3 Hz, prototype scale) and 3) 30 to 40 Hz (9.5 to 12.7 Hz, prototype scale). Figure 4-42 shows S_{xx} plots for the case when $\psi = 165$ deg., high T_u , and Q_4 , which is representative of block response 1. The -1 and -5/3 power laws corresponding to the energy production subrange and energy dissipation range, respectively, are provided for reference. Figure 4-6 shows the location of pressure sensors on the block mold.

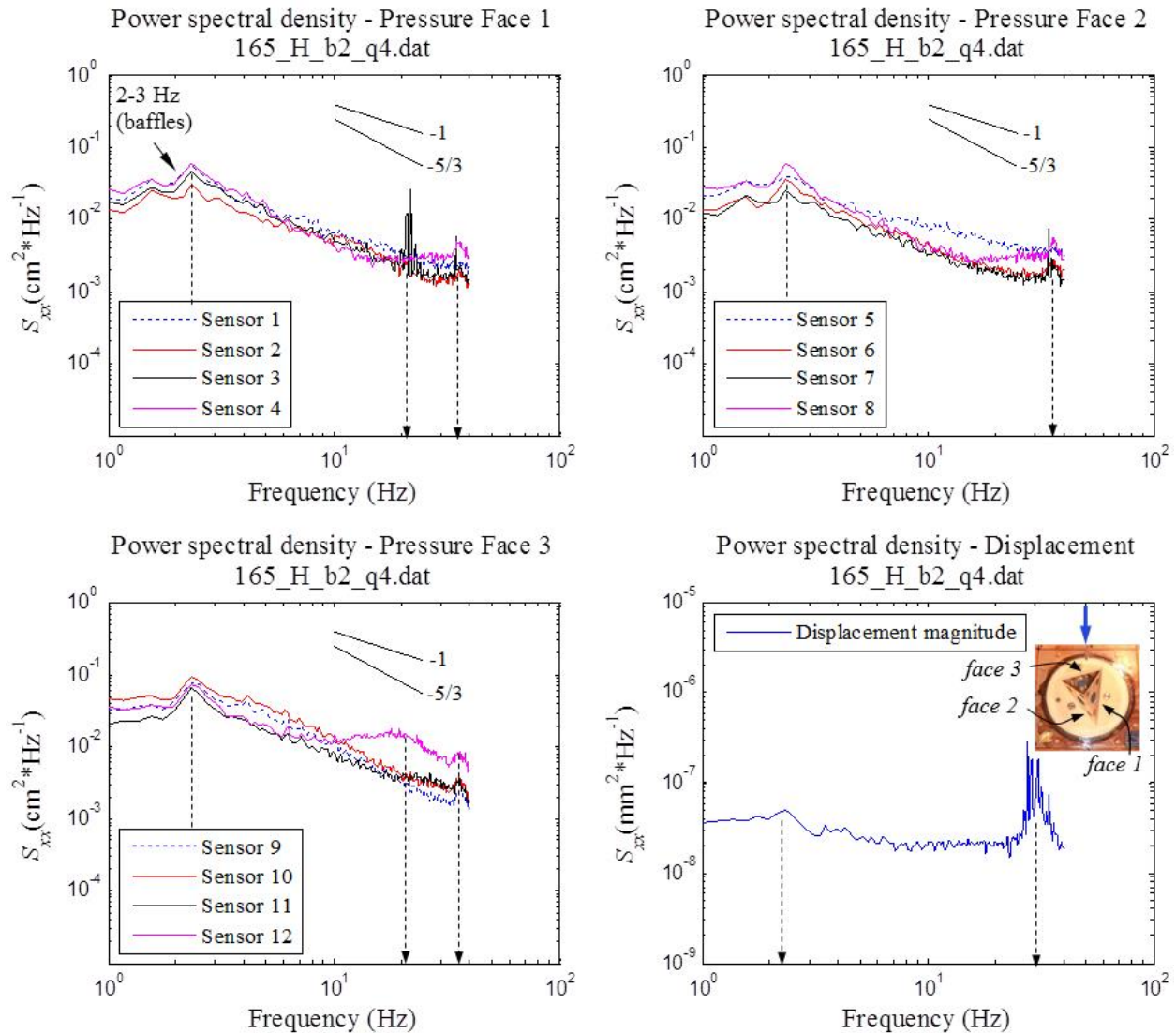


Figure 4-42. Response 1 – Power spectral density for pressure sensors on face 1 (top left), face 2 (top right), face 3 (bottom left) and total displacement (bottom right) for $\psi = 165$ deg., high T_u , and Q_4 . Values presented in model scale.

As shown, predominant block displacements occurred at a frequency of approximately 25 to 40 Hz (7.9 to 12.7 Hz, prototype scale), with a similar peak in pressure data at approximately 35 Hz (11.1 Hz, prototype scale) indicating a fundamental resonance frequency of the block system. This could be related to 1) resonance frequencies of pressure waves traveling through the water column in the discontinuities between the block and mold or 2) a fundamental frequency of the

block itself due to its inertia and contact stiffness with the mold (Federspiel et al. 2011). The presence of the 35 Hz peak across all pressure sensors, both on the channel bottom outside the mold (sensors 1, 5 and 9) and inside the block mold (sensors 2, 3, 4, 6, 7, 8, 10, 11 and 12), suggest it is related to a fundamental frequency of the block itself.

A second peak at approximately 20 Hz (6.3 Hz, prototype scale) was also observed in pressure sensor 3 (face 1) and pressure sensor 12 (face 3), but with no corresponding response in displacement power spectral density. Pressure sensors on the channel bottom near discontinuity openings also produced no response in this range. Accordingly, this peak was likely related to a fundamental resonance frequency of pressure waves traveling through the water-filled discontinuities around the block, inside of the mold. Due to 3D geometry of the block mold, superposition of pressure waves to create this phenomenon only occurred in two localized locations (near sensors 3 and 12), and was not observed across entire block faces.

Finally a third predominant peak in all pressure data was observed at 2 to 3 Hz (0.6 to 0.9 Hz prototype values) related to eddies generated by baffles upstream of the block location. This peak is nearly absent from displacement response as no large impulses in block movement were observed in time series data for these type runs (e.g., Figure 4-18, Figure 4-23). Low T_u flows with no baffles yielded similar results but did not show any response in the 2 to 3 Hz range (Appendix E).

Figure 4-43 shows a characteristic run for block response 2 under low T_u conditions for $\psi = 105$ deg. and Q_3 . For these runs, displacement response was often bimodal with block movements occurring in the 30 to 40 Hz range (9.5 to 12.7 Hz, prototype scale) (as with block response 1) but also at lower frequencies in the 5 to 20 Hz range (1.6 to 6.3 Hz, prototype scale). As indicated in Figure 4-43, small peaks in S_{xx} for displacement occur at approximately 14 Hz and 31 Hz (4.4 and 9.8 Hz, respectively, prototype scale). In contrast to block response 1, block movements were more susceptible to resonance of pressure waves within the discontinuities surrounding the block occurring in the 5 to 20 Hz range. This was most likely related to the increased kinematic resistance associated with the block mold rotation angle in the sense that the smaller, higher frequency pressure fluctuations could not move the block as effectively to dissipate energy which allowed greater build-up of pressure around the block. As the degree of turbulence for these experiments was still relatively low (compared to block response 3), block response in the low frequency range (less than approximately 5 Hz) was generally not observed.

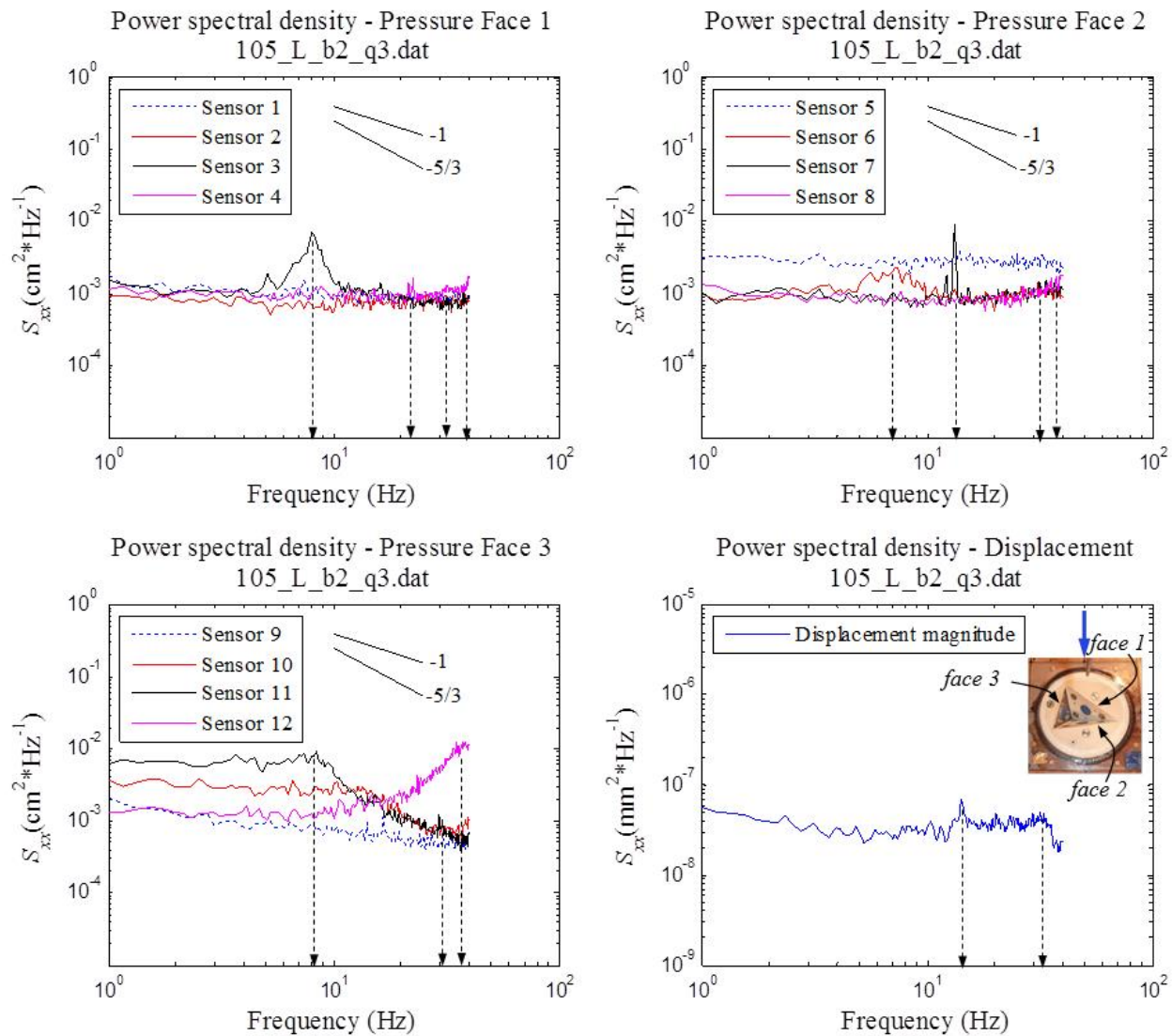


Figure 4-43. Response 2 – Power spectral density for pressure sensors on face 1 (top left), face 2 (top right), face 3 (bottom left) and total displacement (bottom right) for $\psi = 105$ deg., low T_u , and Q_3 . Values presented in model scale.

Figure 4-44 shows a characteristic run for block response 3 for high T_u conditions for $\psi = 0$ deg. and Q_7 . Similar to block responses 1 and 2, excitation of the fundamental block resonance frequency in the 30 to 40 Hz range (9.5 to 12.7 Hz, prototype scale) was witnessed. However, due to the increased kinematic resistance associated with the block mold rotation angle (as described above for block response 2), higher frequency displacements could not adequately move the block and dissipate energy, which increased susceptibility to lower frequency fluctuations in the flow field. As such, these runs were characterized by larger, impulse-driven block movements and exhibited a predominant displacement response for frequencies less than 10 Hz (3.2 Hz, prototype scale).

Plots of S_{xx} for pressure and displacement for additional runs can be found in Appendix E.

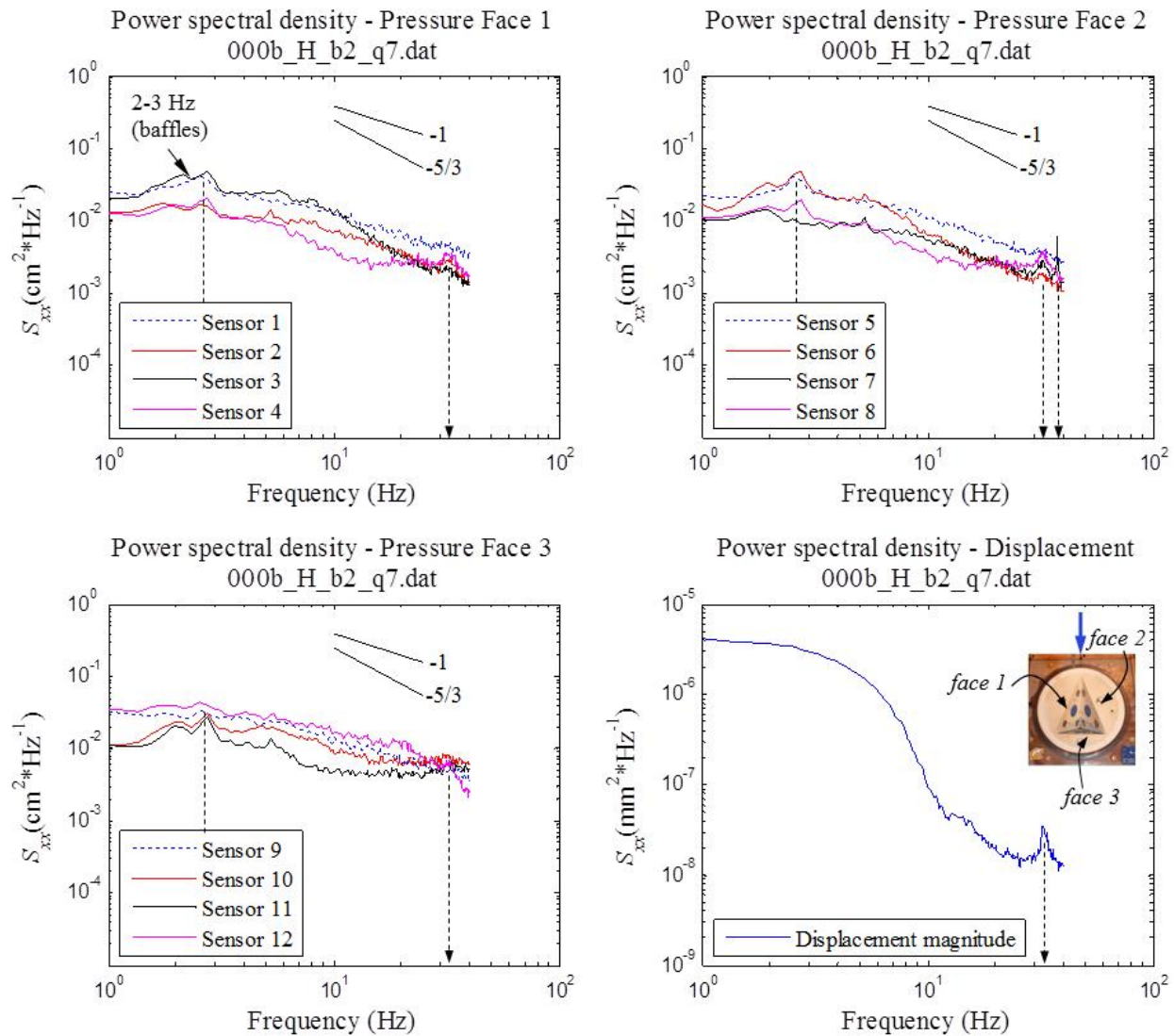


Figure 4-44. Response 3 – Power spectral density for pressure sensors on face 1 (top left), face 2 (top right), face 3 (bottom left) and total displacement (bottom right) for $\psi = 0$ deg., high T_u , and Q_7 . Values presented in model scale.

Post-incipient motion behavior

Position of the block exiting the mold was tracked using still images generated from high speed video taken during model experiments (Figure 4-45). Note that block positions shown represent displacements occurring well beyond those recorded with the proximity (Figure 4-19, Figure 4-24, Figure 4-29, and Figure 4-35). These figures depict movements less than 0.5 mm (model scale) and could not be identified in the video. Accordingly, Figure 4-45 represents block behavior after incipient motion. Images are provided for Block 2 in both high and low T_u flow conditions for four different block mold rotation angles. In general, early displacements appeared to consist of predominantly translational block movement in the downstream direction with a negligible rotational component. As the blocks slide further out of the mold, rotation becomes more prevalent as the blocks tumble about the downstream edge or corner. In all cases,

the time to eject the block was very rapid, ranging from approximately 0.10 to 0.15 s (model scale), once displacements could physically be observed in the video.

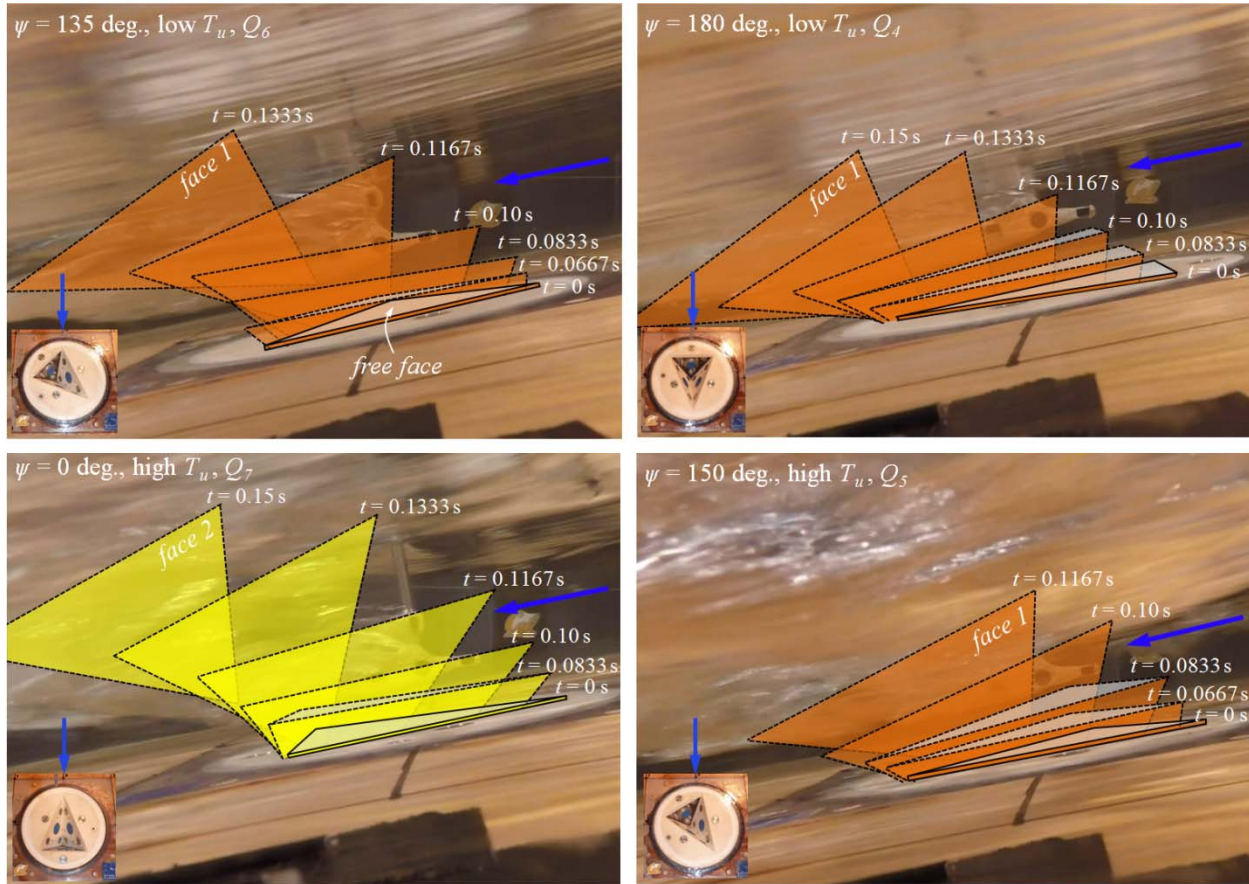


Figure 4-45. Post-incipient motion behavior for Block 2 in low (top) and high (bottom) T_u flow conditions (time values presented in model scale).

4.3.4 Block pressure statistics

For experiments not resulting in block removal, a statistical description of hydrodynamic pressures around the block was made. Of main interest were the average dynamic pressure, fluctuating dynamic pressure (represented by the root mean square (RMS) of pressure measurements), and instantaneous maximum and minimum pressure. These are represented by the dimensionless pressure coefficients, C_p , C'_p , C_p^+ and C_p^- , respectively, and can be calculated as follows:

$$C_p = \frac{P_{avg} - P_{static}}{\frac{1}{2} \cdot \rho_w \cdot u_x^2} \quad (4-9)$$

$$C'_p = \frac{P'}{\frac{1}{2} \cdot \rho_w \cdot u_x^2} \quad (4-10)$$

$$C_p^+ = \frac{P_{max} - P_{static}}{\frac{1}{2} \cdot \rho_w \cdot u_x^2} \quad (4-11)$$

$$C_p^- = \frac{P_{min} - P_{static}}{\frac{1}{2} \cdot \rho_w \cdot u_x^2} \quad (4-12)$$

where P_{avg} = average pressure, P_{static} = static pressure, P' = RMS of pressure fluctuations, P_{max} = maximum instantaneous pressure, P_{min} = minimum instantaneous pressure, and the quantity $\frac{1}{2} \cdot \rho_w \cdot u_x^2$ = the reference dynamic pressure attributed to the mean flow velocity. Note these coefficients represent the dynamic pressure where the static water pressure has been subtracted out.

Model experiments were performed for discharges Q_1 , Q_3 , Q_6 and Q_9 for durations of approximately 5 min. For discharges that exceeded the block erodibility threshold, a narrow metal rod was used to hold the block in place over the duration of the run (Figure 4-46). Two sets of repeat tests were performed for all scenarios for block mold rotation angles, $\psi = 0, 90,$ and 180 deg. Additionally, tests performed more than 15 minutes after the previous operation of the flume/run were discarded. Experiments performed outside this window appeared to yield inconsistent results which were attributed to expansion/contraction in the block mold/ramp from changes in temperature (which ultimately influenced pressure readings).

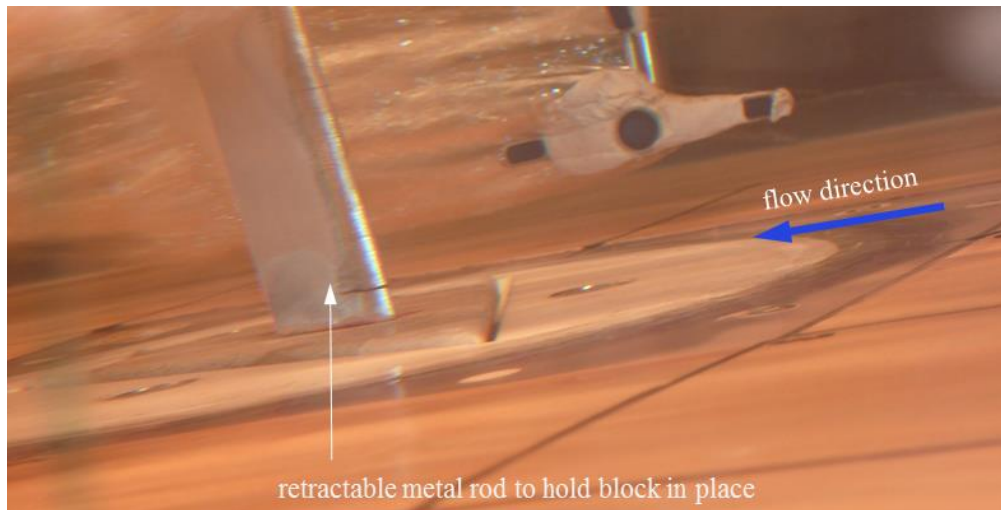


Figure 4-46. Retractable rod used to hold block in position for discharges exceeding the block erodibility threshold.

Average hydrodynamic pressure, C_p

Figure 4-47 and Figure 4-48 show C_p as a function of block mold rotation angle (ψ) for Blocks 1, 2 and 3 on the block faces inside the mold (faces 1, 2 and 3) for high and low T_u flow conditions, respectively. Numerical values for C_p and other pressure coefficients can be found in Appendix F. Note hydrodynamic pressures on the top of the block (face 4) are addressed later on. Values for C_p were consistent between runs for discharges Q_1 , Q_3 , Q_6 and Q_9 (Appendix F) and, accordingly, the below figures represent an average C_p value for all discharges for each ψ .

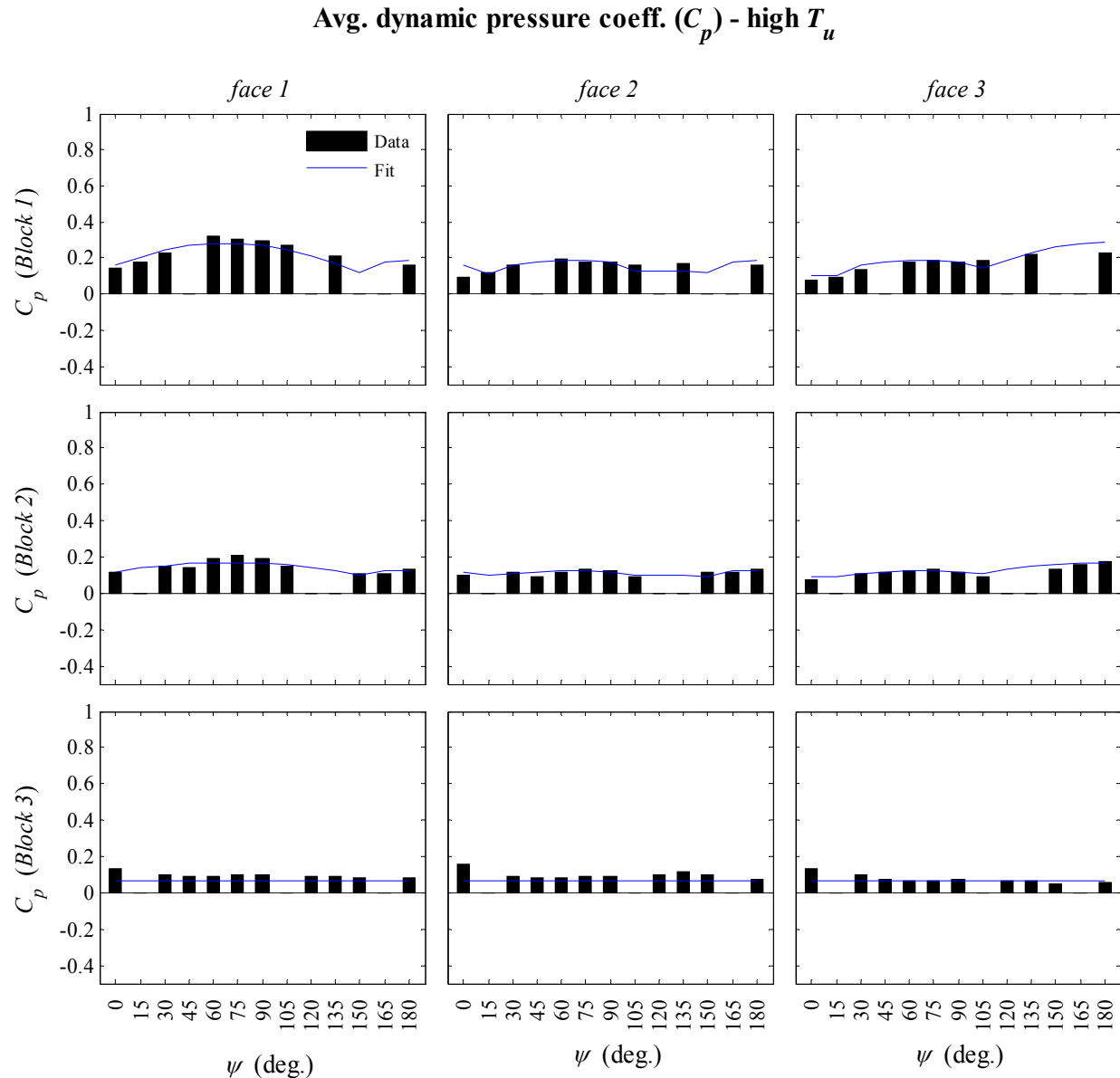


Figure 4-47. Average dynamic pressure coefficient for high T_u flow conditions as a function of block mold rotation angle for Block 1 (top), Block 2 (middle) and Block 3 (bottom) on block faces 1, 2 and 3.

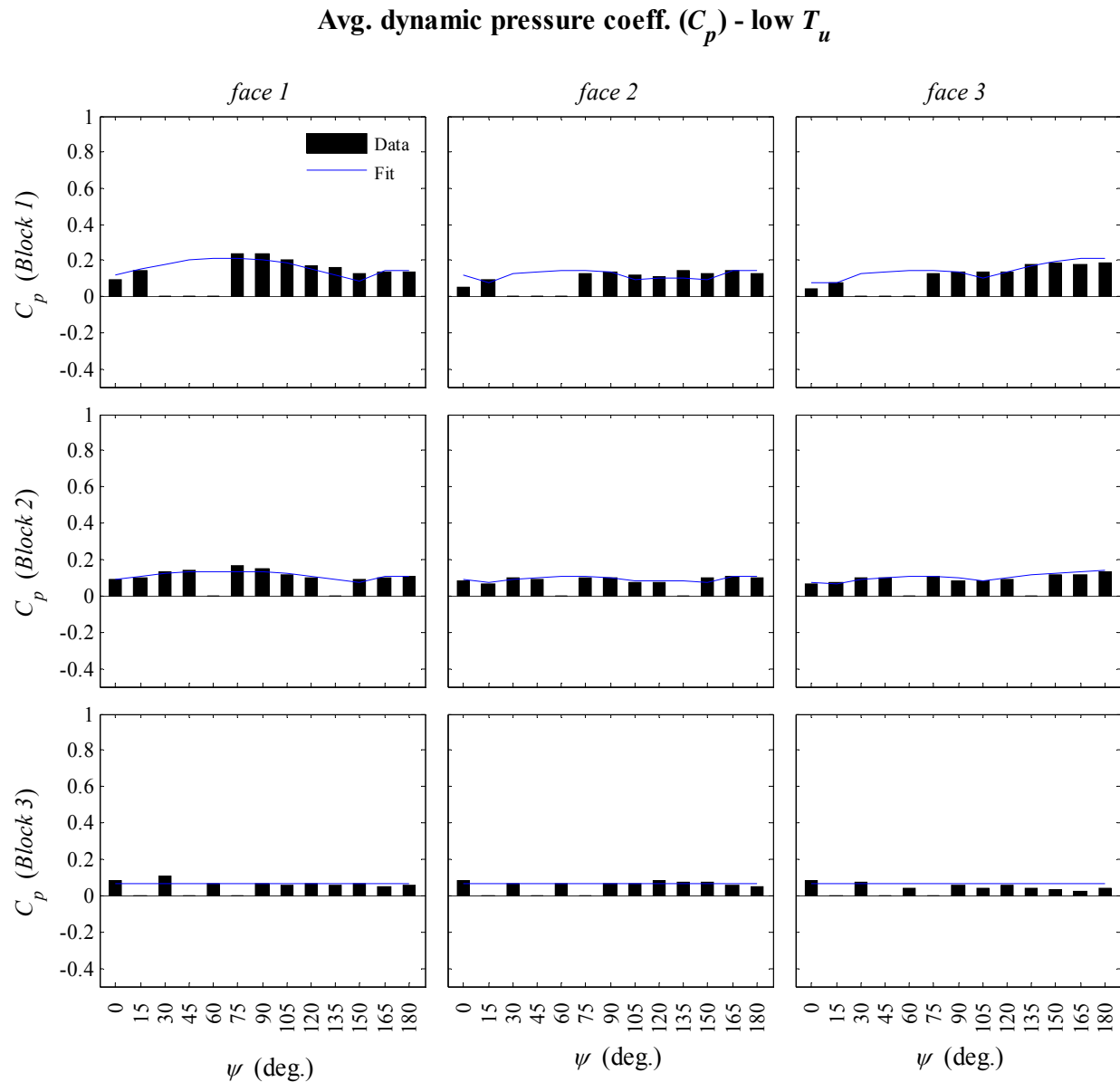


Figure 4-48. Average dynamic pressure coefficient for low T_u flow conditions as a function of block mold rotation angle for Block 1 (top), Block 2 (middle) and Block 3 (bottom) on block faces 1, 2 and 3.

Hydrodynamic pressure within the discontinuities around the block was predominantly controlled by flow impacting the upstream face(s) of the block that protrude above the channel bottom, which is often referred to as the stagnation pressure. This was influenced by the degree of turbulence in the channel, the angle (ξ) at which flow impacts the upstream face(s) (related to the block mold rotation angle), and the geometry of the protrusion itself (i.e., height and shape).

In general, increased turbulence intensity in the channel from low T_u conditions to high T_u conditions resulted in an approximately 30 % increase in the average dynamic pressure across all experiments. This was likely attributed to the larger vertical velocity component (u_z) of the flow field directed downwards toward the blocks caused by larger turbulent eddies in high T_u flows.

Changes in block mold rotation angle (ψ) also yielded a varying response in average dynamic pressure applied to block faces. This was evident for both high and low T_u flow conditions where a portion of the block protruded above the channel bottom (Block 1 and Block 2). For scenarios involving no block protrusion (Block 3), pressure response appeared relatively independent of ψ . Accordingly, a single average value was used to represent C_p for all block mold rotation angles on faces 1, 2 and 3. For high T_u flows, this was found to be $C_p = 0.090$ and for low T_u scenarios, $C_p = 0.062$.

For protruding blocks (Block 1 and Block 2), peak values of C_p occurred when an upstream block face was perpendicular to the flow direction ($\zeta = 90$ deg.). This was observed at $\psi = 75$ deg. for face 1 and $\psi = 180$ deg. for face 3. Note the upstream side of face 2 was never perpendicular to flow for any model tests. This result is logical as the hydraulic force vector acting normal to block face is at a maximum when the face is perpendicular to the flow direction. As ζ diverged from 90 deg., the magnitude of C_p decreased as the normal component of the hydraulic force diminished. This phenomenon is also influenced by the protrusion shape. For rounded block edge geometries, the block protrusion profile along the flow direction becomes more blunt as ζ approaches 90 deg. which results in increased pressure on the upstream block face (Figure 4-49).

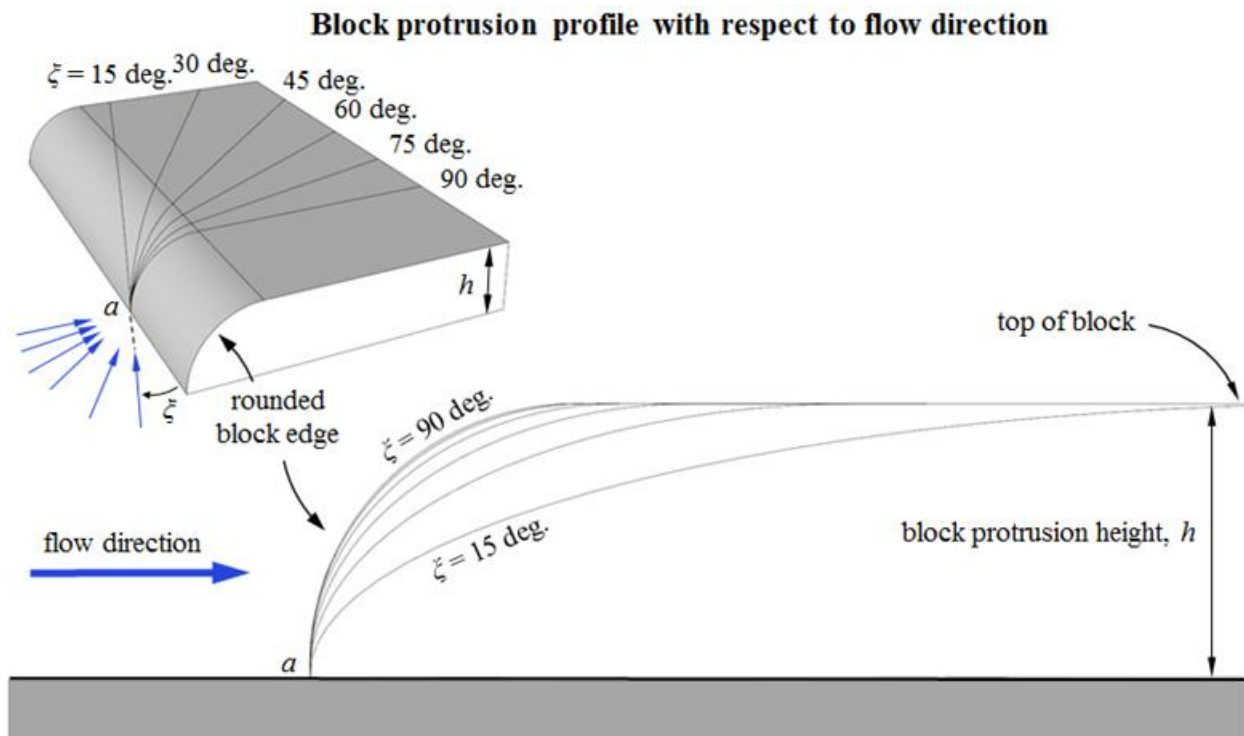


Figure 4-49. Schematic for block protrusion profile with respect to flow direction.

For Block 1 and Block 2, a least squares regression fit for C_p values on the block faces was developed (Figure 4-47 and Figure 4-48). The fit for each block face was based on the angle of the face with respect to the flow direction as well as whether the face was on the upstream or downstream side of the block. For upstream block faces, C_p may be expressed as:

$$C_p = C_1 \cdot \sin(\xi) + C_2 \quad (4-13)$$

where ξ = angle of the block face with respect to the flow direction (Figure 4-49) and C_1 and C_2 = correction coefficients. C_1 adjusts the relative magnitude of C_p , while C_2 accounts for the “background” hydrodynamic pressure. For the latter, C_2 is set equal to 0.090 or 0.062, corresponding to high or low T_u conditions, respectively, when no block protrusion exists. For a downstream block face with *one* upstream face (Figure 4-50), C_p may be expressed as:

$$C_p = C_3 \cdot (C_1 \cdot \sin(\xi) + C_2) \quad (4-14)$$

where ξ = angle of the *upstream* block face with respect to the flow direction and C_3 = correction coefficient that relates the relative magnitude of C_p on the upstream face(s) to the C_p on the downstream face(s). For a downstream block face with *two* upstream faces (Figure 4-50), C_p may be expressed as:

$$C_p = C_3 \cdot \left[\frac{(C_1 \cdot \sin(\xi_1) + C_2) + (C_1 \cdot \sin(\xi_2) + C_2)}{2} \right] \quad (4-15)$$

where ξ_1 = angle of the *first upstream* block face with respect to the flow direction, and ξ_2 = angle of the *second upstream* block face with respect to the flow direction (Figure 4-50). In this case, C_p on the downstream face is related to the average of C_p on the two upstream faces.

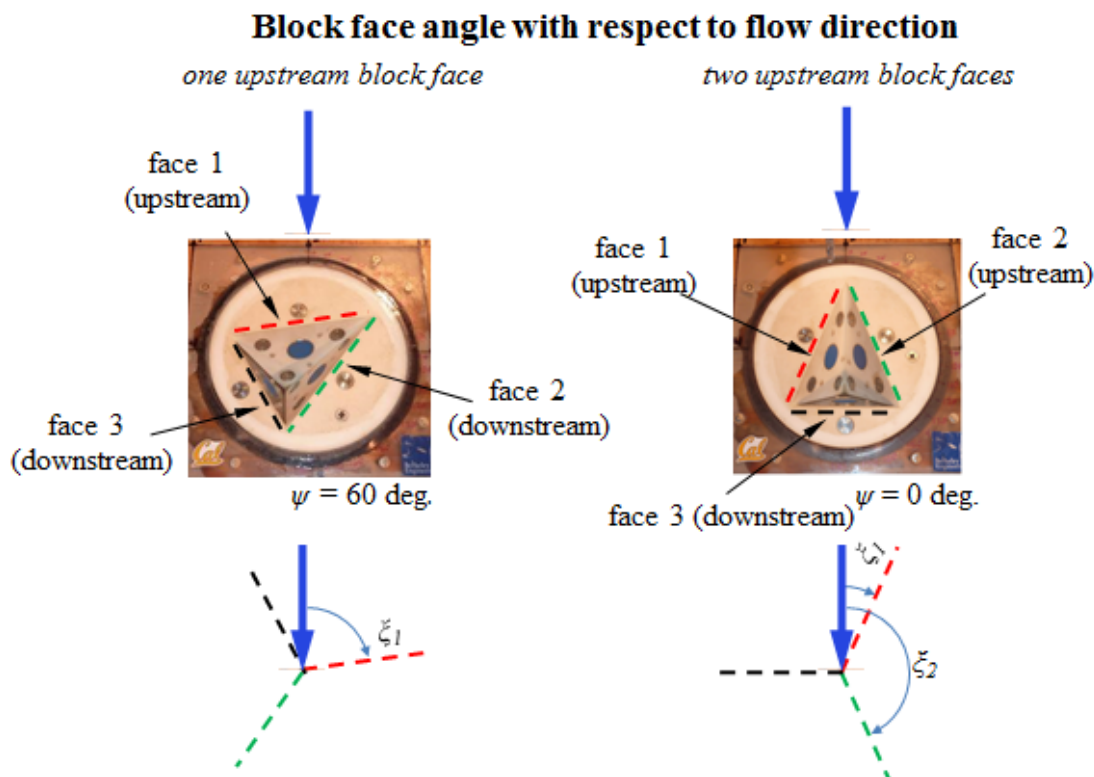


Figure 4-50. Schematic for definition of block face angle with respect to flow direction for one upstream block face (left) and two upstream block faces (right).

Coefficients C_1 and C_3 were determined using a least squares regression with the above equations and the measured C_p data, while keeping the value of C_2 constant. This was done for Block 1, Block 2 and Block 3 for both high and low T_u flow conditions (Appendix F). Numerical values for the coefficients are presented in Table 4-15, and are plotted as a function of block protrusion height in Figure 4-51.

Table 4-15. C_p correction coefficients.

Block	Turb.	C_1	C_2	C_3
1	High	0.195	0.090	0.650
	Low	0.153	0.062	0.680
2	High	0.080	0.090	0.729
	Low	0.075	0.062	0.776
3	High	0	0.090	1
	Low	0	0.062	1

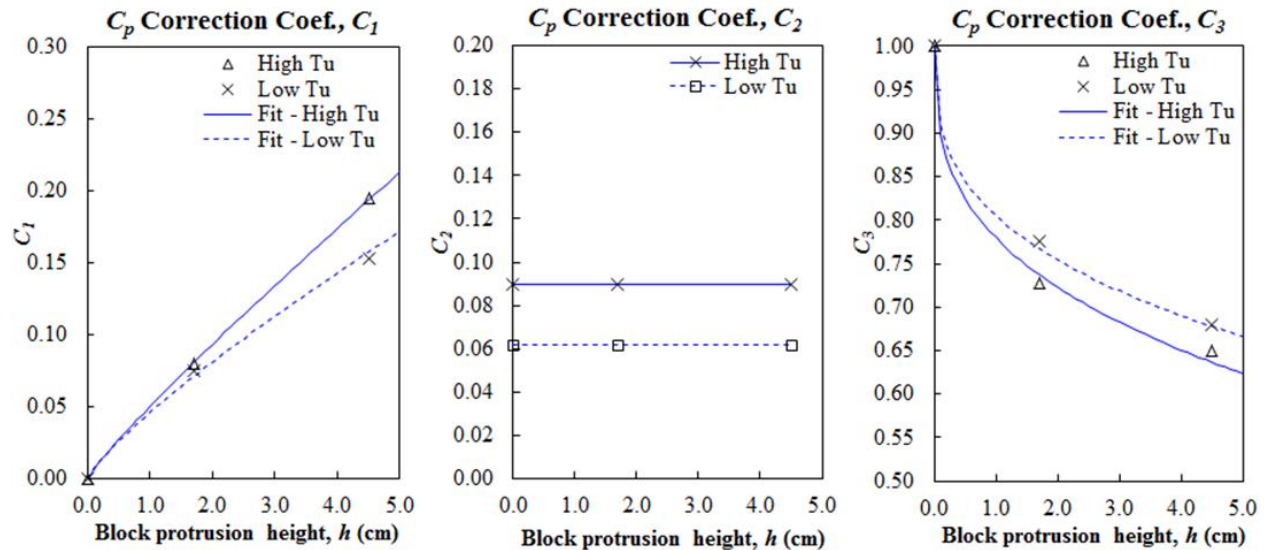


Figure 4-51. C_p correction coefficients C_1 , C_2 and C_3 as a function of block protrusion height.

Empirical expressions for coefficients C_1 and C_3 are presented as a function of block protrusion height (h). Values of fit parameters a and b for C_1 and C_3 are presented in Table 4-16.

$$C_1 = a \cdot h^b \quad (4-16)$$

$$C_3 = 1 - a \cdot h^b \quad (4-17)$$

Table 4-16. Fit parameters for C_p correction coefficients C_1 and C_3 .

Coef.	Turb.	a	b
C_1	High	0.050	0.901
	Low	0.046	0.820
C_3	High	0.220	0.333
	Low	0.195	0.333

Comparison of average hydrodynamic pressure coefficients measured from this study to data collected from a previous study by Frizell (2007) at the United States Bureau of Reclamation (USBR) on hydraulic jacking of concrete spillway slabs (Figure 2-9) was performed. In that study, prototype scale velocities were used ranging from 3 m/s to 17 m/s for slab protrusions of 3 mm to 19 mm oriented perpendicular to the flow direction. C_p values were extracted from Frizell data as a function of block offset (protrusion height) for the case of a vented slab containing a 3 mm radius edge geometry (comparable to the rounded edge geometry of Block 1 and Block 2 from this study) at a flow velocity of 3 m/s. A vented slab refers to a slab with an underlying discontinuity that is open to the channel on the upstream and downstream face. This data was compared to C_p values on block face 3 under high and low T_u flow conditions, for runs with a block rotation angle, $\psi = 180$ deg. (Figure 4-52). At this configuration, face 3 is perpendicular to the flow direction (similar to the Frizell study). C_p values calculated using Equation (4-13 (based on a fit of the entire model data set) are also provided for comparison.

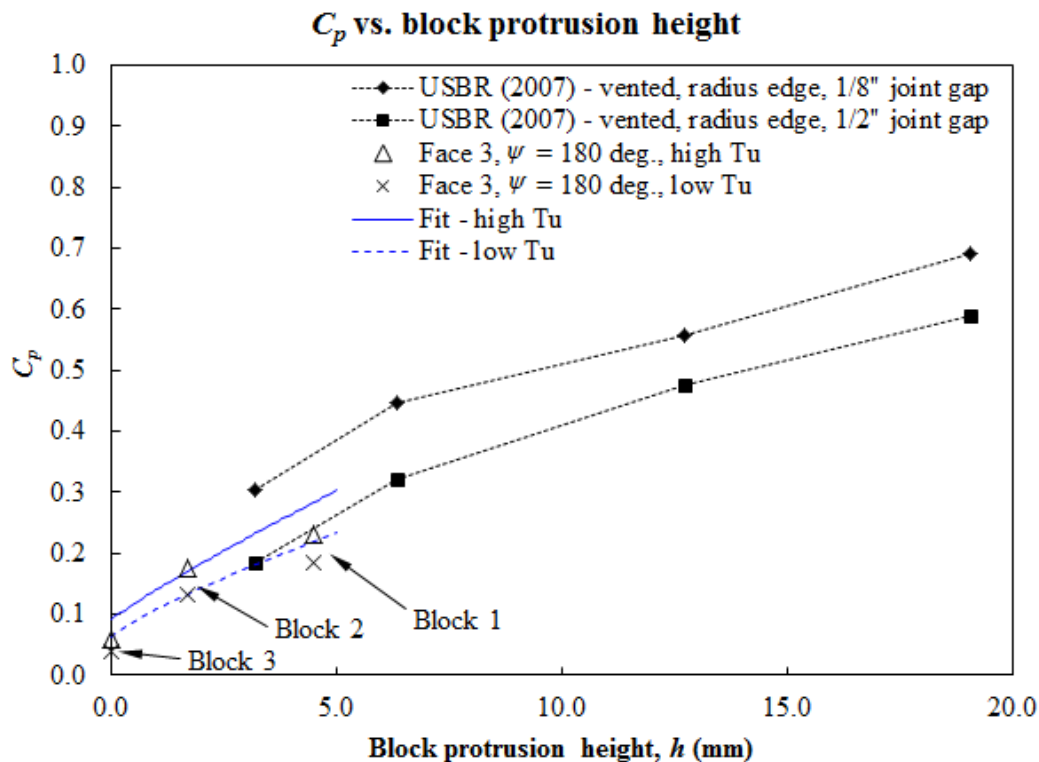


Figure 4-52. Comparison of average hydrodynamic pressure coefficients obtained from the current model study data to previous data from the USBR (Frizell 2007). Note that block protrusion heights for this study are presented in *model scale* to ensure block edge geometries are comparable between the two data sets.

Block protrusion heights examined in this study were near or below the smallest block offset tested by Frizell. Protrusion heights are presented in *model scale* to ensure block edge geometries are comparable between the two data sets. As indicated in Figure 4-52, C_p values on face 3 for runs with $\psi = 180$ deg., as well as values predicted by Equation (4-13, show reasonable agreement with the trend in C_p versus h collected previously by Frizell. A subtle deviation in C_p measured at the highest protrusion height from this study (Block 1) from data of the previous study could potentially be associated with small differences in block edge geometries.

Average hydrodynamic pressures on the block free face (face 4) were not measured directly due to difficulty having sensor wire leads connect with removable blocks. Sensors 1, 5 and 9 were positioned on top of the block mold at the openings of the discontinuities for each block face (1, 2 and 3, respectively) in an attempt to capture pressures near the top of the block (Figure 4-6). In experiments involving Block 3 (no protrusion), the average dynamic pressure coefficient as a function of block mold rotation angle is presented in Figure 4-53 for both high and low T_u flow conditions. Similar to faces 1, 2 and 3, C_p values were consistent on face 4 between all discharges analyzed (Q_1 , Q_3 , Q_6 and Q_9) (Appendix F). Accordingly, Figure 4-53 shows an average C_p value from runs for Q_1 , Q_3 , Q_6 and Q_9 at each ψ value. Average pressures on top of the block were comparable to those measured inside discontinuities surrounding the block in both magnitude and relative independence from the block mold rotation angle. Therefore, an average value of C_p was used to represent data for all orientations of Block 3. For high T_u flows, this was found to be $C_p = 0.095$ and for low T_u flow $C_p = 0.075$.

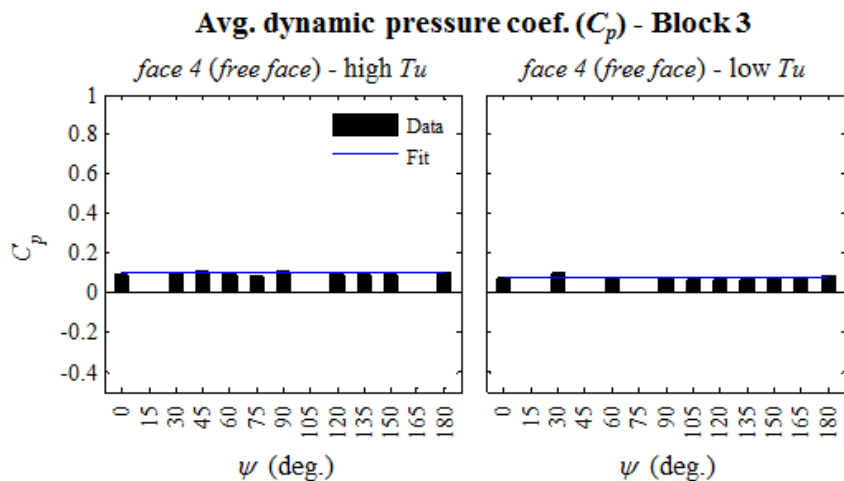


Figure 4-53. Average dynamic pressure coefficient for high (left) and low (right) T_u flow conditions as a function of block mold rotation angle for Block 3 on face 4.

In experiments involving Block 1 and Block 2, proximity of sensors 1, 5, and 9 to the block yielded unreliable measurements due to effects from the block protrusion. Consequently, an estimate of the hydrodynamic force applied to face 4 in these cases was made through calibration of the mean active resultant force vector, \mathbf{r}_{avg} , applied to the block for runs that resulted in block removal. This was done by adjusting the average dynamic pressure coefficient for face 4 until, \mathbf{r}_{avg} , coincided with the block yield condition on a limit equilibrium stereonet (e.g., Figure 4-22), indicating the block was in a state of equilibrium at the threshold of erosion (see Chapter 5 for

calculation of the active resultant force vector and limit equilibrium stereonet). This was also done for runs conducted for pressure statistics analysis where \mathbf{r}_{avg} vectors associated with discharges Q_1 , Q_3 , Q_6 and Q_9 were calibrated on a limit equilibrium stereonet to coincide with the block yield condition. This is shown in Figure 4-54 for low T_u flow conditions and a block mold rotation angle, $\psi = 180$ deg. The mean active resultant force vector orientations for Block 1, Block 2 and Block 3 associated with hydrodynamic loads from discharges Q_1 , Q_3 , Q_6 and Q_9 are plotted. The block yield condition, corresponding to a friction angle, $\phi = 16$ deg. on the block discontinuities, is also shown. For these conditions, the block erodibility threshold for Block 1 occurs just below a discharge of Q_1 , while for Block 2 the threshold occurs at Q_3 (see earlier section on threshold values). As such, the C_p values on face 4 for Blocks 1 and 2 were adjusted such that \mathbf{r}_{avg} for Q_1 (Block 1) plots just outside of the block yield condition, while \mathbf{r}_{avg} for Q_3 (Block 2) plots on the block yield condition. Additional calibrated limit equilibrium stereonet can be found in Appendix F.

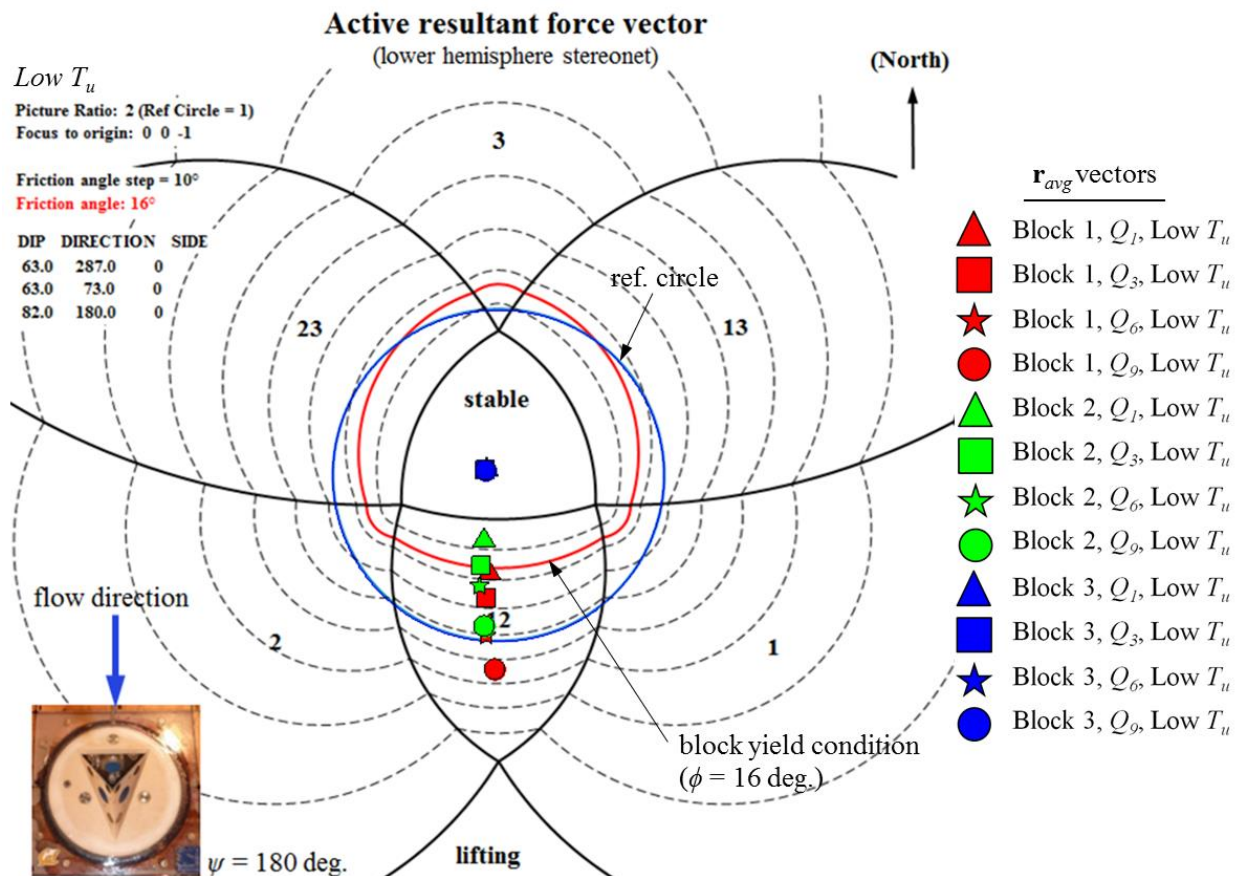


Figure 4-54. Limit equilibrium stereonet for Blocks 1, 2 and 3 showing orientation of mean active resultant force vector (\mathbf{r}_{avg}) for $\psi = 180$ deg., low T_u , and discharges Q_1 , Q_3 , Q_6 and Q_9 . Kinematic mode indicated as 2-plane sliding on face 1 and face 2, except for Block 3 which is stable under all flow conditions.

All calibrated C_p values for face 4 are presented in Figure 4-55. Values correspond to model scenarios with block response type 1 and 2 (described in the previous section on block removal

mechanics) for which a pseudo-static treatment of hydraulic forces on the block appeared appropriate. Values in Figure 4-55 for experiments performed during block erodibility threshold testing are given and additional label of BET. The average value for all ψ is $C_p = 0.005$ for both Block 1 and Block 2, indicating a near hydrostatic pressure distribution for the block free face. Further refinement of the axis scale in Figure 4-55, however, reveals a C_p dependence on ψ (which is more prevalent for Block 1). Potential causes for this could be related to changes in block protrusion profile associated with changes in ψ (Figure 4-49) or additional forces applied to the block not captured by pressure sensors (such as a high pressure region on the upstream side of the block where flow impacts the block protrusion).

Of additional interest in Figure 4-54 is the response of the mean active resultant force vector to changes in block protrusion height and increased flow velocity (associated with increasing discharge). In absence of any hydraulic load (gravity loading only), the initial resultant force vector for a block (\mathbf{r}_0) will plot directly in the center of the reference circle (in a lower hemisphere stereonet) as the orientation of the vector is vertically downward from the self-weight of the block (\mathbf{W}_b). For a flush block with no protrusion (Block 3), \mathbf{r}_{avg} for all discharges plots near the center of the reference circle which suggests the pressure distribution around the block is near hydrostatic and the dominant force is the submerged weight of the block. For block protrusion (Block 2), \mathbf{r}_{avg} rotates outward in the downstream direction in response to the added hydrodynamic forces associated with the block exposure in the channel. Increased flow velocity results in further outward rotation of \mathbf{r}_{avg} along a relatively constant azimuth, which in Figure 4-54 for $\psi = 180$ deg., is directly in the downstream direction. This indicates build-up of hydrodynamic pressure associated with higher flow velocity occurs uniformly across block faces. For increased block protrusion (Block 1), a higher degree of outward rotation in \mathbf{r}_{avg} is observed due increased hydrodynamic pressure applied to Block 1 in comparison to Block 2, but still along the same constant azimuth in the downstream direction. A schematic for the rotation of the active resultant force vector is depicted in Figure 4-56 for Block 2 loading conditions along with kinematic block failure modes (which are discussed in more detail in Chapter 5). As the vector rotates outward, the block becomes unstable at Q_3 and slides along faces 1 and 2.

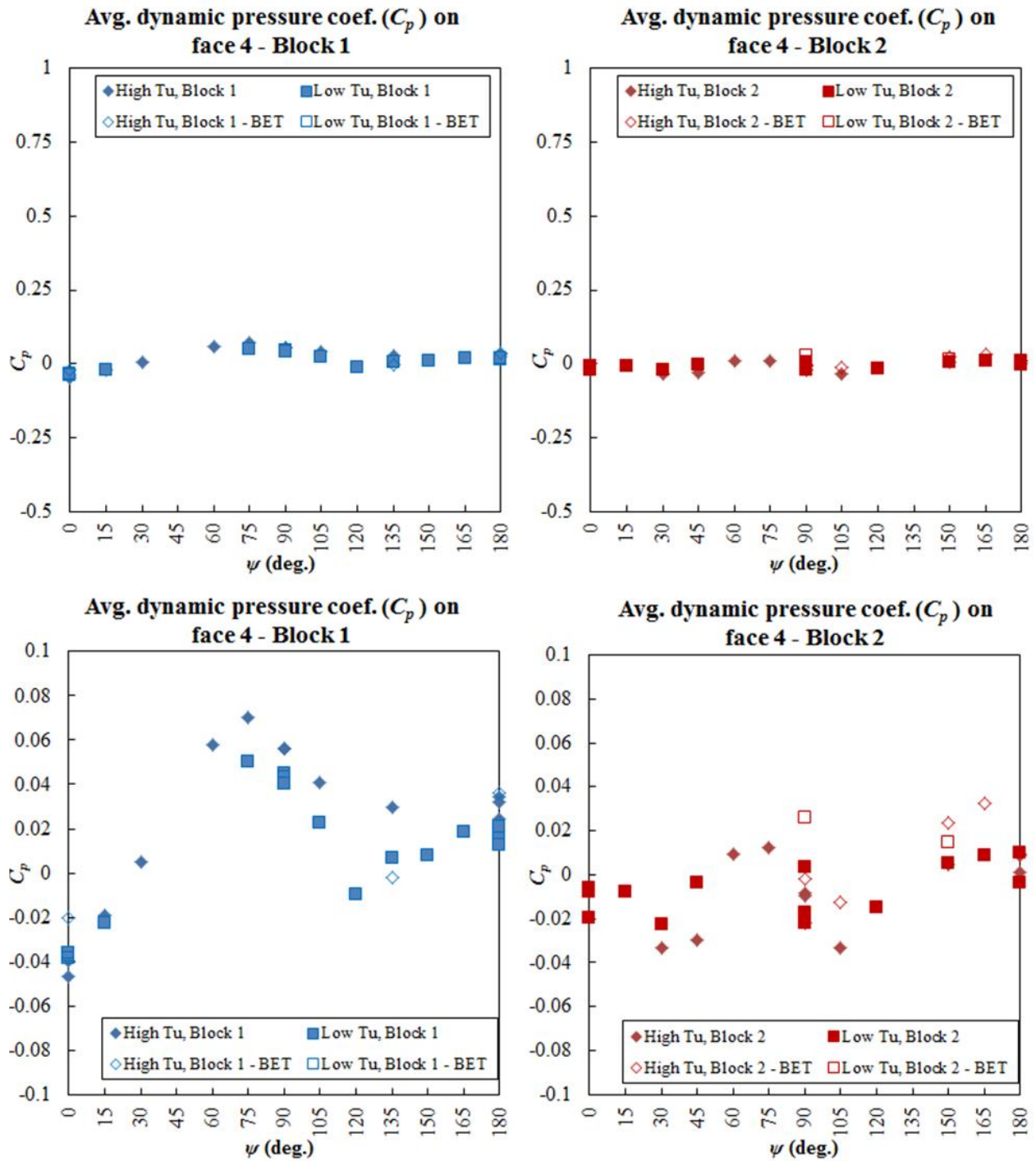


Figure 4-55. Calibrated average dynamic pressure coefficient (C_p) for Block 1 face 4 (left) and Block 2 face 4 (right). Plots with refined axis scale are provided on bottom.

Rotation of mean active resultant force vector, \mathbf{r}_{avg} , due to hydraulic loading

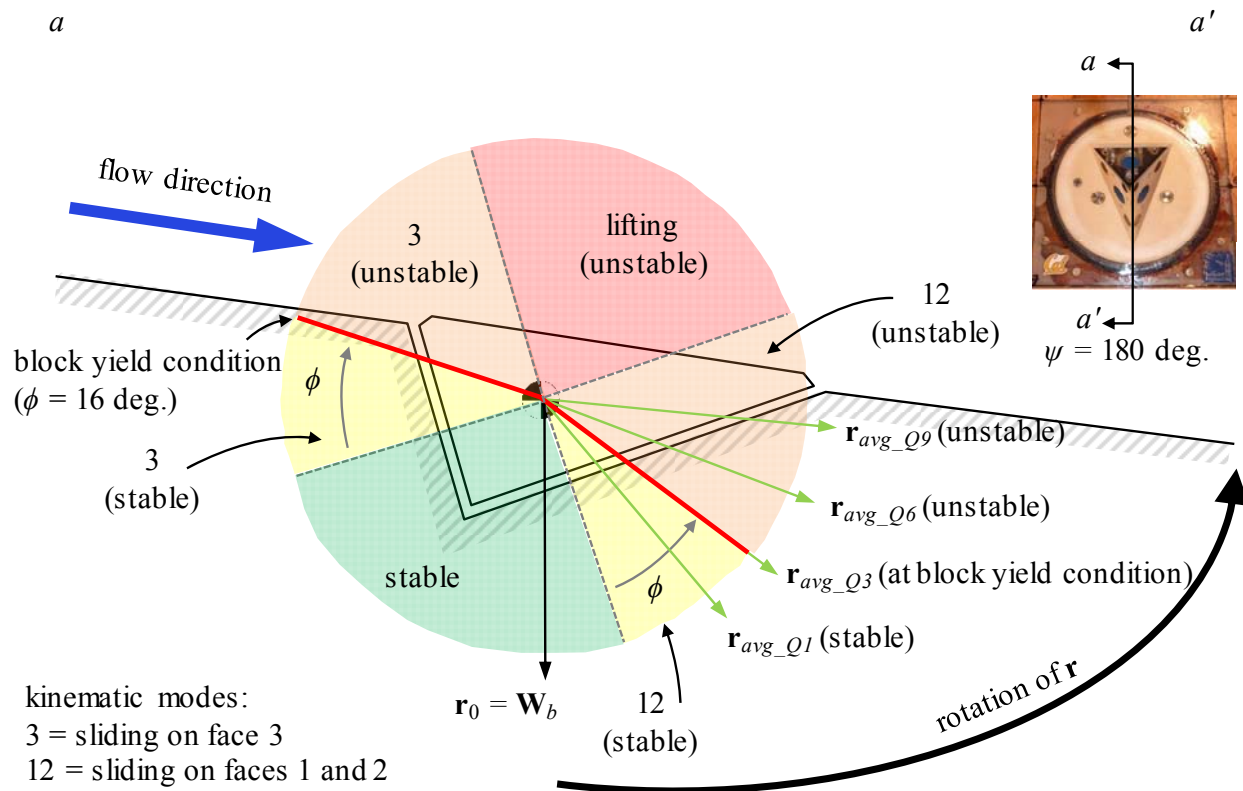


Figure 4-56. Schematic showing rotation of active resultant force vector, \mathbf{r} , for loading of Block 2 due to discharges Q_1 to Q_9 . Block kinematic failure modes (Chapter 5) corresponding to limit equilibrium regions in Figure 4-54 are also shown with respect to orientation of \mathbf{r} .

Fluctuating hydrodynamic pressure, C'_p

Figure 4-57 and Figure 4-58 show C'_p as a function of block mold rotation angle (ψ) for Blocks 1, 2 and 3 on the block faces inside the mold (faces 1, 2 and 3) for high and low T_u flow conditions, respectively. Note the scale on the plots was adjusted to be consistent with plots for C_p above as well as those for C_p^+ and C_p below to allow comparison of the relative magnitude between pressure coefficients. Numerical values for C'_p can be found in Appendix F. As with C_p , values for C'_p were consistent between runs for discharges Q_1 , Q_3 , Q_6 and Q_9 (Appendix F) and, accordingly, the below figures represent an average C'_p value for all discharges for each ψ .

In general, the magnitude of RMS pressures was approximately 5 to 20% of the average dynamic pressure. C'_p values were relatively independent of block mold rotation angle and consistent between block faces. Accordingly, average values of C'_p were used to represent data for all orientations of Block 1, Block 2 and Block 3. For high T_u flow, this was found to be $C'_p = 0.022$, 0.019 and 0.017, respectively. Values for low T_u flows were approximately 50 % less and were $C'_p = 0.012$, 0.012 and 0.008, respectively. A small increase in C'_p is observed with increasing block protrusion height (h) as fluctuations from turbulent eddies in the flow field are less influenced by the channel bottom boundary. The fluctuating hydrodynamic pressures on the top of Block 3 (face 4) were similar to those inside the block mold on faces 1, 2 and 3, and were

$C'_p = 0.018$ and 0.007 for high and low T_u conditions, respectively. Values for face 4 on Block 3 are shown in Figure 4-59.

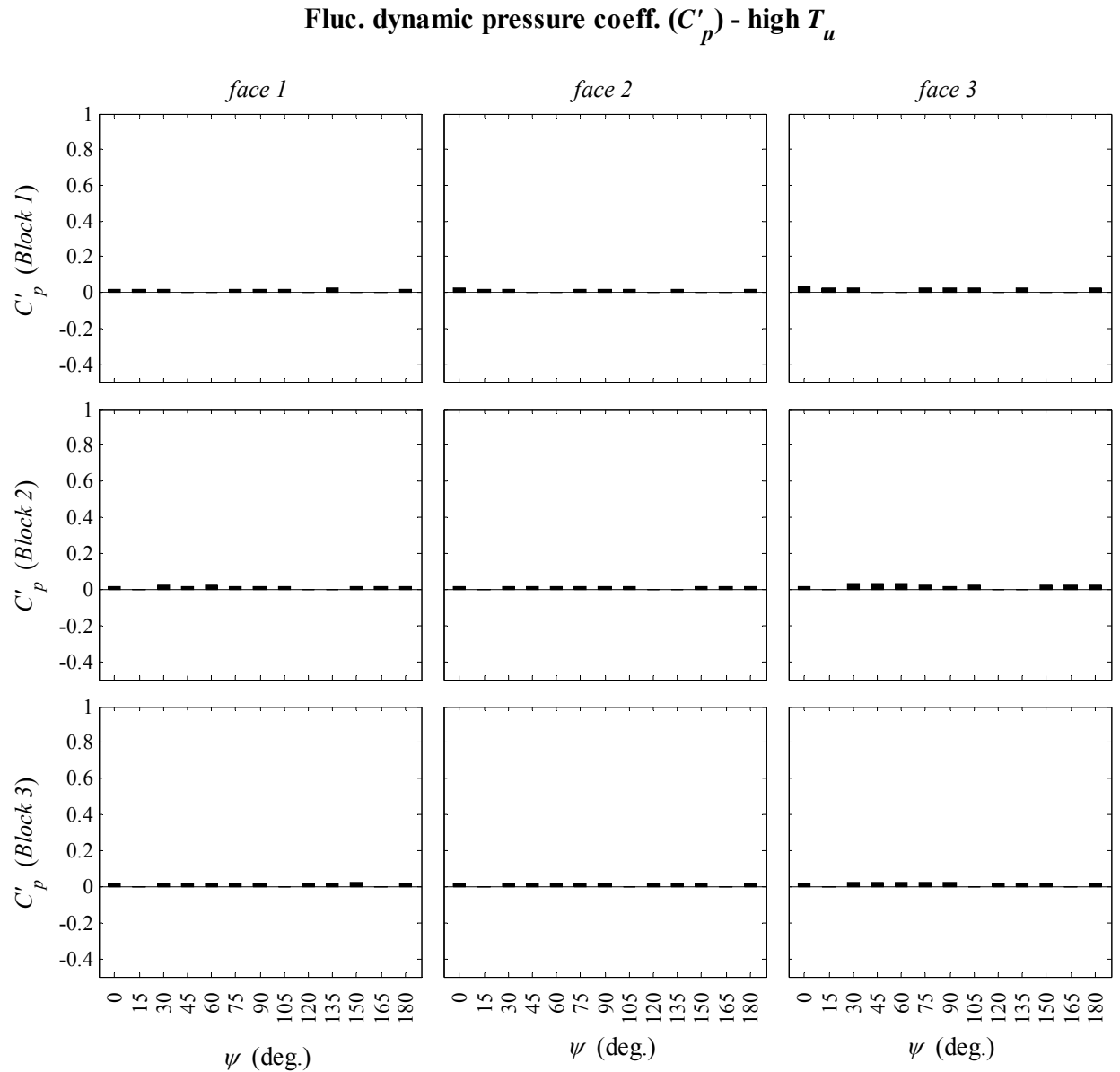


Figure 4-57. Fluctuating dynamic pressure coefficient for high T_u flow conditions as a function of block mold rotation angle for Block 1 (top), Block 2 (middle) and Block 3 (bottom) on block faces 1, 2 and 3.

Fluc. dynamic pressure coeff. (C'_p) - low T_u

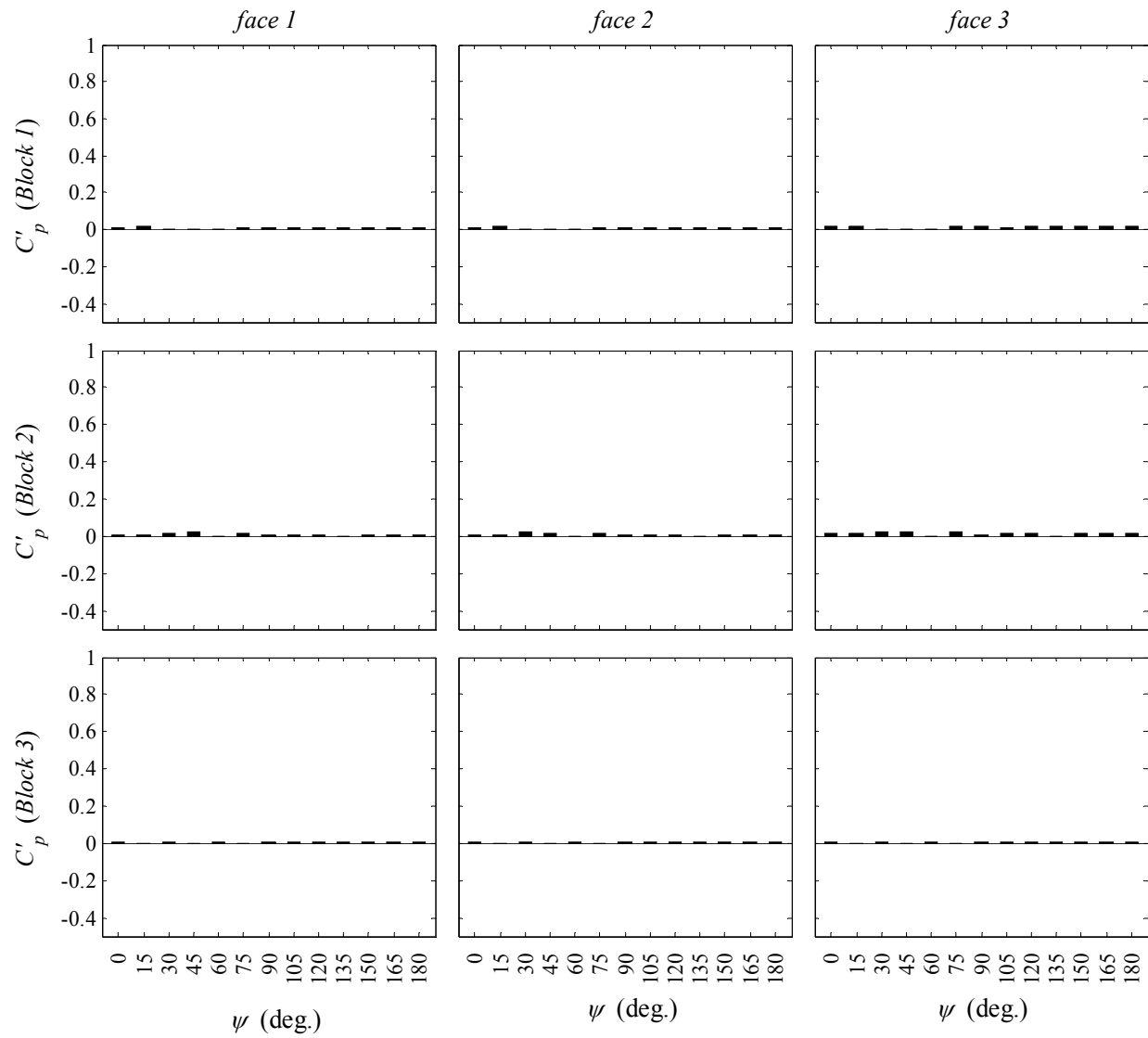


Figure 4-58. Fluctuating dynamic pressure coefficient for low T_u flow conditions as a function of block mold rotation angle for Block 1 (top), Block 2 (middle) and Block 3 (bottom) on block faces 1, 2 and 3.

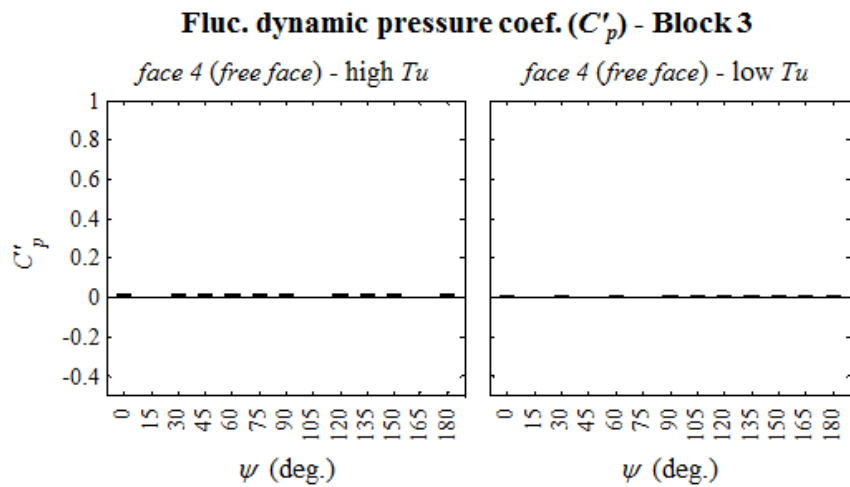


Figure 4-59. Fluctuating dynamic pressure coefficient for high (left) and low (right) T_u flow conditions as a function of block mold rotation angle for Block 3 on face 4.

Maximum and minimum instantaneous hydrodynamic pressure, C_p^+ and C_p^-

Figure 4-60 and Figure 4-61 show C_p^+ and C_p^- as a function of block mold rotation angle (ψ) for Blocks 1, 2 and 3 on the block faces inside the mold (faces 1, 2 and 3) for high and low T_u flow conditions, respectively. Note the scale on the plots was adjusted to be consistent with plots for C_p and C'_p above to allow comparison of the relative magnitude between pressure coefficients. Numerical values for C_p^+ and C_p^- can be found in Appendix F. Values represent an average maximum and minimum dynamic pressure coefficient of all discharges (Q_1 , Q_3 , Q_6 and Q_9) for each ψ . Individual maximum and minimum values for each flow rate on each block face can also be found in Appendix F.

On average, maximum instantaneous values on block faces inside the mold were approximately 150 % higher than corresponding average hydrodynamic pressures for high T_u flows and 100 % higher for low T_u flows. Minimum instantaneous values were approximately 120 % lower than corresponding C_p values for high T_u cases and about 80% lower for low T_u cases. Although the magnitude of C_p^+ and C_p^- values were greater for runs involving protruding blocks (Block 1 and Block 2), the percent change in the maximum and minimum hydrodynamic pressures relative to C_p was greatest for Block 3 (with no protrusion). Values for C_p^+ and C_p^- on the top of Block 3 (face 4) are shown in Figure 4-62. The average increase for C_p^+ and the average decrease for C_p^- with respect to C_p were consistent with results for the other block faces.

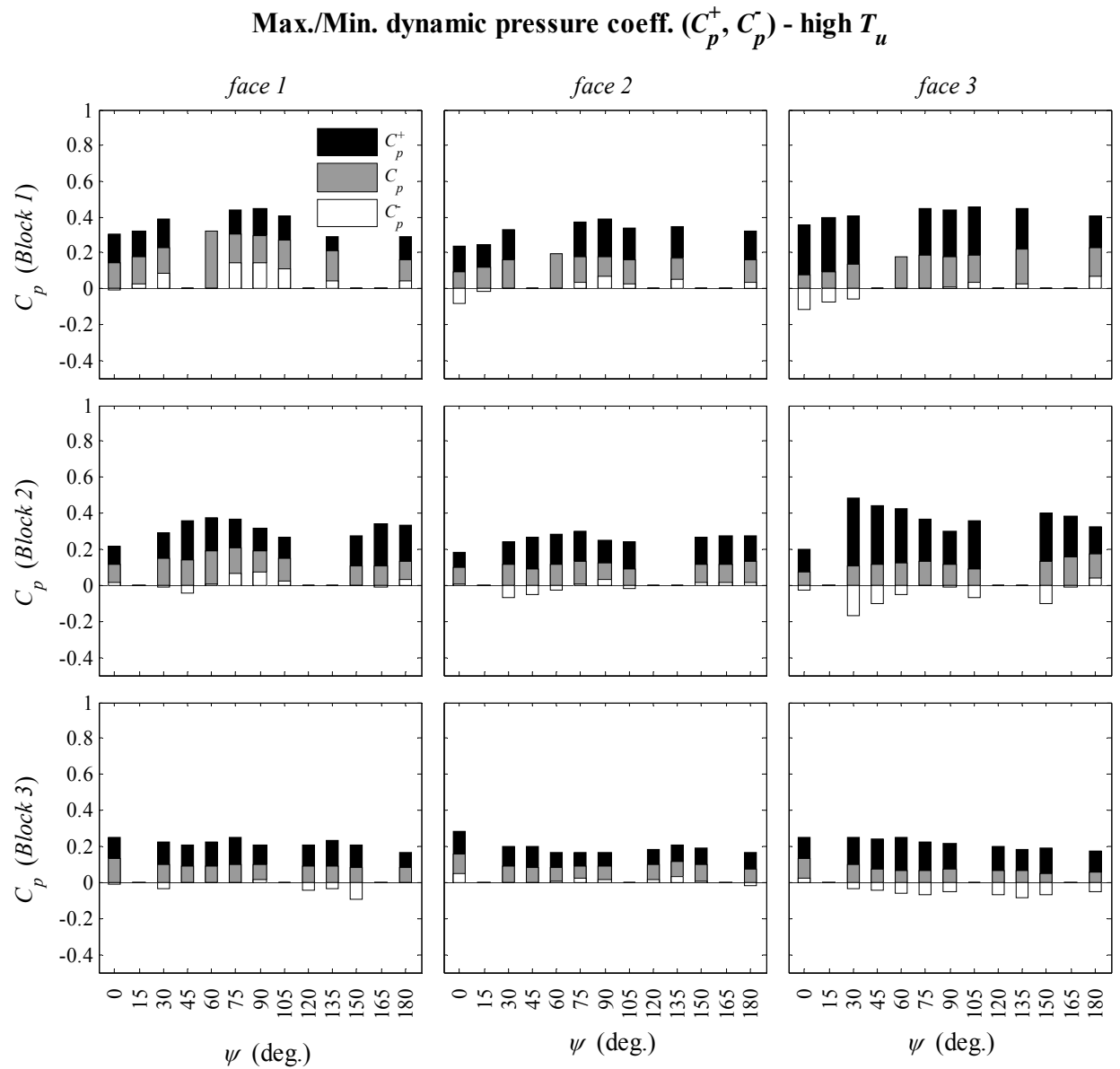


Figure 4-60. Maximum (black bar) and minimum (white bar) instantaneous dynamic pressure coefficient for high T_u flow conditions as a function of block mold rotation angle for Block 1 (top), Block 2 (middle) and Block 3 (bottom) on block faces 1, 2 and 3. The average dynamic pressure coefficient (gray bar) is provided for reference.

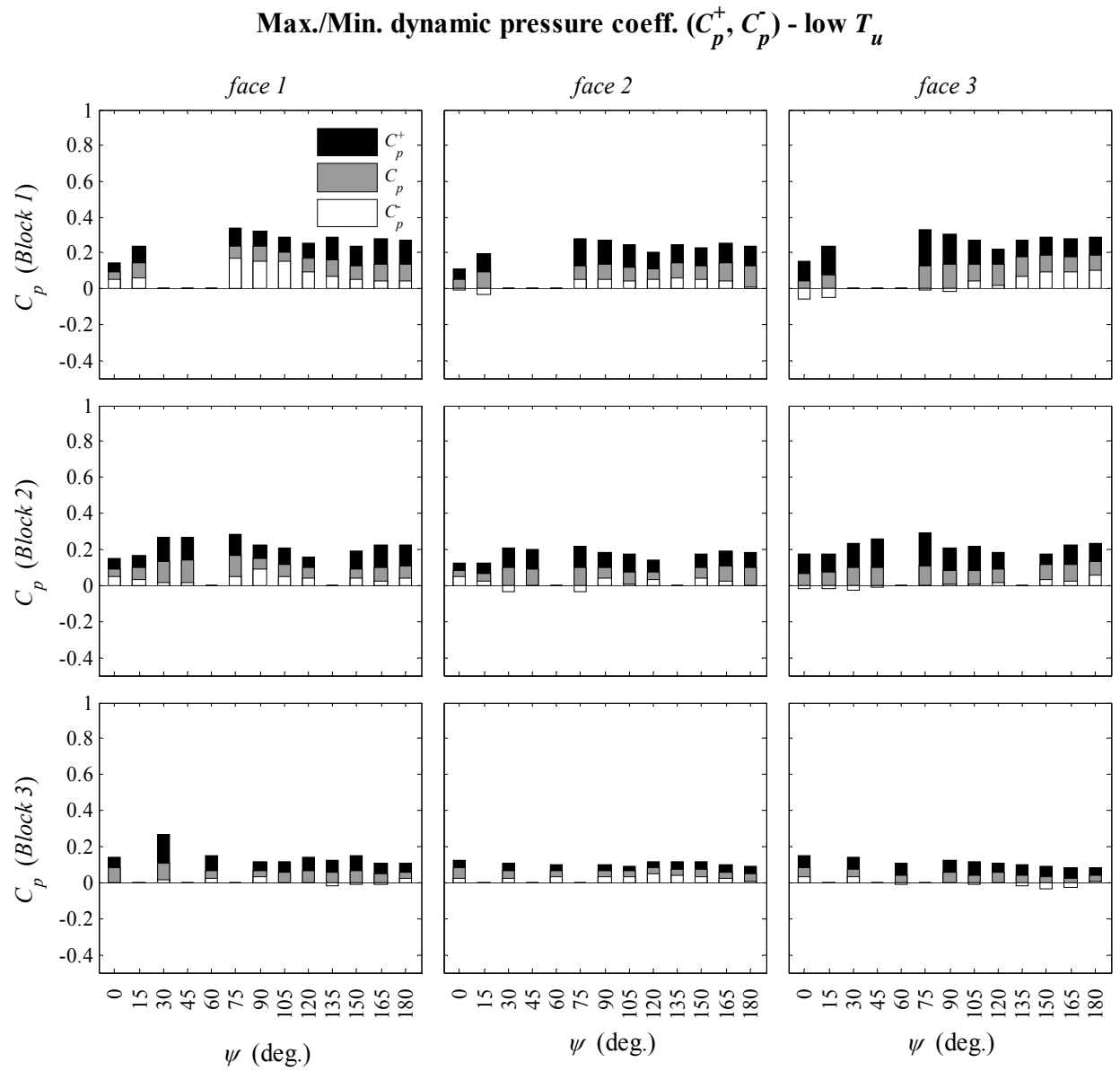


Figure 4-61. Maximum (black bar) and minimum (white bar) instantaneous dynamic pressure coefficient for low T_u flow conditions as a function of block mold rotation angle for Block 1 (top), Block 2 (middle) and Block 3 (bottom) on block faces 1, 2 and 3. The average dynamic pressure coefficient (gray bar) is provided for reference.

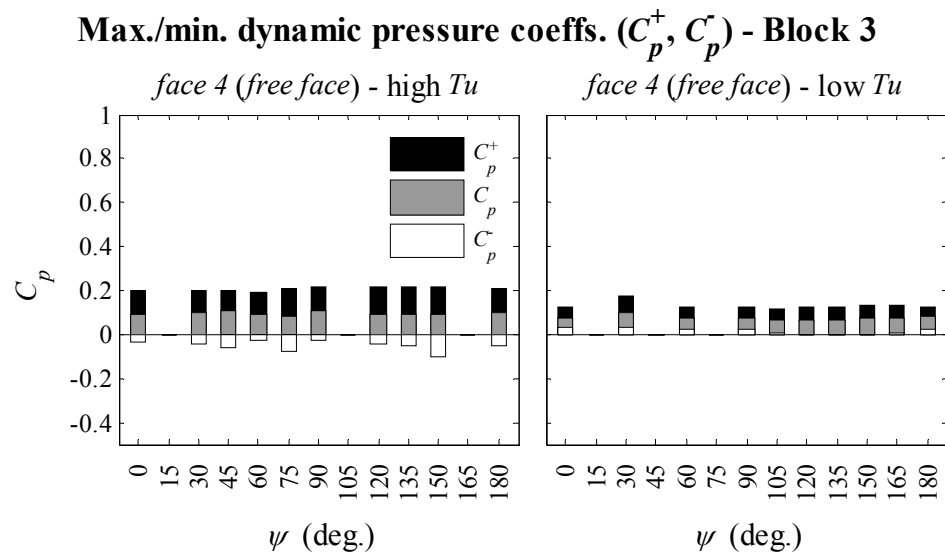


Figure 4-62. Maximum (black bar) and minimum (white bar) instantaneous dynamic pressure coefficient for high (left) and low (right) T_u flow conditions as a function of block mold rotation angle for Block 3 on face 4. The average dynamic pressure coefficient (gray bar) is provided for reference.

4.4 Summary

A scaled physical hydraulic model study was performed in an open channel flume at the University of California's RFS to examine scour of 3D rock blocks (Figure 4-3 and Figure 4-4). An instrumented 3D block mold was constructed that could be rotated with respect to the flow direction to study the influence of discontinuity orientation on block erodibility over a range of flow conditions (Figure 4-4). Four main variables were monitored within the realm of this study and included the block mold rotation angle (ψ), turbulence intensity (T_u), block protrusion height (h), and the flow velocity (\mathbf{u}). Results were presented in four main sections: flow characterization, block erodibility threshold, block removal mechanics and block pressure statistics. The key findings of each section are summarized below. *Values are presented in prototype scale unless otherwise noted.* All supplementary model data can be found in Appendices B, C, D, E and F.

4.4.1 Flow characterization

- A general description of flow conditions in the channel and in the vicinity of the block was made. Removable baffle blocks upstream of the block location (Figure 4-3) allowed for analysis of high and low turbulence conditions. Nine flow rates were analyzed and ranged from 6.6 to 89.8 m^3/s (Q_1 to Q_9 , respectively) (Table 4-10). The corresponding mean stream-wise channel flow velocity at the block location (location 5, Figure 4-7) ranged from $u_x = 7.38$ to 9.35 m/s for the low turbulence flow to $u_x = 6.59$ to 8.57 m/s for the high turbulence flows (Table 4-6). The relative degree of turbulence was expressed using the turbulence intensity (T_u) which related the root mean square (RMS) of the

vertical velocity component (u'_z) to u_x . Values ranged from $T_u = 2.2\%$ to 2.8% for the low turbulence cases to $T_u = 6.0\%$ to 7.4% for the high turbulence cases (Table 4-11).

- Flow conditions at the block location for all model runs were supercritical as indicated by Froude numbers significantly greater than unity (Table 4-12). These values ranged from $Fr = 2.5$ to approximately 7.0 for both high and low T_u cases. The relatively large mean flow velocities in this section also ensured that Reynolds numbers were sufficiently high to adequately represent form drag forces on the block. Re values ranged from approximately $2.0 \cdot 10^4$ to $3.0 \cdot 10^5$ (Table 4-13).
- Despite minimizing the prototype/model length scale ratio (L_r), prototype Re values were still more than 30 times greater than those obtained in the model (i.e., $Re_r = L_r^{3/2} = 10^{3/2} = 32$). In these experiments, model flows tend to dampen high frequency (small length scale) turbulent eddies more so than in prototype settings due to the increased influence of viscosity. These eddies influence the amount of air entrained at the free surface boundary, which can explain the lack of air present in the model runs. This is only problematic in the sense that resonance phenomena attributed to high frequency pressure fluctuations and air entrainment in the rock discontinuities cannot be adequately represented in this model. This specific process was, however, beyond the scope of this research.
- Spectral density analysis of velocity time-series data transformed to a frequency domain indicated that the presence of the baffle blocks within the flow field introduces a predominant turbulent eddy frequency of approximately 0.6 to 1.3 Hz (Figure 4-12). This frequency is not present when baffles are absent from the channel (Figure 4-13).

4.4.2 Block erodibility threshold

- The critical (threshold) mean flow velocity resulting in removal of the 3D block was determined for each flow condition as a function of block mold rotation angle, turbulence intensity and block protrusion height.
- Results presented in Figure 4-14 to Figure 4-17 show that the block erodibility threshold is strongly dependent on the orientation of the block with respect to the flow direction. This result is namely related to two factors: 1) change in the dominant kinematic constraints resulting from changes in orientation of the applied load (this is addressed in more detail in Chapter 5), and 2) changes in the block profile in the flow. The former influences the ease at which the block may be removed from its mold, while the latter influences the relative magnitude of the drag force applied to the block.
- Experiments with varying degrees of block protrusion indicate the block erodibility threshold decreased as the amount of protrusion increased (Figure 4-16 and Figure 4-17). This result is intuitive as greater amounts of block protrusion into the flow field yield increased drag forces applied to the block. The block flush with the channel bottom (Block 3) did not fail under any tested flow conditions and highlights the significance of form drag on block erodibility in channel flow conditions.
- Experiments with varying degrees of turbulence intensity indicated the block erodibility threshold was reduced for cases with a higher T_u . For the case of Block 2, an increase in

T_u from approximately 2.5 % to 7.0 % resulted in an approximately 10 % reduction in the critical mean channel velocity needed to erode the block (Figure 4-15). This indicates blocks may be eroded at a relatively lower mean flow velocity provided the flow also has a higher degree of turbulent fluctuations. This is a particularly important result in the sense that velocity alone would not be a particularly good indicator parameter of erosion threshold. Accordingly, assessment of flow erosive capacity should address both flow velocity and degree of turbulence.

4.4.3 Block removal mechanics

- Analysis of real-time data for hydrodynamic pressures around the block and for block displacements was performed to characterize block removal mechanics for runs resulting in erosion of the block from its mold. Block response was a function of kinematic constraints associated with the orientation of the block mold as well as flow conditions around the block. Three general block behaviors were observed:
 - *Block response 1* – Block mold orientations of $\psi = 135, 150, 165,$ and 180 deg. that have a relatively low kinematic resistance to block movement in the general downstream direction resulted in gradual displacement of the block leading up to removal (Figure 4-18, Figure 4-23) in a consistent direction (Figure 4-19, Figure 4-24). A “low” kinematic resistance refers to a block with a shallow dipping downstream face or shallow plunging line of intersection between two block faces such that the block can easily slide in the downstream direction (see Chapter 5). For these runs, this occurred for both high and low T_u flow conditions. Displacements predominantly occurred along the path of least resistance, which for this study, was always 2-plane sliding along the low angle intersection between block faces 1 and 2, i_{12} . (Figure 4-20, Figure 4-25). Pressure values on all block faces remain fairly constant leading up to removal, with no obvious impulses applied to any of the block faces (Figure 4-21, Figure 4-26), which suggests a pseudo-static treatment of the hydrodynamic forces applied to the block is appropriate for describing the overall stability of the block in these scenarios.
 - *Block response 2* – Block mold orientations $\psi = 0, 15, 30, 45, 60, 75, 90, 105, 120$ and 135 deg. that have a higher kinematic resistance to erosion also resulted in gradual displacement response until removal (similar to response 1) (Figure 4-28), however orientation of block displacements were considerably more variable (Figure 4-29, Figure 4-30). A “high” kinematic resistance refers to blocks with a steep angle downstream face or a steep angle intersection of downstream faces such that blocks cannot easily be removed (see Chapter 5). For these runs, identification of the kinematic mode of failure was often more difficult to deduce. Block response 2 was observed for low T_u flows as well as high T_u flows of discharge Q_3 and below. High T_u flows Q_3 and below are relatively similar in characteristics to low T_u discharges (see flow characterization section). Pressure values on all block faces remain fairly constant leading up to removal, with no obvious impulses applied to any of the block faces (Figure 4-31), which suggests a pseudo-static

treatment of the hydrodynamic forces applied to the block is appropriate for describing the overall stability of the block in these scenarios as well.

- *Block response 3* - For higher T_u flow conditions and orientations where block mold geometry yielded higher kinematic resistance to erosion, block displacement response was significantly more dynamic in comparison with the previous two response types (Figure 4-33, Figure 4-34). In these cases, block movements typically occurred as a result of hydraulic impulses caused by the larger turbulent eddies in the flow field surround the block, one of which would finally remove the block from the mold (Figure 4-39). Displacement direction was typically variable and erratic (Figure 4-35, Figure 4-36). Impulses causing larger displacements, however, generally resulted in consistent kinematic modes of movement between different impulses (Figure 4-37, Figure 4-38).
- Power spectral density (S_{xx}) analysis for pressure and displacement fluctuations was performed for runs that resulted in block removal. Dominant frequencies in both pressure and displacement data were typically present in one or more of three main regions: 1) 0.6 to 0.9 Hz (2 to 3 Hz, model scale) 2) 1.6 to 6.3 Hz (5 to 20 Hz, model scale) and 3) 9.5 to 12.7 Hz (30 to 40 Hz, model scale). Response in the 0.6 to 0.9 Hz range was attributed to installation of the baffles on high T_u runs and was observed in those scenarios. Response in the 1.6 to 6.3 Hz range, however, was attributed to a fundamental resonance frequency of pressure waves traveling through the discontinuities surrounding the block. Due to 3D geometry of the block mold, superposition of pressure waves to create this phenomenon only occurred in localized locations around the block, which varied between runs. Response in the 9.5 to 12.7 Hz range was attributed to excitation of a fundamental resonance frequency of the block itself, as peaks in S_{xx} generally existed across all sensors on the block mold and nearly all runs. Frequency response for each block behavior is discussed below:
 - *Block response 1* – Displacements in runs with block response 1 occurred predominantly in the 9.5 to 12.7 Hz range (30 to 40 Hz model scale), despite dominant loading from hydrodynamic pressures at lower frequencies (associated with the presence of the baffles or from resonance of pressure waves in the discontinuities surrounding the block) (Figure 4-42). This can likely be attributed to the relatively low kinematic resistance afforded by the block mold orientation, which made it more feasible for smaller, higher frequency displacements to occur. Small displacements dissipate energy, preventing the excessive build-up of pressure within the block mold that would cause larger movements to occur.
 - *Block response 2* – Displacements in runs with block response 2 were more susceptible to resonance of pressure waves within the discontinuities and, accordingly, an additional peak in displacement response was observed in the 1.6 to 6.3 Hz range (5 to 20 Hz, model scale) (Figure 4-43). This was most likely related to the increased kinematic resistance associated with the block mold orientation in the sense that the smaller, higher frequency pressure

fluctuations could not move the block as effectively to dissipate energy (compared to block response 1). This allowed slightly greater build-up of pressure around the block resulting in slightly lower frequency displacement response. As the degree of turbulence for these runs was still relatively low (compared to block response 3), block response in the lower frequency range was generally not observed, i.e., less than approximately 1.6 Hz (5 Hz, model scale).

- *Block response 3* – Displacements in runs with block response 3 were susceptible to lower frequency hydrodynamic loading associated with the installation of baffle blocks as well as from resonance of pressure waves within the discontinuities. Similar to block response 2, this can likely be attributed to the increased kinematic resistance associated with the block mold orientation. As such, these runs were characterized by larger, impulse-driven block movements and exhibited a predominant displacement response for frequencies less than approximately 3.2 Hz (10 Hz, model scale) (Figure 4-44).

4.4.4 Block pressure statistics

- A statistical description of hydrodynamic pressures on block faces was made as a function of block mold rotation angle, turbulence intensity, flow velocity and block protrusion height. Dimensionless pressure coefficient C_p , C'_p , C_p^+ and C_p^- were calculated to represent the average hydrodynamic pressure, fluctuating hydrodynamic pressure (represented by the root mean square (RMS) of pressure fluctuations), and instantaneous maximum and minimum pressure, respectively.
- Results for average dynamic pressure presented in Figure 4-47, Figure 4-48, Figure 4-53, Figure 4-55 show a strong dependence on the block mold rotation angle (ψ) for blocks protruding above the channel bottom (Block 1 and Block 2). Intuitively, block faces perpendicular to the flow direction experienced the highest average pressure. The block edge profile (Figure 4-49), which becomes more blunt as the block face is rotated towards a perpendicular orientation to flow direction, also likely contributed to this phenomenon. The addition of the baffle blocks to generate turbulence resulted in an average increase in C_p values of approximately 30 %. Increased flow velocity, however, did not significantly change C_p values on block faces (Appendix F), but did rotate the mean active resultant force vector (\mathbf{r}_{avg}) outward from its initial downward orientation towards the block yield condition (Figure 4-54 and Figure 4-56). The rotation of \mathbf{r}_{avg} generally occurred along a constant azimuth indicating a uniform increase in hydrodynamic pressure applied to the block faces. For runs with no block protrusion (Block 3), C_p values were relatively independent of ψ and a single average value was used to describe each flow scenario. For block faces 1, 2 and 3, $C_p = 0.090$ (high T_u) and 0.062 (low T_u). For face 4 on Block 3, C_p values were found to be similar ($C_p = 0.095$ for high T_u cases and 0.075 for low T_u cases). Accordingly, minimal rotation of \mathbf{r}_{avg} was observed over a range of loading conditions indicating the pressure distribution around the block was near hydrostatic (Figure 4-54).

- A simplistic expression was fit to measured C_p values on block faces based on the angle of the face with respect to the flow direction (ζ , Figure 4-50). For block faces on the upstream side of the block, Equation (4-13) can be used to determine the average dynamic pressure coefficient. For block faces on the downstream side of the block either Equation (4-14) or Equation (4-15) can be used depending on if there are one or two upstream block faces, respectively. Coefficients to account for turbulence intensity and block protrusion height are presented in Table 4-15, Table 4-16, Equation (4-16) and Equation (4-17). As indicated in Figure 4-47 and Figure 4-48, the expression does reasonably well capturing the trend and magnitude of average dynamic pressure on the block faces over the range of block mold rotation angles.
- Comparison of measured values of C_p as well as those calculated from Equation (4-13) show good agreement with those obtained in a related study by Frizell (2007) at the USBR for hydraulic jacking of concrete slabs (Figure 4-52). Data from Frizell were collected over a greater range of flow velocities (3 m/s to 17 m/s), block offsets (3 mm to 19 mm), and block edge types (radius, chamfer, and square) but were limited to protrusion configurations perpendicular to flow direction. Subsequently, both studies may be used concurrently to extend their applicability to a broader range of flow conditions and block configurations.
- Results for the fluctuating component of hydrodynamic pressures presented in Figure 4-57, Figure 4-58 and Figure 4-59 were relatively independent from the block mold rotation angle. Accordingly, an average value that ranged between approximately 0.02 (high T_u condition) to approximately 0.01 (low T_u condition) was used to represent C'_p across all blocks for all block faces. In general, C'_p was approximately 5 to 20 % of the corresponding C_p value.
- Results for the maximum and minimum instantaneous hydrodynamic pressures presented in Figure 4-60, Figure 4-61, and Figure 4-62 indicate C_p^+ values were approximately 150 % higher than corresponding average hydrodynamic pressures in high T_u flows and 100 % higher in low T_u flows. Conversely, C_p values were approximately 120 % lower than corresponding C_p values for high T_u cases and about 80% lower for low T_u cases. No trend was fit to maximum or minimum instantaneous pressure data.

Chapter 5. Block theory framework

Block theory provides a rigorous analytical methodology to identify removable blocks, determine potential failure modes, and assess 3D block stability. This section provides an overview of block theory concepts as well as applicability to the rock scour process. Results from the physical hydraulic model are examined within the block theory framework and a predictive model for block erodibility threshold is presented.

5.1 Overview

The importance of rock mass discontinuity orientations in block analysis is a direct consequence of the relatively high intact strength of the rock material itself. In most typical situations near the ground surface, intact rock strength far exceeds applied loads. Accordingly, failure of a rock mass tends to occur along existing discontinuities that are created by, for example, cooling of the rock during its formation, tectonic stresses, unloading (i.e., exfoliation jointing), or deposition of sedimentary layers (i.e., bedding planes). Discontinuities divide the rock mass into a variety of discrete polyhedral block shapes, some of which are removable from the rock mass. The movements, or kinematics, of removable blocks are ultimately controlled by the orientations of the bounding discontinuities. As such, any simplification or idealization of block geometry would likely render any analysis on block stability inadequate.

For an arbitrary polyhedral block shape a number of kinematic failure modes exist. These consist of 1) pure translational modes, such as lifting and sliding (1-plane or 2-plane), 2) pure rotational modes, such as rotation about an edge or a corner, or 3) some combination of translation and rotation, such as slumping or torsional sliding (Figure 2-3). The significance of kinematics in block stability analysis has been discussed by numerous researchers through

characterization and assessment of these different block failure modes (e.g. Wittke (1965), Londe et al. (1969, 1970), Goodman & Bray (1977), Warburton (1981), Goodman & Shi (1985), Mauldon (1992), Mauldon & Goodman (1990, 1996), Tonon (1998), and Kieffer (1998)). In particular, the ground-breaking work by Goodman & Shi (1985) provided a rigorous approach to 3D characterization of rock mass structure for block stability analysis called “block theory”. Block theory is significant in the sense that it provides a general analytical methodology to identify removable blocks, determine potential failure modes, and assess block stability.

The initial work on block theory focused on analysis of pure translational failure modes for arbitrary polyhedral shaped blocks. This work was expanded by Mauldon (1992) and Mauldon & Goodman (1990, 1996) to include pure rotational failure modes for tetrahedral blocks. Rotational analysis was later generalized by Tonon (1998) to include all loading types on tetrahedral blocks (i.e., those causing a significant moment on the block centroid so as not to result in pure rotational movement). Extension of rotational failure modes to arbitrary polyhedral shaped blocks has currently only been performed through more complex numerical codes such as discrete element method (DEM) (Cundall 1971), discontinuous deformation analysis (DDA) (Shi 1988, 2001), block stability 3D (BS3D) (Tonon (2007), Asadollahi (2009)) and Pötsch (2011).

A major goal of this research is to examine erodibility of non-idealized (non-cubic) 3D rock blocks. With no data regarding hydraulic loads for these block types, efforts focused on tetrahedral block shapes which represent the most basic non-cubic 3D block geometry. While this may appear to be limiting, a study performed by Hatzor (1992) examining block molds for a number of case histories indicated the majority of blocks removed from rock masses were actually tetrahedral. This section outlines a framework for evaluating block erodibility using a block theory approach.

5.2 Block theory basics

5.2.1 Assumptions

The basic assumptions in block theory are: 1) all joint surfaces are planar, 2) all joints extend completely through the volume of interest, and 3) blocks are assumed to be rigid. For the purposes of this research, and for the reasons described in the previous section, 4) only tetrahedral blocks are considered (i.e., blocks defined by three joint planes and one free planar face). Additionally, 5) blocks are assumed to be initially at rest such that incipient motion is of sole interest. Finally, 6) only pure translational kinematic modes are considered. A study by Mauldon (1990) indicated the probability that a tetrahedral block is both removable and rotatable is fairly low (approximately 16 %) and, even in the case that both are true, the critical mode will almost always be one of the translations unless the friction angle of the rock joint is very high.

5.2.2 Block removability

For a given set of i non-repeating joints ($J_1, J_2 \dots J_i$) and one free face (J_f), a number of possible block shapes exist, some of which will be removable from the rock mass. Each block is termed a “joint pyramid (JP)” and is identified by an i -number binary code relating to the side of the joint plane on which the block resides in space. A “0” indicates the block lies in the upper half-space above the joint plane while a “1” indicates the block lies in the lower half-space below

the joint plane. For the case of tetrahedral blocks, eight possible block shapes exist, one of which is removable. A block with JP code 001, for example, would indicate the block in question is above joint 1 (J_1), above joint 2 (J_2), and below joint 3 (J_3). A hierarchal structure exists for classifying each of the block types that occur in a rock mass (Figure 5-1). There are five block types, the first of which is an infinite block (type V). An infinite block extends boundlessly into the rock mass and therefore cannot be removed. The remaining blocks are finite and can be classified as non-removable and removable. A non-removable, finite block (type IV) has a tapered geometry such that any movement in the direction of the opening is impossible with collision into the adjacent rock mass. Accordingly all tapered blocks are non-removable without prior or simultaneous movement of neighboring blocks. Finally, only blocks that are non-tapered and finite are removable. Removable blocks are further distinguished based on if the block is stable without friction (type III), stable with sufficient friction (type II) or unstable without support (type I). The latter two block types are termed “potential key blocks” and “key blocks,” respectively, due to their potential for unsafe behavior (Goodman & Shi 1985). For erodibility assessment, all removable block types (I, II and III) are of interest.

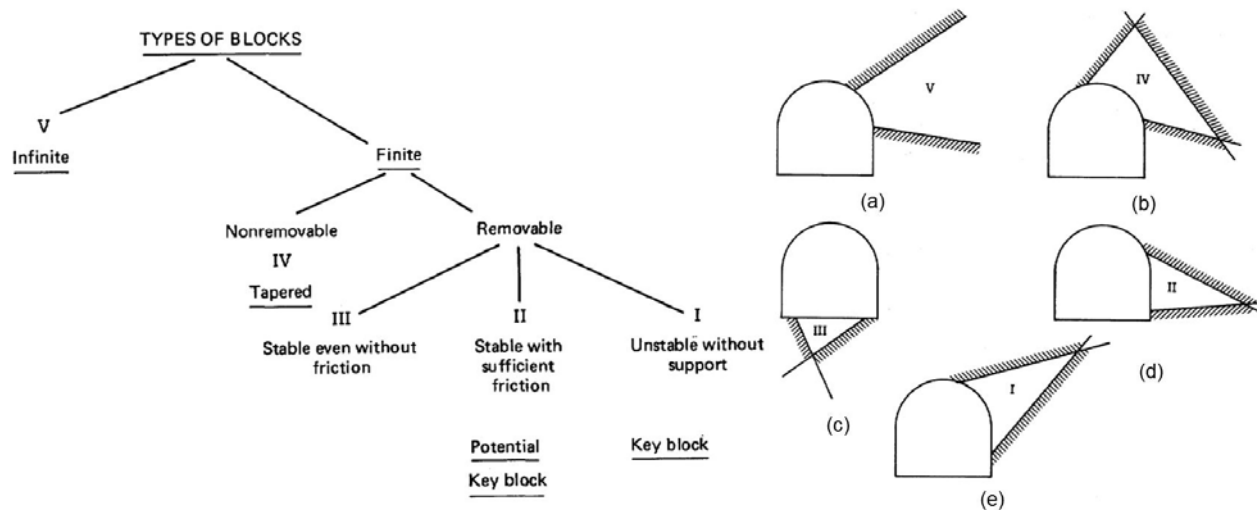


Figure 5-1. Hierarchal structure of rock block types with illustrations (Goodman & Shi 1985).

Using stereographic projection (Goodman 1976), the great circle corresponding to each joint set can be plotted thus subdividing the stereonet into regions corresponding to each JP (Figure 5-2). For an upper hemisphere stereonet, anything plotting inside the great circle for a particular joint is considered above that joint plane, while anything plotting outside is considered below.

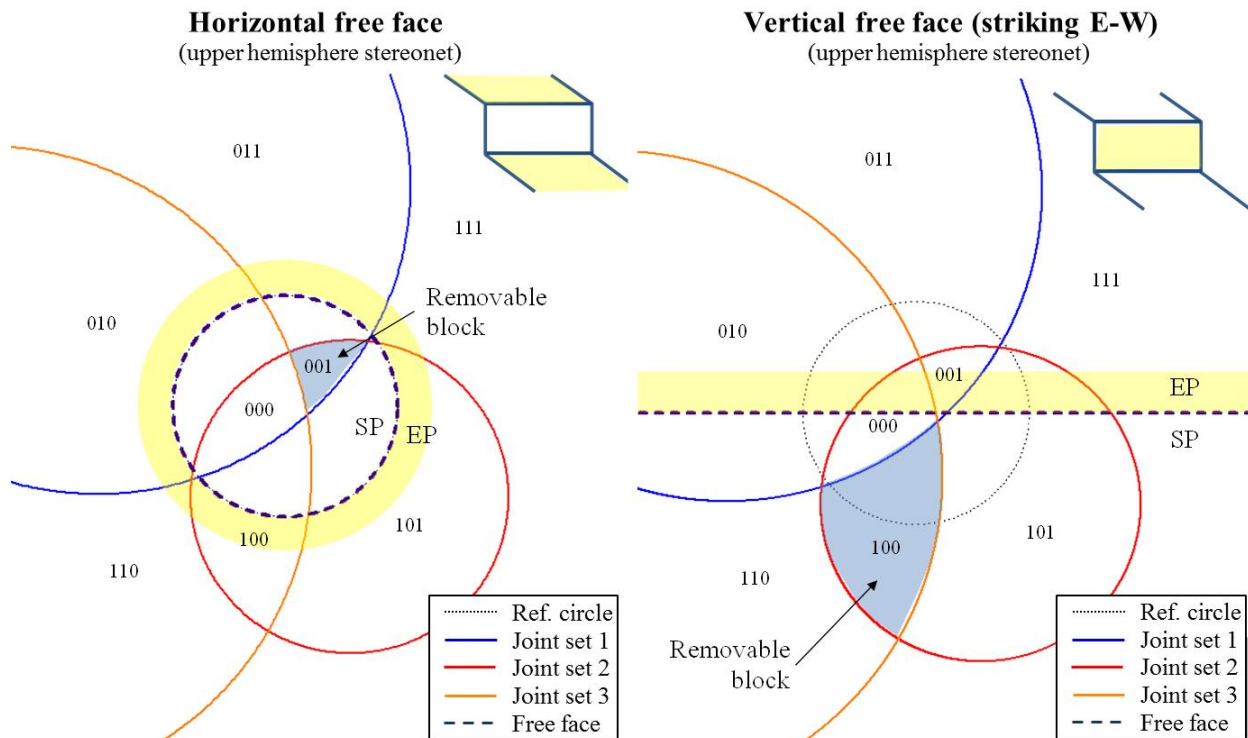


Figure 5-2. Upper hemisphere stereonet showing JP codes and removable blocks for horizontal free face (left) and vertical free face striking East-West (right)

According to Shi's theorem, to be removable the JP region for a particular block must be finite and plot completely within the "space pyramid (SP)" as defined by the free face. This ensures the block is finite and can move into the opening from the rock mass. The free face is the rock/water or rock/air interface (assumed to be planar over the region of interest) that divides the SP (the region into which a removable block moves) from the "excavation pyramid (EP)" (the region where the block resides). In Figure 5-2, JP 001 is a removable block from a horizontal free face, while JP 100 is a removable block from a vertical face striking East-West.

For rock masses with more than three joint sets, multiple combinations of three joint sets should be analyzed to find removable tetrahedral blocks in all cases. For example, if the total number of joint sets is four, the following sets should be analyzed with the free face: (J_1, J_2, J_3) , (J_1, J_2, J_4) , (J_1, J_3, J_4) and (J_2, J_3, J_4) .

5.2.3 Block kinematics

Failure of a removable block in a particular failure mode is subject to several kinematic constraints that must be satisfied for a block to be eroded. This is a function of 3D block geometry and orientation of the active resultant force vector applied to the block. For scour assessment, this vector is namely comprised of the hydraulic forces on the block faces and the self-weight of the block. Criteria were developed by Goodman & Shi (1985) for assessing plausible kinematic failure modes for pure block translations. A general schematic of a removable block is shown in Figure 5-3.

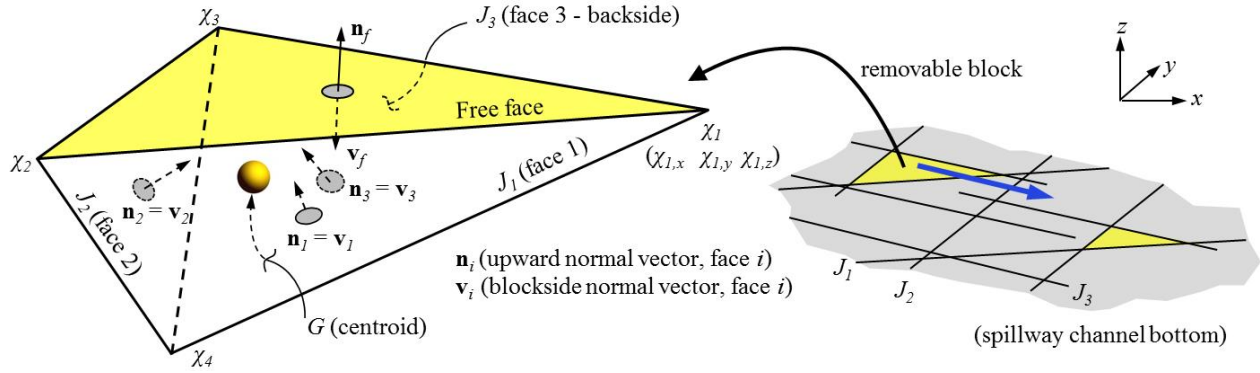


Figure 5-3. Removable block schematic.

For pure translation modes, lifting of a block is kinematically feasible when:

$$\mathbf{s} \cdot \mathbf{v}_i > 0, \text{ for all } i \quad (5-1)$$

where \mathbf{s} = direction of block movement (equal to the direction of the active resultant (\mathbf{r}) for lifting), and \mathbf{v}_i is the block-side normal vector for i^{th} joint plane. **Bold** font signifies a vector/matrix quantity. This condition ensures the block moves away (lifts) from each of the bounding joint planes. The block-side normal may be calculated by:

$$\mathbf{n}_i = \begin{bmatrix} \sin(\delta_i) \cdot \sin(\theta_i) \\ \sin(\delta_i) \cdot \cos(\theta_i) \\ \cos(\delta_i) \end{bmatrix}, \quad (5-2)$$

$\mathbf{v}_i = \mathbf{n}_i$ (block is above i^{th} joint plane), or

$\mathbf{v}_i = -\mathbf{n}_i$ (block is below i^{th} joint plane),

where \mathbf{n}_i is the upward normal for the i^{th} joint plane and δ_i , θ_i are the dip and dip direction, respectively, of the i^{th} joint plane. For block sliding on plane i only, the sliding direction is given by:

$$\mathbf{s} = \mathbf{s}_i = \frac{(\mathbf{n}_i \times \mathbf{r}) \times \mathbf{n}_i}{|\mathbf{n}_i \times \mathbf{r}|} \quad (5-3)$$

This is the orthographic projection of the active resultant force vector (\mathbf{r}) onto the sliding plane. Kinematic feasibility of 1-plane sliding is subject to the following constraints:

$$\begin{aligned} \mathbf{v}_i \cdot \mathbf{r} &\leq 0, \text{ and} \\ \mathbf{s}_i \cdot \mathbf{v}_j &> 0 \text{ for all } j \neq i, \end{aligned} \quad (5-4)$$

where j represents the remaining two joint planes. The first condition ensures a component of the resultant is projected onto the plane of sliding, while the second guarantees the block is being lifted from the remaining joint planes. For block sliding on planes i and j simultaneously, the sliding direction is given by:

$$\mathbf{s} = \mathbf{s}_{ij} = \frac{\mathbf{n}_i \times \mathbf{n}_j}{|\mathbf{n}_i \times \mathbf{n}_j|} \cdot \text{sign}[(\mathbf{n}_i \times \mathbf{n}_j) \cdot \mathbf{r}] \quad (5-5)$$

where $\text{sign}(\cdot)$ is a function that returns 1 if “ (\cdot) ” is positive and -1 if “ (\cdot) ” is negative. The sliding direction is along the line of intersection between the two planes. The sign function determines which direction sliding occurs along this line considering the orientation of the active resultant. Kinematic feasibility of 2-plane sliding on planes i and j is subject to the following constraints:

$$\begin{aligned} \mathbf{s}_{ij} \cdot \mathbf{v}_k &> 0, \text{ and} \\ \mathbf{s}_i \cdot \mathbf{v}_j &\leq 0, \text{ and} \\ \mathbf{s}_j \cdot \mathbf{v}_i &\leq 0, \end{aligned} \quad (5-6)$$

where k represents the remaining joint plane from which the block is lifted. The first condition ensures the block slides away from joint plane k . The second condition ensures the direction of block sliding on plane i is towards plane j , while the third condition ensures the direction of sliding on plane j is towards plane i .

5.2.4 Block stability

For block stability, the corresponding limit equilibrium expressions for the pure translational movements are below (Goodman & Shi 1985). For lifting,

$$F = |\mathbf{r}|, \quad (5-7)$$

for 1 – plane sliding on joint plane i ,

$$F_i = |\mathbf{n}_i \times \mathbf{r}| - |\mathbf{n}_i \cdot \mathbf{r}| \cdot \tan(\phi_i) \quad (5-8)$$

for 2 – plane sliding on joint planes i and j ,

$$F_{ij} = \frac{1}{|\mathbf{n}_i \times \mathbf{n}_j|^2} \cdot \left[\begin{aligned} &|\mathbf{r} \cdot (\mathbf{n}_i \times \mathbf{n}_j)| \cdot |\mathbf{n}_i \times \mathbf{n}_j| - \\ &|(\mathbf{r} \times \mathbf{n}_j) \cdot (\mathbf{n}_i \times \mathbf{n}_j)| \cdot \tan(\phi_i) - \\ &|(\mathbf{r} \times \mathbf{n}_i) \cdot (\mathbf{n}_i \times \mathbf{n}_j)| \cdot \tan(\phi_j) \end{aligned} \right] \quad (5-9)$$

where F is scalar value of the required stabilizing force applied in the direction of movement to maintain equilibrium, and ϕ_i , ϕ_j = friction angle on joints i and j , respectively. When F is negative the block is considered stable, and when F is positive the block is unstable. When F is zero, the block is in equilibrium such that any further increase in load will result in removal of the block. The vector form of the stabilizing force (\mathbf{F}) may be written as:

$$\mathbf{F} = -F \cdot \mathbf{s}, \quad (5-10)$$

Solutions for 3D block stability for the pure translational failure modes can be represented graphically using whole-sphere stereographic projection or as a function of the orientation of the active resultant force vector (Figure 5-4). An example solution is shown for a tetrahedral block

with joint orientations (dip direction/dip angle) = 080/60, 220/45 and 180/75 and JP code 001. Numbered regions represent the kinematic failure modes (e.g., 0 = lifting, 12 = sliding on joint planes 1 & 2, etc.). Dashed lines represent contours of the required joint friction angle (ϕ) to maintain block stability (the red contour corresponds to a block with $\phi = 40$ deg. for all joint planes and represents the block yield condition, i.e., when $F = 0$). When \mathbf{r} plots inside of this contour, as currently shown, the block is stable and when \mathbf{r} plots outside of this contour the block is unstable.

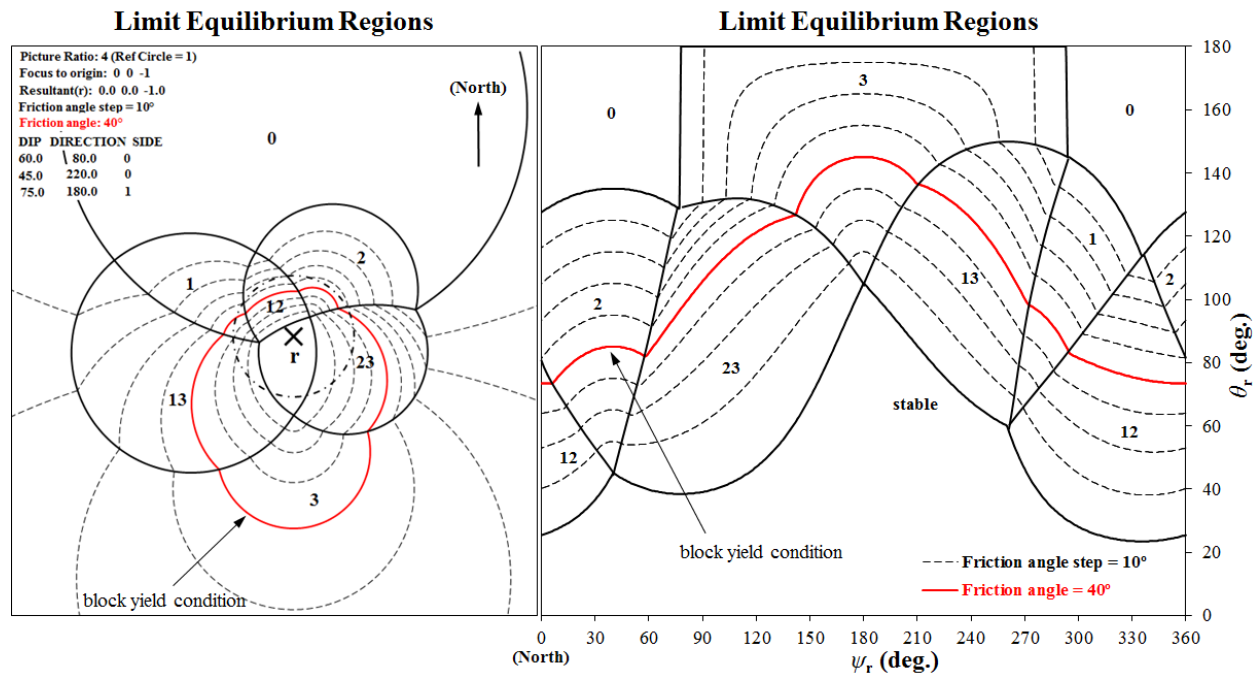


Figure 5-4. Graphical solution for 3D block stability based on stereographic projection (left) and orientation of active resultant force vector (right).

Display of block stability as a function of the active resultant force vector orientation is particularly insightful as the 3D variability of block resistance to removal can readily be shown. This is done incrementally from 0 deg. to 360 deg. for the azimuth of the active resultant force (ψ_r). For each increment of ψ_r , the required angle (θ_r) to rotate the active resultant force vector from its initial orientation (\mathbf{r}_0) to the orientation corresponding to the limit-state condition when the block will yield is calculated (Figure 5-5). In general a larger degree of rotation indicates a larger force is required to cause block instability. In the absence of any hydraulic loading, the orientation of \mathbf{r}_0 is directly downward due to the weight of the block (\mathbf{W}_b). As load \mathbf{F}_a is applied, \mathbf{r} can rotate towards an unstable orientation resulting in removal of the block.

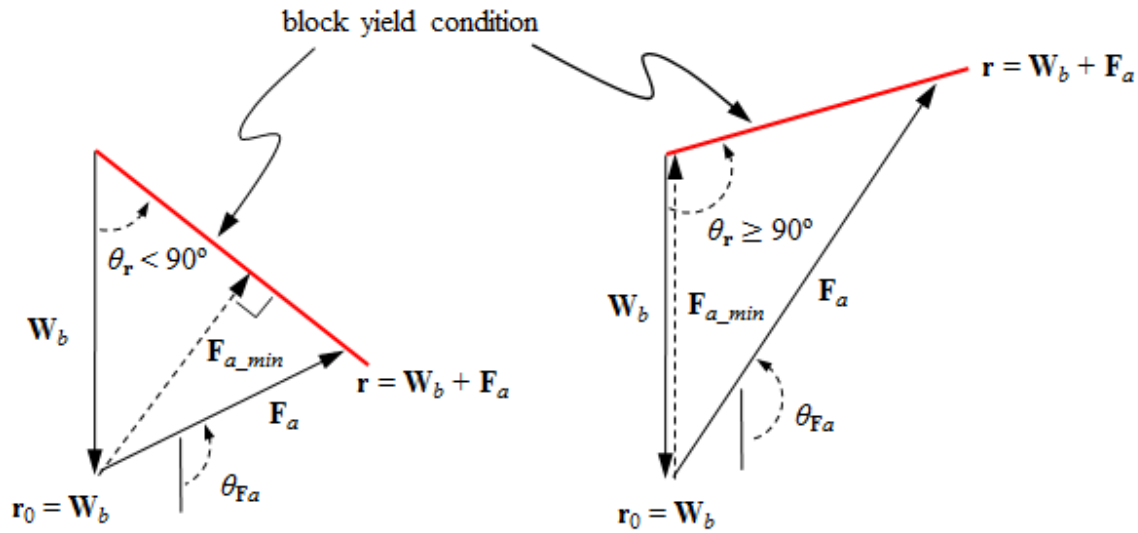


Figure 5-5. Vector diagram for rotation of \mathbf{r} to θ_r . Modified from Kieffer & Goodman (2012).

The magnitude of the load required to rotate \mathbf{r} to θ_r is dependent on the orientation of \mathbf{F}_a which is represented by θ_{Fa} . This may be expressed as:

$$F_a = |\mathbf{F}_a| = \begin{cases} |\mathbf{W}_b| \cdot \frac{\sin(\theta_r)}{\sin(\theta_{Fa} - \theta_r)} & \text{if } \theta_{Fa} > \theta_r \\ \infty & \text{otherwise} \end{cases} \quad (5-11)$$

In lieu of information regarding the orientation of the applied load, the magnitude of the minimum required applied force (\mathbf{F}_{a_min}) can be written as:

$$F_{a_min} = |\mathbf{F}_{a_min}| = \begin{cases} |\mathbf{W}_b| \cdot \sin(\theta_r) & \text{if } \theta_r < 90^\circ \\ |\mathbf{W}_b| & \text{otherwise} \end{cases} \quad (5-12)$$

When $\theta_r < 90$ deg., \mathbf{F}_{a_min} is oriented perpendicular to the yield surface. For the case when $\theta_r \geq 90$ deg., \mathbf{F}_{a_min} is oriented vertically upward and is equal in magnitude to the block weight. Figure 5-6 shows the required magnitude of \mathbf{F}_a (normalized by the block weight) as a function of its orientation to cause instability for the example removable block presented in Figure 5-4. The necessary applied force increases drastically when oriented sub-vertically with an azimuth ranging between approximately 60 deg. and 300 deg. As the block (JP 001) resides below J_3 , any force directed towards J_3 will push the block towards the surrounding rock mass. Accordingly, the only kinematically feasible translational movements are opposite the direction of loading. This causes a significant increase in magnitude of the force required to move the block in comparison to force vectors oriented in alternate directions. This example readily highlights the influence of 3D block geometry and kinematics on block stability.

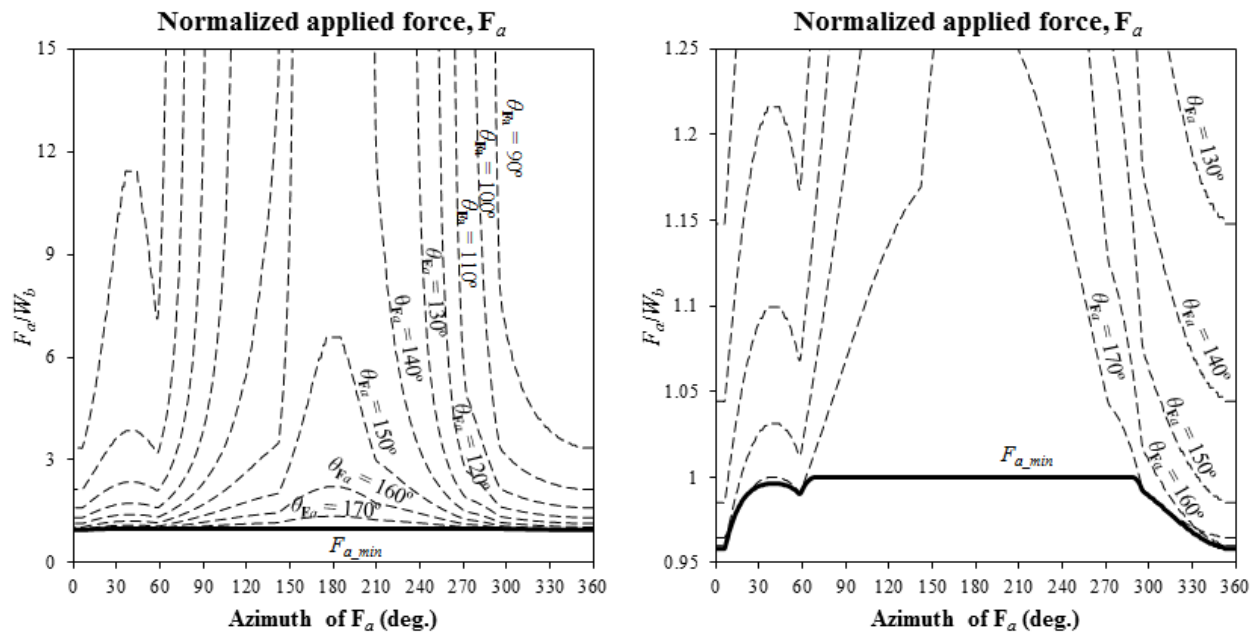


Figure 5-6. Normalized applied force F_a , as a function of θ_{Fa} , required to destabilize a removable tetrahedral block with JP 001, joint orientations (dip direction/dip angle) = 080/60, 220/45 and 180/75 and a yield condition corresponding to $\phi = 40$ deg. (same as presented in Figure 5-4). The region near F_{a_min} is emphasized on the right.

5.3 Rock scour application

Application of block theory to rock scour evaluation occurs through modification of the active resultant force vector, r , which accounts for the hydraulic load applied to the rock block resulting from flowing water. This ultimately influences dominant block kinematic failure modes and stability, however, block removability and kinematic constraints are unaltered. The latter two are purely related to 3D block and rock mass geometry and thus independent of any type of applied forces.

5.3.1 Pseudo-static analysis

To assess block stability, it is necessary to quantify the magnitude, duration and distribution hydraulic forces applied to the block. In doing so, it is important to consider the nature of the flow conditions in the vicinity of the block. Flows for scour applications are predominantly turbulent, and the scouring process is inherently dynamic. In contrast, block theory concepts have been developed for static analysis using limit equilibrium methods for block stability. There is, however, potential for a wide range of variability regarding the degree of turbulence (i.e., turbulence intensity, T_u) such that a pseudo-static treatment of the hydraulic loads is adequate for a large variety of flow scenarios and the full benefit of block theory can be realized.

For a given set of flow conditions, consider a corresponding characteristic dynamic pressure, P_{char} , for a single location in the vicinity of a removable block as defined by an average dynamic pressure, P_{avg} , a fluctuating dynamic pressure, P' and a frequency, f_{char} (Figure 5-7).

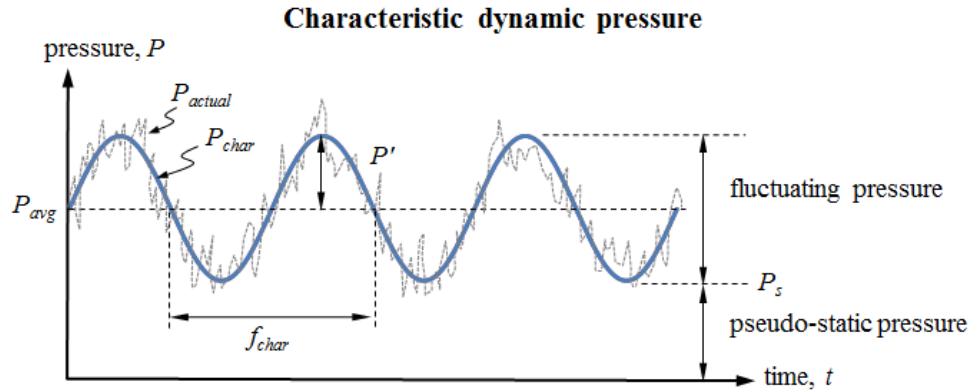


Figure 5-7. Characteristic dynamic pressure in the vicinity of a removable block for a given flow condition.

The characteristic dynamic pressure attempts to represent the main features of a flow field (as defined by the geometry, location, flow type, etc.) in a simplified manner. This characteristic pressure may be expressed as:

$$P_{char} = P' \cdot \sin(2\pi \cdot f_{char} \cdot t) + P_{avg} \quad (5-13)$$

As indicated in Figure 5-7, the characteristic dynamic pressure is comprised of two regions. The first is the fluctuating pressure region which represents the influence of the turbulent nature of the flow field. The second is the pseudo-static region where, for all practical purposes, the pressure is relatively constant and may be treated as such. When the pressure fluctuations are relatively small (i.e., $P' \ll P_{avg}$), the pseudo-static pressure is approximately equal to the mean pressure and accordingly the flow may be analyzed in a pseudo-static manner (Figure 5-8). The characteristic dynamic pressure can therefore be approximated by the pseudo-static pressure, P_s .

$$P_{char} \cong P_s = P_{avg} - P' \cong P_{avg} \quad (5-14)$$

Should the magnitude of the pressure fluctuations comprise a significant portion of the characteristic dynamic pressure, a pseudo-static treatment may not be appropriate. In such instances, examination of a dynamic impulse applied to the block may better represent block response (see, e.g., Bollaert (2002)). As discussed later on, however, a pseudo-static approach appears to perform reasonably well for analysis of experiments conducted for this study with model blocks under high turbulence flow conditions.

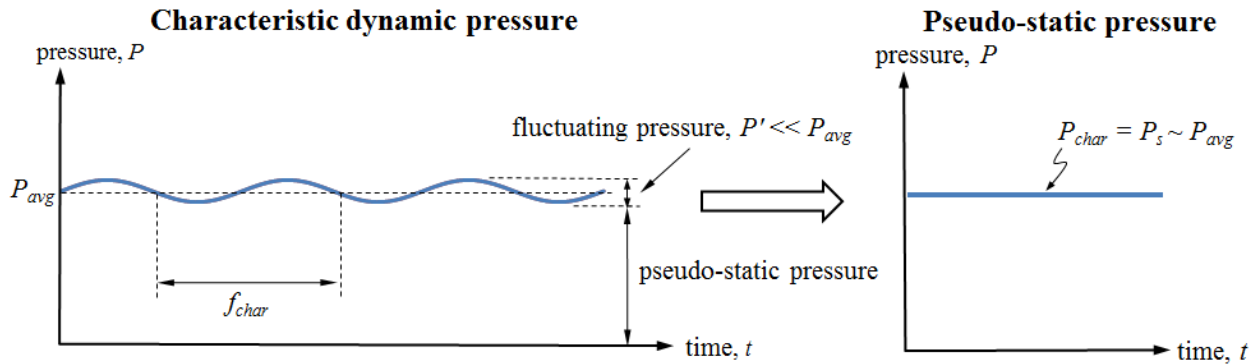


Figure 5-8. Simplification of characteristic dynamic pressure for pseudo-static analysis.

5.3.2 Active resultant force vector

Applied loads are incorporated into the active resultant force vector (\mathbf{r}) which represents a vector sum of all active forces acting on the block. For rock scour purposes, these are predominantly the pseudo-static pressure applied normal to the block faces and the self-weight of the block due to gravity. This can be expressed as:

$$\mathbf{r} = \sum_i^n S_i \cdot \mathbf{v}_i + \mathbf{W}_b \quad (5-15)$$

where S_i is the integral of the hydraulic pressure acting over i^{th} face and n is the total number of block faces. For simplicity, it is often sufficiently accurate to use a uniform distribution of pressure over the block faces, such that the above equation may be written:

$$\mathbf{r} = \sum_i^n P_{si} \cdot A_i \cdot \mathbf{v}_i + \mathbf{W}_b = \sum_i^n \frac{1}{2} \cdot \rho_w \cdot u^2 \cdot C_{pi} \cdot A_i \cdot \mathbf{v}_i + \mathbf{W}_b \quad (5-16)$$

where P_{si} is the pseudo-static pressure on the i^{th} block face, A_i is the area of the i^{th} block face, ρ_w is the density of water, u is the flow velocity, and C_{pi} is the average dynamic pressure coefficient on the i^{th} face. Note that when using the dynamic pressure coefficient, the submerged weight of the block should also be used. Other forces can be incorporated (such as flow shear force, cohesion or rock bolt force) through addition of their respective vector quantities to the above equation. The assumption of uniform pressure distribution likely becomes invalid as the size of the block becomes large relative to dominant length scales in within the flow field.

5.3.3 Application to hydraulic model experiments

The block theory methodology was used to verify results obtained from the hydraulic model experiments. The block erodibility thresholds presented in Figure 4-14 and Figure 4-15 for Block 1 and Block 2, respectively, are theoretically reproduced in Figure 5-9 and Figure 5-10. A block yield condition, corresponding to $\phi = 16$ deg., was used based on dry and wet testing of the blocks in the block mold (Appendix E). Average dynamic pressure coefficients (C_p) on the block faces were calculated using Equations 4-13 to 4-15 which were derived from pressure measurements from the hydraulic model experiments. For the free face a value of $C_p = 0.005$ was used corresponding to the average of data presented in Figure 4-55 for Block 1 and Block 2. C_p values were used to determine the active resultant force vector, \mathbf{r} , which was calculated using

Equation 5-16. With \mathbf{r} known, the stability of each block at every block mold rotation angle (ψ) was evaluated using block theory Equations 5-7 to 5-9. To determine the theoretical block erodibility threshold, the flow velocity was increased incrementally until \mathbf{r} rotated outward to the block yield condition. Figure 5-11 presents the required angle of rotation (θ_r) to cause instability as a function of ψ for a block yield condition corresponding to $\phi = 16$ deg.

As indicated in both Figure 5-9 and Figure 5-10, the theoretical erodibility threshold captures the overall trend exhibited by the experimental data as a function of the block mold rotation angle. For Block 1, the threshold in general is over-predicted for both high and low T_u flow conditions. Over-prediction of the threshold can result from underestimation of flow erosive capacity or overestimation of the block resistance. For high T_u conditions, a better result is achieved particularly where $\psi > 120$ deg., corresponding to the region for Block response 1 (see Chapter 4). For Block 2, good agreement with experimental data is similarly observed in the region where $\psi > 120$ deg., but also when $\psi \leq 15$ deg. For $\psi \leq 15$ deg., Block 2 did not fail under low T_u conditions, which is correctly predicted by the theoretical approach. Additionally, for high T_u flow conditions where a more dynamic block response was observed (Block response 3, Chapter 4), the pseudo-static approach appears to adequately represent the block erodibility threshold (i.e., $\psi = 0, 120$ and 135 deg., Block 2).

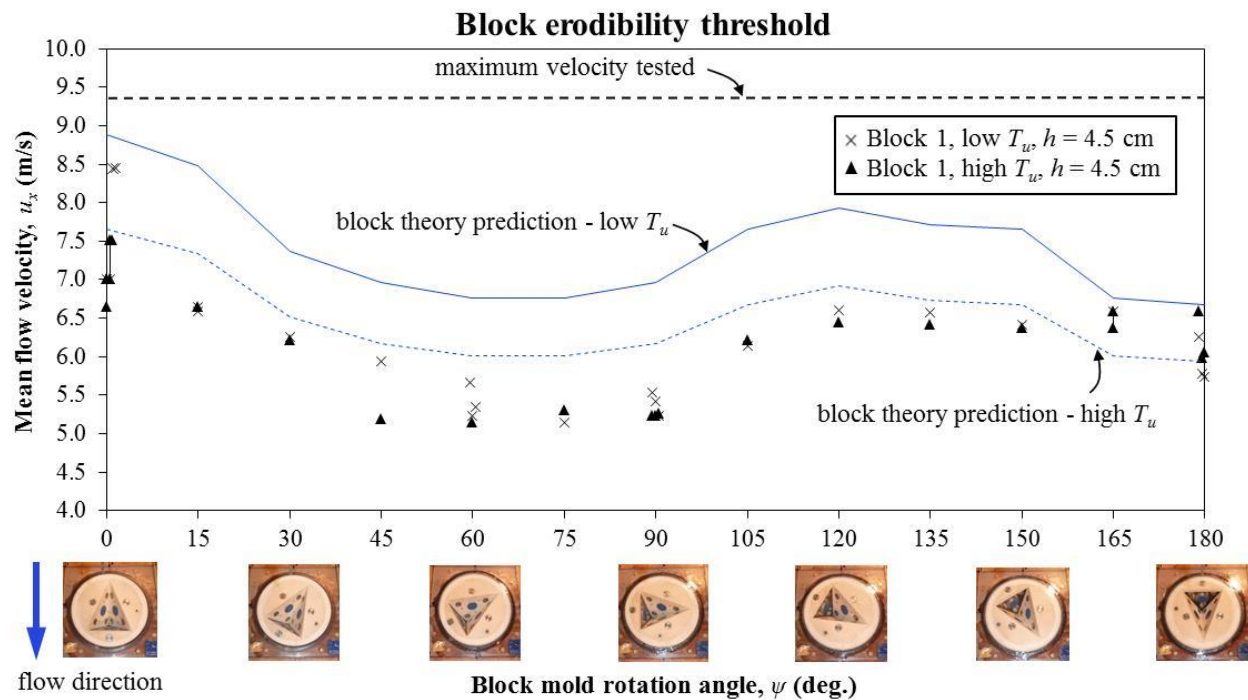


Figure 5-9. Prediction of block erodibility threshold for high and low T_u flow conditions compared to measured data from hydraulic model experiment for Block 1.

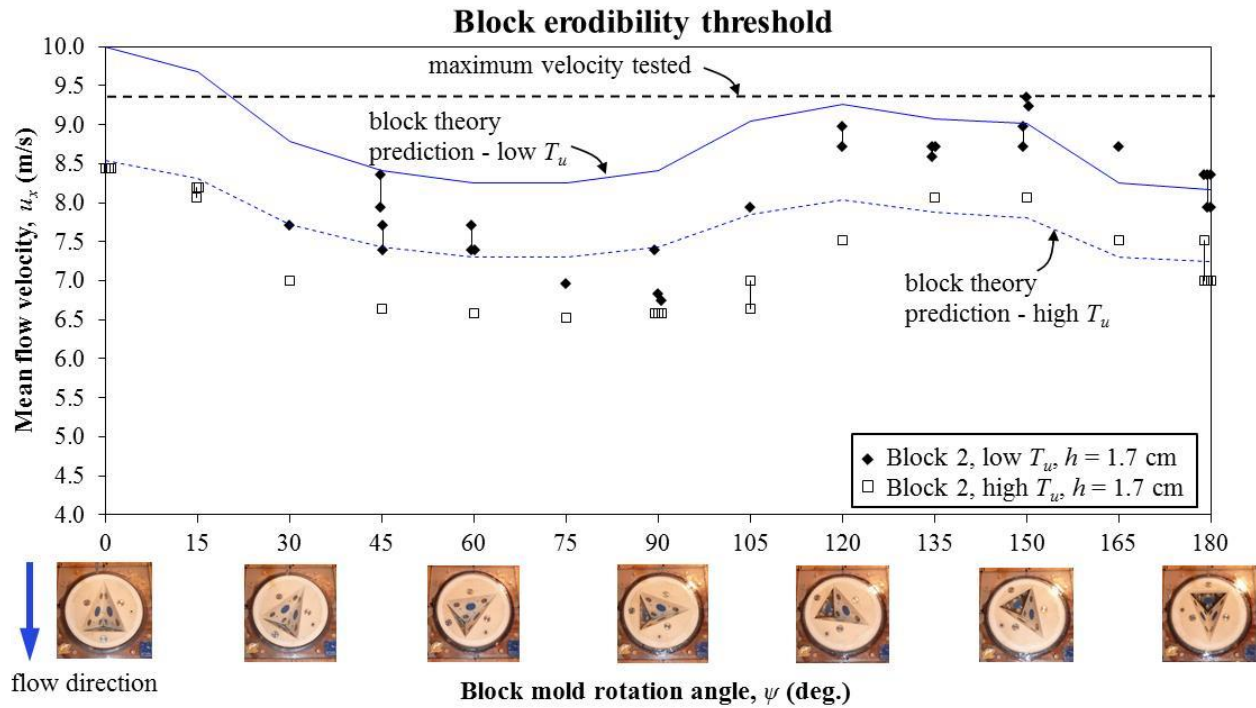


Figure 5-10. Prediction of block erodibility threshold for high and low T_u flow conditions compared to measured data from hydraulic model experiment for Block 2.

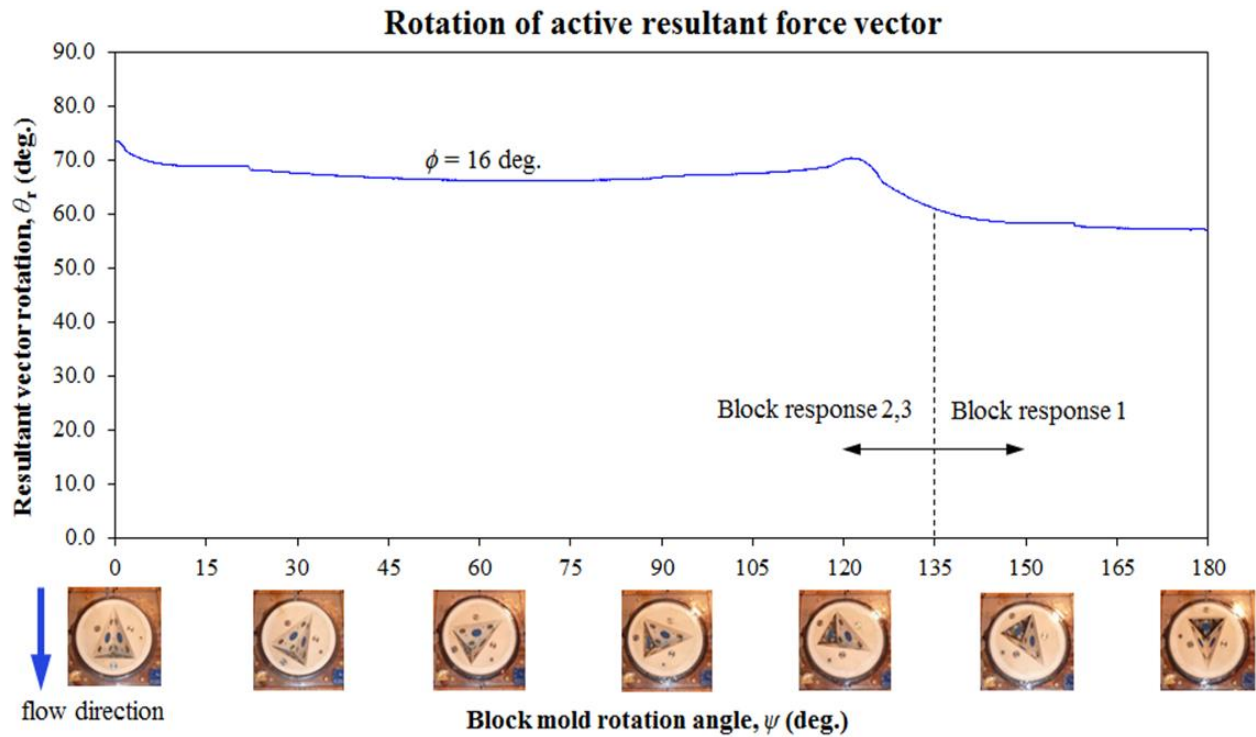


Figure 5-11. Required rotation angle (θ_r) of active resultant force vector to reach block yield condition as a function of block mold rotation angle (ψ).

Overall, the block theory approach appears to represent the block erodibility threshold reasonably well. In block mold rotation angles where the threshold is theoretically over-predicted, there are a couple of possible explanations. Namely, this occurs where ψ is approximately 15 deg. to 120 deg. For these mold rotation angles, the discharges in the hydraulic model experiments resulting in block removal were relatively low (predominantly Q_2 and below). Accordingly, one explanation for the discrepancy may be related to model scale effects associated with low flow depths (corresponding to low discharges) such that similitude is not achieved with the other discharges.

Alternatively, another explanation may be related to the difference in block response described in Chapter 4. For block mold rotation angles $\psi < 135$ deg., a slightly more dynamic response is observed (block response 2) compared to $\psi \geq 135$ deg. (block response 1). For block response 2, block movements occur at a lower frequency range (approximately 5 to 20 Hz (model scale)) in addition to movements at in the 30 to 40 Hz range (model scale) versus block 1 response where only higher frequency response is witnessed. This phenomenon is hypothesized to be associated with the higher kinematic resistance resulting from the orientation of the block mold. The additional movements of the block may have been enough to decrease the shear resistance on the block faces, such that the friction angle for the joints was lower and more representative of a mobilized friction value. For the block mold material used in the model study, the mobilized value of ϕ is likely very small. Figure 5-12 and Figure 5-13 represent a revised theoretical block erodibility threshold for Block 1 and Block 2, respectively, assuming that $\phi = 0$ deg. for the cases when $\psi < 135$ deg. As indicated, a much improved agreement is obtained with the experimental data for both Block 1 and 2 in high and low T_u flow conditions. Accordingly, it may be appropriate to represent the joint shear strength with a mobilized friction angle in scenarios where the block mold geometry provides added kinematic resistance and a Block response 2 and 3 is anticipated. For the blocks tested in the hydraulic model study, this occurred when the required rotation angle of the active resultant force vector was approximately $\theta_r > 60$ deg. (Figure 5-11).

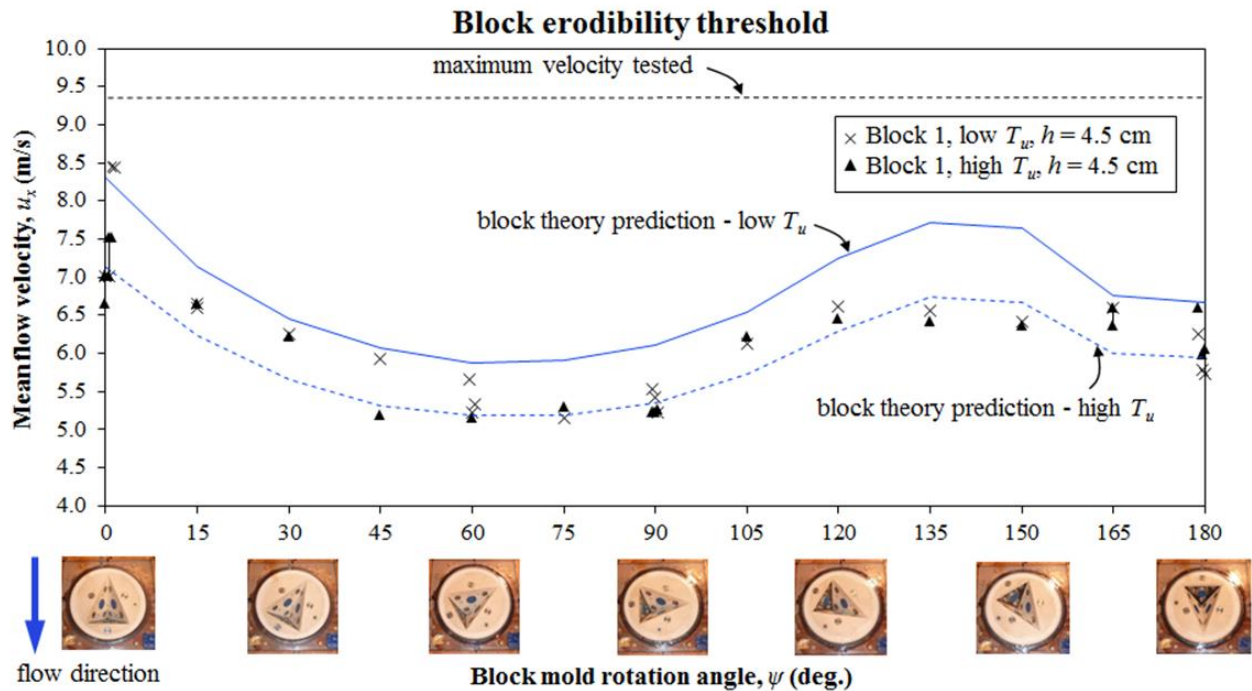


Figure 5-12. Alternate prediction of block erodibility threshold for high and low T_u flow conditions compared to measured data for Block 1 using a mobilized friction angle, $\phi = 0$ deg. for $\psi < 135$ deg. (corresponding to block response 2 and 3).

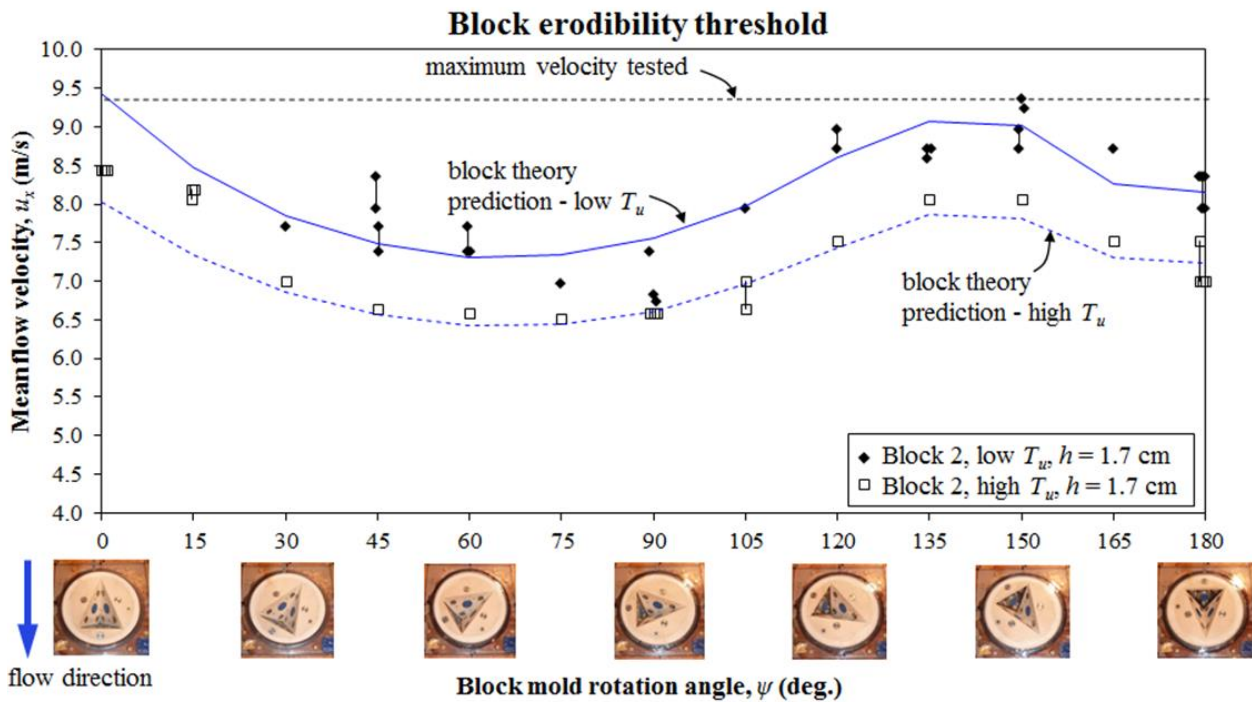


Figure 5-13. Alternate prediction of block erodibility threshold for high and low T_u flow conditions compared to measured data for Block 2 using a mobilized friction angle, $\phi = 0$ deg. for $\psi < 135$ deg. (corresponding to block response 2 and 3).

5.4 Example Analysis

An example analysis was performed using a block theory framework above to assess scour potential of the actively eroding unlined rock spillway channel at the Spaulding Dam No. 2 site in northern California (Chapter 3). Field investigations were performed to collect pertinent rock mass information and analyses were conducted to identify removable blocks and determine their susceptibility to scour. For simplicity, erodibility assessment of the spillway has been limited to a single free rock face, although more thorough analysis would consider all pertinent locations / faces. The free face in question is that directly downstream of the spillway gates. Based on field measurement, the spillway face has an orientation of 320 / 10 (dip direction / dip) in degrees. A schematic of the idealized geometry is shown in Figure 5-15, which is loosely analogous to the original (pre-erosion) landscape (Figure 3-4).

5.4.1 Removability

Since only tetrahedral blocks are considered, the joint sets in Table 3-4 were broken down into groups of three that, when combined with the free spillway face, yield a four-sided (tetrahedral) block with no repeated joint sets. In doing so, there were ten different combinations (joint groups) that required analysis, each of which produced one removable block. Using stereographic projection, the removable JP code was determined and block geometry calculated (Figure 5-14, with supplemental plots in Appendix G). The JP codes are identified by joint group in Table 5-1 along with pertinent geometry data for stability analysis. Block weight was kept constant between blocks to allow comparison of stability results. Figure 5-15 shows the surficial trace of the ten removable blocks on the spillway surface.

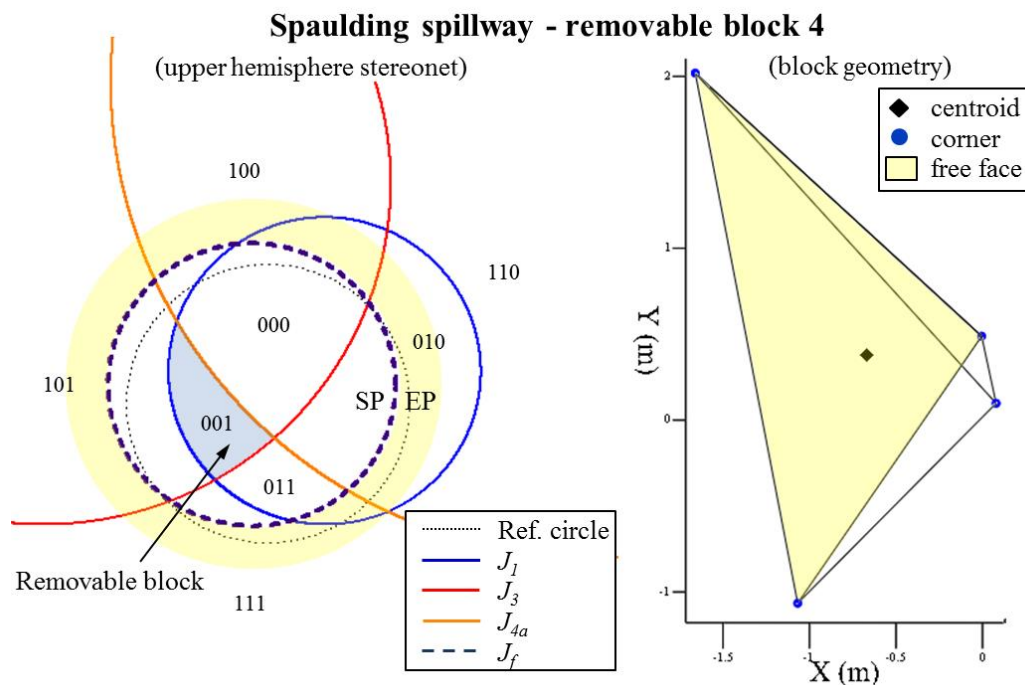


Figure 5-14. Stereographic projection showing removable block with JP 001 (contained completely within the space pyramid (SP) region) (left) and block geometry (right).

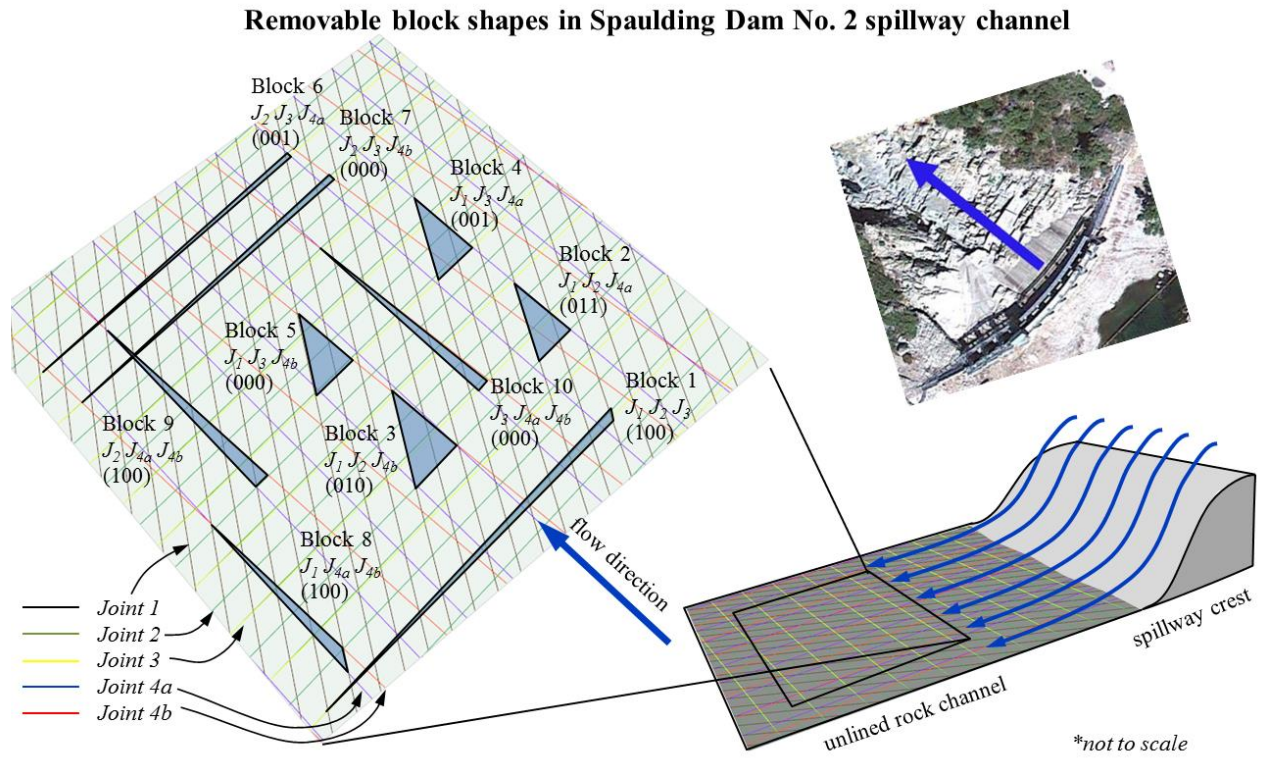


Figure 5-15. Schematic showing idealized spillway geometry (analogous to original configuration, Figure 3-4) and removable block shapes. Note block sizes are not to scale.

Table 5-1. Removable block data for Spaulding Dam No. 2 spillway

Block	Joint group	JP code	Volume V_b (m ³)	Face area A (m ²)	Trace length l_b (m)	Angle w/ flow ζ (deg.) ^a
1	J_1	100	0.5	0.117	0.499	29
	J_2			5.721	32.97	264
	J_3			4.388	32.685	85
	J_f			6.735	-	-
2	J_1	011	0.5	2.945	2.553	209
	J_2			1.119	1.31	84
	J_{4a}			1.205	2.095	358
	J_f			1.368	-	-
3	J_1	010	0.5	2.636	2.572	209
	J_2			1.111	1.464	84
	J_{4b}			1.027	2.104	354
	J_f			1.54	-	-
4	J_1	001	0.5	2.339	3.189	209
	J_3			0.687	1.635	85
	J_{4a}			0.965	2.636	358
	J_f			2.151	-	-
5	J_1	000	0.5	2.135	3.148	209
	J_3			0.696	1.791	85
	J_{4b}			0.839	2.598	354
	J_f			2.327	-	-
6	J_2	001	0.5	5.676	32.973	264
	J_3			4.388	32.944	85
	J_{4a}			0.048	0.413	358
	J_f			6.789	-	-
7	J_2	000	0.5	5.669	32.986	264
	J_3			4.386	32.985	85
	J_{4b}			0.046	0.412	354
	J_f			6.8	-	-
8	J_1	100	0.5	1.226	0.603	29
	J_{4a}			5.105	5.03	178
	J_{4b}			4.386	4.523	354
	J_f			0.775	-	-
9	J_2	100	0.5	0.401	0.398	84
	J_{4a}			3.965	5.839	178
	J_{4b}			3.778	5.823	354
	J_f			1.159	-	-
10	J_3	000	0.5	0.277	0.447	85
	J_{4a}			3.531	6.553	178
	J_{4b}			3.367	6.54	354
	J_f			1.46	-	-

Notes:

^a see Figure 4-50 for definition sketch.

5.4.2 Block erodibility threshold

Once all removable blocks have been identified, their stability was assessed. As mentioned above, the block weight was kept constant between blocks to facilitate comparison of the block erodibility threshold. Accordingly, some block sizes are impractical which correspond to the long, narrow geometries of Blocks 1, 6, 7, 8, 9 and 10. In actuality these blocks would not exist to such lengths and would be subdivided into smaller blocks by other joints. Additionally, the assumption of uniform pressure distribution on the block faces would likely be invalid. For comparative purposes, these blocks were still analyzed for stability.

In this analysis, a block yield condition corresponding to $\phi = 40$ deg. was assumed. Average dynamic pressure coefficients (C_p) on the block faces were calculated using Equations 4-13 to 4-15. C_p values were used to determine the active resultant force vector (\mathbf{r}) which was calculated using Equation 5-16. With \mathbf{r} known, the pseudo-static stability of each block was evaluated using limit equilibrium Equations 5-7 to 5-9 for the pure translational modes subject to kinematic constraints in Equations 5-1, 5-4 and 5-6.

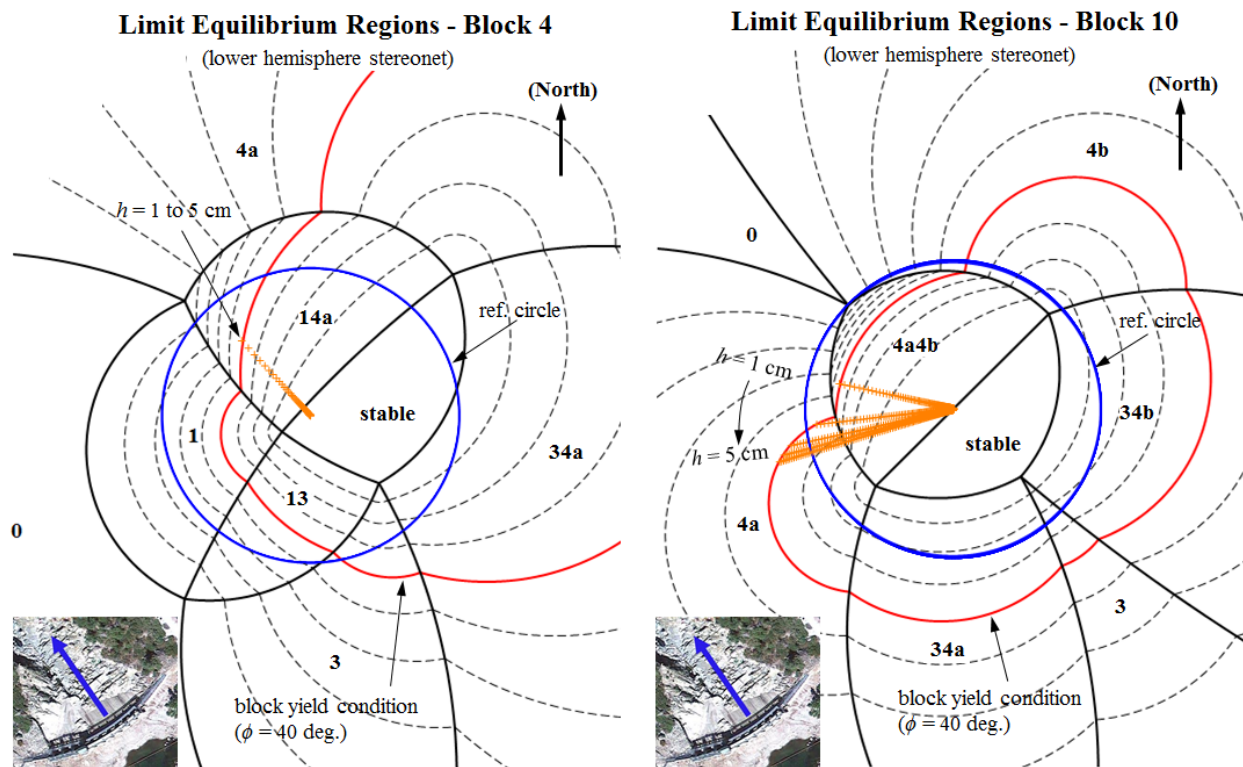


Figure 5-16. Limit equilibrium stereonets showing active resultant force vector path with increasing mean channel velocity for Blocks 4 (left) and 10 (right) for low T_u flow conditions.

The flow velocity was increased incrementally until \mathbf{r} rotated outward to the block yield condition. This is shown for Blocks 4 and 10 in Figure 5-16 assuming low T_u flow conditions for a range of block protrusion heights, $h = 1, 2, 3, 4$ and 5 cm. In both instances, the initial orientation of \mathbf{r} was downward (corresponding to the self-weight of the block), which plotted at the center of the reference circle (in the stable region). As flow velocity was increased, \mathbf{r} rotated outward, away from the origin of the stereonet. The azimuth of the vector as well as the rate of

outward rotation is dependent on the orientation and size of the block faces. For Block 4 (Figure 5-16 – left) the azimuth of \mathbf{r} remained constant with increased block protrusion height. The kinematic mode also remained constant, corresponding to 2-plane sliding on J_1 and J_{4a} . For Block 10 (Figure 5-16 – right), \mathbf{r} rotated counter-clockwise with increased block protrusion height, which caused a change in the kinematic mode from 2-plane sliding on J_{4a} and J_{4b} to 1-plane sliding on J_{4a} . This also resulted in an increase in the block erodibility threshold with increased protrusion height (Figure 5-17). Results for other blocks are also provided in Figure 5-17 and, more intuitively, show a decrease in block erodibility threshold with increased block protrusion height. Block 10 is an exception, but highlights the importance of block kinematics on stability and scour potential. Results are also summarized in Table 5-2.

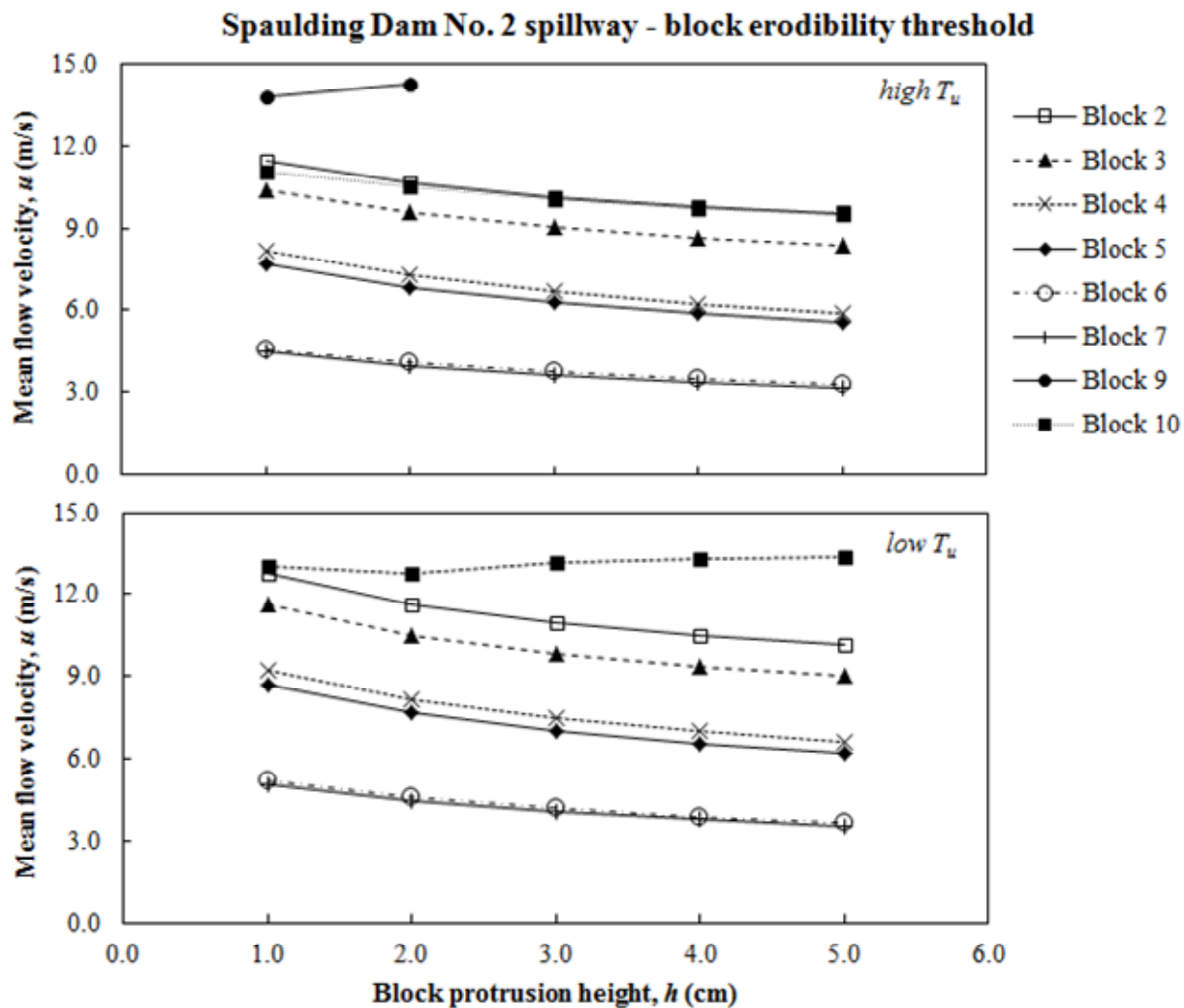


Figure 5-17. Calculated erodibility threshold for removable blocks from Spaulding Dam No. 2 spillway for high (top) and low (bottom) T_u flow conditions.

As anticipated, a range of critical flow velocities was predicted for the different block shapes. Blocks 4 and 5 were the most critical cases (not considering the long narrow Blocks 1, 6, 7, 8, 9 and 10). Compared to Blocks 2 and 3 which have a similar surficial trace (Figure 5-15), Blocks

4 and 5 reside above an upstream joint (J_3) that dips in the direction of flow. Blocks 2 and 3, however, are located below an upstream face defined by J_2 and dips against the direction of flow. For the latter, hydraulic pressure applied normal to this face acts to stabilize the block. Accordingly, the predicted erodibility threshold for Blocks 2 and 3 is approximately 50% higher than for Blocks 4 and 5. It should also be noted that two blocks, despite being removable, were stable over the range of flow velocities considered for this analysis (Blocks 1 and 8).

Table 5-2. Calculated erodibility threshold for removable blocks from Spaulding Dam No. 2.

Block	Block erodibility threshold, u_x (m/s)									
	High T_u					Low T_u				
	$h=1\text{cm}$	$h=2\text{cm}$	$h=3\text{cm}$	$h=4\text{cm}$	$h=5\text{cm}$	$h=1\text{cm}$	$h=2\text{cm}$	$h=3\text{cm}$	$h=4\text{cm}$	$h=5\text{cm}$
1	-	-	-	-	-	-	-	-	-	-
2	11.4	10.7	10.1	9.8	9.5	12.8	11.7	11.0	10.5	10.2
3	10.4	9.6	9.0	8.6	8.4	11.6	10.5	9.8	9.4	9.0
4	8.2	7.3	6.7	6.3	5.9	9.2	8.2	7.5	7.0	6.6
5	7.7	6.9	6.3	5.9	5.6	8.7	7.7	7.0	6.6	6.2
6	4.6	4.1	3.7	3.5	3.3	5.2	4.6	4.2	3.9	3.7
7	4.5	4.0	3.6	3.4	3.2	5.1	4.5	4.1	3.8	3.6
8	-	-	-	-	-	-	-	-	-	-
9	13.8	14.2	-	-	-	-	-	-	-	-
10	11.0	10.5	10.1	9.7	9.6	13.0	12.8	13.2	13.3	13.3

Predicted kinematic modes for each block are presented in Table 5-3, while supplemental limit equilibrium stereonet plots showing the active resultant force vector orientation are provided in Appendix G.

Table 5-3. Predicted kinematic modes for removable block from Spaulding Dam No. 2 spillway

Block	JP code	Mode ^a
1	100	-
2	011	14a
3	010	14b
4	001	14a
5	000	14b
6	001	24a
7	000	24b
8	100	-
9	100	4a4b, 4a
10	000	4a4b, 4a

Notes:

^a e.g., Mode 14a = 2-plane sliding on J_1 and J_{4a}

5.5 Summary

- A block theory framework for rock scour assessment allows incorporation of site-specific geologic structure into determination of the erodibility threshold of 3D rock blocks. Application to erodibility analysis occurs through modification of the active resultant force vector (\mathbf{r}) to include hydrodynamic loads (Equation 5-16). Average dynamic pressure coefficients (C_p) for loads on block faces can be determined from Equations 4-13 to 4-15 and Figure 4-55 based on hydraulic model testing of 2D channel flow conditions. Pseudo-static block stability is evaluated using block theory limit equilibrium Equations 5-7 to 5-9 subject to kinematic constraints in Equations 5-1, 5-4 and 5-6.
- Theoretical predictions for block erodibility thresholds from the hydraulic model (Chapter 4) are presented in Figure 5-9 and Figure 5-10. The overall trend as a function of block mold rotation angle showed good agreement with experimental data, however, the critical flow velocity resulting in removal was over-predicted mainly for experiments where ψ ranged between approximately 15 to 120 deg.
- Potential causes for the discrepancy could be related to scale effects in the model associated with low flow depths during these experiments or additional block movements associated with block response 2 (Chapter 4) causing a reduction in the shear strength of the block joints prior to removal. For the latter, Figure 5-12 and Figure 5-13 present alternative predictions for the block erodibility thresholds assuming a mobilized joint friction angle with no shear strength ($\phi = 0$ deg.) which provide improved agreement with experimental data. Block response 2 is hypothesized to occur as a result of increased kinematic resistance associated with the block mold geometry/orientation. This response appears to occur when \mathbf{r} must be rotated beyond approximately 60 deg. to reach the block yield condition (Figure 5-11) based on hydraulic model experiments, but may vary with other flow conditions/block geometries.
- For high T_u flow conditions exhibiting a more dynamic block response (block response 3), the pseudo-static approach appears to adequately represent the block erodibility threshold (i.e., $\psi = 0, 120$ and 135 deg. for Block 2). This suggests the block theory framework can be applicable to higher turbulence flows, although in extreme turbulence cases, a more dynamic analysis may be required (e.g., directly beneath a turbulent jet in a plunge pool).
- An example analysis shows the application of the block theory framework to assess scour potential at Spaulding Dam No. 2 spillway. Results indicated that there is a wide range of critical flow conditions that strongly depend on block shape (Figure 5-17). In general, increasing flow velocity rotates \mathbf{r} outwards, typically along same the azimuth until the block yield condition is reached (Figure 5-16). Some removable blocks are stable under all flow conditions, while others become more stable with increasing protrusion. In all cases, the influence of kinematics on block erodibility highlights the need to incorporate block geometry to properly assess stability.

Chapter 6. Reliability analysis: General system formulation

The influence of the variability in rock mass and flow conditions is evaluated using a general system reliability approach within the block theory framework. Monte Carlo sampling is used to determine block failure probability under hydraulic loading, while the first-order reliability method (FORM) provides a convenient means to estimate importance of system parameters and their overall influence on block erodibility.

6.1 Overview

Material properties and processes in most geologic settings are inherently variable and accounting for their variability can be problematic from a design perspective when trying to decide on selecting appropriate values for analysis. For scour analysis, reliable quantification of rock erodibility is of particular importance due to the high risk of infrastructure damage or even loss of life, should excessive erosion occur. Accordingly, a probabilistic approach is a natural choice for scour evaluation. Quantification of the rock scour process requires a joint assessment of the erosive capacity of water and the resistive capacity of the rock mass. Variability in erosive capacity is predominantly produced by unsteadiness and turbulent flow conditions, which can change both spatially and temporally; while variability in rock block resistance is dominated by the spacing, orientation and sliding friction of the discontinuities bounding the block (Figure 6-1).

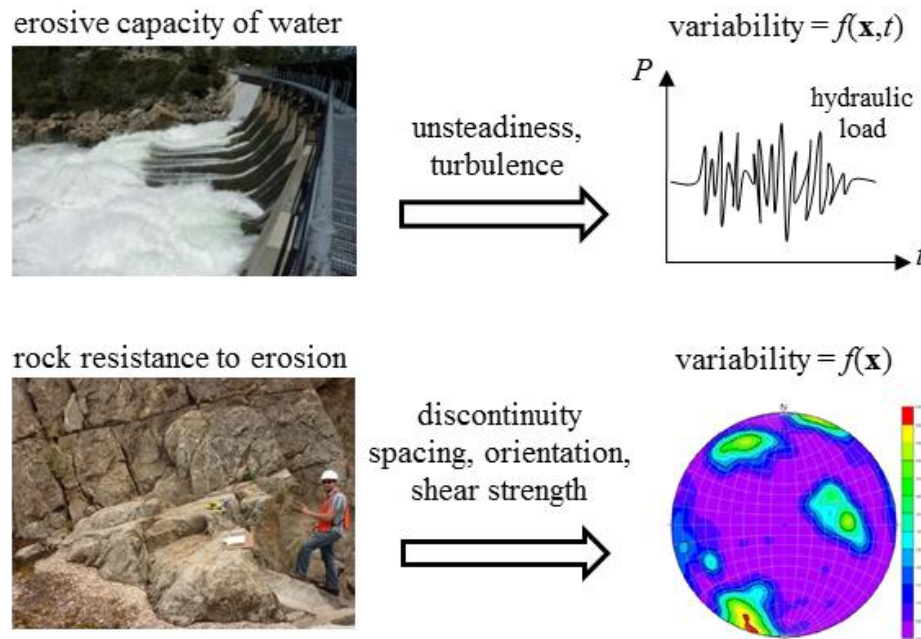


Figure 6-1. Variability in the rock scour process.

In recent years, risk and reliability methods have seen increased use among practitioners and researchers for quantification of event failure probability to aid in hazard analysis and the decision-making process. However, these studies have had limited use in the current state-of-the-art rock scour prediction models, e.g., Annandale (1995, 2006), Bollaert (2002). Reliability methods have been successfully applied to general rock slope stability in 2D by, e.g., Jimenez-Rodriguez et al. (2006) and for 3D rock wedges defined by two discontinuity planes by Low (1997, 2008), Jimenez-Rodriguez & Sitar (2005), and Li et al. (2009). Herein, the systems reliability approach is extended to 3D rock blocks bound by three discontinuity planes and one free face. While the analysis is presented for hydraulic loading by channel flow, the method can be readily applied to block stability problems of similar geometry with other loading conditions (e.g., gravity, seepage, overtopping jet).

6.2 Model Formulation

A general system reliability approach is used to determine the probability that scour of the rock mass will occur by removal (failure) of individual rock blocks. The state of the system in a domain, Ω , defined by a set of n random variables, $\mathbf{x} = [x_1 \dots x_n]$, is uniquely determined by the state of N_g components comprising the system. Each individual component, i , is represented by a limit state function (LSF), $g_i(\mathbf{x})$, and has two potential states: safe ($g_i(\mathbf{x}) > 0$) or fail ($g_i(\mathbf{x}) \leq 0$).

The performance of the overall system (i.e., the stability of the block) is modeled using a minimum cut-set formulation (Der Kiureghian 2005). For this purpose, the system is represented by a series assemblage of N_{cs} parallel sub-systems, or cut-sets, each of which corresponds to one of the potential kinematic failure modes of the block (Figure 6-2).

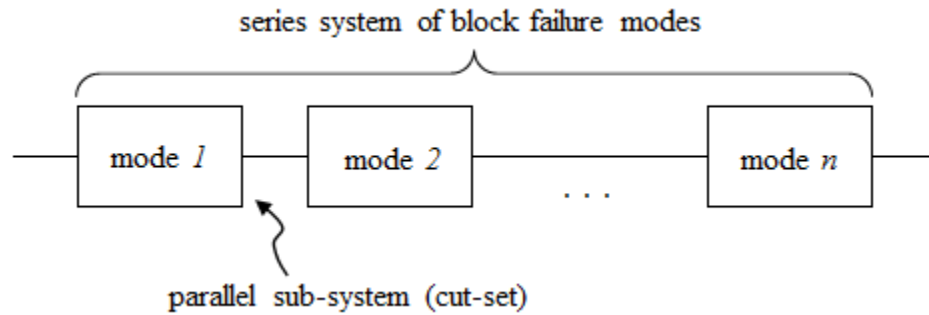


Figure 6-2. General system representation of 3D block stability with n different failure modes.

Each cut-set, C_k , is represented by a set of parallel components corresponding to the minimum criteria necessary to define failure of the block in a particular mode (i.e., the limit equilibrium and kinematic constraint expressions). A cut-set fails when all of its parallel components fail, and hence represents the intersection of component failure regions, i.e., $C_k = \cap g_i(\mathbf{x}) \leq 0$ (for $i \in C_k$) (Figure 6-3). For the block, this means that 1) the equilibrium expression must indicate the block is unstable, and 2) the kinematic conditions must be met to guarantee the block can be physically removed in accordance with the prescribed failure mode.

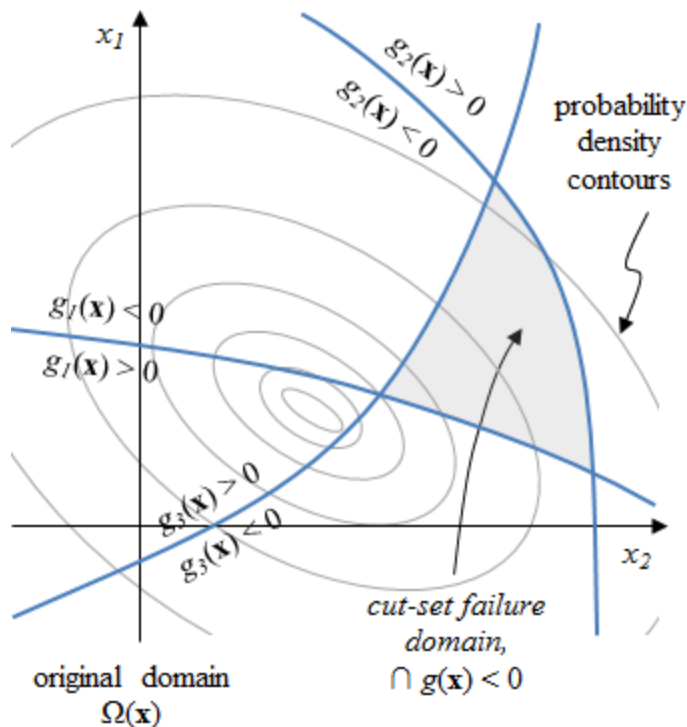


Figure 6-3. Physical interpretation of cut-set (parallel system) defined by three LSFs.

The overall system (block) fails when one of the cut-sets fails. Figure 6-4 shows the cut-set formulation for a block subject to pure translational modes of failure, while Table 6-1 lists the LSFs and their physical interpretation. These are taken directly from the original block theory

formulation presented by Goodman & Shi (1985) for the pure translational modes of failure. For lifting mode, a limit equilibrium condition is not required, i.e., Equation (5-7), as the kinematic criteria guarantee block instability when satisfied. Other block failure modes may be considered, such as rotation about a corner or edge, by adding other cut-sets with the appropriate expressions for stability and kinematics in series with the existing cut-sets.

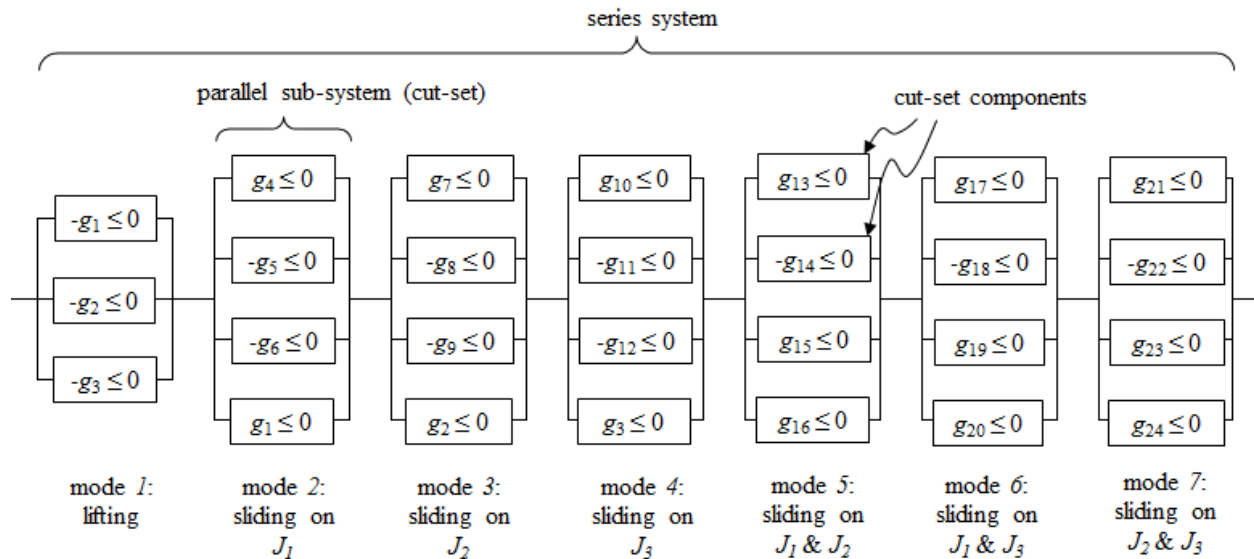


Figure 6-4. General system formulation of 3D block stability with translational failure modes.

Table 6-1. Limit state functions for 3-D block stability model with translational failure modes.

Failure mode	Limit state function	Physical interpretation	Eqn.
Lifting	$g_1 = \mathbf{r} \cdot \mathbf{v}_1$	Block lifting dir. away from J_1	(5-1)
	$g_2 = \mathbf{r} \cdot \mathbf{v}_2$	Block lifting dir. away from J_2	(5-1)
	$g_3 = \mathbf{r} \cdot \mathbf{v}_3$	Block lifting dir. away from J_3	(5-1)
Sliding on J_1	$g_4 = -F_1$	Limit equilibrium eqn. for sliding on J_1	(5-8)
	$g_5 = \mathbf{s}_1 \cdot \mathbf{v}_2$	Block sliding dir. away from J_2	(5-4)
	$g_6 = \mathbf{s}_1 \cdot \mathbf{v}_3$	Block sliding dir. away from J_3	(5-4)
	g_2 (same as above)	Active resultant oriented towards J_1	(5-1)
Sliding on J_2	$g_7 = -F_2$	Limit equilibrium eqn. for sliding on J_2	(5-8)
	$g_8 = \mathbf{s}_2 \cdot \mathbf{v}_1$	Block sliding dir. away from J_1	(5-4)
	$g_9 = \mathbf{s}_2 \cdot \mathbf{v}_3$	Block sliding dir. away from J_3	(5-4)
	g_3 (same as above)	Active resultant oriented towards J_2	(5-1)
Sliding on J_3	$g_{10} = -F_3$	Limit equilibrium eqn. for sliding on J_3	(5-8)
	$g_{11} = \mathbf{s}_3 \cdot \mathbf{v}_1$	Block sliding dir. away from J_1	(5-4)
	$g_{12} = \mathbf{s}_3 \cdot \mathbf{v}_2$	Block sliding dir. away from J_2	(5-4)
	g_4 (same as above)	Active resultant oriented towards J_3	(5-1)
Sliding on J_1 & J_2	$g_{13} = -F_{12}$	Limit equilibrium eqn. for sliding on J_1 & J_2	(5-9)
	$g_{14} = \mathbf{s}_{12} \cdot \mathbf{v}_3$	Block sliding dir. away from J_3	(5-6)
	$g_{15} = \mathbf{s}_1 \cdot \mathbf{v}_2$	Block sliding along J_1 towards J_2	(5-6)
	$g_{16} = \mathbf{s}_2 \cdot \mathbf{v}_1$	Block sliding along J_2 towards J_1	(5-6)
Sliding on J_1 & J_3	$g_{17} = -F_{13}$	Limit equilibrium eqn. for sliding on J_1 & J_3	(5-9)
	$g_{18} = \mathbf{s}_{13} \cdot \mathbf{v}_2$	Block sliding dir. away from J_2	(5-6)
	$g_{19} = \mathbf{s}_1 \cdot \mathbf{v}_3$	Block sliding along J_1 towards J_3	(5-6)
	$g_{20} = \mathbf{s}_3 \cdot \mathbf{v}_1$	Block sliding along J_3 towards J_1	(5-6)
Sliding on J_2 & J_3	$g_{21} = -F_{23}$	Limit equilibrium eqn. for sliding on J_2 & J_3	(5-9)
	$g_{22} = \mathbf{s}_{23} \cdot \mathbf{v}_1$	Block sliding dir. away from J_1	(5-6)
	$g_{23} = \mathbf{s}_2 \cdot \mathbf{v}_3$	Block sliding along J_2 towards J_3	(5-6)
	$g_{24} = \mathbf{s}_3 \cdot \mathbf{v}_2$	Block sliding along J_3 towards J_2	(5-6)

6.3 System failure probability

The probability of failure of a system, $P_{f,s}$, consisting of N_{cs} cut-sets can be expressed as:

$$P_{f,s} = P\left(\bigcup_{k=1}^{N_{cs}} C_k\right) = P\left(\bigcup_{k=1}^{N_{cs}} \bigcap_{i \in C_k} g_i(\mathbf{x}) \leq 0\right) \quad (6-1)$$

which is interpreted as the probability of failure of the union of all system cut-sets. Although a number of options exist for calculating the system failure probability (including approximate methods using first order reliability method (FORM) (e.g., Der Kiureghian (2005)) and bound methods based on low-order probabilities (e.g., Kounias (1968), Hunter (1976), Ditlevsen (1979), Yong Cang (1993), Song & Der Kiureghian (2003)), Monte Carlo simulation method is utilized here. Monte Carlo sampling provides an “exact” solution for the failure probability of the block system and is relatively straight forward to implement. Furthermore, discontinuous LSFs can be used which can be problematic for approximate methods like FORM. The tradeoff in using Monte Carlo is increased computational effort when system failure probability is low as large numbers of samples are required to achieve a tolerable level of confidence in the failure probability value.

For Monte Carlo analysis, a set of random numbers for each of the variables, \mathbf{x} , is generated and the system is solved deterministically N times. For each trial run an indicator function, $I(\mathbf{x})$, is given a Boolean value depending on whether failure of the block occurs (0 = safe/stable, 1 = fail/unstable). Failure probability of the system is computed by dividing the number failure occurrences by the total number of simulations:

$$I(\mathbf{x}) = \begin{cases} 1 & \text{if } \bigcup_{k=1}^{N_{cs}} \bigcap_{i \in C_k} g_i(\mathbf{x}) \leq 0, \\ 0 & \text{otherwise} \end{cases} \quad (6-2)$$

$$P_{f,s} \cong P_{f_MC} = \frac{1}{N} \cdot \sum_{i=1}^N I(\mathbf{x}_i) \quad (6-3)$$

The total number of trials, N , is determined when the coefficient of variation of the failure probability, δ_{P_f} , is below a specified tolerance, δ_0 , or when a specified maximum number of trials, N_0 , is achieved. The coefficient of variation is expressed as:

$$\delta_{P_f} = \frac{\sqrt{N \cdot \sum_{i=1}^N I(\mathbf{x}_i)^2 - \left(\sum_{i=1}^N I(\mathbf{x}_i)\right)^2}}{\sqrt{N} \cdot \sum_{i=1}^N I(\mathbf{x}_i)} = \sqrt{\frac{1 - (P_{f_MC})_i}{N \cdot (P_{f_MC})_i}} \quad (6-4)$$

The individual cut-set with the highest failure probability represents the most probable block failure mode.

6.4 Parameter importance

Information regarding the relative importance of the individual random variables can conveniently be obtained through FORM analysis. A key criterion for FORM requires LSFs to be continuous and differentiable to facilitate solution of a minimization algorithm to find the most probable failure point (design point) for a particular LSF (discussed in further detail below). This criterion can be relaxed for discontinuous functions, such as some of those considered in the block system formulation, as long they are continuous and differentiable in the vicinity of the design point (Der Kiureghian 2005). To this end, FORM is implemented to compute relative parameter importance for specific LSFs corresponding to the most probable block failure mode determined from MC analysis.

FORM utilizes a transformation of the variables, \mathbf{x} , and LSF, $g(\mathbf{x})$, from their original defined domain $\Omega(\mathbf{x})$ to the standard normal domain $\phi(\mathbf{u})$ where $\mathbf{u} = [u_1 \dots u_n]$ is the vector of transformed variables, and $g(\mathbf{u})$ is the transformed LSF in the standard normal space (Figure 6-5).

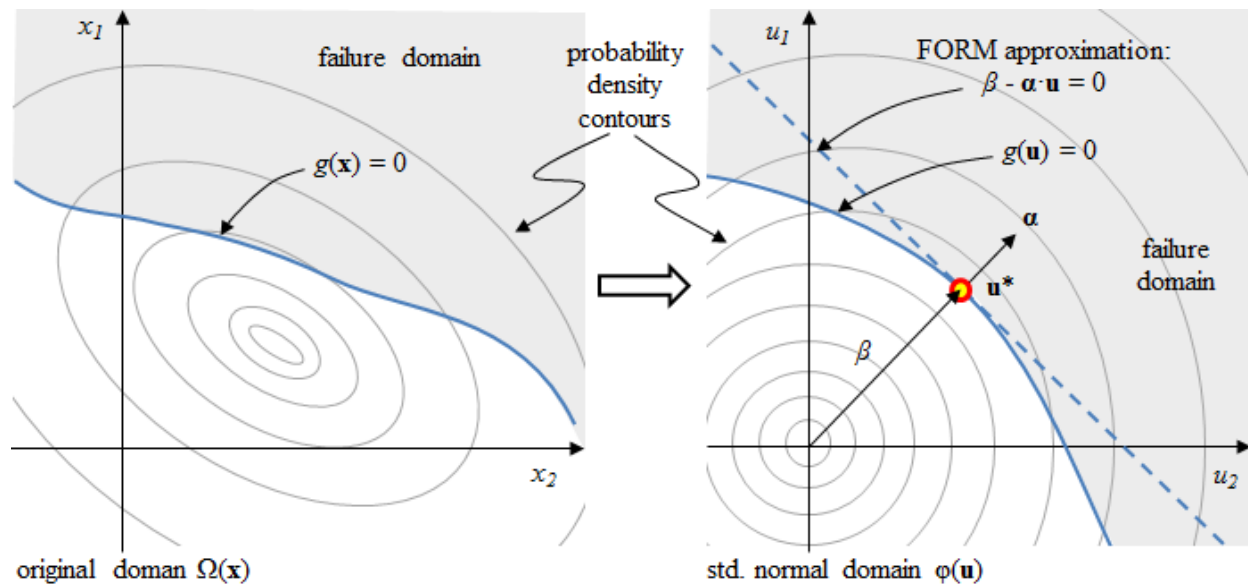


Figure 6-5. First order approximation of failure probability for a component reliability problem transformed from 2-D original domain (left) to 2-D standard normal domain (right).

This transformation requires knowledge of joint probability distributions between variables in the original domain, which can be difficult or impractical to obtain. As such, variables are assumed to be related through a Nataf distribution such that the transformation may be performed with only the information regarding their prescribed marginal distributions and correlation coefficients (Liu & Der Kiureghian 1986). This is expressed as:

$$\mathbf{u} = \mathbf{L}_0^{-1} \cdot \begin{bmatrix} \Phi^{-1}(F_{x_1}(x_1)) \\ \vdots \\ \Phi^{-1}(F_{x_n}(x_n)) \end{bmatrix} \quad (6-5)$$

where $\Phi(\cdot)$ is the univariate standard normal cumulative density function (CDF), $F_{x_i}(x_i)$ is the marginal CDF of x_i , and \mathbf{L}_0 is the Choleski decomposition of the correlation matrix \mathbf{R}_0 . $\mathbf{R}_0 = [\rho_{ij}]$ for $i, j = 1 \dots n$, where ρ_{ij} is the correlation coefficient between x_i and x_j .

In the standard normal space, probability density contours form concentric circles around the origin (Figure 6-5 – right). The location on the LSF closest to the origin, \mathbf{u}^* , represents the location of maximum probability density, i.e., the point of most probable occurrence. This location is referred to as the design point and is found by solving a minimization problem using the improved Hasofer/Lind-Rackwitz/Fiessler (iHL-RF) algorithm (Zhang & Der Kiureghian 1995). At \mathbf{u}^* , a first order (linear) approximation of the limit state function is made:

$$g(\mathbf{u}) \cong \nabla g(\mathbf{u}^*) \cdot (\mathbf{u} - \mathbf{u}^*) = |\nabla g(\mathbf{u}^*)| \cdot (\beta - \boldsymbol{\alpha} \cdot \mathbf{u}) \quad (6-6)$$

where $\nabla g(\mathbf{u}^*) = [\partial g/\partial u_1 \dots \partial g/\partial u_n]$ is the gradient row vector evaluated at the design point, $\boldsymbol{\alpha} = -\nabla g(\mathbf{u}^*)/|\nabla g(\mathbf{u}^*)|$ is a unit vector normal to the limit state surface at the design point and $\beta = \boldsymbol{\alpha} \cdot \mathbf{u}^*$ is the reliability index. The reliability index can be viewed as an alternative measure of safety (e.g., analogous to a factor of safety in a purely deterministic problem). For statistically independent random variables, the individual terms of vector $\boldsymbol{\alpha} = [\alpha_1 \dots \alpha_n]$ represent the relative importance (or contribution) of each variable, x_i , on the total variance of the linearized LSF. A larger magnitude of α_i indicates a stronger influence from x_i . A positive value of α_i signifies x_i is a demand variable and works to destabilize the system while a negative value of α_i signifies x_i is a capacity variable and works to stabilize the system. For dependent random variables, the importance vector with similar implications is represented by $\boldsymbol{\gamma}$ (Der Kiureghian 2005):

$$\boldsymbol{\gamma} = \frac{\boldsymbol{\alpha} \cdot \mathbf{J}_{\mathbf{x},\mathbf{u}}^{-1} \cdot \mathbf{D}'}{|\boldsymbol{\alpha} \cdot \mathbf{J}_{\mathbf{x},\mathbf{u}}^{-1} \cdot \mathbf{D}'|} \quad (6-7)$$

where $\mathbf{J}_{\mathbf{x},\mathbf{u}}$ is the Jacobian matrix for the transformation from \mathbf{x} to \mathbf{u} space evaluated at the design point, and \mathbf{D}' is the diagonal standard deviation matrix of equivalent normal random variables $\mathbf{x}' = \mathbf{x}^* + \mathbf{J}_{\mathbf{x},\mathbf{u}} \cdot (\mathbf{u} - \mathbf{u}^*)$ evaluated at the design point. Note that at the design point, $\mathbf{x}' = \mathbf{x}^*$ where \mathbf{x}^* is the design point in the original domain.

6.5 Numerical implementation

The reliability code FERUM, developed in Matlab (Haukaas & Der Kiureghian 1999), is utilized for Monte Carlo simulation of the failure probability of the block system, and for FORM analysis of individual system components to determine parameter importance. The original Monte Carlo sampling module is modified to include simulation for a multiple component block system.

6.6 Example analysis

The deterministic block theory approach presented in Chapter 5 to evaluate block erodibility threshold was extended here to incorporate variability in the scouring process at the Spaulding Dam No. 2 site. For this analysis, one of the removable tetrahedral blocks (Block 5, JP 000 - Figure 5-15 and Table 5-1) from the unlined spillway channel was analyzed to demonstrate

applicability of the block theory-based, reliability methods presented above. A schematic of the spillway and block geometry is shown in Figure 6-6.

Schematic for reliability analysis of removable block in Spaulding Dam No. 2 spillway

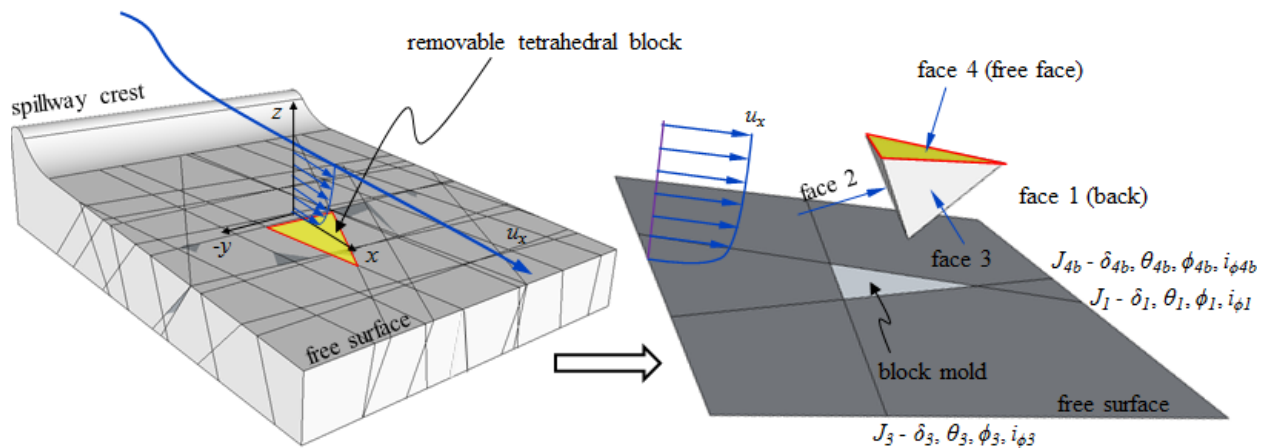


Figure 6-6. Schematic for Spaulding Dam No. 2 spillway channel used in reliability analysis of removable tetrahedral blocks.

6.6.1 Variable distributions and correlation

Joint orientations defining the block geometry (dip (δ) and dip direction (θ)) were considered variable as were the friction (ϕ) and dilation (i_ϕ) angles representing the discontinuity shear strength on the block faces. The block protrusion height (h) and the magnitude of the stream-wise velocity (u_x) were also considered variable. The latter two, combined with the orientation of block discontinuities, define the relative magnitude of the hydrodynamic pressure applied to the block faces. As previously, flow is assumed parallel to the dip vector of the spillway surface. The orientation of the spillway channel was considered to be constant for this analysis and, therefore, was evaluated deterministically (Table 6-2). Other deterministic parameters are also listed in Table 6-2.

Table 6-2. Deterministic block parameters.

Parameter	Description	Value	Notes
g	gravitational constant (m/s^2)	9.81	
ρ_b	block density (kg/m^3)	2,700	
ρ_w	water density (kg/m^3)	1,000	
a	fit parameter for C_1	0.050 (0.046)	High T_u (Low T_u) - Table 4-16
b	fit parameter for C_1	0.901 (0.820)	High T_u (Low T_u) - Table 4-16
a	fit parameter for C_3	0.220 (0.195)	High T_u (Low T_u) - Table 4-16
b	fit parameter for C_3	0.333	High & Low T_u - Table 4-16
C_2	C_p correction coefficient.	0.090 (0.062)	High T_u (Low T_u) - Table 4-15
C_{pf}	C_p on free block face	0.005	High & Low T_u - Figure 4-55
δ_f	dip angle of free surface (deg.)	10	
θ_f	dip direction of free surface (deg.)	320	

Marginal distributions for all variables are presented in Table 6-3. For joint orientations defining the block geometry, as well as joint dilation angles, a Beta distribution was used. Distribution parameters were determined based on statistical analysis of LiDAR data collected at the field site presented in Chapter 3. Correlation values, ρ , between the dip and dip direction for joint sets J_1 , J_3 and J_{4b} (also determined from LiDAR analysis) are -0.123, 0.164 and 0.135, respectively (Table 6-4).

Joint friction angles were also modeled using a Beta distribution. The bounds for each friction angle were assumed to range between $\phi = 35$ to 45 deg. for all discontinuities. The general distribution shape was presumed to be symmetric as defined by parameters $p_1 = 3$, and $p_2 = 3$. A positive correlation $\rho = 0.3$ (Table 6-4) was assumed between friction angles on opposing discontinuities, suggesting if a high value friction angle is observed on one joint plane, the friction angle on the other joint planes would also likely be high. Similarly, if a low value is observed on one joint plane, the values on the other joint planes would also likely be low. Note that in highly foliated or layered rock, no correlation or a negative correlation of joint friction angles may be more appropriate.

For the block protrusion height, a Log Normal distribution with parameters $p_1 = 2$ cm and $p_2 = 0.5$ cm was arbitrarily selected. The protrusion height was assumed uncorrelated with the other block parameters (i.e., $\rho = 0$), but inversely correlated with the flow velocity ($\rho = -0.1$). The latter implies that as the protrusion height increases the flow velocity decreases and vice versa. This is intuitive as a higher block protrusion relates to a more hydraulically rough channel which results in slower flow velocity (assuming other surface roughness asperities in the channel are of the same relative magnitude).

Normal distribution was assumed for flow velocity. The mean velocity was increased from $u_x = 5$ to 10 m/s to encompass a range of conditions likely encountered at the field site. The standard deviation was determined based on hydraulic model experiments presented in Chapter 4 and set equal to $T_u u_x$, where $T_u = 0.06$ (high turbulence conditions) and $T_u = 0.02$ (low turbulence conditions) (Table 4-11). No correlation of flow velocity with other variables was assumed (except the block protrusion height as discussed above).

Definitions for Beta, Normal and Log Normal distributions can be found in Appendix A.

Table 6-3. Variable statistical distributions.

Variable	Distribution	Distribution Parameters				Description
		p_1	p_2	p_3	p_4	
δ_1	Beta ^a	5.903	5.271	10	38	dip angle J_1 (deg.)
δ_3	Beta ^a	3.469	3.681	53	81	dip angle J_3 (deg.)
δ_{4b}	Beta ^a	1.923	0.943	76	90	dip angle J_{4b} (deg.)
θ_1	Beta ^a	3.333	2.679	023	090	dip direction J_1 (deg.)
θ_3	Beta ^a	2.577	3.146	304	328	dip direction J_3 (deg.)
θ_{4b}	Beta ^a	1.412	1.522	214	237	dip direction J_{4b} (deg.)
ϕ_1	Beta ^a	3	3	35	45	friction angle on J_1 (deg.)
ϕ_3	Beta ^a	3	3	35	45	friction angle on J_3 (deg.)
ϕ_{4b}	Beta ^a	3	3	35	45	friction angle on J_{4b} (deg.)
$i_{\phi 1}$	Beta ^a	5.816	8.137	0	5.6	dilation angle on J_1 (deg.)
$i_{\phi 3}$	Beta ^a	3.926	17.927	0	14.8	dilation angle on J_3 (deg.)
$i_{\phi 4b}$	Beta ^a	4.456	4.285	0	4.3	dilation angle on J_{4b} (deg.)
h	Log Normal ^b	2	0.5	-	-	block protrusion height (cm)
u_x	Normal ^c	u_x^d	$T_u u_x^e$	-	-	flow velocity (m/s)

Notes:

^a p_1, p_2 = distribution shape parameters, $p_3 = a$ (min. value), $p_4 = b$ (max. value),^b $p_1 = \lambda$ (mean log normal space), $p_2 = \zeta$ (std. dev. log normal space), p_3, p_4 not required^c $p_1 = \mu$ (mean), $p_2 = \sigma$ (std. dev.), p_3, p_4 not required^d Mean value of u_x varied from 5 m/s to 10 m/s^e $T_u = 0.06$ (high T_u analysis), 0.02 (low T_u analysis)Table 6-4. Correlation matrix, \mathbf{R}_0 , for input variables.

	δ_1	δ_3	δ_{4b}	θ_1	θ_3	θ_{4b}	ϕ_1	ϕ_3	ϕ_{4b}	$i_{\phi 1}$	$i_{\phi 3}$	$i_{\phi 4b}$	h	u_x
δ_1	1													
δ_3	0	1												
δ_{4b}	0	0	1											
θ_1	-0.123 ^a	0	0	1										
θ_3	0	0.164 ^a	0	0	1									
θ_{4b}	0	0	0.135 ^a	0	0	1								
ϕ_1	0	0	0	0	0	0	1							
ϕ_3	0	0	0	0	0	0	0.3	1						
ϕ_{4b}	0	0	0	0	0	0	0.3	0.3	1					
$i_{\phi 1}$	0	0	0	0	0	0	0.5	0.3	0.3	1				
$i_{\phi 3}$	0	0	0	0	0	0	0.3	0.5	0.3	0.3	1			
$i_{\phi 4b}$	0	0	0	0	0	0	0.3	0.3	0.5	0.3	0.3	1		
h	0	0	0	0	0	0	0	0	0	0	0	0	1	
u_x	0	0	0	0	0	0	0	0	0	0	0	0	-0.1	1

Notes:

^a Correlation values, ρ , determined from field investigation (Chapter 3)

6.6.2 Block failure probability and parameter importance

Calculated failure probabilities for the block (system) and individual kinematic failure modes (sub-systems) are provided in Figure 6-7 for increasing values of mean channel flow velocity for both high and low turbulence conditions. Monte Carlo simulation was performed until the coefficient of variation for the block system failure probability was below a threshold of $\delta_{Pf} = \delta_0 = 0.05$ or until 10,000 trials had been performed. Note, the approximate time to perform 10,000 simulations was two hours and therefore represented a reasonable ceiling for this example study. In most cases the $\delta_{Pf} = 0.05$ criterion was achieved, except when $u_x = 5$ and 6 m/s. In these scenarios the analysis stopped when $\delta_{Pf} \sim 0.15$ to 0.2 because of the low failure probability of the system for these two cases ($P_{f,s} < 0.005$). Systems with such low failure probability would require nearly 100,000 simulations (~ 1 day run time) in order to reliability characterize $P_{f,s}$ to a threshold of $\delta_{Pf} = 0.05$. This highlights one of the limitations of the Monte Carlo method. The other modeled scenarios required significantly fewer simulations to achieve the threshold coefficient of variation (Table 6-5). Figure 6-9 shows the evolution of $P_{f,s}$ and δ_{Pf} for low turbulence conditions and $u_x = 7$ m/s.

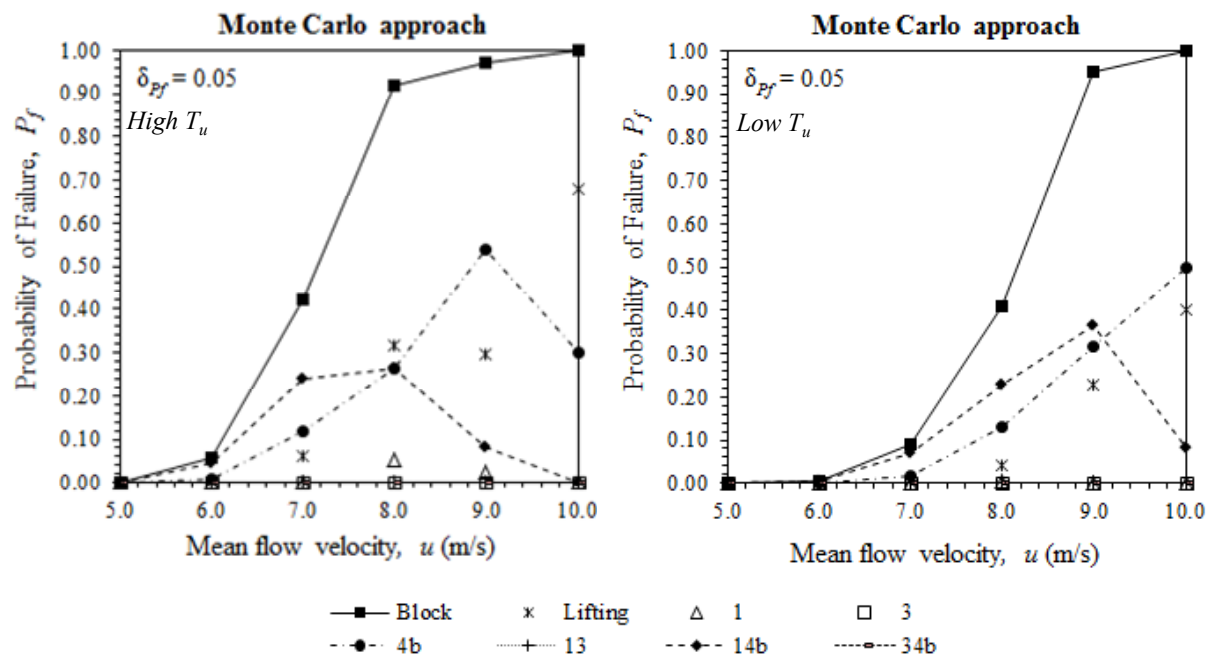


Figure 6-7. Monte Carlo simulation results for high (left) and low (right) T_u flow conditions.

Overall a trend of increasing block failure probability versus increasing mean channel flow velocity is witnessed, as anticipated. The failure probability begins to increase rapidly when $u_x > 6$ m/s (high T_u) and $u_x > 7$ m/s (low T_u). Three failure modes are identified as the most probable to occur which include 1-plane sliding on J_{4b} (4b), 2-plane sliding on J_1 and J_{4b} (14b) and lifting (0). These are modes corresponding to the individual cut-sets with the highest failure probability. For lower mean u_x values the dominant mode is 14b, while for higher u_x values 4b and 0 are more prevalent. Block removal by the other kinematic modes (1, 3, 13, 34b) yielded P_f values at or near zero indicating their unlikely occurrence.

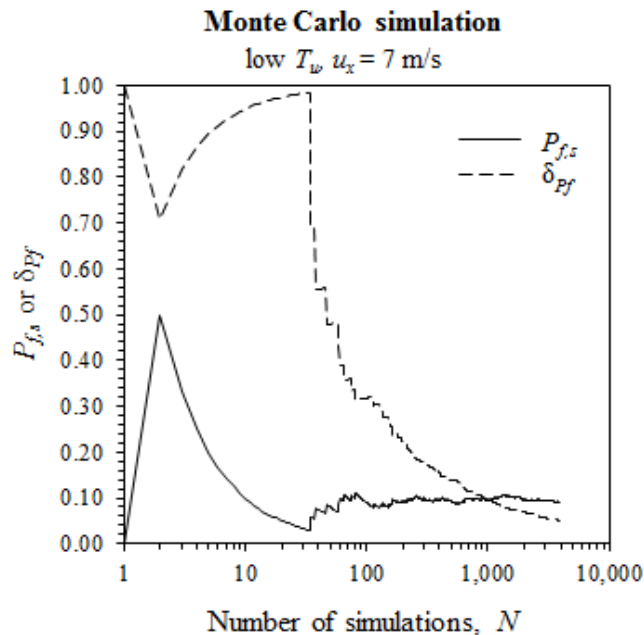
Figure 6-8. Evolution of $P_{f,s}$ and δ_{Pf} for $u_x = 7$ m/s.

Table 6-5. Monte Carlo simulation results.

Flow velocity u_x (m/s)	Turb. T_u	Failure probability $P_{f,s}$	Coef. of var. δ_{Pf}	Number of simulations N
5	High	0.002	0.22	10000
6	High	0.058	0.05	6465
7	High	0.421	0.05	551
8	High	0.919	0.05	37
9	High	0.972	<0.05	36
10	High	1.000	<0.05	49
5	Low	0	-	10000
6	Low	0.005	0.14	10000
7	Low	0.092	0.05	3970
8	Low	0.409	0.05	579
9	Low	0.952	0.05	21
10	Low	1.000	<0.05	49

A comparison between high and low T_u flow conditions is provided in Figure 6-9. The high turbulence case shows increased block failure probability at lower flow velocities. This is attributed to greater variability in the active resultant force orientation (\mathbf{r}) due to greater variability in the flow velocity, thus creating a higher probability for block instability. At $P_{f,s} = 0.5$, u_x values for both high and low T_u conditions compare very well with critical velocities obtained from the block erodibility threshold deterministic analysis presented in Chapter 5 (i.e., $u_x = 7.2$ m/s and 8.2 m/s (Figure 6-9) versus $u_x = 6.9$ m/s and 7.9 m/s (Figure 5-17, Table 5-2) for

high and low T_u , respectively, when block protrusion height, $h = 2$ cm). This was anticipated as the deterministic analysis was performed using average values for block variables.

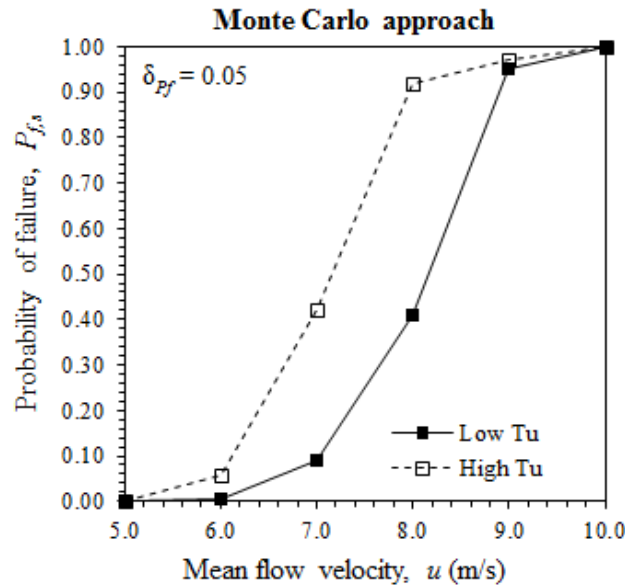


Figure 6-9. Comparison of block failure probability, $P_{f,s}$, for high and low T_u flow conditions.

Table 6-6 presents values of the importance vector (γ) for LSF g_{17} corresponding to the limit equilibrium expression for 2-plane sliding on J_1 and J_{4b} , one of the most probable kinematic failure modes. As anticipated, individual γ values for ϕ and i_ϕ are negative indicating that friction on the joint bounding the block acts in a capacitive (stabilizing) manner. Importance values for the block joint orientations are both positive and negative. This is solely a function of block face orientation as hydraulic pressure acts normal to the block face. Depending on how the face is oriented and the failure mode under consideration, the hydraulic force on that face may work to stabilize or destabilize the block. In this example, values are predominantly positive indicating a destabilizing tendency. This is logical for Block 5 because the block-side normal vector for each block face is orientated upwards out of the block mold (as the block sits above each joint plane, i.e., JP 000).

As expected, γ values for block protrusion height (h) and u_x are positive indicating these variables work to destabilize the block. Interestingly, at higher flow speeds ($u_x \geq 9$ m/s) these values become negative and act in a stabilizing capacity. This corresponds with the change in dominant kinematic failure mode observed Figure 6-7. At higher flow velocities, 2-plane sliding on J_1 and J_{4b} is less relevant, while 1-plane sliding on J_{4b} and lifting become more probable. The increased load associated with the higher flow velocity changed the orientation of the active resultant force vector (\mathbf{r}) such that sliding on J_1 and J_{4b} became kinematically more difficult. This, again, highlights the importance of kinematics in the evaluation of block stability/erodibility.

Finally, examination of the relative magnitude of the importance values for each variable (i.e., $|\gamma|$) in Table 6-6 shows that the block protrusion height has, by far, the most influence on block stability in this analysis ($|\gamma| \sim 0.75$ to 0.95). Also of significant importance is the flow velocity ($|\gamma| \sim 0.15$ to 0.20) and the orientation of the downstream block face (defined by δ_I and θ_I) ($|\gamma| \sim$

0.2 to 0.45). The magnitude of importance values for ϕ and i_ϕ representing the sliding friction are much lower than those for h , u_x , and δ_l and θ_l . This indicates the influence of the friction angle on the stability of the block is not very significant.

Table 6-6. Parameter importance vector, γ , when $u_x = 5$ to 10 m/s (low T_u)

Variable	Importance vector (γ) ^a					
	$u_x = 5$ m/s	$u_x = 6$ m/s	$u_x = 7$ m/s	$u_x = 8$ m/s	$u_x = 9$ m/s	$u_x = 10$ m/s
δ_l	0.201	0.211	0.229	0.258	-0.335	-0.308
δ_3	-0.003	0.009	0.017	0.024	0.008	0.009
δ_{4b}	0.037	0.038	0.040	0.042	-0.093	-0.078
θ_l	0.086	0.074	0.065	0.059	0.322	0.439
θ_3	0.065	0.072	0.081	0.092	-0.065	-0.074
θ_{4b}	-0.005	0.000	0.008	0.019	-0.255	-0.318
ϕ_l	-0.035	-0.032	-0.033	-0.037	-0.067	-0.092
ϕ_3	~0	~0	~0	~0	~0	~0
ϕ_{4b}	-0.018	-0.016	-0.016	-0.018	-0.027	-0.031
$i_{\phi l}$	-0.012	-0.011	-0.012	-0.013	-0.024	-0.032
$i_{\phi 3}$	~0	~0	~0	~0	~0	~0
$i_{\phi 4b}$	-0.006	-0.006	-0.006	-0.006	-0.009	-0.011
h	0.961	0.958	0.950	0.935	-0.816	-0.742
u_x	0.149	0.157	0.175	0.207	-0.186	-0.196

Notes:

^a γ values provided for LSF g_{17} corresponding to the limit equilibrium equation for 2-plane sliding on J_l & J_{4b})

6.7 Summary

A general system reliability approach for evaluation of 3D rock block stability within a block theory framework was developed to assess the relative influence of the key variables on the probability of block removal by hydraulic forces, as follows:

- A minimum cut-set formulation was implemented, where the block is treated as a series system comprised of individual cut-sets corresponding to each block failure mode (Figure 6-4). Each cut-set is a parallel sub-system comprised of LSFs corresponding to the block limit equilibrium and kinematic constraint equations (Table 6-1). The system (block) is considered to have failed when each of the LSFs for a particular cut-set have failed. For this to occur, the block limit equilibrium expression must indicate the block is unstable and the kinematic criteria must show the direction of block movement is physically feasible.
- This formulation was cast within the original block theory framework developed by Goodman & Shi (1985) for pure translational block failure modes (i.e., lifting, 1-plane sliding, and 2-plane sliding). Other kinematic block modes can be readily be considered by inclusion of additional cut-sets (Figure 6-2).

- Although the focus of the present research is hydraulic loading of rock blocks in channel flow scenarios, the method can be readily applied to block stability problems of similar geometry for other loading conditions (e.g., gravity, seepage, overtopping jet) through modification of the active resultant force vector, \mathbf{r} .
- The reliability approach provides a convenient methodology to incorporate uncertainty associated with variables considered in 3D block stability analysis (e.g., discontinuity orientation, friction angle, hydraulic loads, etc.). Variables are described by their marginal probability density distributions and related to other variables using correlation coefficients, both of which can be determined through field and laboratory investigations.
- Two key outcomes of the reliability-based block stability approach include 1) block failure probability, calculated using Monte Carlo simulation, and 2) parameter importance, determined using FORM. Block failure probability information can help guide designers in decision making and risk management for key infrastructure projects, while parameter importance provides insight into the most influential variables affecting 3D block stability. The latter can be particularly useful to optimize future field or laboratory investigations to focus on variables that have the most impact on the overall system.

An example analysis using the reliability approach to evaluate 3D block erodibility is presented to incorporate variability in the analysis of the scouring process at the Spaulding Dam No. 2 site. Variable statistics were determined from analysis of terrestrial LiDAR scan data of the rock mass (Chapter 3) and from hydraulic model testing (Chapter 4). The failure probability of an individual block was calculated as a function of increasing mean channel flow velocity (Figure 6-7). The computed parameter importance factors show that the block protrusion height (h) is by far the most influential variable on block stability/erodibility in this example, followed by the discontinuity orientations (δ and θ) and the flow velocity (u_x) (Table 6-6). Sliding friction, represented by the friction (ϕ) and dilation (i_ϕ) angles, is the least influential. Accordingly, from a design standpoint, future erodibility investigations would be best focused on determination of h , u_x , δ and θ , particularly if given budgetary constraints. This highlights the usefulness of the reliability approach to systematically (and optimally) identify variables that most impact a system.

Chapter 7. Conclusions

Erosion of rock is a complex process with applicability to both geomorphology and engineering practice, where removal of individual blocks is one of the primary mechanisms by which rock scour can occur. The objectives of this research have been aimed at understanding basic mechanics of the process as well as developing a predictive framework for block erodibility. Specifically, these were (from Chapter 1):

- Investigate influence of 3D geologic structure on the erodibility of blocks from rock masses.
- Collect high-resolution experimental data for hydraulic and rock mass parameters from both field and laboratory settings to help bridge the gap between idealized model and actual prototype conditions.
- Identify dominant modes/mechanisms for removal of 3D rock blocks subject to hydraulic loading.
- Address uncertainty in the scour process associated with natural variability in rock mass and flow parameters.
- Develop a framework to incorporate 3D geologic structure and natural variability into predictive analysis of block erodibility.

A multifaceted research program was developed in order to accomplish these objectives. Field investigation of a prototype site in the Sierra Nevada was used as a basis for the development of an extensive series of hydraulic model experiments, which were complemented

by theoretical deterministic and stochastic analyses based on 3D block theory. The key findings of this effort are summarized below.

7.1 Block response to hydraulic loading

A scaled physical hydraulic model study was performed in an open channel flume to examine scour of 3D rock blocks (Figure 4-2 and Figure 4-3). An instrumented 3D block mold was constructed that could be rotated with respect to the flow direction to study the influence of discontinuity orientation on block erodibility over a range of flow conditions (Figure 4-4). Four main variables were monitored within the realm of this study and included the block mold rotation angle (ψ), turbulence intensity (T_u), block protrusion height (h), and the flow velocity (u).

Block erodibility was highly dependent on its orientation with respect to the flow direction (Figure 4-16 and Figure 4-17). This was a function of the kinematic resistance afforded by the block mold geometry as well as the relative profile of the block protruding into the flow field. Block orientations with higher kinematic resistance (e.g., a steep downstream face angle) and a more aerodynamic flow profile (e.g., block edges oriented at an angle to flow direction) resulted in higher block erodibility thresholds. Increased turbulence intensity in the flow field resulted in an overall decrease in the block erodibility threshold despite lower mean channel flow velocities associated with the higher T_u flows (Figure 4-14 and Figure 4-15). This highlights the importance to consider the fluctuating component of the flow field in addition to the mean flow velocity when evaluating block erodibility. Intuitively, the block erodibility threshold decreased with increased block protrusion height (Figure 4-16 and Figure 4-17).

Spectral analysis of pressure and displacement time series data for experiments resulting in block removal indicated three different block response types. Block response appeared closely related to the kinematic resistance associated with the block mold geometry as well as the flow conditions. In general, increased kinematic resistance allowed greater susceptibility of the block to dynamic block behavior (i.e., impulse-like movements). When the kinematic resistance was relatively low (block response 1), block displacements occurred predominantly at the higher end of the analyzed frequency spectrum, regardless of high or low turbulence conditions (9.5 to 12.7 Hz (30 to 40 Hz model scale), Figure 4-42). This behavior was hypothesized to be associated with a fundamental resonance frequency of the block. The small displacements dissipate energy, preventing the excessive build-up of pressure within the block mold that would cause larger movements to occur. With increased kinematic resistance, lower frequency response became more pronounced. For low turbulence flow conditions (block response 2), an additional peak in displacement response was observed in the 1.6 to 6.3 Hz range (5 to 20 Hz, model scale) (Figure 4-43), which was potentially associated with resonance of pressure waves in the water-filled joints surrounding the block in the mold. For high turbulence flow conditions (block response 3), response was predominantly characterized by larger, impulse-driven block movements. These movements exhibited dominant frequencies less than approximately 3.2 Hz (10 Hz, model scale) and were associated with eddies generated from the upstream baffle blocks (Figure 4-44). The more variable displacement behavior of block response 2 and 3 was potentially associated with a decrease in block capacity to resist erosion, which is discussed in more detail in the following section.

Hydrodynamic pressures around the block faces, represented by the average dynamic pressure coefficient (C_p), were found to be a function of the angle of the upstream block face(s) with respect to the flow direction (ζ), turbulence intensity, the block protrusion height and whether or not the block face was on the upstream or downstream side of the block (Figure 4-47, Figure 4-48 and Figure 4-55). Block protrusion was the dominant factor in transmitting hydrodynamic pressure to block faces inside the block mold. This was caused by stagnation pressure at the joint entrance associated with flow in the channel impacting the protrusion. Measured dynamic pressures agreed reasonably well with those obtained from a USBR study by Frizell (2007) for rounded block edge geometries. Equations 4-13 to 4-15 were fit to C_p data using coefficients C_1 , C_2 , and C_3 to account for affects due to ψ , T_u , and h (Figure 4-51). Accordingly, the data presented herein may be applied to a variety of flow conditions.

7.2 Reliability-based, block theory framework for block erodibility

A reliability-based, block theory framework was developed for evaluation of 3D block erodibility given parameter uncertainty associated with the inherent variability within the rock scour process. Block theory provides a rigorous analytical methodology to identify removable blocks, determine potential failure modes, and assess 3D block stability. Application to erodibility analysis occurs through modification of the active resultant force vector (\mathbf{r}) to include hydrodynamic loads (Equation 5-16). Average dynamic pressure coefficients for loads on block faces can be determined from Equations 4-13 to 4-15 and Figure 4-55 based on hydraulic model testing of 2D channel flow conditions. Block stability is evaluated in a pseudo-static manner using block theory limit equilibrium and kinematic constraint equations.

Theoretical predictions for block erodibility threshold compared reasonably well with those obtained from hydraulic model testing. Improved prediction was observed for blocks exhibiting block response 2 when a mobilized joint friction angle was used (Figure 5-12 and Figure 5-13). This was thought to be a result of increased kinematic resistance associated with the block mold geometry/orientation causing more erratic block displacements leading up to removal. For the blocks tested in the model study, this response appears to occur when \mathbf{r} must be rotated beyond approximately $\theta_r = 60$ deg. to reach the block yield condition (Figure 5-11). This condition may be specific to the model blocks and should therefore be investigated for other geometries. Pseudo-static assessment of block erodibility threshold also provided adequate results for blocks showing dynamic impulse displacements (block response 3) suggesting the block theory framework can be applicable to higher turbulence flows. In cases of extreme turbulence (e.g., directly beneath a turbulent jet in a plunge pool), this should be investigated further.

Parameter uncertainty associated with natural variability within the rock scour process was addressed through development of a general system reliability approach for evaluation of 3D rock block stability. This formulation was cast within the block theory framework developed for pure translational block failure modes. A minimum cut-set formulation was implemented, where the block is treated as a series system comprised of individual cut-sets corresponding to each block failure mode (Figure 6-4). Each cut-set is a parallel sub-system comprised of limit state functions corresponding to the block limit equilibrium and kinematic constraint equations (Table 6-1). In this regard, other block failure modes can be readily be considered by inclusion of additional cut-sets in the block system (Figure 6-2). The block failure probability is determined through Monte Carlo simulation while parameter importance (i.e., the relative influence of

variables on the system) is determined using the first order reliability method (FORM). The use of remote sensing technologies, such as LiDAR and photogrammetry, allow for rapid collection of high resolution topographic data which can be used to develop statistical distributions for rock mass parameters such as joint orientation and dilation angle (Figure 3-28 to Figure 3-31).

Applicability of the reliability-based, block theory methodology was demonstrated in the example analyses presented in Chapters 5 and 6. From a design standpoint, the benefit of the proposed methodology is that 3D site specific geologic structure information can be incorporated into evaluation of rock mass erodibility. Variability in site parameters can be addressed in a probabilistic manner to classify locations most susceptible to erosion as well as identify the most influential variables affecting rock block stability. This can lead to more efficient scour remediation designs as well as more focused field and laboratory efforts to investigate parameters with the most impact on the system. Furthermore, reliability data can be useful for designers and infrastructure owners in decision making and management of risk at a specific site.

7.3 Recommendations for future study

The research study presented herein focused on erodibility of tetrahedral block shapes subject to pure translational movements. Future research could be extended to investigate other block configurations (e.g., blocks with more than four sides or multiple free faces) and other flow scenarios (e.g., overtopping jets, plunge pools, hydraulic jumps, or knickpoints). This could translate to exploring behavior of multiple block systems and hydrodynamic pressures in near-surface joint networks from hydraulic loading, particularly the influence of rock joint structure on the progressive failure of large, multi-block systems and how it relates to the formation of rock gorges by erosion. Furthermore, numerical modeling of the hydraulic model experiments could be performed to compare calculated versus actual block erodibility thresholds as well as hydrodynamic pressures on block faces. A calibrated numerical model could readily be used to evaluate a greater variety of flow conditions and block geometries.

References

- Achterberg, D., Gotzmer, J.W., Spath, R., Tseng, M., Woodward, D.E., Miller, N. and Shipman, S.A. (1998). Federal guidelines for dam safety: selecting and accommodating inflow design floods for dams. Federal Emergency Management Agency (FEMA).
- AgiSoft (2015). PhotoScan photogrammetry software Version 1.1.6. <http://www.agisoft.com>.
- Annandale, G.W. (1995). Erodibility. *Journal of Hydraulic Research*, 33(4): 471-494.
- Annandale, G.W. (2006). *Scour technology: mechanics and engineering practice*, New York, McGraw-Hill.
- Asadollahi, P. (2009). *Stability analysis of a single three dimensional rock block: effect of dilatancy and high-velocity water jet impact*. Ph.D. Dissertation. University of Texas - Austin.
- Atkinson, B.K. (1987). *Fracture mechanics of rock*, London, Academic Press Inc.
- Barton, N. (1988). Rock mass classification and tunnel reinforcement selection using the Q-system *Rock Classification Systems for Engineering Purposes ASTM STP 984*. L. Kirkaldie (Ed.), Philadelphia, American Society for Testing and Materials, 59-88.
- Barton, N., Lien, R. and Lunde, J. (1974). Engineering classification of rock masses for the design of tunnel support. *Rock Mechanics*, 6(4): 189-236.
- Bollaert, E.F.R. (2002). *Transient water pressures in joints and formation of rock scour due to high-velocity jet impact*, *Communication No. 13*. Ph.D. Dissertation. Laboratory of Hydraulic Constructions. Ecole Polytechnique Federale de Lausanne, Switzerland.
- Bollaert, E.F.R. (2010). Numerical modeling of scour at bridge foundations on rock. *Proc. of the 5th Int. Conf. on Scour and Erosion*, San Francisco, CA, 767-776.
- Bollaert, E.F.R. and Schleiss, A.J. (2005). Physically based model for evaluation of rock scour due to high-velocity jet impact. *Journal of Hydraulic Engineering*, 131(3): 153-165.
- Carling, P.A., Hoffmann, M., Blatter, A.A. and Dittrich, A. (2002). Drag of emergent and submerged rectangular obstacles in turbulent flow above bedrock surface. *Rock scour due to falling high-velocity jets*. E. F. R. Bollaert & A. J. Schleiss (Ed.), Lisse, Swets and Zeitlinger, 83-94.
- Castillo, L.G., Puertas, J. and Dolz, J. (2007). Discussion: Scour of rock due to the impact of plunging high velocity jets Part I: A state-of-the-art review. *Journal of Hydraulic Research*, 45(6): 853-858.

- Chatanantavet, P. and Parker, G. (2009). Physically based modeling of bedrock incision by abrasion, plucking, and macroabrasion. *Journal of Geophysical Research: Earth Surface*, 114(F4): F04018.
- Chatanantavet, P. and Parker, G. (2011). Quantitative testing of model of bedrock channel incision by plucking and macroabrasion. *Journal of Hydraulic Engineering*, 137(11): 1311-1317.
- Coleman, S.E., Melville, B.W. and Gore, L. (2003). Fluvial entrainment of protruding fractured rock. *Journal of Hydraulic Engineering*, 129(11): 872-884.
- Cundall, P.A. (1971). A computer model for simulating progressive large scale movements in blocky rock systems. *Proc. of the Int. Symposium on Rock Fracture (ISRM)*, Nancy, France, Paper II-8.
- Dasgupta, B., Basu, D., Das, K. and Green, R. (2011). Development of computational methodology to assess erosion damage in dam spillways. *Proc. of the 31st USSD Annual Meeting and Conf.*, San Diego, CA, April 11-15.
- Der Kiureghian, A. (2005). First-and second-order reliability methods. *Engineering design reliability handbook*. Nikolaidis E, Ghiocel D M & S. S (Ed.), Boca Raton, FL, CRC Press, Chap. 14.
- Ditlevsen, O. (1979). Narrow reliability bounds for structural systems. *Journal of Structural Mechanics*, 7(4): 453-472.
- Duarte, R.X.M. (2014). *Influence of air entrainment on rock scour development and block stability in plunge pools*, Communication No. 59. Ph.D. Dissertation. Laboratory of Hydraulic Constructions. Ecole Polytechnique Federale de Lausanne, Switzerland.
- Dubinski, I.M. (2009). *Physical modeling of jointed bedrock erosion by block quarrying*. Ph.D. Dissertation. Colorado State University, USA.
- Dubinski, I.M. and Wohl, E. (2013). Relationships between block quarrying, bed shear stress, and stream power: A physical model of block quarrying of a jointed bedrock channel. *Geomorphology*, 180–181(0): 66-81.
- Emmerling, R. (1973). The instantaneous structure of the wall pressure under a turbulent boundary layer flow, *Report No. 9*. Max-Planck-Inst. f. Strömungsforschung.
- Ervine, D.A. and Falvey, H.T. (1987). Behaviour of turbulent water jets in the atmosphere and in plunge pools. *ICE Proceedings*, 83(1): 295-314.
- Ervine, D.A., Falvey, H.T. and Withers, W. (1997). Pressure fluctuations on plunge pool floors. *Journal of Hydraulic Research*, 35(2): 257-279.

- Federspiel, M.P.E.A., Bollaert, E.F.R. and Schleiss, A.J. (2009). Response of an intelligent block to symmetrical core jet impact. *Proc. of the 33rd IAHR Congress*, Vancouver, British Columbia, 3573-3580.
- Federspiel, M.P.E.A., Bollaert, E.F.R. and Schleiss, A.J. (2011). Dynamic response of a rock block in a plunge pool due to asymmetrical impact of a high-velocity jet. *Proc. of the 34th IAHR World Congress*, Brisbane, Australia, 2404-2411.
- Fiorotto, V. and Rinaldo, A. (1992). Fluctuating uplift and lining design in spillway stilling basins. *Journal of Hydraulic Engineering*, 118(4): 578-596.
- Fiorotto, V. and Salandin, P. (2000). Design of anchored slabs in spillway stilling basins. *Journal of Hydraulic Engineering*, 126(7): 502-512.
- Fisher, R. (1953). Dispersion on a Sphere. *Proc. Royal Society London*, A217(1130): 295-305.
- Frizell, W. (2007). Uplift and crack flow resulting from high velocity discharges over open offset joints - laboratory studies, *Report 12-2007*. U.S. Dept. of the Interior - Bureau of Reclamation.
- GEI Consultants Inc. (2003). Supporting Technical Information for Lake Spaulding Dams No. 1, No. 2 and No. 3 - FERC Project 2310. Prepared for Pacific Gas & Electric
- GEI Consultants Inc. and Pacific Gas & Electric (1998). Mitigation of Erosion at Lake Spaulding Spillway, Placer County - FERC Project No. 2310.
- George, M.F. and Annandale, G.W. (2006). Dam failure by rock scour: evaluation & prevention (a case study). *Proc. of the 41st US Symposium on Rock Mechanics*, Golden, CO, June 17-21.
- George, M.F., Canali, G. and Annandale, G.W. (2010). Private consulting report prepared for Freeport McMoRan Copper & Gold. Golder Associates Inc.
- Goodman, R.E. (1976). *Methods of geological engineering in discontinuous rocks*, St. Paul, MN, West Publishing Company.
- Goodman, R.E. (1995). Block theory and its application. *Géotechnique*, 45(3): 383-423.
- Goodman, R.E. and Bray, J.W. (1977). Toppling of rock slopes. *Proc. of Rock Engineering for Foundations & Slopes*, Boulder, CO, August 15-18, 1976, 2: 201-234.
- Goodman, R.E. and Hatzor, Y. (1991). Kendrick Project, Wyoming - Safety of dam deficiencies due to overtopping: results of preliminary analysis of abutments stability based on block theory and the critical key block concept. Submitted to USBR Missouri Basin Region.
- Goodman, R.E. and Powell, C. (2003). Investigations of blocks in foundations and abutments of concrete dams. *Journal of Geotechnical and Geoenvironmental Engineering*, 129(2): 105-116.

- Goodman, R.E. and Shi, G. (1985). *Block theory and its application to rock engineering*, Englewood Cliffs, NJ, Prentice Hall.
- Goring, D. and Nikora, V. (2002). Despiking acoustic doppler velocimeter data. *Journal of Hydraulic Engineering*, 128(1): 117-126.
- Grohmann, C.H. and Campanha, G.A.C. (2010). OpenStereo: open source, cross-platform software for structural geology analysis. *Proc. of the American Geophysical Union Fall Meeting*, San Francisco, CA, December 13-17.
- Hancock, G.S., Anderson, R.S. and Whipple, K.X. (1998). Beyond power: Bedrock river incision process and form. *Rivers over rock: fluvial processes in bedrock channels - Geophysical Monograph 107*. K. J. Tinkler & E. Wohl (Ed.), Washington, D.C., American Geophysical Union, 35-65.
- Hatzor, Y. (1992). *Validation of block theory using field case histories*. Ph.D. Dissertation. University of California - Berkeley.
- Haukaas, T. and Der Kiureghian, A. (1999). FERUM users guide. Dept. of Civil & Environmental Engineering, University of California - Berkeley, www.ce.berkeley.edu/projects/ferum/.
- Henderson, F.M. (1966). *Open channel flow*, New York, The Macmillan Company.
- Hinze, J.D. (1975). *Turbulence*. 2nd Ed., New York, McGraw-Hill.
- Hoffmans, G. (2012). *The influence of turbulence on soil erosion*, Delft, Eburon Academic Publishers.
- Howard, A.D., Dietrich, W.E. and Seidl, M.A. (1994). A detachment-limited model of drainage basin evolution. *Water Resources Research*, 30(7): 2261-2285.
- Hunter, D. (1976). An upper bound for the probability of a union. *Journal of Applied Probability*, 13(3): 597-603.
- Jimenez-Rodriguez, R. and Sitar, N. (2005). Rock wedge stability analysis using system reliability methods. *Proc. of the Int. Conf. Landslide Risk Management*. O. Hungr & R. Couture (Ed.), Vancouver, British Columbia.
- Jimenez-Rodriguez, R., Sitar, N. and Chacón, J. (2006). System reliability approach to rock slope stability. *International Journal of Rock Mechanics and Mining Sciences*, 43(6): 847-859.
- Kader, B.A. and Yaglom, A.M. (1991). Spectra and correlation functions of surface layer atmospheric turbulence in unstable thermal stratification. *Turbulence and coherent structures*. O. Metais & M. Lesieur (Ed.), Dordrecht, Netherlands, Kluwer Academy, 387-412.

- Katul, G.G., Chu, C.R., Parlange, M.B., Albertson, J.D. and Ortenburger, T.A. (1995). Low wavenumber spectral characteristics of velocity and temperature in the atmospheric boundary layer. *Journal of Geophysical Research*, 100: 14,243-14,255.
- Kieffer, D.S. (1998). *Rock slumping: A compound failure mode of jointed hard rock slopes*. Ph.D. Dissertation. University of California - Berkeley
- Kieffer, D.S. and Goodman, R.E. (2012). Assessing scour potential of unlined rock spillways with the Block Scour Spectrum / Beurteilung der Kolkbildung in nicht ausgekleideten Hochwasserentlastungen in Fels mittels des Block Scour Spectrums. *Geomechanics and Tunnelling*, 5(5): 527-536.
- Kirsten, H.A.D. (1982). A classification system for excavation in natural materials. *The Engineer in South Africa*, July: 292-308.
- Kirsten, H.A.D. (1988). Case histories of groundmass characterization for excavatability. *Rock Classification Systems for Engineering Purposes ASTM STP 984*. L. Kirkaldie (Ed.), Philadelphia, American Society for Testing and Materials, 189-236.
- Kolmogorov, A.N. (1941). Dissipation of energy in the locally isotropic turbulence English translation. *Proc. Royal Society London*, A(434): 15-17.
- Kounias, E.G. (1968). Bounds for the probability of a union, with applications. *The Annals of Mathematical Statistics*, 39(6): 2154-2158.
- Lague, D. (2014). The stream power river incision model: evidence, theory and beyond. *Earth Surface Processes and Landforms*, 39(1): 38-61.
- Lamb, M.P. and Dietrich, W.E. (2009). The persistence of waterfalls in fractured rock. *Geological Society of America Bulletin*, 121(7-8): 1123-1134.
- Lamb, M.P., Finnegan, N.J., Scheingross, J.S. and Sklar, L.S. (2015). New insights into the mechanics of fluvial bedrock erosion through flume experiments and theory. *Geomorphology*, In press.
- Leica Geosystems (2015). Cyclone 3D point cloud processing software. http://hds.leica-geosystems.com/en/Leica-Cyclone_6515.htm.
- Li, A. and Liu, P. (2010). Mechanism of rock-bed scour due to impinging jet. *Journal of Hydraulic Research*, 48(1): 14-22.
- Li, D., Zhou, C., Lu, W. and Jiang, Q. (2009). A system reliability approach for evaluating stability of rock wedges with correlated failure modes. *Computers and Geotechnics*, 36(8): 1298-1307.

- Lin, J.S. and Wibowo, J.L. (2008). Stability analysis of rock surface spillways using a partition of unity method. *Proc. of the 42nd US Rock Mechanics Symposium*, San Francisco, CA, June 29 - July 2.
- Liu, P., Dong, J. and Yu, C. (1998). Fluctuating uplift on rock blocks at the bottom of a scour pool by overfall jets. *Science in China Series E: Technological Sciences*, 41(2): 130-139.
- Liu, P.L. and Der Kiureghian, A. (1986). Multivariate distribution models with prescribed marginals and covariances. *Probabilistic Engineering Mechanics*, 1(2): 105-112.
- Londe, P., Vigier, G. and Vormeringer, R. (1969). Stability of rock slopes, a three-dimensional study. *Journal of Soil Mechanics & Foundations Div*, 95(1): 235-262.
- Londe, P., Vigier, G. and Vormeringer, R. (1970). Stability of rock slopes, graphical methods. *Journal of Soil Mechanics & Foundations Div*, 96(4): 1411-1434.
- Low, B.K. (1997). Reliability analysis of rock wedges. *Journal of Geotechnical and Geoenvironmental Engineering*, 123(6): 498-505.
- Low, B.K. (2008). Efficient probabilistic algorithm illustrated for a rock slope. *Rock Mechanics and Rock Engineering*, 41(5): 715-734.
- Mansfield, C.H. and Kemeny, J. (2009). The use of terrestrial LiDAR in determining direction joint dilation angle values. *Proc. of the 43rd US Symposium on Rock Mechanics*, Asheville, NC, June 28 - July 1.
- Manso, P. (2006). *The influence of pool geometry and induced flow patterns in rock scour by high-velocity plunging jets*, Communication No. 25. Laboratory of Hydraulic Constructions. Ecole Polytechnique Federale de Lausanne, Switzerland.
- Maptek (2015). I-Site Studio point cloud processing software. http://www.maptek.com/products/i-site/i-site_studio.html.
- Martins, R. (1973). Contribution to the knowledge on the scour action of free jets on rocky river beds. *Proc. of the 11th Int. Congress of Large Dams*, Madrid, Spain, 799-814.
- Mattson, J. (1996). Memorandum: Spaulding 25k cfs Spill. Pacific Gas & Electric.
- Mauldon, M. (1990). Probability aspects of the removability and rotatability of tetrahedral blocks. *International Journal of Rock Mechanics and Mining Sciences & Geomechanics Abstracts*, 27(4): 303-307.
- Mauldon, M. (1992). *Rotational failure modes in jointed rock: A generalization of block theory*. Ph.D. Dissertation. University of California - Berkeley.

- Mauldon, M. and Goodman, R.E. (1990). Rotational kinematics and equilibrium of blocks in a rock mass. *International Journal of Rock Mechanics and Mining Sciences & Geomechanics Abstracts*, 27(4): 291-301.
- Mauldon, M. and Goodman, R.E. (1996). Vector analysis of keyblock rotations. *Journal of Geotechnical Engineering*, 122(12): 976-987.
- Melo, J.F., Pinheiro, A.N. and Ramos, C.M. (2006). Forces on plunge pool slabs: Influence of joints location and width. *Journal of Hydraulic Engineering*, 132(1): 49-60.
- Melville, B.W., van Ballegooy, R. and van Ballegooy, S. (2006). Flow-Induced Failure of Cable-Tied Blocks. *Journal of Hydraulic Engineering*, 132(3): 324-327.
- Miller, J.R. (1991). The influence of bedrock geology on knickpoint development and channel-bed degradation along downcutting streams in south-central Indiana. *The Journal of Geology*, 99(4): 591-605.
- National Park Service. (2015). Grand Canyon DEIS aerial: Colorado River, Solomon Temple. Retrieved April 7, from www.flickr.com/photos/grand_canyon_nps/5477454812/in/album-72157626136162880.
- Page, W.D. (1997). Assessment of Erosion at Lake Spaulding Spillway, Placer County. Pacific Gas & Electric Geosciences Department.
- Page, W.D. (1998). Proposed Erosion Protection Measures Lake Spaulding Spillway, Placer County. Pacific Gas & Electric Hydro Engineering Department & Geosciences Department.
- Paris, P.C., Gomez, M.P. and Anderson, W.P. (1961). A rational analytic theory of fatigue. *The Trend in Engineering*, 13: 9-14.
- Peakall, J. and Warburton, J. (1996). Surface tension in small hydraulic river models - the significance of the Weber number. *Journal of Hydrology*, 35(2): 199-212.
- Pötsch, M. (2011). *The analysis of rotational and sliding modes of failure for slopes, foundations, and underground structures in blocky, hard rock*. Ph.D. Dissertation. Technische Universität Graz.
- Reinius, E. (1986). Rock erosion. *Water Power and Dam Construction*, (June): 43-48.
- Robinson, K. and Kadavy, K. (2001). Pressure forces in a fractured matrix. *Proc. of the ASAE Int. Annual Meeting*, Sacramento, CA.
- Schoklitsch, A. (1932). Kolkbildung unter ueberfallstrahlen. *Die Wasserwirtschaft*, 24: 341-343.
- Shi, G. (1988). *Discontinuous deformation analysis - A new numerical model for the statics and dynamics of block systems*. Ph.D. Dissertation. University of California - Berkeley.

- Shi, G. (2001). Three dimensional discontinuous deformation analyses. *Proc. of the 4th Int. Conf on Analysis of Discontinuous Deformation (ICADD-4)*. B. N (Ed.), Glasgow, Scotland, 1-21.
- Shields, A. (1936). Application of similarity principles and turbulence research to bed-load movement, *Hydrodynamics Laboratory Publication 167*. U.S. Dept of Agriculture Soil Conservation Service Cooperative Laboratory.
- Singh, A., Porte-Agel, F. and Fofoula-Georgiou, E. (2010). On the influence of gravel bed dynamics on velocity power spectra. *Water Resources Research*, 46(W04509).
- Sklar, L.S. and Dietrich, W.E. (2004). A mechanistic model for river incision into bedrock by saltating bed load. *Water Resources Research*, 40(6): W06301.
- Song, J. and Der Kiureghian, A. (2003). Bounds on system reliability by linear programming. *Journal of Engineering Mechanics*, 129(6): 627-636.
- Split Engineering (2015). Split FX rock mass characterization software Version 2.3. <http://www.spliteng.com/products/split-fx-software>.
- Stratford, C.E., Bollaert, E.F.R. and Lesleighter, E.J. (2013). Plunge pool rock scour analysis techniques - Wivenhoe dam spillway, Australia. *Proc. of HYDRO2013*, Innsbruck, Austria, 1567-1608.
- Tonon, F. (1998). Generalization of Mauldon's and Goodman's vector analysis of keyblock rotations. *Journal of Geotechnical and Geoenvironmental Engineering*, 124(10): 913-922.
- Tonon, F. (2007). Analysis of single rock blocks for general failure modes under conservative and non-conservative forces. *International Journal for Numerical and Analytical Methods in Geomechanics*, 31(14): 1567-1608.
- Trimble Navigation (2015). SketchUp 3D drafting software. <http://www.sketchup.com/>.
- Veronese, A. (1937). *Erosion of a bed downstream from an outlet*. Colorado A&M College, Fort Collins, CO.
- Wahl, T.L. (2000). Analyzing ADV data using WinADV. *Proc. of the Joint Conf. on Water Resources Engineering & Water Resources Planning & Management (ASCE)*, Minneapolis, MN, July 30-August 2, www.usbr.gov/wrrl/twahl/winadv.
- Wahl, T.L. (2003). Discussion of "Despiking acoustic doppler velocimeter data". *Journal of Hydraulic Engineering*, 129(6): 484-487.
- Warburton, P.M. (1981). Vector stability analysis of an arbitrary polyhedral rock block with any number of free faces. *International Journal of Rock Mechanics and Mining Sciences & Geomechanics Abstracts*, 18(5): 415-427.

Whipple, K.X., Hancock, G.S. and Anderson, R.S. (2000). River incision into bedrock: Mechanics and relative efficacy of plucking, abrasion, and cavitation. *Geological Society of America Bulletin*, 112(3): 490-503.

Wittke, W. (1965). Methods to analyze the stability of rock slopes with and without additional loading. *Felsmechanik und Ingenieurgeologie, Supp*, 11(30): 52-79.

Yong Cang, Z. (1993). High-order reliability bounds for series systems and application to structural systems. *Computers & Structures*, 46(2): 381-386.

Yuditskii, G.A. (1967). Actual pressure on the channel bottom below ski-jump spillways (in Russian). *Izvestiya Vsesoyuznogo Nauchno - Issledovatel - Skogo Instuta Gidrotekhiki*, 67: 231-240.

Zhang, Y. and Der Kiureghian, A. (1995). Two improved algorithms for reliability analysis. *Reliability and Optimization of Structural Systems*. R. Rackwitz, G. Augusti & A. Borri (Ed.), Springer US, Chap. 32: 297-304.

Appendix A – Statistical distributions

Beta distribution

$$\beta(x) = \frac{(x - p_3)^{p_1 - 1} \cdot (p_4 - x)^{p_2 - 1}}{B(p_1, p_2) \cdot (p_4 - p_3)^{p_1 + p_2 - 1}}$$

where:

$\beta(x)$ = Beta probability density distribution for variable x

p_1 = distribution parameter, $0 < p_1$

p_2 = distribution parameter, $0 < p_2$

p_3 = distribution parameter, lower bound, $x \leq p_3$

p_4 = distribution parameter, upper bound, $x \leq p_4$

$B(i, j)$ = Beta function = $\Gamma(i) \cdot \Gamma(j) / \Gamma(i + j)$

$\Gamma(k)$ = Gamma function = $\int_0^\infty e^{-u} \cdot u^{k-1} du$

Normal distribution

$$\varphi(x) = \frac{1}{\sqrt{2\pi}\sigma} \exp\left[-\frac{1}{2}\left(\frac{x - \mu}{\sigma}\right)^2\right]$$

where:

$\varphi(x)$ = Normal probability density distribution for variable x

μ = mean value of $x = p_1$ (distribution parameter)

σ = standard deviation of $x = p_2$ (distribution parameter)

Log normal distribution

$$\varphi_{\ln}(x) = \frac{1}{\sqrt{2\pi}\zeta x} \exp\left[-\frac{1}{2}\left(\frac{\ln(x) - \lambda}{\zeta}\right)^2\right]$$

where:

$\varphi_{\ln}(x)$ = Log normal probability density distribution for variable x

$\lambda = p_1$ (distribution parameter) = mean in log normal space > 0

$\zeta = p_2$ (distribution parameter) = std. dev. in log normal space > 0

μ = mean value of $x = \exp\left(\lambda + \frac{\zeta^2}{2}\right)$

σ = standard deviation of $x = \exp\left(\lambda + \frac{\zeta^2}{2}\right) \cdot \left[\exp(\zeta^2) - 1\right]^{\frac{1}{2}}$

Appendix B – Hydraulic model experiment: Model development

Pressure sensor coefficients

Linear equation relating measured voltage (mV) to pressure head (cm):

$$V = m \cdot P + b$$

where V is the measured voltage from datalogger (mV), P is the pressure head (cm), m is the slope (mV/cm) and b is the initial condition corresponding to atmospheric pressure conditions. Values for m were calibrated three times during the experiments and are presented here. For data analysis purposes, an average value of m was used. Due to temperature changes in the block mold/ramp, b was not always zero at atmospheric conditions and accordingly values for b were determined prior to every run for each sensor. These values were recorded in the initial data files associated with each block run and not presented here.

Date	Time	<i>m</i> (slope) (mV/cm)											
		Sensor 1	Sensor 2	Sensor 3	Sensor 4	Sensor 5	Sensor 6	Sensor 7	Sensor 8	Sensor 9	Sensor 10	Sensor 11	Sensor 12
6/4/2014	10 am to 1 pm	9.7800	9.7938	9.7793	9.4886	9.7847	9.7961	9.7823	9.7804	9.7806	9.8318	9.8879	9.8676
12/23/2014	1 pm to 3 pm	9.7885	9.8367	9.7387	9.6911	9.8297	9.8651	9.8431	9.7126	9.7435	9.9218	9.9083	9.8471
12/24/2014	11:30 am to 1:30 pm	9.8953	9.9341	9.8846	9.8376	9.9036	9.8905	9.9089	9.7856	9.8579	9.8652	9.9497	9.9221
Average		9.8213	9.8549	9.8008	9.6724	9.8393	9.8506	9.8448	9.7595	9.7940	9.8729	9.9153	9.8789

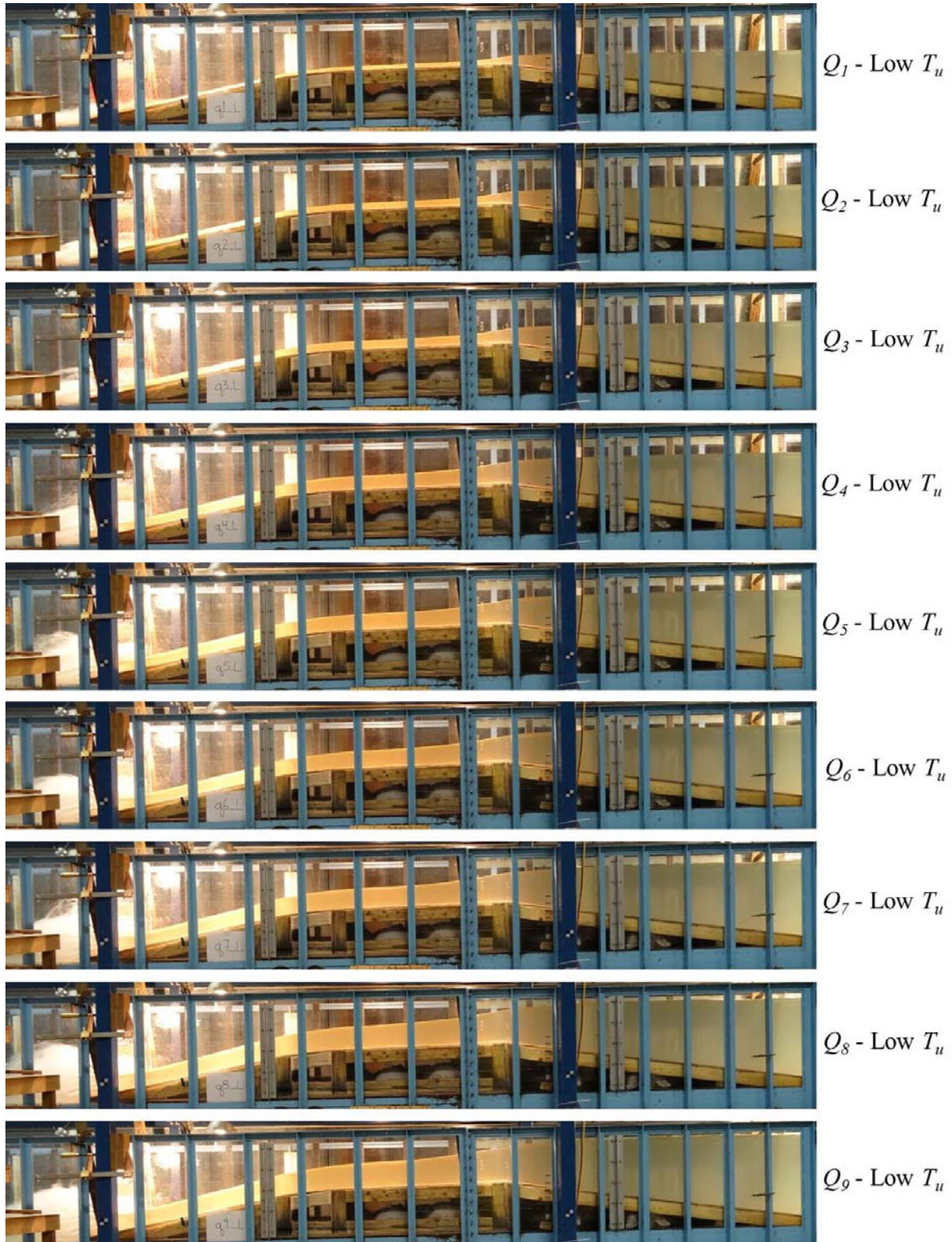
Appendix C – Hydraulic model experiment: Flow characterization

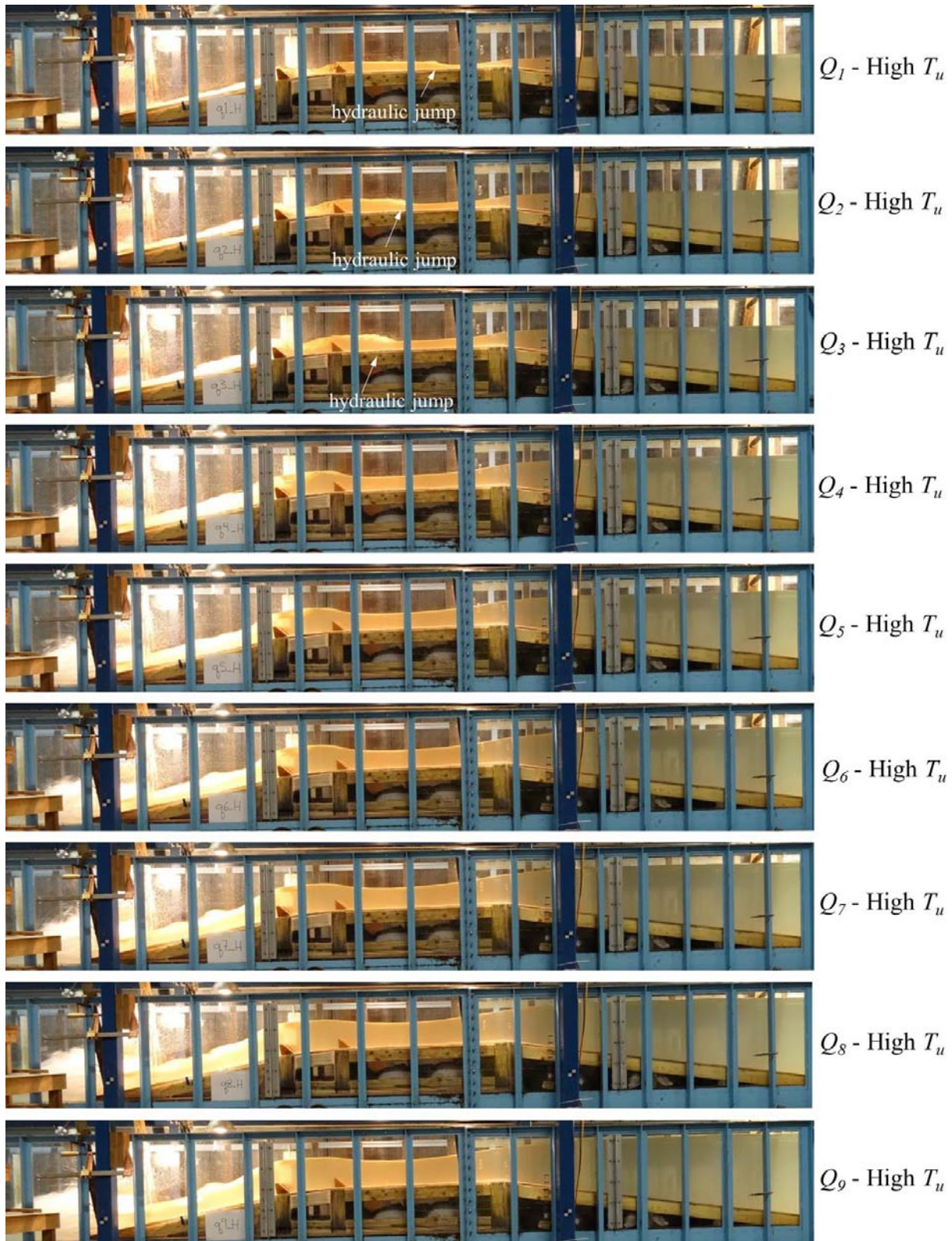
Correlation coefficients for pitot & ADV measurements

Instrument	Correlation	Correlation																	
		Low T_u									High T_u								
		Q_1	Q_2	Q_3	Q_4	Q_5	Q_6	Q_7	Q_8	Q_9	Q_1	Q_2	Q_3	Q_4	Q_5	Q_6	Q_7	Q_8	Q_9
1/8" Pitot	Location 2 / Location 0	0.962	0.955	0.958	0.951	0.949	0.951	0.950	0.952	0.957	0.906	0.969	0.977	0.921	0.937	0.941	0.936	0.928	0.926
Pitot/ADV	Location 2 Pitot / Location 2 ADV	0.697	0.697	0.696	0.691	0.693	0.691	0.681	0.677	0.676	0.750	0.747	0.791	0.753	0.754	0.742	0.739	0.738	0.738
1/8" Pitot	Location 4 / Location 0	0.934	0.929	0.936	0.949	0.950	0.941	0.946	0.958	0.956	0.961	1.008	0.980	0.921	0.930	0.912	0.896	0.910	0.900
Pitot/ADV	Location 4 Pitot / Location 4 ADV	0.662	0.660	0.663	0.672	0.663	0.659	0.660	0.659	0.657	0.760	0.760	0.746	0.763	0.781	0.769	0.756	0.754	0.748
1/8" Pitot	Location 5 / Location 0	0.966	0.979	0.971	0.963	0.951	0.957	0.954	0.964	0.969	1.020	1.011	0.990	0.927	0.940	0.929	0.939	0.933	0.925
Pitot/ADV	Location 5 Pitot / Location 5 ADV	0.676	0.678	0.680	0.683	0.676	0.678	0.671	0.669	0.669	0.772	0.772	0.772	0.730	0.732	0.731	0.727	0.730	0.726
1/8" Pitot	Location 8 / Location 0	0.942	0.959	0.947	0.962	0.955	0.961	0.963	0.966	0.963	1.003	1.048	0.989	0.928	0.947	0.946	0.935	0.929	0.928
Pitot/ADV	Location 8 Pitot / Location 8 ADV	0.657	0.649	0.656	0.663	0.661	0.657	0.659	0.658	0.654	0.745	0.744	0.745	0.711	0.721	0.714	0.705	0.702	0.705

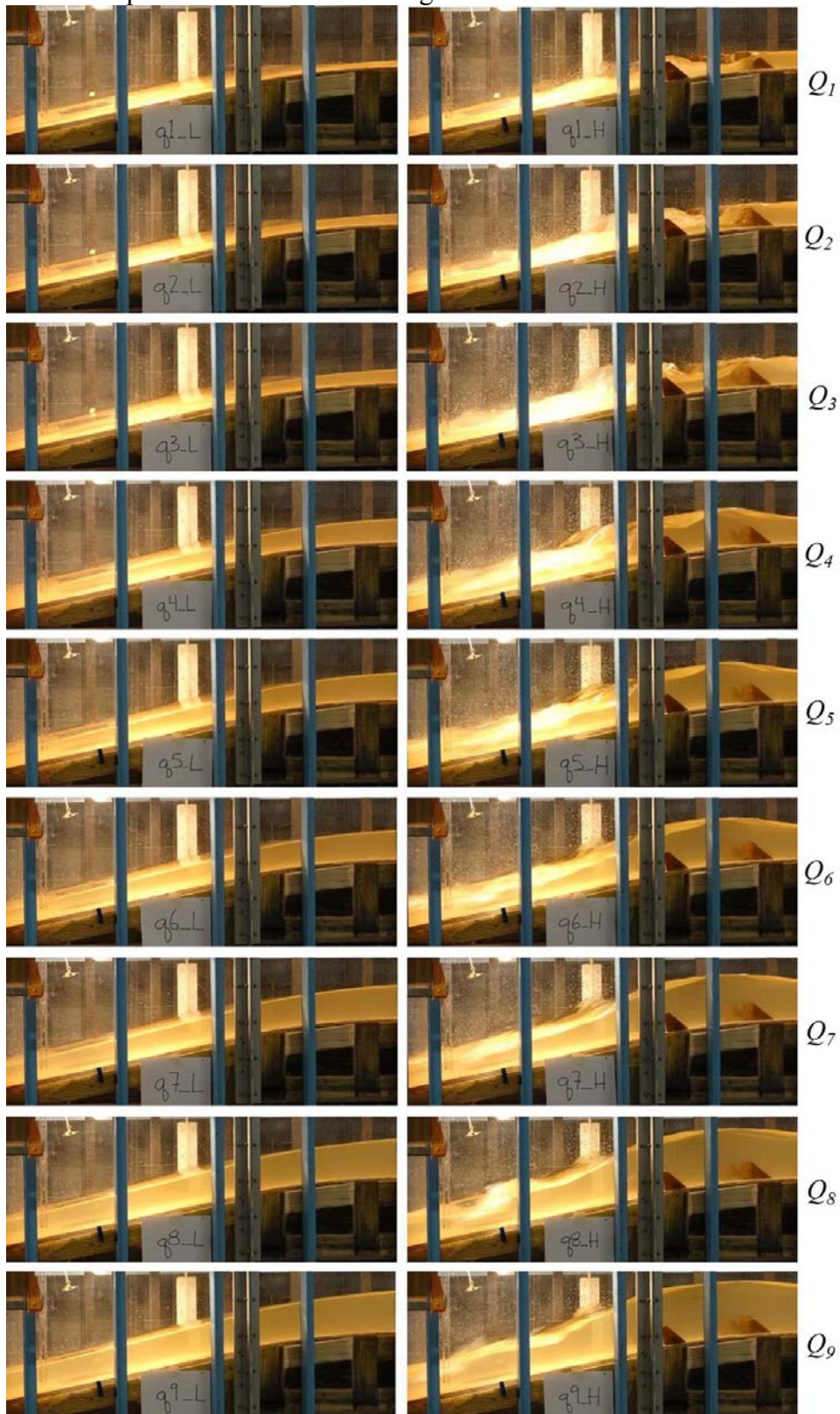
Calculated

Flow profiles





Close-up view near block mold region



Flow velocity

Height (cm) Method Location			Velocity MEAN, u_x (cm/s) - Model																	
			Low T_u									High T_u								
			Q_1	Q_2	Q_3	Q_4	Q_5	Q_6	Q_7	Q_8	Q_9	Q_1	Q_2	Q_3	Q_4	Q_5	Q_6	Q_7	Q_8	Q_9
0.16	1/8" Pitot	0	166.1	173.1	177.7	187.7	189.9	193.5	197.7	200.6	202.9	159.9	160.4	172.0	196.6	201.0	204.6	209.4	210.8	213.5
0.16	1/8" Pitot	4	155.1	160.7	166.3	178.1	180.3	182.0	186.9	192.1	194.0	153.7	161.6	168.6	181.0	186.8	186.5	187.7	191.8	192.2
1.10	ADV	4	234.4	243.4	250.9	265.0						202.3	212.7	226.0	237.3					
2.60	ADV	4					272.1	276.2	283.4	291.5	295.3					239.3	242.5	248.1	254.3	256.9
31.70	ADV	C	7.6	15.2	21.2	35.7	41.4	45.0	51.8	60.3	64.1	Same as Low T_u								
1.10	ADV	B		198.4	209.6	230.9	237.8	242.5	251.3	260.6	264.4		184.7		198.6	203.9	205.0	205.7	203.8	202.9
1.10	ADV	A				240.4	247.7	252.6	260.6	269.5	273.4				223.3	226.3	227.8	230.2	229.9	229.3
0.16	1/8" Pitot	0	160.4	168.7	173.5	184.3	190.5	192.3	196.5	200.1	202.0	157.4	156.3	168.1	199.5	199.9	200.9	203.8	206.7	205.7
0.16	1/8" Pitot	0					191.6	194.4	196.1	201.6	202.1				198.1	198.6	198.8	201.2	204.3	208.1
0.16	1/8" Pitot	0							196.4	201.2	203.5						199.1	201.6	205.0	205.9
		Avg	160.4	168.7	173.5	184.3	191.1	193.3	196.4	201.0	202.5	157.4	156.3	168.1	198.8	199.3	199.6	202.2	205.4	206.6
0.16	1/8" Pitot	2	154.3	161.2	166.2	175.2	181.2	184.2	187.5	190.7	194.2	142.6	151.4	164.1	182.7	187.9	190.0	189.5	192.1	192.1
0.16	1/8" Pitot	2					181.3	183.6	185.5	191.7	193.3				183.4	185.5	187.8	189.8	190.1	191.6
0.16	1/8" Pitot	2							186.8	191.4	193.7						185.5	188.7	189.8	190.2
		Avg	154.3	161.2	166.2	175.2	181.2	183.9	186.6	191.3	193.8	142.6	151.4	164.1	183.1	186.7	187.8	189.3	190.7	191.3
1.10	ADV	2	221.4	231.2	239.0	253.5	260.3	265.1	272.8	281.5	285.7	190.0	202.6	207.6	238.1	243.5	245.5	248.5	250.7	251.7
2.60	ADV	2					262.8	267.4	274.8	283.6	287.8				247.9	251.5	252.5	254.5	256.0	256.4
5.60	ADV	2							275.0	282.3	286.2						261.1	265.7	268.2	269.5
		Avg	221.4	231.2	239.0	253.5	261.6	266.2	274.2	282.4	286.6	190.0	202.6	207.6	243.0	247.5	253.0	256.2	258.3	259.2
0.16	1/8" Pitot	0	163.3	168.8	175.7	187.3	191.0	193.6	198.0	202.7	203.1	157.8	160.4	172.7	187.1	198.0	204.1	204.6	210.9	214.2
0.16	1/8" Pitot	0					194.6	196.9	199.6	202.1	205.2					199.5	203.7	206.3	211.7	213.0
0.16	1/8" Pitot	0							200.9	203.6	204.6							209.2	211.8	211.4
		Avg	163.3	168.8	175.7	187.3	192.8	195.3	199.5	202.8	204.3	157.8	160.4	172.7	187.1	198.8	203.9	206.7	211.5	212.9
0.16	1/8" Pitot	5	157.8	165.2	170.6	180.4	183.1	185.9	190.5	195.8	198.2	160.8	162.2	171.0	173.5	185.7	189.6	193.2	195.0	197.5
0.16	1/8" Pitot	5					183.7	187.7	189.0	195.2	197.9					187.8	189.2	193.1	198.8	196.8
0.16	1/8" Pitot	5							191.4	195.3	197.7							196.1	198.0	196.5
		Avg	157.8	165.2	170.6	180.4	183.4	186.8	190.3	195.4	197.9	160.8	162.2	171.0	173.5	186.8	189.4	194.1	197.2	196.9
1.10	ADV	5	233.5	243.6	250.9	264.1	269.8	274.1	281.4	291.0	294.8	208.3	210.2	221.5	237.7	251.8	255.9	259.7	262.6	263.6
2.60	ADV	5					272.9	277.1	284.1	292.5	296.6					258.6	262.3	265.4	268.3	268.8
5.60	ADV	5							285.1	292.2	296.0							276.2	279.7	281.1
		Avg	233.5	243.6	250.9	264.1	271.4	275.6	283.5	291.9	295.8	208.3	210.2	221.5	237.7	255.2	259.1	267.1	270.2	271.2
0.16	1/8" Pitot	0	168.7	174.1	181.7	188.1	192.3	193.8	200.2	202.5	205.9	156.6	158.9	174.6	195.0	200.0	202.0	209.1	214.2	215.0
0.16	1/8" Pitot	0					195.6	195.2	200.8	204.9	206.7				195.7	198.6	201.3	208.1	210.3	212.6
0.16	1/8" Pitot	0							200.7	207.2	207.7							208.8	212.1	215.6
		Avg	168.7	174.1	181.7	188.1	194.0	194.5	200.5	204.8	206.8	156.6	158.9	174.6	195.4	199.3	201.6	208.7	212.2	214.4
0.16	1/8" Pitot	8	159.0	167.0	172.1	181.0	184.9	185.3	192.5	196.4	198.0	157.0	166.6	172.7	181.2	190.3	192.9	197.8	197.3	198.8
0.16	1/8" Pitot	8					185.7	188.3	192.1	197.4	198.3				181.5	187.3	188.5	192.3	196.2	197.6
0.16	1/8" Pitot	8							194.5	199.8	200.8							195.1	198.1	200.8
		Avg	159.0	167.0	172.1	181.0	185.3	186.8	193.1	197.9	199.0	157.0	166.6	172.7	181.4	188.8	190.7	195.1	197.2	199.1
1.10	ADV	8	241.9	257.2	262.4	273.2	278.9	283.0	290.5	298.7	302.5	210.8	223.9	231.9	252.0	257.8	263.5	270.2	273.5	274.9
2.60	ADV	8					282.0	286.1	293.4	301.4	305.2				257.9	266.0	270.7	275.3	279.3	280.7
5.60	ADV	8							294.6	301.6	305.2							284.5	290.1	291.6
		Avg	241.9	257.2	262.4	273.2	280.4	284.5	292.8	300.6	304.3	210.8	223.9	231.9	254.9	261.9	267.1	276.7	281.0	282.4

	Calculated
	Low COR, Low SNR, Wide 95% Conf. Int.
	Low COR, Low SRN
	Low COR or Low SNR, Wide 95% Conf. Int.
	Low COR or Low SNR
	Wide 95% Conf. Int.

Appendix C – Hydraulic model experiment: Flow characterization

Height (cm)	Method	Location	Velocity MEAN, u_x (m/s) - Prototype																	
			Low T_u									High T_u								
			Q_1	Q_2	Q_3	Q_4	Q_5	Q_6	Q_7	Q_8	Q_9	Q_1	Q_2	Q_3	Q_4	Q_5	Q_6	Q_7	Q_8	Q_9
0.16	1/8" Pitot	0	5.25	5.47	5.62	5.94	6.00	6.12	6.25	6.34	6.42	5.06	5.07	5.44	6.22	6.36	6.47	6.62	6.67	6.75
0.16	1/8" Pitot	4	4.90	5.08	5.26	5.63	5.70	5.76	5.91	6.08	6.13	4.86	5.11	5.33	5.72	5.91	5.90	5.93	6.06	6.08
1.10	ADV	4	7.41	7.70	7.93	8.38						6.40	6.73	7.15	7.51					
2.60	ADV	4					8.60	8.74	8.96	9.22	9.34					7.57	7.67	7.85	8.04	8.13
31.70	ADV	C	0.24	0.48	0.67	1.13	1.31	1.42	1.64	1.91	2.03	Same as Low T_u								
1.10	ADV	B		6.27	6.63	7.30	7.52	7.67	7.95	8.24	8.36	5.84		6.28	6.45	6.48	6.51	6.44	6.42	
1.10	ADV	A			7.60	7.83	7.99	8.24	8.52	8.65		7.06		7.16	7.20	7.28	7.27	7.25		
0.16	1/8" Pitot	0	5.07	5.34	5.49	5.83	6.02	6.08	6.21	6.33	6.39	4.98	4.94	5.31	6.31	6.32	6.35	6.44	6.54	6.51
0.16	1/8" Pitot	0					6.06	6.15	6.20	6.37	6.39				6.27	6.28	6.29	6.36	6.46	6.58
0.16	1/8" Pitot	0							6.21	6.36	6.43						6.30	6.37	6.48	6.51
		Avg	5.07	5.34	5.49	5.83	6.04	6.11	6.21	6.35	6.40	4.98	4.94	5.31	6.29	6.30	6.31	6.39	6.49	6.53
0.16	1/8" Pitot	2	4.88	5.10	5.26	5.54	5.73	5.82	5.93	6.03	6.14	4.51	4.79	5.19	5.78	5.94	6.01	5.99	6.08	6.07
0.16	1/8" Pitot	2					5.73	5.81	5.87	6.06	6.11				5.80	5.87	5.94	6.00	6.01	6.06
0.16	1/8" Pitot	2							5.91	6.05	6.13						5.87	5.97	6.00	6.02
		Avg	4.88	5.10	5.26	5.54	5.73	5.82	5.90	6.05	6.13	4.51	4.79	5.19	5.79	5.90	5.94	5.99	6.03	6.05
1.10	ADV	2	7.00	7.31	7.56	8.02	8.23	8.38	8.63	8.90	9.04	6.01	6.41	6.56	7.53	7.70	7.76	7.86	7.93	7.96
2.60	ADV	2					8.31	8.45	8.69	8.97	9.10				7.84	7.95	7.98	8.05	8.10	8.11
5.60	ADV	2							8.69	8.93	9.05						8.26	8.40	8.48	8.52
		Avg	7.00	7.31	7.56	8.02	8.27	8.42	8.67	8.93	9.06	6.01	6.41	6.56	7.68	7.83	8.00	8.10	8.17	8.20
0.16	1/8" Pitot	0	5.16	5.34	5.56	5.92	6.04	6.12	6.26	6.41	6.42	4.99	5.07	5.46	5.92	6.26	6.45	6.47	6.67	6.77
0.16	1/8" Pitot	0					6.15	6.23	6.31	6.39	6.49				6.31	6.44	6.53	6.70	6.74	
0.16	1/8" Pitot	0							6.35	6.44	6.47							6.62	6.70	6.69
		Avg	5.16	5.34	5.56	5.92	6.10	6.17	6.31	6.41	6.46	4.99	5.07	5.46	5.92	6.29	6.45	6.54	6.69	6.73
0.16	1/8" Pitot	5	4.99	5.23	5.39	5.71	5.79	5.88	6.02	6.19	6.27	5.09	5.13	5.41	5.49	5.87	6.00	6.11	6.16	6.25
0.16	1/8" Pitot	5					5.81	5.94	5.98	6.17	6.26				5.94	5.98	6.11	6.29	6.22	
0.16	1/8" Pitot	5							6.05	6.18	6.25							6.20	6.26	6.21
		Avg	4.99	5.23	5.39	5.71	5.80	5.91	6.02	6.18	6.26	5.09	5.13	5.41	5.49	5.91	5.99	6.14	6.24	6.23
1.10	ADV	5	7.38	7.70	7.93	8.35	8.53	8.67	8.90	9.20	9.32	6.59	6.65	7.00	7.52	7.96	8.09	8.21	8.30	8.34
2.60	ADV	5					8.63	8.76	8.98	9.25	9.38				8.18	8.29	8.39	8.48	8.50	
5.60	ADV	5							9.02	9.24	9.36							8.73	8.84	8.89
		Avg	7.38	7.70	7.93	8.35	8.58	8.72	8.97	9.23	9.35	6.59	6.65	7.00	7.52	8.07	8.19	8.45	8.54	8.57
0.16	1/8" Pitot	0	5.34	5.50	5.75	5.95	6.08	6.13	6.33	6.40	6.51	4.95	5.03	5.52	6.17	6.32	6.39	6.61	6.77	6.80
0.16	1/8" Pitot	0					6.19	6.17	6.35	6.48	6.54				6.19	6.28	6.36	6.58	6.65	6.72
0.16	1/8" Pitot	0							6.35	6.55	6.57							6.60	6.71	6.82
		Avg	5.34	5.50	5.75	5.95	6.13	6.15	6.34	6.48	6.54	4.95	5.03	5.52	6.18	6.30	6.38	6.60	6.71	6.78
0.16	1/8" Pitot	8	5.03	5.28	5.44	5.73	5.85	5.86	6.09	6.21	6.26	4.97	5.27	5.46	5.73	6.02	6.10	6.26	6.24	6.29
0.16	1/8" Pitot	8					5.87	5.96	6.08	6.24	6.27				5.74	5.92	5.96	6.08	6.20	6.25
0.16	1/8" Pitot	8							6.15	6.32	6.35							6.17	6.26	6.35
		Avg	5.03	5.28	5.44	5.73	5.86	5.91	6.10	6.26	6.29	4.97	5.27	5.46	5.74	5.97	6.03	6.17	6.24	6.30
1.10	ADV	8	7.65	8.13	8.30	8.64	8.82	8.95	9.19	9.45	9.57	6.67	7.08	7.33	7.97	8.15	8.33	8.54	8.65	8.69
2.60	ADV	8					8.92	9.05	9.28	9.53	9.65				8.15	8.41	8.56	8.71	8.83	8.88
5.60	ADV	8							9.32	9.54	9.65							9.00	9.17	9.22
		Avg	7.65	8.13	8.30	8.64	8.87	9.00	9.26	9.50	9.62	6.67	7.08	7.33	8.06	8.28	8.45	8.75	8.89	8.93

Appendix C – Hydraulic model experiment: Flow characterization

			Velocity MEAN, u_y (cm/s) - Model																		
			Low T_u									High T_u									
Height (cm)	Method	Location	Q_1	Q_2	Q_3	Q_4	Q_5	Q_6	Q_7	Q_8	Q_9	Q_1	Q_2	Q_3	Q_4	Q_5	Q_6	Q_7	Q_8	Q_9	
1.10	ADV	4		-15.4	-13.8	-5.8							-27.1	-14.2	-3.6						
2.60	ADV	4					-15.3	-13.6	-12.1	-11.5	-11.4					-1.6	0.1	0.003	-1.0	-1.2	
31.70	ADV	C	0.03	-0.1	-0.03	0.1	-0.1	-0.2	-0.5	-0.3	-0.4	Same as Low T_u									
1.10	ADV	B		-16.8	-14.1	-8.0	-7.2	-7.2	-6.6	-6.4	-7.0		-13.6	-13.6	-13.2	-13.7	-13.9	-13.9	-14.0		
1.10	ADV	A				-9.5	-8.2	-7.9	-7.2	-7.2	-7.4		-7.5	-11.7	-11.5	-11.0	-11.1	-11.1	-11.4	-11.4	
1.10	ADV	2			-11.4	-5.3	-4.2	-3.7	-2.7	-2.5	-2.4		-7.5	-13.7	-6.0	-8.2	-8.7	-8.3	-7.8	-7.9	
2.60	ADV	2				-7.6	-6.5	-5.2	-4.3	-4.1				-7.4	-9.9	-10.3	-9.2	-8.5	-8.3		
5.60	ADV	2							-11.3	-7.6	-6.8					-12.7	-10.7	-8.6	-8.1		
		Avg			-11.4	-5.3	-5.9	-5.1	-6.4	-4.8	-4.4		-7.5	-13.7	-6.7	-9.0	-10.6	-9.4	-8.3	-8.1	
1.10	ADV	5			-14.7	-8.0	-6.4	-6.0	-5.3	-6.2	-5.8		-17.4	-12.6	-7.9	-9.5	-9.6	-9.0	-8.2	-7.8	
2.60	ADV	5				-9.9	-8.6	-6.9	-6.0	-5.9					-9.0	-9.5	-8.6	-7.4	-7.1		
5.60	ADV	5							-13.8	-10.1	-9.0							-11.7	-9.7	-8.8	
		Avg			-14.7	-8.0	-8.2	-7.3	-8.7	-7.4	-6.9		-17.4	-12.6	-7.9	-9.2	-9.6	-9.8	-8.4	-7.9	
1.10	ADV	8		-19.2	-17.7	-10.2	-8.7	-8.4	-6.5	-6.7	-6.9		-19.0	-13.3	-10.8	-9.6	-8.9	-7.6	-6.5	-6.6	
2.60	ADV	8				-15.8	-14.3	-12.5	-11.6	-11.4					-13.9	-13.0	-12.5	-11.2	-9.6	-8.8	
5.60	ADV	8							-17.9	-13.9	-12.5							-13.8	-11.3	-10.3	
		Avg		-19.2	-17.7	-10.2	-12.2	-11.3	-12.3	-10.7	-10.3		-19.0	-13.3	-12.3	-11.3	-10.7	-10.9	-9.1	-8.5	

- Calculated
- Low COR, Low SNR, Wide 95% Conf. Int.
- Low COR, Low SNR
- Low COR or Low SNR, Wide 95% Conf. Int
- Low COR or Low SNR
- Wide 95% Conf. Int

			Velocity MEAN, u_y (m/s) - Prototype																		
			Low T_u									High T_u									
Height (cm)	Method	Location	Q_1	Q_2	Q_3	Q_4	Q_5	Q_6	Q_7	Q_8	Q_9	Q_1	Q_2	Q_3	Q_4	Q_5	Q_6	Q_7	Q_8	Q_9	
1.10	ADV	4		-0.49	-0.44	-0.18							-0.86	-0.45	-0.11						
2.60	ADV	4					-0.48	-0.43	-0.38	-0.36	-0.36					-0.05	0.004	0.0001	-0.03	-0.04	
31.70	ADV	C	0.001	-0.004	-0.001	0.002	-0.004	-0.006	-0.015	-0.010	-0.011	Same as Low T_u									
1.10	ADV	B		-0.53	-0.45	-0.25	-0.23	-0.23	-0.21	-0.20	-0.22		-0.43	-0.43	-0.42	-0.43	-0.44	-0.44	-0.44		
1.10	ADV	A				-0.30	-0.26	-0.25	-0.23	-0.23	-0.23		-0.24	-0.37	-0.36	-0.35	-0.35	-0.35	-0.36	-0.36	
1.10	ADV	2			-0.36	-0.17	-0.13	-0.12	-0.09	-0.08	-0.07		-0.24	-0.43	-0.19	-0.26	-0.27	-0.26	-0.25	-0.25	
2.60	ADV	2				-0.24	-0.21	-0.16	-0.13	-0.13				-0.23	-0.31	-0.33	-0.29	-0.27	-0.26		
5.60	ADV	2							-0.36	-0.24	-0.22					-0.40	-0.34	-0.27	-0.26		
		Avg			-0.36	-0.17	-0.19	-0.16	-0.20	-0.15	-0.14		-0.24	-0.43	-0.21	-0.29	-0.33	-0.30	-0.26	-0.26	
1.10	ADV	5			-0.47	-0.25	-0.20	-0.19	-0.17	-0.19	-0.18		-0.55	-0.40	-0.25	-0.30	-0.30	-0.29	-0.26	-0.25	
2.60	ADV	5				-0.31	-0.27	-0.22	-0.19	-0.19					-0.28	-0.30	-0.27	-0.23	-0.23		
5.60	ADV	5							-0.44	-0.32	-0.28							-0.37	-0.31	-0.28	
		Avg			-0.47	-0.25	-0.26	-0.23	-0.27	-0.24	-0.22		-0.55	-0.40	-0.25	-0.29	-0.30	-0.31	-0.27	-0.25	
1.10	ADV	8		-0.61	-0.56	-0.32	-0.27	-0.27	-0.21	-0.21	-0.22		-0.60	-0.42	-0.34	-0.30	-0.28	-0.24	-0.21	-0.21	
2.60	ADV	8				-0.50	-0.45	-0.39	-0.37	-0.36				-0.44	-0.41	-0.40	-0.35	-0.30	-0.28		
5.60	ADV	8							-0.57	-0.44	-0.39							-0.44	-0.36	-0.32	
		Avg		-0.61	-0.56	-0.32	-0.39	-0.36	-0.39	-0.34	-0.32		-0.60	-0.42	-0.39	-0.36	-0.34	-0.34	-0.29	-0.27	

Appendix C – Hydraulic model experiment: Flow characterization

			Velocity MEAN, u_z (cm/s) - Model																			
			Low T_u									High T_u										
Height (cm)	Method	Location	Q_1	Q_2	Q_3	Q_4	Q_5	Q_6	Q_7	Q_8	Q_9	Q_1	Q_2	Q_3	Q_4	Q_5	Q_6	Q_7	Q_8	Q_9		
1.10	ADV	4	-20.8									-22.7										
2.60	ADV	4	-25.1 -26.8 -28.8 -31.2 -32.2									-19.0 -17.9 -19.5 -23.7 -25.4										
31.70	ADV	C	-0.90	-1.9	-2.6	-4.9	-5.9	-6.2	-6.9	-7.9	-8.4	Same as Low Tu										
1.10	ADV	B	-26.2 -27.6 -28.4 -29.3 -31.0 -31.6									-31.1 -31.7 -31.8 -31.7 -32.0 -31.7										
1.10	ADV	A	-27.2 -28.3 -29.3 -30.4 -32.0 -32.6									-31.8 -32.2 -32.5 -32.8 -33.2 -33.2										
1.10	ADV	2	-20.7 -22.4 -23.4 -24.4 -25.7 -26.5									-22.4 -27.7 -29.5 -30.8 -31.7 -32.2										
2.60	ADV	2	-21.8 -23.6 -25.5 -27.9 -29.1									-22.3 -30.8 -34.1 -35.9 -37.2 -37.4										
5.60	ADV	2	-22.8 -26.7 -28.4									-23.7 -32.7 -36.3 -38.0										
		Avg	-20.7 -22.1 -23.5 -24.2 -26.8 -28.0									-22.4 -29.2 -29.1 -33.1 -35.1 -35.9										
1.10	ADV	5	-20.5 -21.5 -22.4 -23.3 -25.1 -25.8									-16.2	-17.0	-21.5	-23.4	-24.7	-25.5	-25.7				
2.60	ADV	5	-22.4 -24.0 -25.7 -28.5 -29.3									-21.3 -25.4 -28.6 -29.9 -30.1										
5.60	ADV	5	-27.2 -30.7 -32.6									-32.3 -37.3 -38.7										
		Avg	-20.5 -21.9 -23.2 -25.4 -28.1 -29.2									-16.2	-17.0	-21.4	-24.4	-28.5	-30.9	-31.5				
1.10	ADV	8	-17.1 -18.0 -18.6 -18.8 -20.0 -20.6									-9.0	-11.6	-14.4	-15.2	-16.6	-17.3	-17.6				
2.60	ADV	8	-16.3 -17.9 -20.1 -22.6 -23.7									-16.2 -19.7 -21.8 -24.2 -25.6 -26.2										
5.60	ADV	8	-17.2 -21.5 -23.5									-21.8 -28.0 -29.5										
		Avg	-17.1 -17.1 -18.2 -18.7 -21.4 -22.6									-13.9 -17.0 -18.5 -20.9 -23.6 -24.4										

- Calculated
- Low COR, Low SNR, Wide 95% Conf. Int.
- Low COR, Low SRN
- Low COR or Low SNR, Wide 95% Conf. Int
- Low COR or Low SNR
- Wide 95% Conf. Int

			Velocity MEAN, u_z (m/s) - Prototype																	
			Low T_u									High T_u								
Height (cm)	Method	Location	Q_1	Q_2	Q_3	Q_4	Q_5	Q_6	Q_7	Q_8	Q_9	Q_1	Q_2	Q_3	Q_4	Q_5	Q_6	Q_7	Q_8	Q_9
1.10	ADV	4	-0.66									-0.72								
2.60	ADV	4	-0.79 -0.85 -0.91 -0.99 -1.02									-0.60 -0.56 -0.62 -0.75 -0.80								
31.70	ADV	C	-0.03	-0.06	-0.08	-0.15	-0.19	-0.20	-0.22	-0.25	-0.27	Same as Low Tu								
1.10	ADV	B	-0.83 -0.87 -0.90 -0.93 -0.98 -1.00									-0.98 -1.00 -1.00 -1.00 -1.01 -1.00								
1.10	ADV	A	-0.86 -0.89 -0.93 -0.96 -1.01 -1.03									-1.01 -1.02 -1.03 -1.04 -1.05 -1.05								
1.10	ADV	2	-0.65 -0.71 -0.74 -0.77 -0.81 -0.84									-0.71 -0.88 -0.93 -0.97 -1.00 -1.02								
2.60	ADV	2	-0.69 -0.74 -0.81 -0.88 -0.92									-0.70 -0.97 -1.08 -1.13 -1.18 -1.18								
5.60	ADV	2	-0.72 -0.84 -0.90									-0.75 -1.03 -1.15 -1.20								
		Avg	-0.65 -0.70 -0.74 -0.77 -0.85 -0.89									-0.71 -0.92 -0.92 -1.05 -1.11 -1.13								
1.10	ADV	5	-0.65 -0.68 -0.71 -0.74 -0.79 -0.81									-0.51 -0.54 -0.68 -0.74 -0.78 -0.81 -0.81								
2.60	ADV	5	-0.71 -0.76 -0.81 -0.90 -0.93									-0.67 -0.80 -0.90 -0.95 -0.95								
5.60	ADV	5	-0.86 -0.97 -1.03									-1.02 -1.18 -1.22								
		Avg	-0.65 -0.69 -0.73 -0.80 -0.89 -0.92									-0.51 -0.54 -0.68 -0.77 -0.90 -0.98 -1.00								
1.10	ADV	8	-0.54 -0.57 -0.59 -0.60 -0.63 -0.65									-0.28 -0.37 -0.45 -0.48 -0.53 -0.55 -0.56								
2.60	ADV	8	-0.52 -0.57 -0.64 -0.72 -0.75									-0.51 -0.62 -0.69 -0.76 -0.81 -0.83								
5.60	ADV	8	-0.54 -0.68 -0.74									-0.69 -0.89 -0.93								
		Avg	-0.54 -0.54 -0.58 -0.59 -0.68 -0.71									-0.44 -0.54 -0.59 -0.66 -0.75 -0.77								

Appendix C – Hydraulic model experiment: Flow characterization

			Velocity RMS, u'_x (cm/s) - Model																		
			Low T_u									High T_u									
Height (cm)	Method	Location	Q_1	Q_2	Q_3	Q_4	Q_5	Q_6	Q_7	Q_8	Q_9	Q_1	Q_2	Q_3	Q_4	Q_5	Q_6	Q_7	Q_8	Q_9	
1.10	ADV	4	7.4	8.3	5.4							16.5	19.7								
2.60	ADV	4					3.7	3.7	3.7	3.8	4.0					20.3	20.7	22.1	23.5	24.1	
31.70	ADV	C	1.3	1.3	1.6	2.9	3.0	3.3	4.0	4.1	4.8	Same as Low Tu									
1.10	ADV	B	9.1	7.9	5.1	5.3	5.6	5.7	5.9	6.3		15.9	12.8	14.5	15.9	17.7	20.9	22.2			
1.10	ADV	A			4.6	4.8	5.0	5.0	5.4	5.9			12.0	13.6	15.0	17.0	19.6	20.8			
1.10	ADV	2	3.9	4.8	5.0	5.2	5.5	5.6	6.1	6.2		12.2	20.7	13.0	14.2	15.4	16.8	19.1	20.0		
2.60	ADV	2				3.6	3.6	3.6	3.9	4.1			11.5	12.0	13.8	16.3	18.8	20.2			
5.60	ADV	2							3.4	3.5	3.7					10.2	10.9	13.9	15.2		
		Avg	3.9	4.8	5.0	4.4	4.5	4.2	4.5	4.7		12.2	20.7	12.2	13.1	13.1	14.7	17.3	18.5		
1.10	ADV	5	4.6	5.0	4.8	4.9	5.2	5.4	5.4	5.8		10.6	16.1	14.1	14.2	15.2	16.5	18.5	19.4		
2.60	ADV	5				3.5	3.6	3.6	3.8	4.0					12.6	13.7	15.8	18.3	19.6		
5.60	ADV	5							3.4	3.5	3.6							12.3	14.6	16.2	
		Avg	4.6	5.0	4.8	4.2	4.4	4.1	4.2	4.5		10.6	16.1	14.1	13.4	14.4	14.9	17.1	18.4		
1.10	ADV	8	11.6	10.7	6.0	6.3	6.6	7.1	7.3	7.6		9.2	13.0	15.1	17.2	17.4	17.5	19.3	20.1		
2.60	ADV	8				3.6	3.7	3.7	3.9	4.1				13.6	13.6	14.4	15.9	18.1	19.0		
5.60	ADV	8							3.5	3.6	3.7							13.0	14.6	15.8	
		Avg	11.6	10.7	6.0	5.0	5.2	4.8	4.9	5.1		9.2	13.0	14.3	15.4	15.9	15.4	17.3	18.3		

			Velocity RMS, u'_x (m/s) - Prototype																		
			Low T_u									High T_u									
Height (cm)	Method	Location	Q_1	Q_2	Q_3	Q_4	Q_5	Q_6	Q_7	Q_8	Q_9	Q_1	Q_2	Q_3	Q_4	Q_5	Q_6	Q_7	Q_8	Q_9	
1.10	ADV	4	0.23	0.26	0.17							0.00	0.52	0.62							
2.60	ADV	4				0.12	0.12	0.12	0.12	0.13					0.64	0.65	0.70	0.74	0.76		
31.70	ADV	C	0.04	0.04	0.05	0.09	0.09	0.10	0.13	0.13	0.15	Same as Low Tu									
1.10	ADV	B	0.29	0.25	0.16	0.17	0.18	0.18	0.19	0.20		0.50	0.41	0.46	0.50	0.56	0.66	0.70			
1.10	ADV	A			0.15	0.15	0.16	0.16	0.17	0.19			0.38	0.43	0.48	0.54	0.62	0.66			
1.10	ADV	2	0.12	0.15	0.16	0.16	0.17	0.18	0.19	0.19		0.39	0.66	0.41	0.45	0.49	0.53	0.60	0.63		
2.60	ADV	2				0.11	0.11	0.11	0.12	0.13				0.36	0.38	0.44	0.51	0.59	0.64		
5.60	ADV	2							0.11	0.11	0.12					0.32	0.35	0.44	0.48		
		Avg	0.12	0.15	0.16	0.14	0.14	0.13	0.14	0.15		0.39	0.66	0.39	0.41	0.42	0.46	0.55	0.58		
1.10	ADV	5	0.14	0.16	0.15	0.15	0.16	0.17	0.17	0.18		0.34	0.51	0.45	0.45	0.48	0.52	0.58	0.61		
2.60	ADV	5				0.11	0.11	0.11	0.12	0.13					0.40	0.43	0.50	0.58	0.62		
5.60	ADV	5							0.11	0.11	0.12							0.39	0.46	0.51	
		Avg	0.14	0.16	0.15	0.13	0.14	0.13	0.13	0.14		0.34	0.51	0.45	0.42	0.46	0.47	0.54	0.58		
1.10	ADV	8	0.37	0.34	0.19	0.20	0.21	0.22	0.23	0.24		0.29	0.41	0.48	0.54	0.55	0.55	0.61	0.64		
2.60	ADV	8				0.12	0.12	0.12	0.12	0.13				0.43	0.43	0.45	0.50	0.57	0.60		
5.60	ADV	8							0.11	0.11	0.12							0.41	0.46	0.50	
		Avg	0.37	0.34	0.19	0.16	0.16	0.15	0.16	0.16		0.29	0.41	0.45	0.49	0.50	0.49	0.55	0.58		

Appendix C – Hydraulic model experiment: Flow characterization

			Velocity RMS, u'_y (cm/s) - Model																		
			Low T_u									High T_u									
Height (cm)	Method	Location	Q_1	Q_2	Q_3	Q_4	Q_5	Q_6	Q_7	Q_8	Q_9	Q_1	Q_2	Q_3	Q_4	Q_5	Q_6	Q_7	Q_8	Q_9	
1.10	ADV	4	2.4	2.9	2.8							18.9	10.8	15.7							
2.60	ADV	4					2.2	2.4	2.8	3.2	3.5					16.2	17.3	18.1	18.2	18.1	
31.70	ADV	C	0.4	0.6	0.9	1.9	2.0	2.4	2.8	3.0	3.5	Same as Low T_u									
1.10	ADV	B	2.6	2.7	2.9	3.2	3.6	4.0	4.4	4.8		8.7	11.5	12.6	13.8	15.1	16.8	17.4			
1.10	ADV	A				2.7	3.0	3.4	3.7	4.2	4.8	11.5	15.3	9.4	10.9	12.2	13.7	15.3	16.0		
1.10	ADV	2	1.4	1.8	2.7	3.1	3.5	3.8	4.5	4.7		9.9	12.6	9.5	10.6	12.1	13.7	15.0	15.5		
2.60	ADV	2				2.1	2.5	2.8	3.4	3.8				8.6	8.8	10.2	12.4	13.9	14.6		
5.60	ADV	2							2.9	2.9	3.2					8.5	8.3	10.1	10.8		
		Avg	1.4	1.8	2.7	2.6	3.0	3.2	3.6	3.9		9.9	12.6	9.1	9.7	10.2	11.5	13.0	13.6		
1.10	ADV	5	1.7	1.9	2.7	3.0	3.4	3.9	4.3	4.8		8.4	10.7	10.0	10.1	11.3	12.9	14.1	14.5		
2.60	ADV	5				2.1	2.4	2.8	3.4	3.6					9.2	9.8	11.5	13.1	13.7		
5.60	ADV	5							2.8	3.0	3.1							9.3	10.3	10.9	
		Avg	1.7	1.9	2.7	2.6	2.9	3.2	3.5	3.8		8.4	10.7	10.0	9.6	10.6	11.2	12.5	13.1		
1.10	ADV	8	3.4	3.4	3.1	3.3	3.8	4.3	4.7	5.0		6.7	9.2	10.3	10.9	11.5	12.6	13.7	13.9		
2.60	ADV	8				2.1	2.4	2.8	3.3	3.6				9.9	9.6	9.9	11.1	12.6	12.9		
5.60	ADV	8							3.0	3.0	3.2							9.5	9.9	10.5	
		Avg	3.4	3.4	3.1	2.7	3.1	3.4	3.7	4.0		6.7	9.2	10.1	10.2	10.7	11.1	12.0	12.4		

			Velocity RMS, u'_y (m/s) - Prototype																		
			Low T_u									High T_u									
Height (cm)	Method	Location	Q_1	Q_2	Q_3	Q_4	Q_5	Q_6	Q_7	Q_8	Q_9	Q_1	Q_2	Q_3	Q_4	Q_5	Q_6	Q_7	Q_8	Q_9	
1.10	ADV	4	0.07	0.09	0.09							0.60	0.34	0.50							
2.60	ADV	4					0.07	0.08	0.09	0.10	0.11					0.51	0.55	0.57	0.58	0.57	
31.70	ADV	C	0.01	0.02	0.03	0.06	0.06	0.08	0.09	0.09	0.11	Same as Low T_u									
1.10	ADV	B	0.08	0.09	0.09	0.10	0.11	0.13	0.14	0.15		0.27	0.36	0.40	0.44	0.48	0.53	0.55			
1.10	ADV	A				0.08	0.09	0.11	0.12	0.13	0.15	0.37	0.48	0.30	0.34	0.39	0.43	0.48	0.51		
1.10	ADV	2	0.04	0.06	0.09	0.10	0.11	0.12	0.14	0.15		0.31	0.40	0.30	0.34	0.38	0.43	0.47	0.49		
2.60	ADV	2				0.07	0.08	0.09	0.11	0.12				0.27	0.28	0.32	0.39	0.44	0.46		
5.60	ADV	2							0.09	0.09	0.10					0.27	0.26	0.32	0.34		
		Avg	0.04	0.06	0.09	0.08	0.09	0.10	0.11	0.12		0.31	0.40	0.29	0.31	0.32	0.36	0.41	0.43		
1.10	ADV	5	0.05	0.06	0.08	0.09	0.11	0.12	0.14	0.15		0.26	0.34	0.32	0.32	0.36	0.41	0.45	0.46		
2.60	ADV	5				0.07	0.08	0.09	0.11	0.11					0.29	0.31	0.36	0.41	0.43		
5.60	ADV	5							0.09	0.09	0.10							0.29	0.33	0.35	
		Avg	0.05	0.06	0.08	0.08	0.09	0.10	0.11	0.12		0.26	0.34	0.32	0.30	0.33	0.35	0.39	0.41		
1.10	ADV	8	0.11	0.11	0.10	0.11	0.12	0.14	0.15	0.16		0.21	0.29	0.32	0.34	0.36	0.40	0.43	0.44		
2.60	ADV	8				0.07	0.08	0.09	0.10	0.12				0.31	0.30	0.31	0.35	0.40	0.41		
5.60	ADV	8							0.09	0.09	0.10							0.30	0.31	0.33	
		Avg	0.11	0.11	0.10	0.09	0.10	0.11	0.12	0.12		0.21	0.29	0.32	0.32	0.34	0.35	0.38	0.39		

Appendix C – Hydraulic model experiment: Flow characterization

			Velocity RMS, u'_z (cm/s) - Model																	
			Low T_u									High T_u								
Height (cm)	Method	Location	Q_1	Q_2	Q_3	Q_4	Q_5	Q_6	Q_7	Q_8	Q_9	Q_1	Q_2	Q_3	Q_4	Q_5	Q_6	Q_7	Q_8	Q_9
1.10	ADV	4	7.2									20.6								
2.60	ADV	4	6.6 6.7 6.3 6.4 6.5									26.7 27.2 28.6 30.1 30.8								
31.70	ADV	C	2.2	2.1	2.5	3.6	3.8	4.1	4.3	4.4	5.0	Same as Low Tu								
1.10	ADV	B	7.3 7.2 7.2 6.5 6.5 6.6									19.0 20.5 21.9 23.4 25.9 27.0								
1.10	ADV	A	7.4 6.8 6.7 6.2 6.1 6.2									16.8 18.3 19.6 21.2 23.2 24.4								
1.10	ADV	2	7.4 7.2 7.2 6.6 6.7 6.7									15.8 16.7 17.8 19.2 21.2 21.9								
2.60	ADV	2	6.4 6.5 6.1 6.2 6.4									15.4 15.9 17.6 20.2 22.8 24.2								
5.60	ADV	2	6.0 6.2 6.4									14.8 12.4 15.5 16.9								
		Avg	7.4 6.8 6.8 6.3 6.4 6.5									15.6 16.3 16.7 17.3 19.9 21.0								
1.10	ADV	5	7.3 7.2 7.2 6.7 6.4 6.6									15.7 15.4 16.3 17.5 19.5 20.4								
2.60	ADV	5	6.3 6.4 6.0 6.2 6.3									15.1 16.0 17.9 20.6 21.9								
5.60	ADV	5	6.1 6.3 6.4									13.5 16.0 17.7								
		Avg	7.3 6.7 6.8 6.3 6.3 6.4									15.7 15.2 16.2 16.3 18.7 20.0								
1.10	ADV	8	8.9 8.4 8.3 7.5 7.4 7.5									15.0 15.9 16.1 16.1 17.7 18.4								
2.60	ADV	8	6.5 6.7 6.4 6.4 6.5									16.2 15.5 15.9 17.0 19.2 20.2								
5.60	ADV	8	6.6 6.4 6.6									13.7 15.0 16.4								
		Avg	8.9 7.5 7.5 6.8 6.8 6.9									15.6 15.7 16.0 15.6 17.3 18.3								

			Velocity RMS, u'_z (m/s) - Prototype																	
			Low T_u									High T_u								
Height (cm)	Method	Location	Q_1	Q_2	Q_3	Q_4	Q_5	Q_6	Q_7	Q_8	Q_9	Q_1	Q_2	Q_3	Q_4	Q_5	Q_6	Q_7	Q_8	Q_9
1.10	ADV	4	0.23									0.65								
2.60	ADV	4	0.21 0.21 0.20 0.20 0.20									0.84 0.86 0.90 0.95 0.97								
31.70	ADV	C	0.07	0.07	0.08	0.11	0.12	0.13	0.14	0.14	0.16	Same as Low Tu								
1.10	ADV	B	0.23 0.23 0.23 0.21 0.20 0.21									0.60 0.65 0.69 0.74 0.82 0.85								
1.10	ADV	A	0.23 0.22 0.21 0.20 0.19 0.20									0.53 0.58 0.62 0.67 0.73 0.77								
1.10	ADV	2	0.23 0.23 0.23 0.21 0.21 0.21									0.50 0.53 0.56 0.61 0.67 0.69								
2.60	ADV	2	0.20 0.21 0.19 0.20 0.20									0.49 0.50 0.56 0.64 0.72 0.77								
5.60	ADV	2	0.19 0.20 0.20									0.47 0.39 0.49 0.54								
		Avg	0.23 0.22 0.22 0.20 0.20 0.21									0.49 0.51 0.53 0.55 0.63 0.67								
1.10	ADV	5	0.23 0.23 0.23 0.21 0.20 0.21									0.50 0.49 0.52 0.55 0.62 0.65								
2.60	ADV	5	0.20 0.20 0.19 0.20 0.20									0.48 0.51 0.57 0.65 0.69								
5.60	ADV	5	0.19 0.20 0.20									0.43 0.51 0.56								
		Avg	0.23 0.21 0.21 0.20 0.20 0.20									0.50 0.48 0.51 0.52 0.59 0.63								
1.10	ADV	8	0.28 0.27 0.26 0.24 0.24 0.24									0.47 0.50 0.51 0.51 0.56 0.58								
2.60	ADV	8	0.21 0.21 0.20 0.20 0.21									0.51 0.49 0.50 0.54 0.61 0.64								
5.60	ADV	8	0.21 0.20 0.21									0.43 0.47 0.52								
		Avg	0.28 0.24 0.24 0.22 0.21 0.22									0.49 0.50 0.51 0.49 0.55 0.58								

Flow depth

			Flow depth, d (cm) - Model																		
			Low T_u									High T_u									
Height ADV (cm)	Meas. Method	Location	Q_1	Q_2	Q_3	Q_4	Q_5	Q_6	Q_7	Q_8	Q_9	Q_1	Q_2	Q_3	Q_4	Q_5	Q_6	Q_7	Q_8	Q_9	
1.10	UltSonic	4	1.0	2.2	3.1	5.6						1.1	2.8	4.1	6.2						
2.60	UltSonic	4					6.6	7.4	8.7	10.3	11.0					6.8	7.7	9.4	11.5	12.2	
31.70	Ruler	C	38.6	42.2	44.7	51.0	53.5	55.2	57.8	61.4	62.8	Same as Low T_u									
1.10	UltSonic	B	1.5	2.8	3.8	6.6	7.6	8.6	10.1	11.9	12.8	1.0	3.0	4.9	7.2	8.9	10.2	12.3	14.7	16.2	
1.10	UltSonic	A	1.2	2.6	3.6	6.1	7.4	8.3	9.7	11.3	12.1	0.8	3.1	4.9	6.7	8.1	9.2	10.9	13.0	14.2	
1.10	UltSonic	2	1.2	2.4	3.4	5.8	6.8	7.6	9.0	10.8	11.6	1.3	3.5	5.0	5.5	7.1	8.4	10.1	12.1	13.1	
2.60	UltSonic	2					6.9	7.6	9.0	10.7	11.6				5.7	7.4	8.6	10.6	12.2	13.1	
5.60	UltSonic	2							8.9	10.6	11.3							8.7	10.4	12.5	13.4
		Avg	1.2	2.4	3.4	5.8	6.8	7.6	9.0	10.7	11.5	1.3	3.5	5.0	5.6	7.3	8.6	10.4	12.3	13.2	
1.10	UltSonic	5	1.0	2.2	3.0	5.4	6.7	7.2	8.5	10.2	11.1	1.0	2.8	4.3	6.7	7.3	8.1	9.5	11.3	12.1	
2.60	UltSonic	5					6.6	7.3	8.8	10.4	10.9					7.3	8.2	9.5	11.2	12.2	
5.60	UltSonic	5							8.7	10.4	11.1								9.3	11.1	12.2
		Avg	1.0	2.2	3.0	5.4	6.7	7.3	8.7	10.3	11.0	1.0	2.8	4.3	6.7	7.3	8.1	9.4	11.2	12.2	
1.10	UltSonic	8	0.9	2.0	2.7	5.5	6.4	7.3	8.3	10.0	10.7	1.5	3.1	3.9	6.3	7.2	8.0	9.2	10.8	11.6	
2.60	UltSonic	8					6.2	7.1	8.3	9.7	10.5				6.2	7.4	8.3	9.4	11.0	11.9	
5.60	UltSonic	8							8.1	9.6	10.3								9.3	10.7	11.6
		Avg	0.9	2.0	2.7	5.5	6.3	7.2	8.2	9.8	10.5	1.5	3.1	3.9	6.2	7.3	8.1	9.3	10.8	11.7	

			Flow depth, d (cm) - Prototype																		
			Low T_u									High T_u									
Height ADV (cm)	Meas. Method	Location	Q_1	Q_2	Q_3	Q_4	Q_5	Q_6	Q_7	Q_8	Q_9	Q_1	Q_2	Q_3	Q_4	Q_5	Q_6	Q_7	Q_8	Q_9	
1.10	UltSonic	4	10	22	31	56						11	28	41	62						
2.60	UltSonic	4					66	74	87	103	110					68	77	94	115	122	
31.70	Ruler	C	386	422	447	510	535	552	578	614	628	Same as Low T_u									
1.10	UltSonic	B	15	28	38	66	76	86	101	119	128	10	30	49	72	89	102	123	147	162	
1.10	UltSonic	A	12	26	36	61	74	83	97	113	121	8	31	49	67	81	92	109	130	142	
1.10	UltSonic	2	12	24	34	58	68	76	90	108	116	13	35	50	55	71	84	101	121	131	
2.60	UltSonic	2					69	76	90	107	116				57	74	86	106	122	131	
5.60	UltSonic	2							89	106	113							87	104	125	134
		Avg	12	24	34	58	68	76	90	107	115	13	35	50	56	73	86	104	123	132	
1.10	UltSonic	5	10	22	30	54	67	72	85	102	111	10	28	43	67	73	81	95	113	121	
2.60	UltSonic	5					66	73	88	104	109					73	82	95	112	122	
5.60	UltSonic	5							87	104	111								93	111	122
		Avg	10	22	30	54	67	73	87	103	110	10	28	43	67	73	81	94	112	122	
1.10	UltSonic	8	9	20	27	55	64	73	83	100	107	15	31	39	63	72	80	92	108	116	
2.60	UltSonic	8					62	71	83	97	105				62	74	83	94	110	119	
5.60	UltSonic	8							81	96	103								93	107	116
		Avg	9	20	27	55	63	72	82	98	105	15	31	39	62	73	81	93	108	117	

Turbulence intensity

			Turbulence intensity, $T_{u_x} (u'_x/u_x)$																		
			Low T_u									High T_u									
Height ADV (cm)	Meas. Method	Location	Q_1	Q_2	Q_3	Q_4	Q_5	Q_6	Q_7	Q_8	Q_9	Q_1	Q_2	Q_3	Q_4	Q_5	Q_6	Q_7	Q_8	Q_9	
1.10	ADV	4		3.0%	3.3%	2.0%							0.0%	7.3%	8.3%						
2.60	ADV	4					1.4%	1.4%	1.3%	1.3%	1.4%					8.5%	8.5%	8.9%	9.2%	9.4%	
31.70	ADV	C	17.4%	8.6%	7.6%	8.0%	7.1%	7.3%	7.7%	6.8%	7.5%	Same as Low Tu									
1.10	ADV	B		4.6%	3.8%	2.2%	2.2%	2.3%	2.3%	2.2%	2.4%		8.6%		6.5%	7.1%	7.8%	8.6%	10.3%	11.0%	
1.10	ADV	A				1.9%	1.9%	2.0%	1.9%	2.0%	2.1%				5.4%	6.0%	6.6%	7.4%	8.5%	9.1%	
1.10	ADV	2		1.7%	2.0%	2.0%	2.0%	2.1%	2.1%	2.2%	2.2%		6.0%	10.0%	5.5%	5.8%	6.3%	6.8%	7.6%	7.9%	
2.60	ADV	2					1.4%	1.4%	1.3%	1.4%	1.4%				4.6%	4.8%	5.5%	6.4%	7.3%	7.9%	
5.60	ADV	2								1.2%	1.2%	1.3%				3.9%	4.1%	5.2%	5.6%		
		Avg		1.7%	2.0%	2.0%	1.7%	1.7%	1.5%	1.6%	1.6%		6.0%	10.0%	5.0%	5.3%	5.2%	5.8%	6.7%	7.2%	
1.10	ADV	5		1.9%	2.0%	1.8%	1.8%	1.9%	1.9%	1.8%	1.9%		5.0%	7.3%	5.9%	5.6%	5.9%	6.2%	6.8%	7.1%	
2.60	ADV	5					1.3%	1.3%	1.3%	1.3%	1.3%				4.9%	5.3%	5.9%	6.8%	7.2%		
5.60	ADV	5								1.2%	1.2%	1.2%					4.6%	5.4%	6.0%		
		Avg		1.9%	2.0%	1.8%	1.5%	1.6%	1.5%	1.4%	1.5%		5.0%	7.3%	5.9%	5.2%	5.6%	5.6%	6.3%	6.8%	
1.10	ADV	8		4.5%	4.1%	2.2%	2.2%	2.3%	2.4%	2.4%	2.5%		4.1%	5.6%	6.0%	6.7%	6.6%	6.5%	7.1%	7.3%	
2.60	ADV	8					1.3%	1.3%	1.3%	1.3%	1.4%				5.3%	5.1%	5.3%	5.8%	6.5%	6.8%	
5.60	ADV	8								1.2%	1.2%	1.2%					4.6%	5.0%	5.4%		
		Avg		4.5%	4.1%	2.2%	1.8%	1.8%	1.6%	1.6%	1.7%		4.1%	5.6%	5.6%	5.9%	6.0%	5.6%	6.2%	6.5%	

			Turbulence intensity, $T_{u_y} (u'_y/u_x)$																		
			Low T_u									High T_u									
Height ADV (cm)	Meas. Method	Location	Q_1	Q_2	Q_3	Q_4	Q_5	Q_6	Q_7	Q_8	Q_9	Q_1	Q_2	Q_3	Q_4	Q_5	Q_6	Q_7	Q_8	Q_9	
1.10	ADV	4		1.0%	1.1%	1.1%							8.9%	4.8%	6.6%						
2.60	ADV	4					0.8%	0.9%	1.0%	1.1%	1.2%					6.8%	7.2%	7.3%	7.2%	7.0%	
31.70	ADV	C	5.6%	4.1%	4.2%	5.3%	4.9%	5.4%	5.4%	5.0%	5.4%	Same as Low Tu									
1.10	ADV	B		1.3%	1.3%	1.3%	1.4%	1.5%	1.6%	1.7%	1.8%		4.7%		5.8%	6.2%	6.7%	7.4%	8.2%	8.6%	
1.10	ADV	A				1.1%	1.2%	1.3%	1.4%	1.6%	1.8%				4.2%	4.8%	5.4%	6.0%	6.7%	7.0%	
1.10	ADV	2		0.6%	0.8%	1.1%	1.2%	1.3%	1.4%	1.6%	1.6%		4.9%	6.0%	4.0%	4.4%	4.9%	5.5%	6.0%	6.2%	
2.60	ADV	2					0.8%	0.9%	1.0%	1.2%	1.3%				3.5%	3.5%	4.0%	4.9%	5.4%	5.7%	
5.60	ADV	2								1.0%	1.0%	1.1%					3.3%	3.1%	3.8%	4.0%	
		Avg		0.6%	0.8%	1.1%	1.0%	1.1%	1.2%	1.3%	1.4%		4.9%	6.0%	3.7%	3.9%	4.1%	4.5%	5.1%	5.3%	
1.10	ADV	5		0.7%	0.7%	1.0%	1.1%	1.2%	1.4%	1.5%	1.6%		4.0%	4.8%	4.2%	4.0%	4.4%	4.9%	5.4%	5.5%	
2.60	ADV	5					0.8%	0.9%	1.0%	1.1%	1.2%				3.6%	3.8%	4.3%	4.9%	5.1%		
5.60	ADV	5								1.0%	1.0%	1.1%					3.4%	3.7%	3.9%		
		Avg		0.7%	0.7%	1.0%	0.9%	1.1%	1.1%	1.2%	1.3%		4.0%	4.8%	4.2%	3.8%	4.1%	4.2%	4.6%	4.8%	
1.10	ADV	8		1.3%	1.3%	1.1%	1.2%	1.3%	1.5%	1.6%	1.7%		3.0%	4.0%	4.1%	4.2%	4.4%	4.7%	5.0%	5.1%	
2.60	ADV	8					0.8%	0.8%	1.0%	1.1%	1.2%				3.8%	3.6%	3.7%	4.0%	4.5%	4.6%	
5.60	ADV	8								1.0%	1.0%	1.0%					3.4%	3.4%	3.6%		
		Avg		1.3%	1.3%	1.1%	1.0%	1.1%	1.2%	1.2%	1.3%		3.0%	4.0%	4.0%	3.9%	4.0%	4.0%	4.3%	4.4%	

Appendix C – Hydraulic model experiment: Flow characterization

Height ADV (cm)	Meas. Method	Location	Turbulence intensity, $T_{u,z}$ (u'_z/u_x)																
			Low T_u									High T_u							
			Q_1	Q_2	Q_3	Q_4	Q_5	Q_6	Q_7	Q_8	Q_9	Q_1	Q_2	Q_3	Q_4	Q_5	Q_6	Q_7	Q_8
1.10	ADV	4	2.7%									8.7%							
2.60	ADV	4	2.4% 2.4% 2.2% 2.2% 2.2%									11.1% 11.2% 11.5% 11.8% 12.0%							
31.70	ADV	C	29.3%	14.0%	12.0%	10.2%	9.2%	9.1%	8.3%	7.3%	7.9%	Same as Low Tu							
1.10	ADV	B	3.2% 3.0% 3.0% 2.6% 2.5% 2.5%									9.6% 10.0% 10.7% 11.4% 12.7% 13.3%							
1.10	ADV	A	3.1% 2.8% 2.7% 2.4% 2.3% 2.3%									7.5% 8.1% 8.6% 9.2% 10.1% 10.6%							
1.10	ADV	2	2.9% 2.8% 2.7% 2.4% 2.4% 2.4%									6.6% 6.8% 7.3% 7.7% 8.5% 8.7%							
2.60	ADV	2	2.4% 2.4% 2.2% 2.2% 2.2%									6.2% 6.3% 7.0% 8.0% 8.9% 9.5%							
5.60	ADV	2	2.2% 2.2% 2.3%									5.7% 4.7% 5.8% 6.3%							
		Avg	2.9% 2.6% 2.6% 2.3% 2.3% 2.3%									6.4% 6.6% 6.6% 6.8% 7.7% 8.1%							
1.10	ADV	5	2.8% 2.6% 2.6% 2.4% 2.2% 2.2%									6.6% 6.0% 6.3% 6.5% 7.2% 7.5%							
2.60	ADV	5	2.3% 2.3% 2.1% 2.1% 2.1%									5.9% 6.2% 6.7% 7.6% 8.1%							
5.60	ADV	5	2.1% 2.1% 2.2%									5.1% 5.9% 6.5%							
		Avg	2.8% 2.5% 2.5% 2.2% 2.2% 2.2%									6.6% 6.0% 6.2% 6.1% 6.9% 7.4%							
1.10	ADV	8	3.3% 3.0% 2.9% 2.6% 2.5% 2.5%									6.0% 6.2% 6.1% 6.0% 6.5% 6.7%							
2.60	ADV	8	2.3% 2.3% 2.2% 2.1% 2.1%									6.3% 5.8% 5.9% 6.2% 6.9% 7.2%							
5.60	ADV	8	2.2% 2.1% 2.2%									4.8% 5.2% 5.6%							
		Avg	3.3% 2.7% 2.6% 2.3% 2.2% 2.3%									6.1% 6.0% 6.0% 5.7% 6.2% 6.5%							

Froude number

		Froude Number, Fr																	
		Low T_u									High T_u								
Location		Q_1	Q_2	Q_3	Q_4	Q_5	Q_6	Q_7	Q_8	Q_9	Q_1	Q_2	Q_3	Q_4	Q_5	Q_6	Q_7	Q_8	Q_9
4		7.3	5.2	4.6	3.6	3.4	3.2	3.1	2.9	2.8	6.3	4.1	3.6	3.0	2.9	2.8	2.6	2.4	2.4
C		0.04	0.1	0.1	0.2	0.2	0.2	0.2	0.2	0.3	Same as Low Tu								
B			3.8	3.4	2.9	2.7	2.6	2.5	2.4	2.4	3.4		2.4	2.2	2.1	1.9	1.7	1.6	
A					3.1	2.9	2.8	2.7	2.6	2.5			2.8	2.5	2.4	2.2	2.0	1.9	
2		6.5	4.8	4.2	3.4	3.2	3.1	2.9	2.8	2.7	5.4	3.5	3.0	3.3	2.9	2.8	2.5	2.4	2.3
5		7.4	5.3	4.6	3.6	3.4	3.3	3.1	2.9	2.8	6.6	4.0	3.4	2.9	3.0	2.9	2.8	2.6	2.5
8		8.2	5.9	5.1	3.7	3.6	3.4	3.3	3.1	3.0	5.5	4.0	3.8	3.3	3.1	3.0	2.9	2.7	2.6

Reynolds number

Location	Reynolds Number * 10 ⁴ , Re																	
	Low T_u									High T_u								
	Q_1	Q_2	Q_3	Q_4	Q_5	Q_6	Q_7	Q_8	Q_9	Q_1	Q_2	Q_3	Q_4	Q_5	Q_6	Q_7	Q_8	Q_9
4	2.3	5.2	7.4	14.2	17.1	19.4	23.3	28.4	30.9	2.0	5.6	8.8	13.9	15.5	17.6	22.2	27.6	29.6
C	2.8	6.1	9.0	17.3	21.0	23.6	28.4	35.1	38.2	Same as Low Tu								
B		5.3	7.6	14.5	17.2	19.7	24.0	29.4	32.0	5.3		13.5	17.1	19.8	24.0	28.5	31.1	
A				14.0	17.4	19.9	23.9	29.0	31.4			14.1	17.4	19.8	23.8	28.4	30.8	
2	2.5	5.2	7.6	13.9	17.0	19.3	23.4	28.6	31.2	2.3	6.6	9.8	12.9	17.1	20.5	25.2	30.1	32.5
5	2.2	5.0	7.1	13.5	17.1	19.0	23.3	28.5	30.9	2.0	5.6	9.0	15.0	17.7	19.9	23.9	28.7	31.3
8	2.0	4.8	6.6	14.1	16.7	19.4	22.8	27.9	30.3	3.0	6.6	8.5	15.1	18.1	20.6	24.4	28.9	31.3

Appendix D – Hydraulic model experiment: Block erodibility threshold

Threshold mean velocity values, u_x

Rotation Angle		Discharge No.				Pitot (m/s) - Ref. Location				0.966 Correlation Factor				0.676 Correlation Factor				Prototype (m/s) - Loc. 5				
										Pitot 5 / Pitot Ref				Pitot 5 / ADV 5								
		Test 1	Test 2	Test 3	Test 4	Test 1	Test 2	Test 3	Test 4	Test 1	Test 2	Test 3	Test 4	Test 1	Test 2	Test 3	Test 4	Test 1	Test 2	Test 3	Test 4	
At least	0	9	9	9										2.96	2.96	2.96						
Heighest	0																	NA	NA	NA		
At least	15	9												2.96								
Heighest	15																	NA				
At least	30																					
Heighest	30	2												2.44						7.70		
At least	45	3	1											2.51	2.33					7.93	7.38	
Heighest	45	4	2											2.64	2.44					8.35	7.70	
At least	60	1												2.33						7.38		
Heighest	60	2	1	1										2.44	2.33	2.33				7.70	7.38	7.38
At least	75																					
Heighest	75	0.5				1.54				1.488				2.20						6.96		
At least	90																					
Heighest	90	1	0.5	0.5		1.51	1.49			1.459	1.439			2.33	2.16	2.13				7.38	6.82	6.73
At least	105																					
Heighest	105	3												2.51						7.93		
At least	120	6												2.76						8.72		
Heighest	120	7												2.84						8.97		
At least	135	5												2.71						8.58		
Heighest	135	6	6											2.76	2.76					8.72	8.72	
At least	150	6												2.76						8.72		
Heighest	150	7	9	8										2.84	2.96	2.92				8.97	9.35	9.23
At least	165																					
Heighest	165	6												2.76						8.72		
At least	180		3	3											2.51	2.51				7.93	7.93	
Heighest	180	4	4	4										2.64	2.64	2.64				8.35	8.35	8.35

NA Did not get eroded

Appendix D – Hydraulic model experiment: Block erodibility threshold

Block 2 - High Tu		1.02 Correlation Factor				0.772 Correlation Factor															
		Discharge No.				Pitot (m/s) - Ref. Location				Pitot 5 / Pitot Ref				Pitot 5 / ADV 5							
		Test 1	Test 2	Test 3	Test 4	Test 1	Test 2	Test 3	Test 4	Test 1	Test 2	Test 3	Test 4	Test 1	Test 2	Test 3	Test 4	Test 1	Test 2	Test 3	Test 4
At least	0																				
Heighest	0	7	7	7										2.67	2.67	2.67		8.45	8.45	8.45	
At least	15	5												2.55				8.07			
Heighest	15	6	6											2.59	2.59			8.19	8.19		
At least	30																				
Heighest	30	3												2.22				7.00			
At least	45																				
Heighest	45	2												2.10				6.65			
At least	60																				
Heighest	60	1												2.08				6.59			
At least	75																				
Heighest	75	0.5			1.56					1.591				2.06				6.52			
At least	90																				
Heighest	90	1	1	1										2.08	2.08	2.08		6.59	6.59	6.59	
At least	105	2												2.10				6.65			
Heighest	105	3												2.22				7.00			
At least	120																				
Heighest	120	4												2.38				7.52			
At least	135																				
Heighest	135	5												2.55				8.07			
At least	150																				
Heighest	150	5												2.55				8.07			
At least	165																				
Heighest	165	4												2.38				7.52			
At least	180	3												2.22				7.00			
Heighest	180	4	3	3										2.38	2.22	2.22		7.52	7.00	7.00	

Block 1 - Low Tu		0.966 Correlation Factor				0.676 Correlation Factor															
		Discharge No.				Pitot (m/s) - Ref. Location				Pitot 5 / Pitot Ref				Pitot 5 / ADV 5							
		Test 1	Test 2	Test 3	Test 4	Test 1	Test 2	Test 3	Test 4	Test 1	Test 2	Test 3	Test 4	Test 1	Test 2	Test 3	Test 4	Test 1	Test 2	Test 3	Test 4
At least	0																				
Heighest	0	3	3	7	7									2.22	2.22	2.67	2.67	7.00	7.00	8.45	8.45
At least	15	1												2.08				6.59			
Heighest	15	2												2.10				6.65			
At least	30																				
Heighest	30	0.5			1.58					1.526				1.98				6.25			
At least	45																				
Heighest	45	0.5			1.5					1.449				1.88				5.94			
At least	60																				
Heighest	60	0.5	0.5	0.5		1.43	1.32	1.35		1.381	1.275	1.304		1.79	1.65	1.69		5.66	5.22	5.34	
At least	75																				
Heighest	75	0.5			1.3					1.256				1.63				5.14			
At least	90																				
Heighest	90	0.5	0.5	0.5		1.4	1.37	1.32		1.352	1.323	1.275		1.75	1.71	1.65		5.54	5.42	5.22	
At least	105																				
Heighest	105	0.5			1.55					1.497				1.94				6.13			
At least	120																				
Heighest	120	0.5			1.67					1.613				2.09				6.61			
At least	135																				
Heighest	135	0.5			1.66					1.604				2.08				6.57			
At least	150																				
Heighest	150	0.5			1.62					1.565				2.03				6.41			
At least	165																				
Heighest	165	1												2.08				6.59			
At least	180																				
Heighest	180	0.5	0.5	0.5		1.58	1.46	1.45		1.526	1.41	1.401		1.98	1.83	1.81		6.25	5.78	5.74	

Appendix D – Hydraulic model experiment: Block erodibility threshold

Block 1 - High Tu		1.02 Correlation Factor								0.772 Correlation Factor											
		Discharge No.				Pitot (m/s) - Ref. Location				Pitot (m/s) - Location 5				ADV (m/s) - Location 5				Prototype (m/s) - Loc. 5			
		Test 1	Test 2	Test 3	Test 4	Test 1	Test 2	Test 3	Test 4	Test 1	Test 2	Test 3	Test 4	Test 1	Test 2	Test 3	Test 4	Test 1	Test 2	Test 3	Test 4
At least	0	2	3										2.10	2.22			6.65	7.00			
Heighest	0	3	4	4									2.22	2.38	2.38		7.00	7.52	7.52		
At least	15																				
Heighest	15	2											2.10				6.65				
At least	30																				
Heighest	30	0.5			1.57				1.517				1.96				6.21				
At least	45																				
Heighest	45	0.5			1.31				1.265				1.64				5.18				
At least	60																				
Heighest	60	0.5			1.3				1.256				1.63				5.14				
At least	75																				
Heighest	75	0.5			1.34				1.294				1.68				5.30				
At least	90																				
Heighest	90	0.5	0.5	0.5	1.32	1.32	1.33		1.275	1.275	1.285		1.65	1.65	1.66		5.22	5.22	5.26		
At least	105																				
Heighest	105	0.5			1.57				1.517				1.96				6.21				
At least	120																				
Heighest	120	0.5			1.63				1.575				2.04				6.45				
At least	135																				
Heighest	135	0.5			1.62				1.565				2.03				6.41				
At least	150																				
Heighest	150	0.5			1.61				1.555				2.01				6.37				
At least	165																				
Heighest	165	0.5			1.61				1.555				2.01				6.37				
At least	180																				
Heighest	180	1	0.5	0.5		1.51	1.53			1.459	1.478		2.08	1.89	1.91		6.59	5.97	6.05		

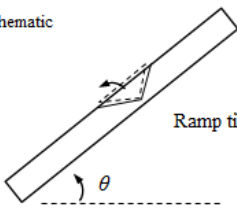
Appendix E – Hydraulic model experiment: Block removal mechanics

Block yield condition tests

Determination of ϕ for model blocks																											
Mold rot. angle	Ramp rotation angle, θ (deg) ¹								Dip (deg)	Dip dir. (deg)	Dip (deg)	Dip dir. (deg)	Dip (deg)	Dip dir. (deg)	JP code			ϕ (deg) ⁴	Failure Mode								
	ψ (deg)	Block 1 ²	AVG	Block 2	AVG	Block 3 ²	AVG	Block2-wet AVG ³	Block 2 - Face 1	Block 2 - Face 2	Block 2 - Face 3	Face 1	Face 2	Face 3	Block 2	Block 2											
0	84	84	85	84	86	85	86	86	88	85	85	86	85	85	85	85	72	296	72	64	16	180	1	1	0	16	S3
15	85	82	83	83	82	81	82	82	87	85	85	86	86	80	310	80	247	32	117	19	131	1	1	0	15	S23	
30	80	83	80	81	83	80	85	83	83	83	84	83	86	80	81	82	48	310	80	247	32	117	1	0	0	18	S23
45					80	79	79	79					86	80	81	82	41	327	65	249	44	107	1	0	0	16	S23
60					77	76	80	78	74	75	82	77					36	348	51	250	58	106	1	0	0	15	S23
75					76	79	82	79					75	80	79	78	35	11	37	246	72	108	1	0	0	16	S23
90					77	76	75	76	75	80	79	78					43	30	23	243	85	109	1	0	0	13	S23
105					77	78	77	77					78	78	77	78	51	45	12	212	81	293	1	0	1	12	S23
120					77	79	77	78	80	80	79	80					62	55	14	147	67	298	1	0	1	14	S2
135					77	78	80	78					78	78	77	78	74	61	25	121	55	305	1	0	1	18	S12
150					75	80	75	77					78	78	77	78	88	65	37	112	44	318	1	0	1	19	S12
165					75	73	72	73					77	77	76	76	77	249	50	106	40	338	0	0	1	17	S12
180					68	69	66	68	77	75	77	76					62	254	62	106	42	0	0	0	1	15	S12

Notes:

1) ramp schematic



Ramp tilted upwards until block slides out

2) block 1 and block 3 yielded similar results to block 2 for first three rotation angles, so only block 2 was tested thereafter.
 3) wet runs yielded similar results to dry runs
 4) back-calculated using a block theory approach

16	AVG
2	STD. DEV

Summary table for block removal mechanics

Run ID	Failure Mode ^a	<i>d</i> freq. (Hz) ^b	<i>P</i> freq. (Hz) ^b	Response
000_H_b2_q7	S3	< 5, 15, 28	2-3, 31	3
000_L_b1_q3	S1 (early), Lifting/S3 (late)	none	10, 21, 34	2
000_L_b1_q3_2	S3 (early), Lifting/S3 (late)	29	10, 21, 35	2
000b_H_b2_q7	Did not capture failure	< 10, 31	2-3, 31, 38	3
000b_L_b1_q7	S3	2-3, 7-9, 15, 30, 35	10, 18, 28, 31, 35	2
000c_H_b1_q4	S2, S23, S3	5, 21	2-3, 7, 18, 35	2
000c_H_b2_q7	S3 (early), S2/S3 (late)	< 10, 29	2-3, 31	3
000c_L_b1_q7	S3	6, 10, 12	10, 18, 21, 31, 35	2
015_H_b1_q2	Lifting (early), S2/S3 /Lifting (late)	11, 33	11, 37	2
015_L_b1_q2	S12/S2 (early), S2/Lifting (late)	too few samples	too few samples	2
030_H_b2_q3	S1 (early), S1/Lifting/S3 (late)	21, 38	25, 38	2
030_L_b2_q2	S1 (early), S1/Lifting/S3 (late)	10-17, 30	8-12, 22, 30, 35	2
045_H_b2_q2	S1/S3 (early), S1/Lifting/S3 (late)	12, 35, 39	22, 35	2
060_H_b2_q1	S1/S2 (early), Lifting/S3 (late)	14	4-5, 9, 13, 25, 34	2
060_L_b2_q1b	S1/S2 (early), Lifting/S2 (late)	7, 37	5-11, 33	2
090_H_b2_q1	S2/S3/S23 (early), Lifting/S2 (late)	11	4, 8, 12, 30	2
090_H_b2_q1a	S3 (early), Lifting/S2 (late)	24, 39	7-11, 23	2
090_L_b2_q1	S2 (early), Lifting/S2 (late)	4, 7, 34	4, 7-10, 12, 16, 22, 29, 38	1, 2
090b_H_b2_i3_q1	Lifting (early), Lifting/S2 (late)	38	20, 32	1, 2
090c_H_b2_i2_q1	S2/S3/S23 (early), Lifting/S2 (late)	too few samples	too few samples	2
105_H_b2_q3	S2 (early), Lifting/S2 (late)	37	10	1, 2
105_L_b2_q3	S2/S3/S23 (early), Lifting/S2 (late)	14, 31	7-8, 12, 21, 31, 38	2
120_H_b2_q4	S1/S2 (early), Lifting/S2 (late)	< 8	2-3, 35	3
135_H_b2_q5	S12/Lifting	5, 24, 31	2, 5-11, 35	1, 3
135_L_b2_q6a	S12	28	5-20, 32	1
150_H_b2_q5	S12	none	2-3, 16, 35	1
150_L_b2_q8a	S12	35	9, 15, 32	1
150_L_b2_q9	S12	21, 32	12, 21, 31	1
165_H_b2_q4	S2(early)/S12(later)	2-3, 30	2-3, 21, 35	1
165_L_b2_q6	S12	7-8,	< 9, 11, 35	1
180_H_b1_q1	S2/S12	35	10, 13, 21, 30, 35	1
180_L_b2_q4	S12	30	21, 33	1
180b_H_b2_q3	S12	30, 40	2, 18, 30	1
180c_H_b2_q3	S12	32	2, 18, 20, 31	1

Notes:

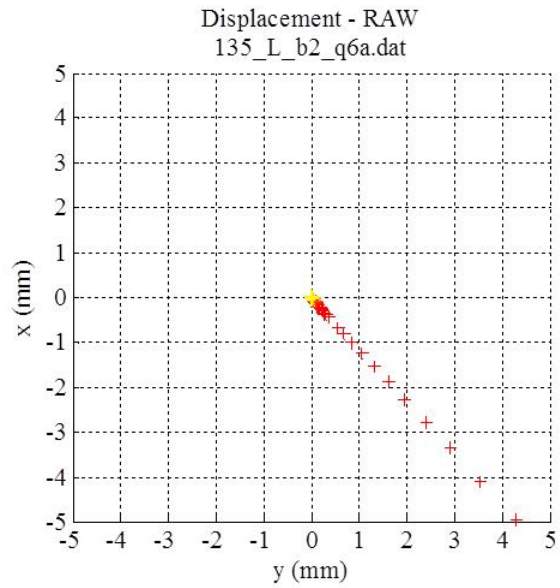
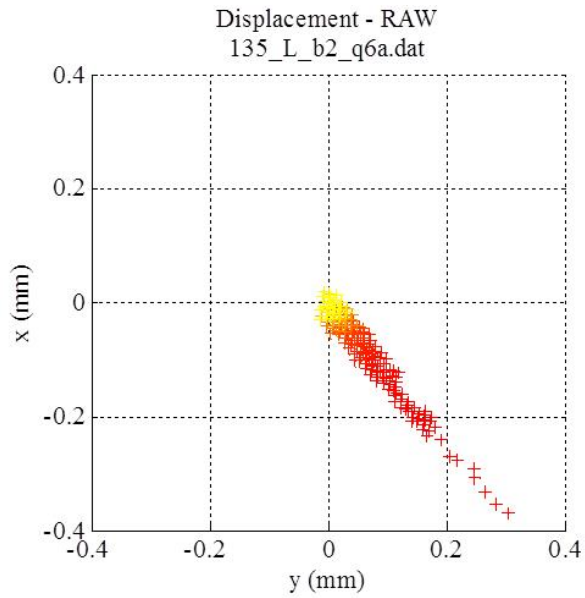
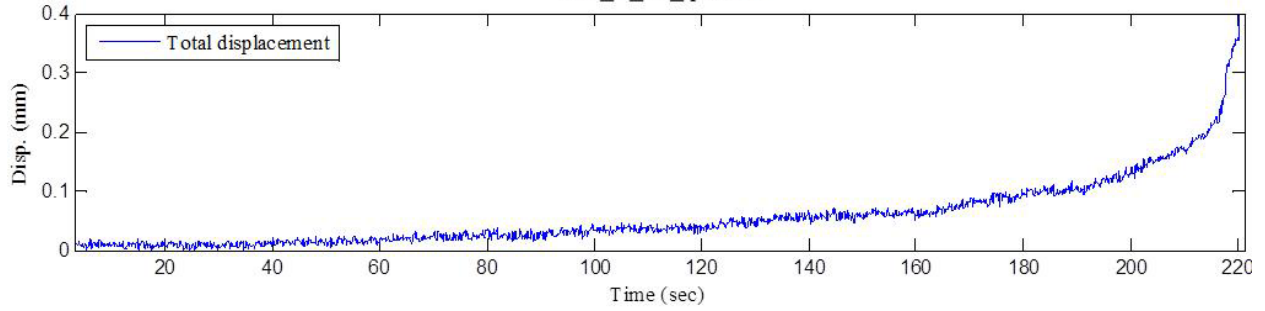
^a Based on displacement data plotted on stereonet

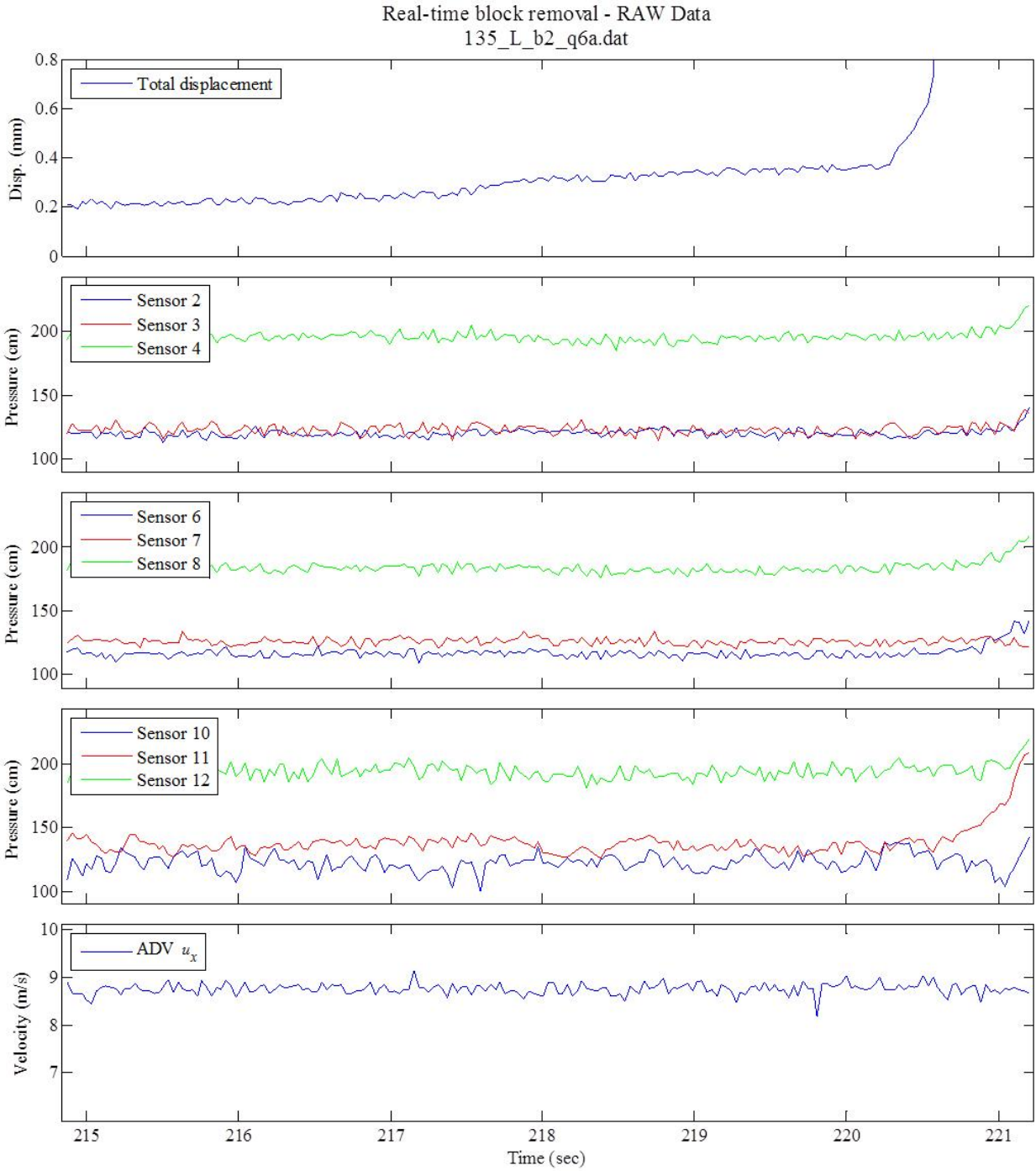
^b Dominant freq. for displacement, *d* and pressure, *P*. From power spectral density analysis (model scale values)

Block response 1 – supplemental figures

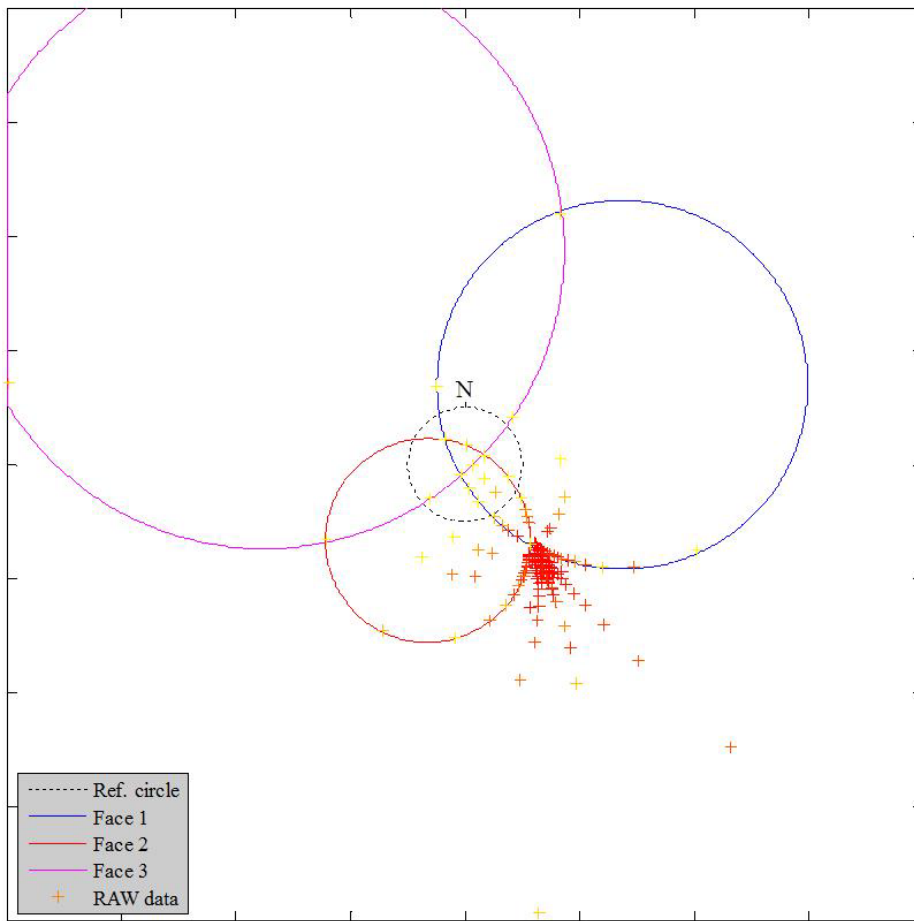
$\psi = 135$ deg., Low T_u , Block 2, Q_6

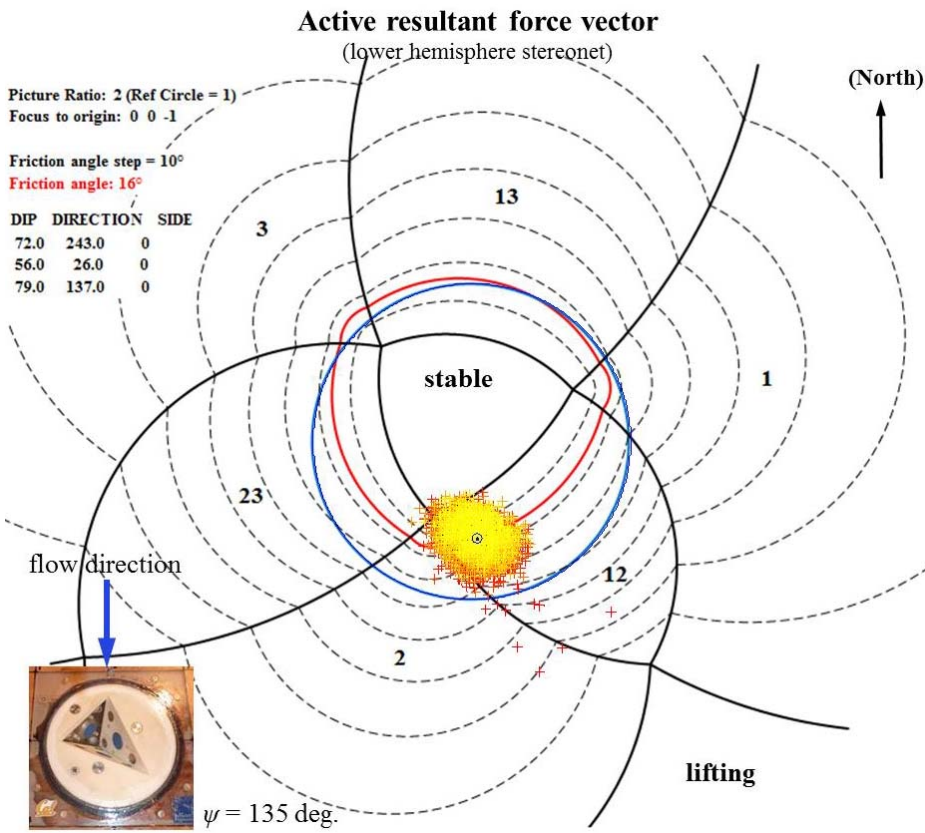
Real-time block removal - FILTERED Data
135_L_b2_q6a.dat



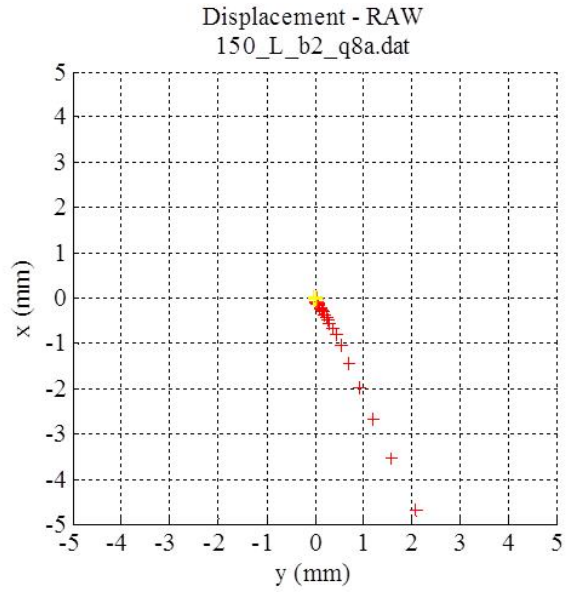
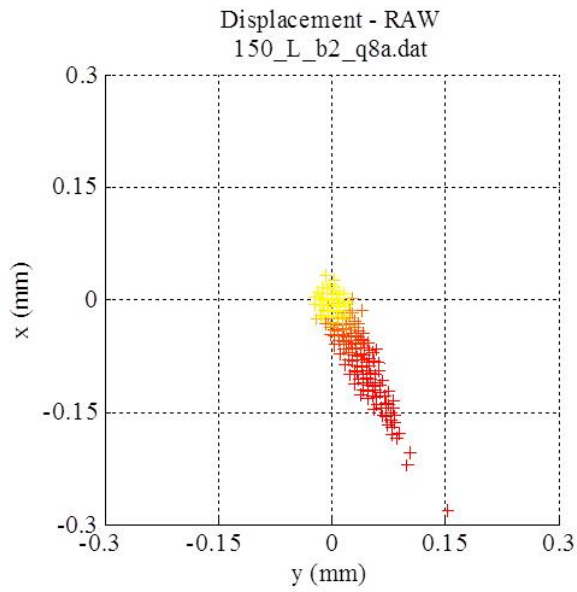
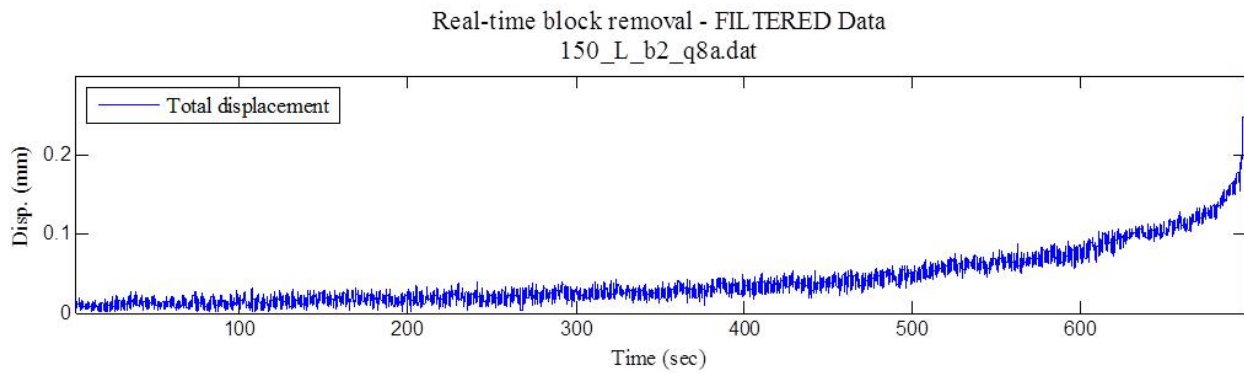


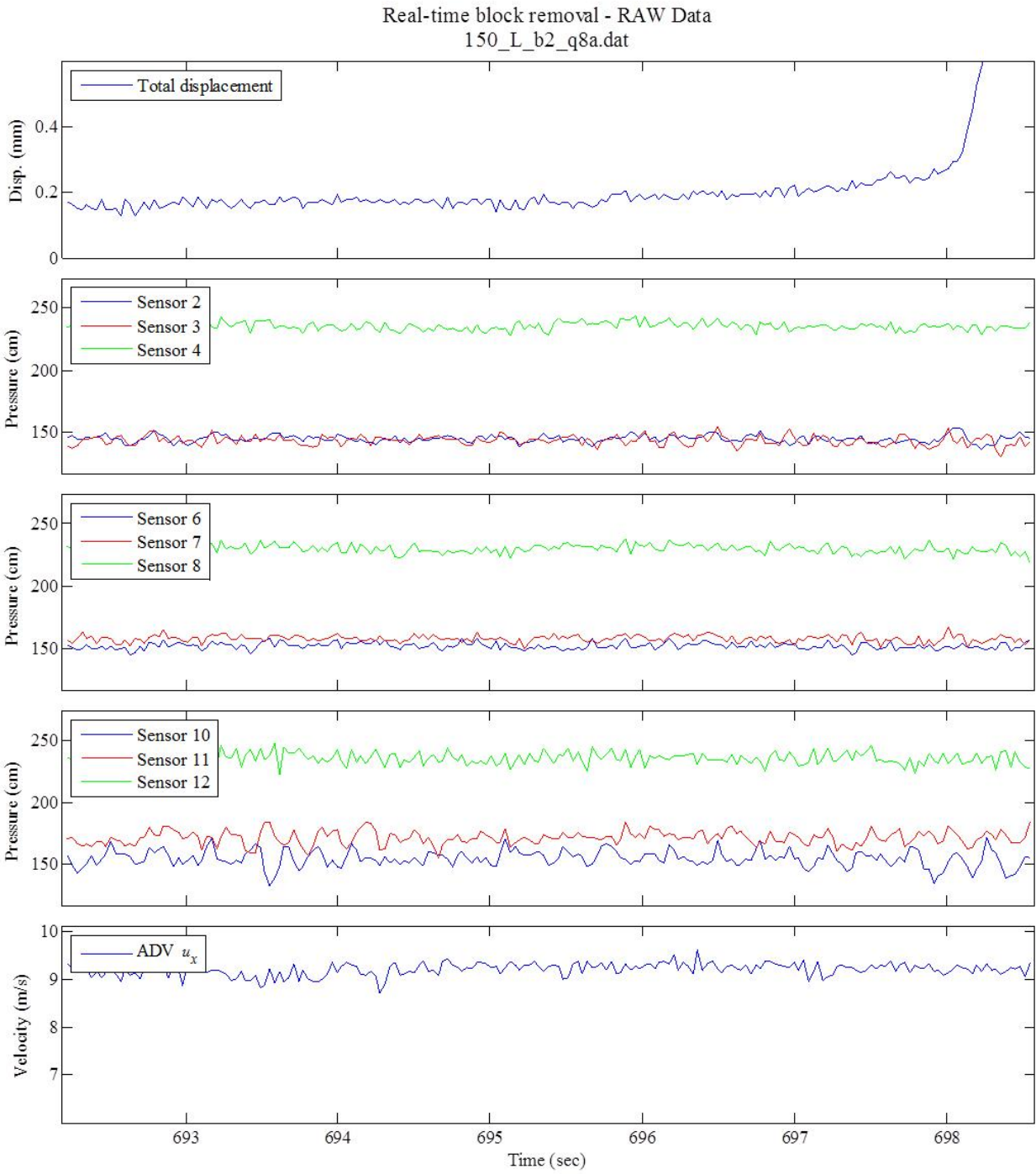
RAW displacement vector - lower hemisphere stereonet
135_L_b2_q6a.dat



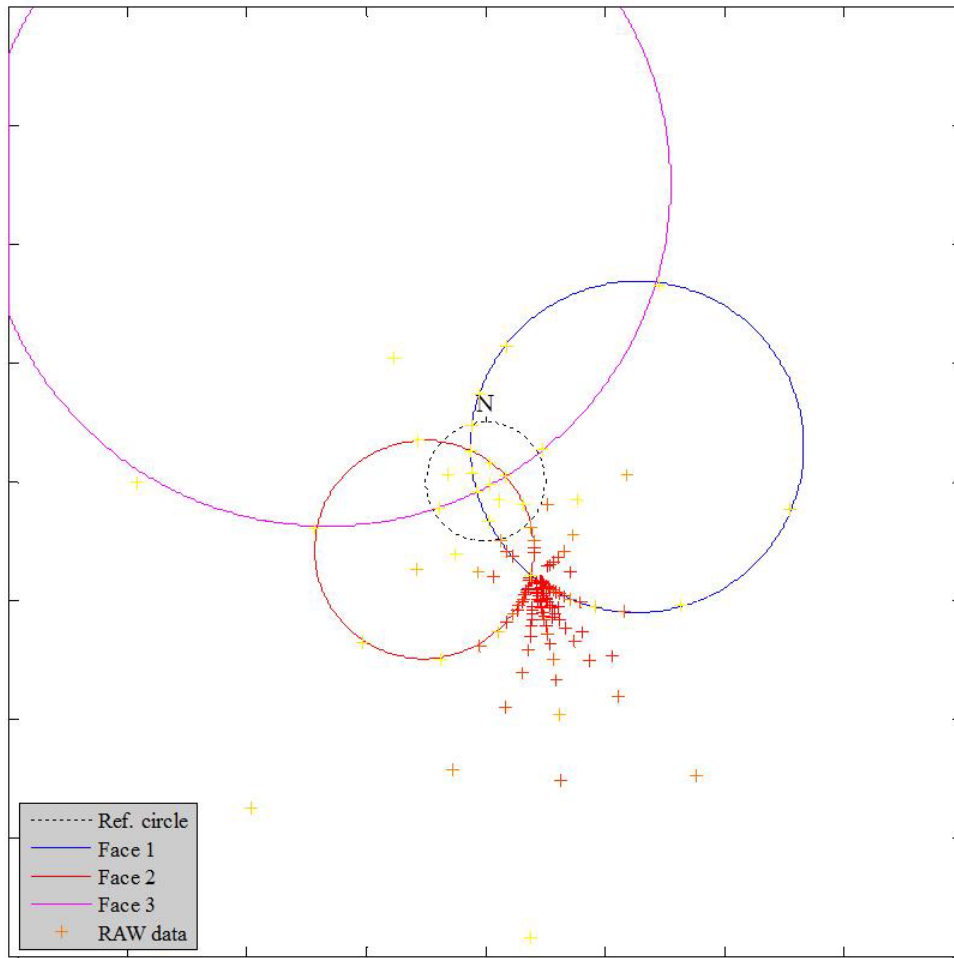


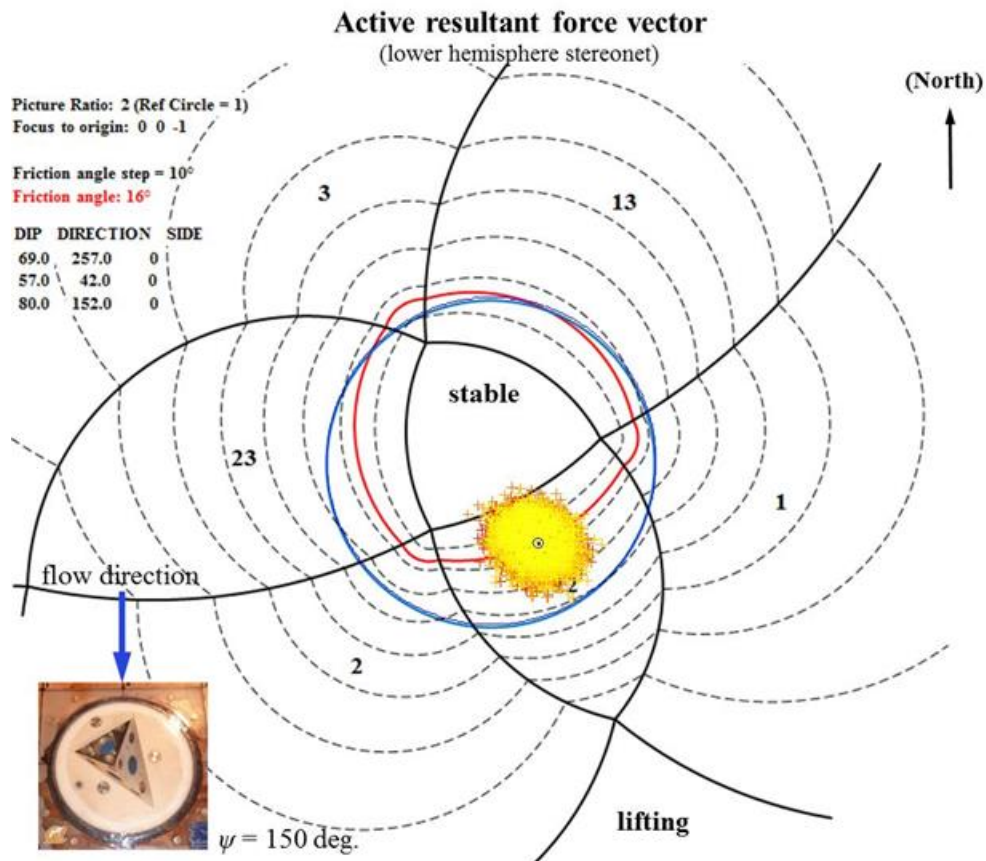
$\psi = 150$ deg., Low T_u , Block 2, Q_8



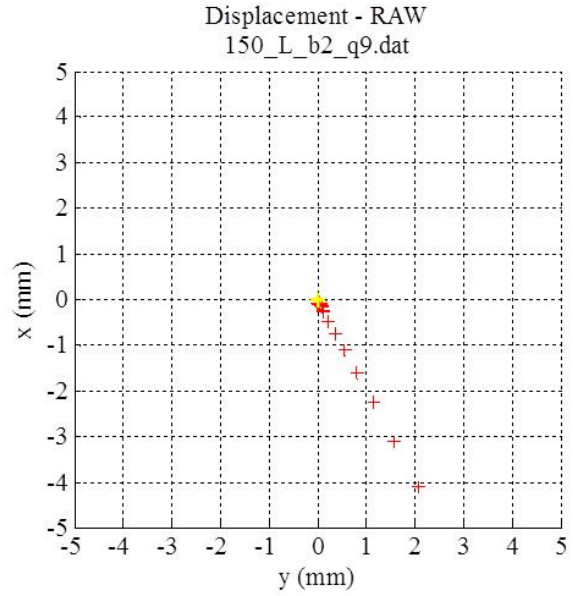
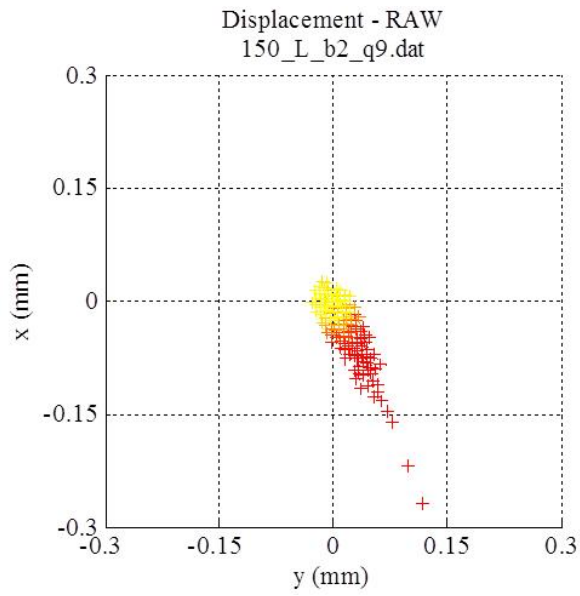
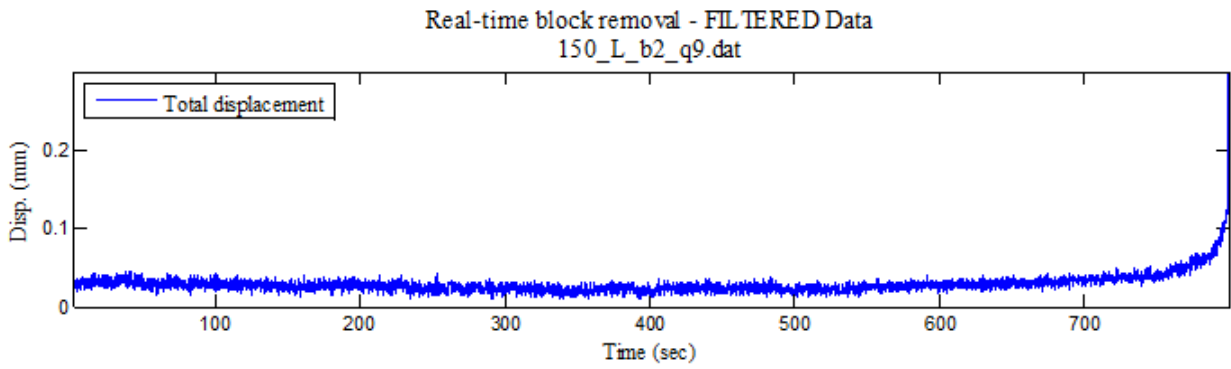


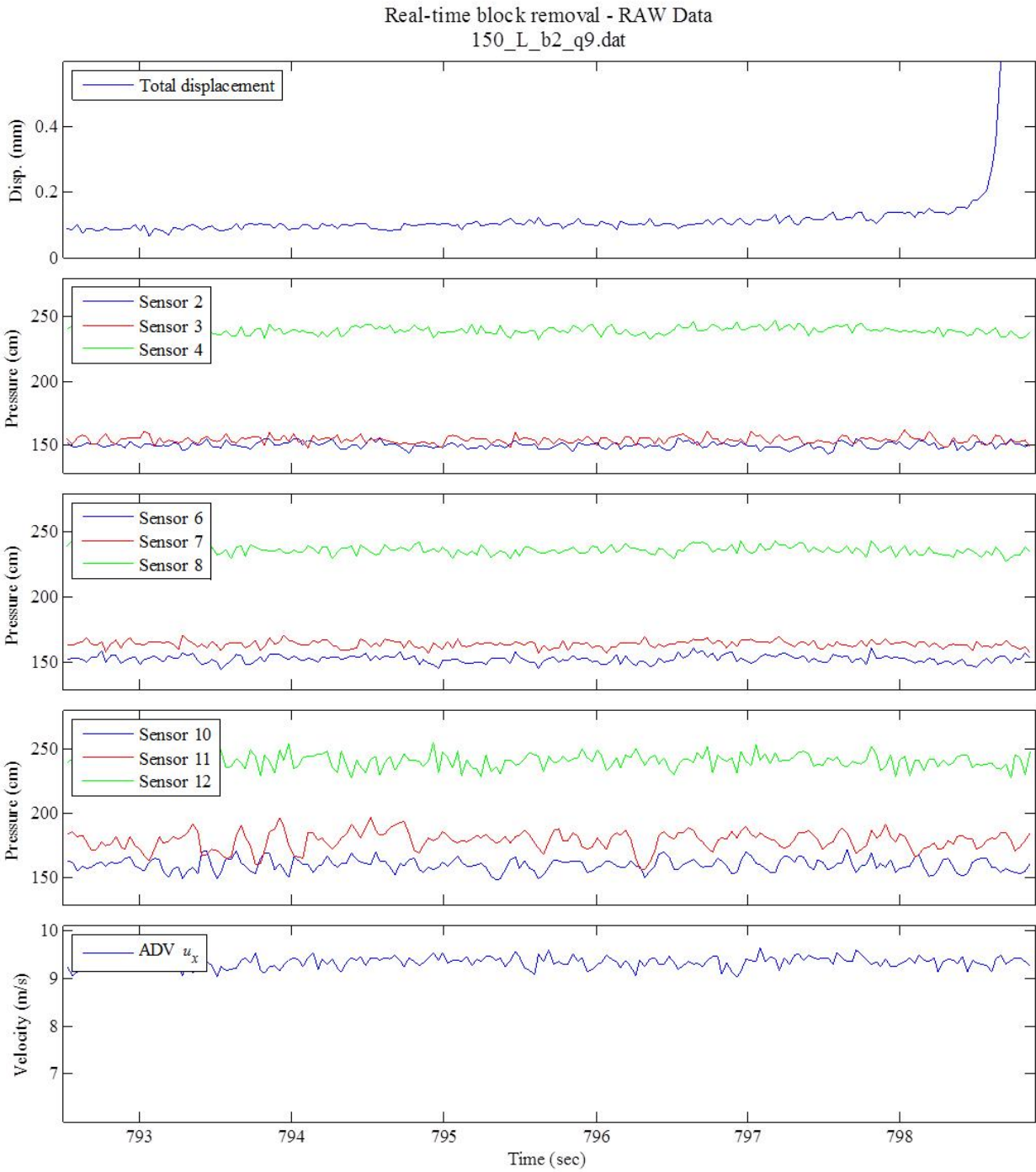
RAW displacement vector - lower hemisphere stereonet
150_L_b2_q8a.dat



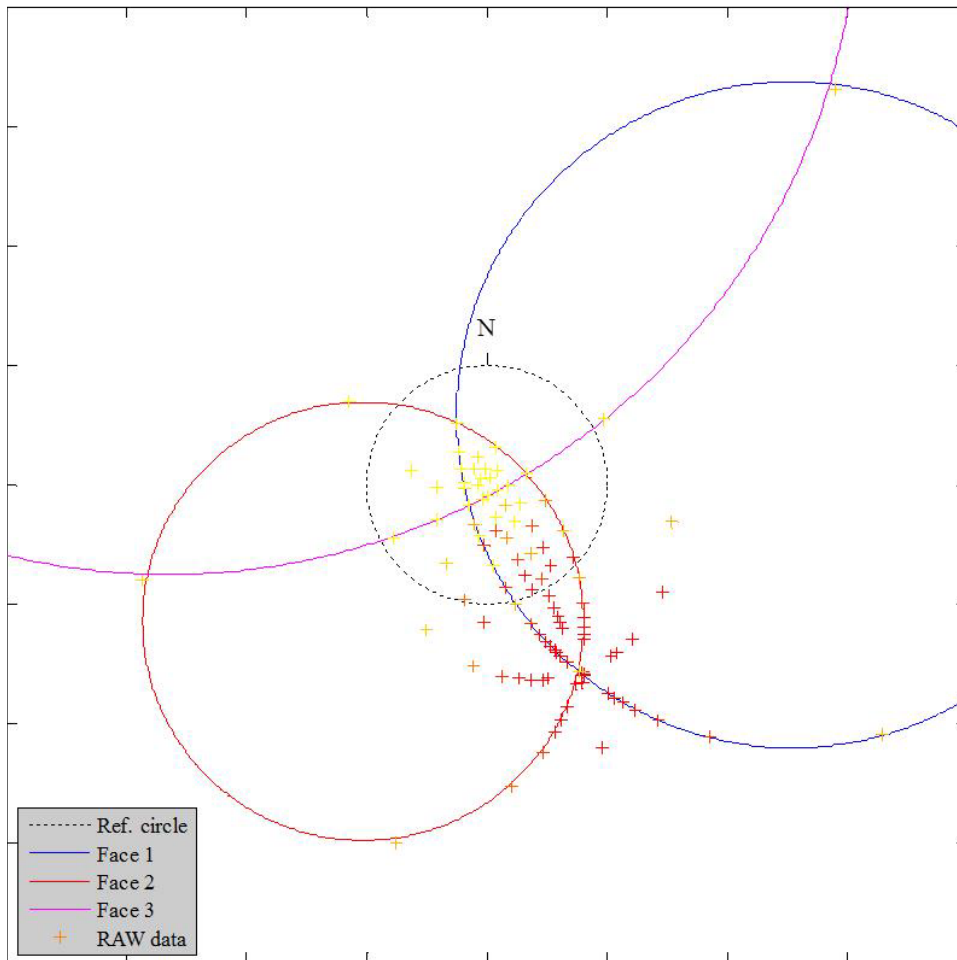


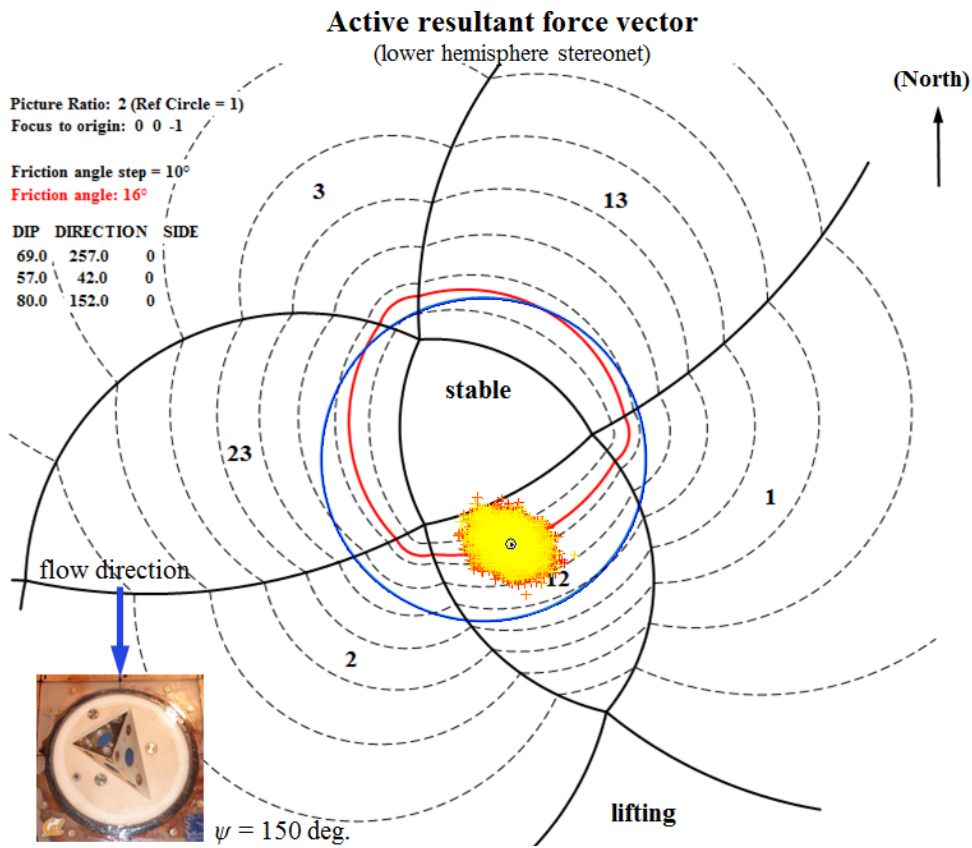
$\psi = 150$ deg., Low T_u , Block 2, Q_9





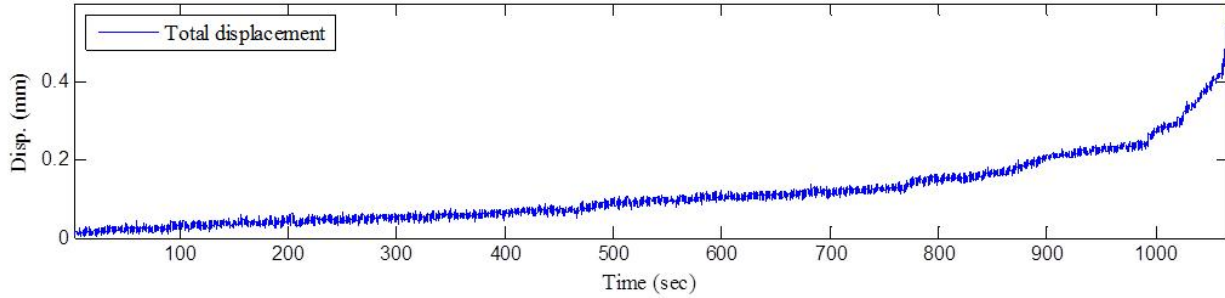
RAW displacement vector - lower hemisphere stereonet
150_L_b2_q9.dat



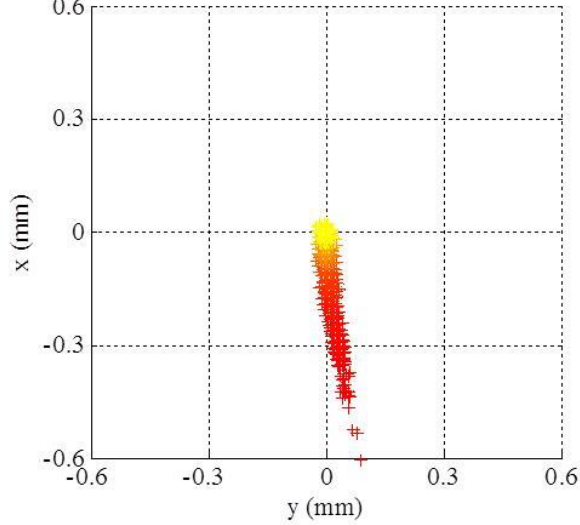


$\psi = 165$ deg., High T_u , Block 2, Q_4

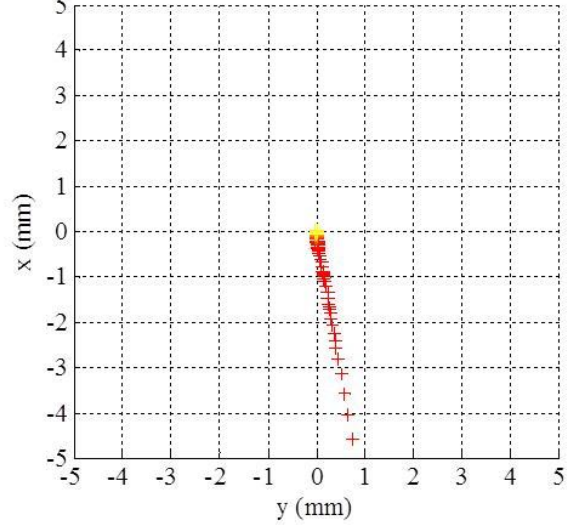
Real-time block removal - FILTERED Data
165_H_b2_q4.dat

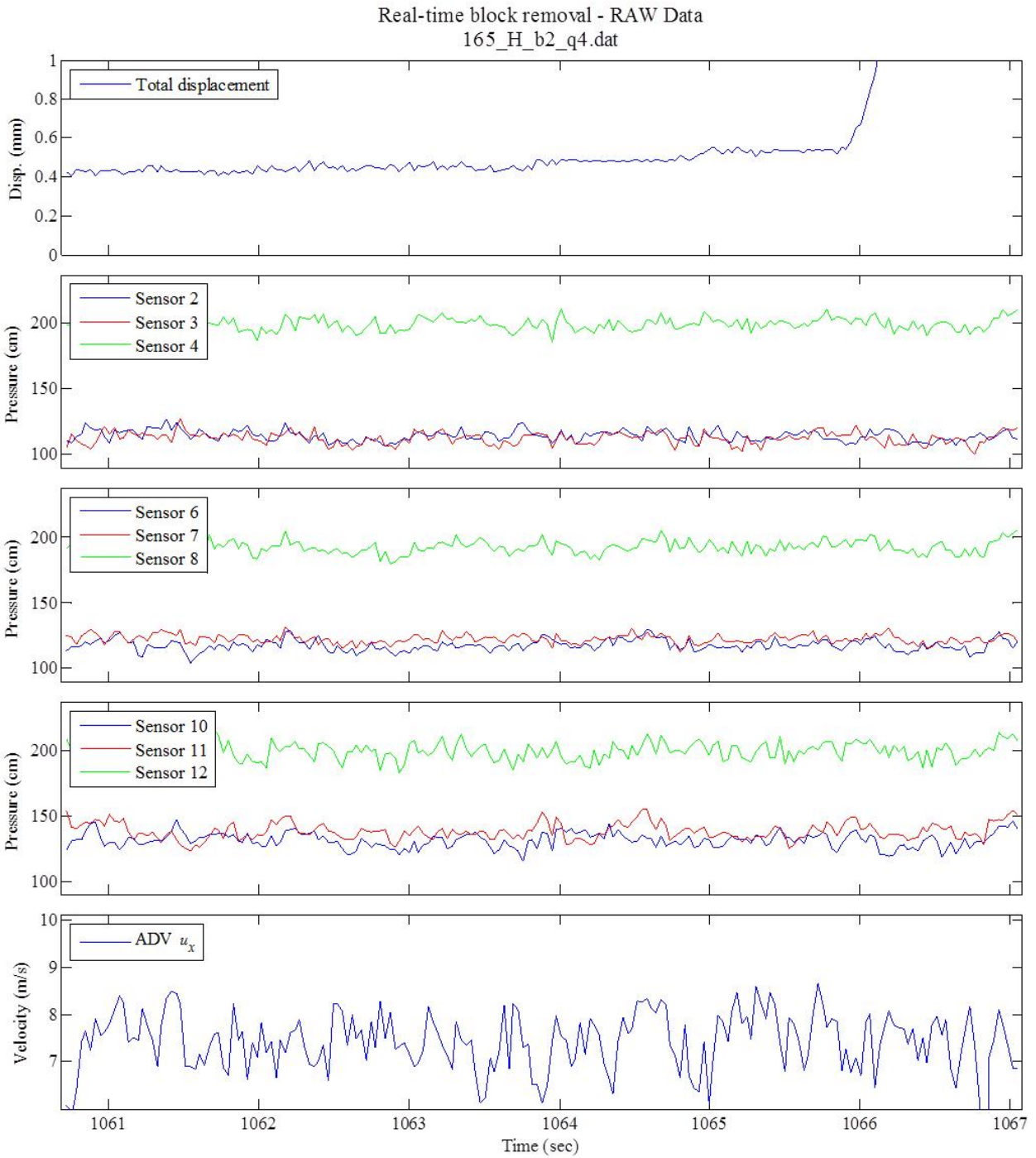


Displacement - RAW
165_H_b2_q4.dat

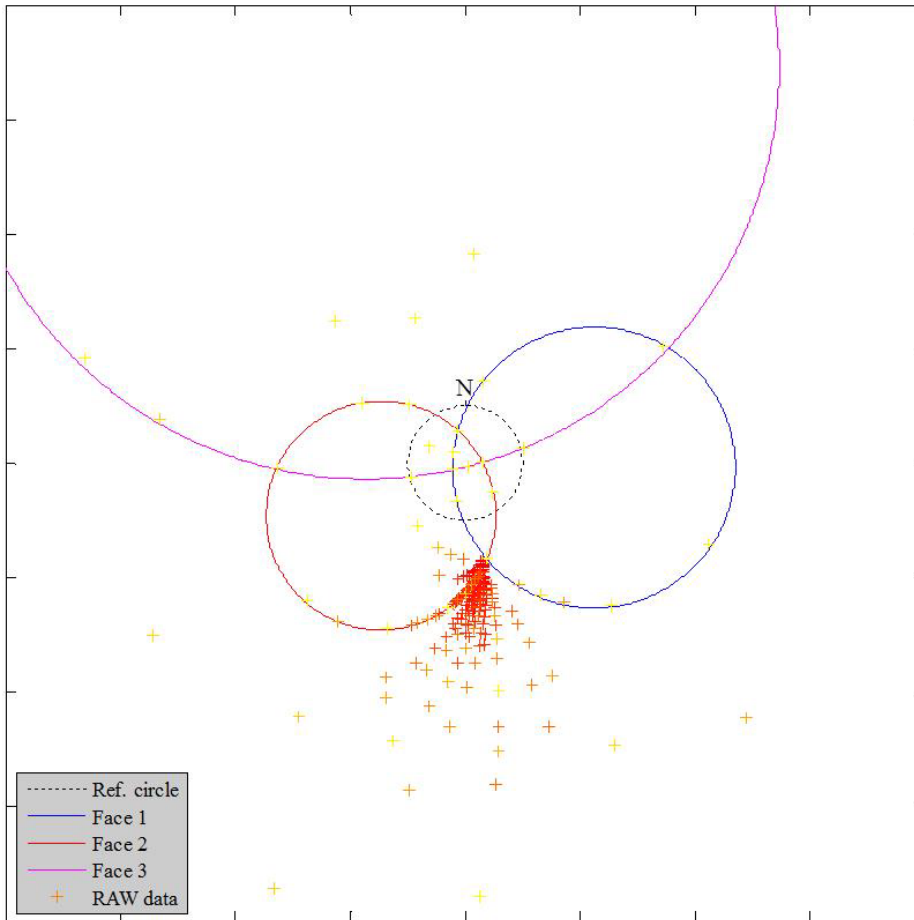


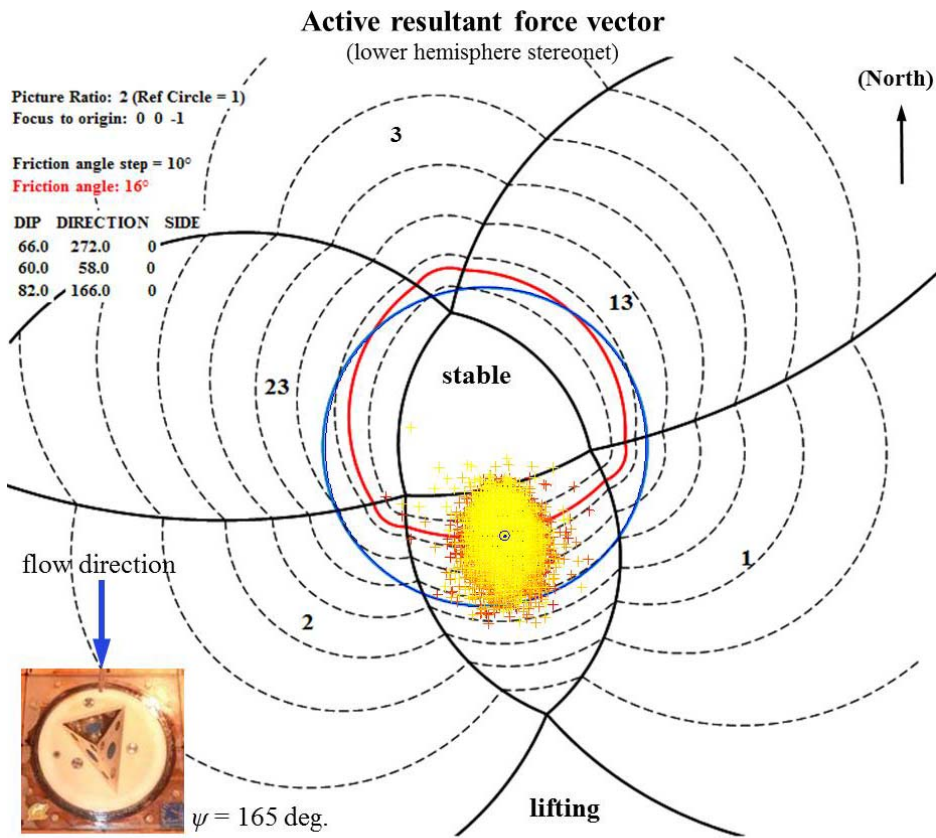
Displacement - RAW
165_H_b2_q4.dat



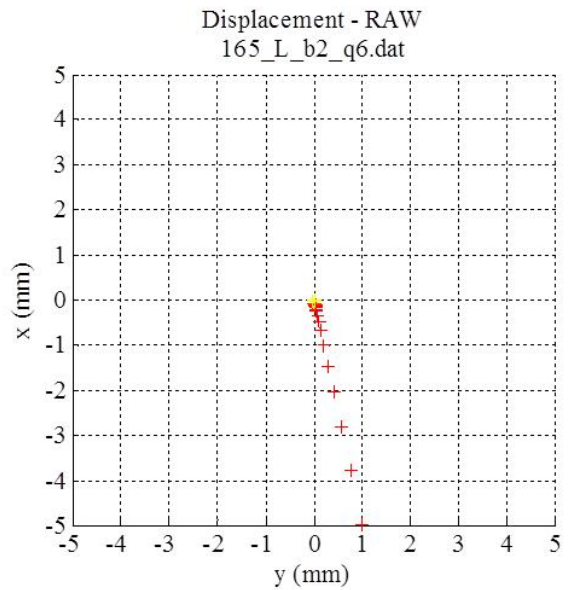
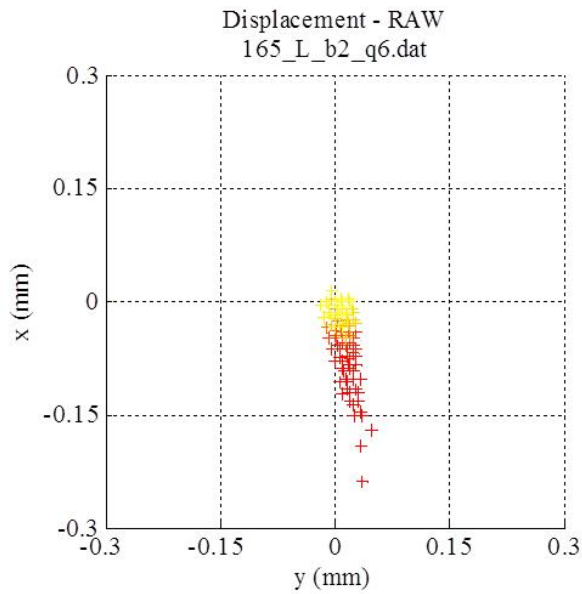
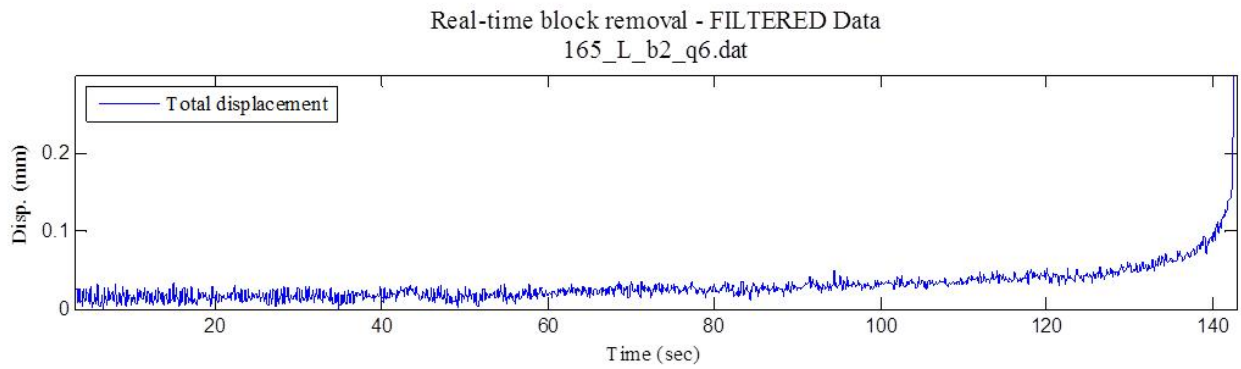


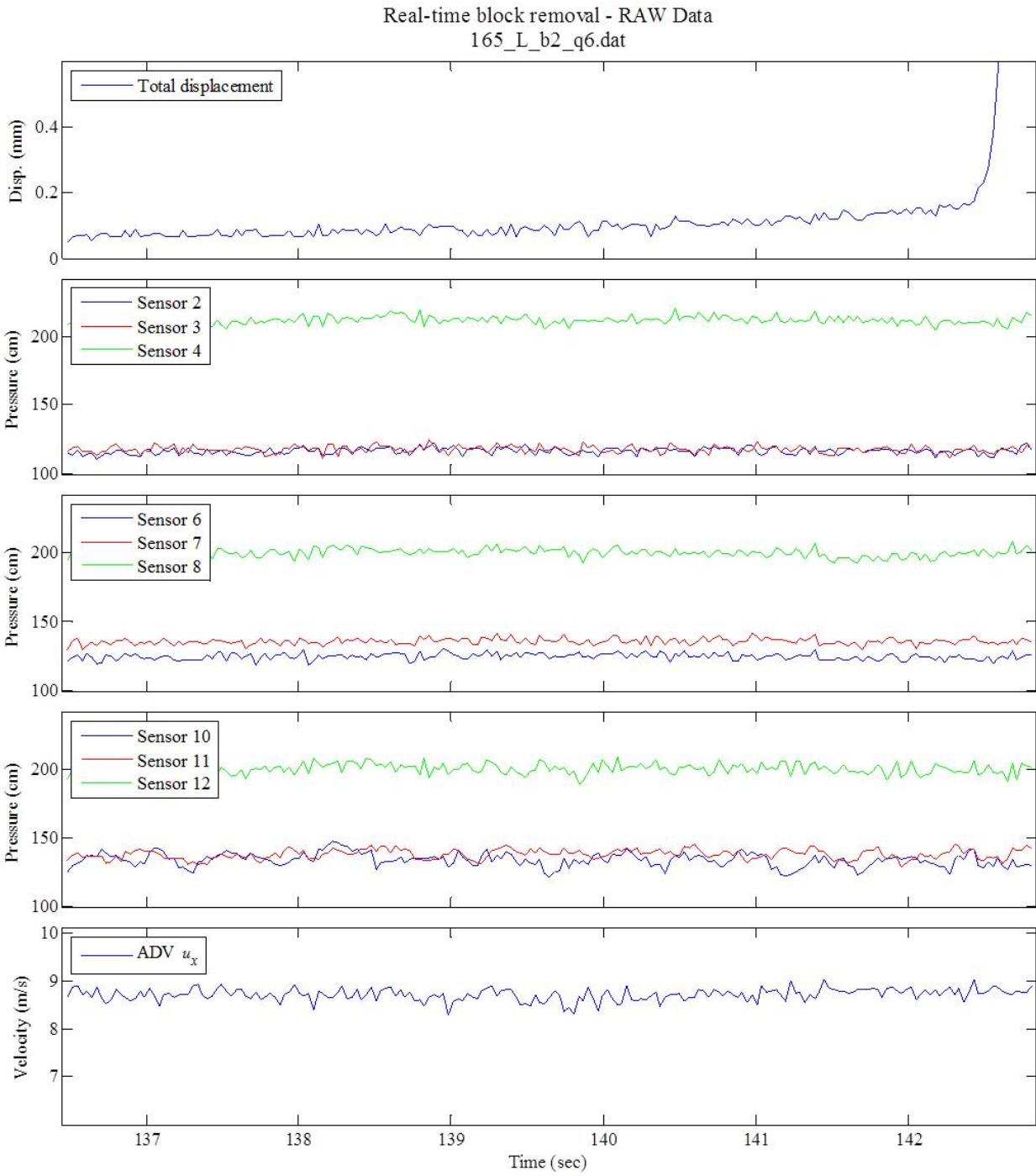
RAW displacement vector - lower hemisphere stereonet
165_H_b2_q4.dat



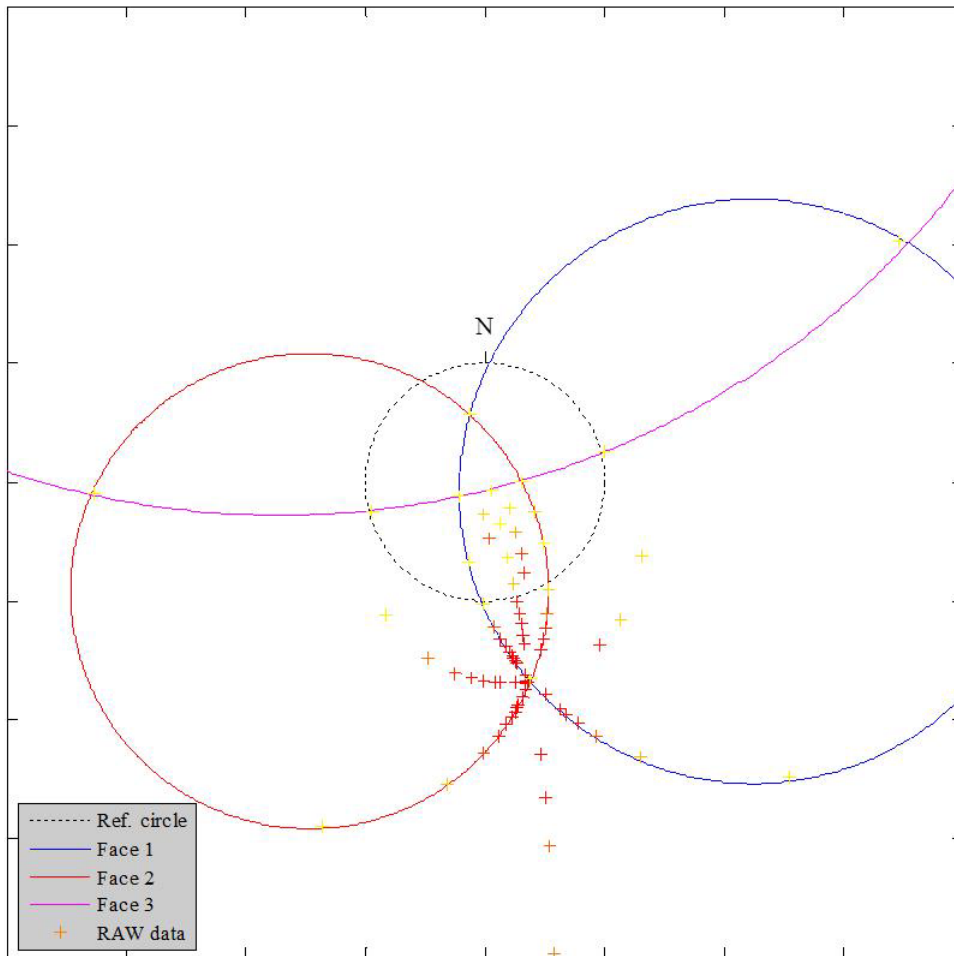


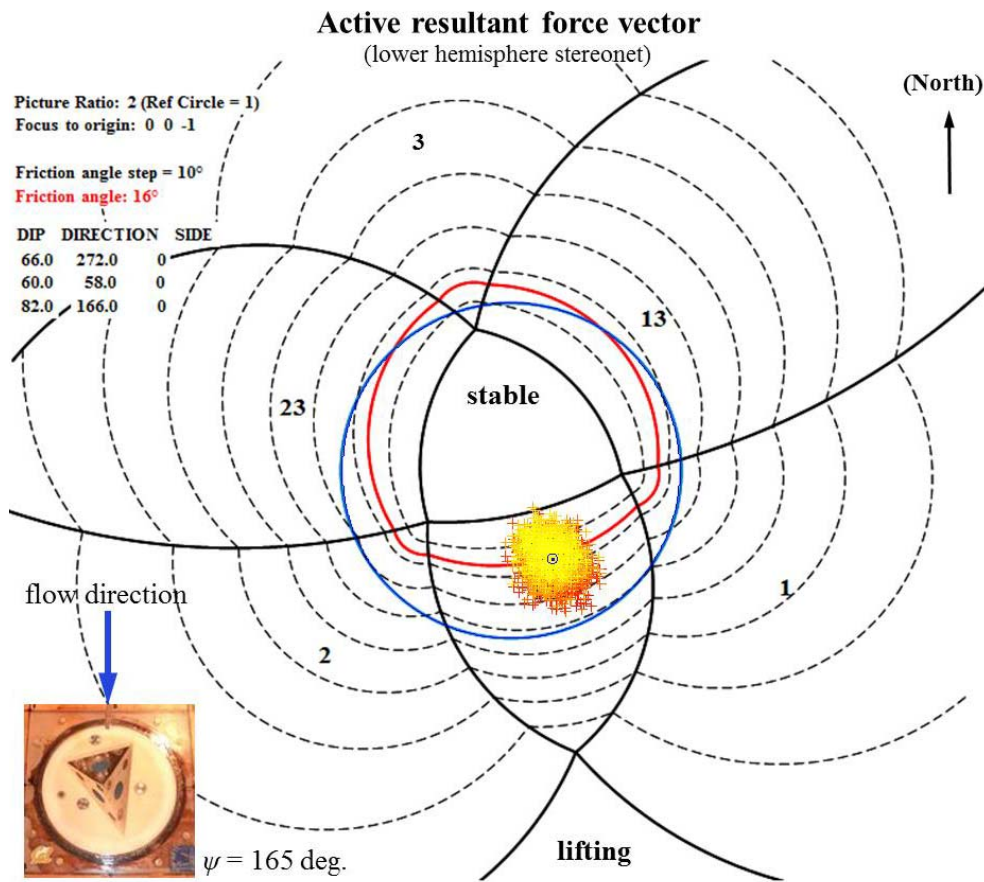
$\psi = 165$ deg., Low T_u , Block 2, Q_6



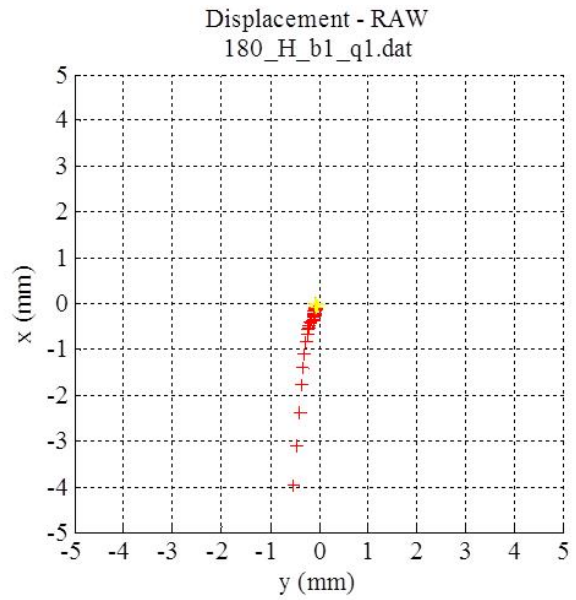
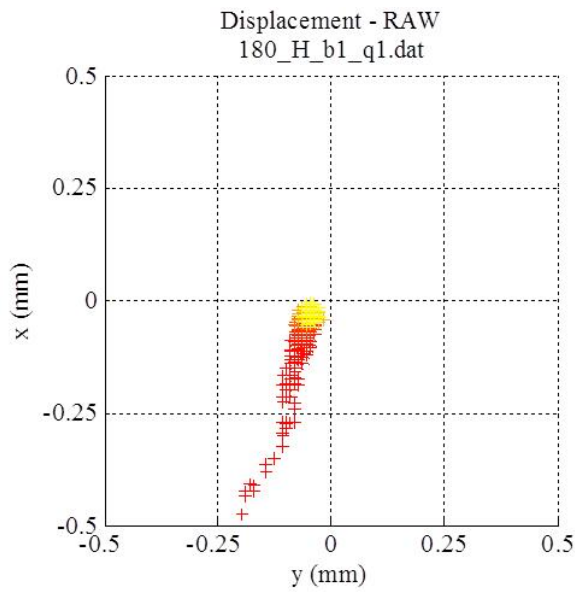
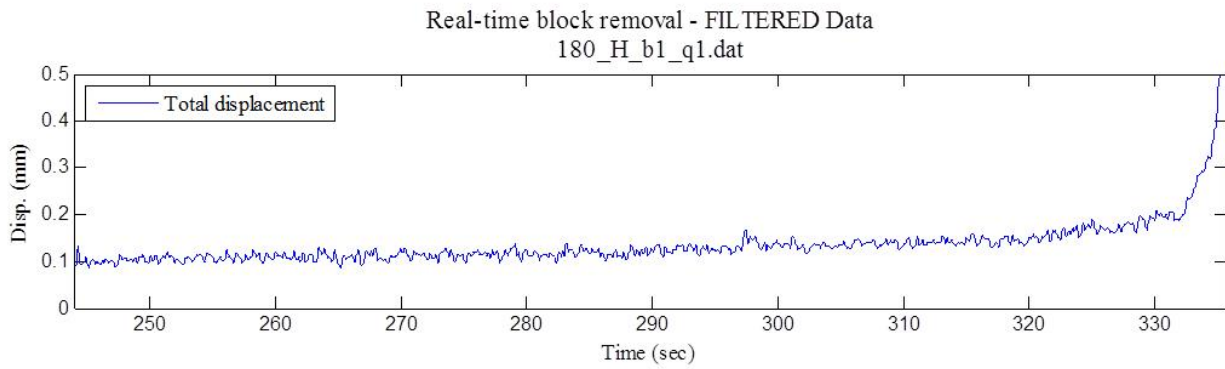


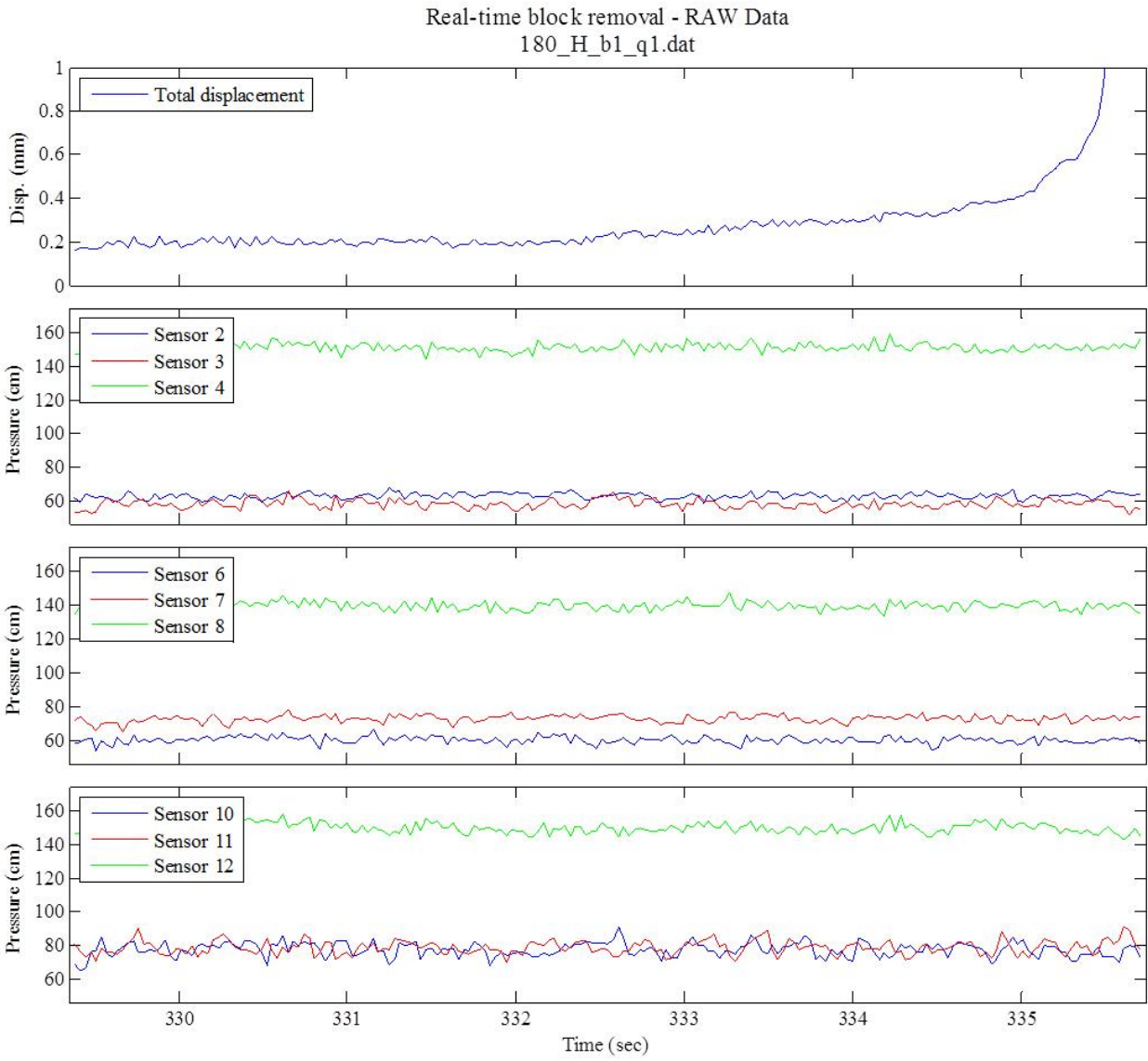
RAW displacement vector - lower hemisphere stereonet
165_L_b2_q6.dat



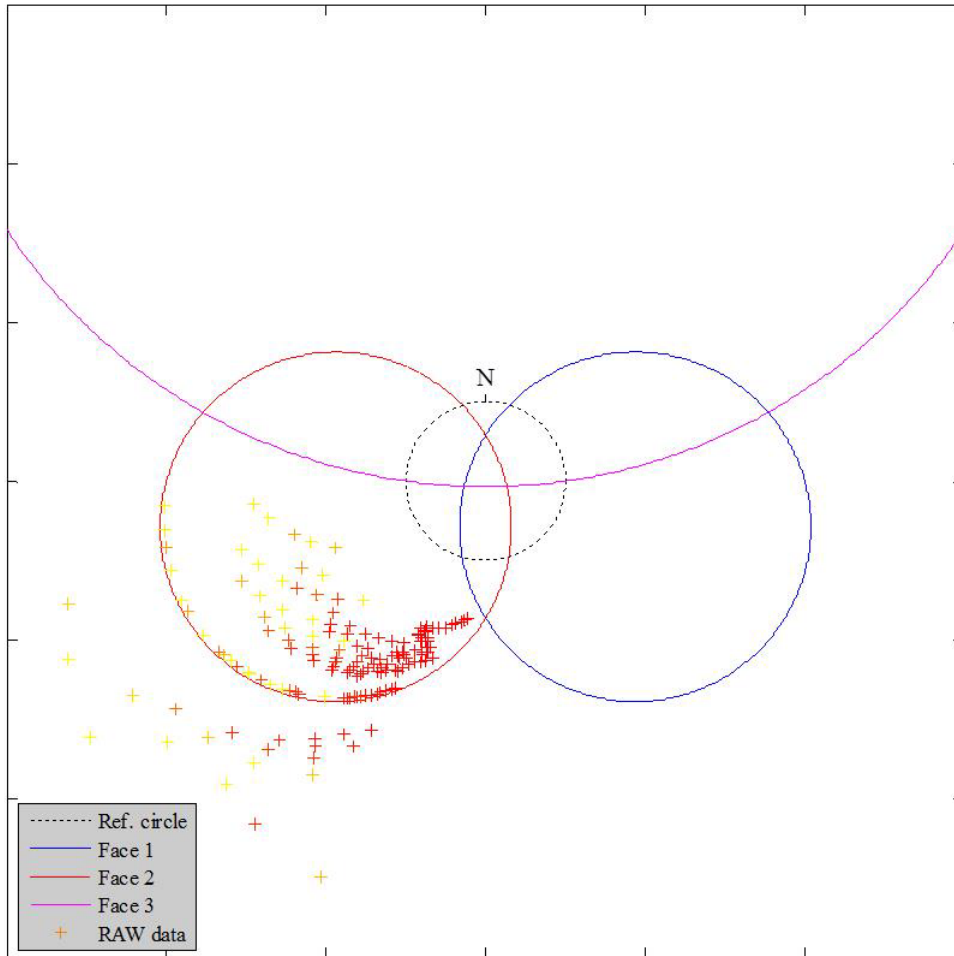


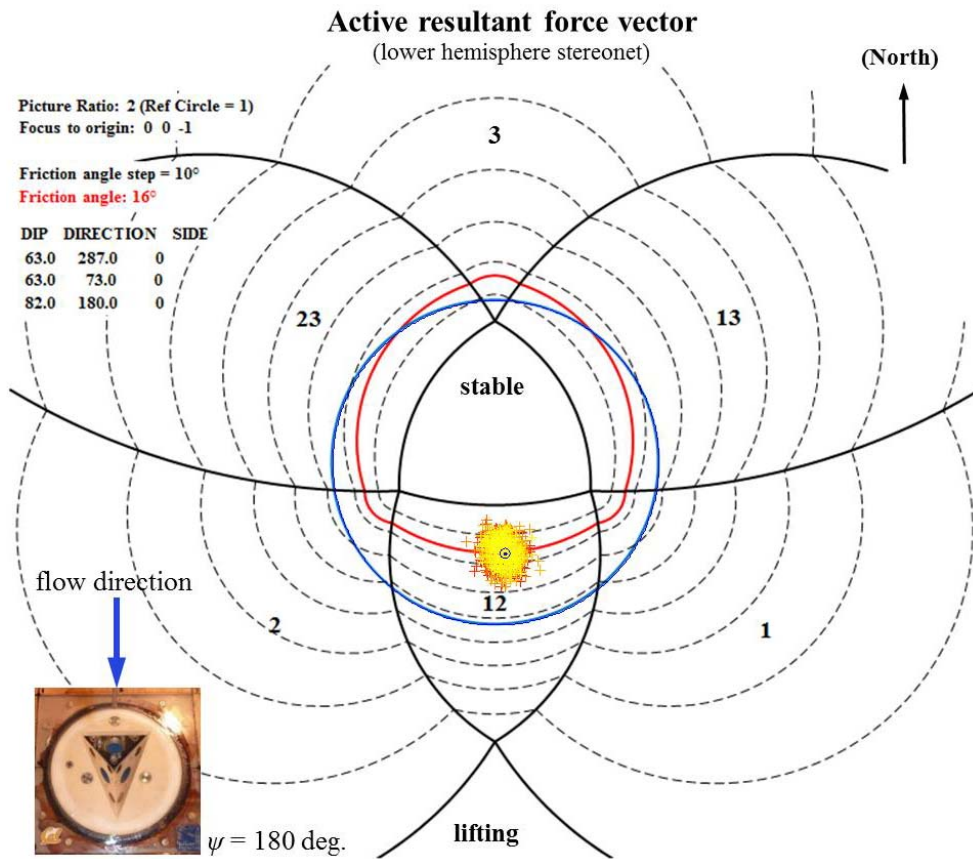
$\psi = 180$ deg., High T_u , Block 1, Q_I



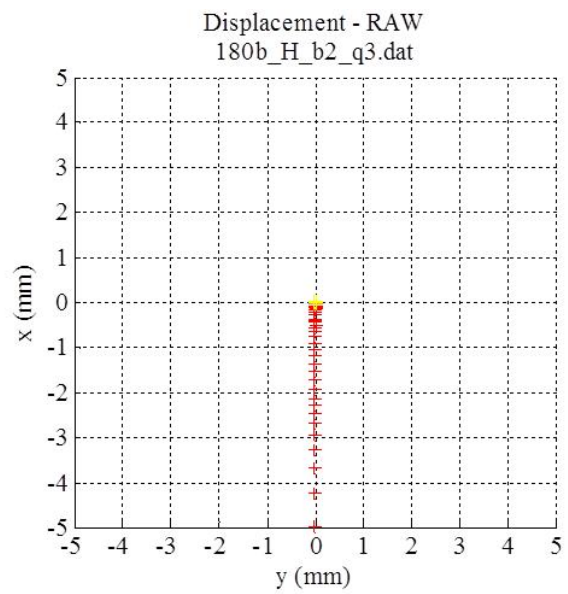
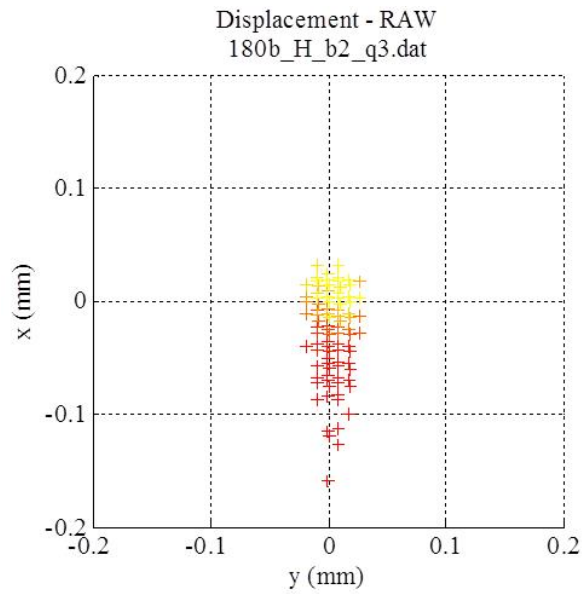
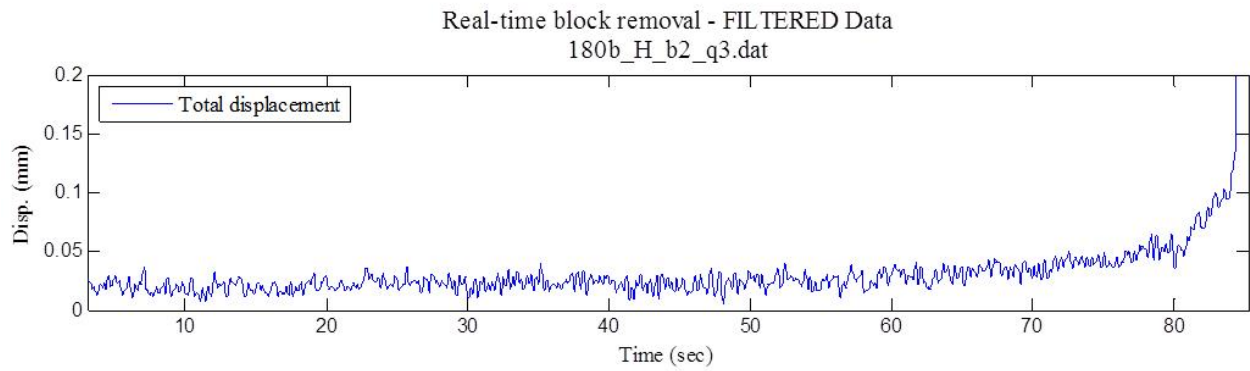


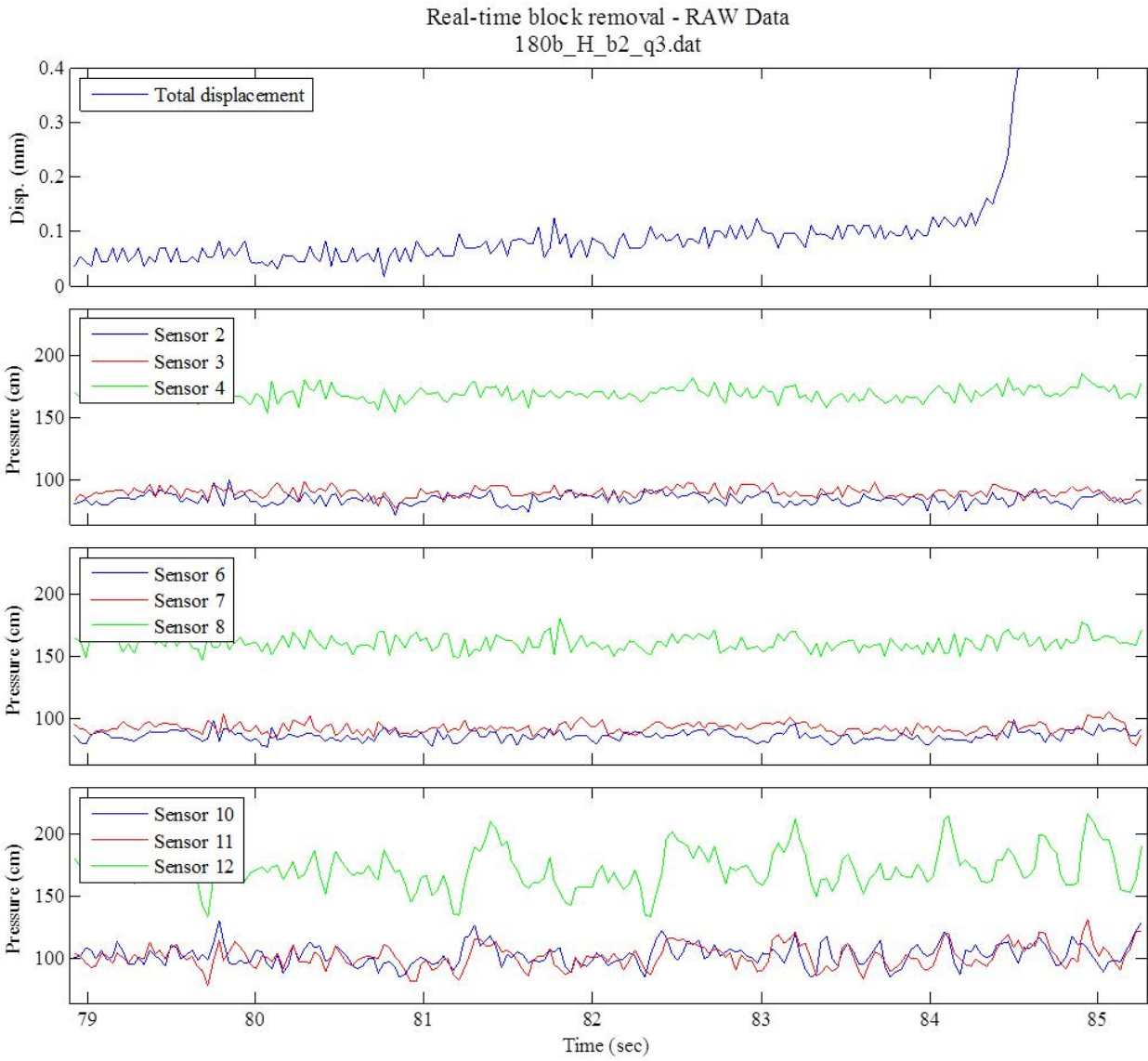
RAW displacement vector - lower hemisphere stereonet
180_H_b1_q1.dat



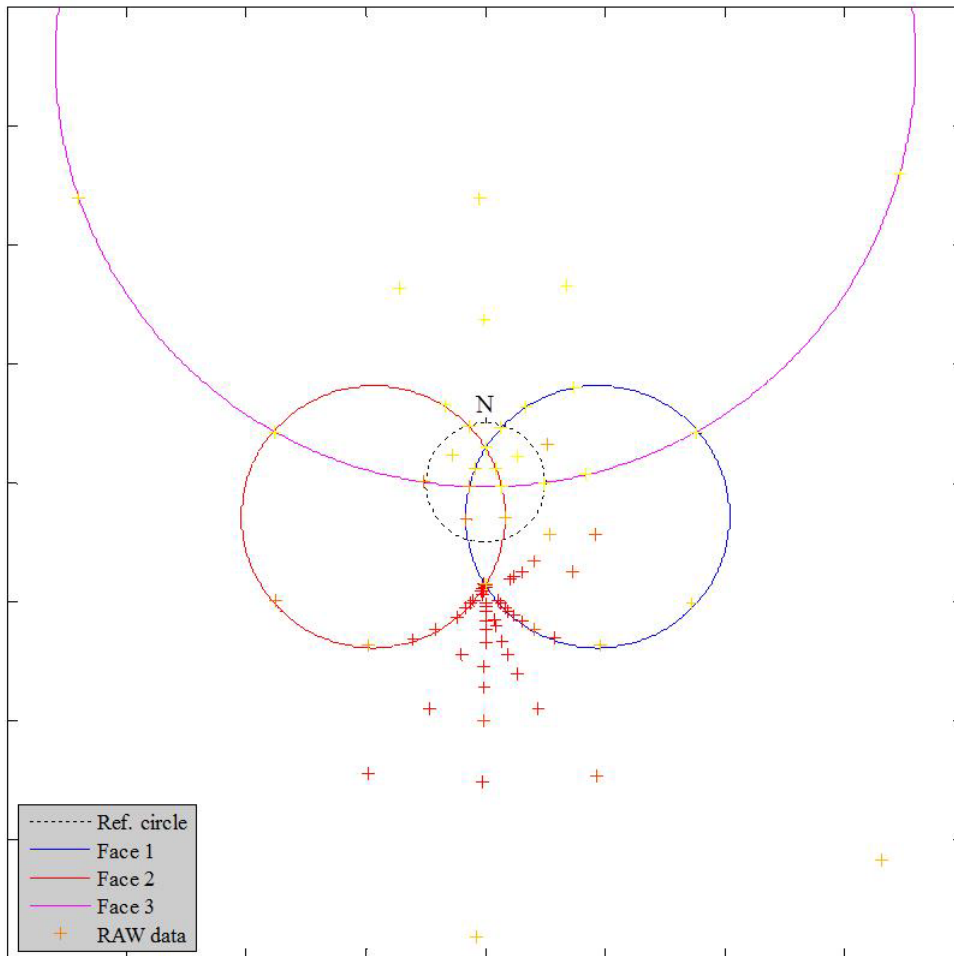


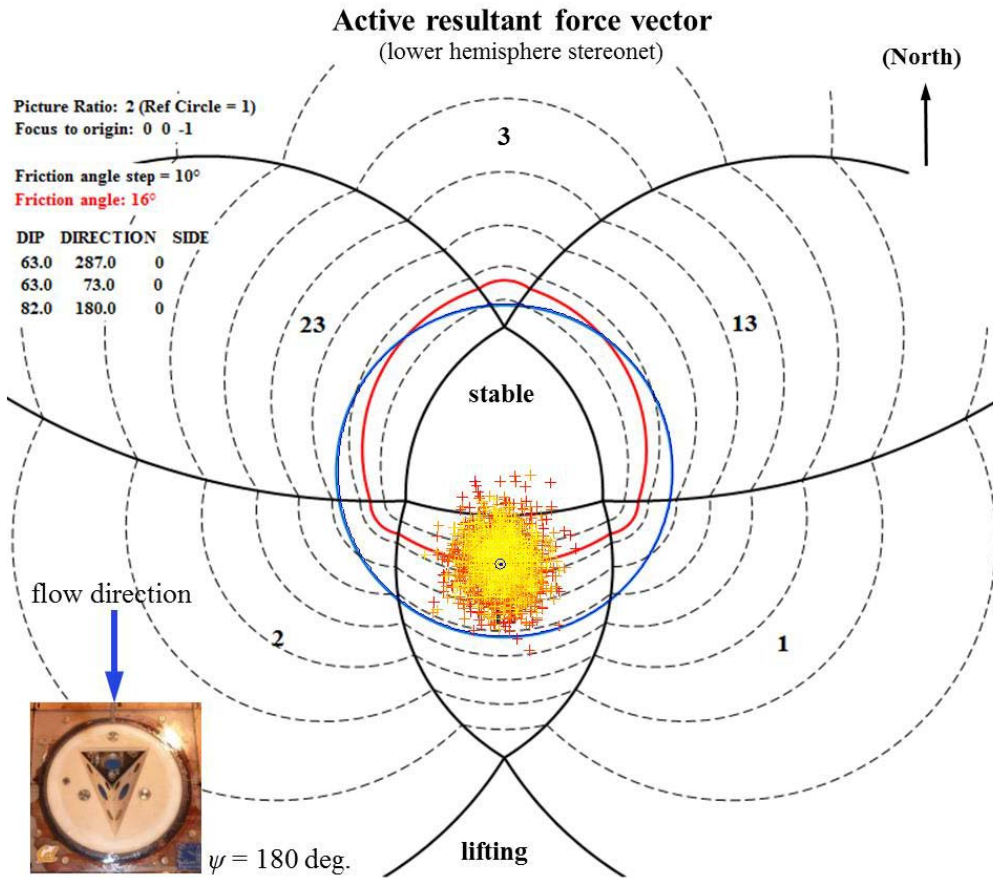
$\psi = 180$ deg., High T_u , Block 2, Q_3



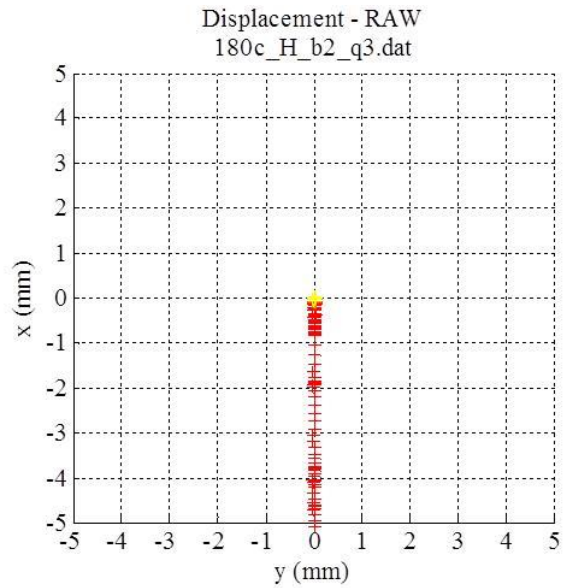
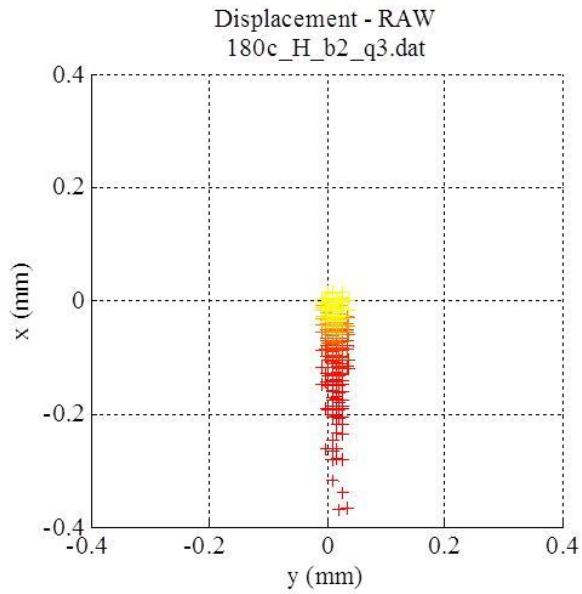
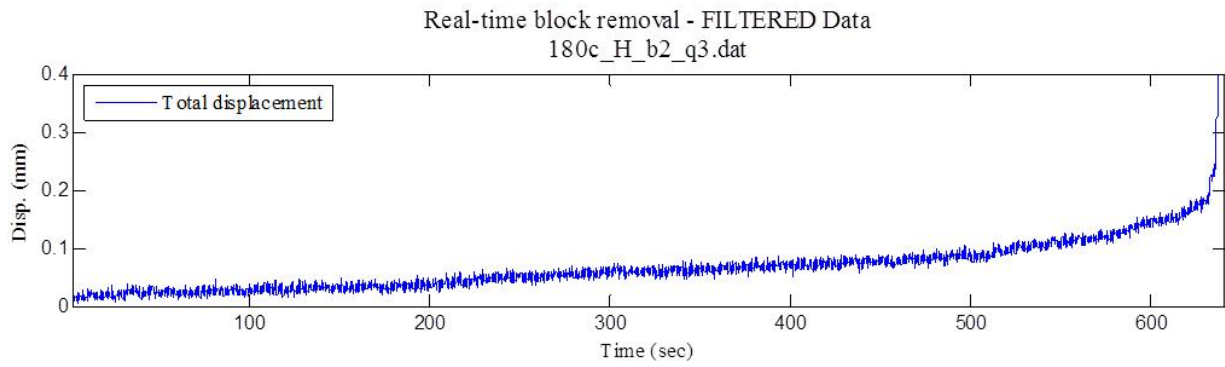


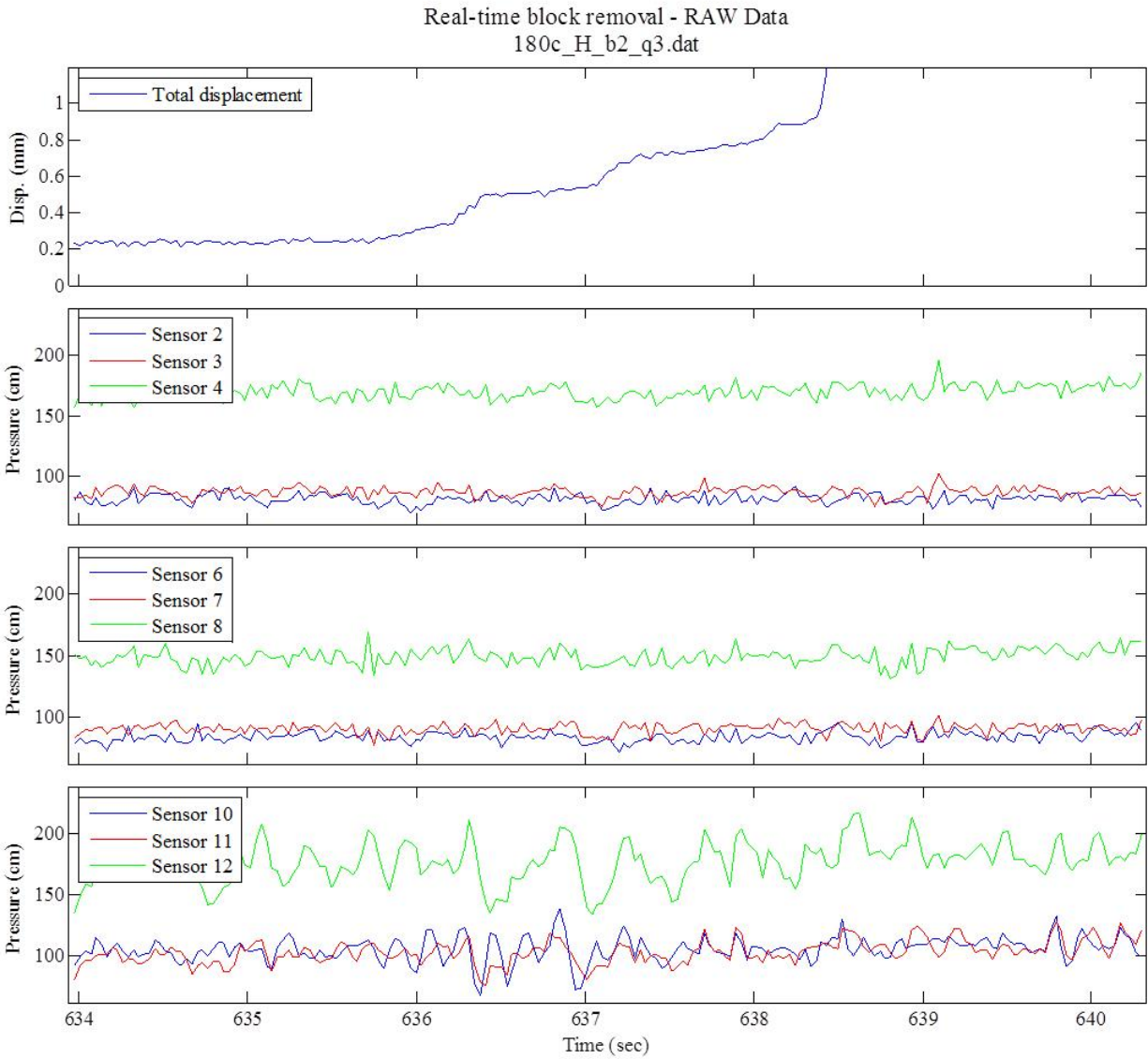
RAW displacement vector - lower hemisphere stereonet
180b_H_b2_q3.dat



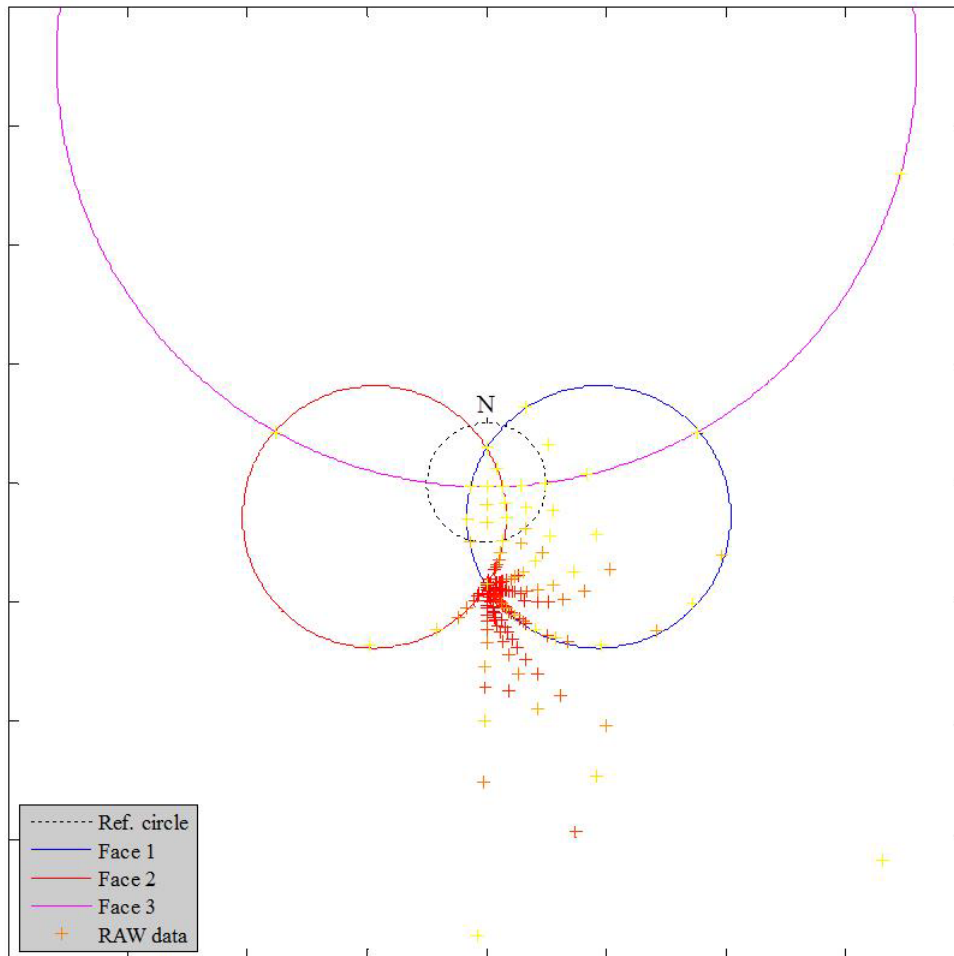


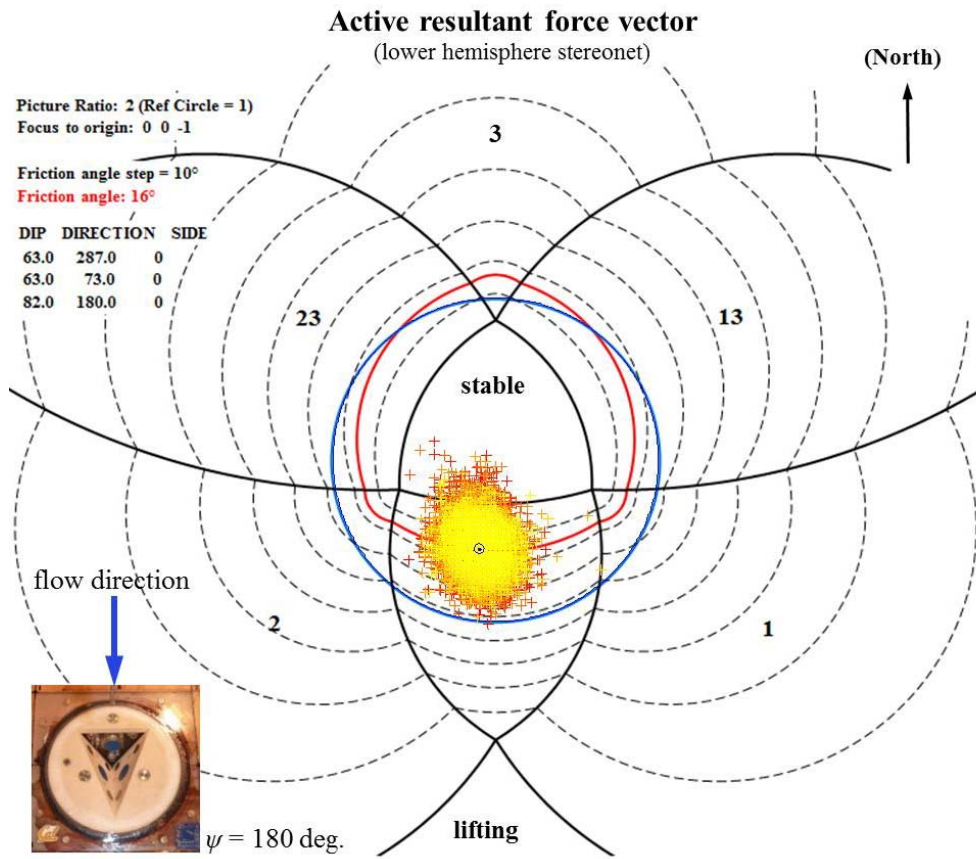
$\psi = 180$ deg., High T_u , Block 2, Q_3





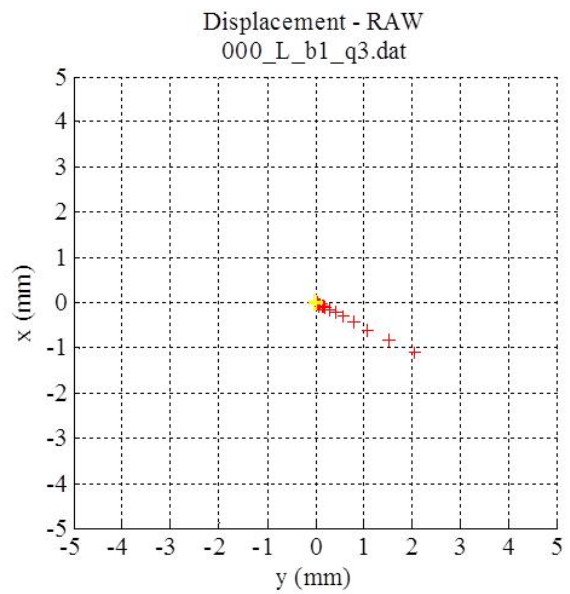
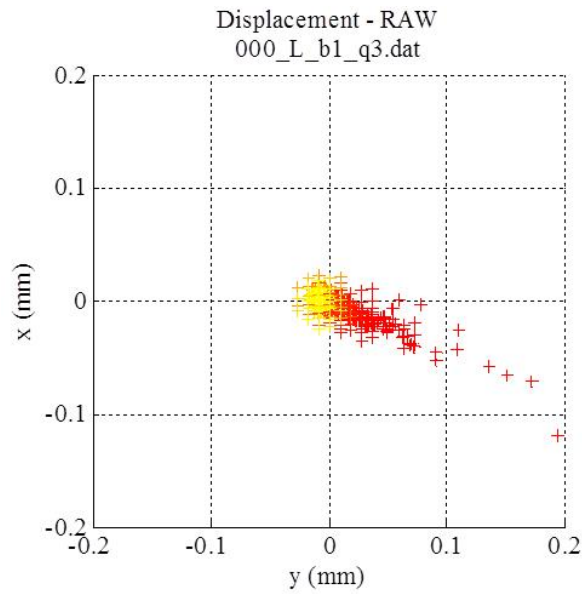
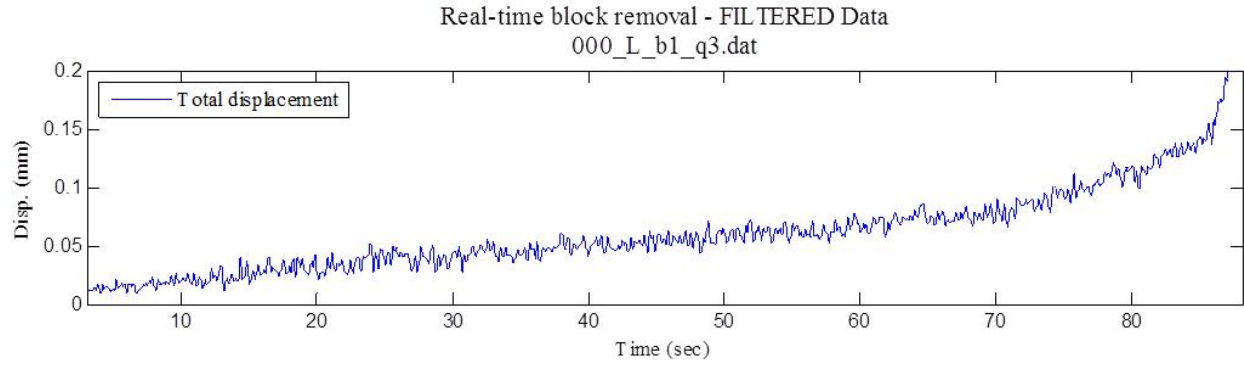
RAW displacement vector - lower hemisphere stereonet
180c_H_b2_q3.dat

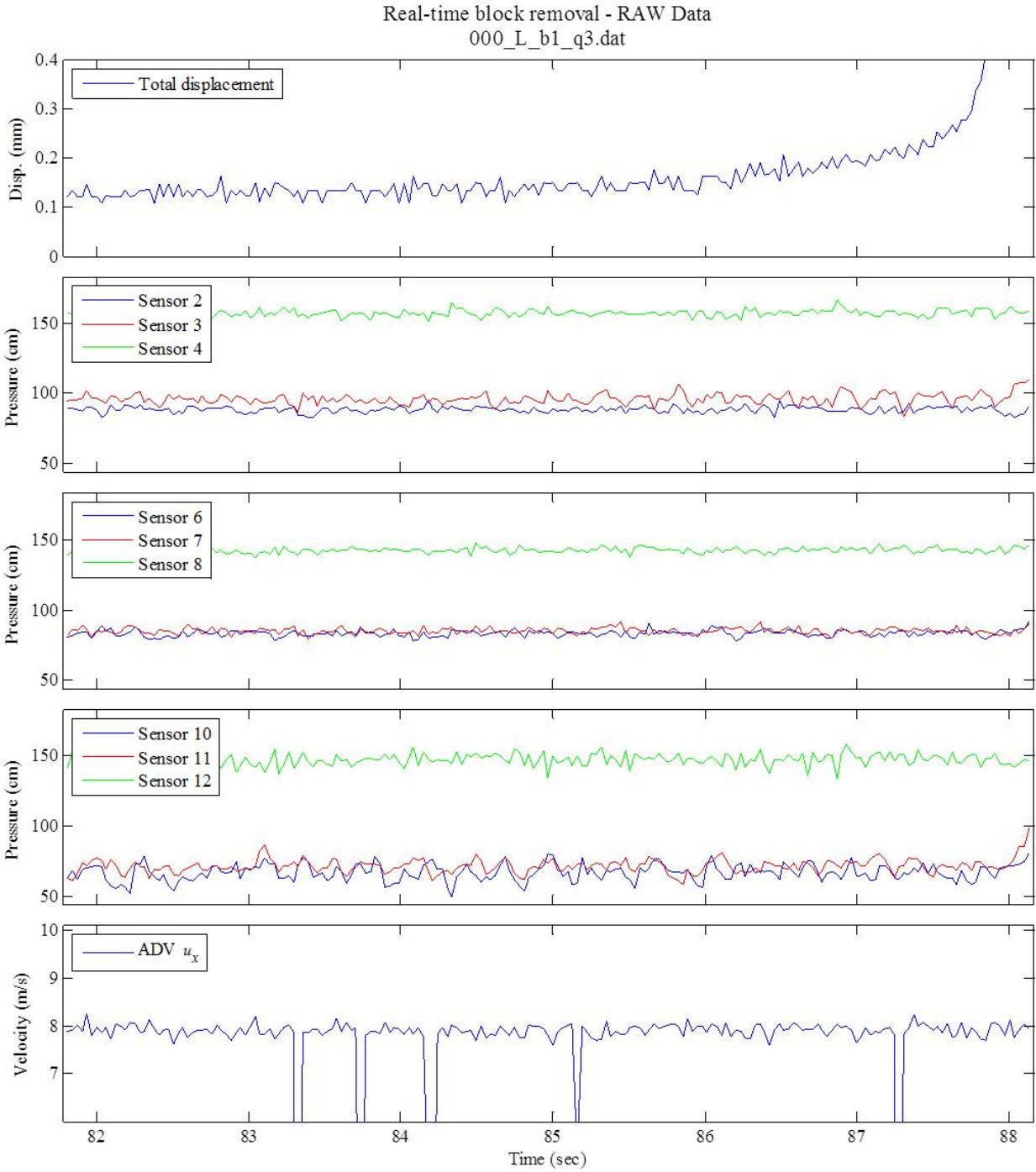




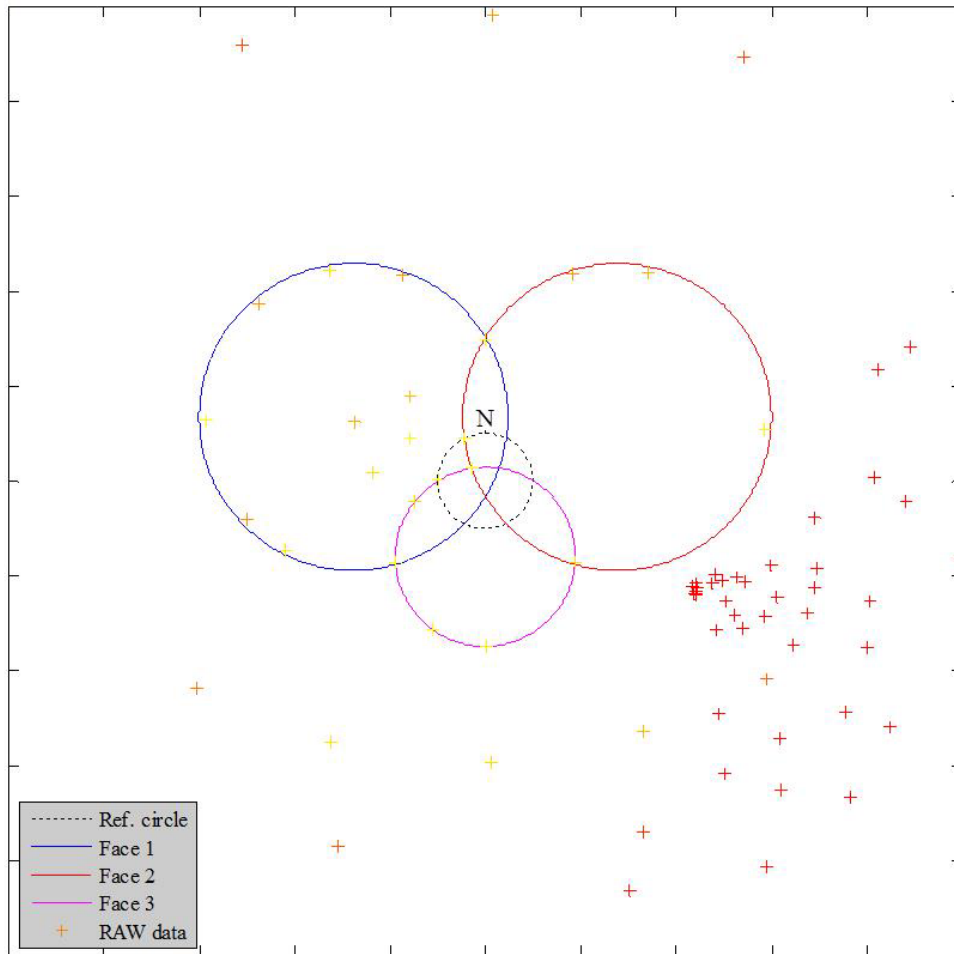
Block response 2 – supplemental figures

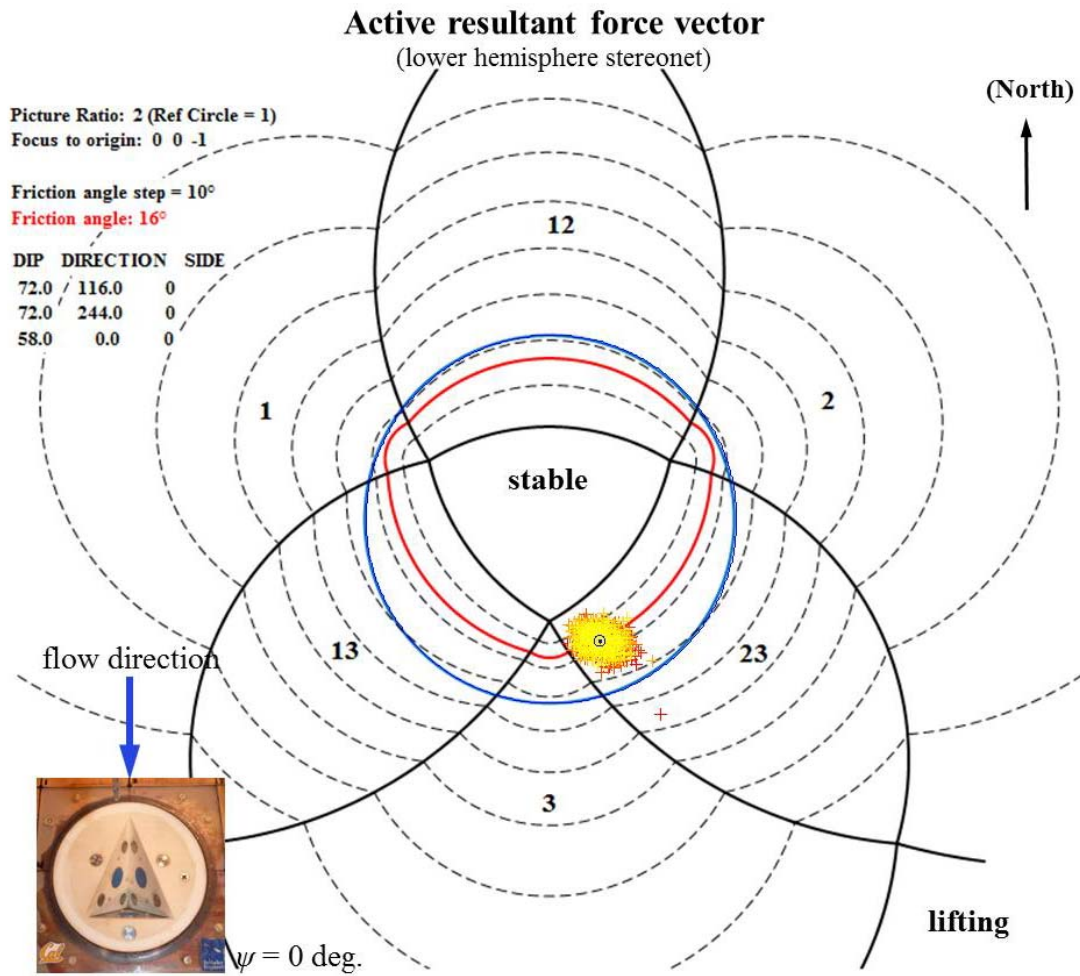
$\psi = 0$ deg., Low T_u , Block 1, Q_3



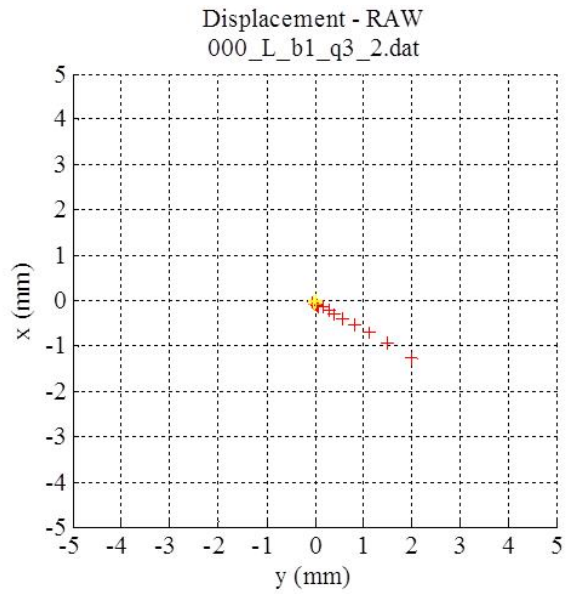
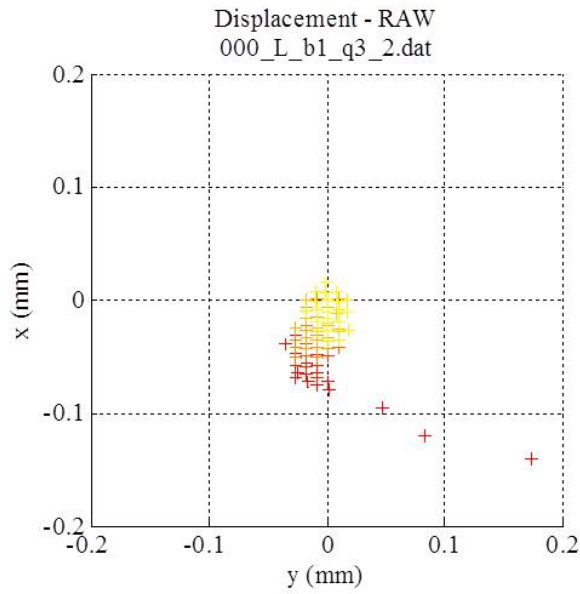
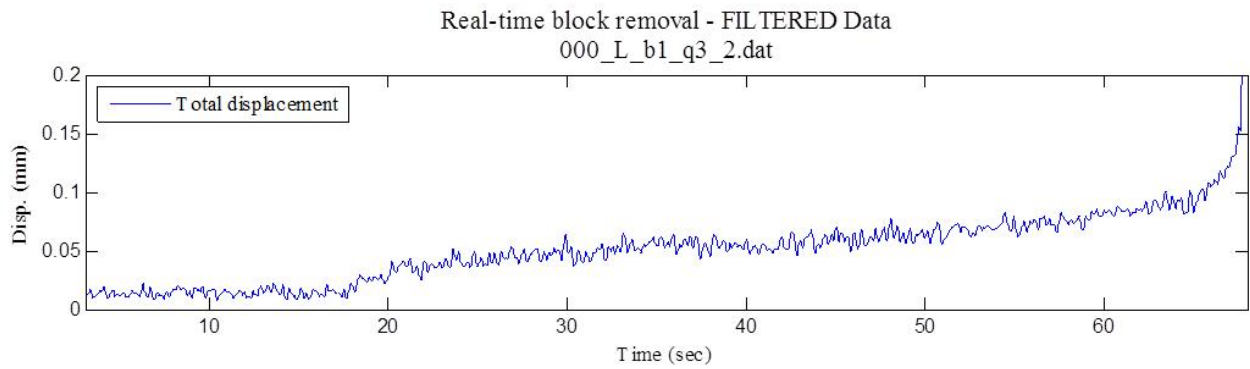


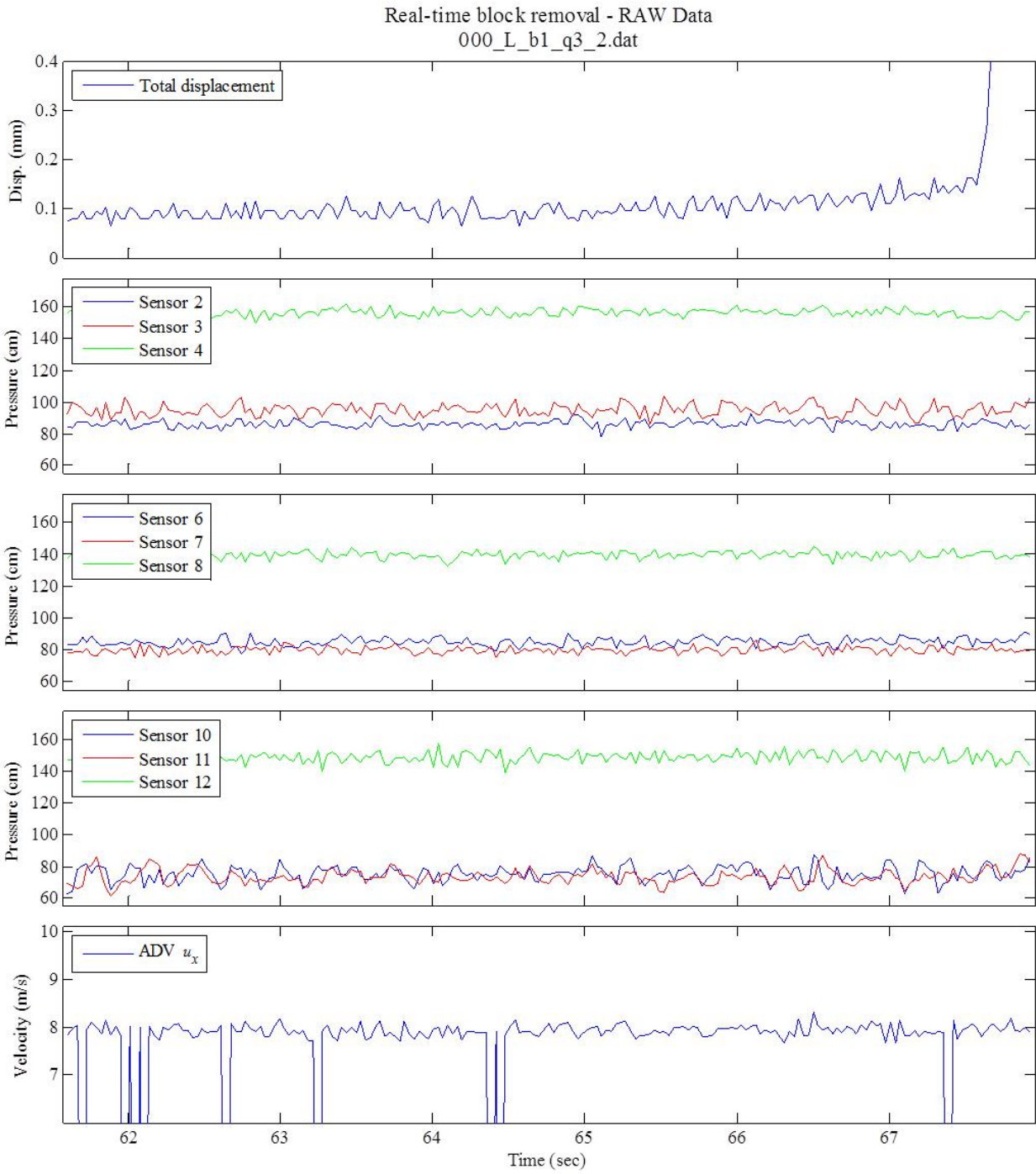
RAW displacement vector - lower hemisphere stereonet
000_L_b1_q3.dat



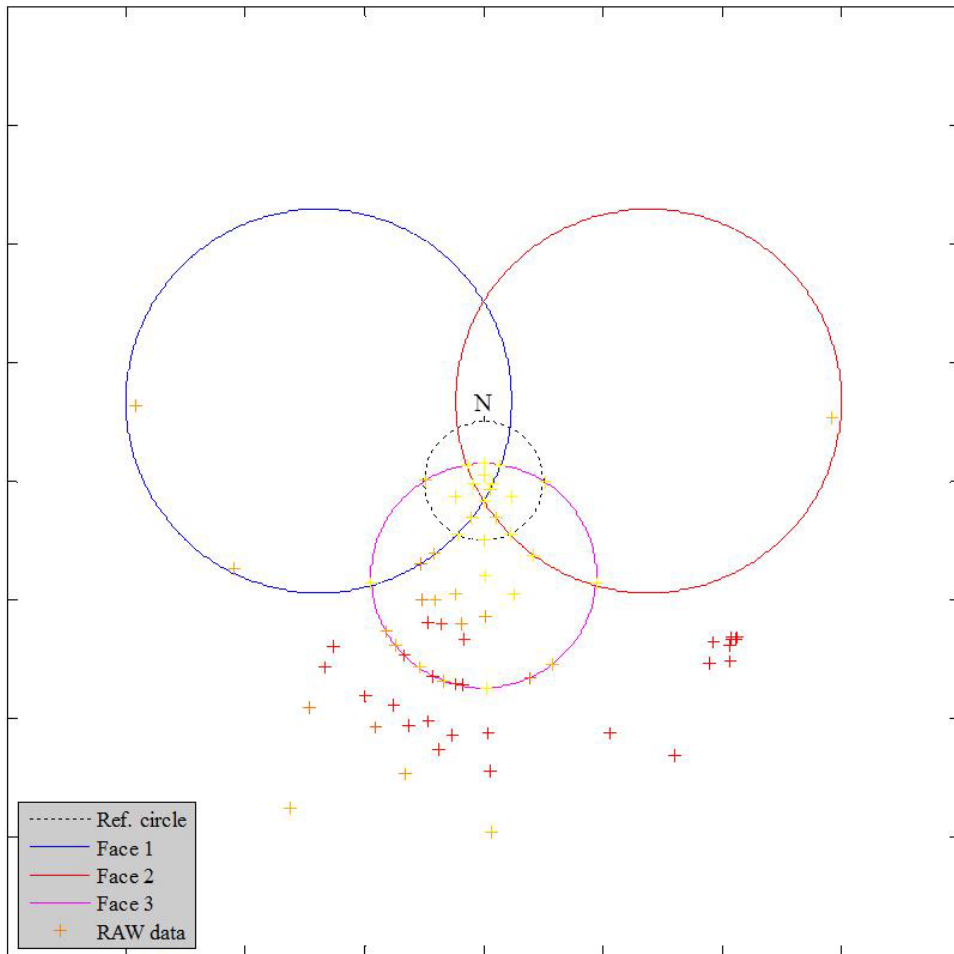


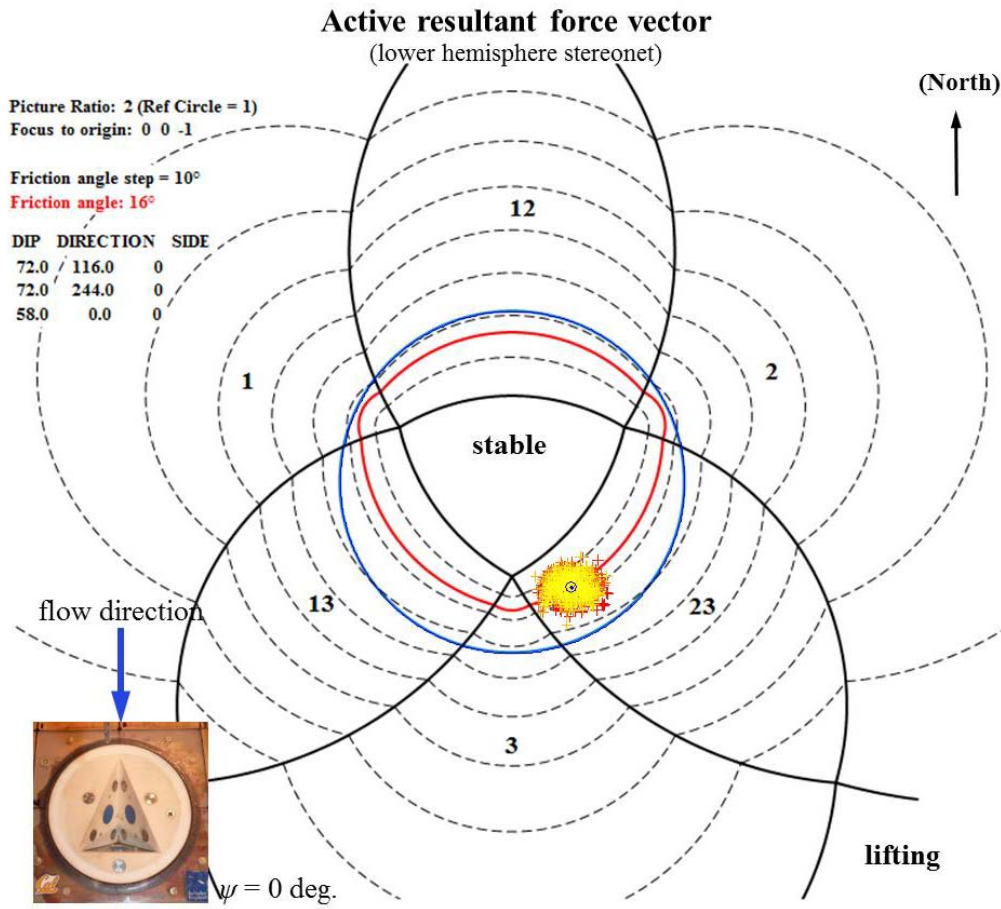
$\psi = 0$ deg., Low T_u , Block 1, Q_3



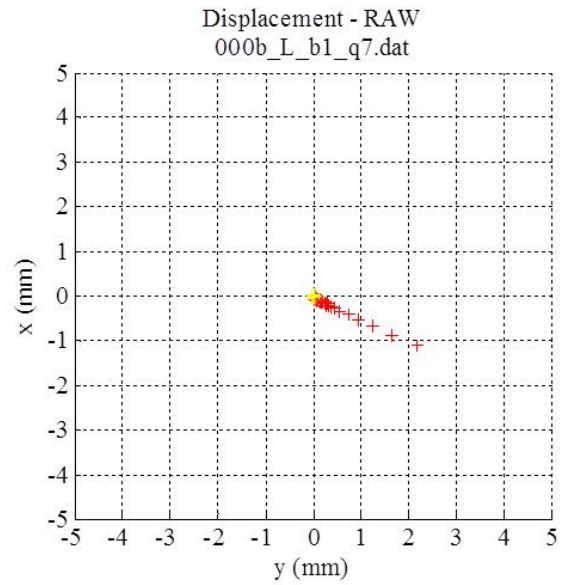
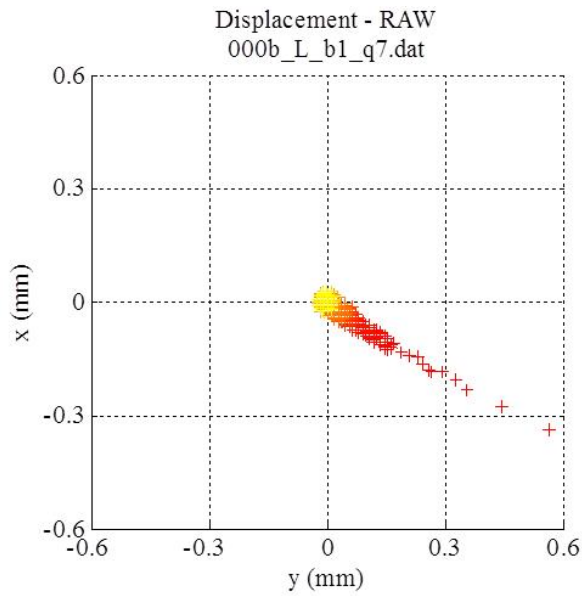
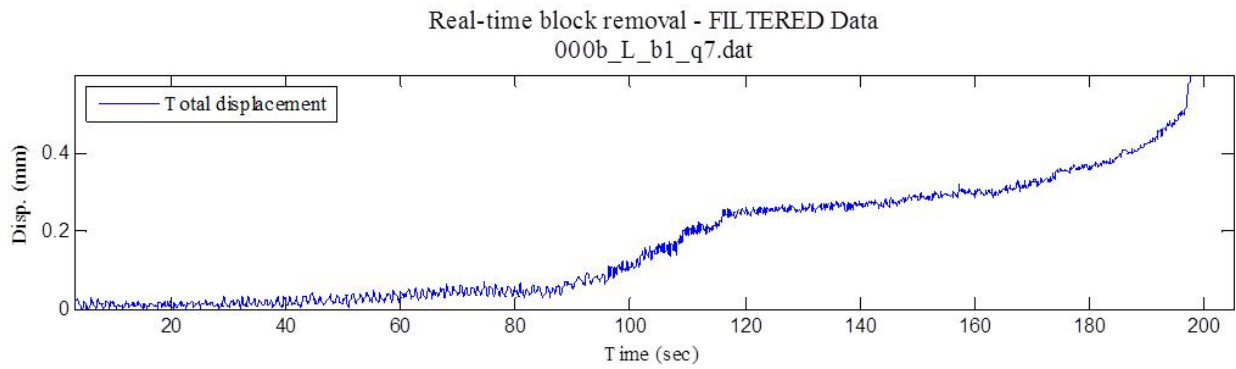


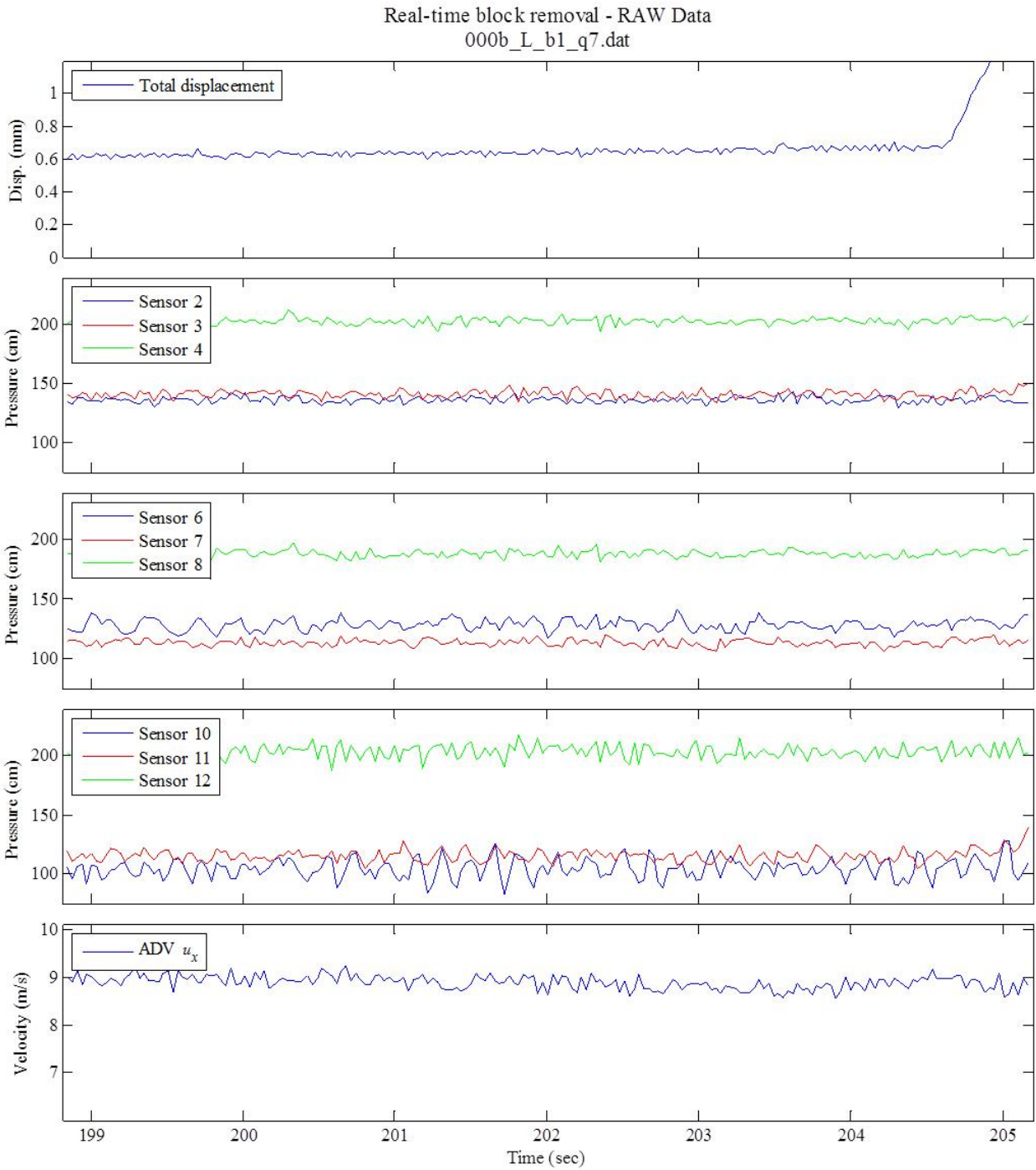
RAW displacement vector - lower hemisphere stereonet
000_L_b1_q3_2.dat



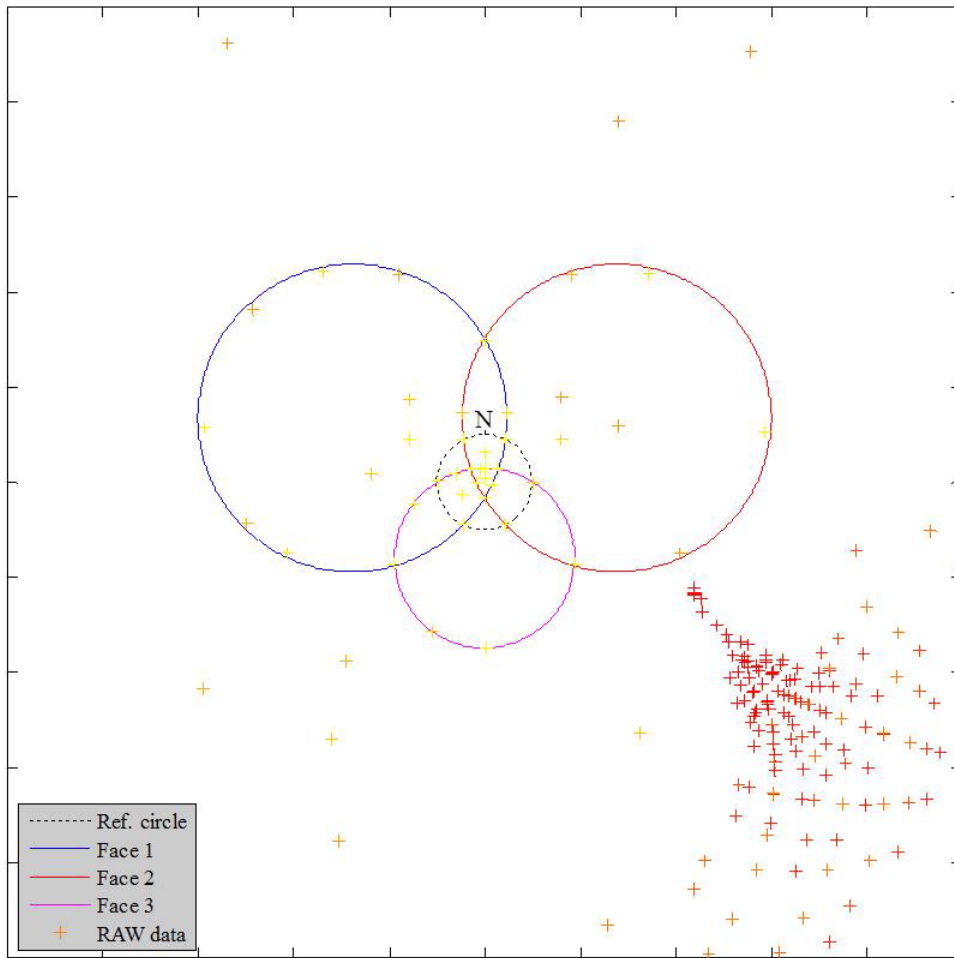


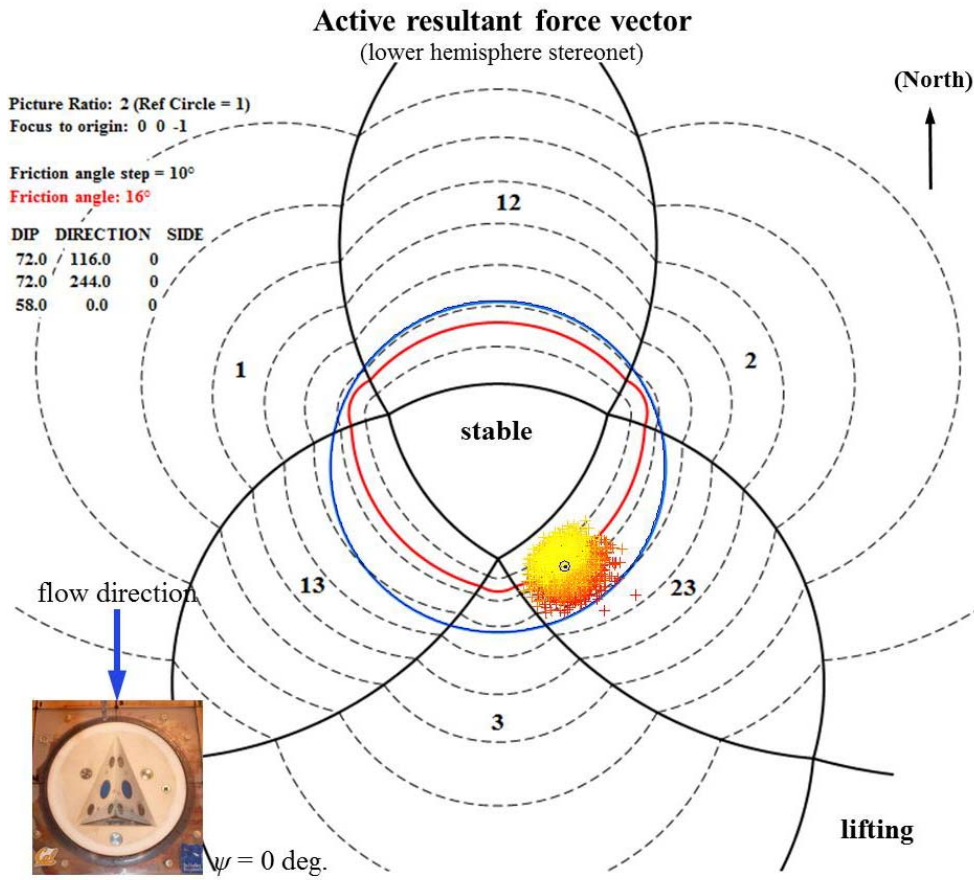
$\psi = 0$ deg., Low T_u , Block 1, Q_7





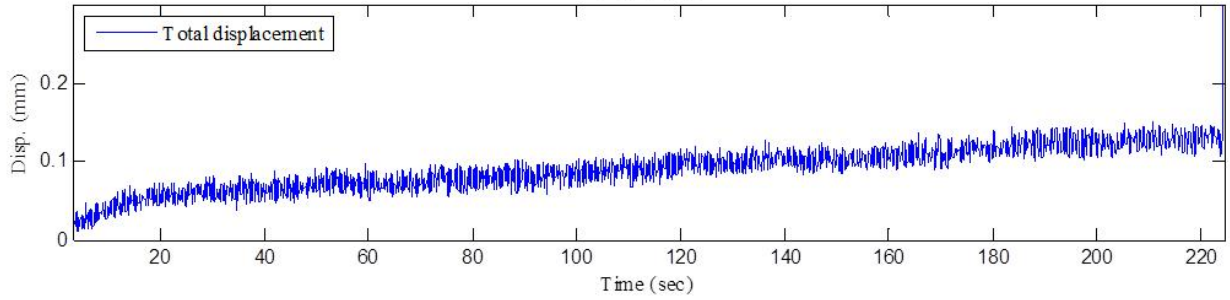
RAW displacement vector - lower hemisphere stereonet
000b_L_b1_q7.dat



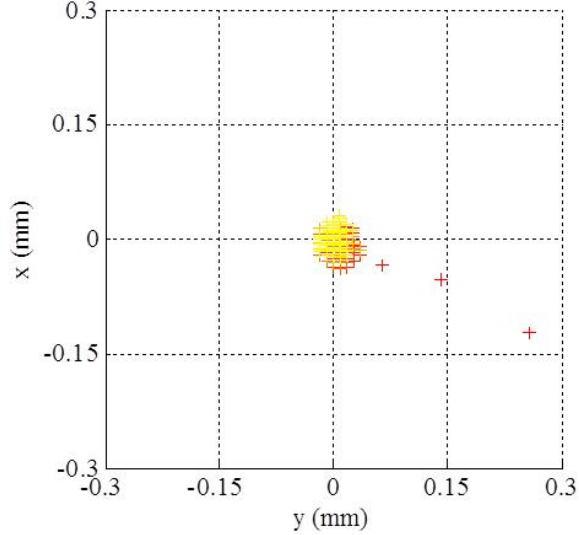


$\psi = 0$ deg., High T_u , Block 1, Q_4

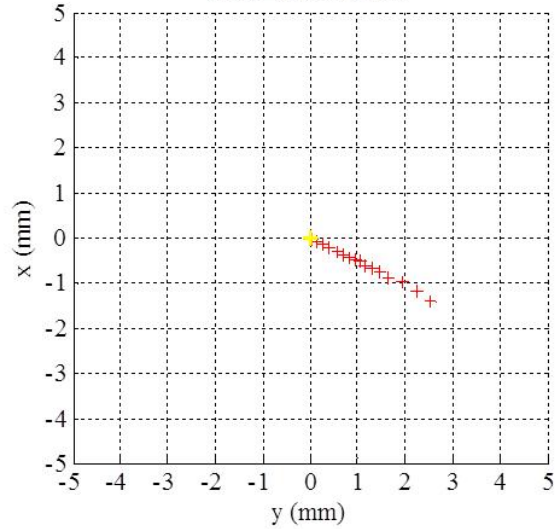
Real-time block removal - FILTERED Data
000c_H_b1_q4.dat

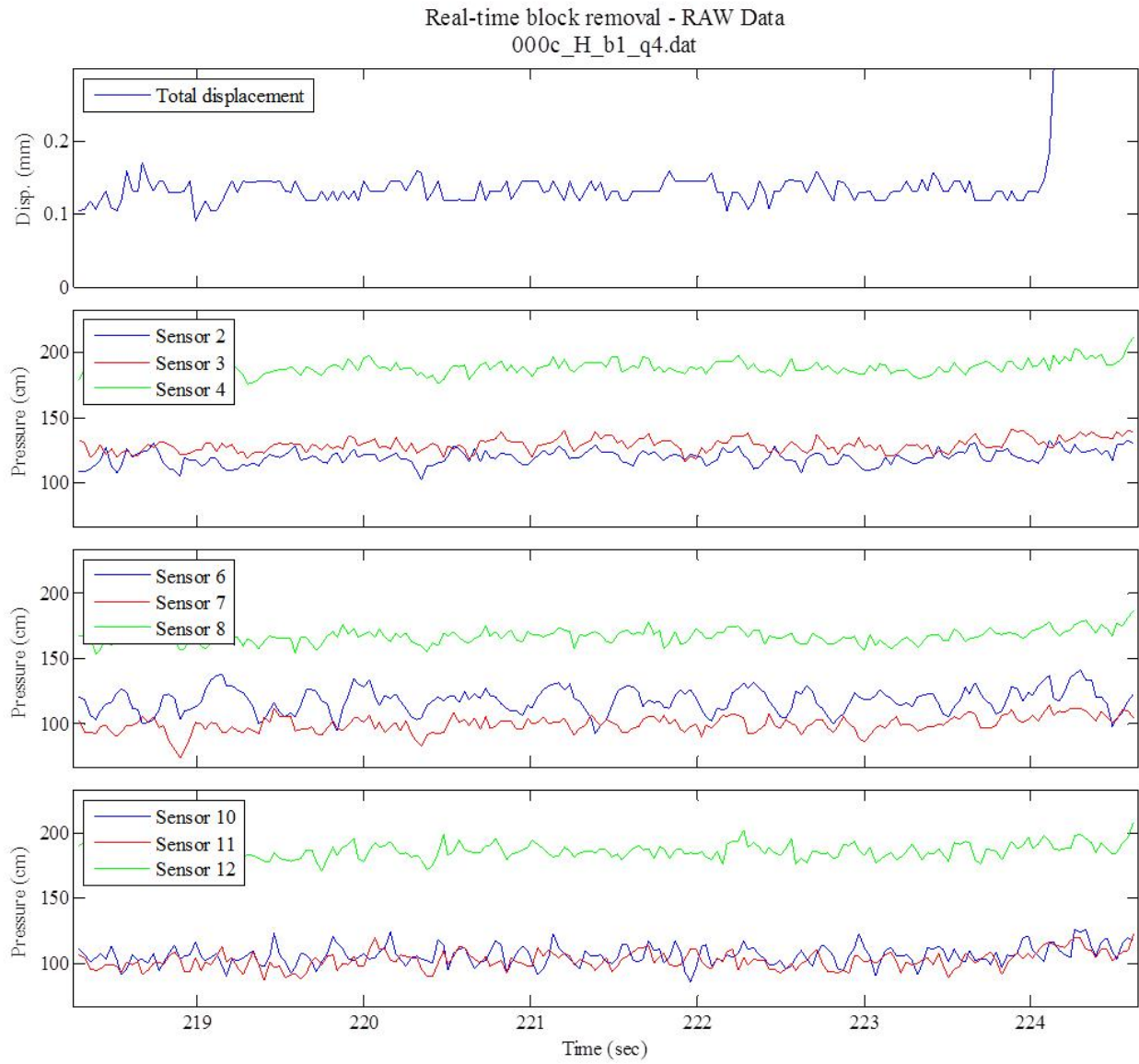


Displacement - RAW
000c_H_b1_q4.dat

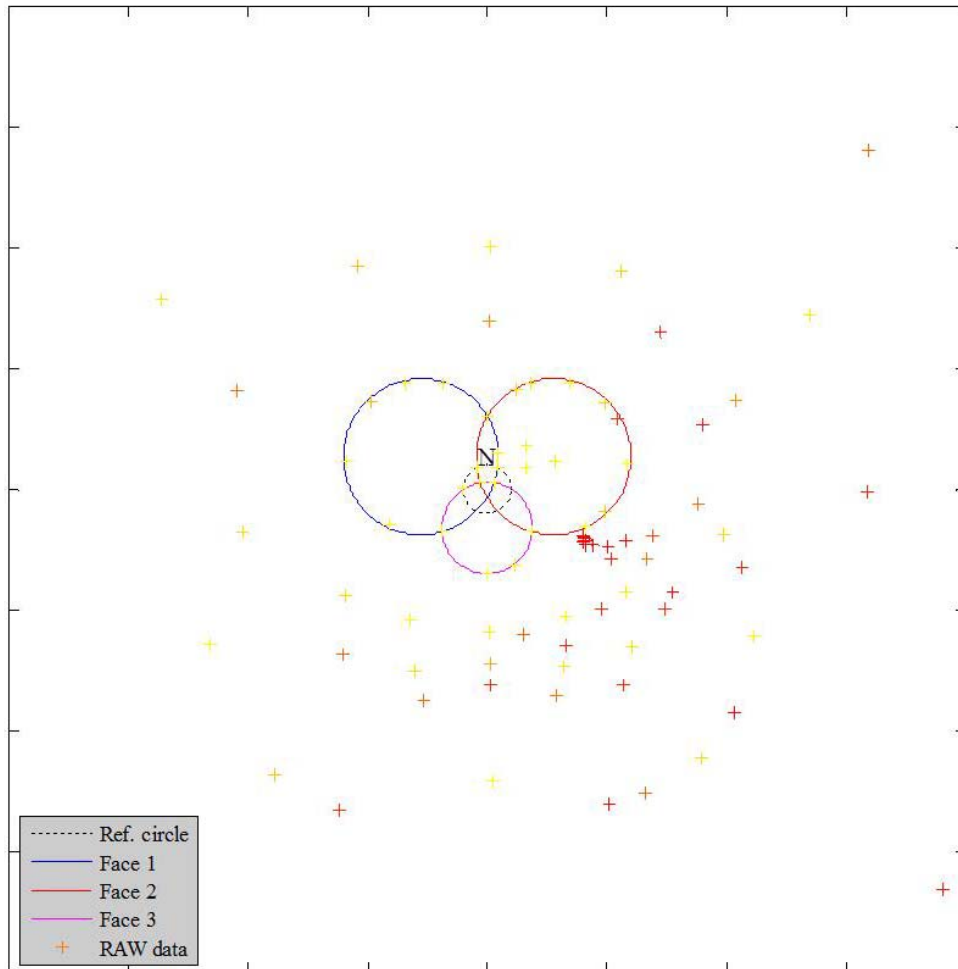


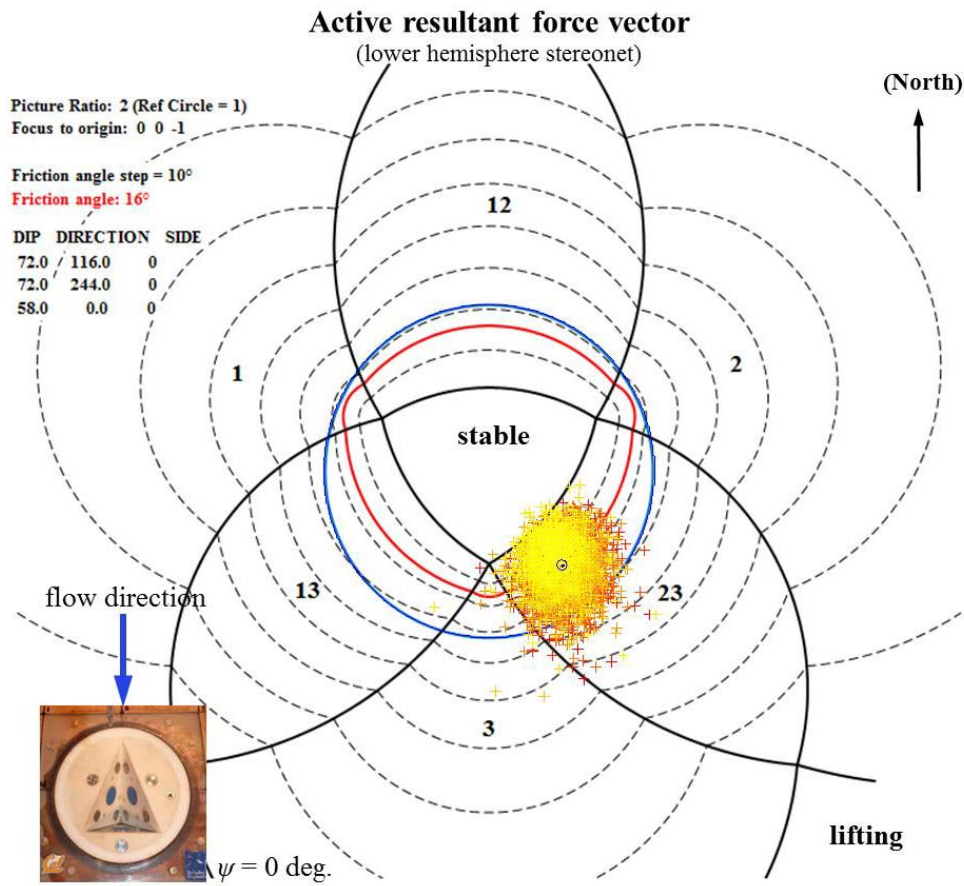
Displacement - RAW
000c_H_b1_q4.dat



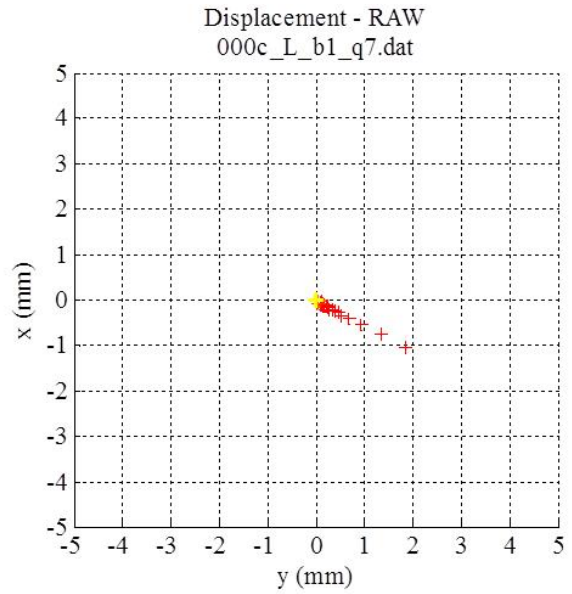
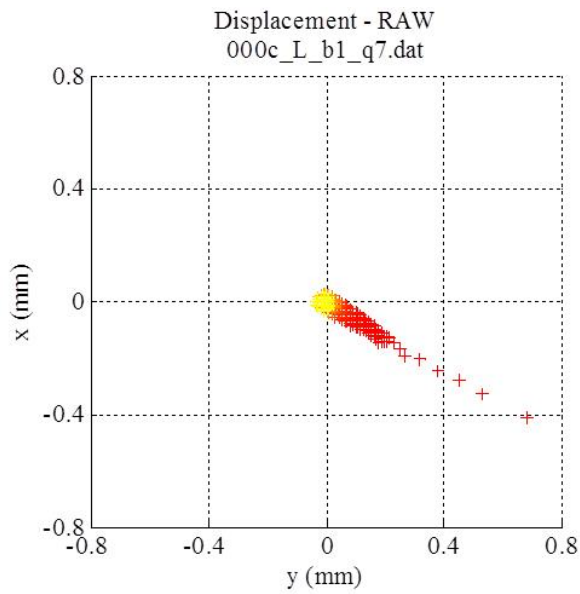
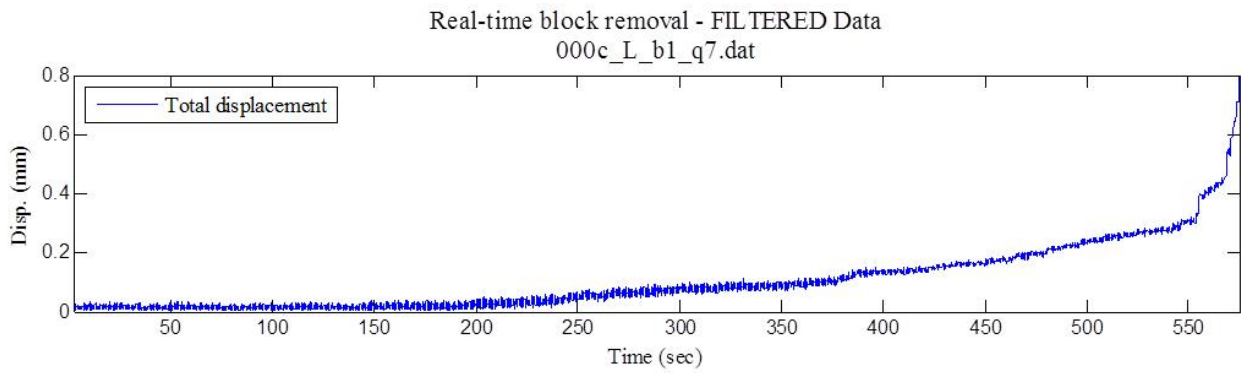


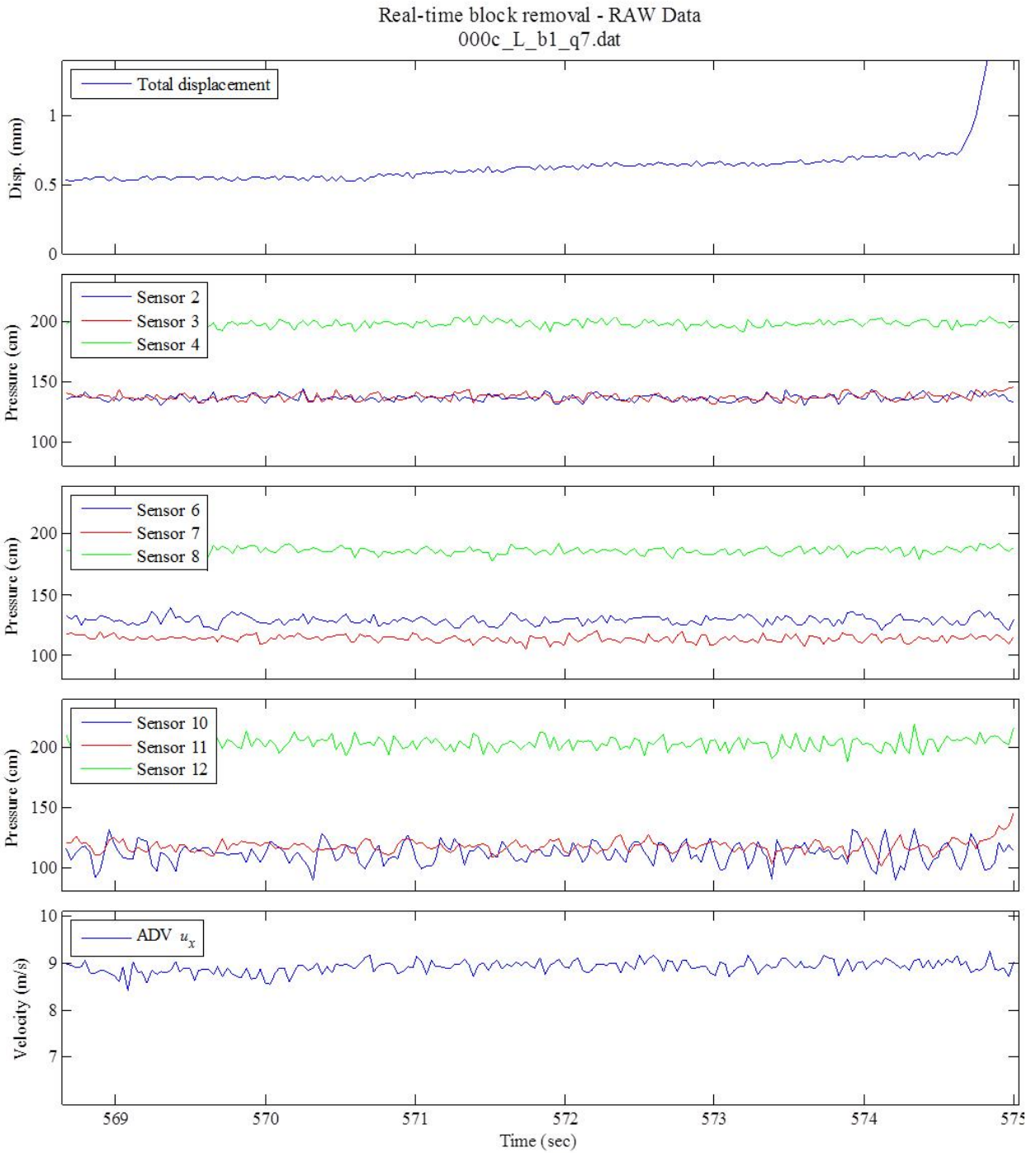
RAW displacement vector - lower hemisphere stereonet
000c_H_b1_q4.dat



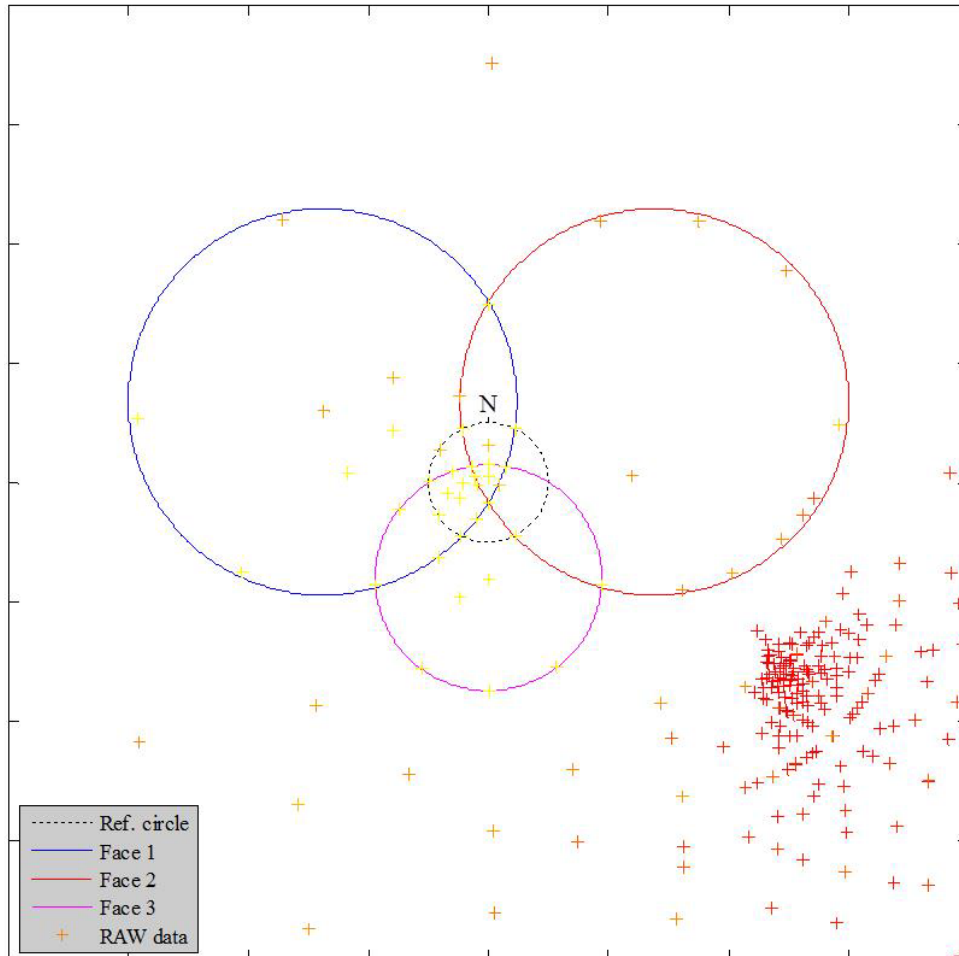


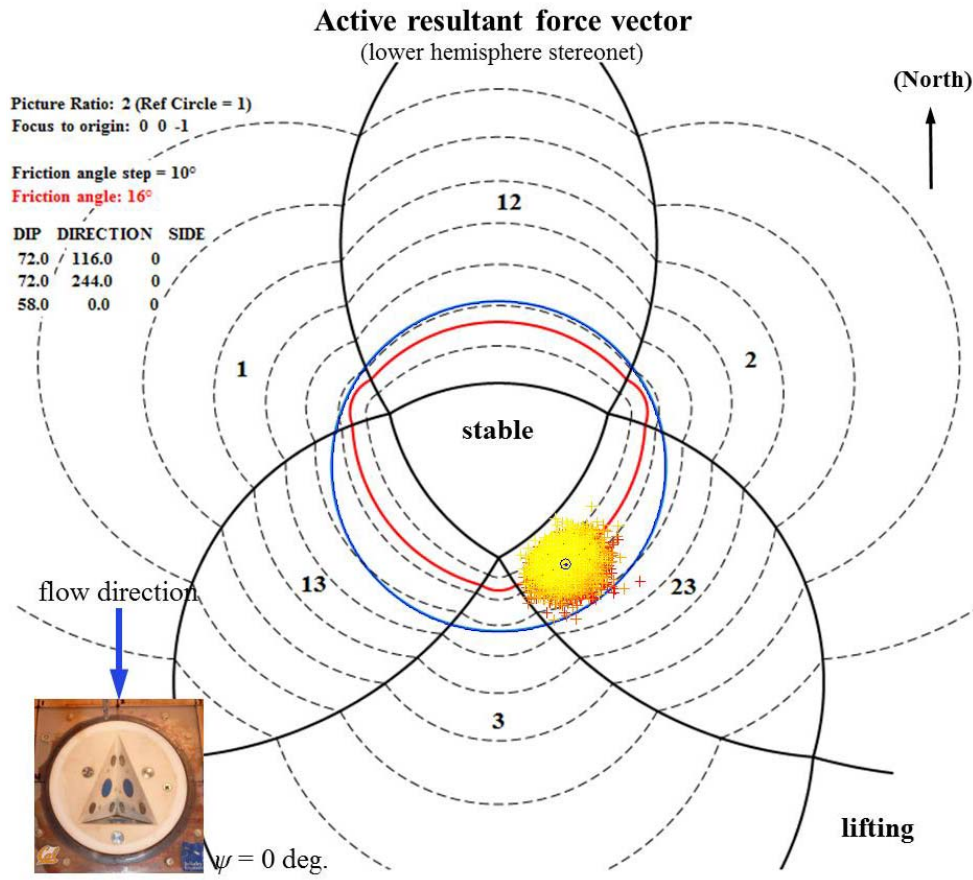
$\psi = 0$ deg., Low T_u , Block 1, Q_7





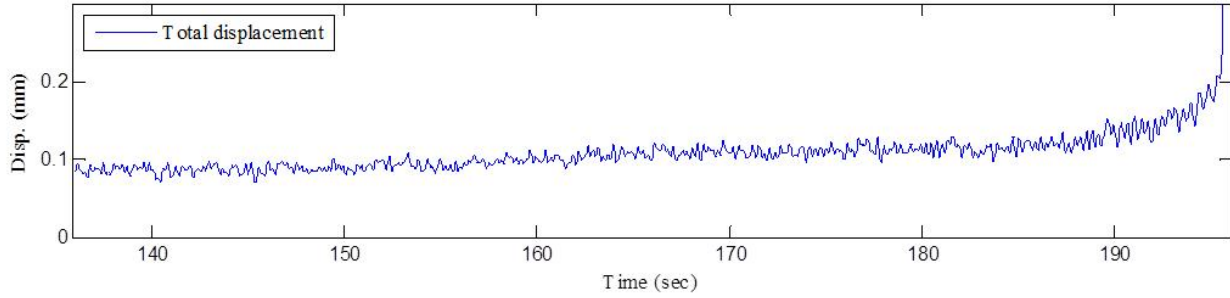
RAW displacement vector - lower hemisphere stereonet
000c_L_b1_q7.dat



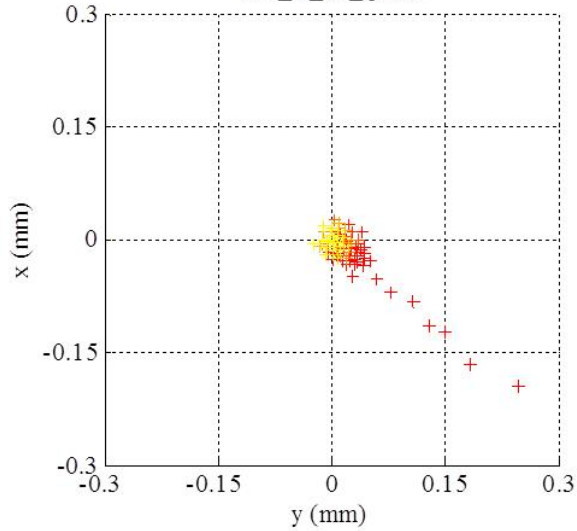


$\psi = 15$ deg., High T_u , Block 1, Q_2

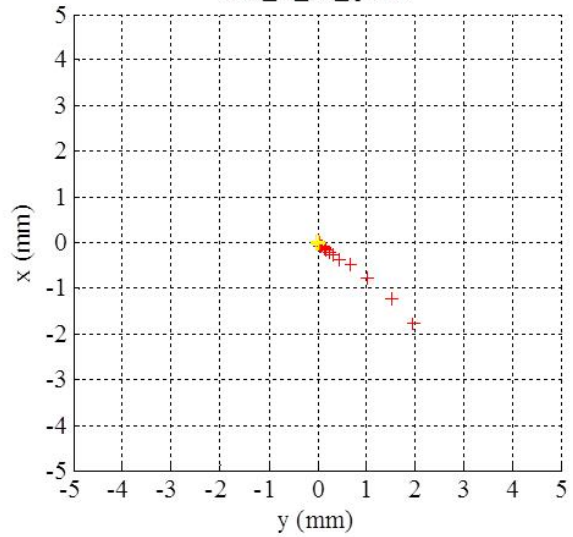
Real-time block removal - FILTERED Data
015_H_b1_q2.dat

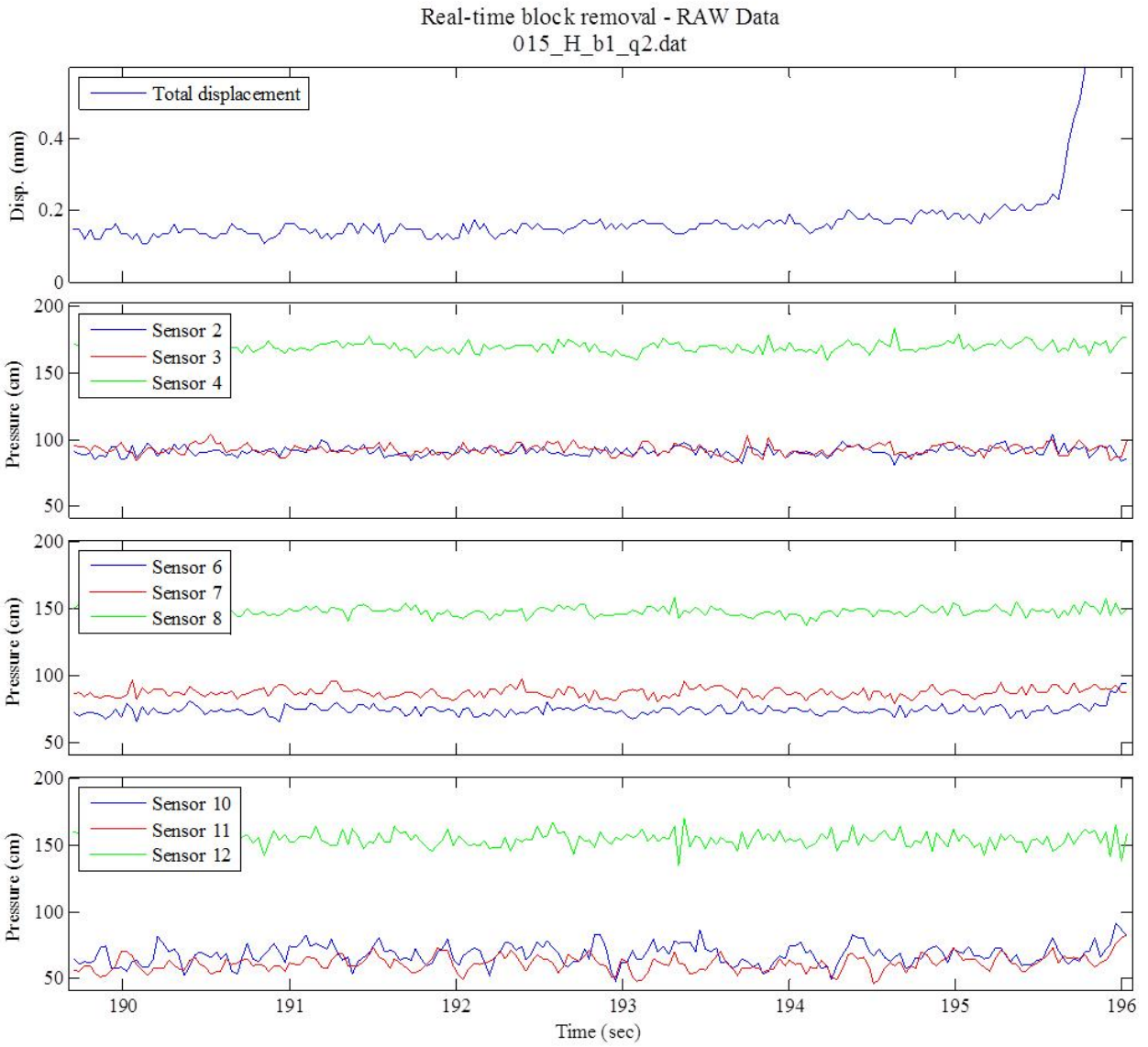


Displacement - RAW
015_H_b1_q2.dat

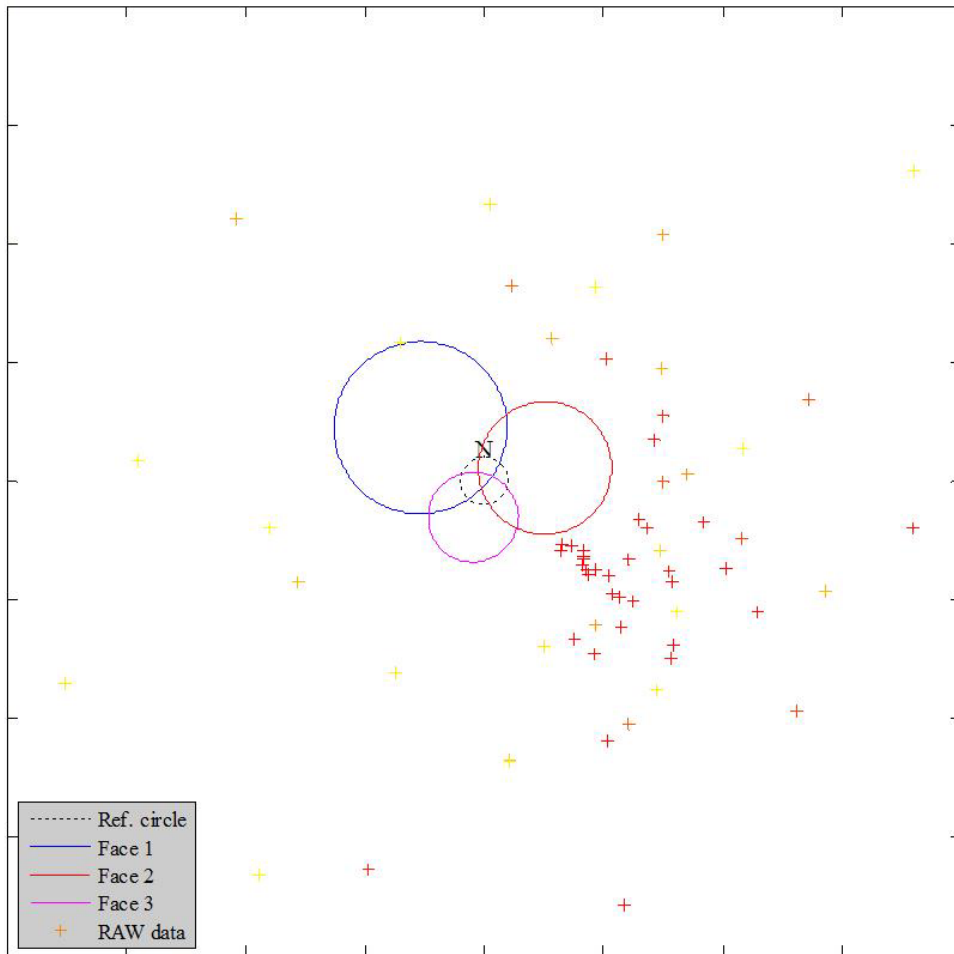


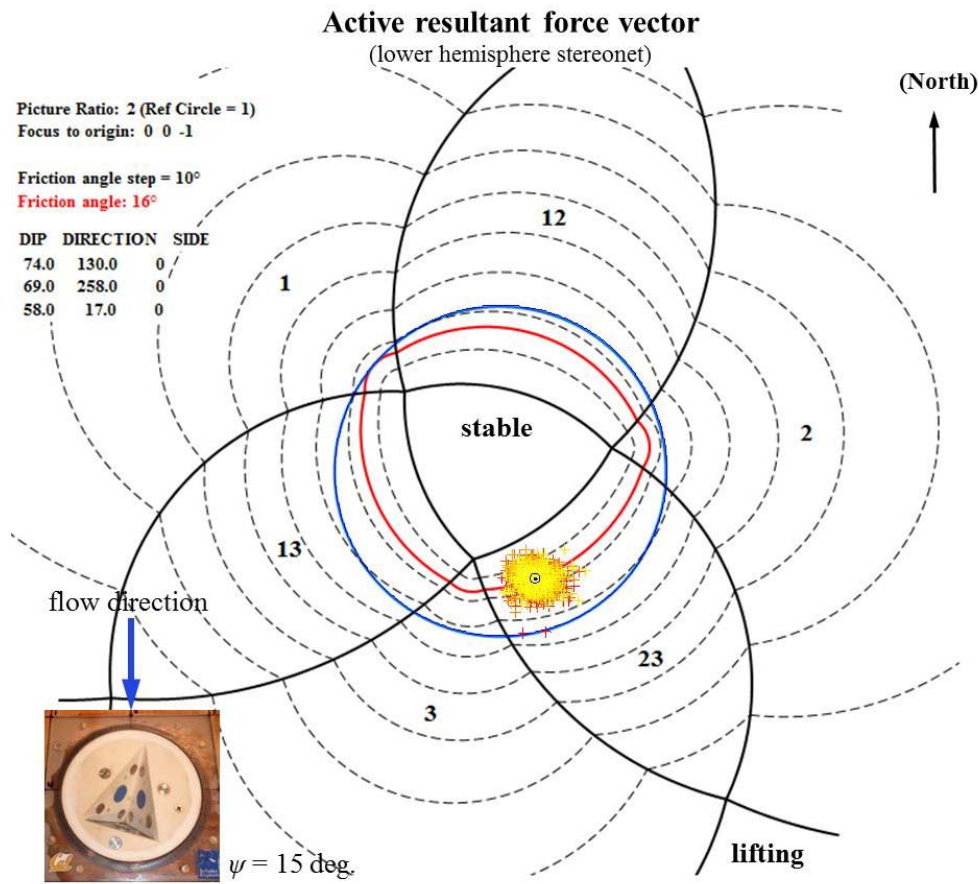
Displacement - RAW
015_H_b1_q2.dat



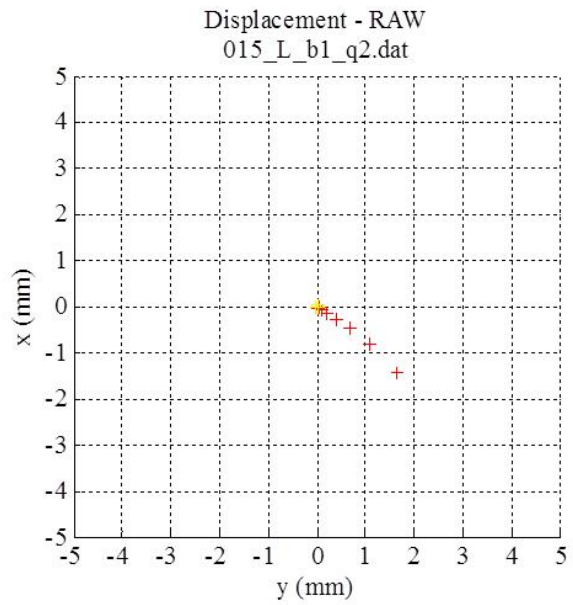
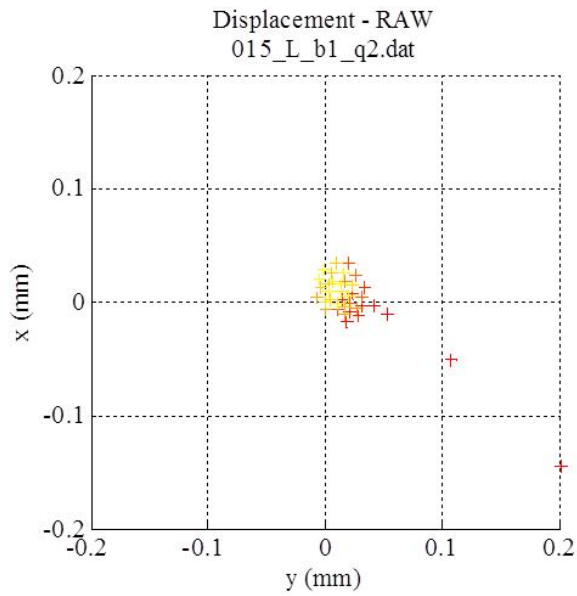
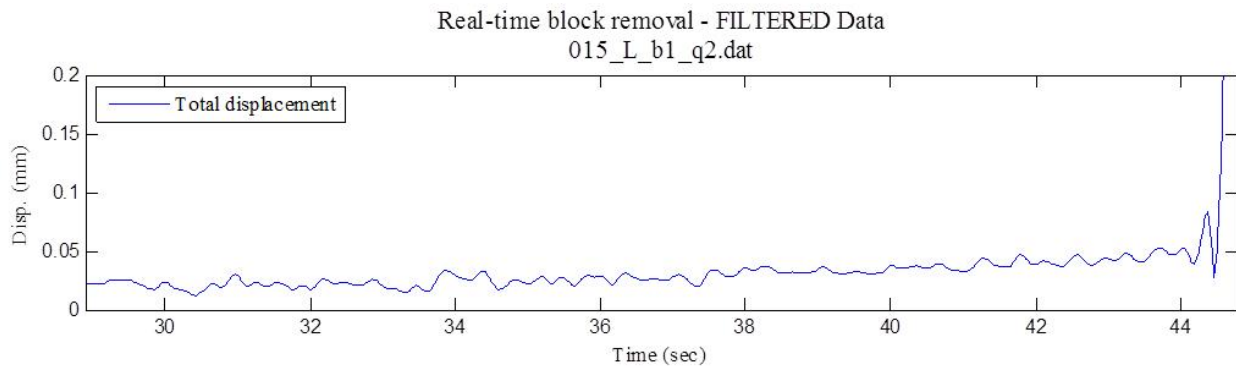


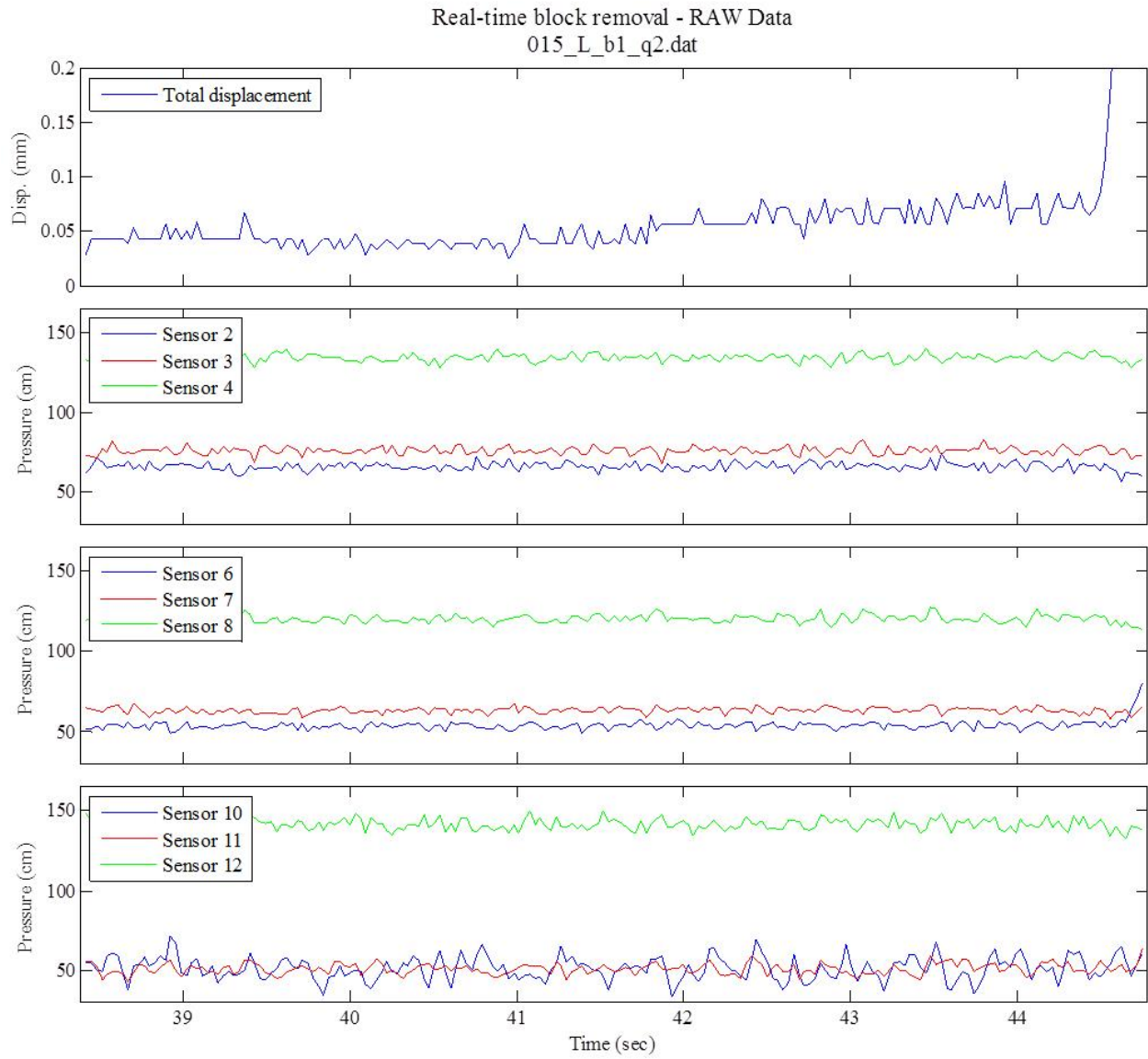
RAW displacement vector - lower hemisphere stereonet
015_H_b1_q2.dat



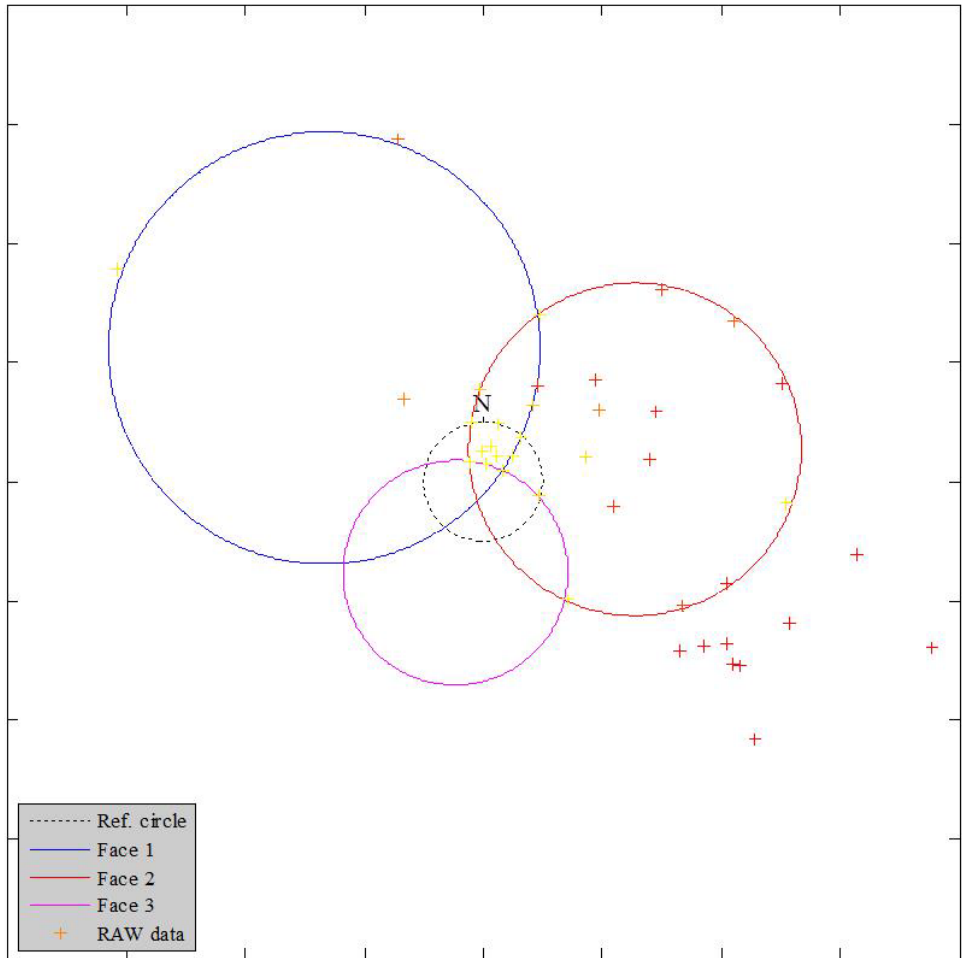


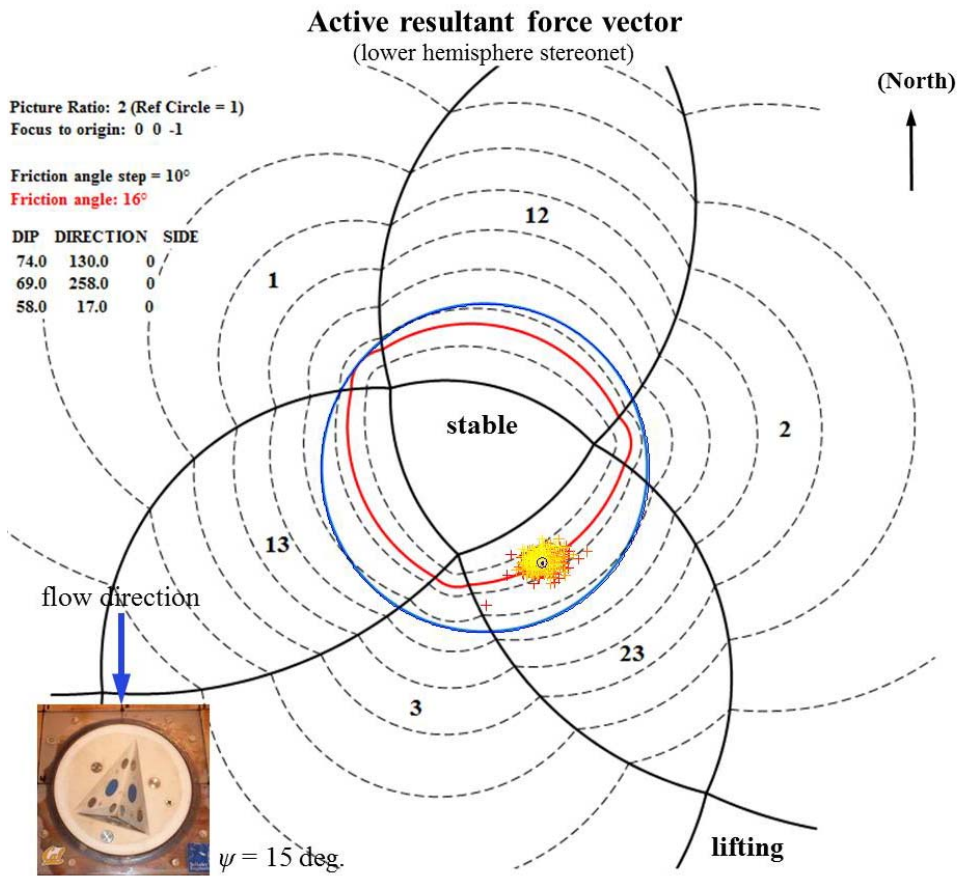
$\psi = 15$ deg., Low T_u , Block 1, Q_2





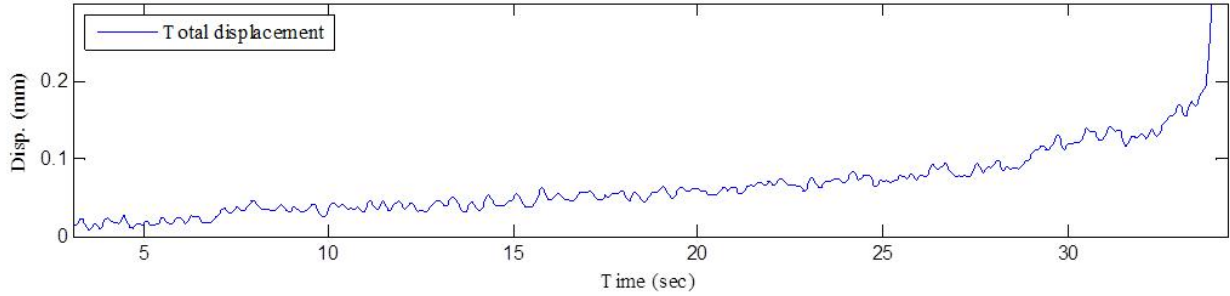
RAW displacement vector - lower hemisphere stereonet
015_L_b1_q2.dat



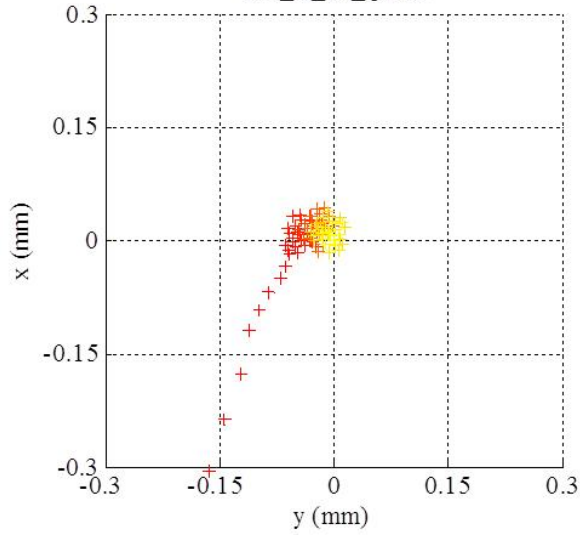


$\psi = 30$ deg., High T_u , Block 2, Q_3

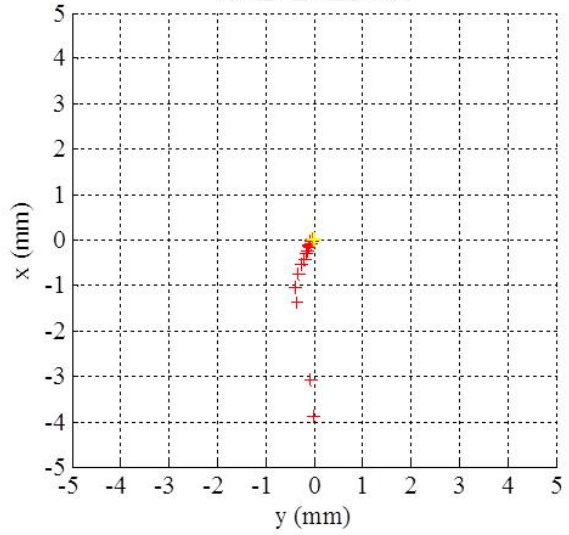
Real-time block removal - FILTERED Data
030_H_b2_q3.dat

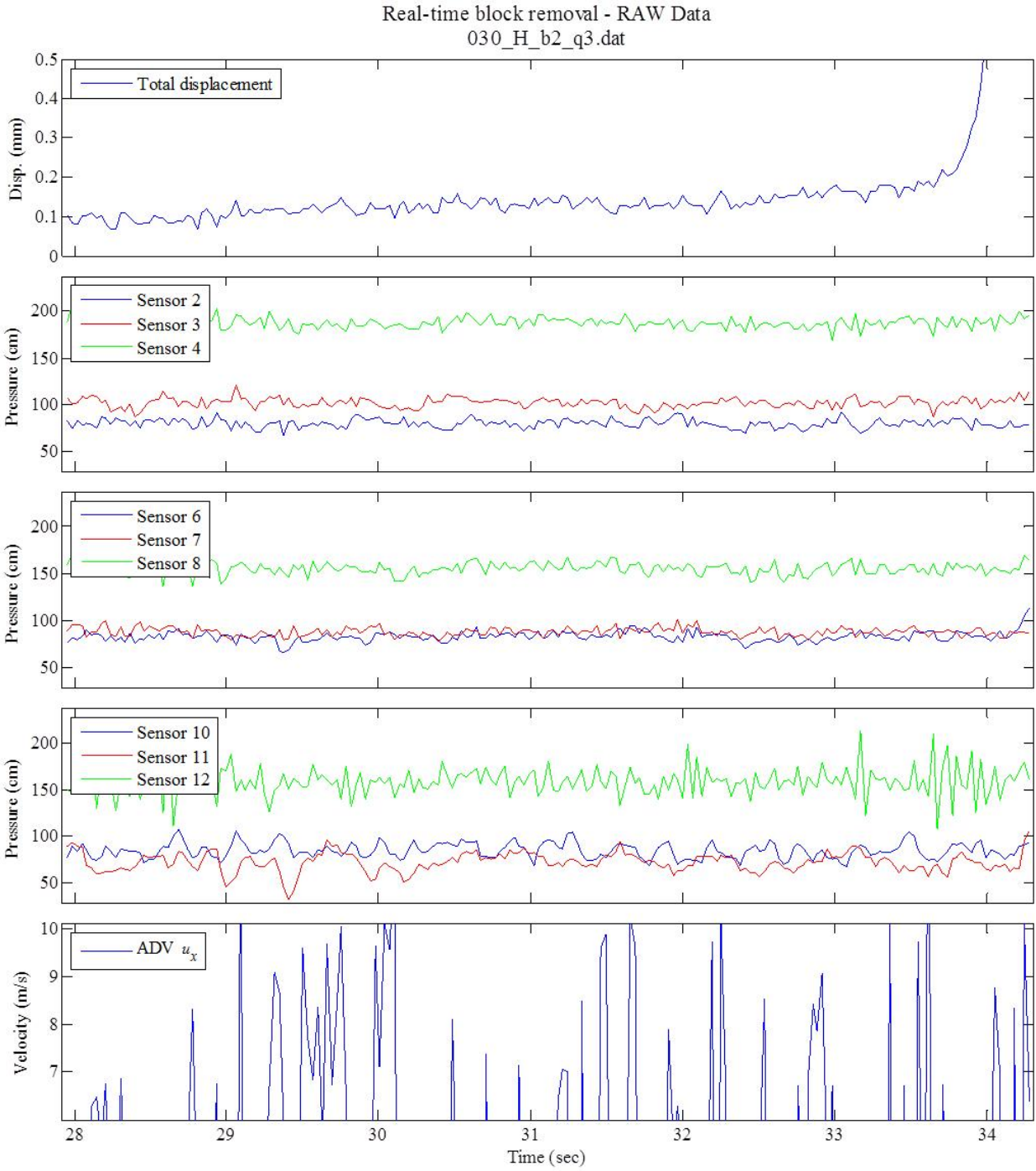


Displacement - RAW
030_H_b2_q3.dat

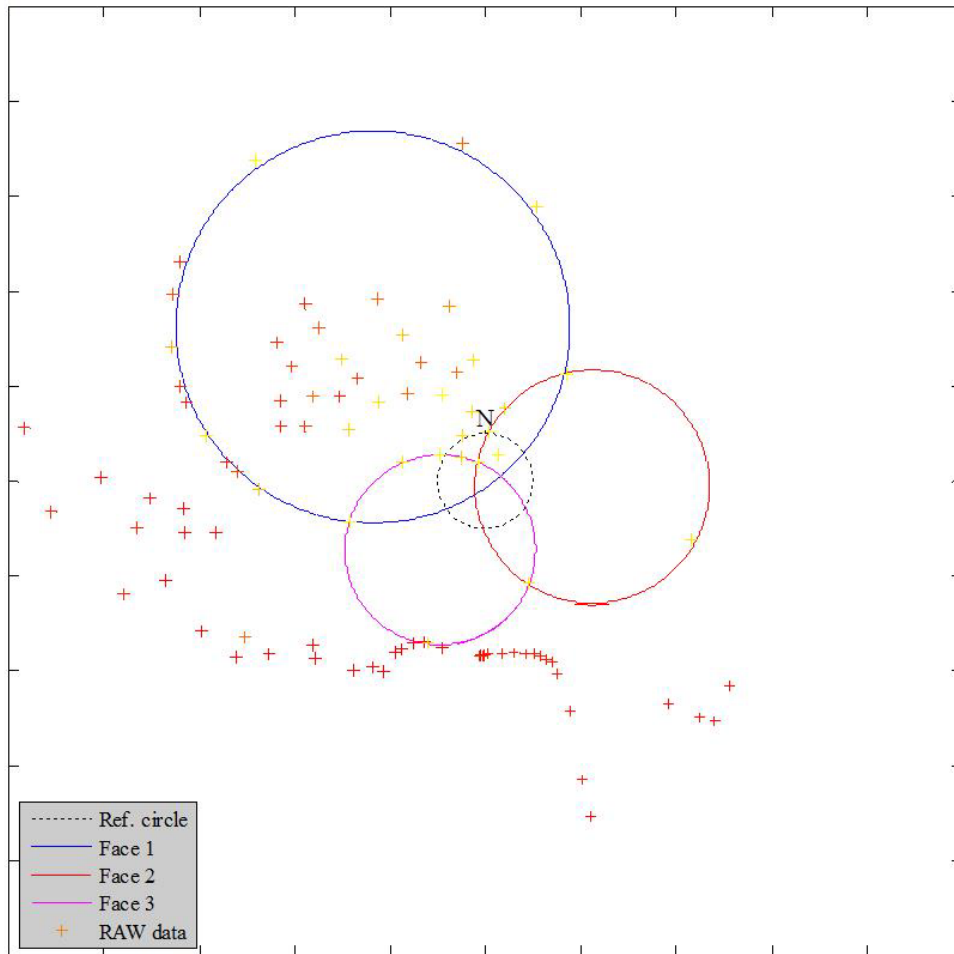


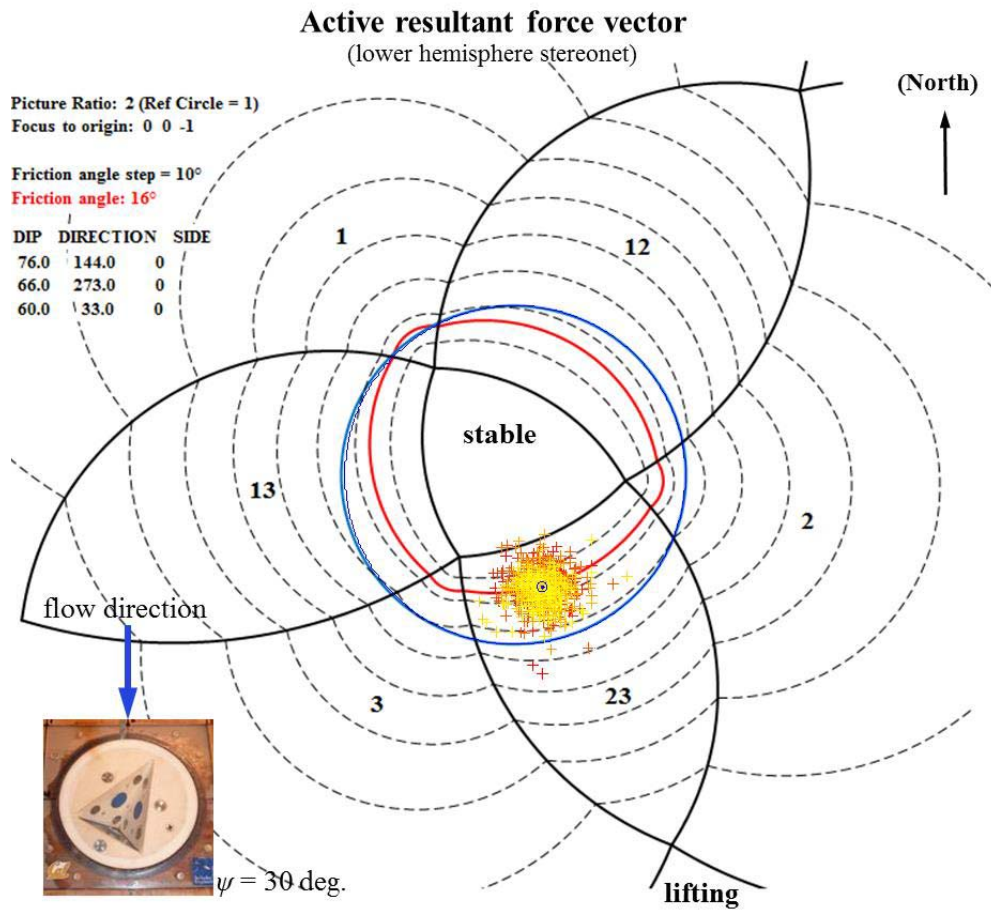
Displacement - RAW
030_H_b2_q3.dat



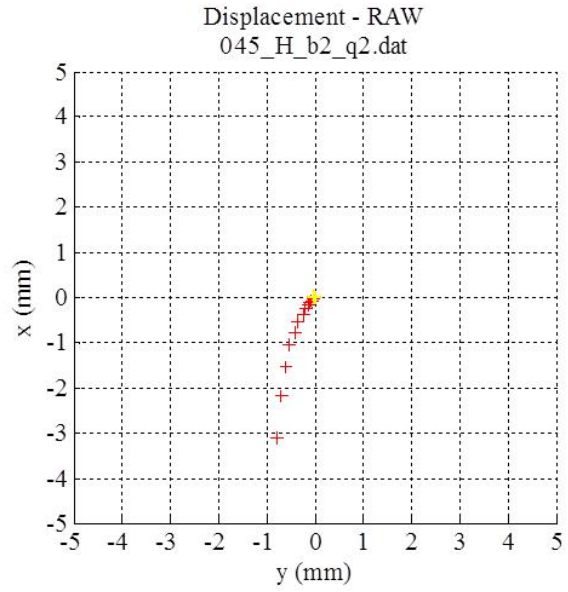
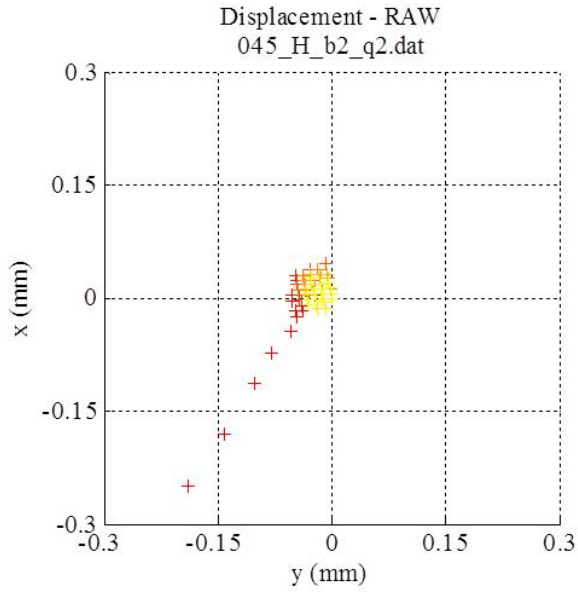
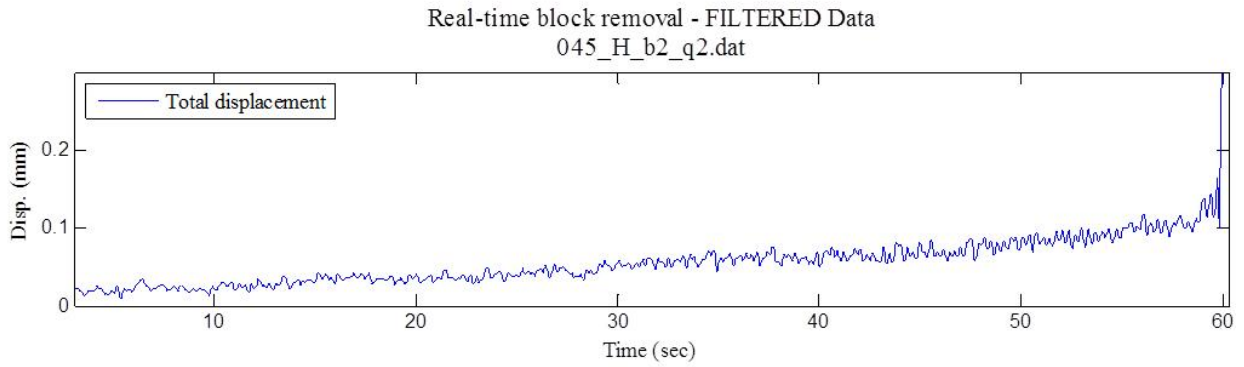


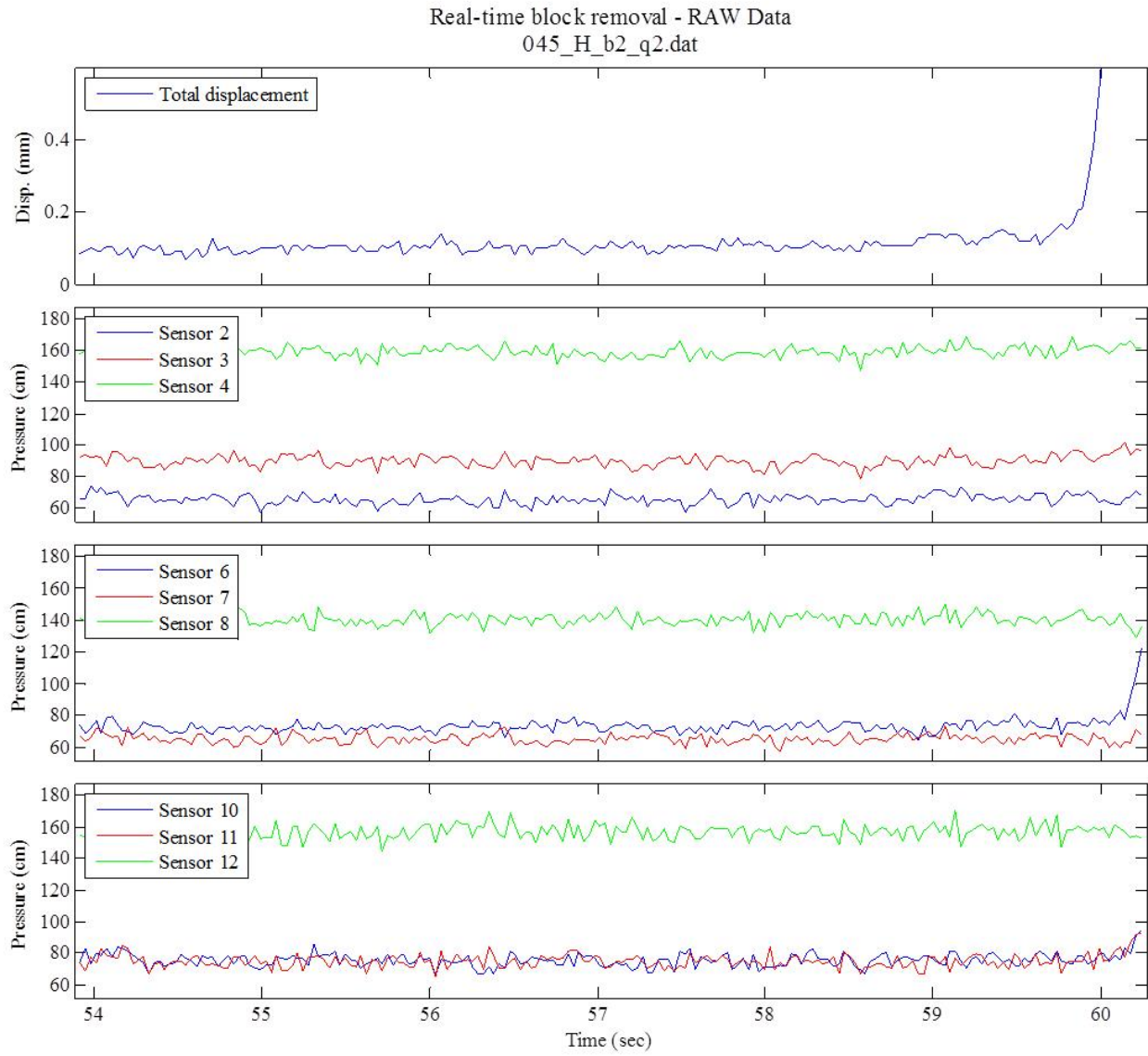
RAW displacement vector - lower hemisphere stereonet
030_H_b2_q3.dat



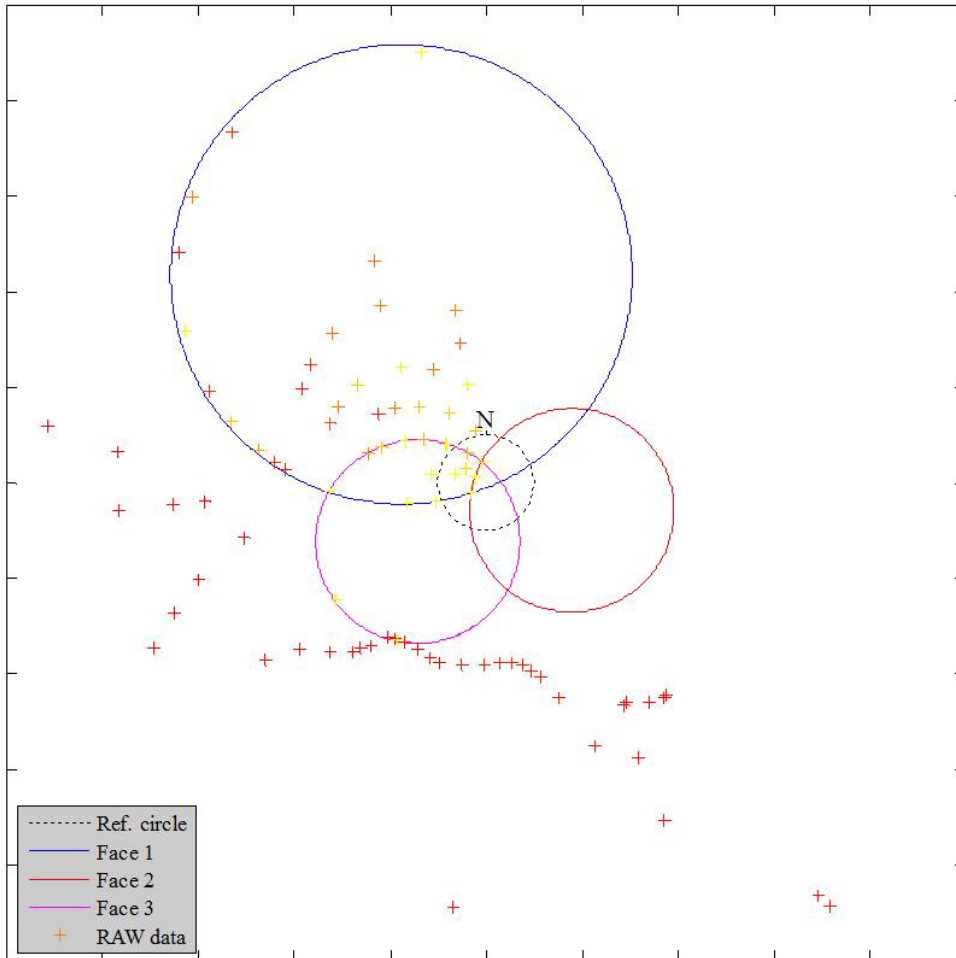


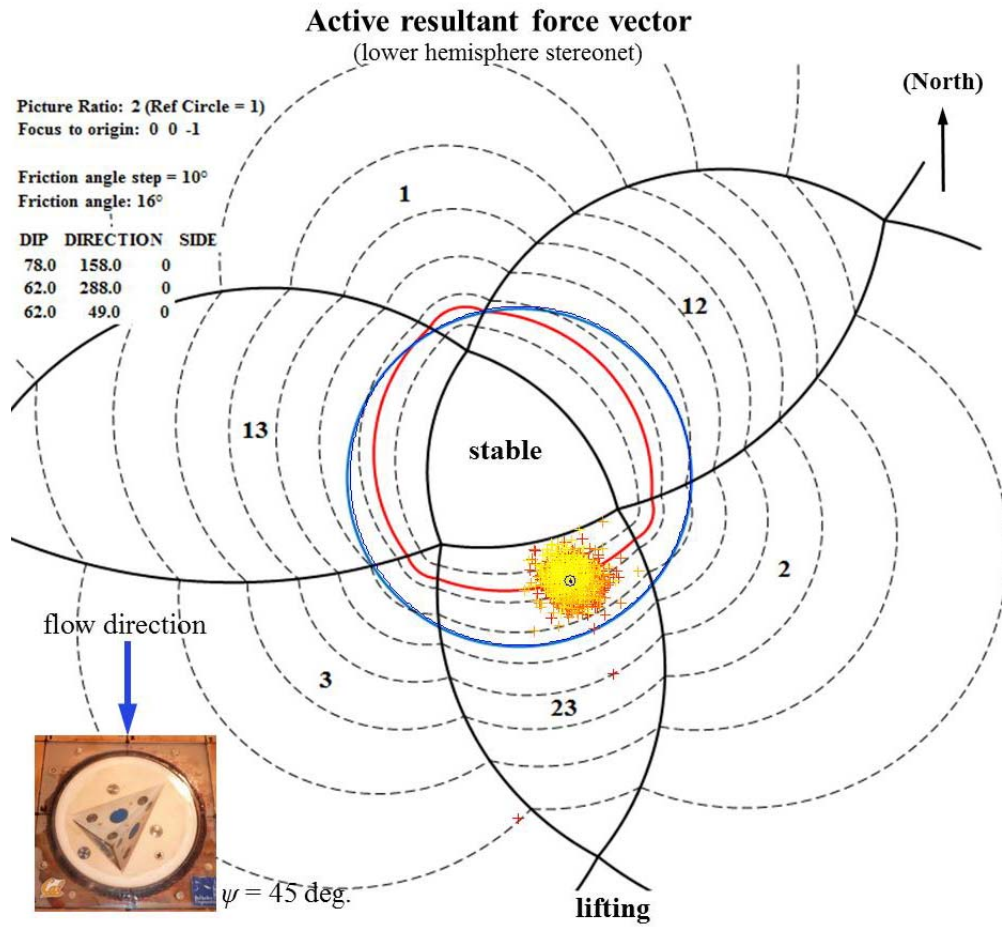
$\psi = 45$ deg., High T_u , Block 2, Q_2





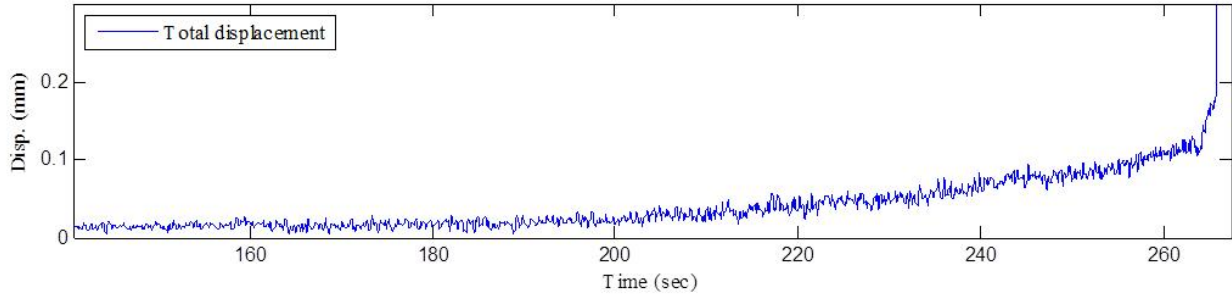
RAW displacement vector - lower hemisphere stereonet
045_H_b2_q2.dat



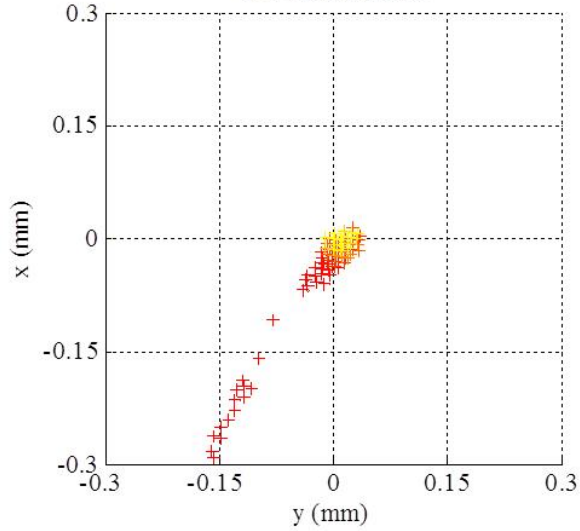


$\psi = 60$ deg., High T_u , Block 2, Q_I

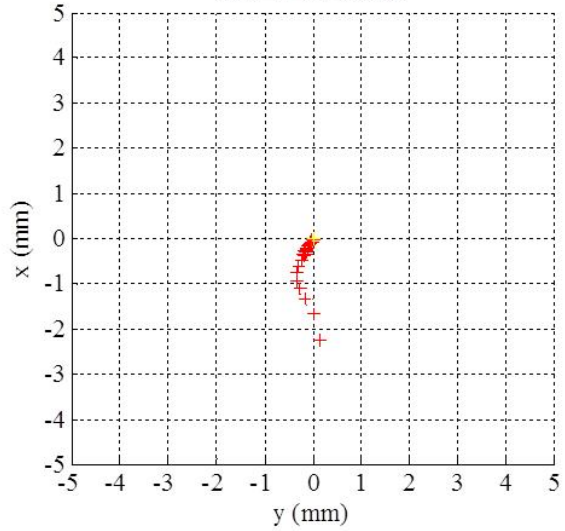
Real-time block removal - FILTERED Data
060_H_b2_q1.dat

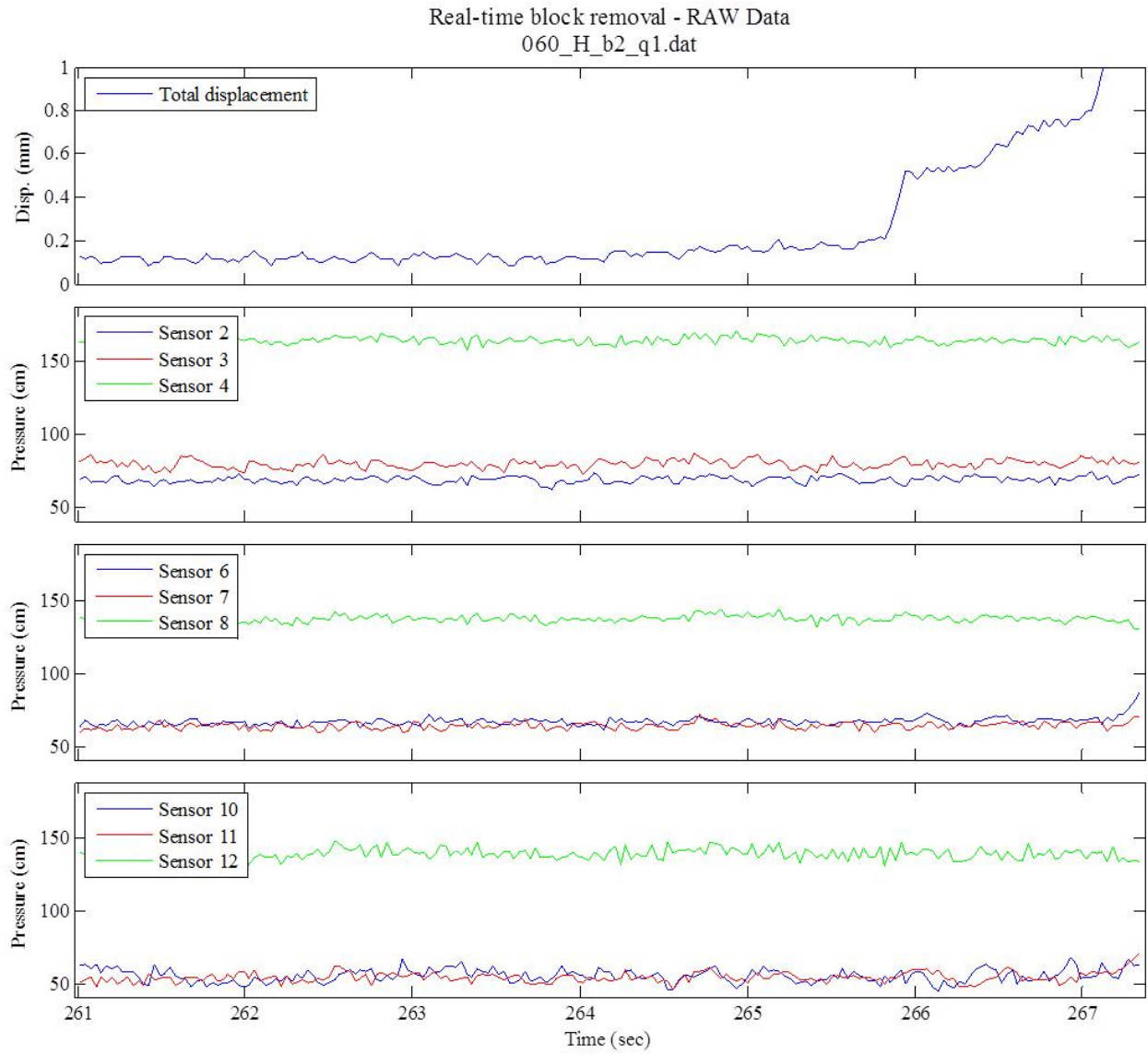


Displacement - RAW
060_H_b2_q1.dat

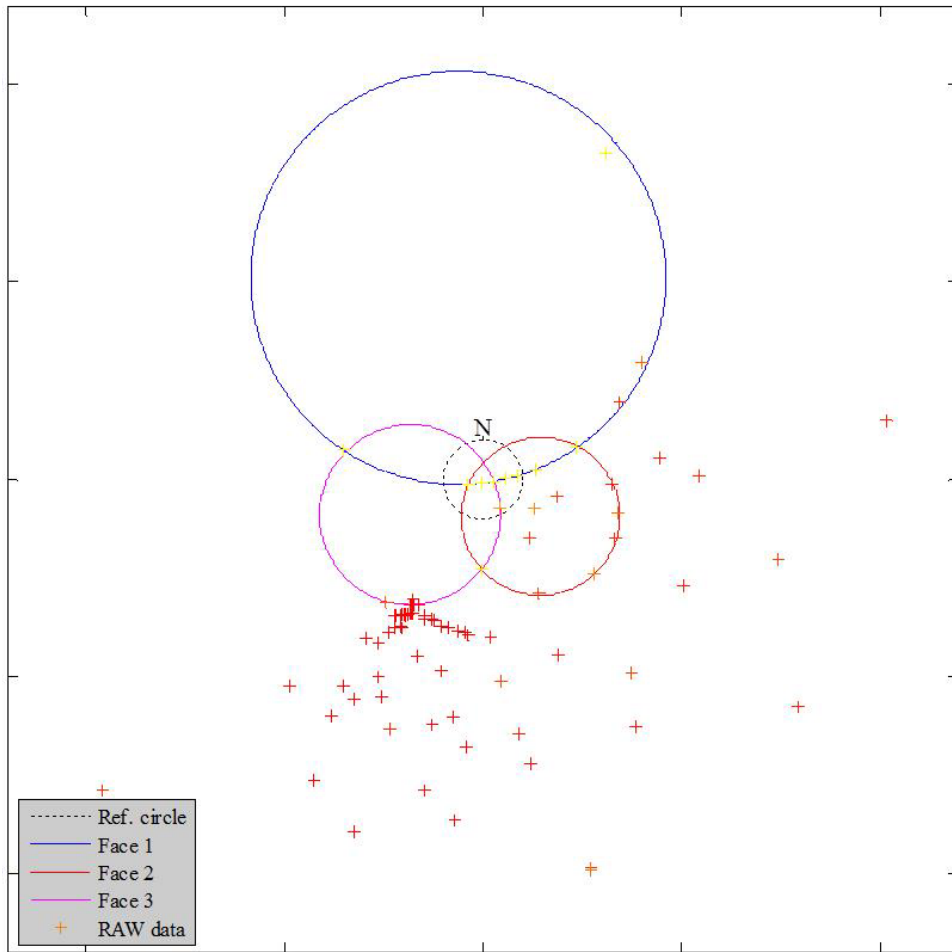


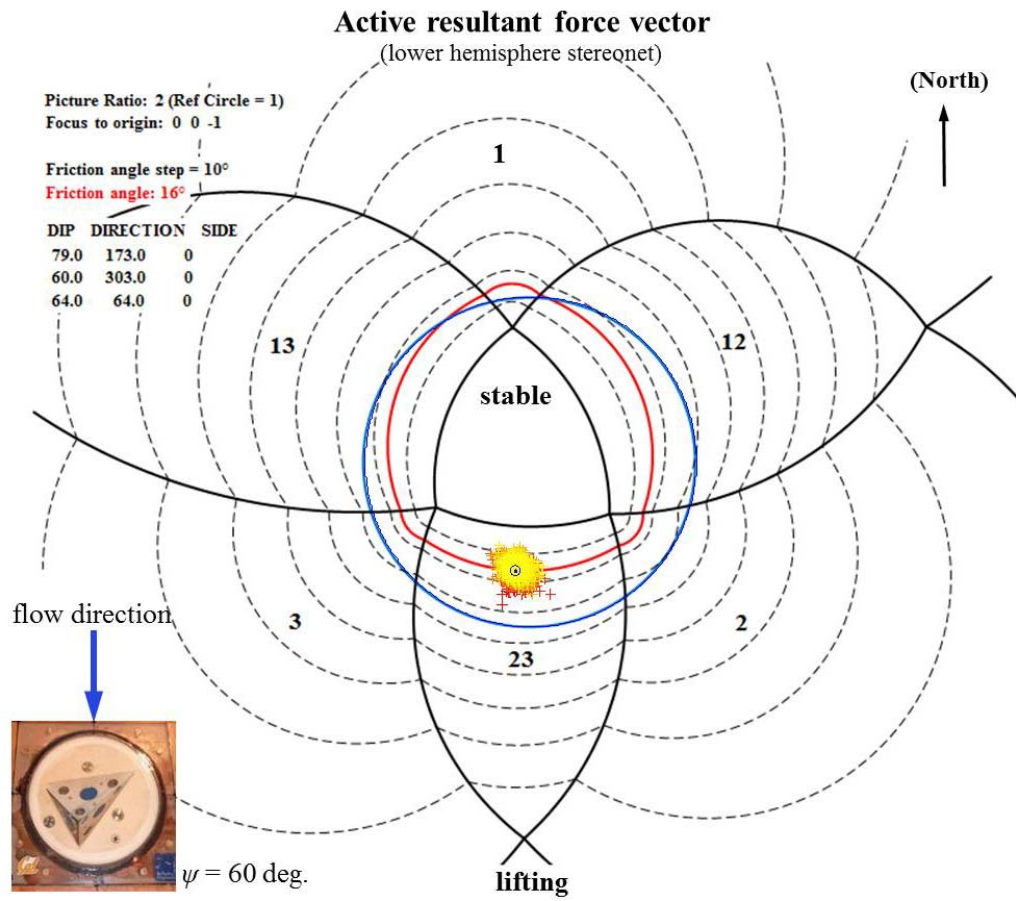
Displacement - FILTERED
060_H_b2_q1.dat



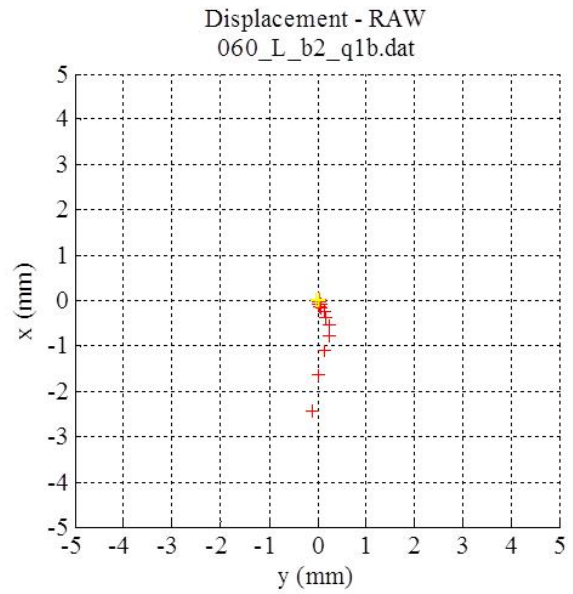
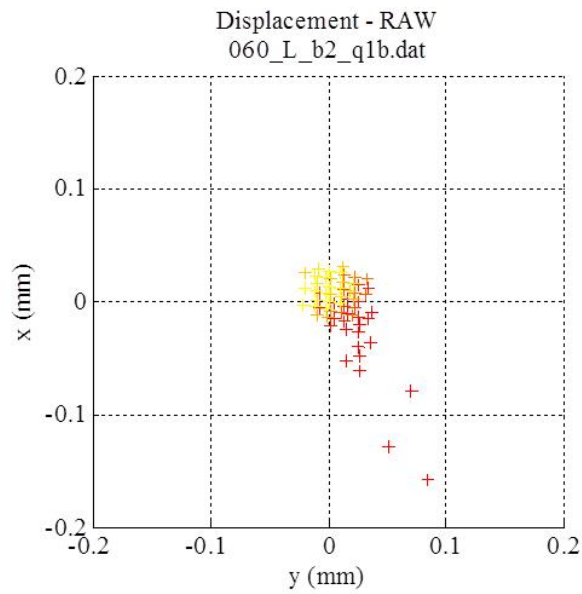
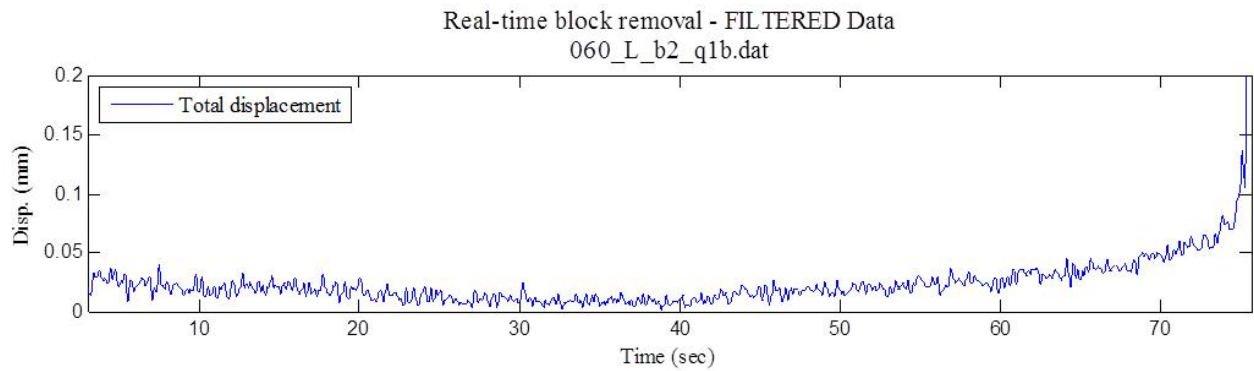


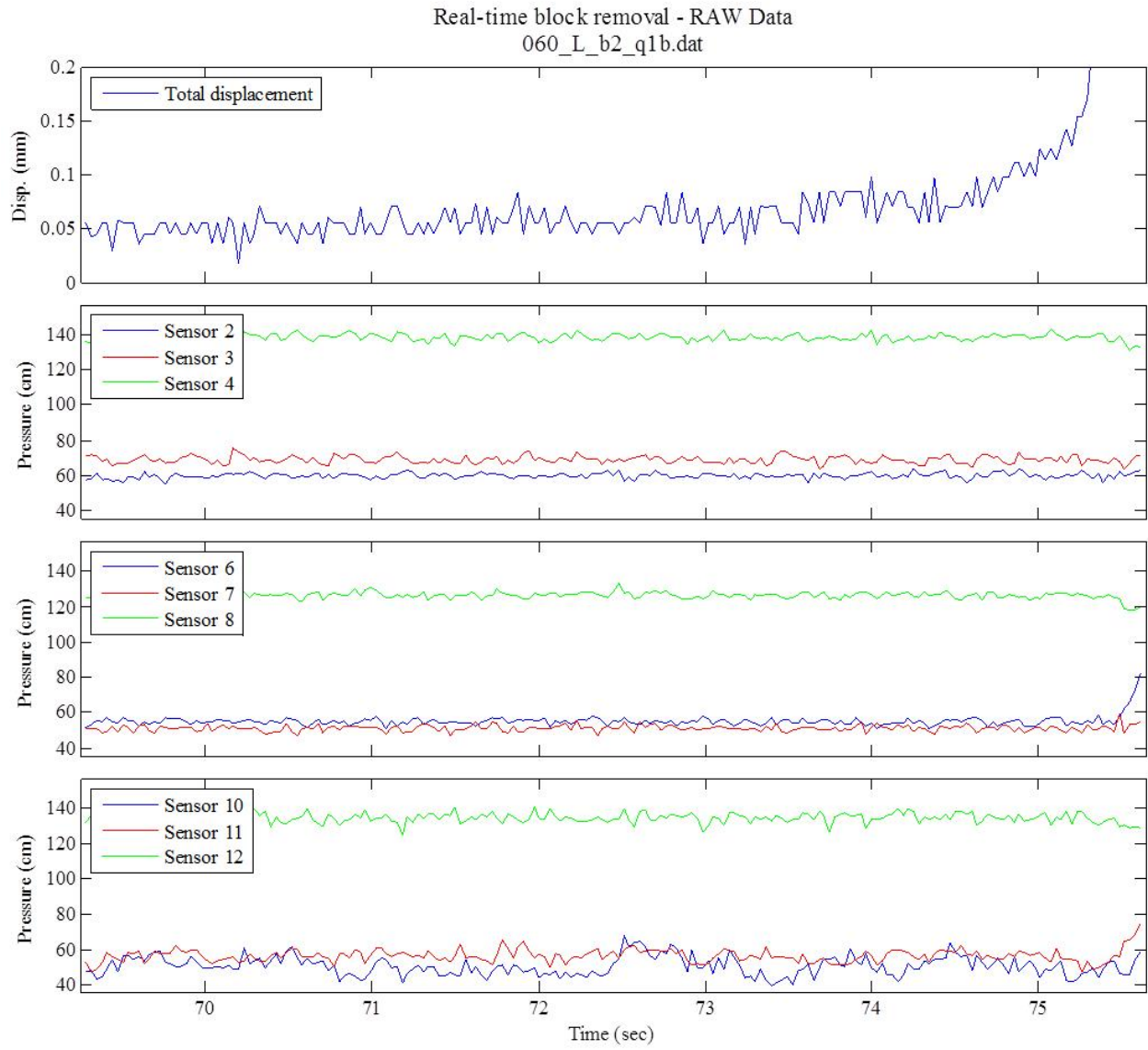
RAW displacement vector - lower hemisphere stereonet
060_H_b2_q1.dat



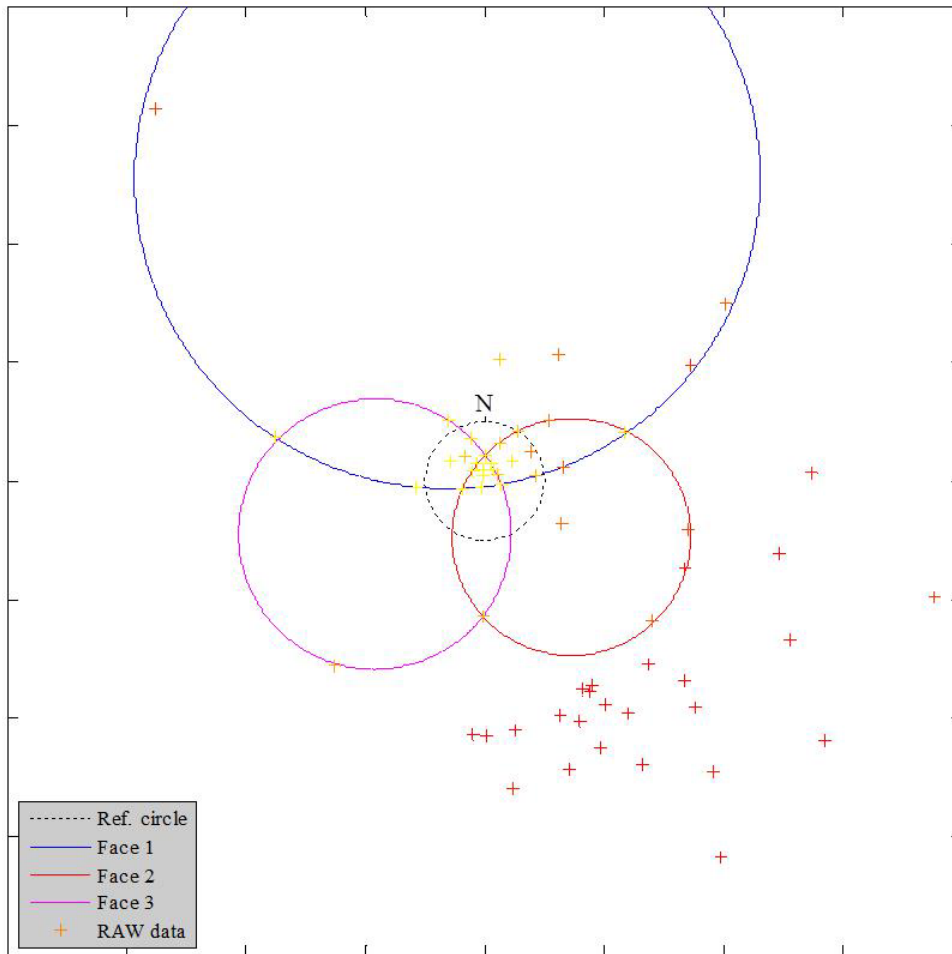


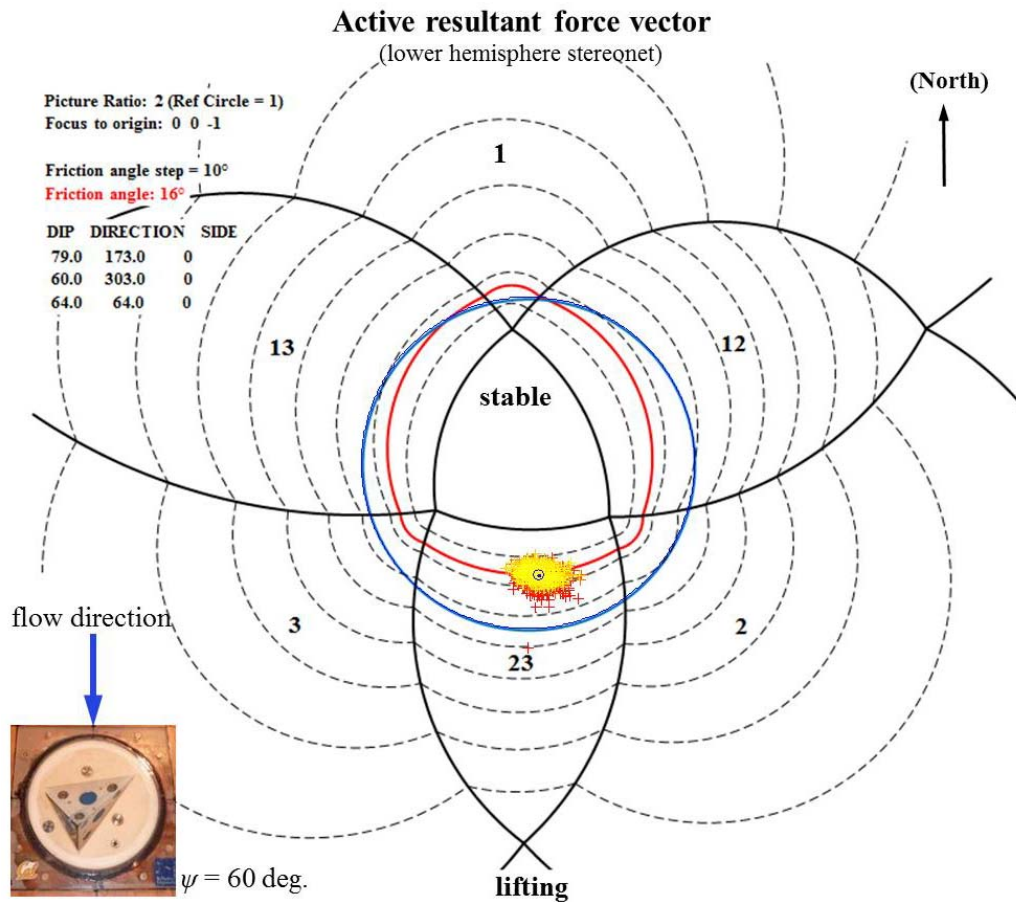
$\psi = 60$ deg., Low T_u , Block 2, Q_I



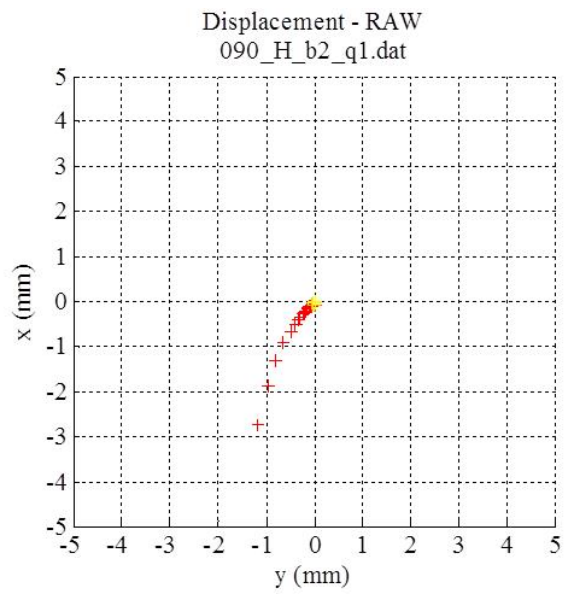
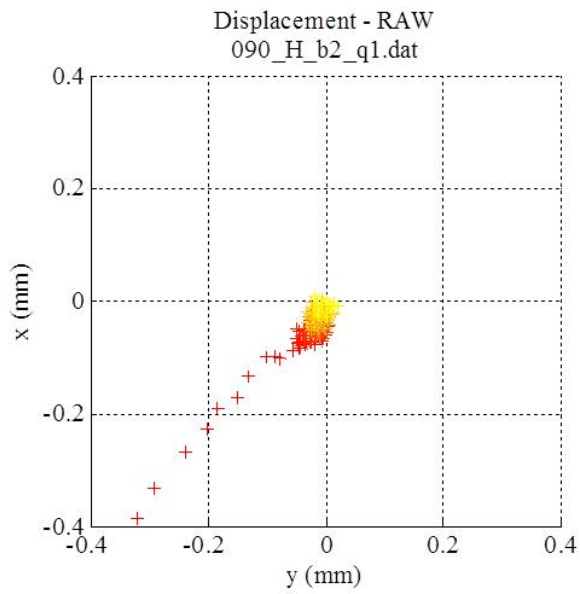
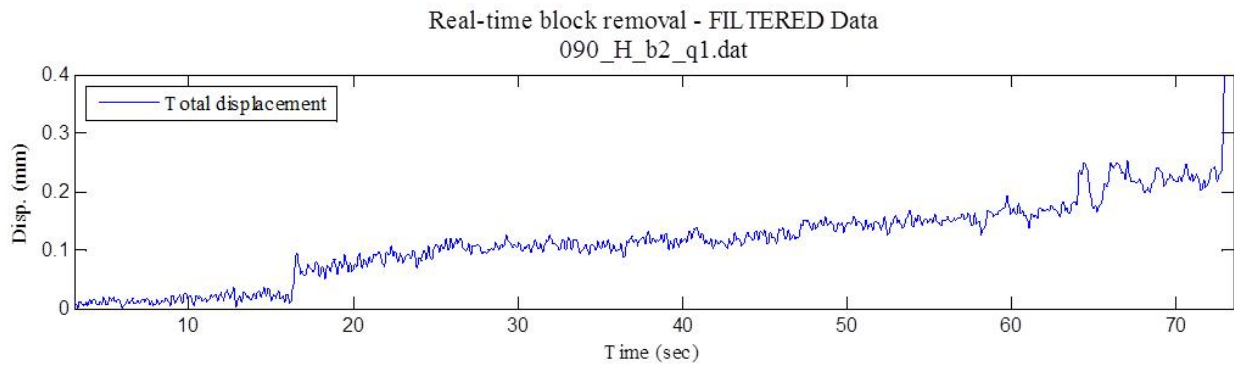


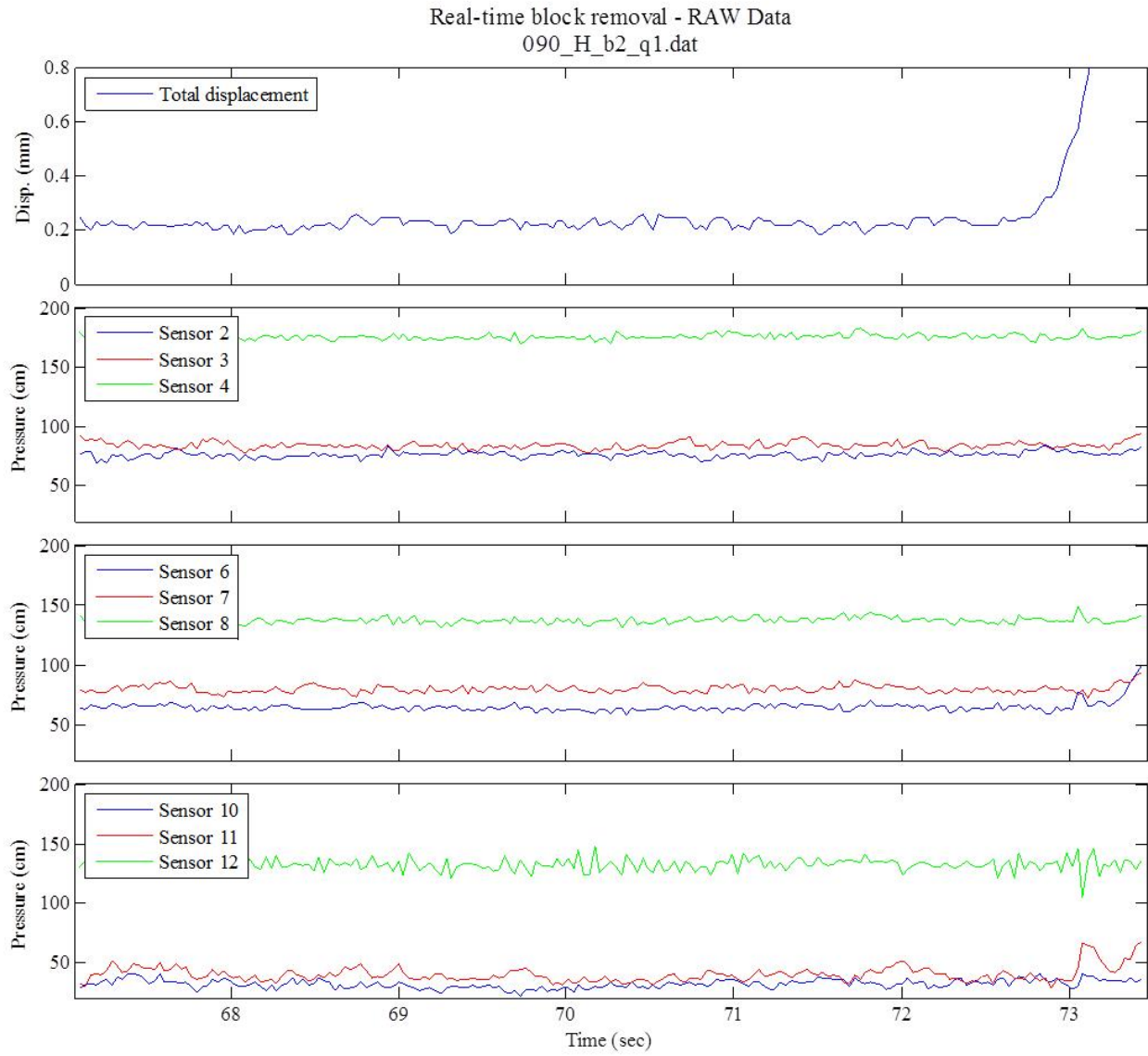
RAW displacement vector - lower hemisphere stereonet
060_L_b2_q1b.dat



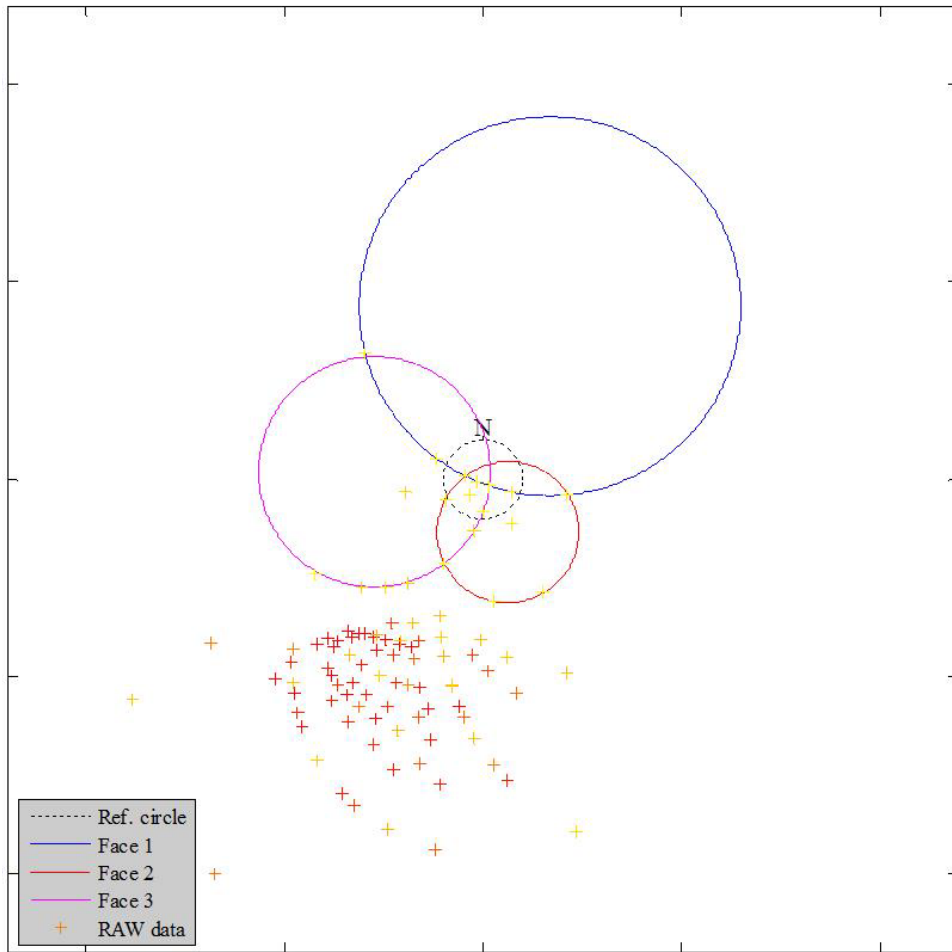


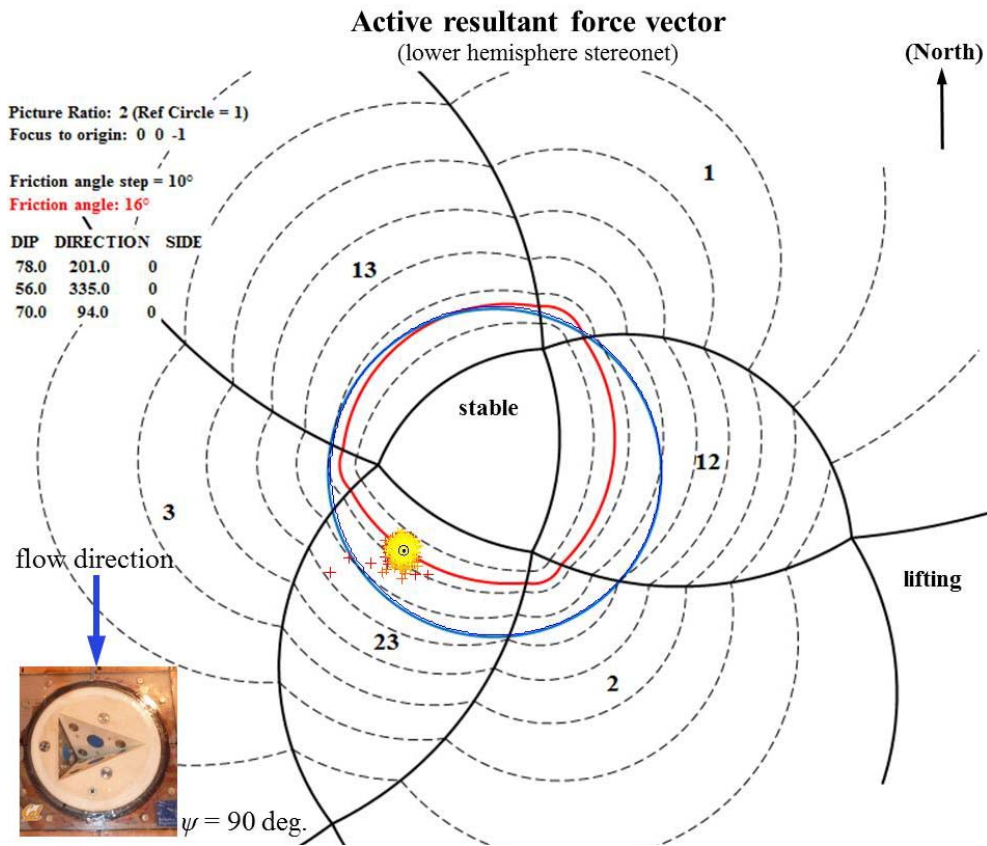
$\psi = 90$ deg., High T_u , Block 2, Q_I



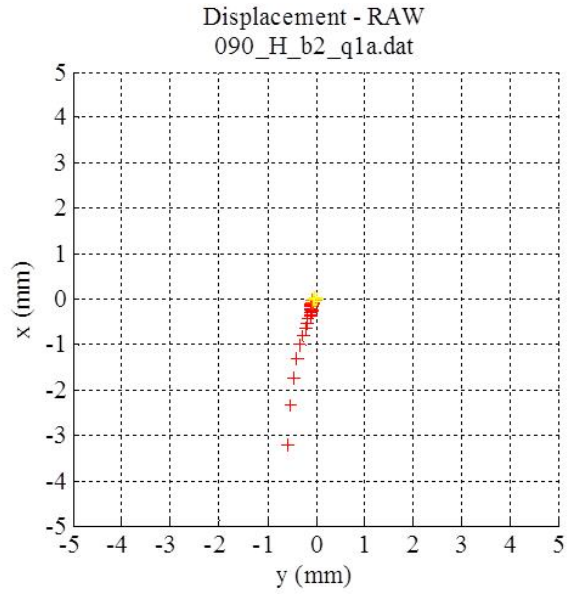
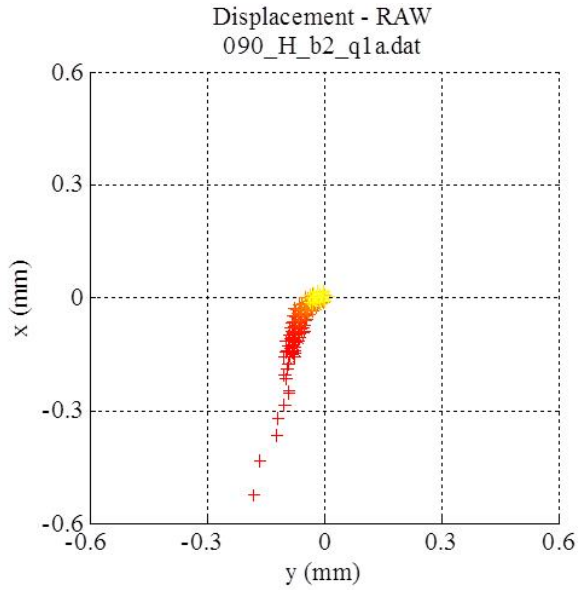
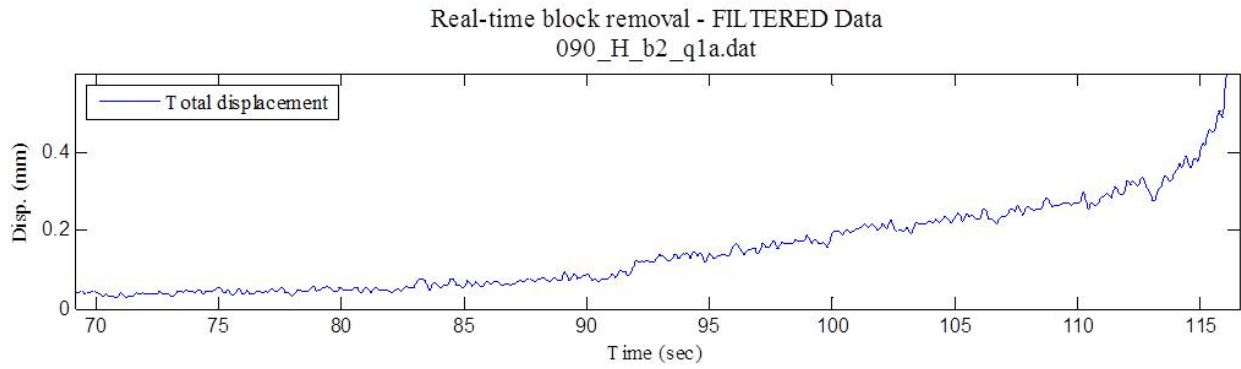


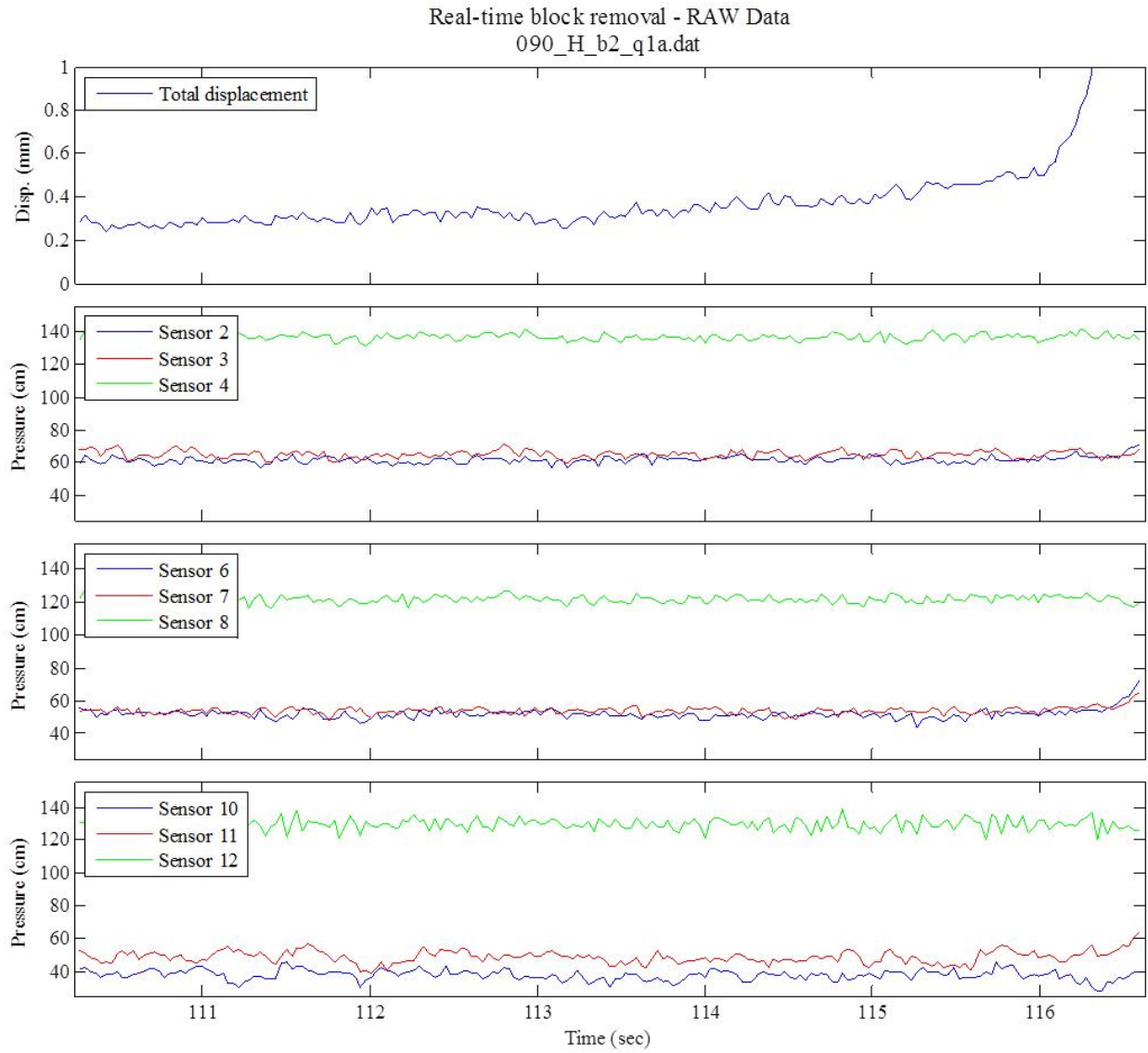
RAW displacement vector - lower hemisphere stereonet
090_H_b2_q1.dat



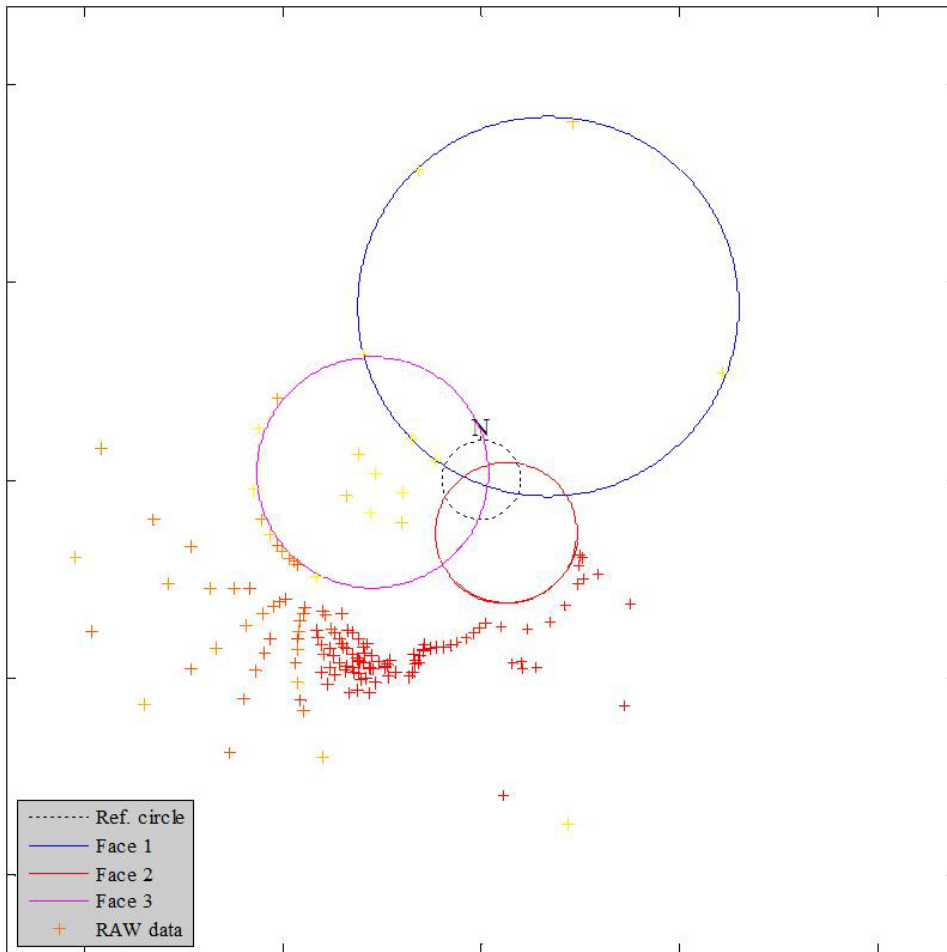


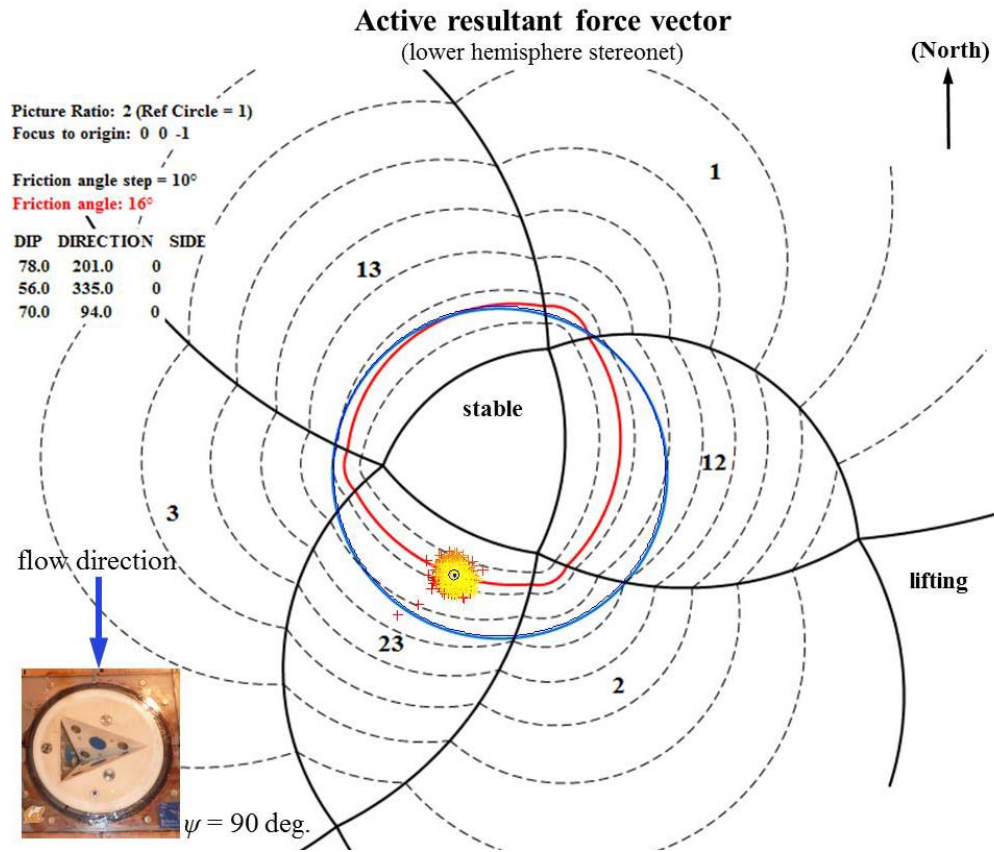
$\psi = 90$ deg., High T_u , Block 2, Q_I



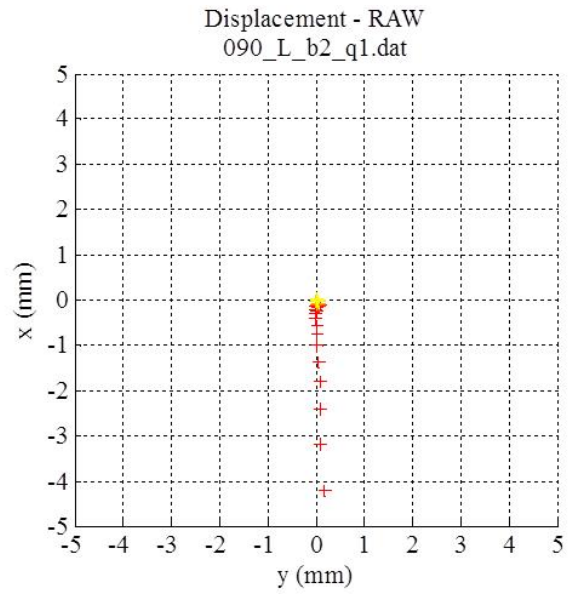
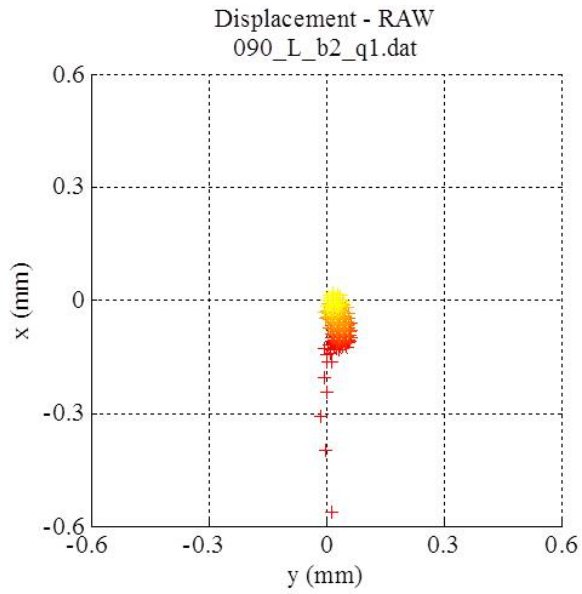
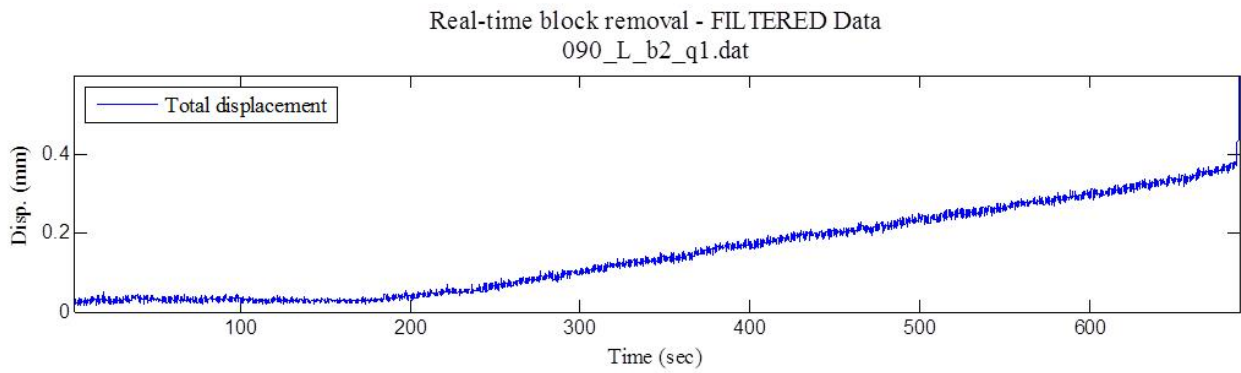


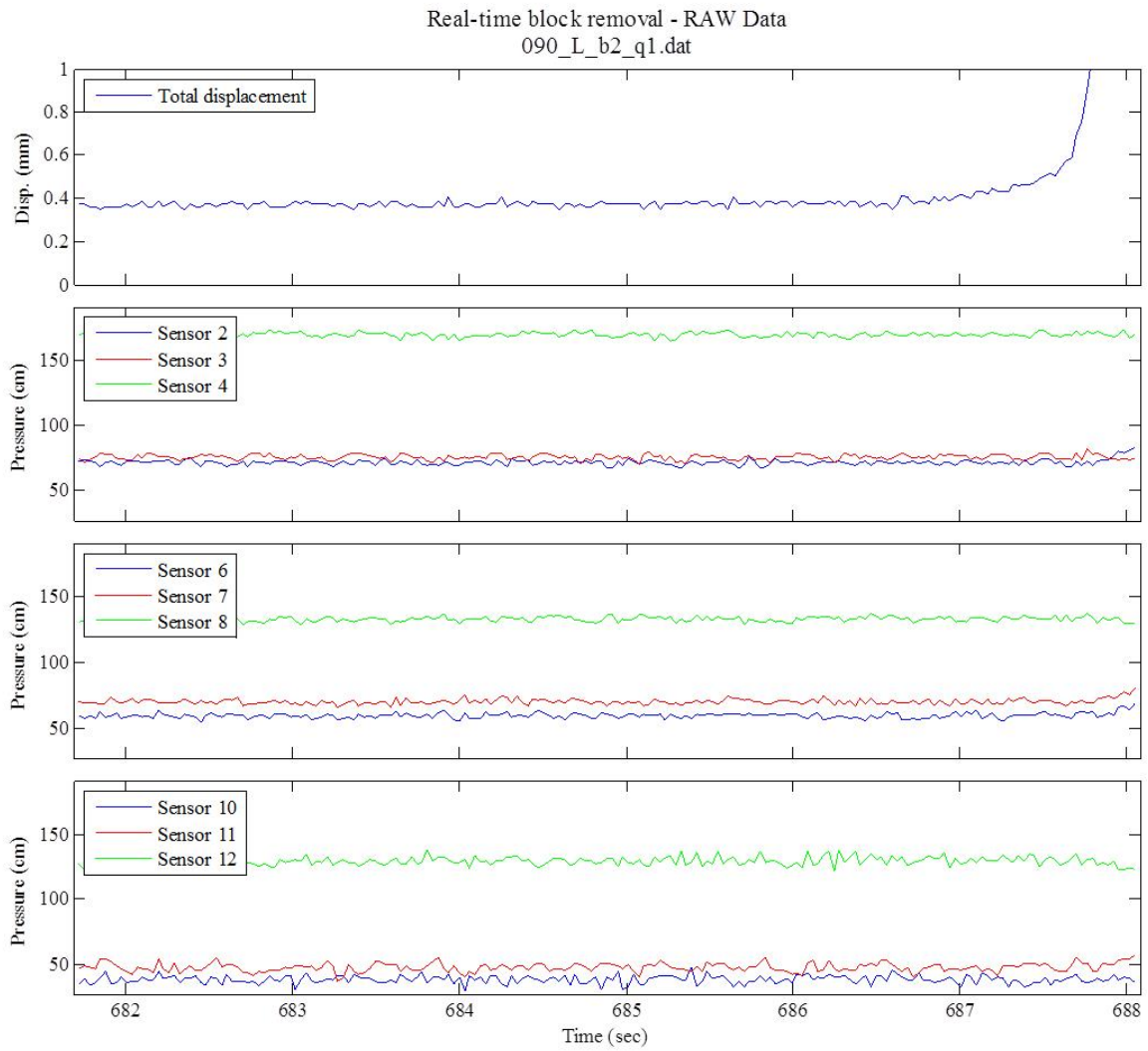
RAW displacement vector - lower hemisphere stereonet
090_H_b2_q1a.dat



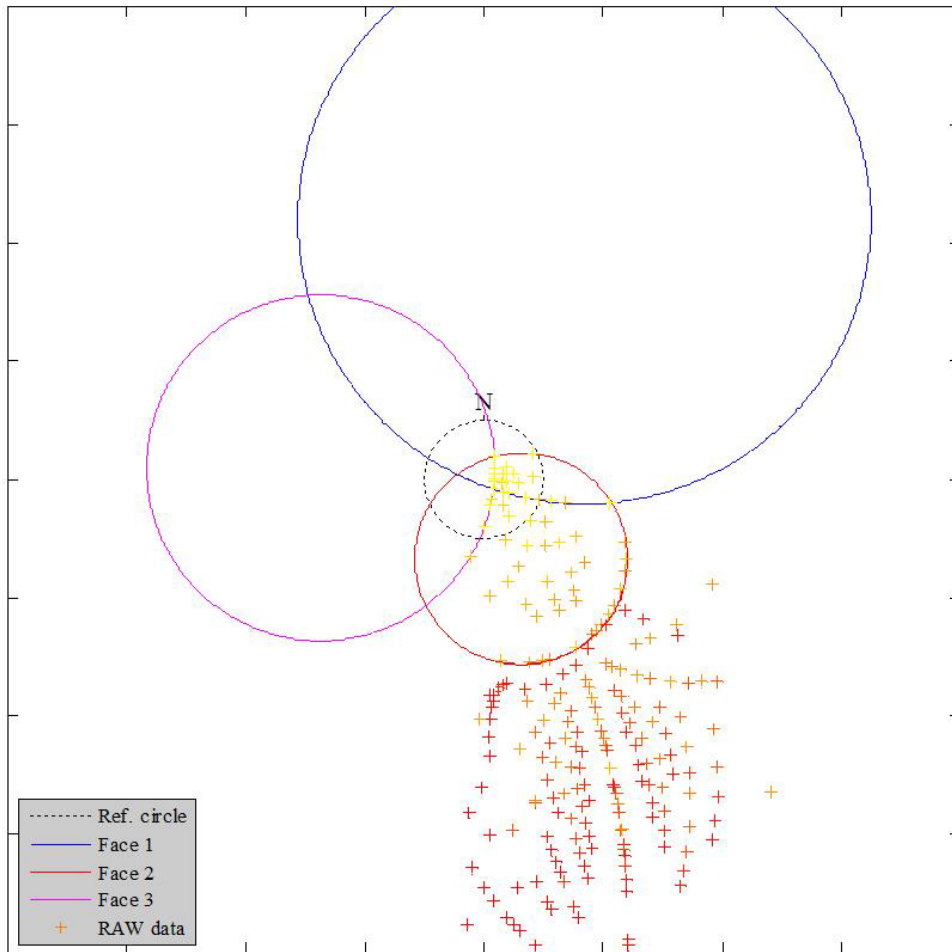


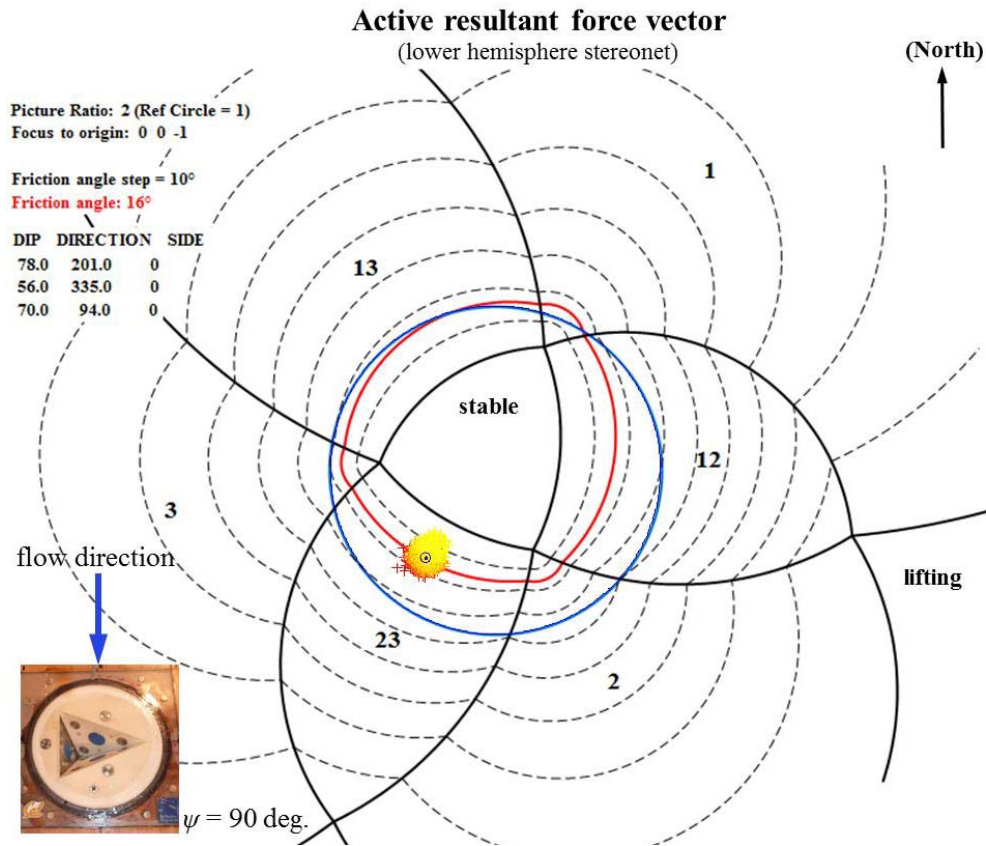
$\psi = 90$ deg., Low T_u , Block 2, Q_I



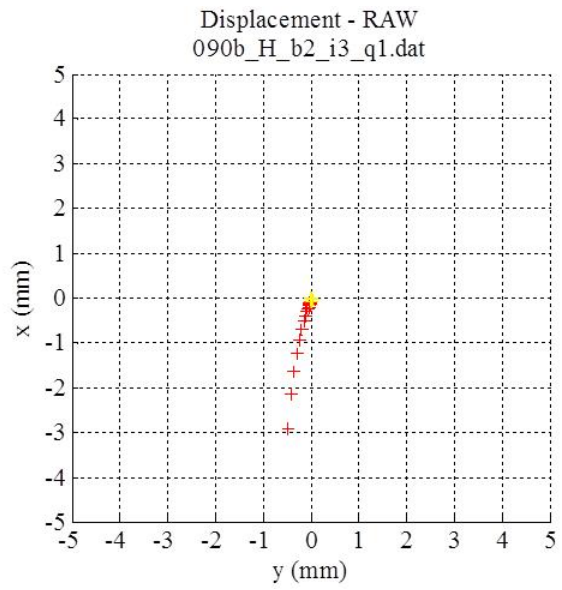
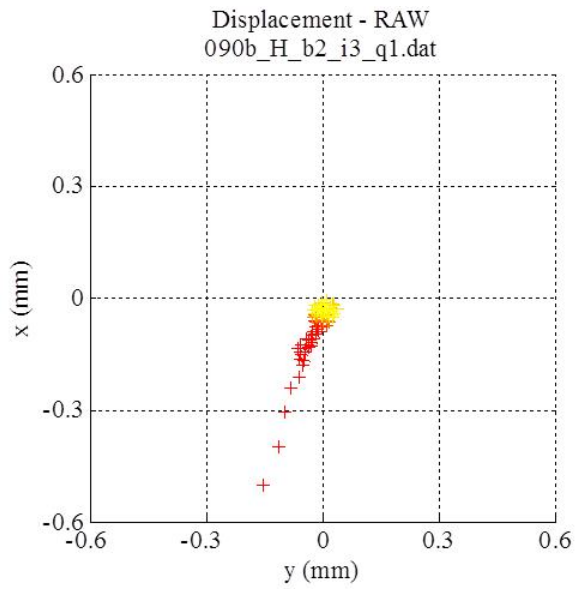
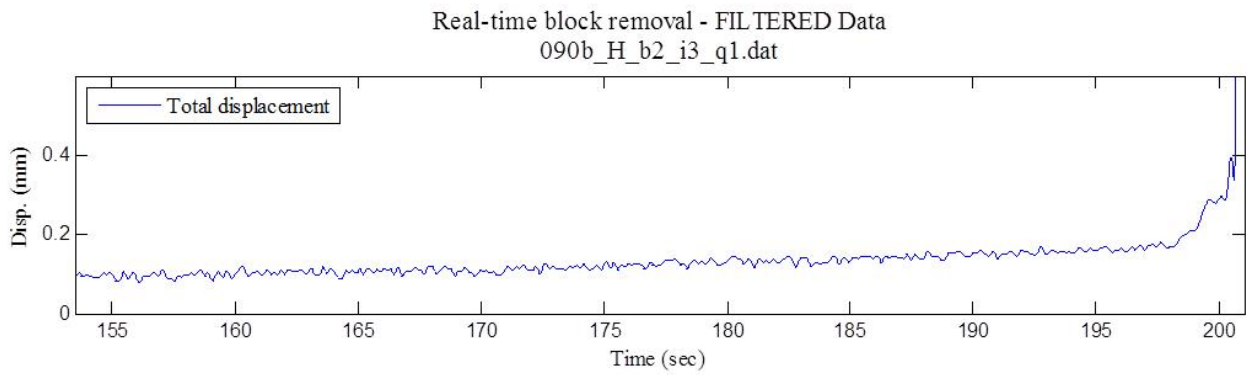


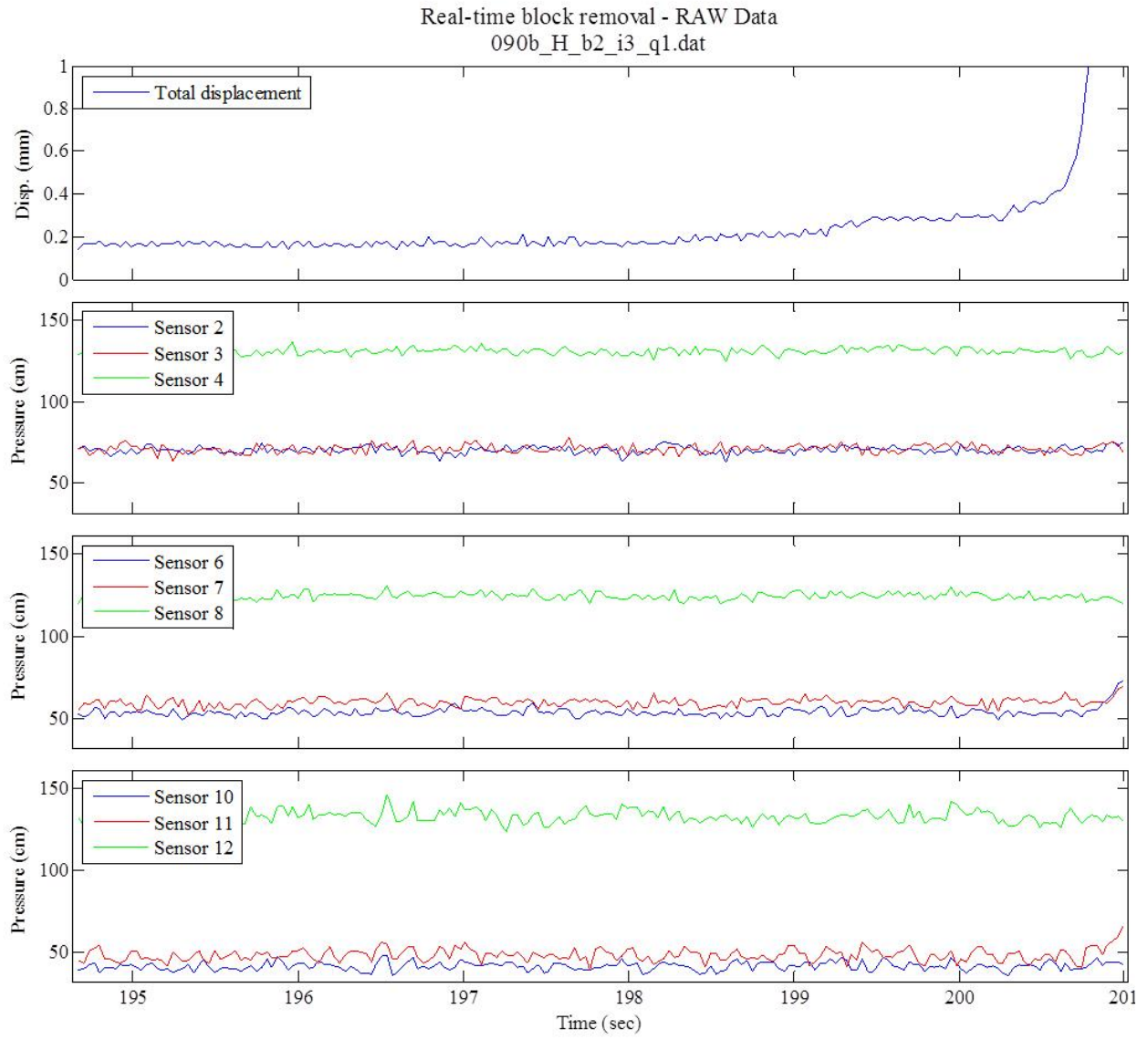
RAW displacement vector - lower hemisphere stereonet
090_L_b2_q1.dat



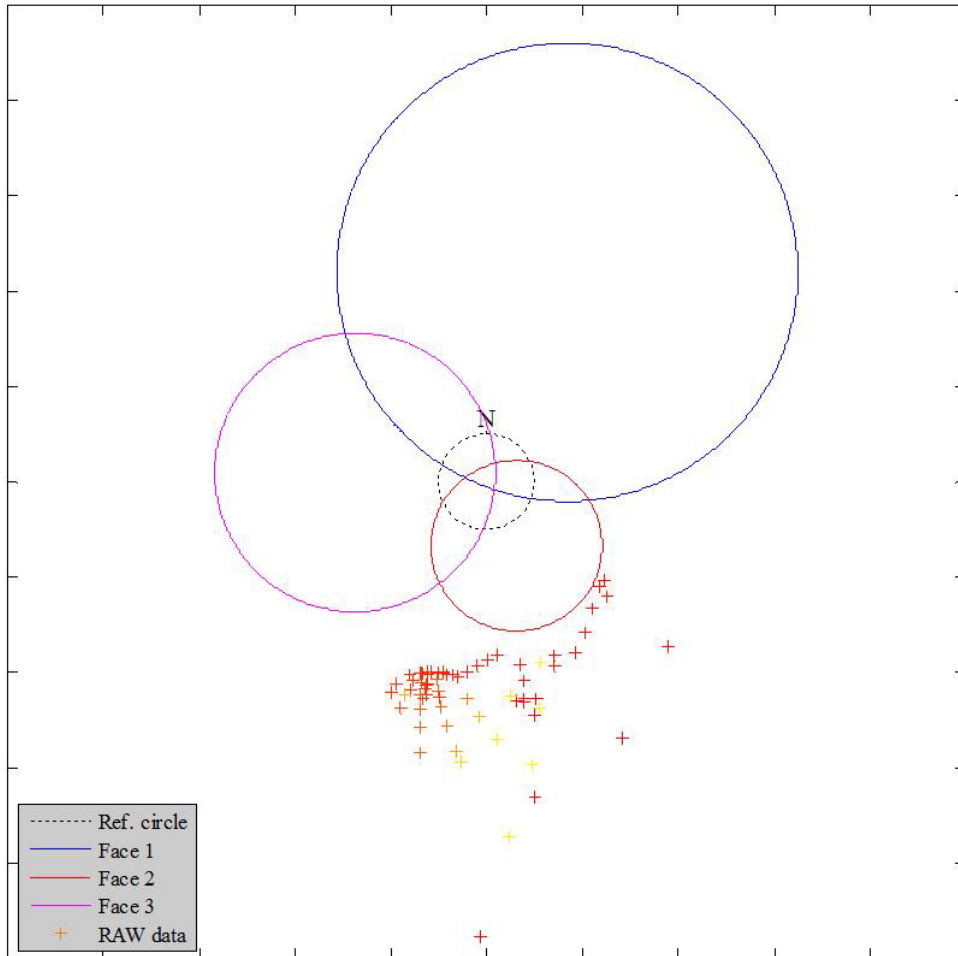


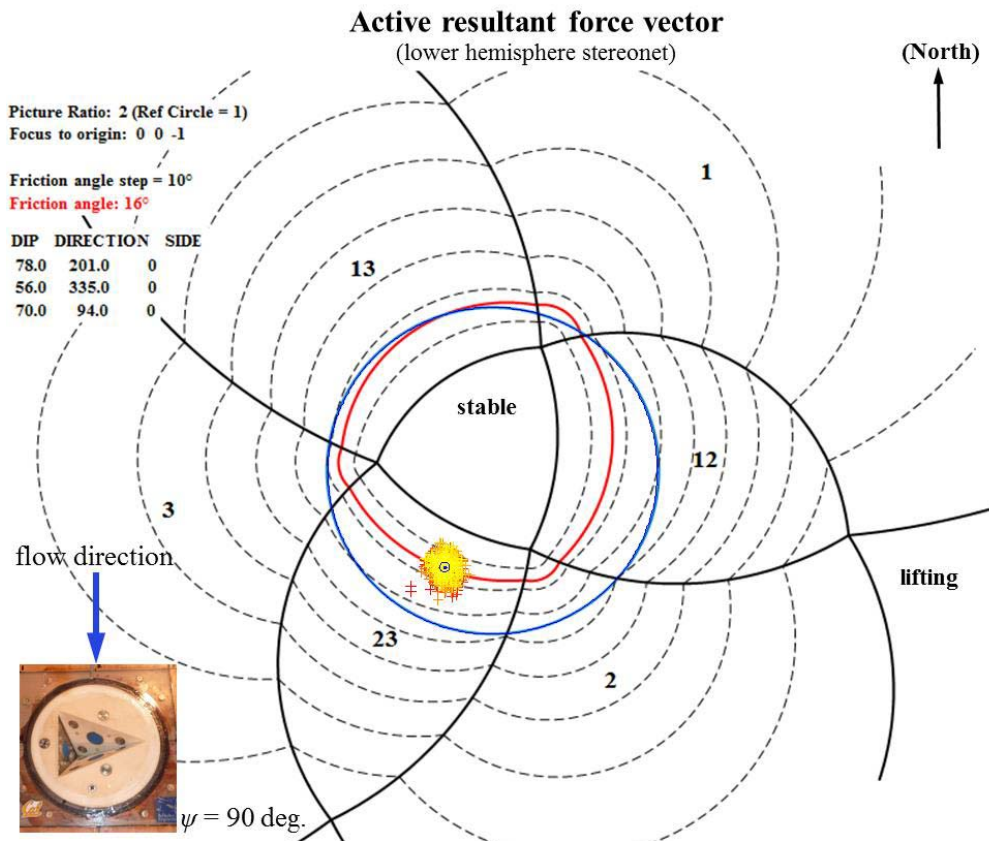
$\psi = 90$ deg., High T_u , Block 2, Q_I



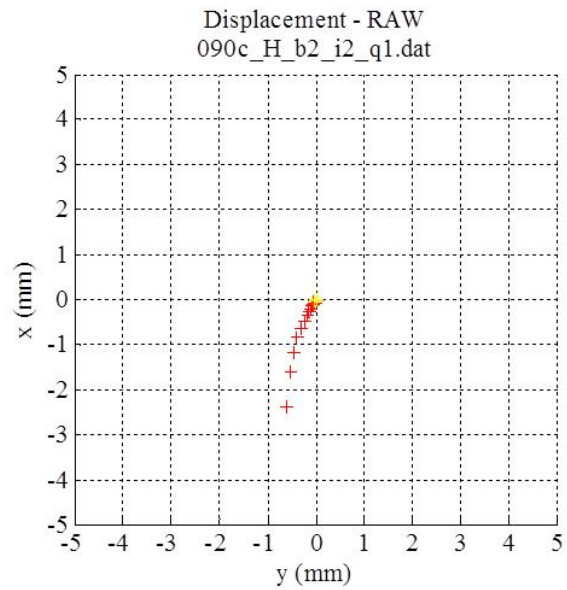
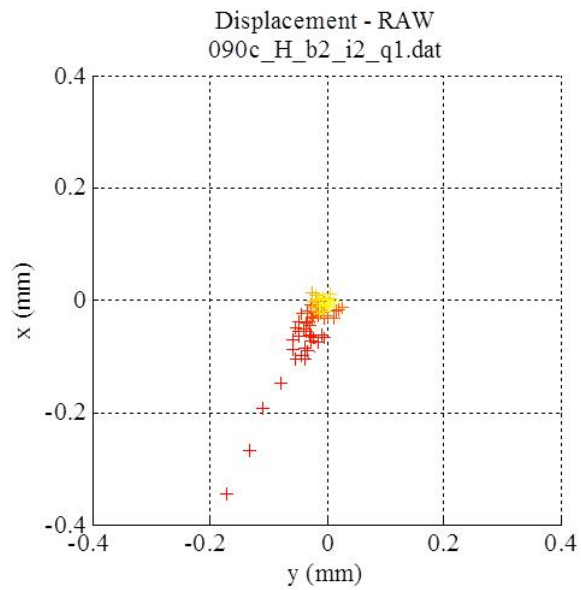
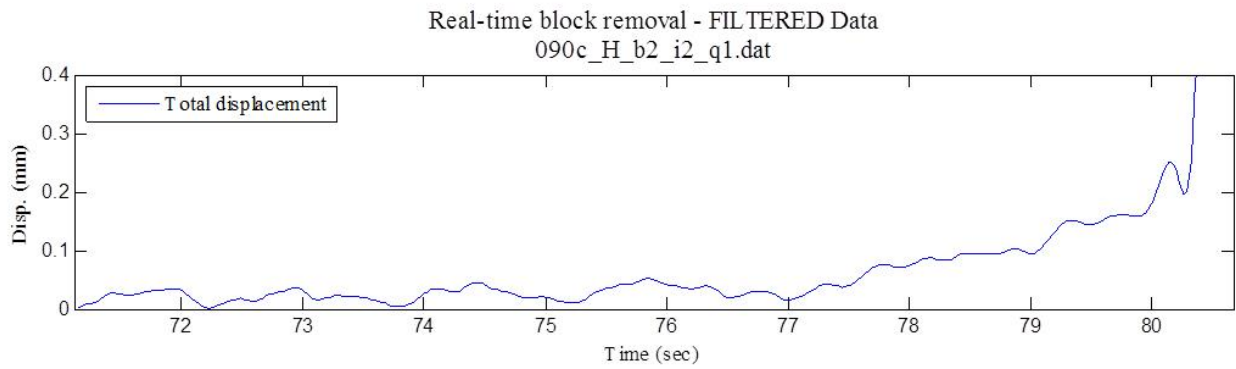


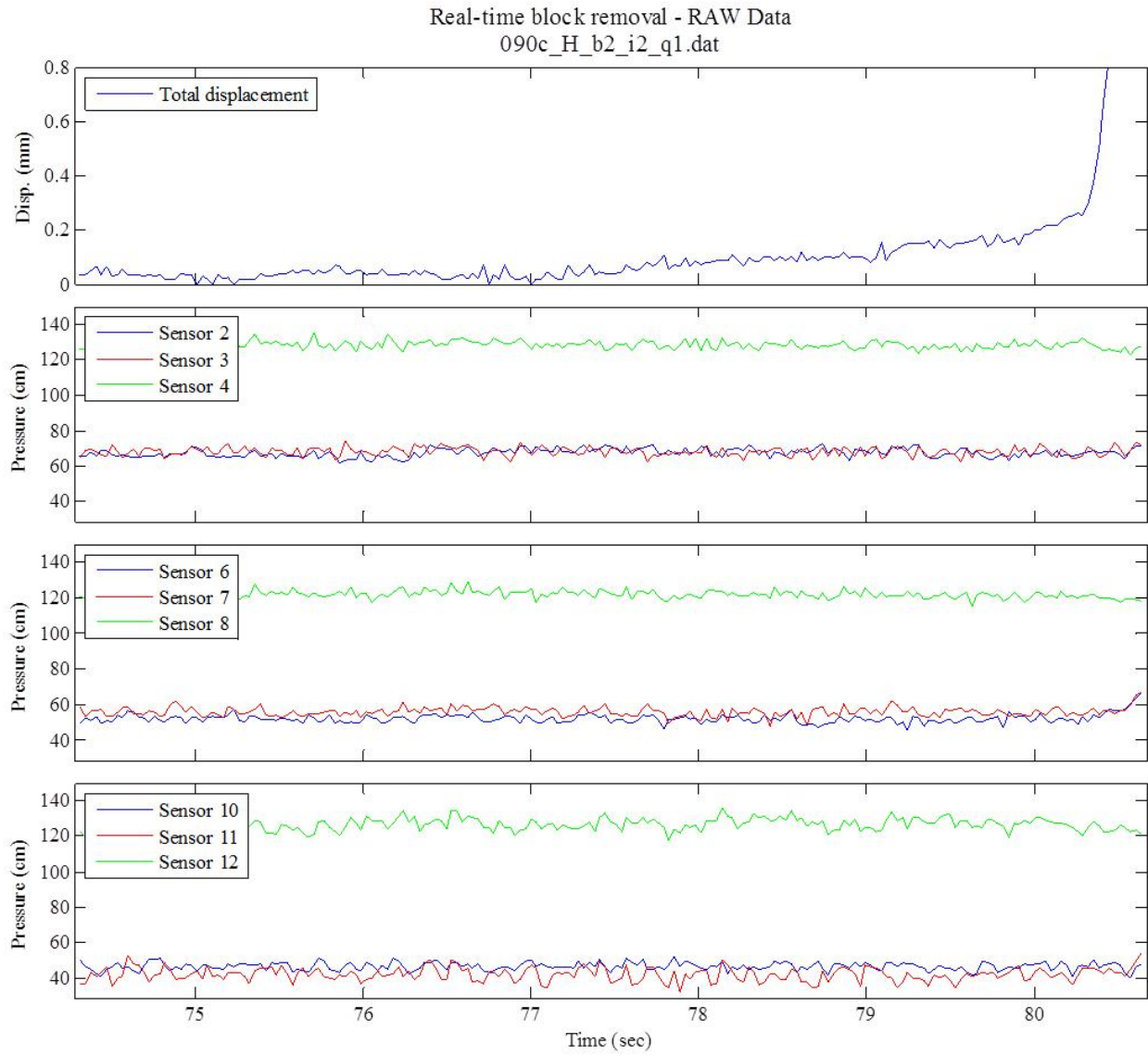
RAW displacement vector - lower hemisphere stereonet
090b_H_b2_i3_q1.dat



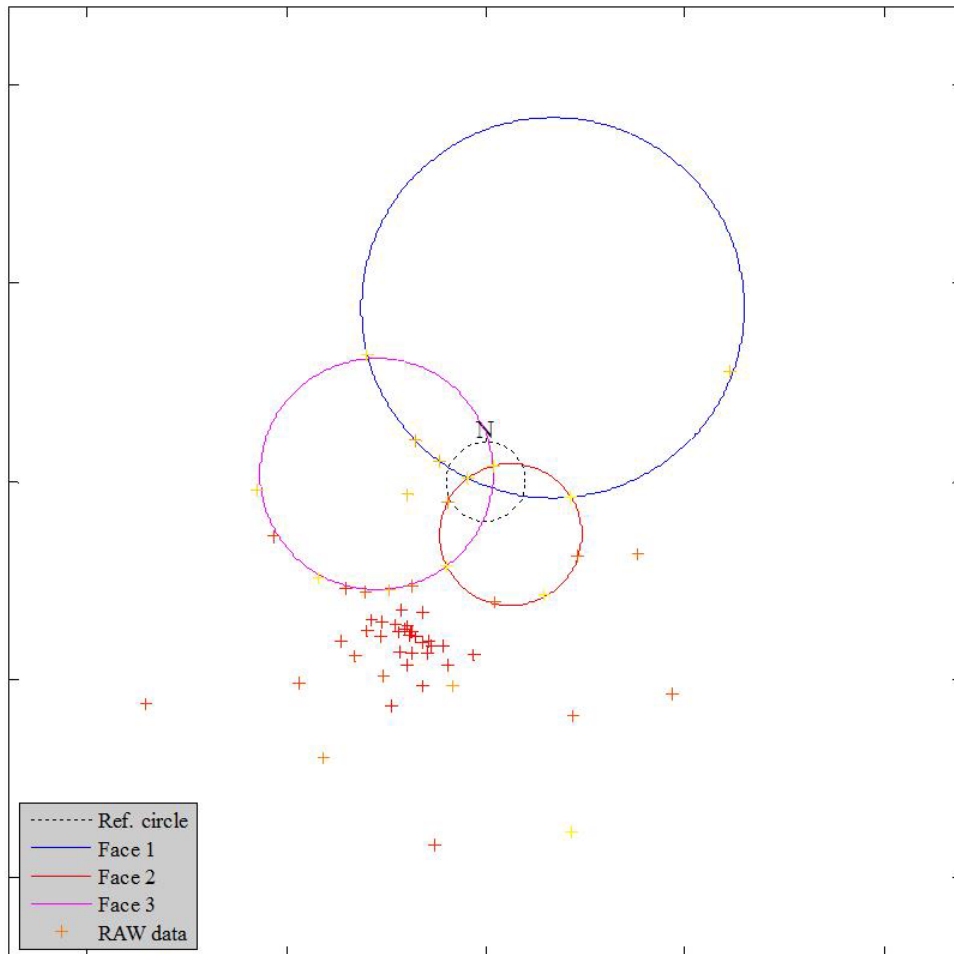


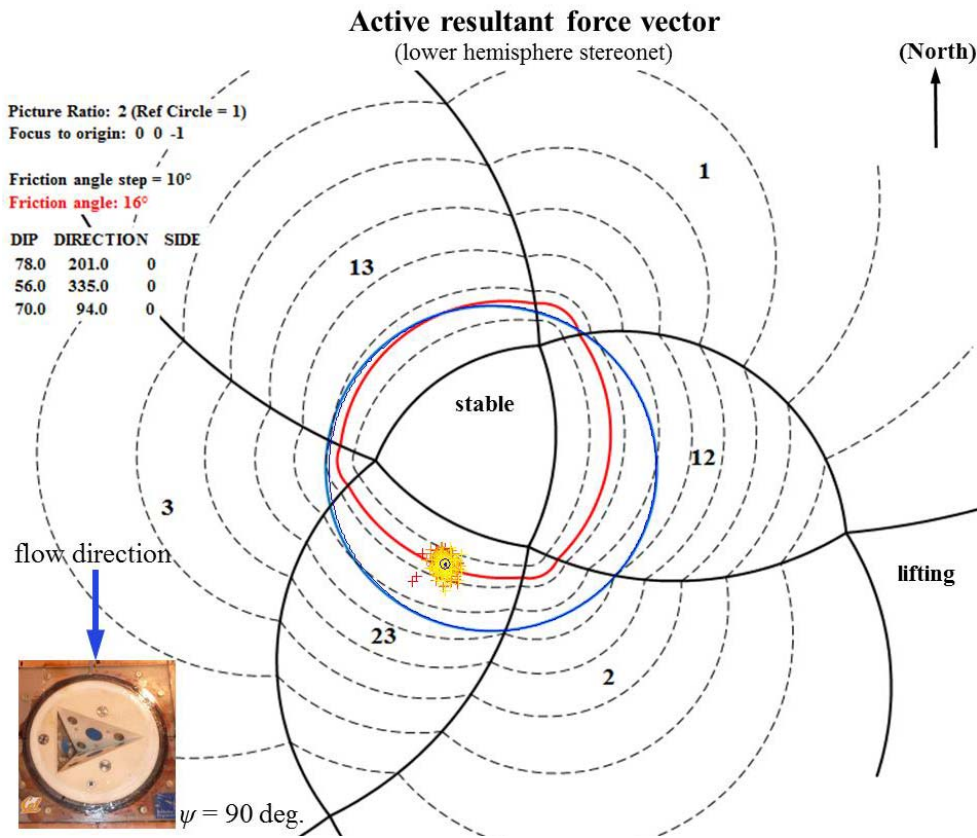
$\psi = 90$ deg., High T_u , Block 2, Q_I



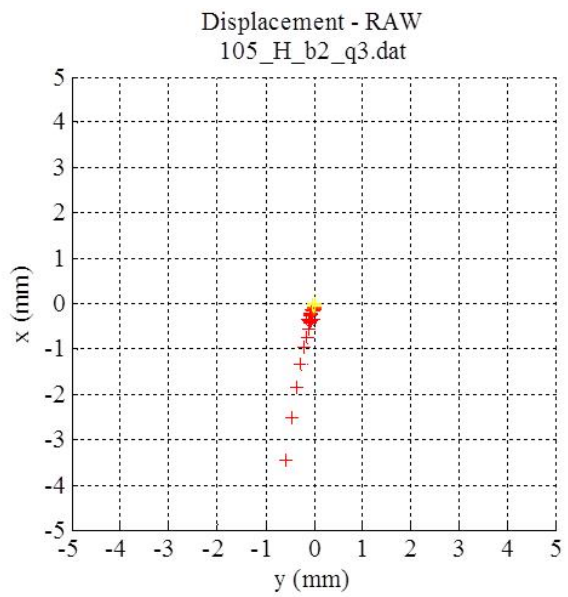
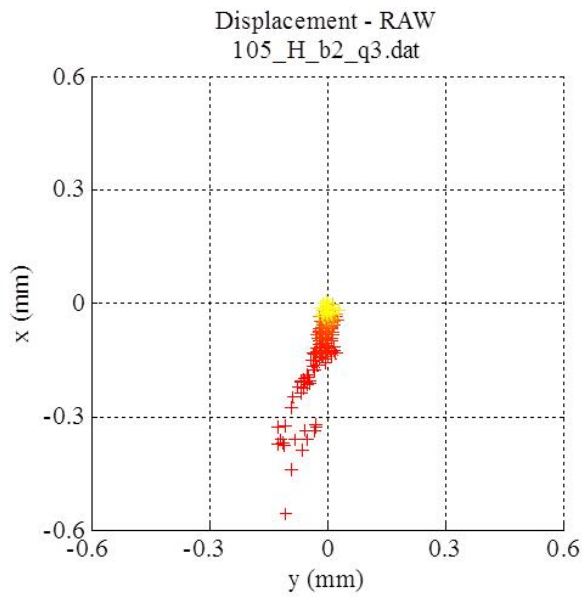
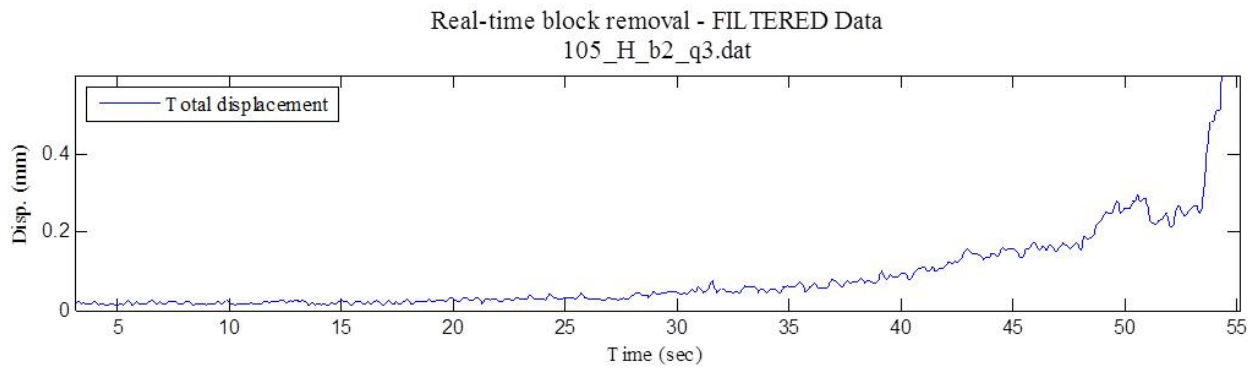


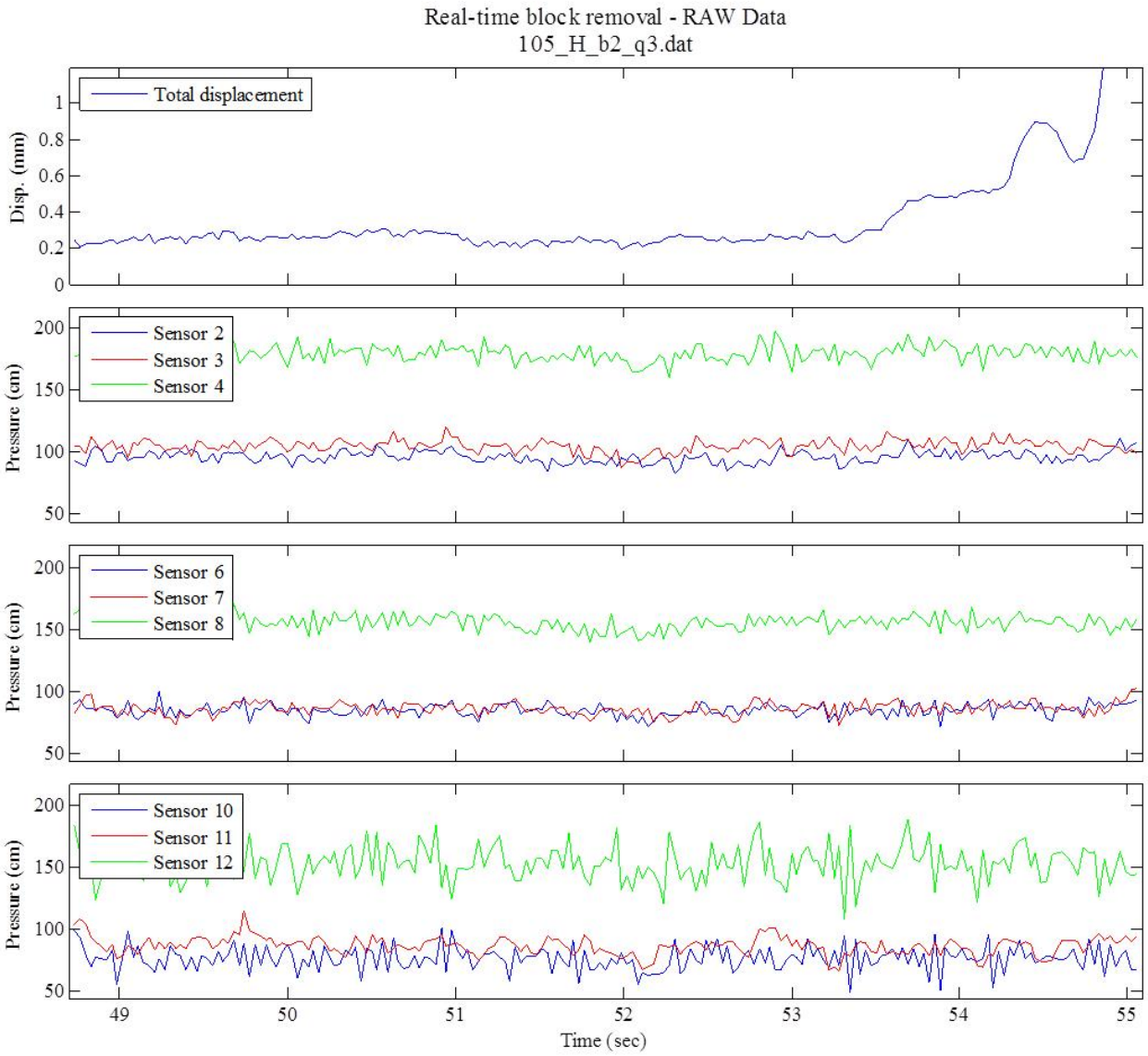
RAW displacement vector - lower hemisphere stereonet
090c_H_b2_i2_q1.dat



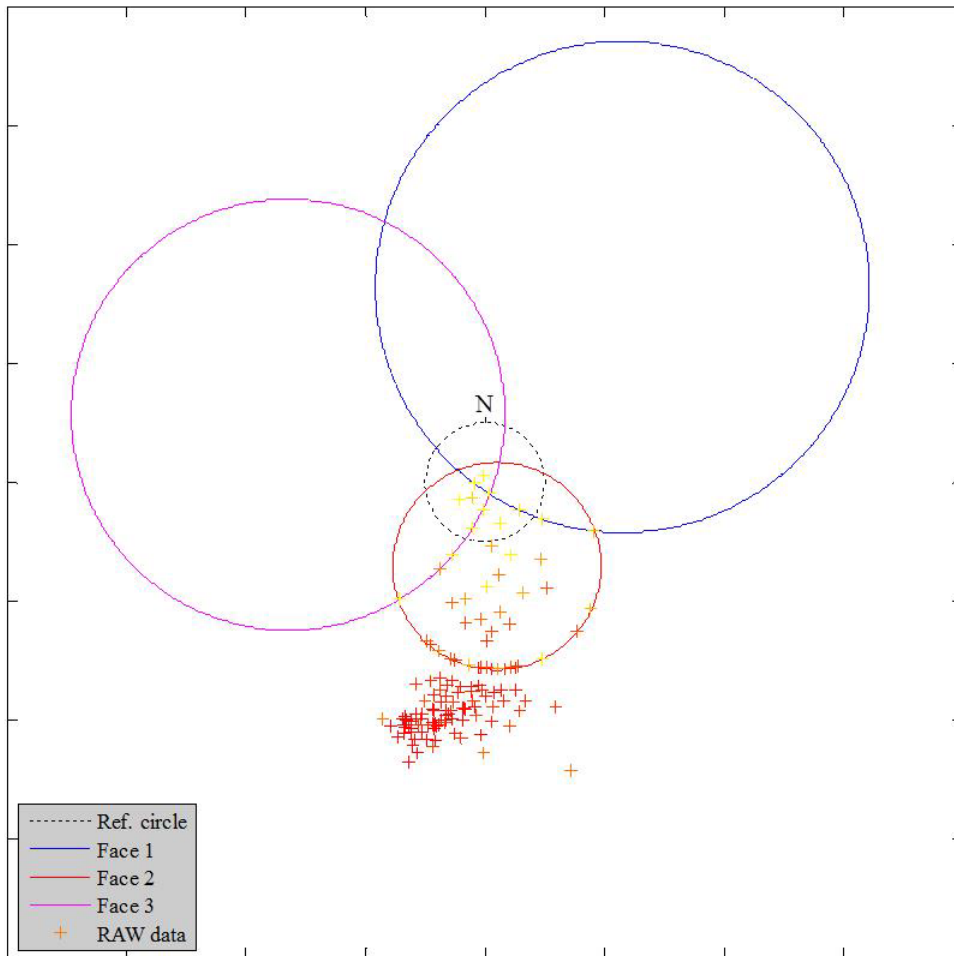


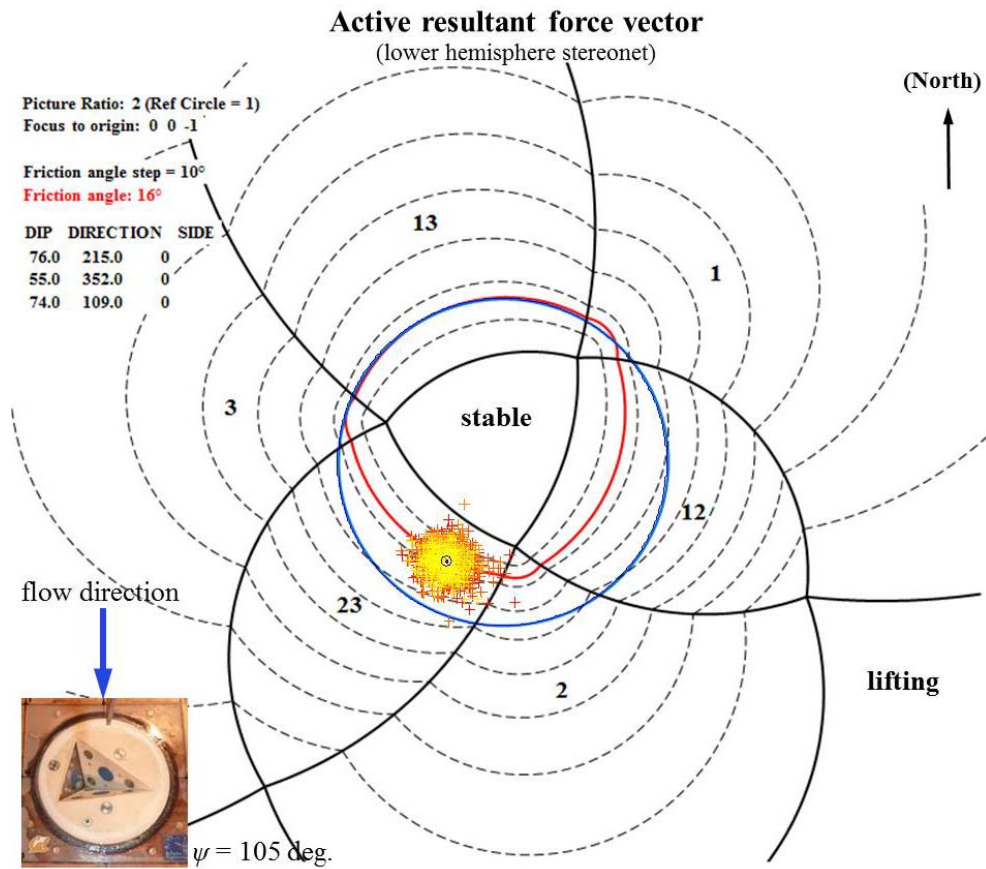
$\psi = 105$ deg., High T_u , Block 2, Q_3



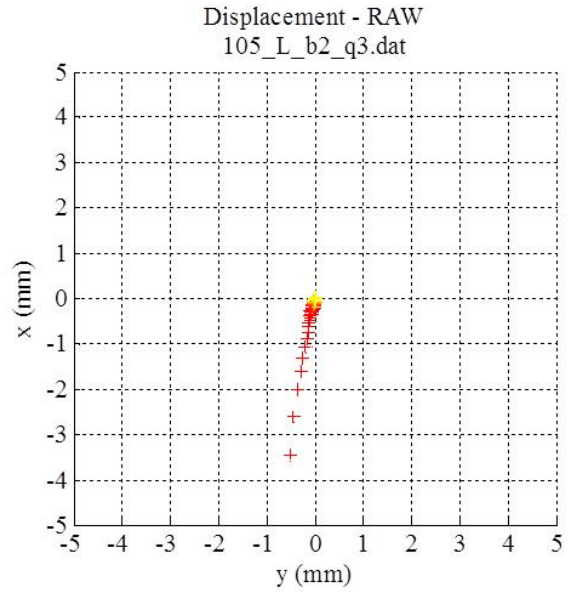
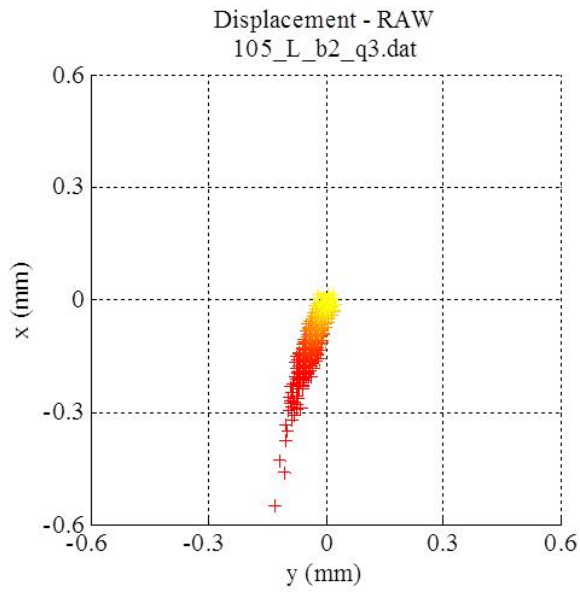
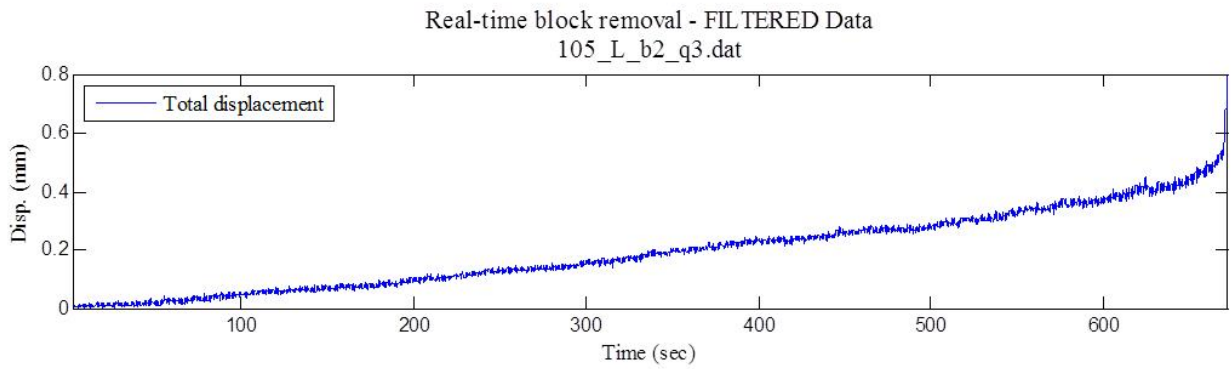


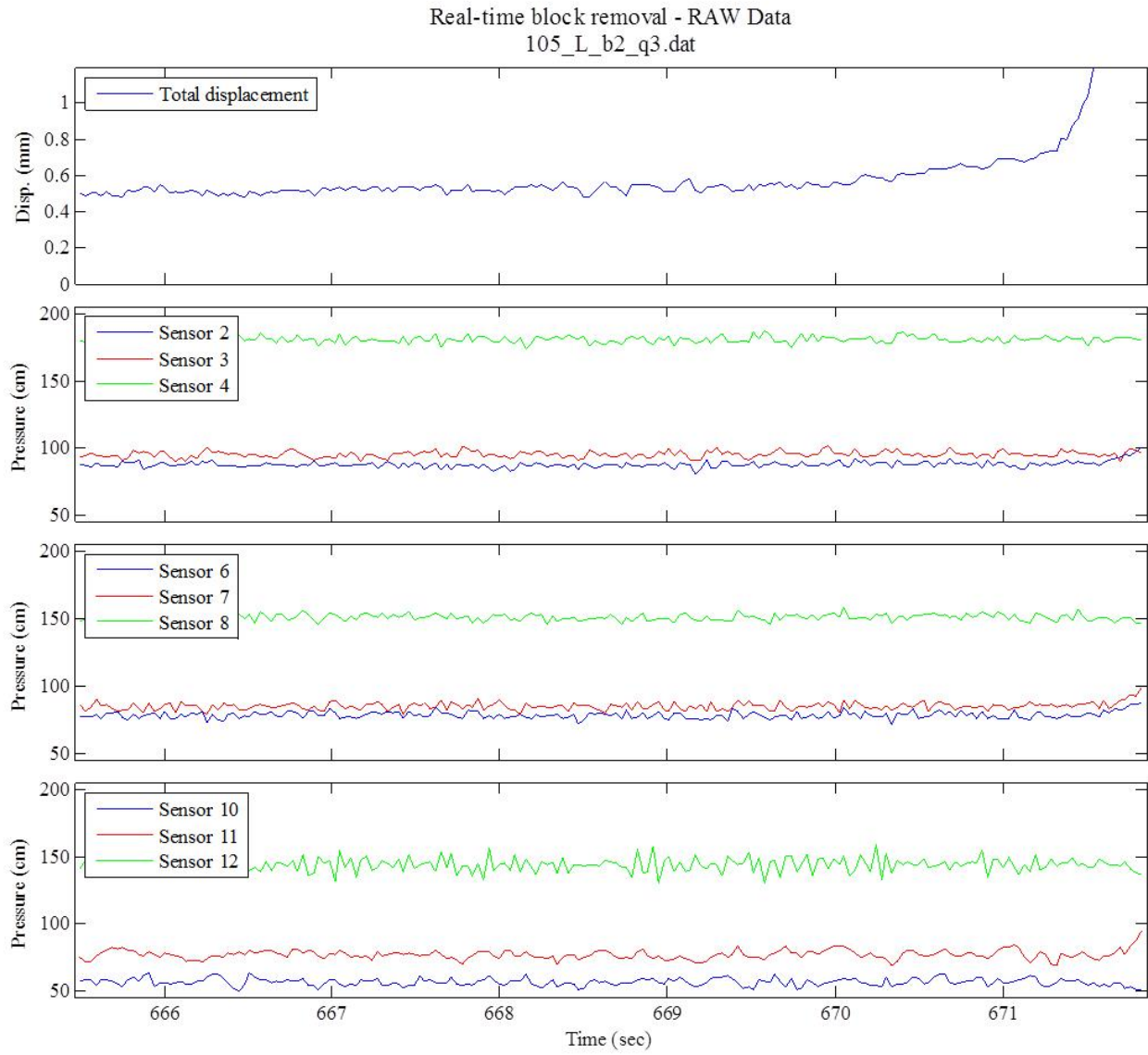
RAW displacement vector - lower hemisphere stereonet
105_H_b2_q3.dat



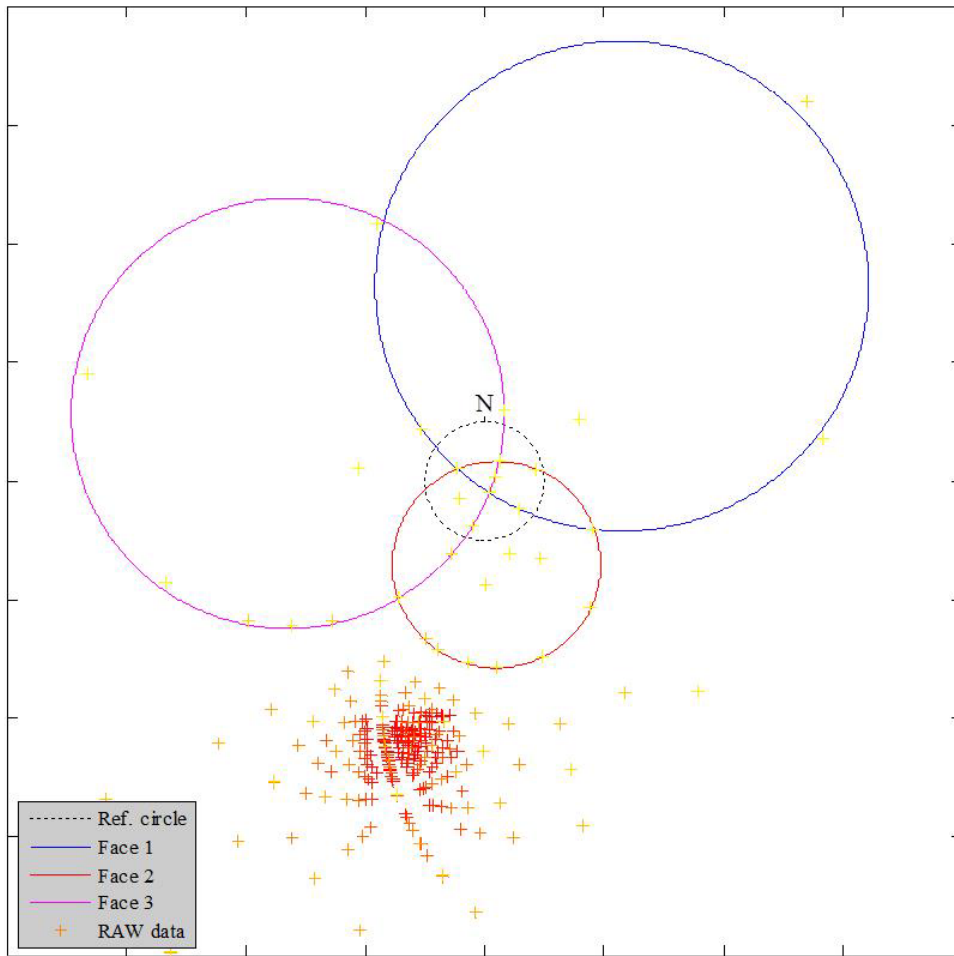


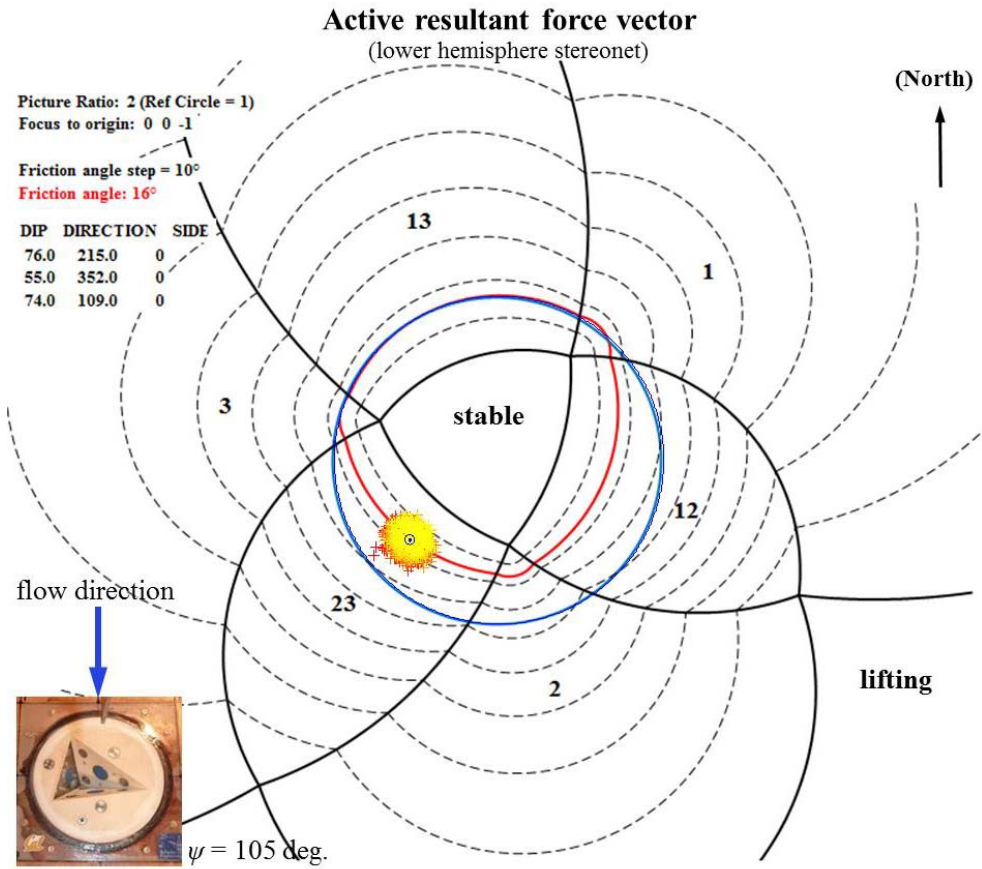
$\psi = 105$ deg., Low T_u , Block 2, Q_3





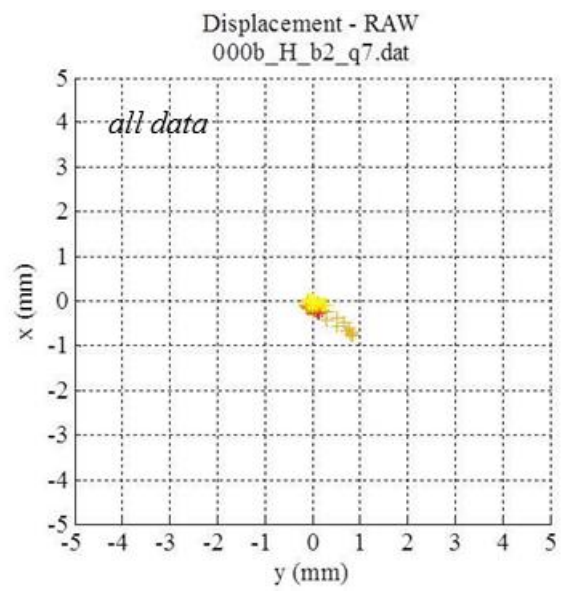
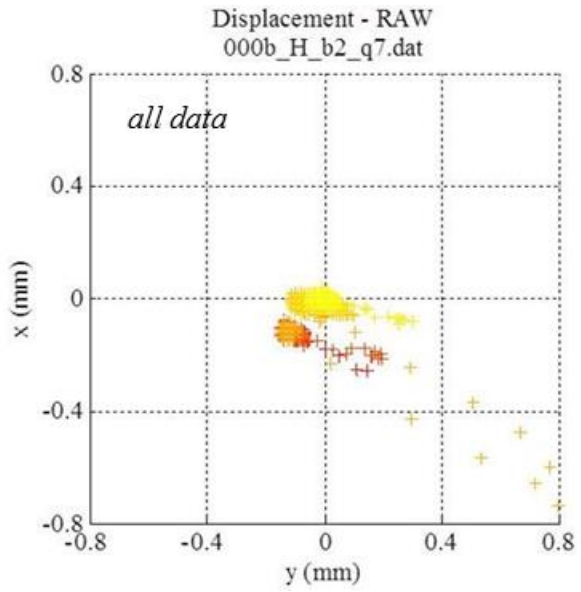
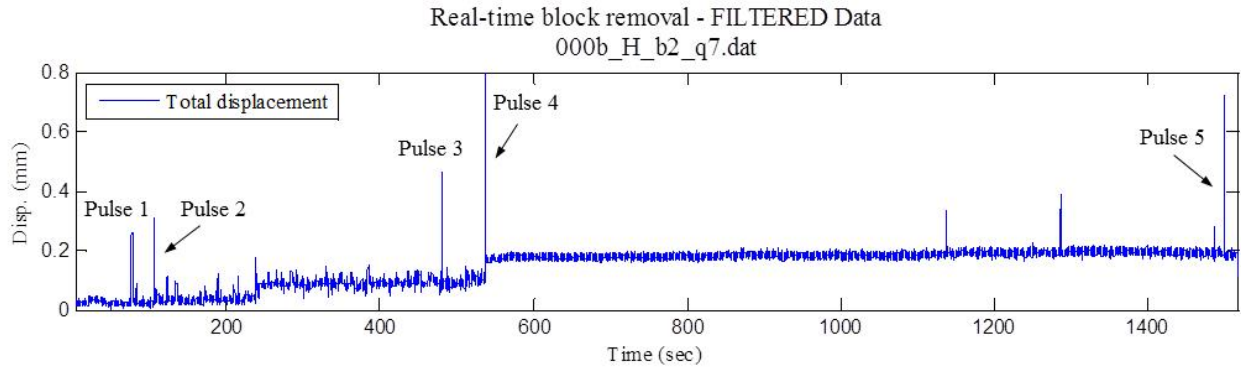
RAW displacement vector - lower hemisphere stereonet
105_L_b2_q3.dat



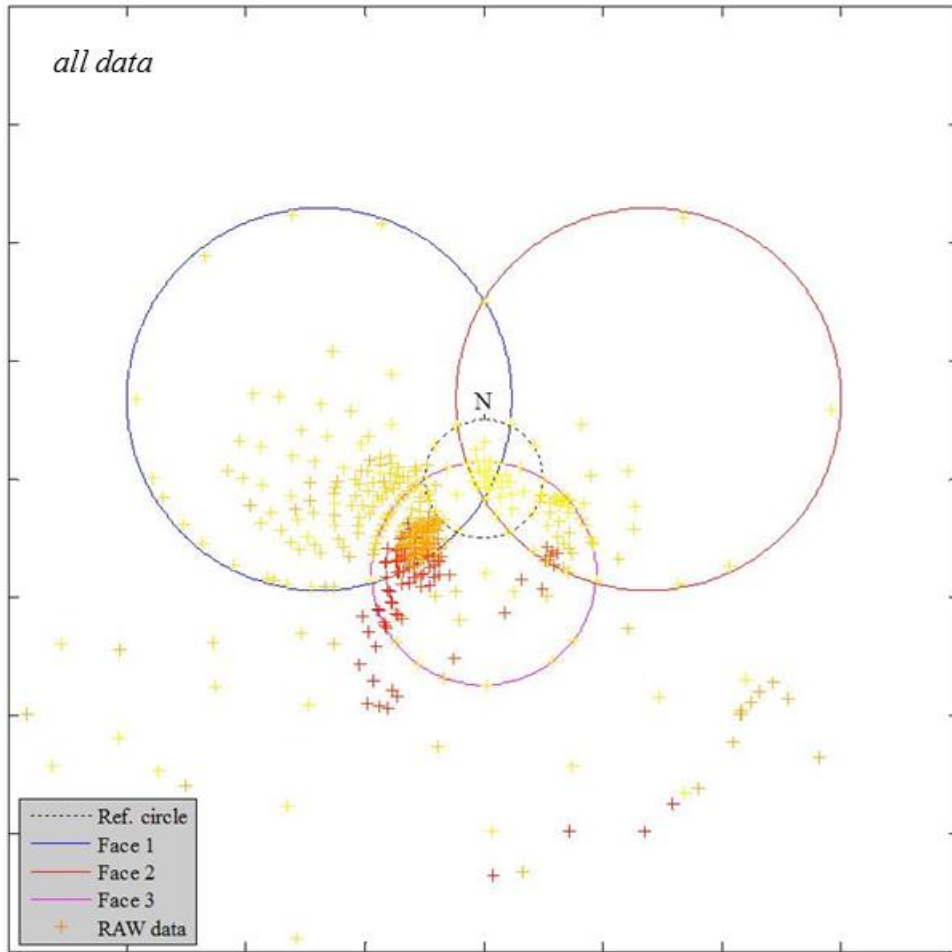


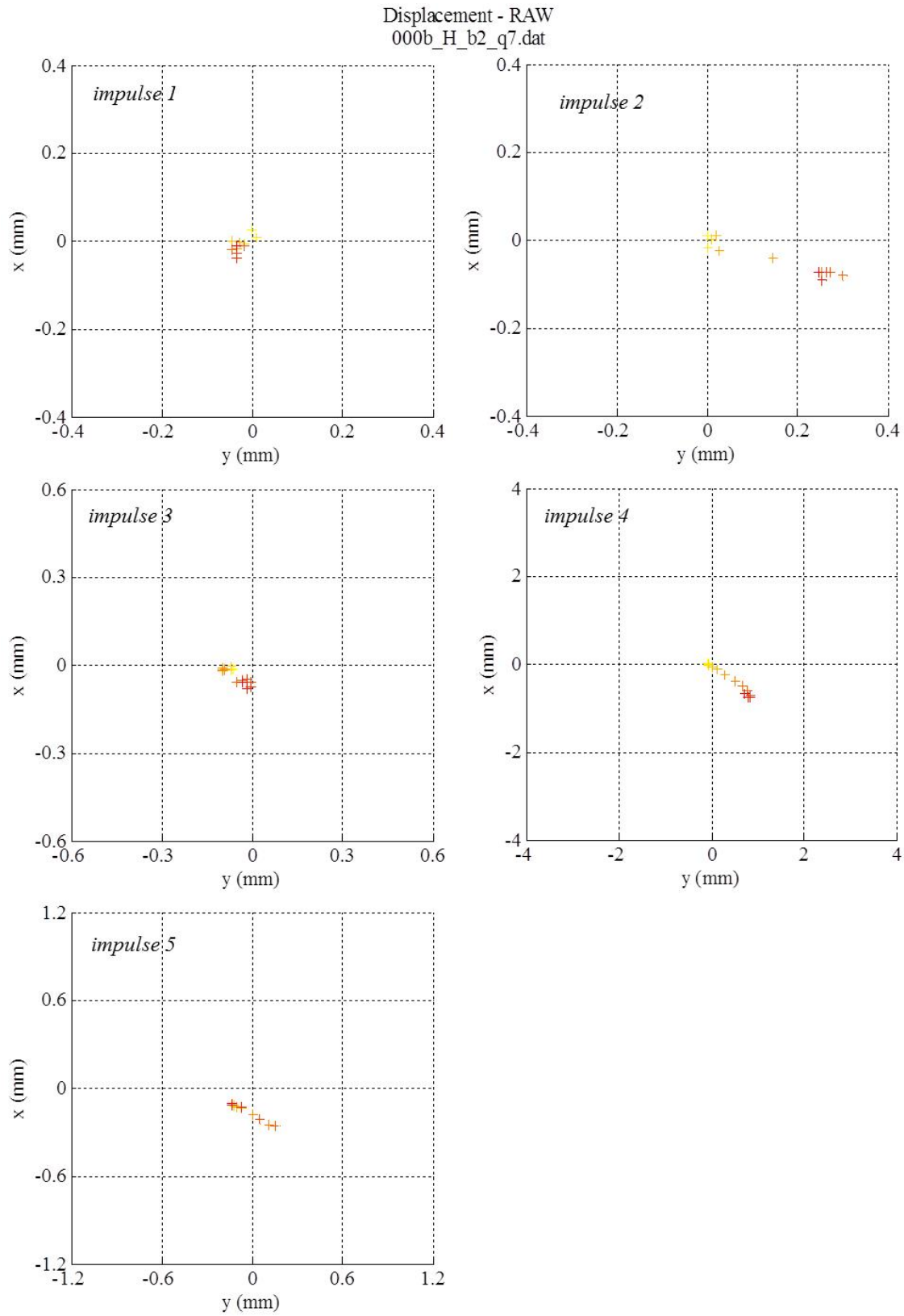
Block response 3 – supplemental figures

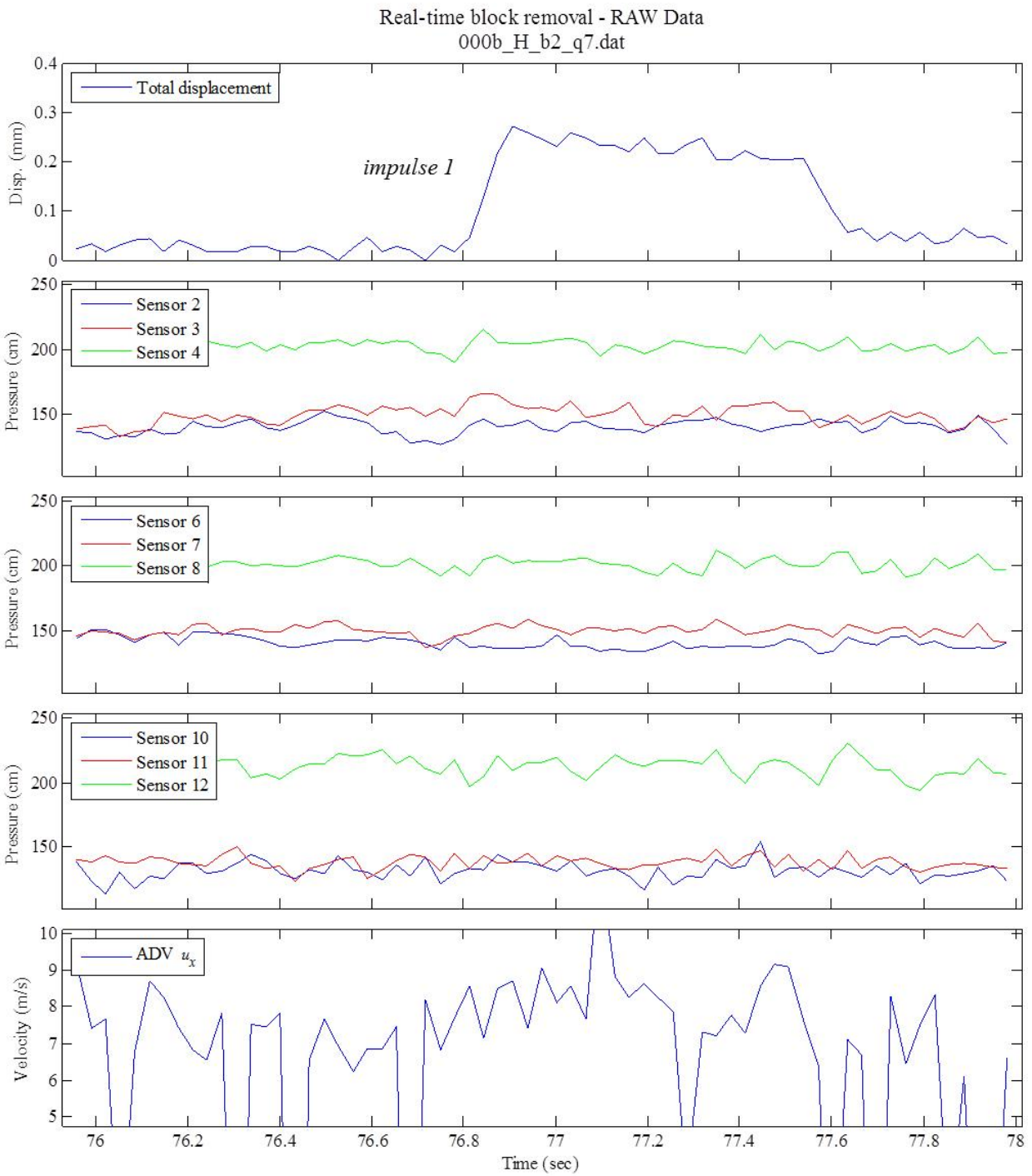
$\psi = 0$ deg., High T_u , Block 2, Q_7

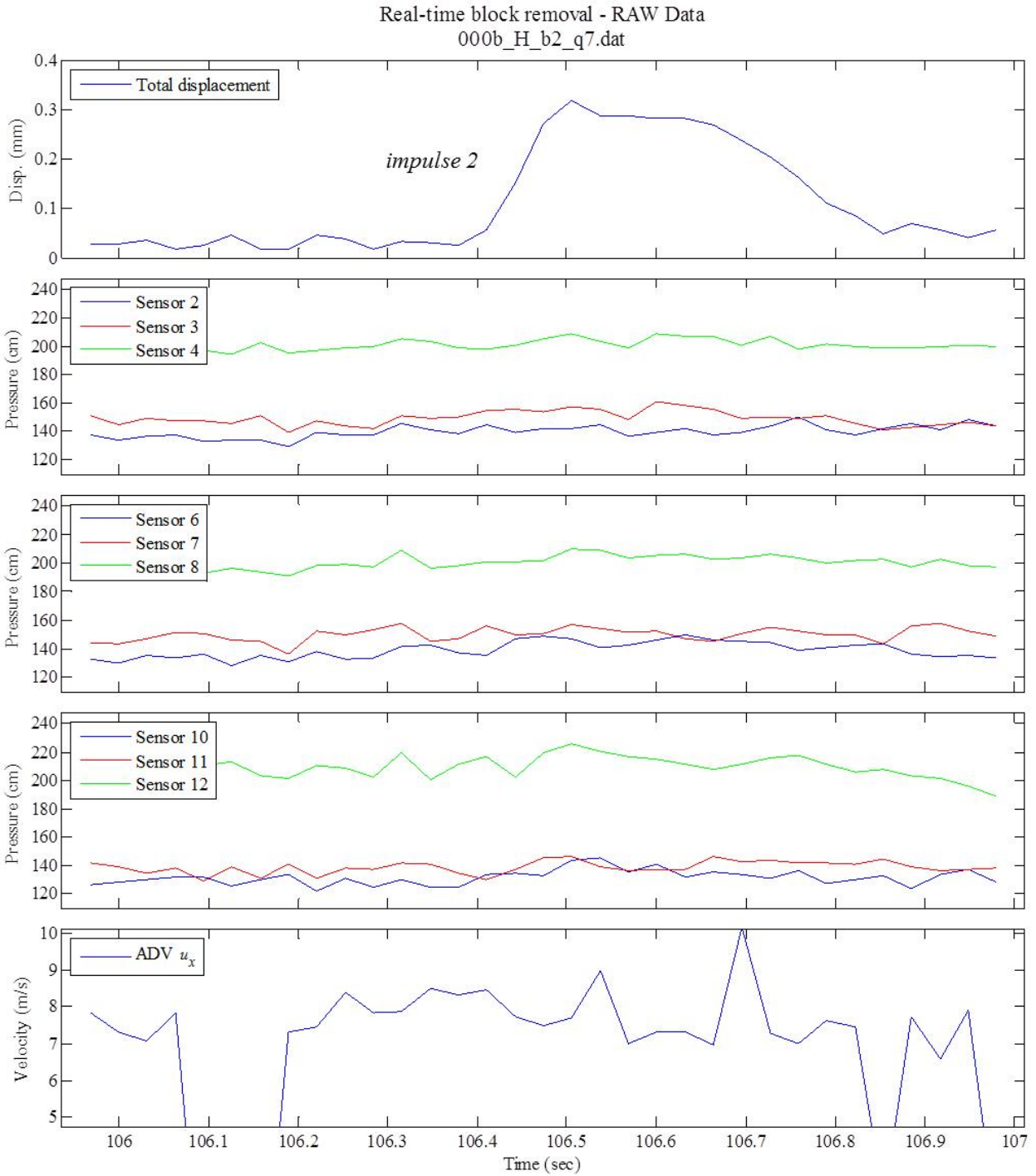


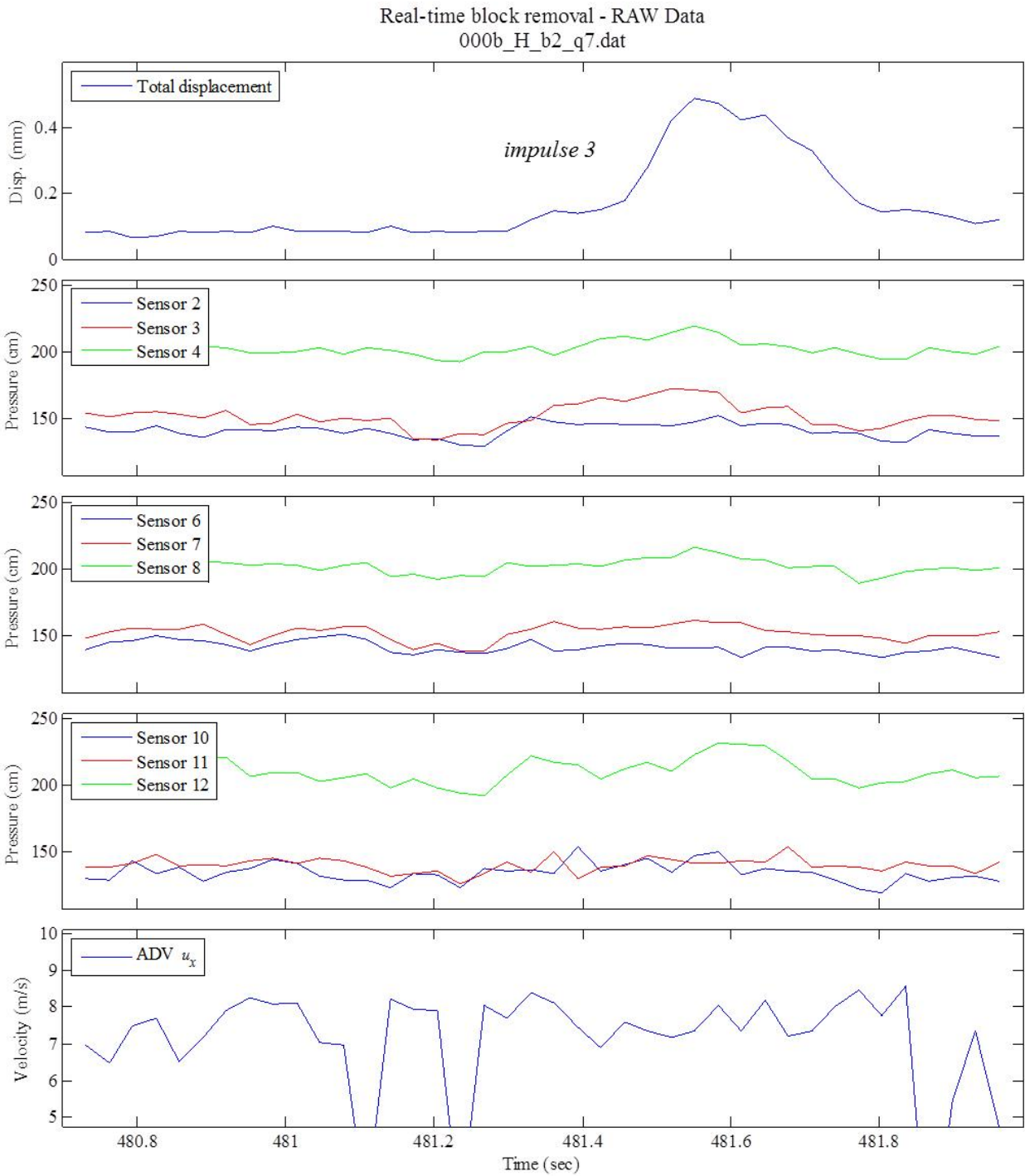
RAW displacement vector - lower hemisphere stereonet
000b_H_b2_q7.dat

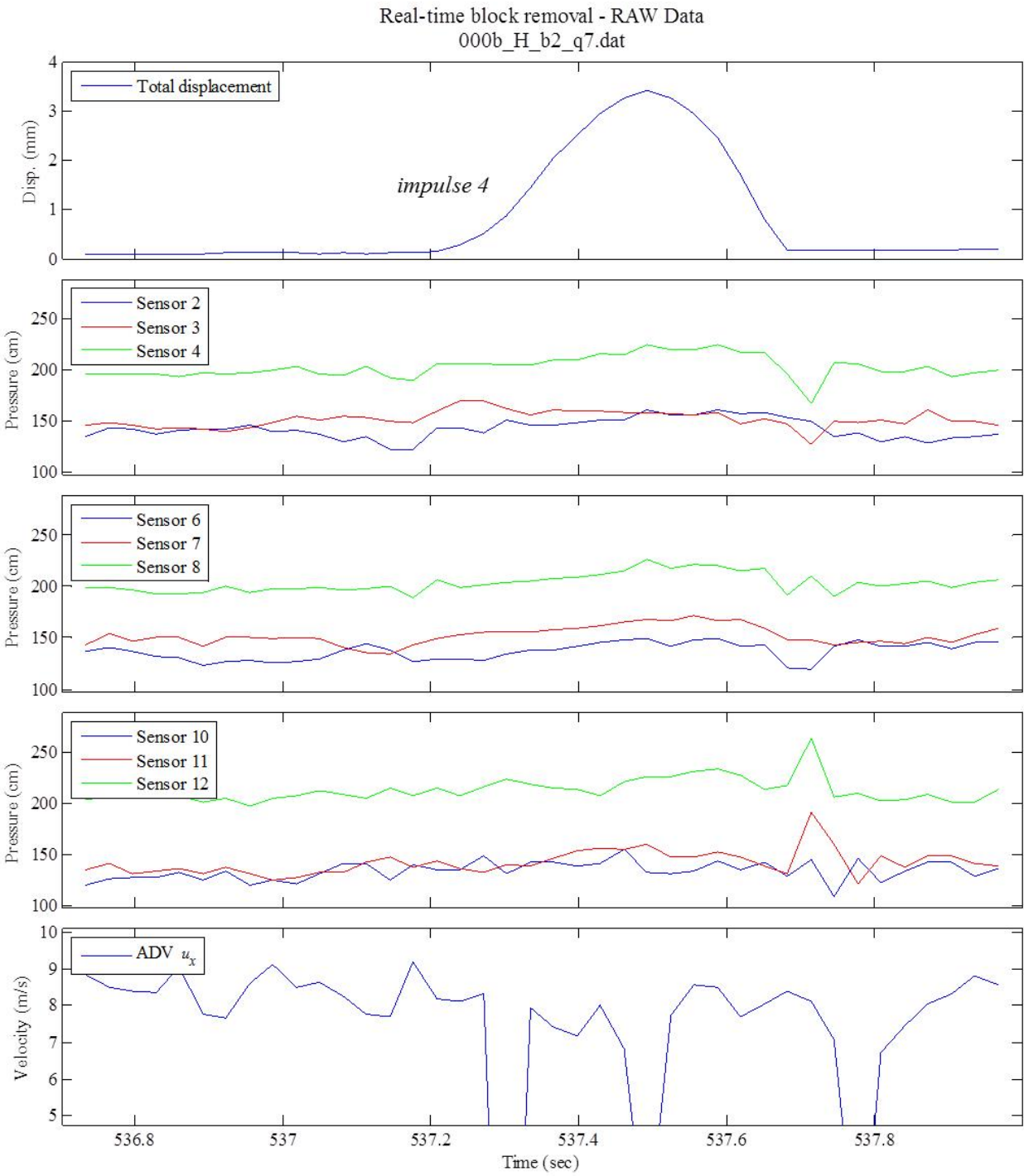


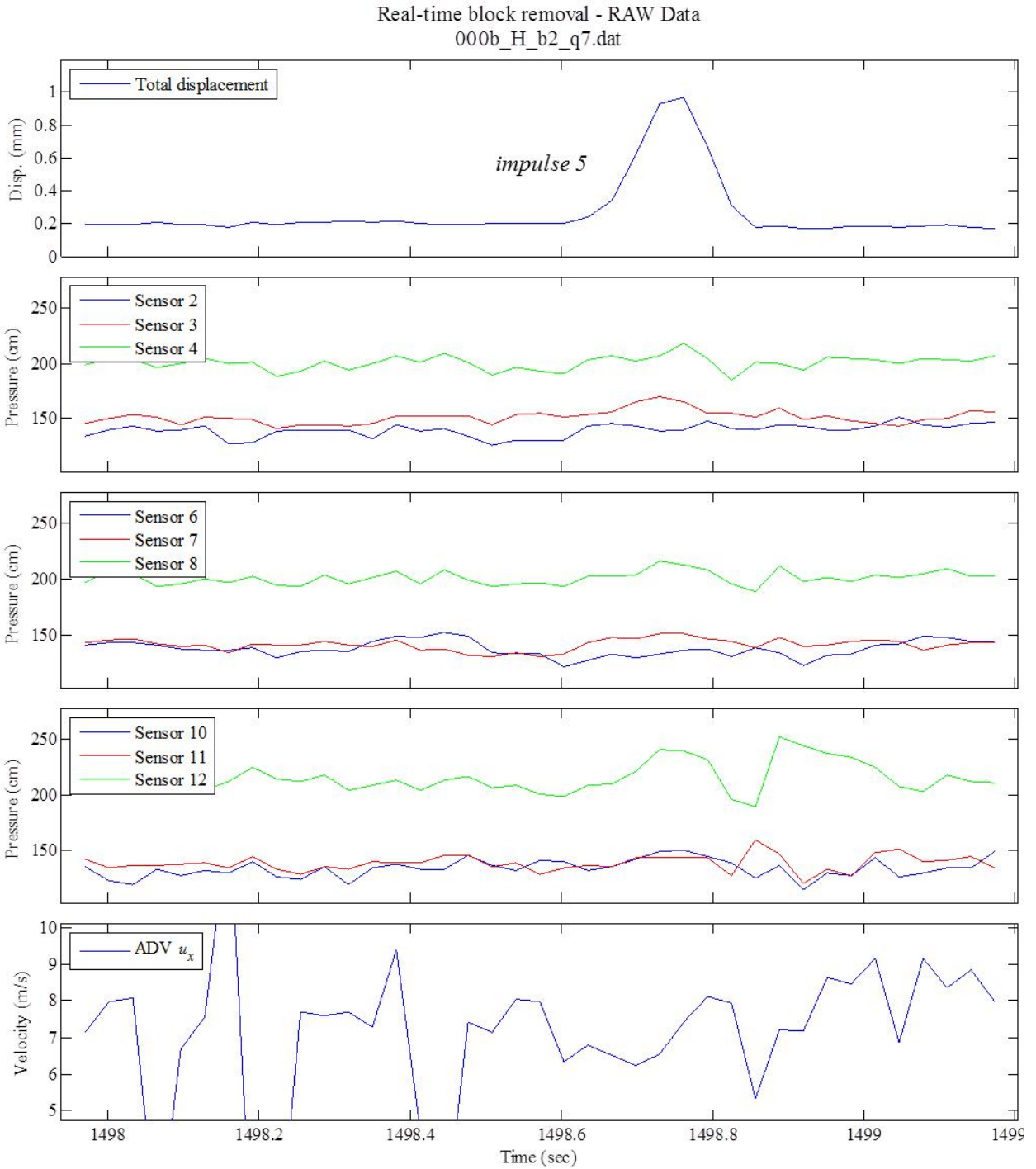




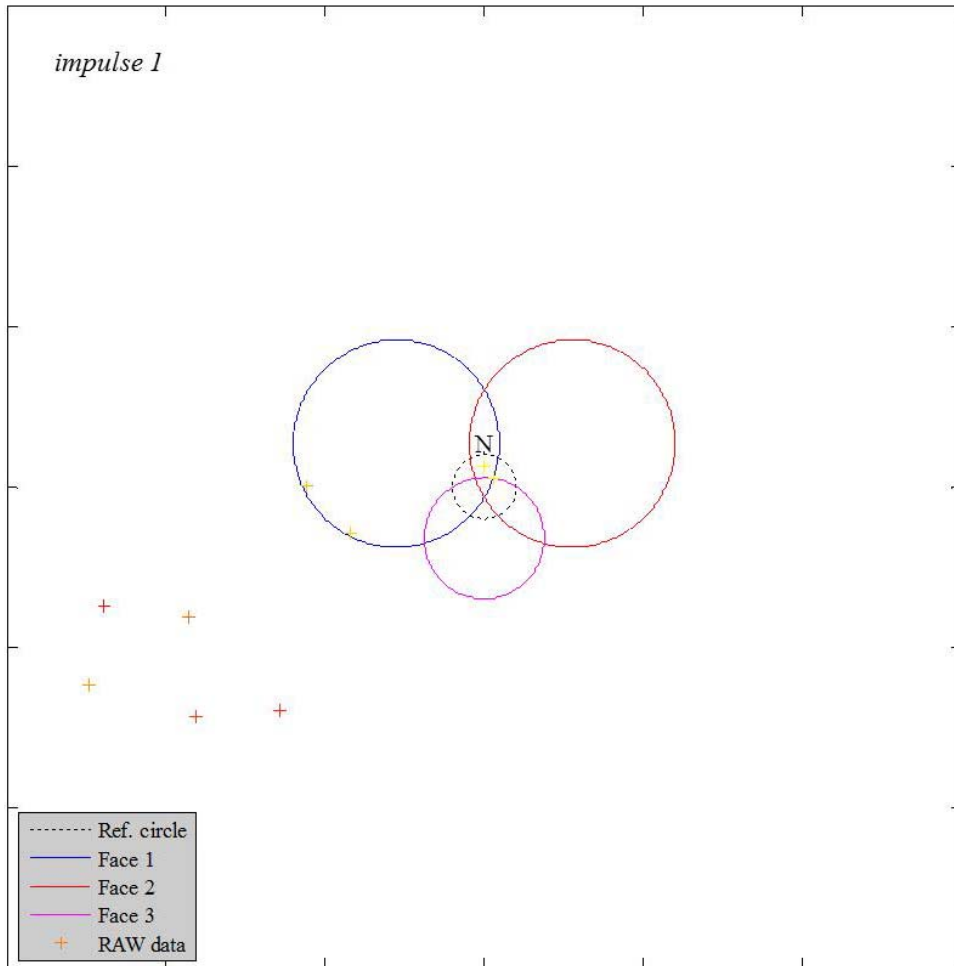




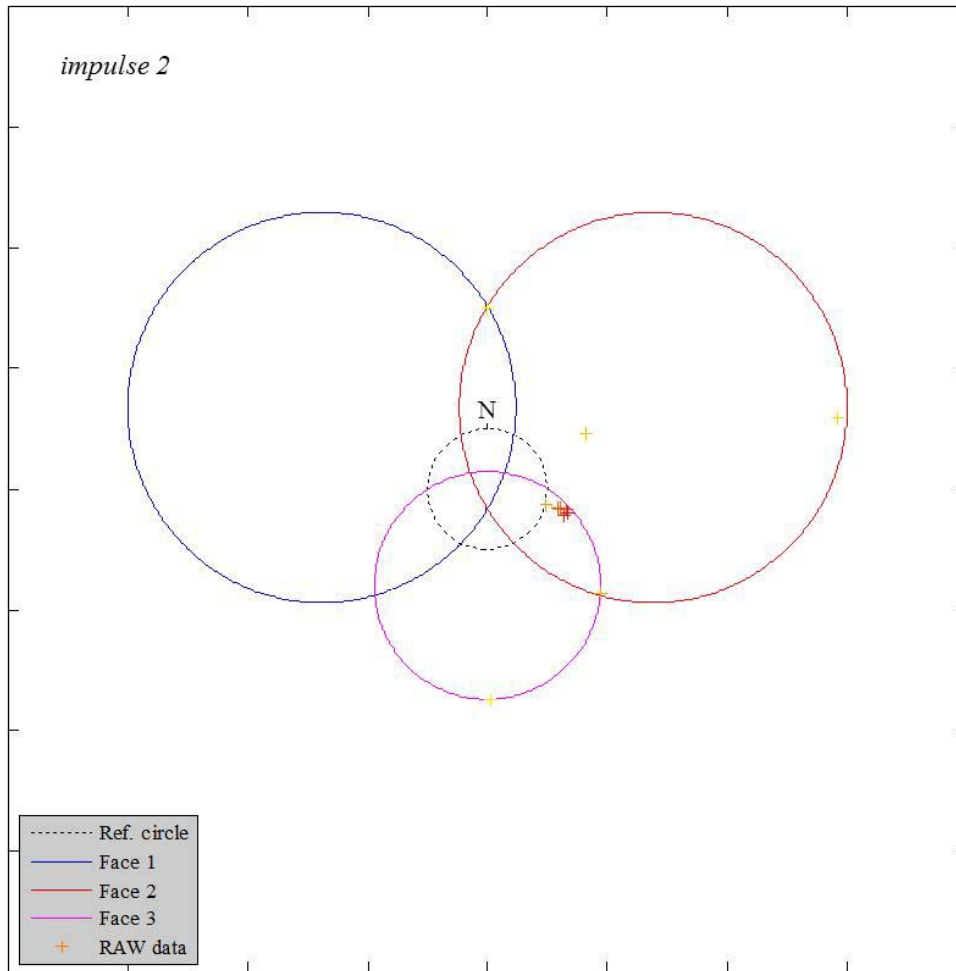




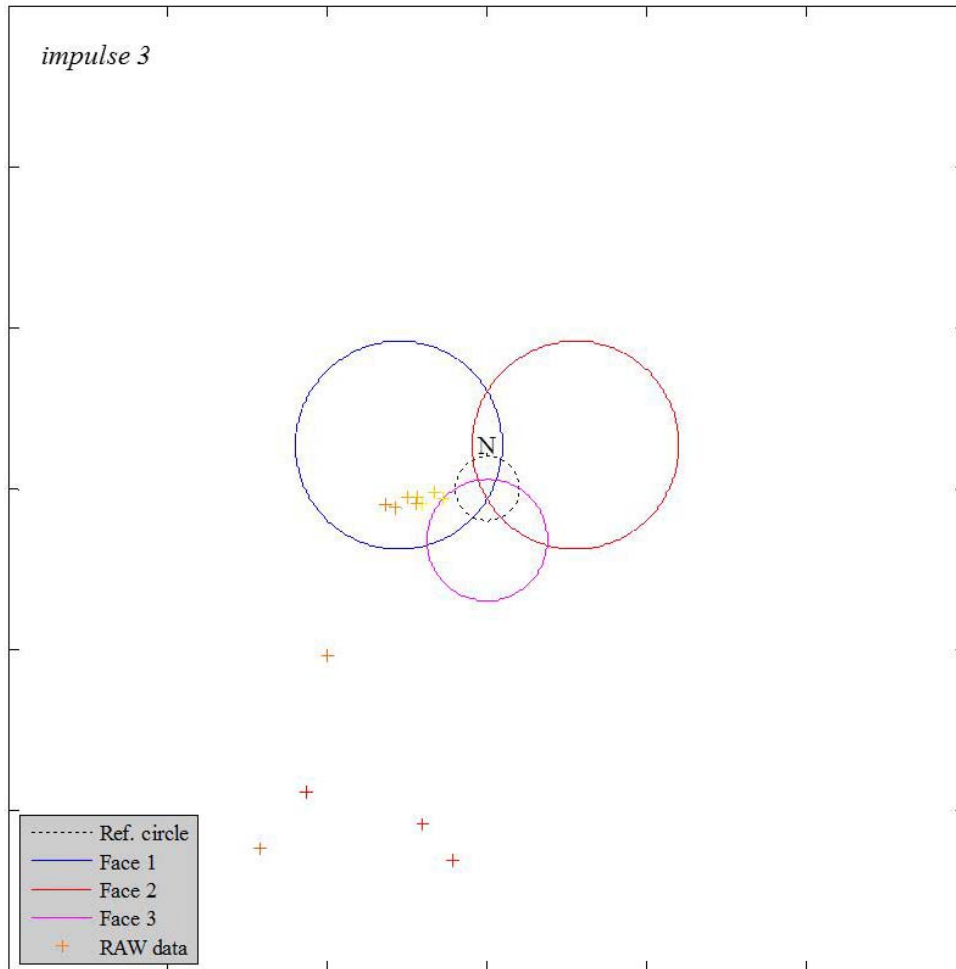
RAW displacement vector - lower hemisphere stereonet
000b_H_b2_q7.dat



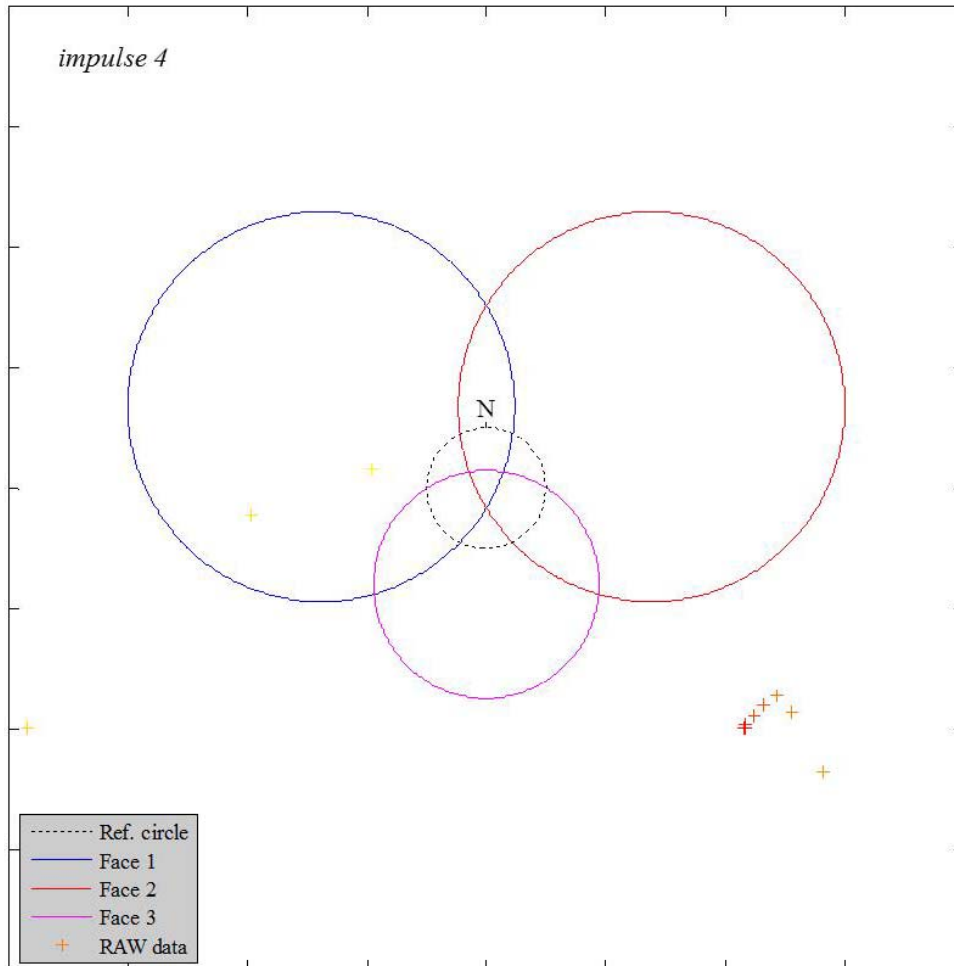
RAW displacement vector - lower hemisphere stereonet
000b_H_b2_q7.dat



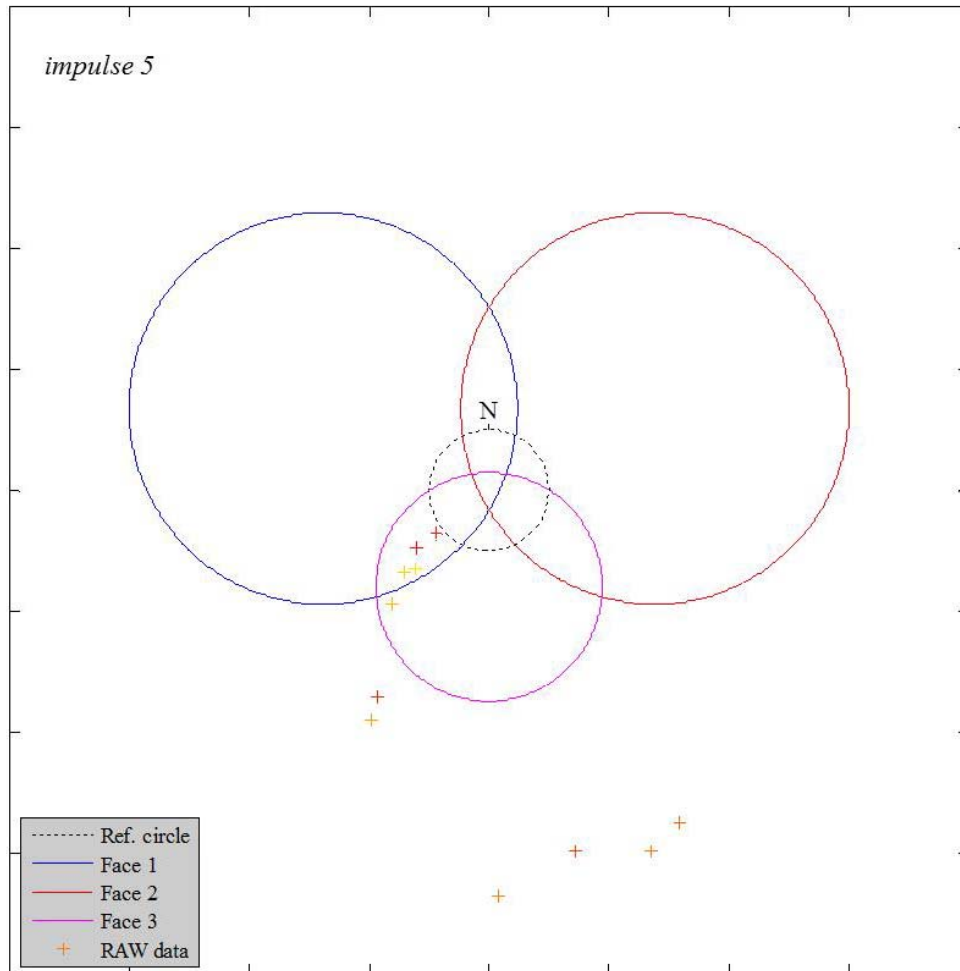
RAW displacement vector - lower hemisphere stereonet
000b_H_b2_q7.dat



RAW displacement vector - lower hemisphere stereonet
000b_H_b2_q7.dat

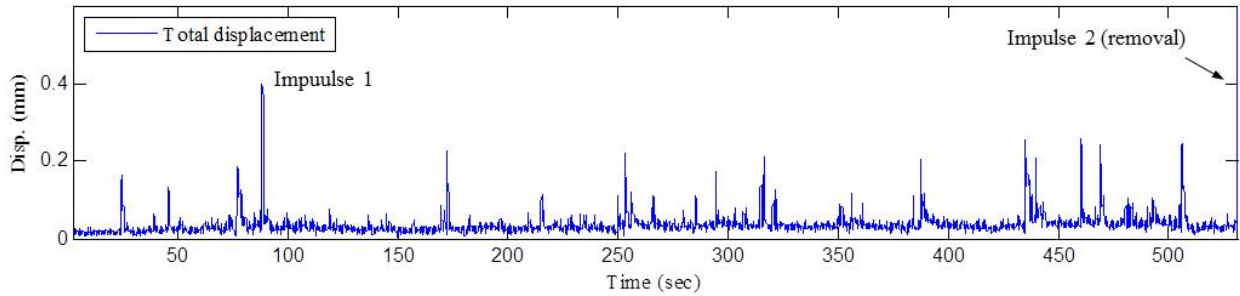


RAW displacement vector - lower hemisphere stereonet
000b_H_b2_q7.dat

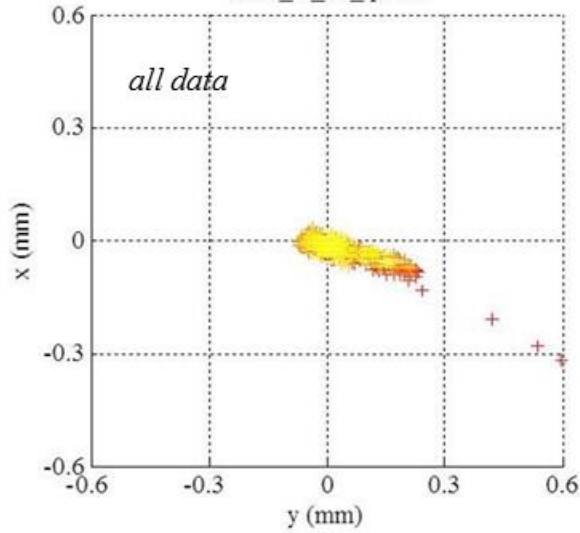


$\psi = 0$ deg., High T_u , Block 2, Q_7

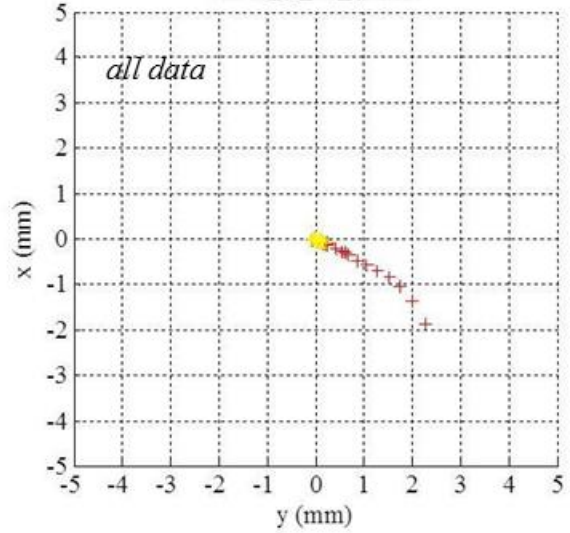
Real-time block removal - FILTERED Data
000c_H_b2_q7.dat



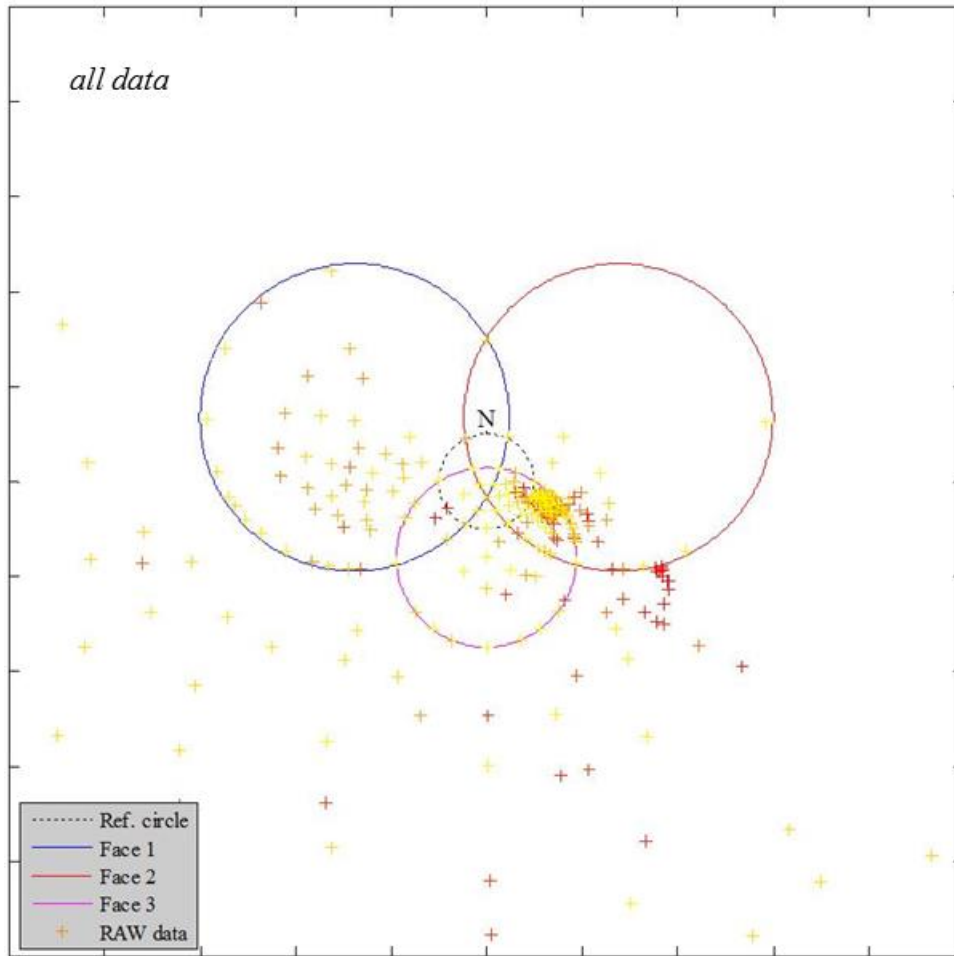
Displacement - RAW
000c_H_b2_q7.dat



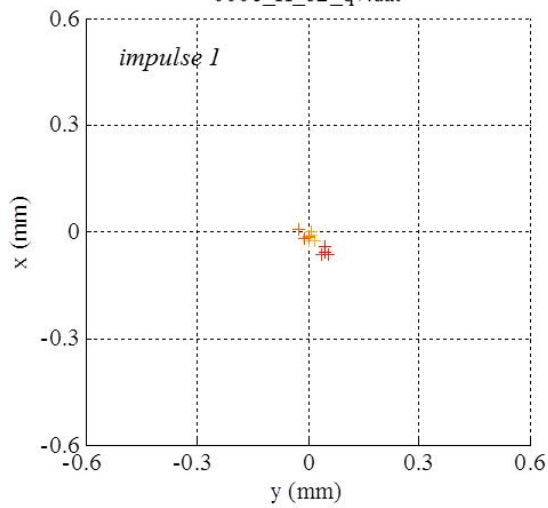
Displacement - RAW
000c_H_b2_q7.dat



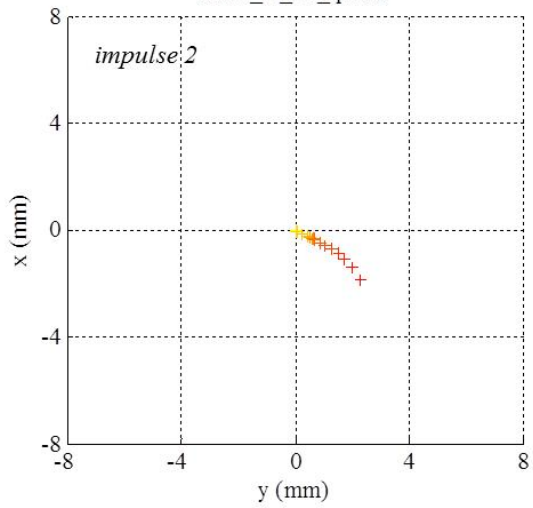
RAW displacement vector - lower hemisphere stereonet
000c_H_b2_q7.dat

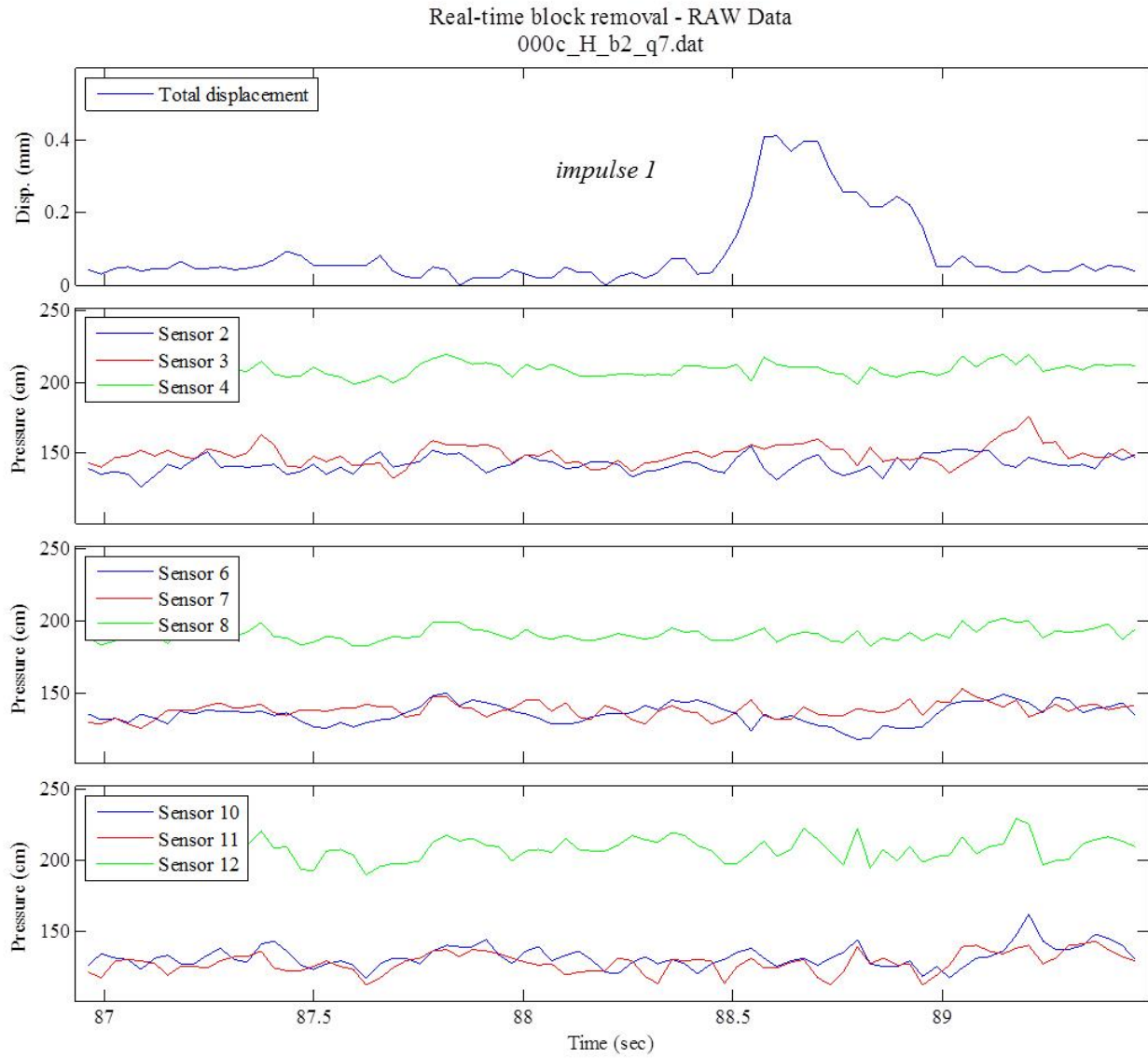


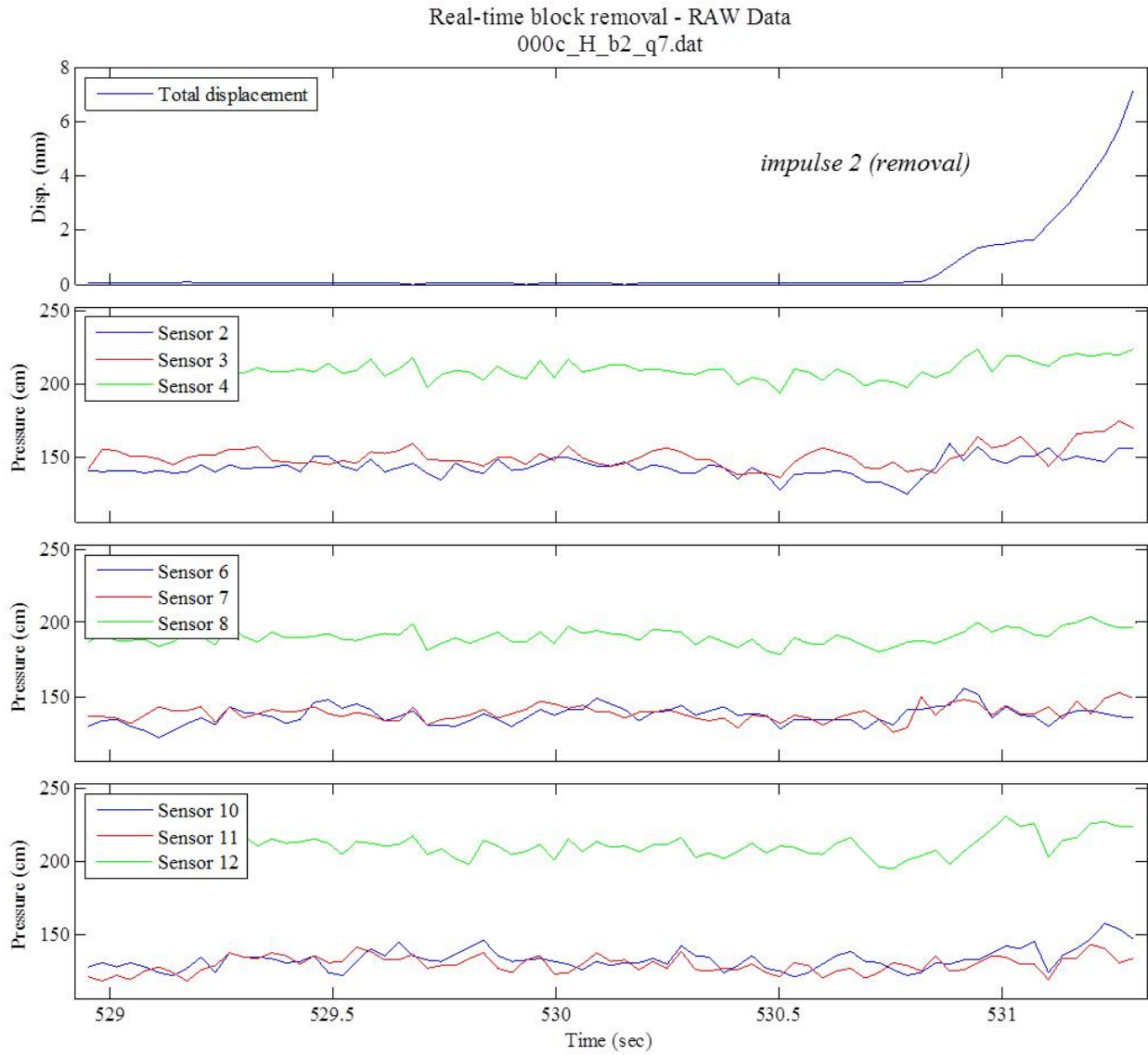
Displacement - RAW
000c_H_b2_q7.dat



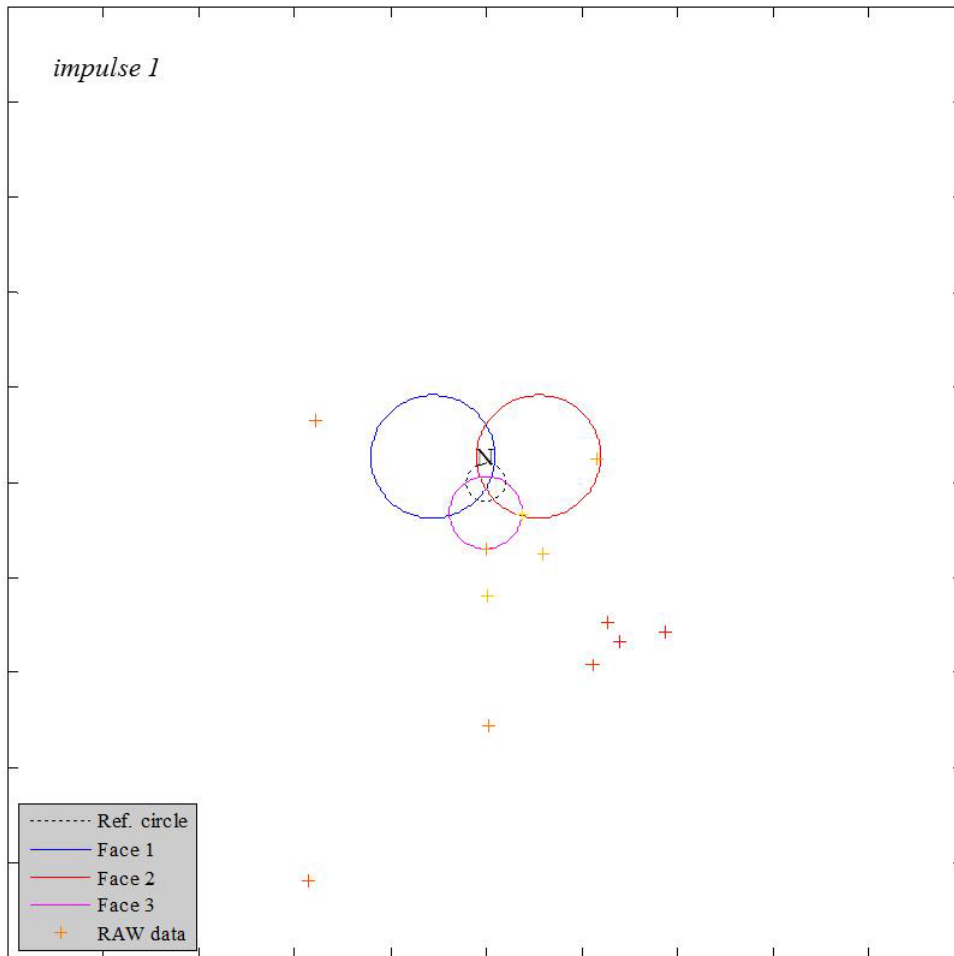
Displacement - RAW
000c_H_b2_q7.dat



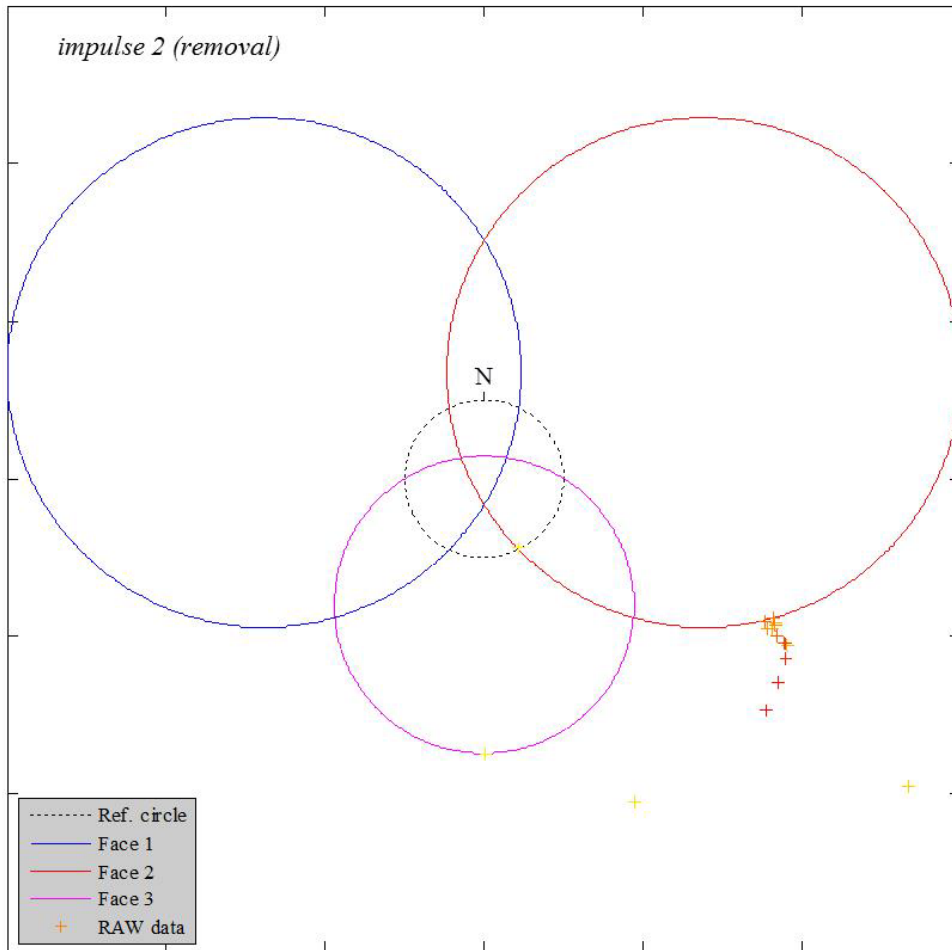




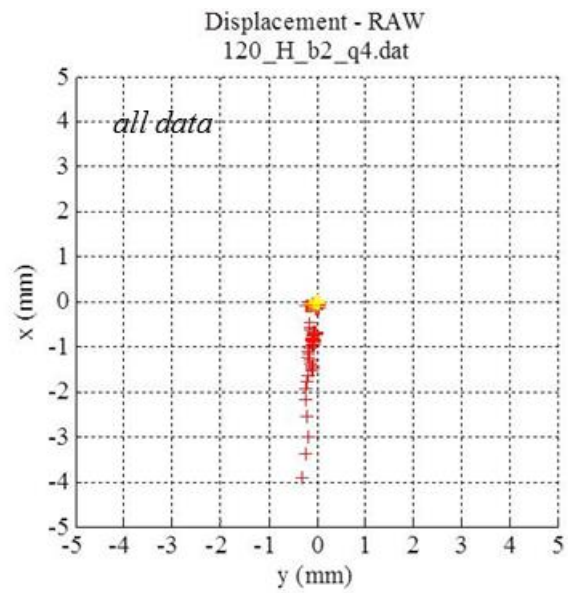
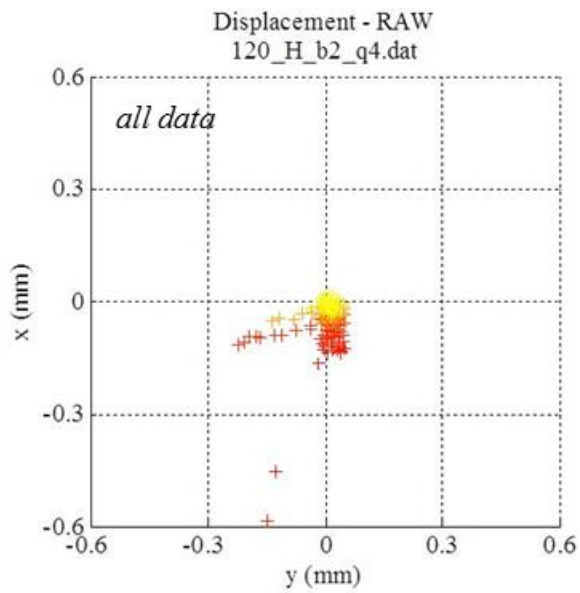
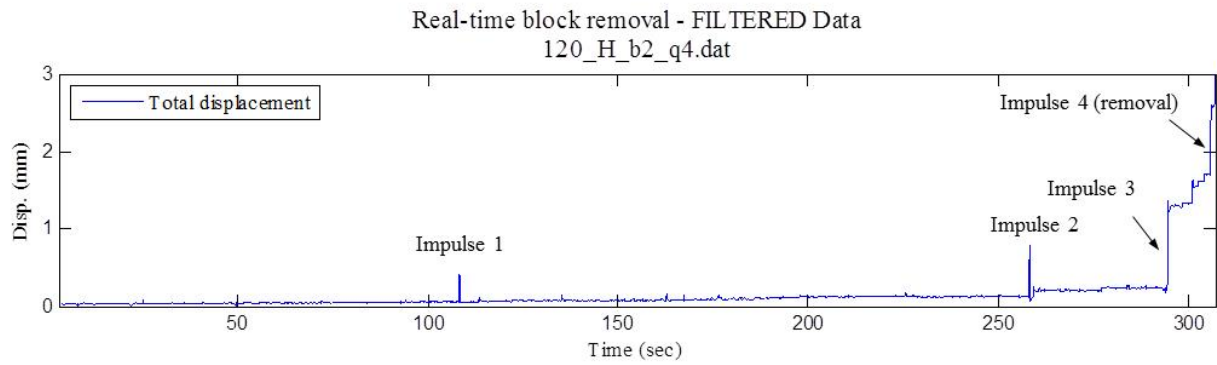
RAW displacement vector - lower hemisphere stereonet
000c_H_b2_q7.dat



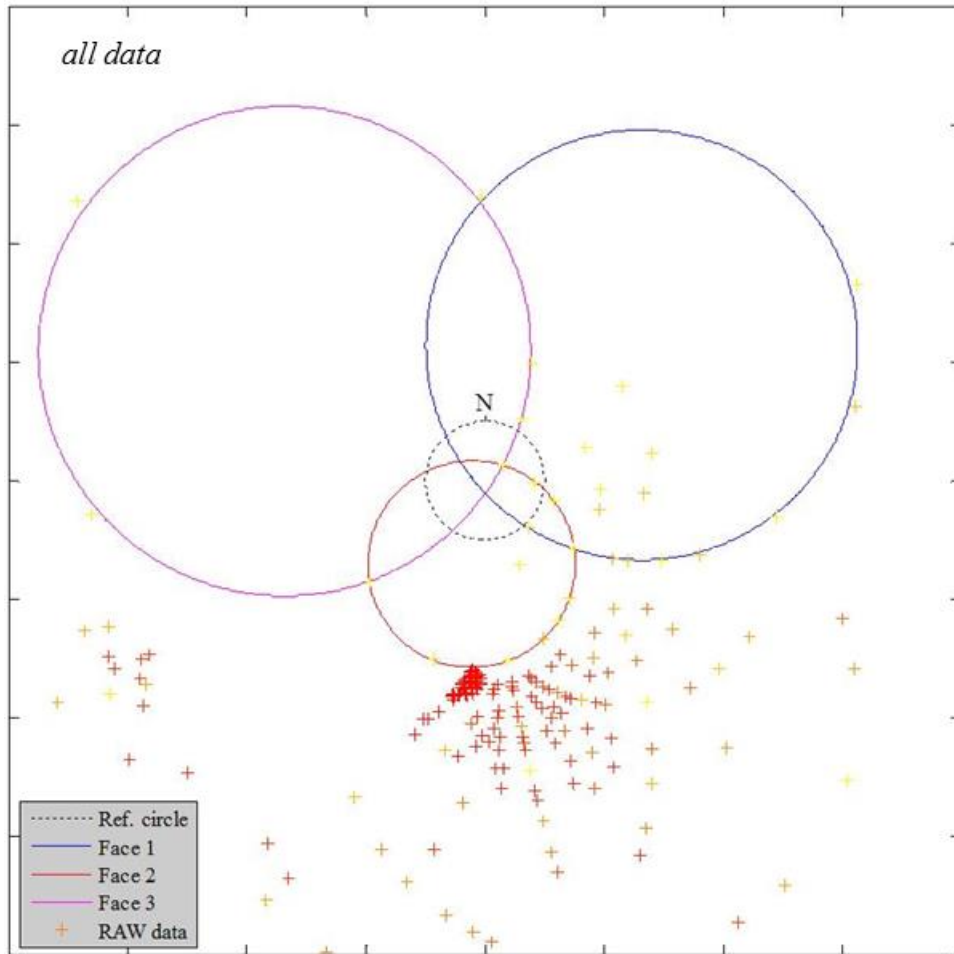
RAW displacement vector - lower hemisphere stereonet
000c_H_b2_q7.dat



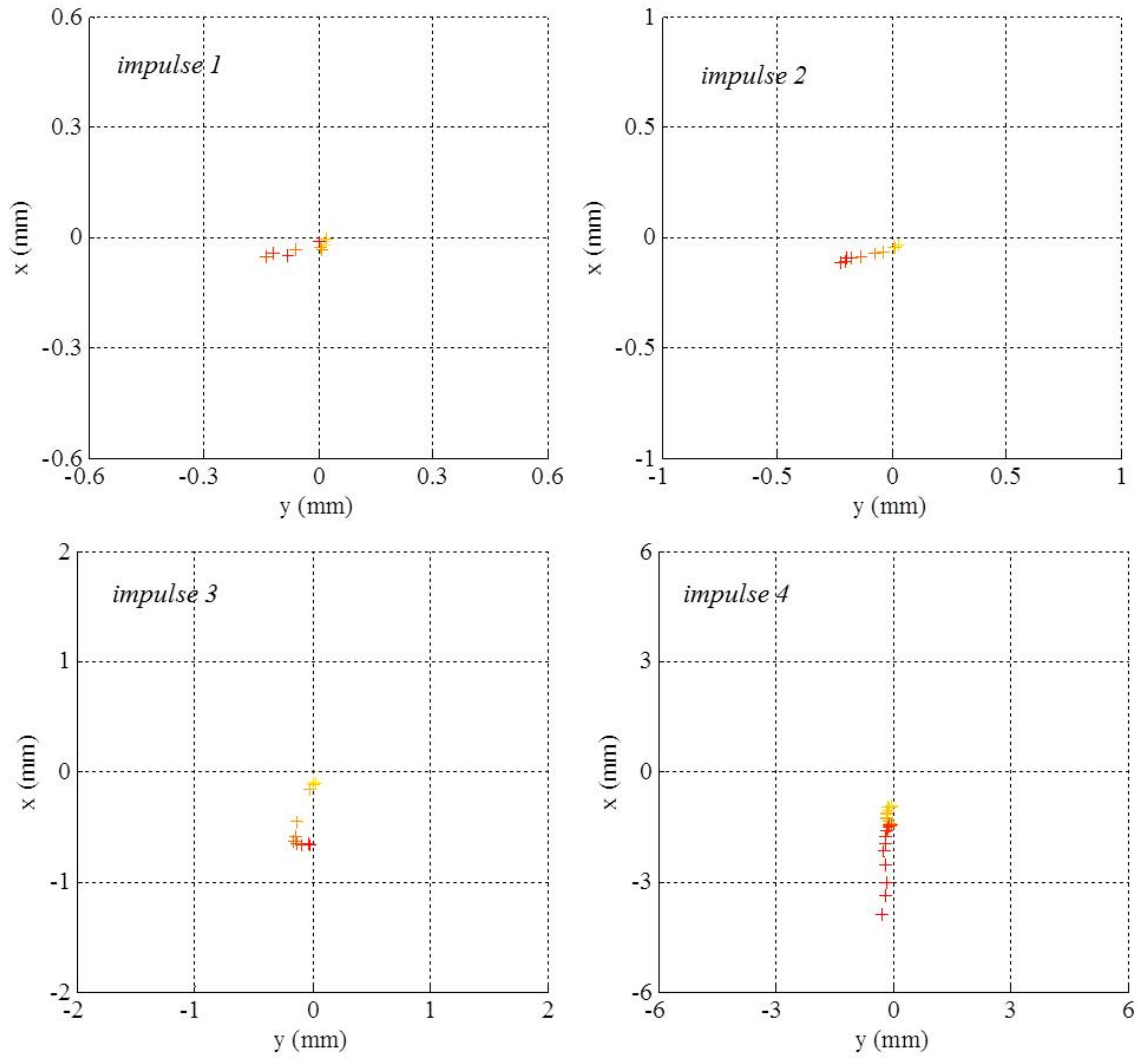
$\psi = 120$ deg., High T_u , Block 2, Q_4

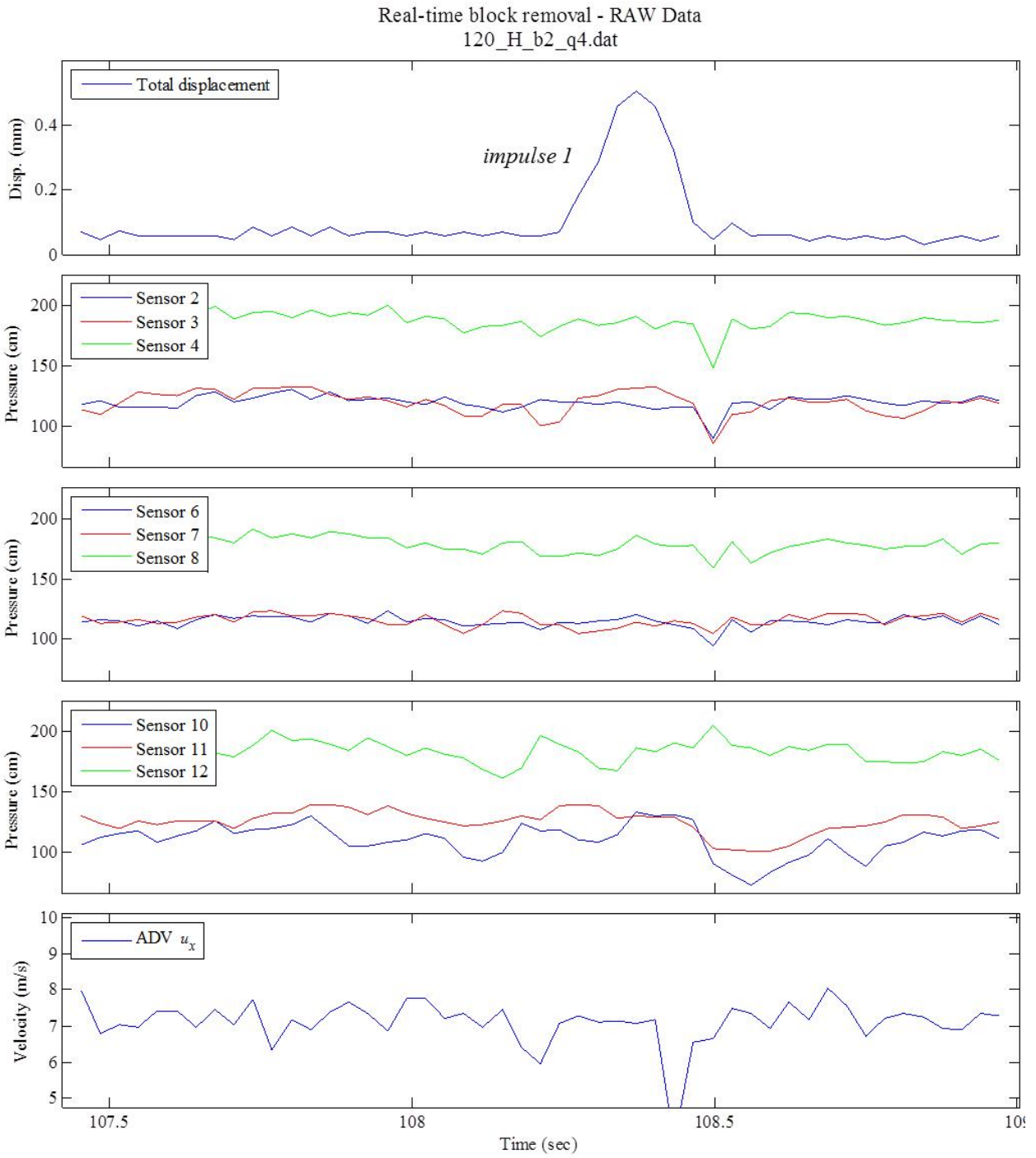


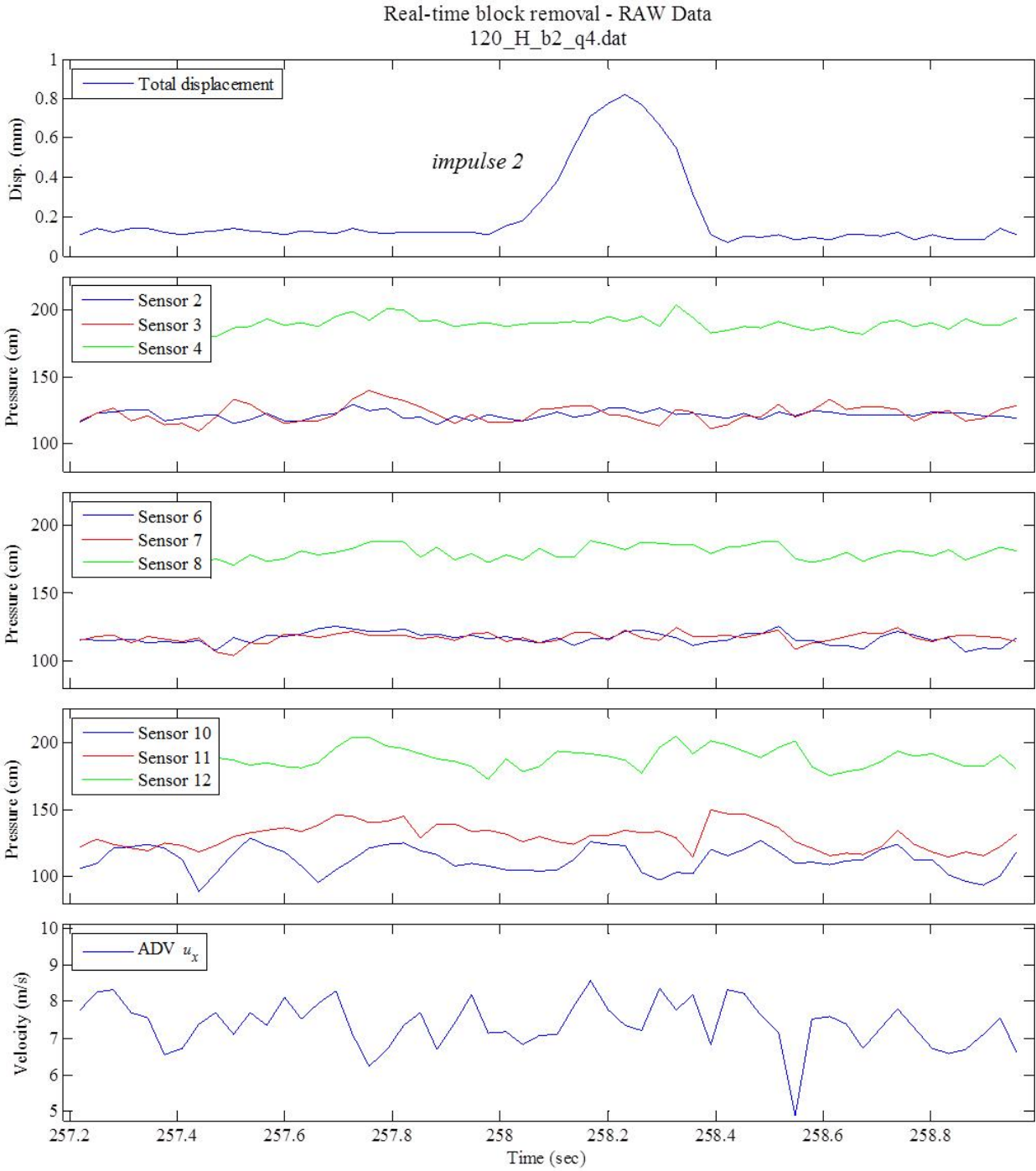
RAW displacement vector - lower hemisphere stereonet
120_H_b2_q4.dat

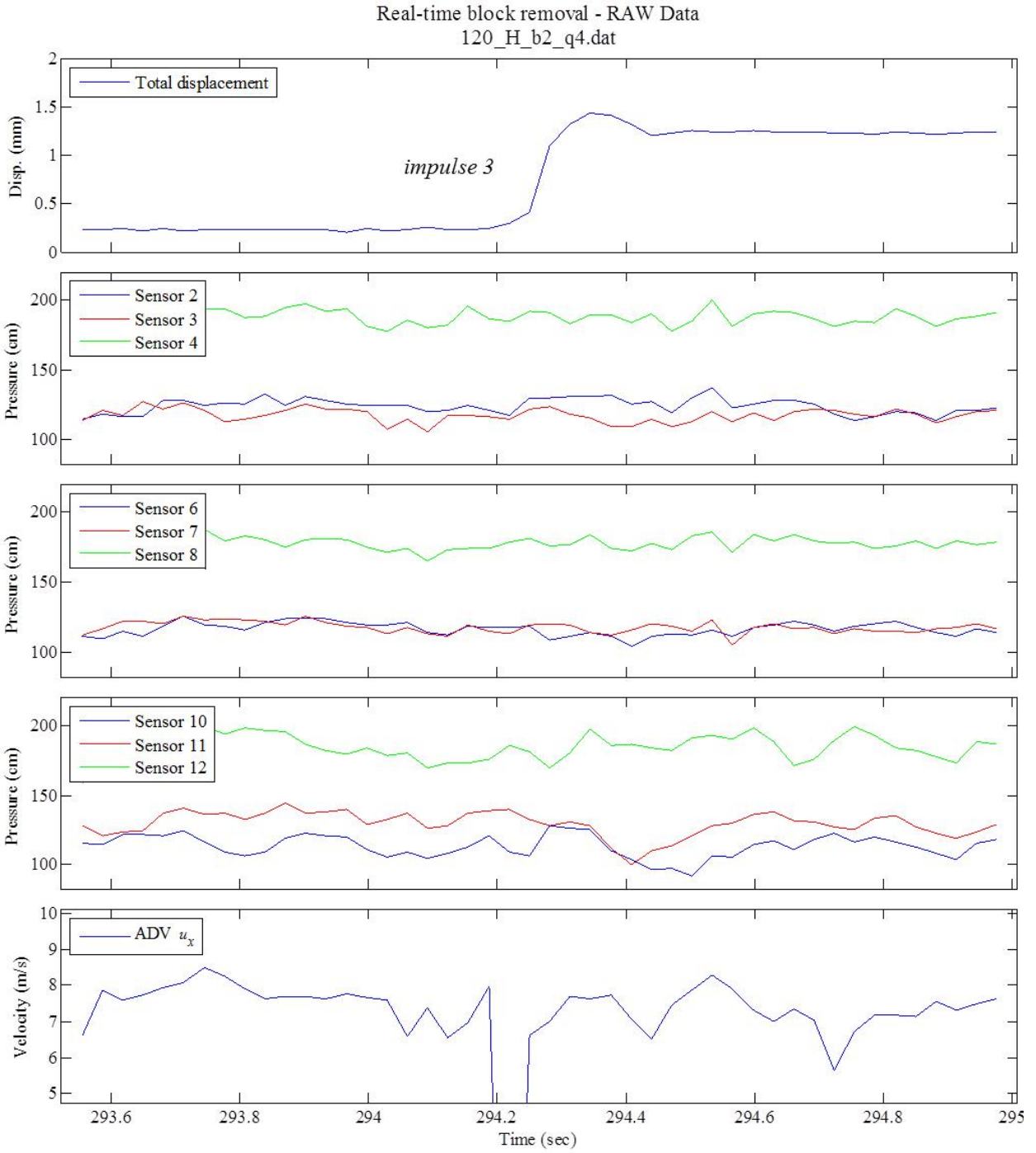


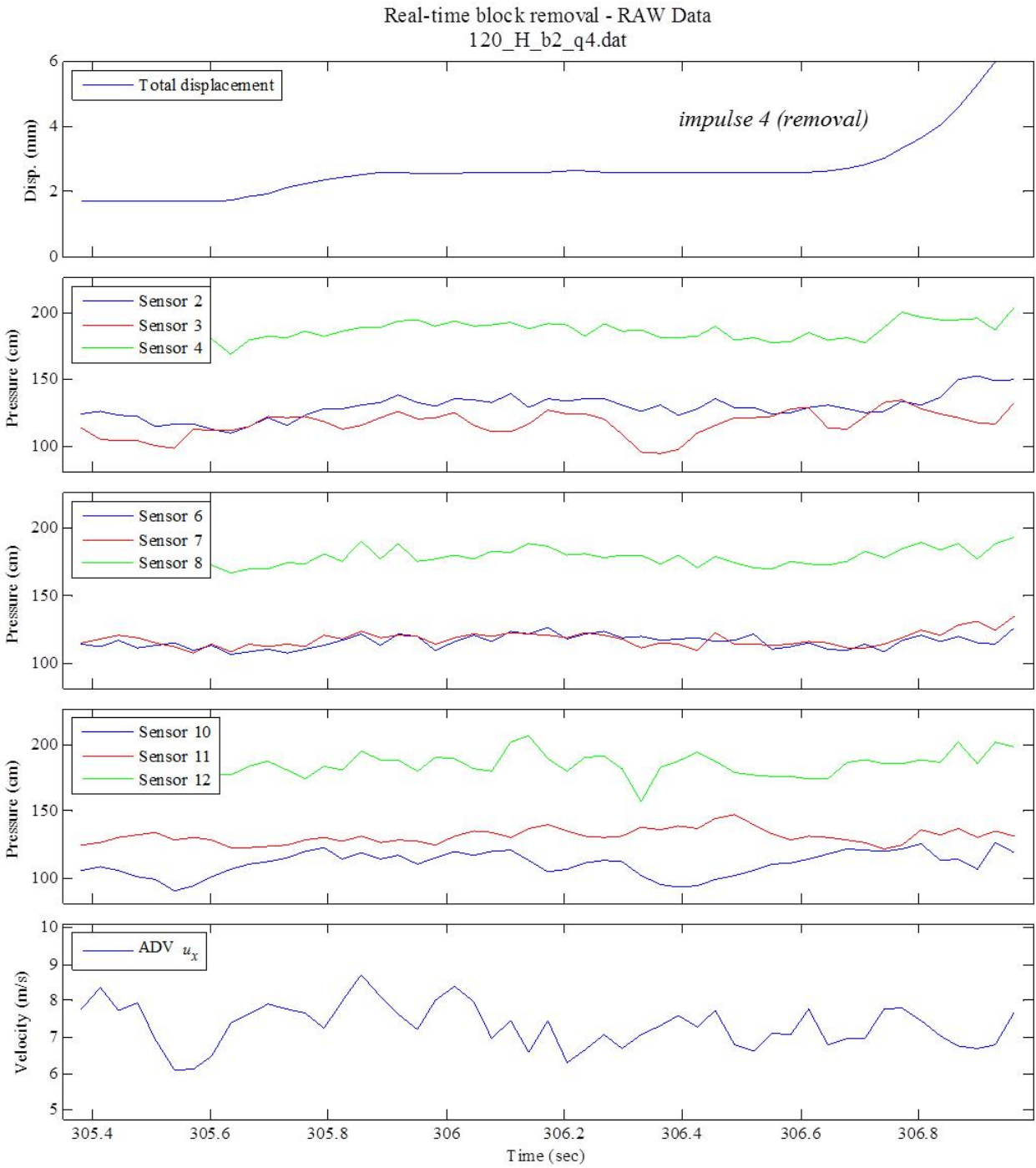
Displacement - RAW
120_H_b2_q4.dat



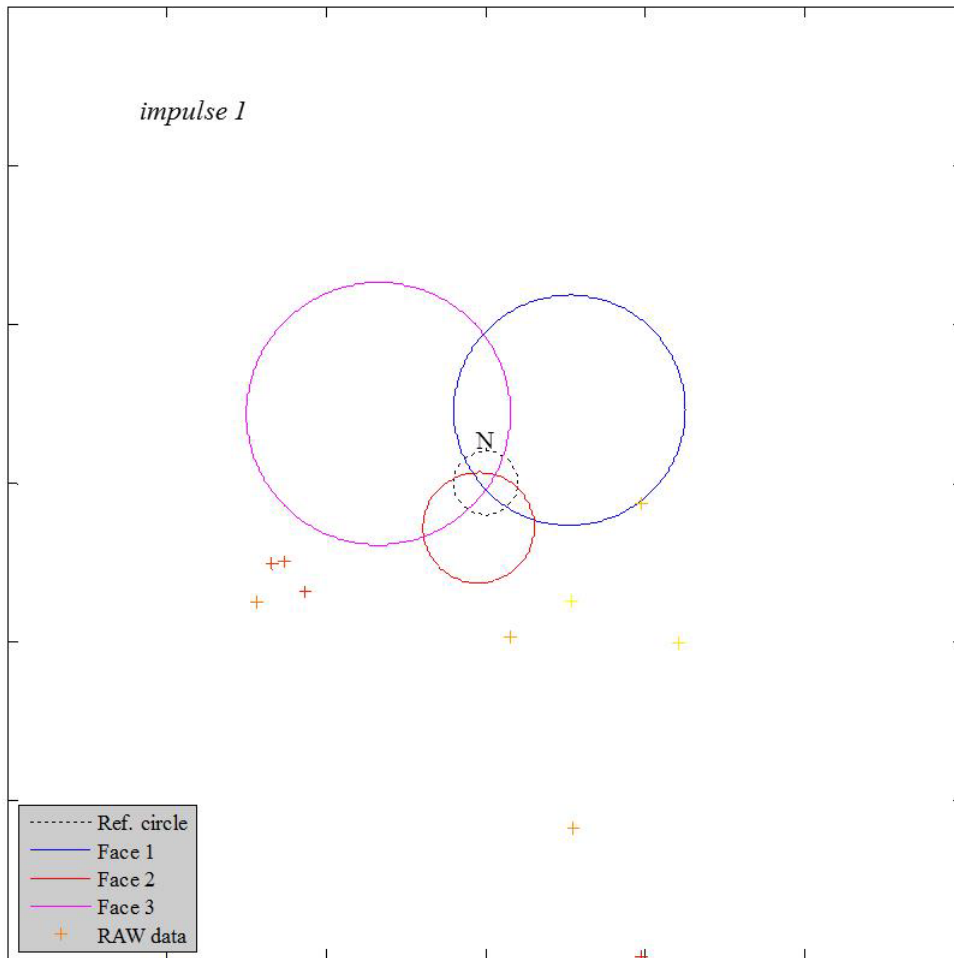




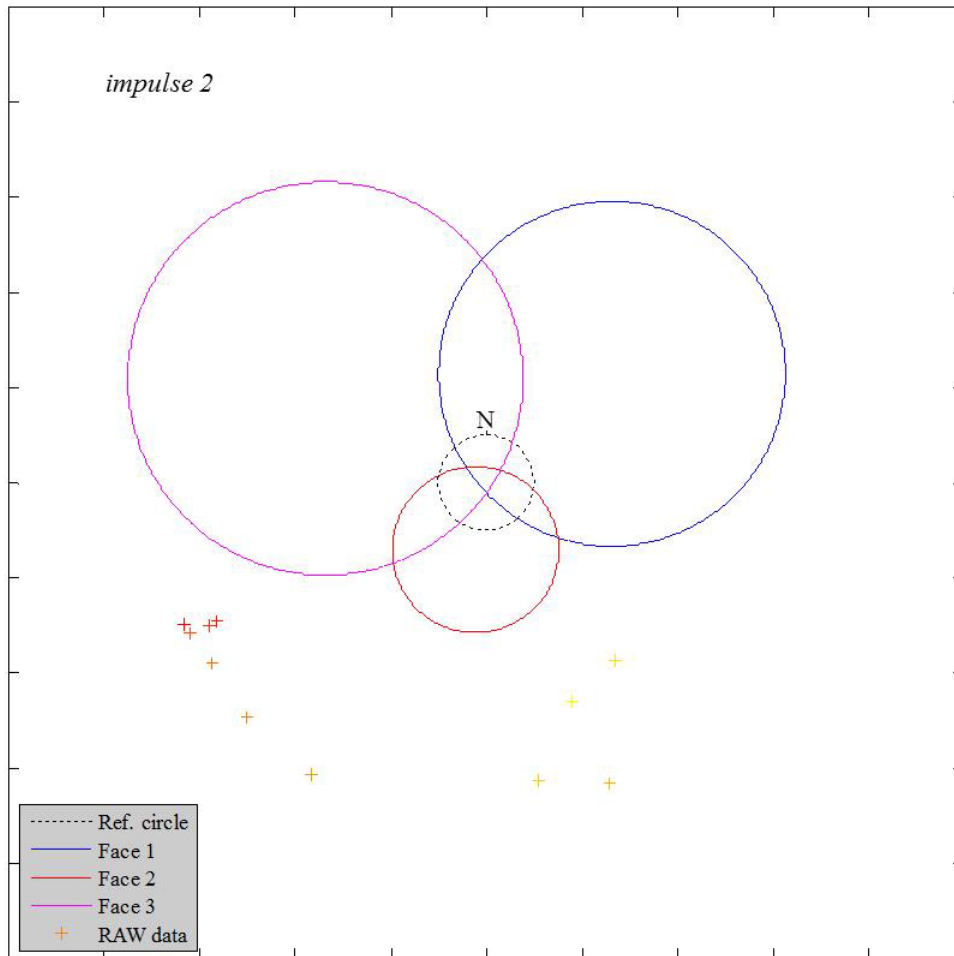




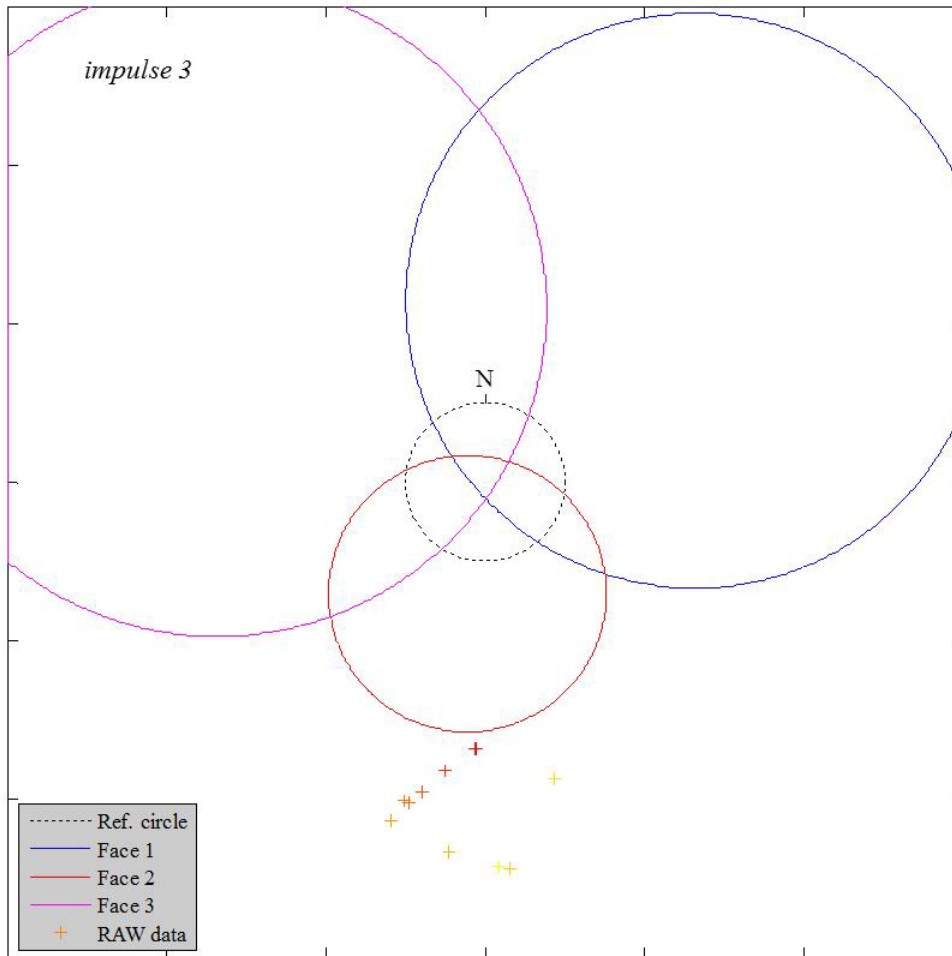
RAW displacement vector - lower hemisphere stereonet
120_H_b2_q4.dat



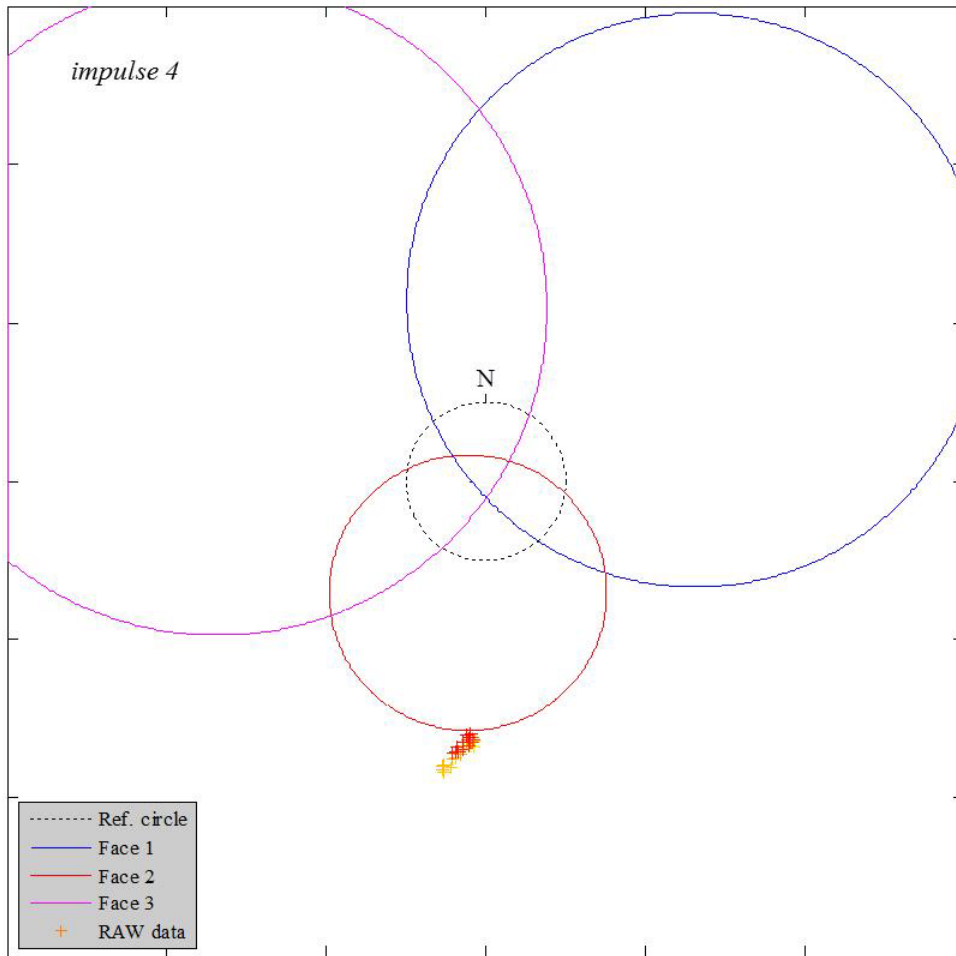
RAW displacement vector - lower hemisphere stereonet
120_H_b2_q4.dat



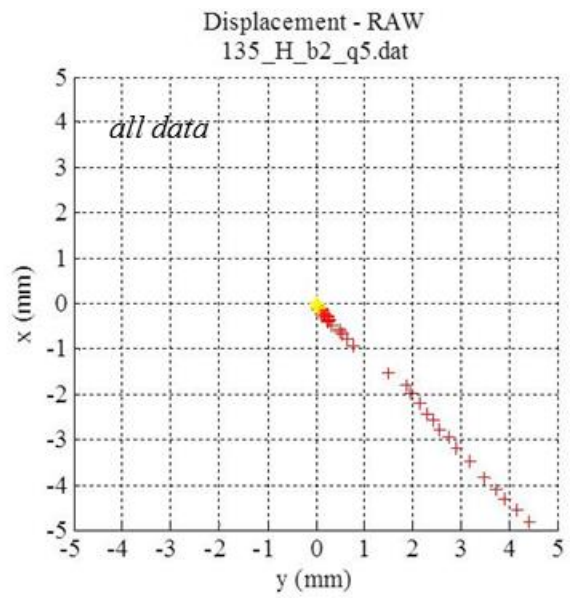
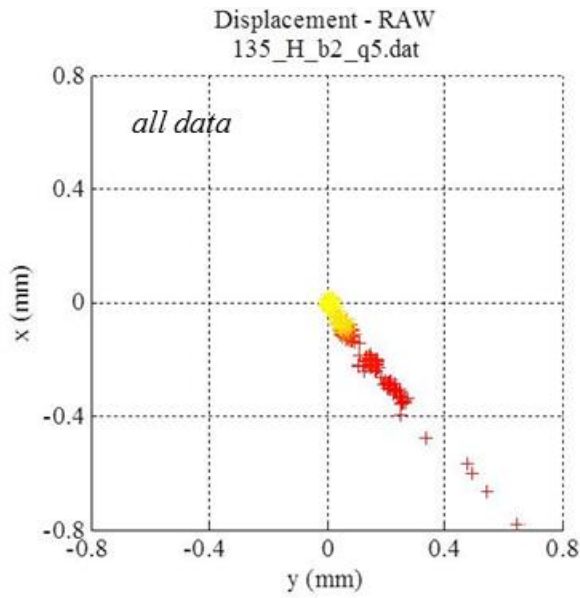
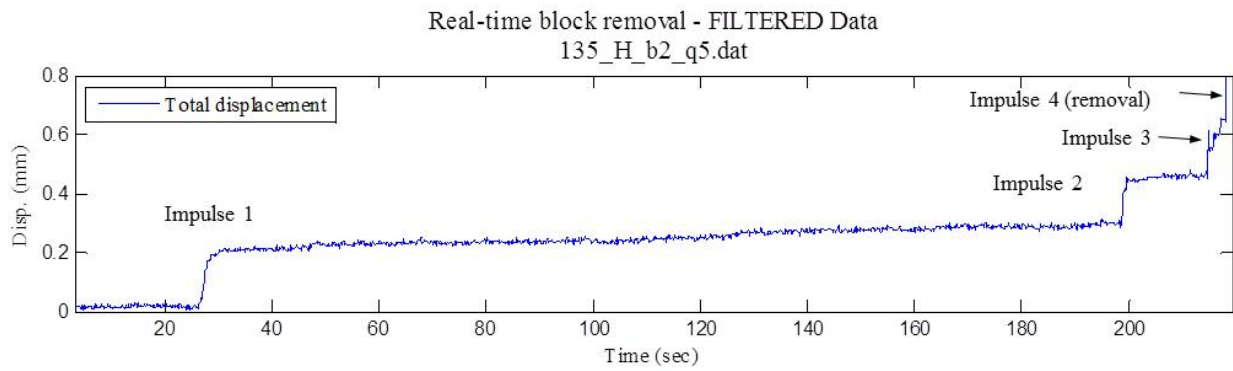
RAW displacement vector - lower hemisphere stereonet
120_H_b2_q4.dat



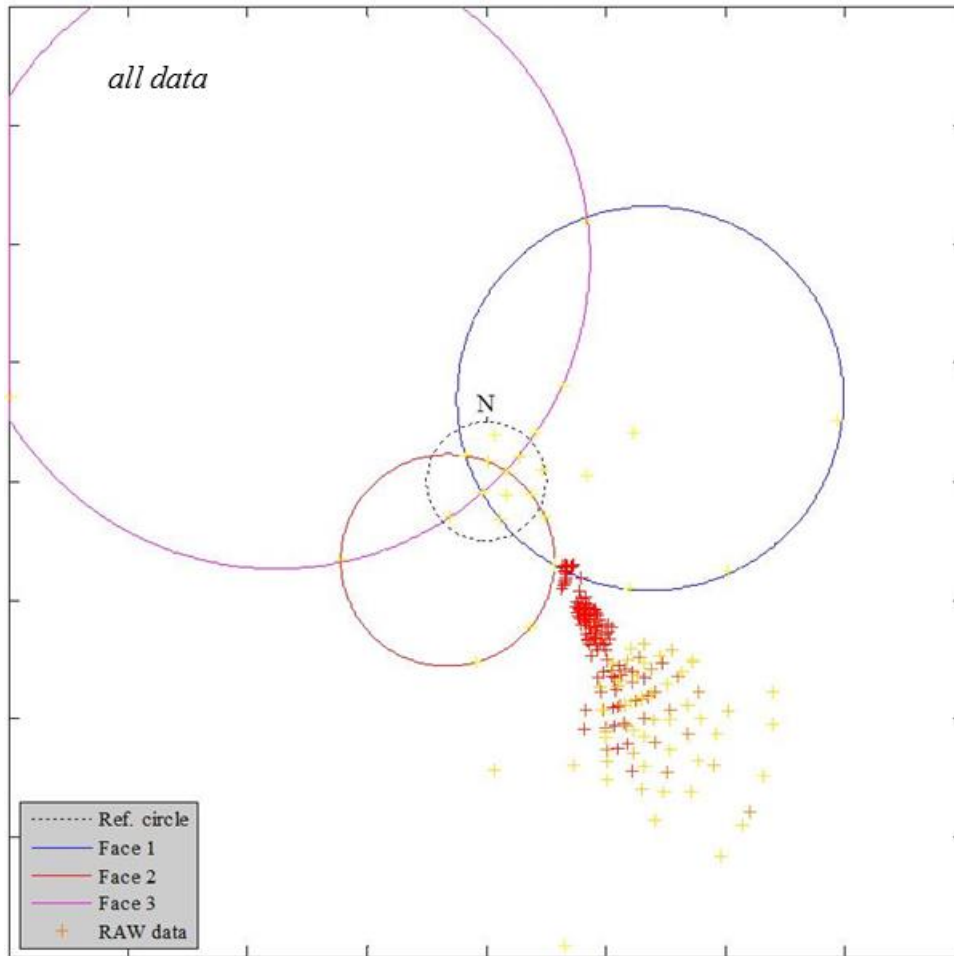
RAW displacement vector - lower hemisphere stereonet
120_H_b2_q4.dat

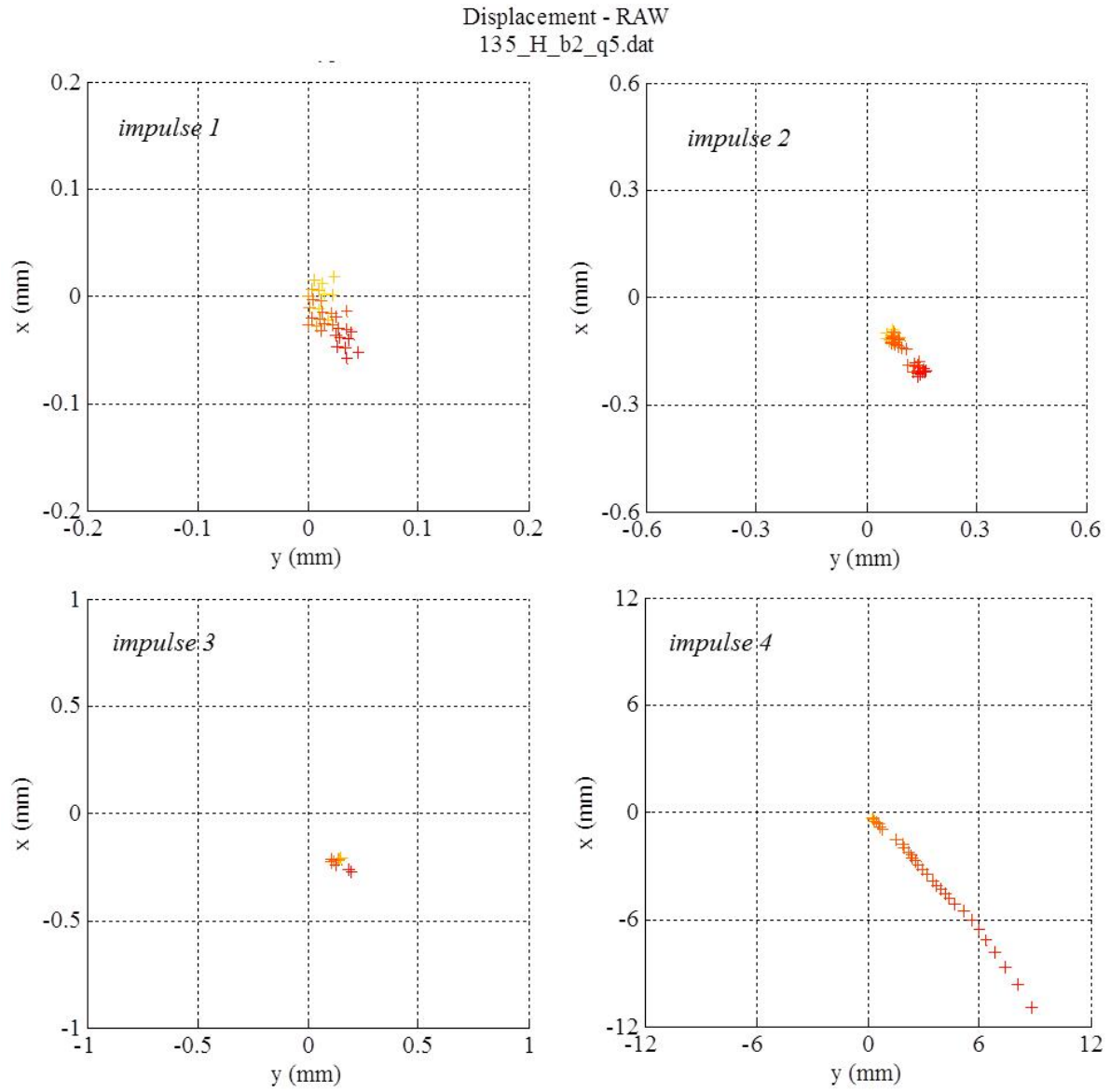


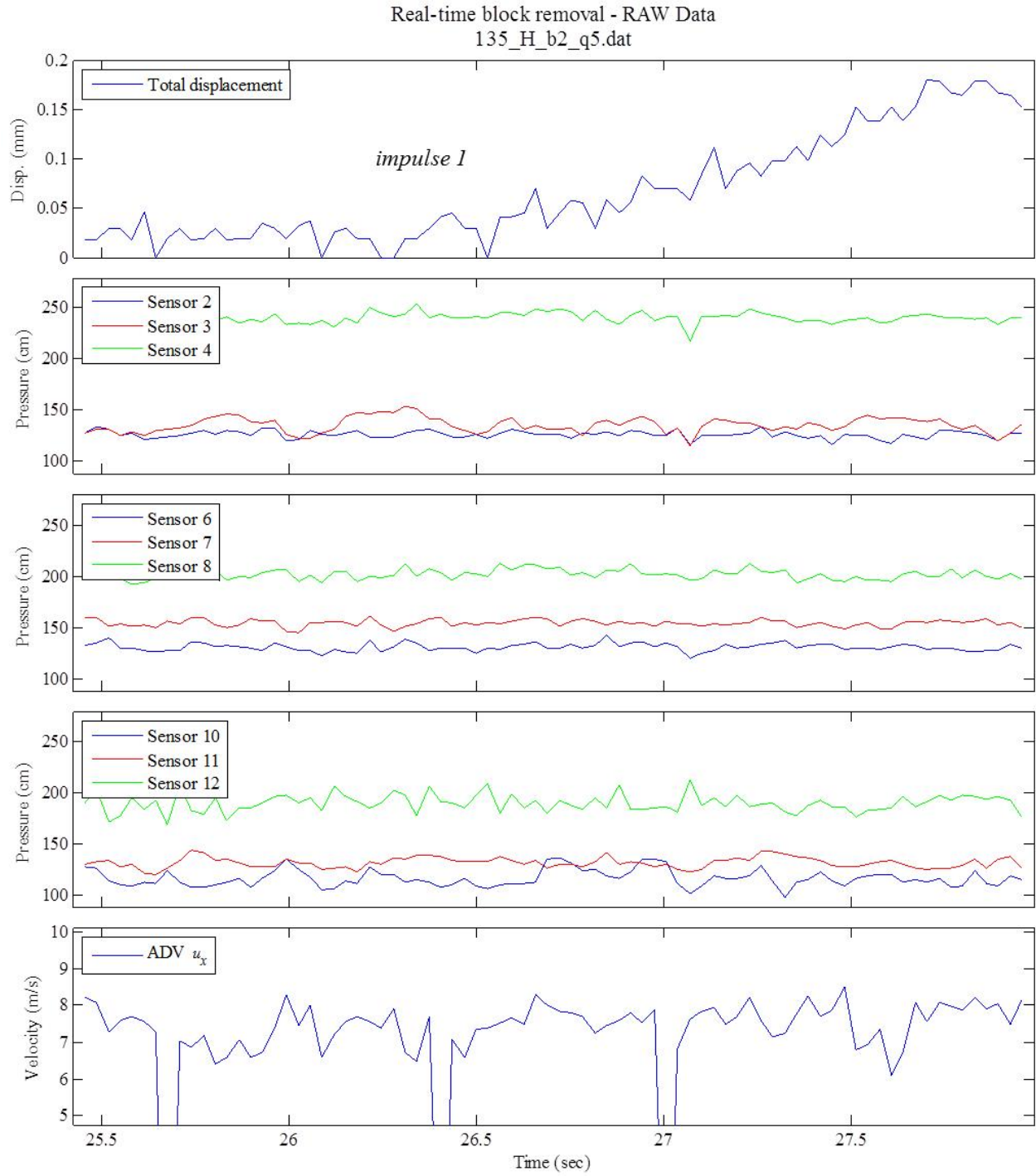
$\psi = 135$ deg., High T_u , Block 2, Q_5

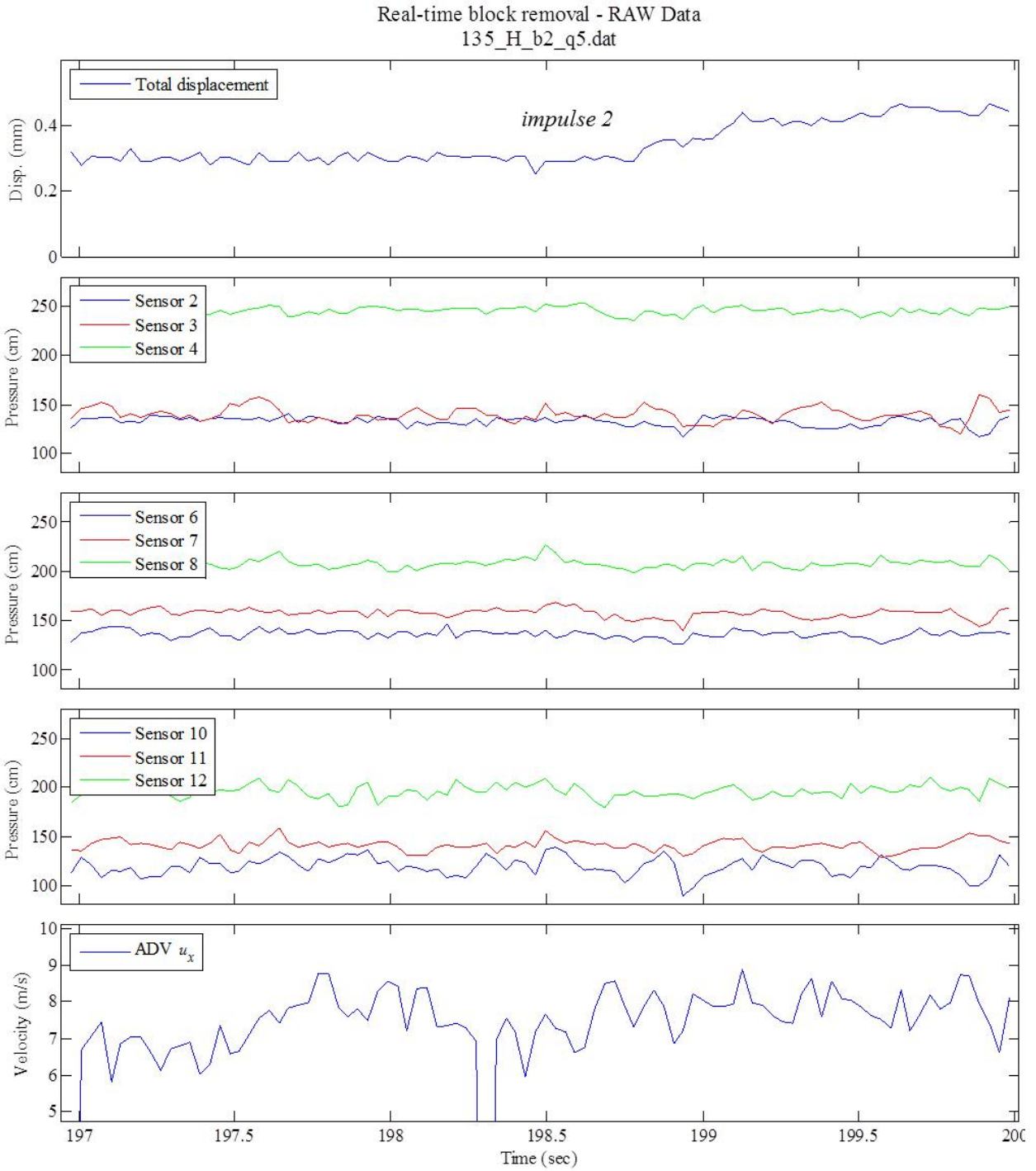


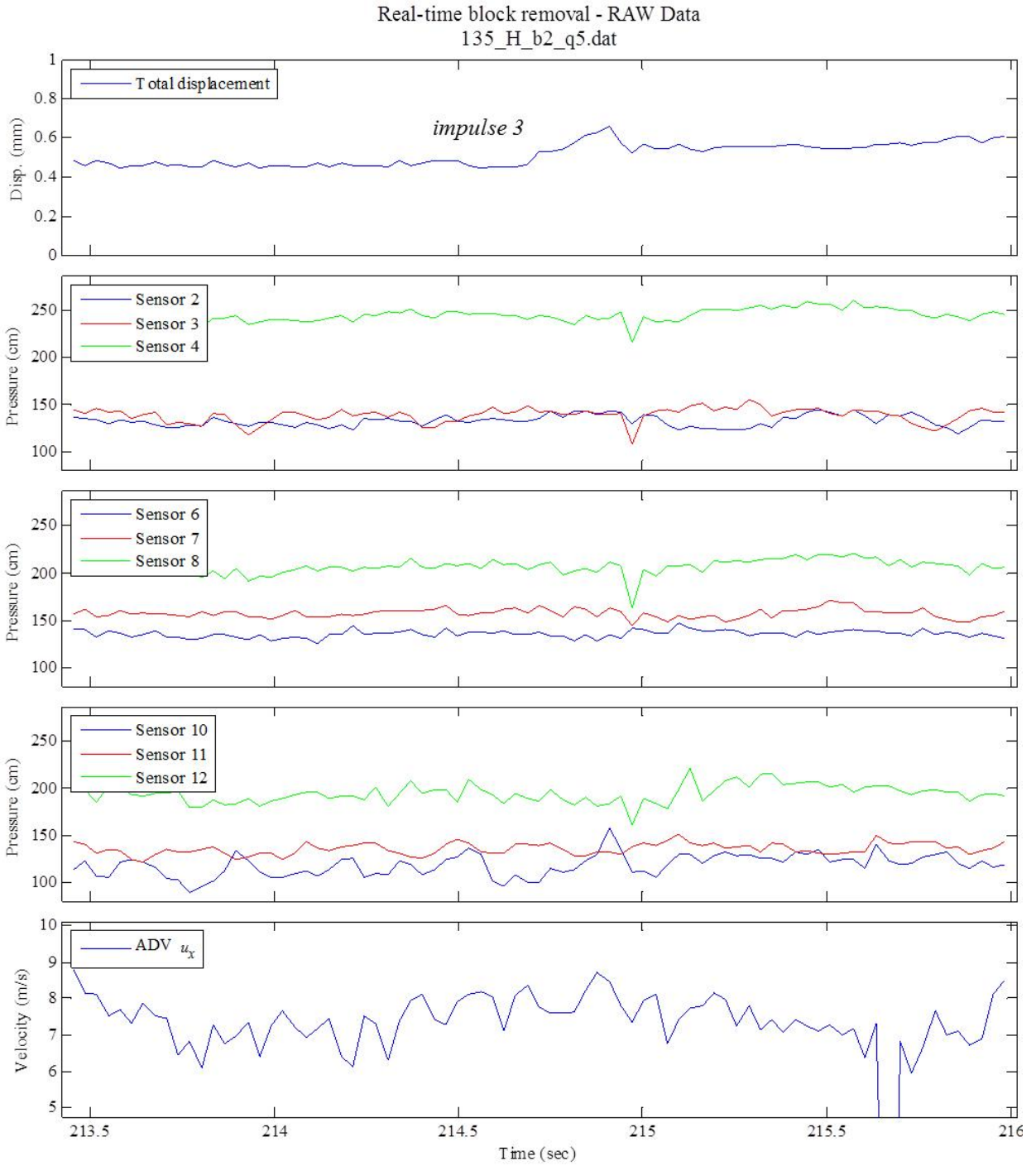
RAW displacement vector - lower hemisphere stereonet
135_H_b2_q5.dat

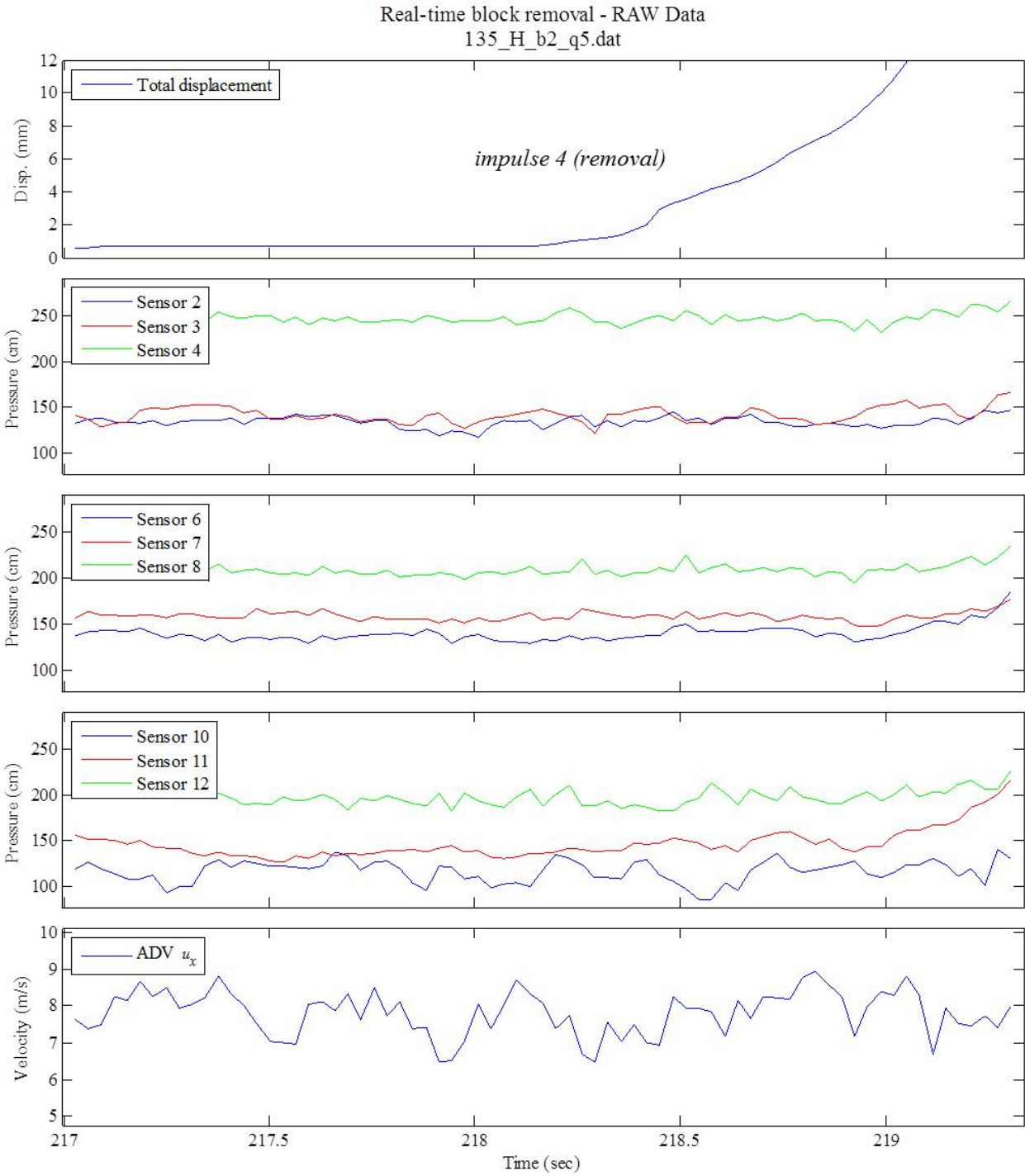




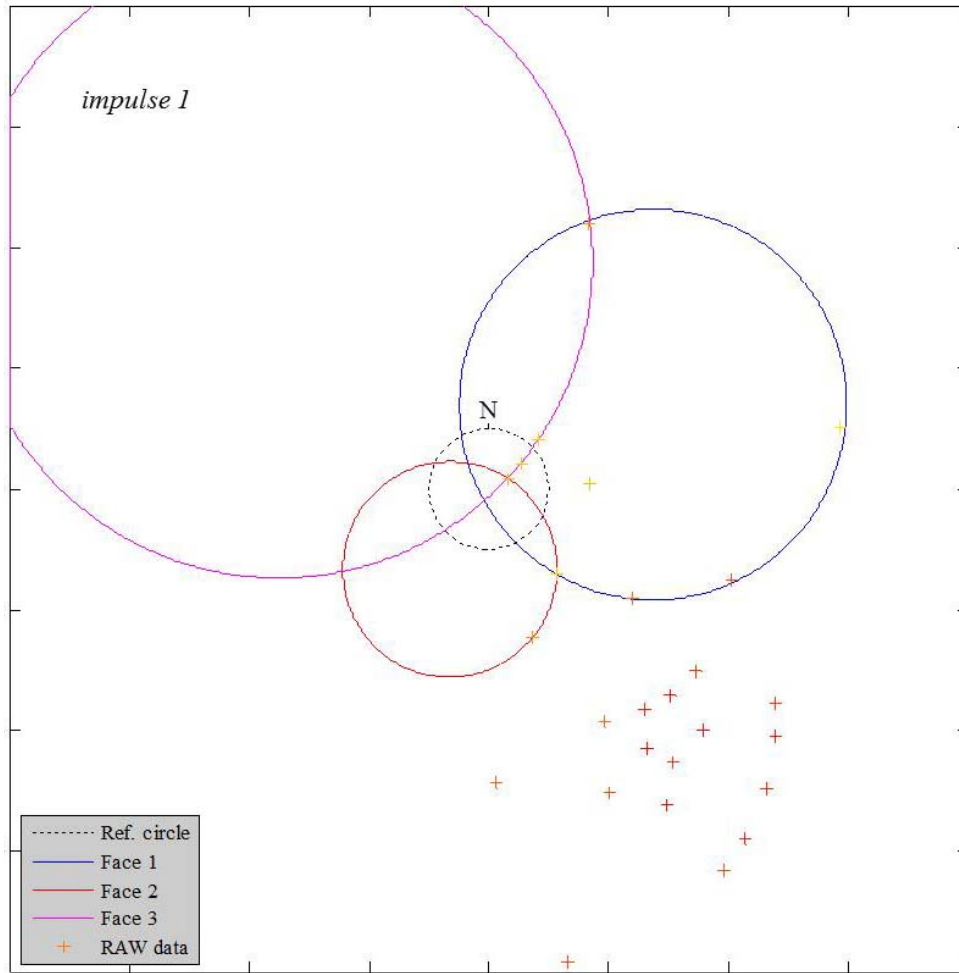




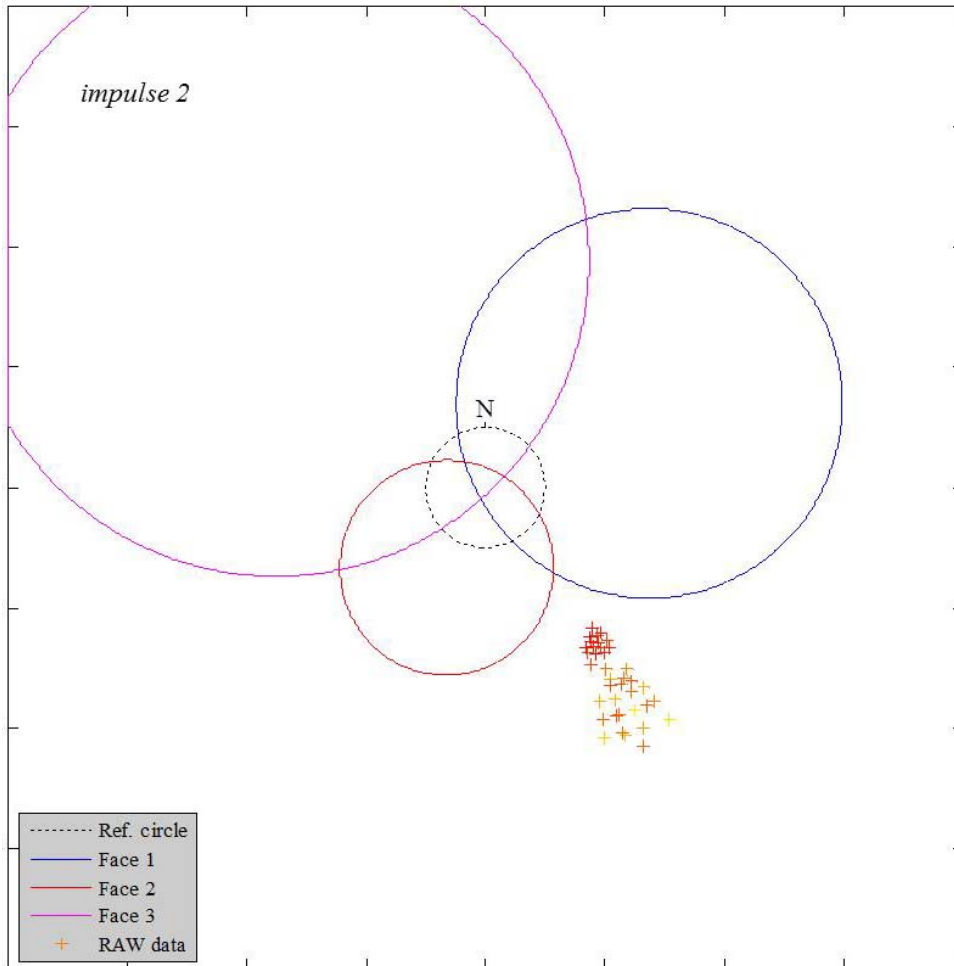




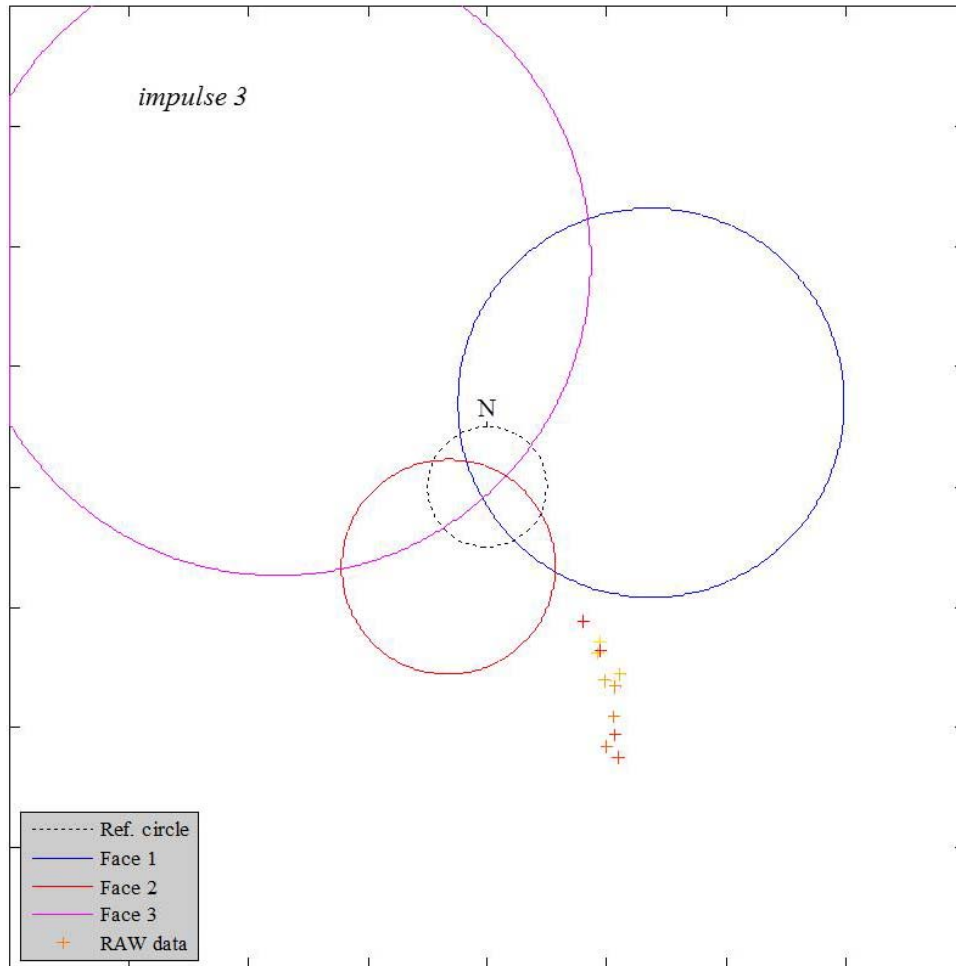
RAW displacement vector - lower hemisphere stereonet
135_H_b2_q5.dat



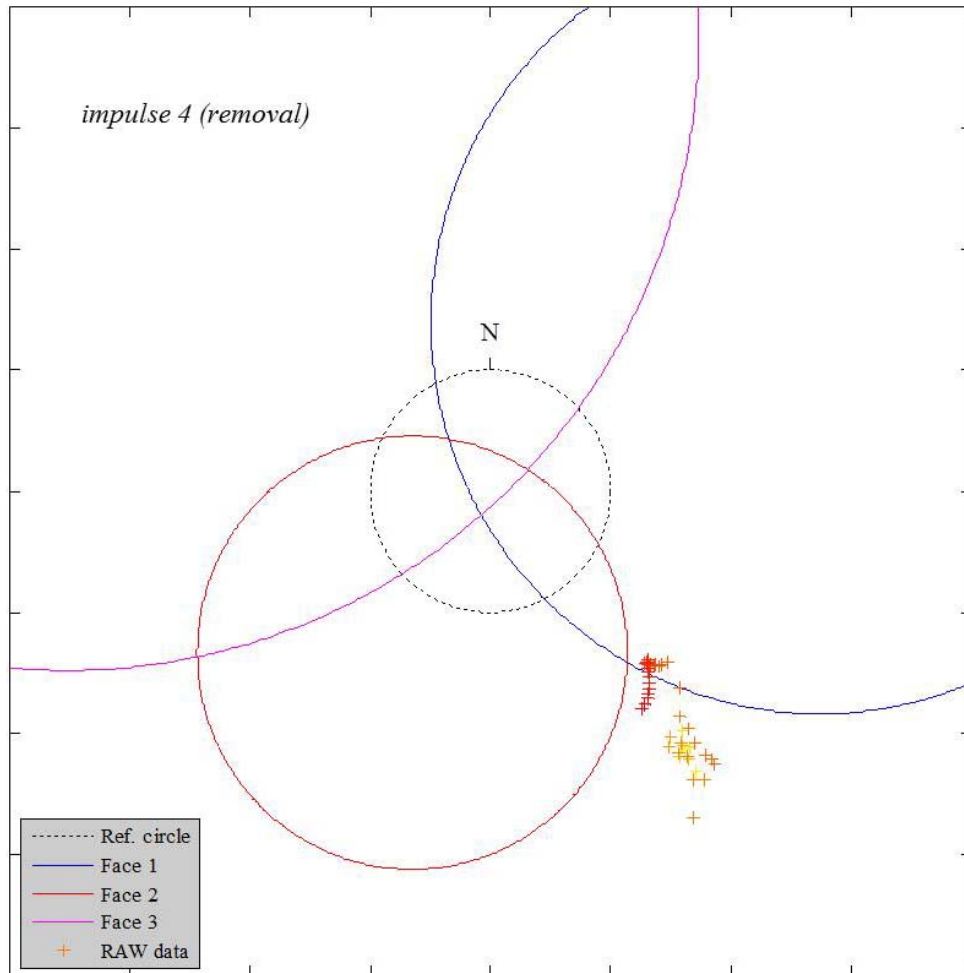
RAW displacement vector - lower hemisphere stereonet
135_H_b2_q5.dat



RAW displacement vector - lower hemisphere stereonet
135_H_b2_q5.dat

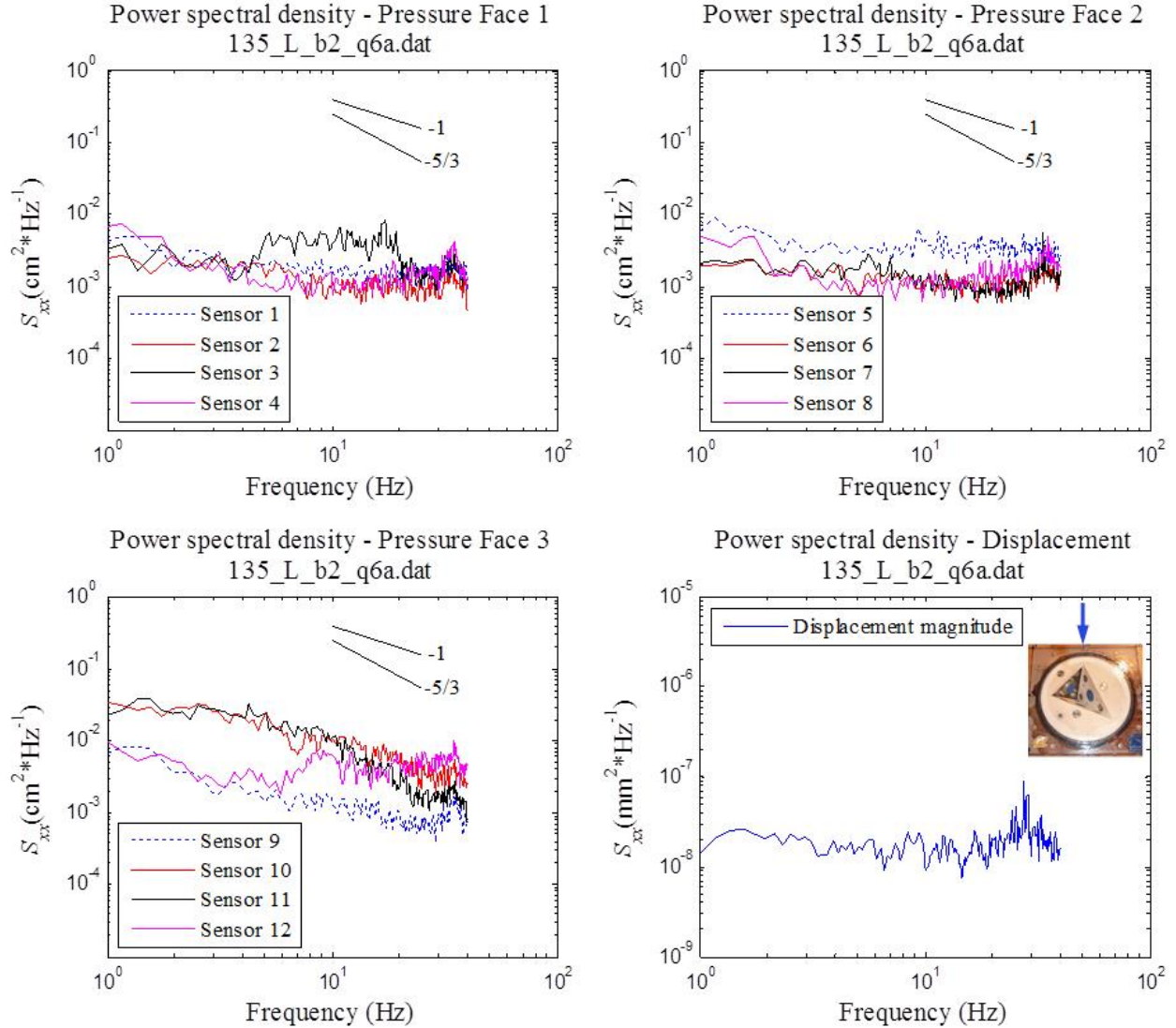


RAW displacement vector - lower hemisphere stereonet
135_H_b2_q5.dat

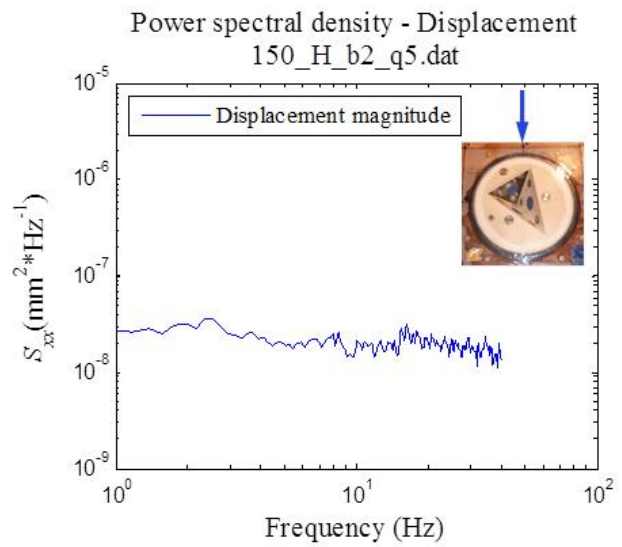
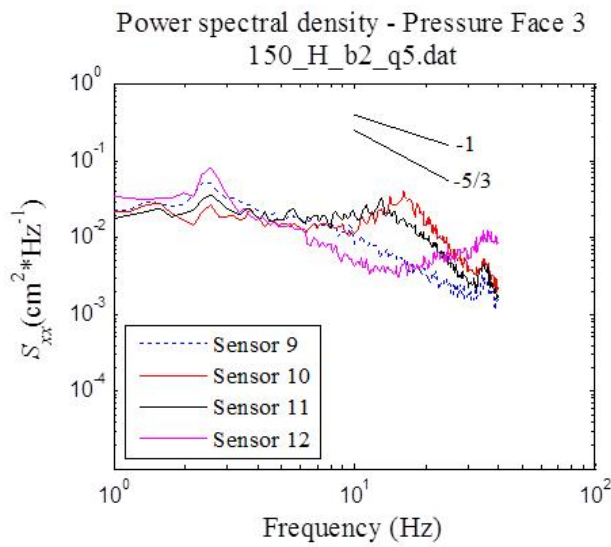
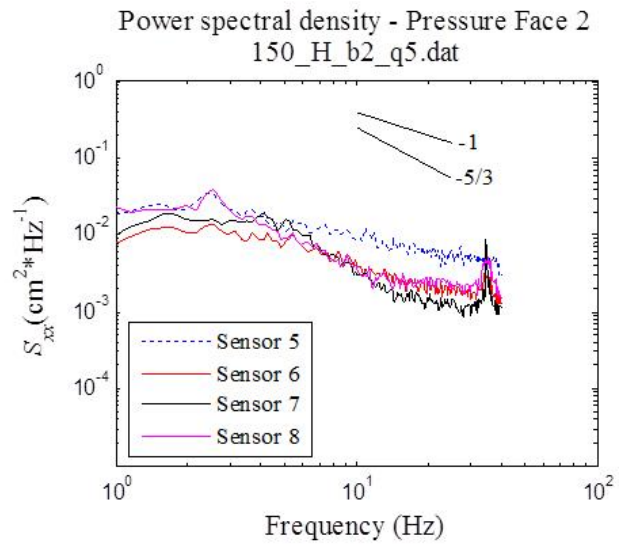
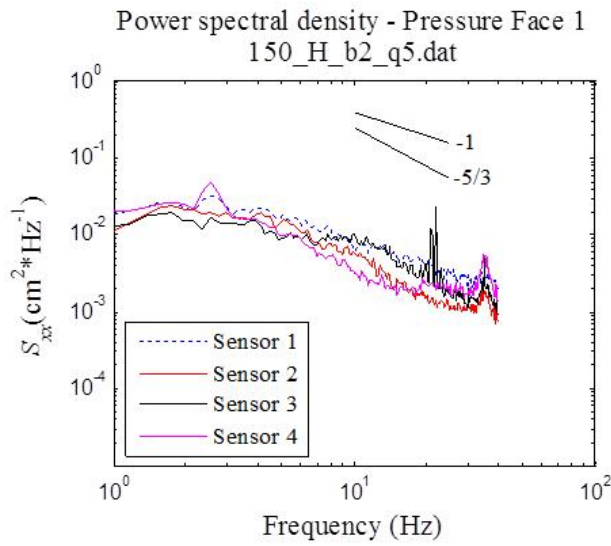


Pressure/displacement spectral analysis – supplemental figures

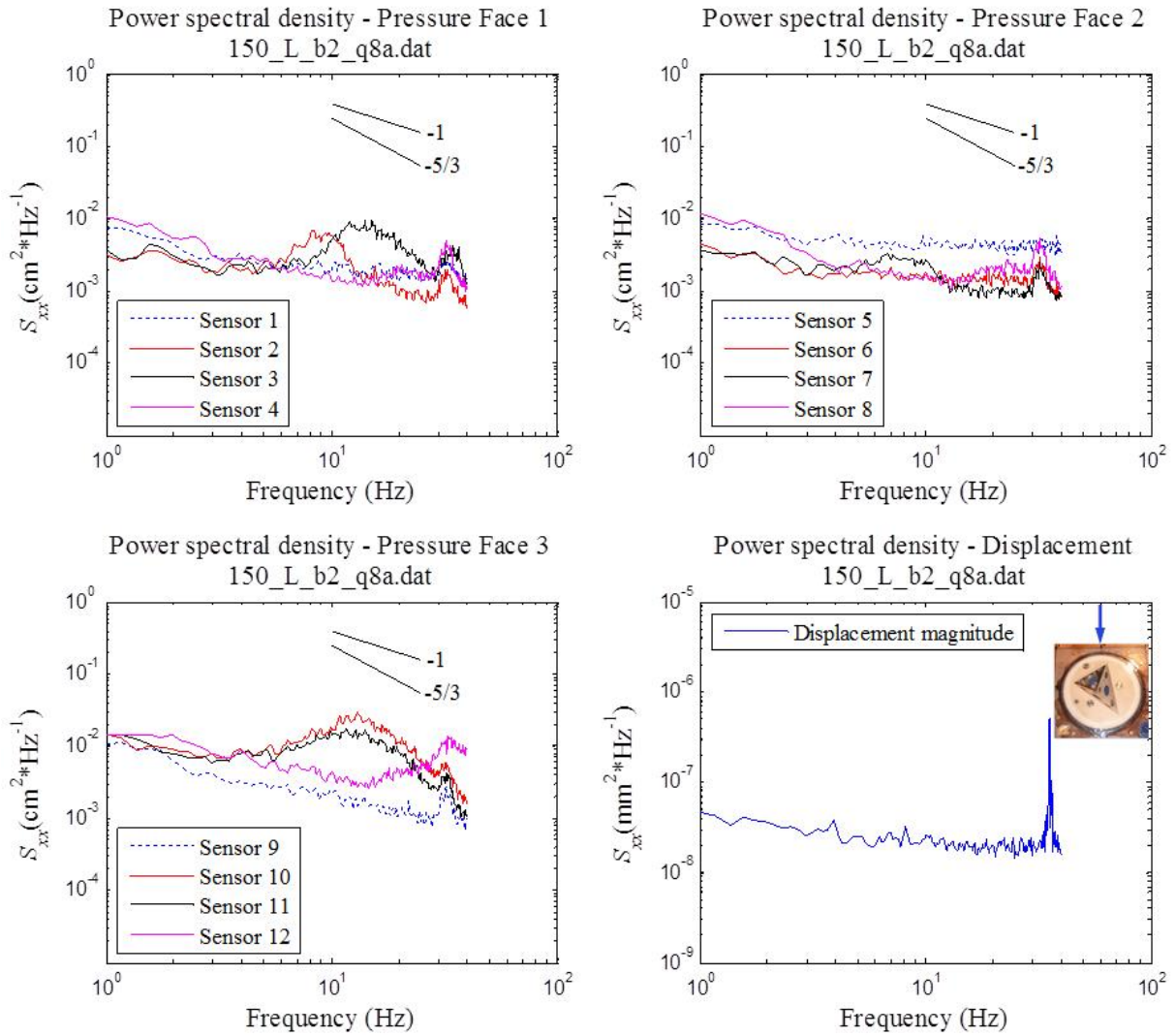
Block response 1, $\psi = 135$ deg., Low T_u , Block 2, Q_6



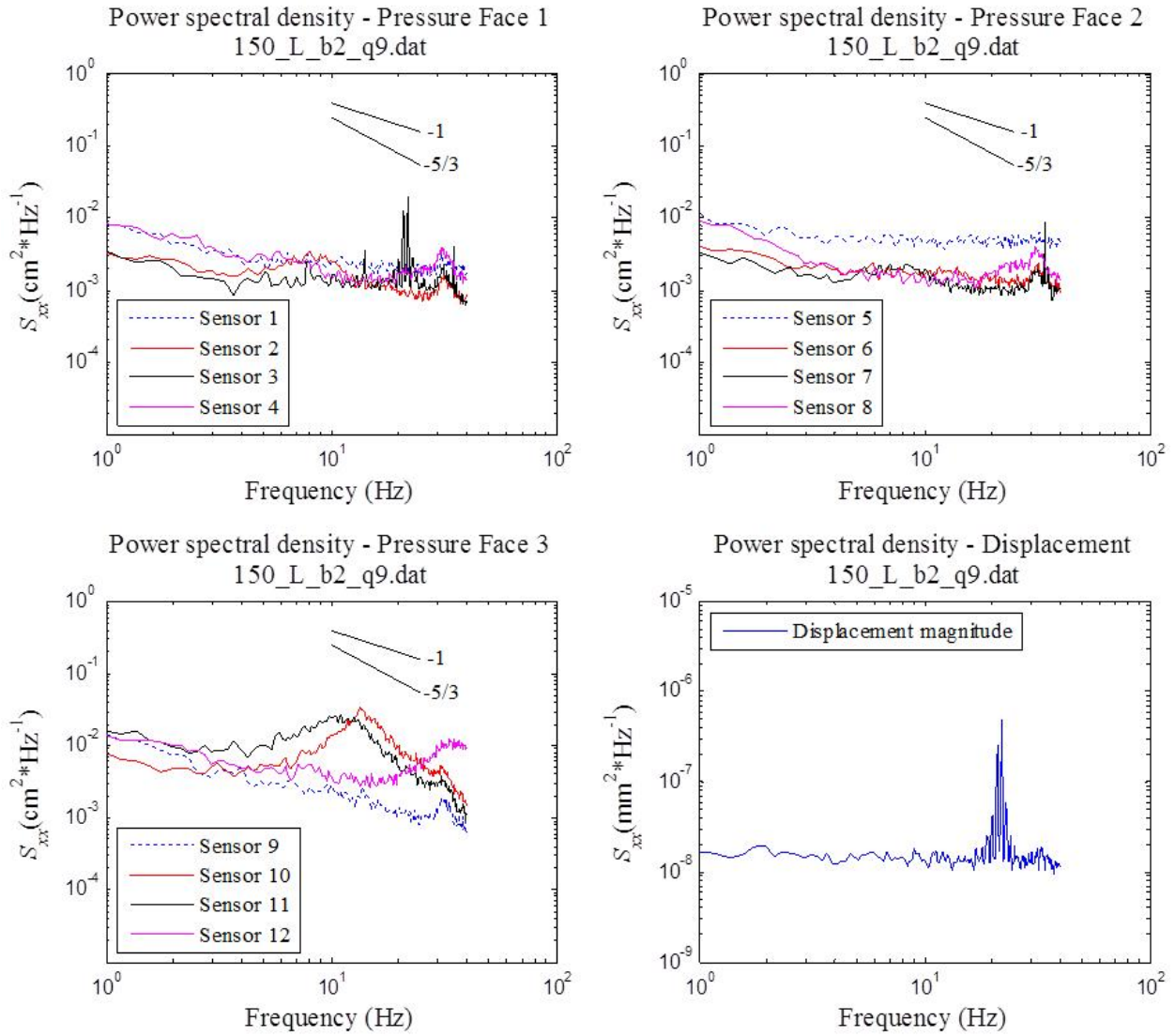
Block response 1, $\psi = 150$ deg., High T_u , Block 2, Q_5



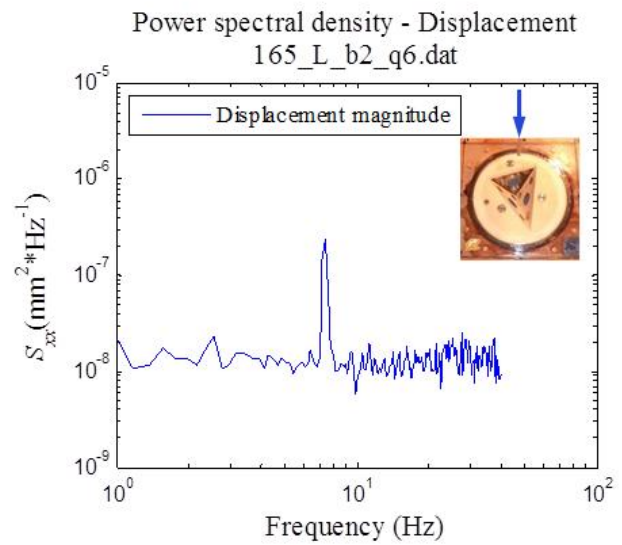
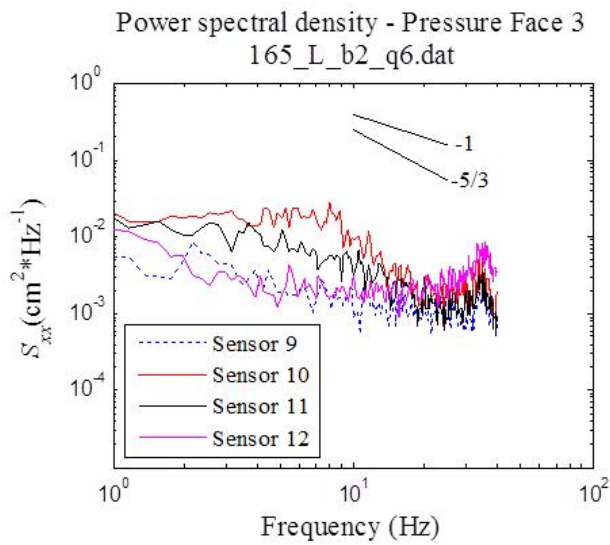
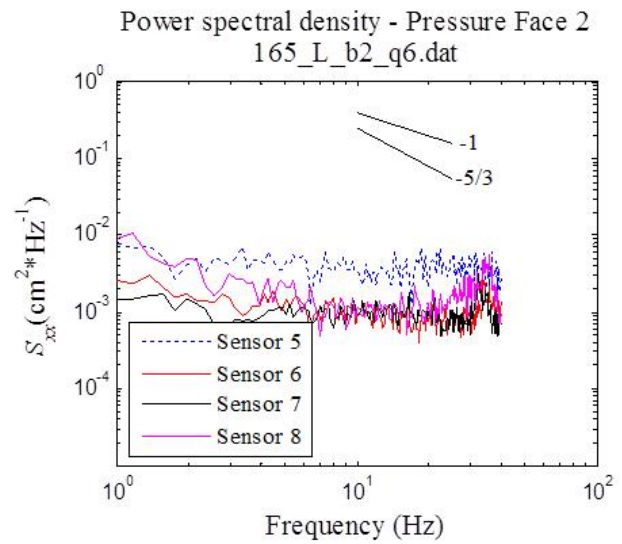
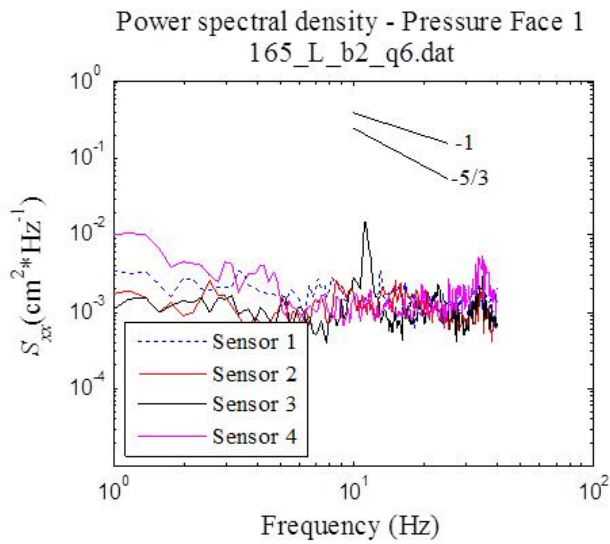
Block response 1, $\psi = 150$ deg., Low T_u , Block 2, Q_8



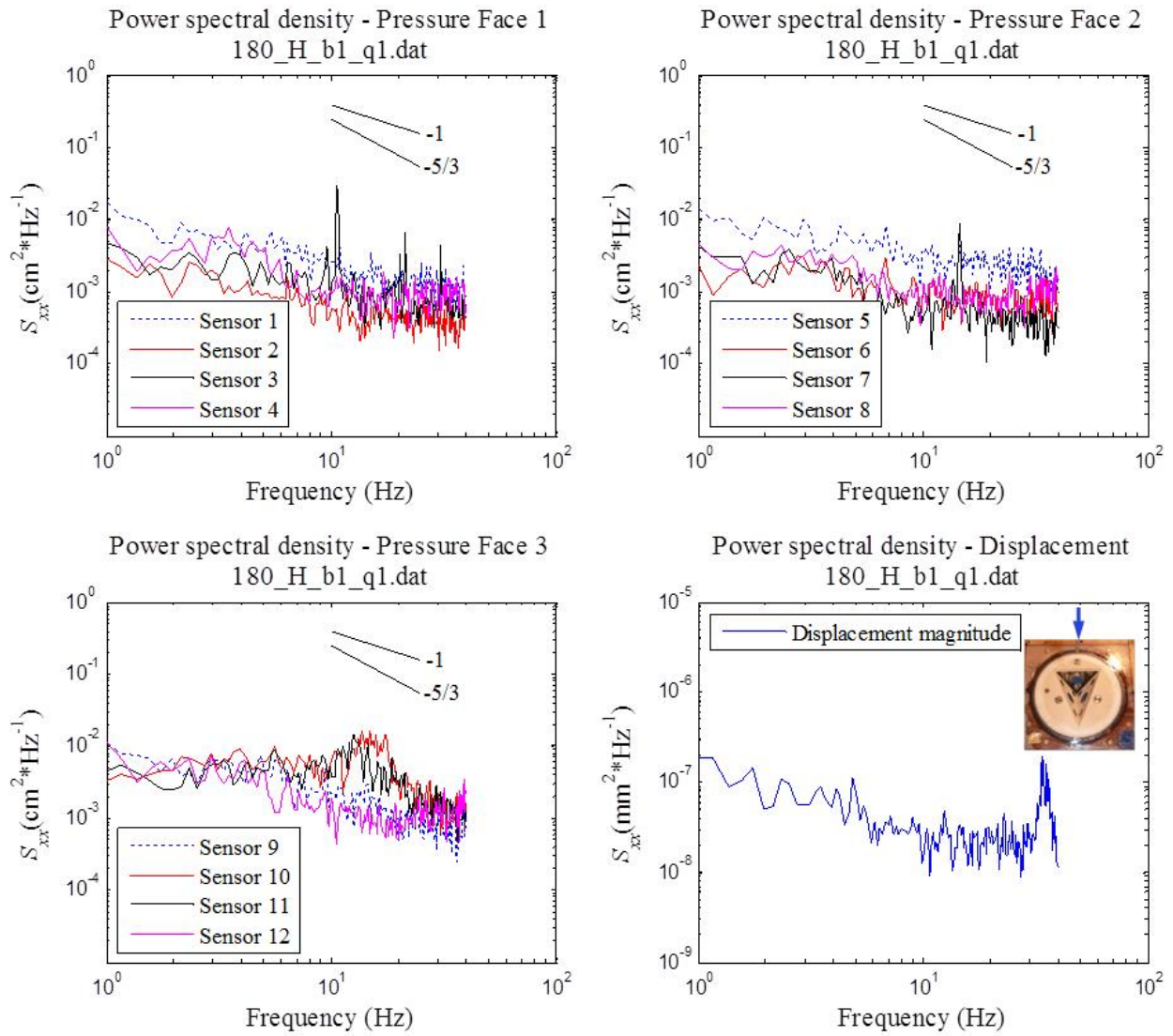
Block response 1, $\psi = 150$ deg., Low T_u , Block 2, Q_8



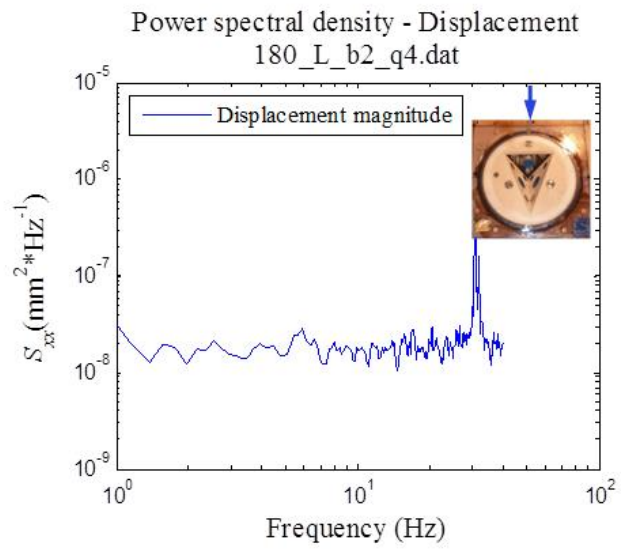
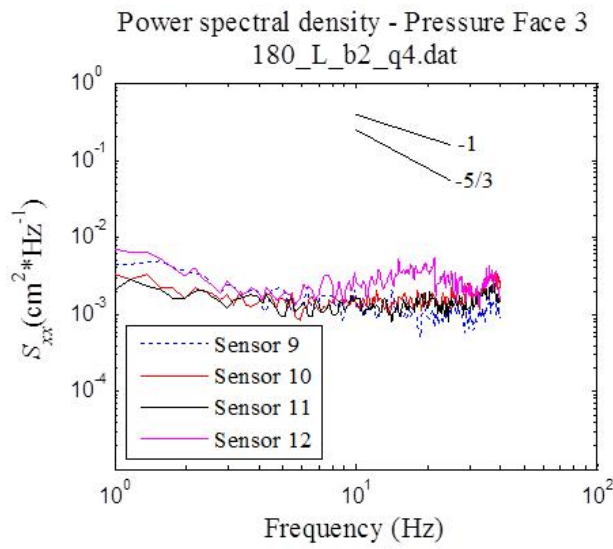
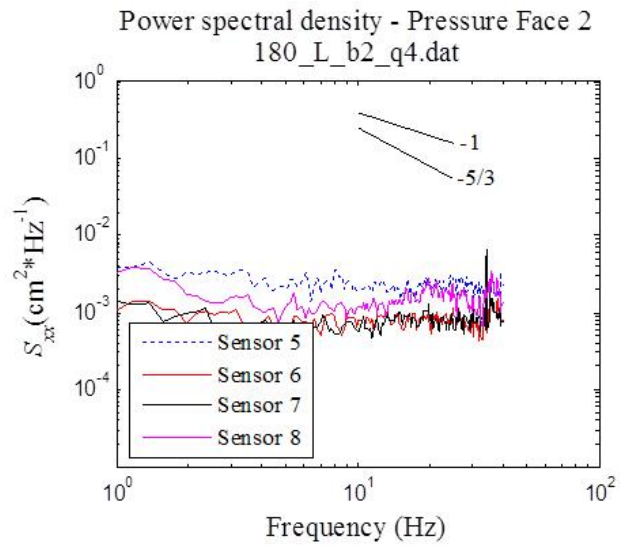
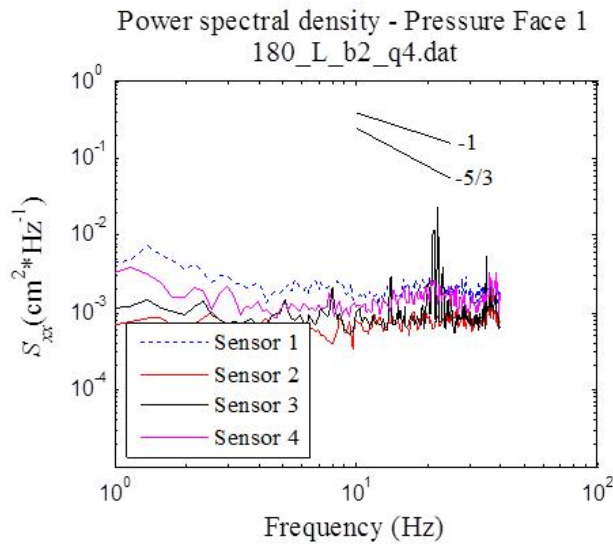
Block response 1, $\psi = 165$ deg., Low T_u , Block 2, Q_6



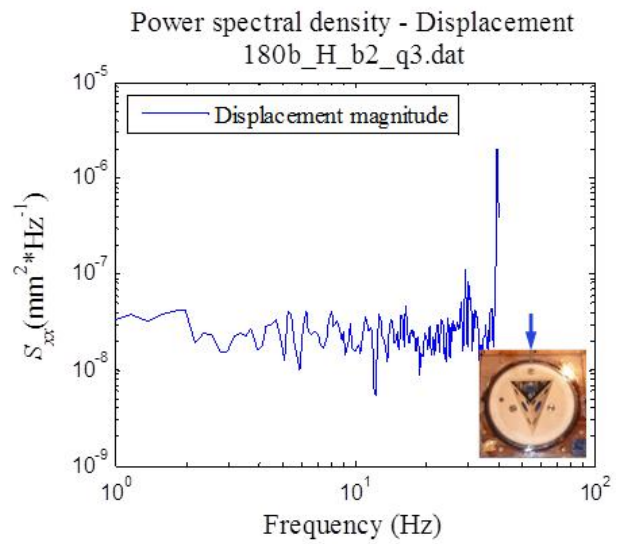
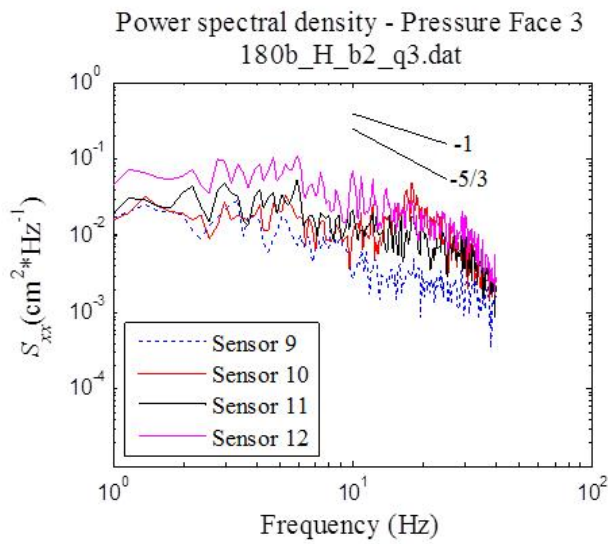
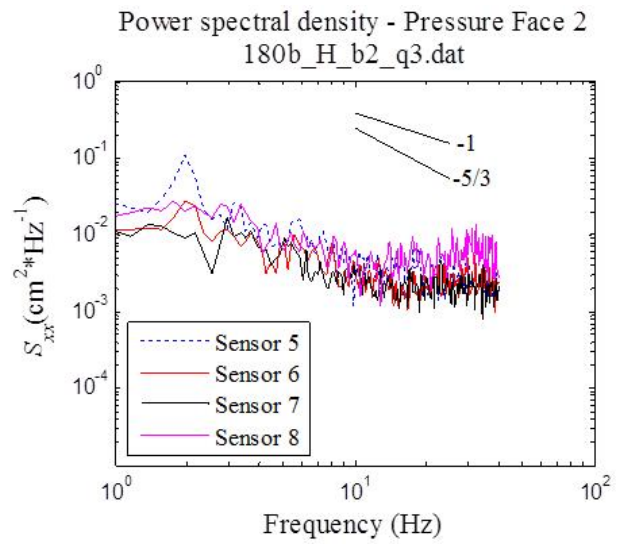
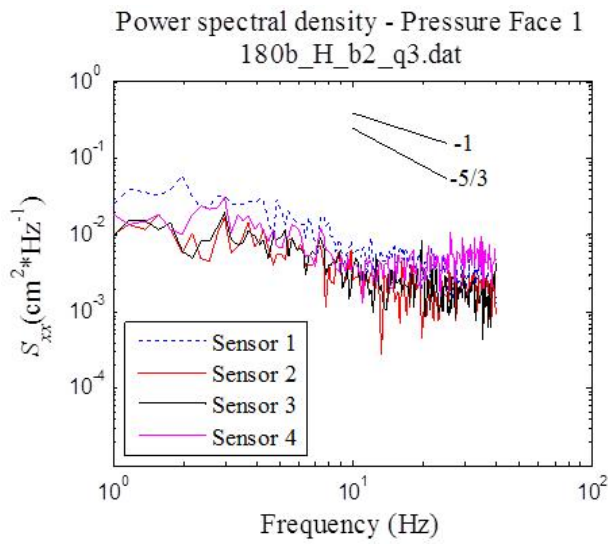
Block response 1, $\psi = 180$ deg., High T_u , Block 1, Q_I



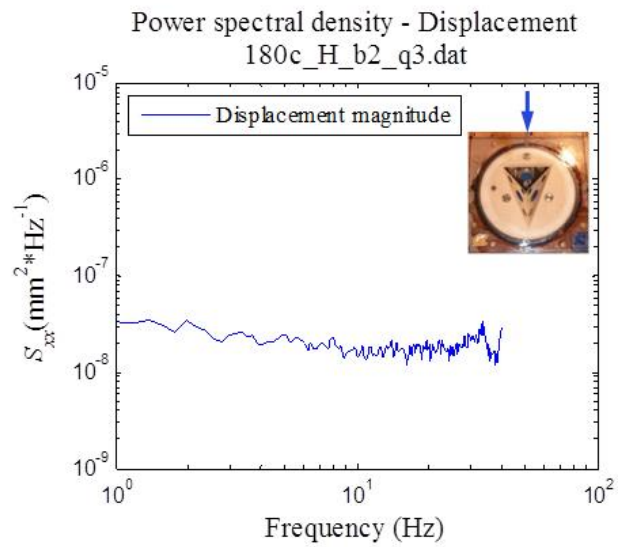
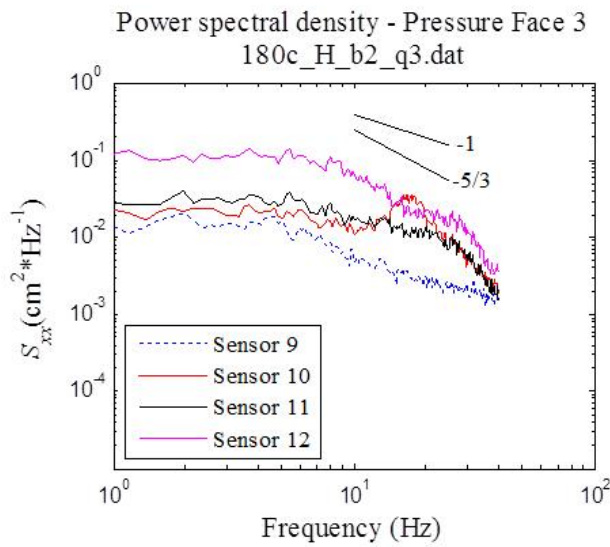
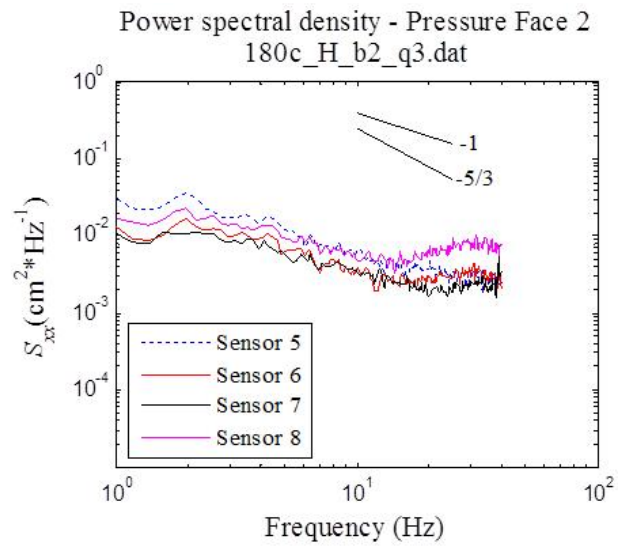
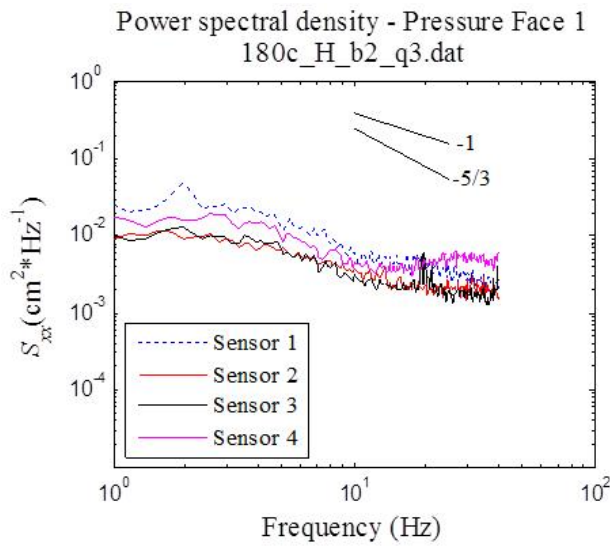
Block response 1, $\psi = 180$ deg., Low T_u , Block 2, Q_4



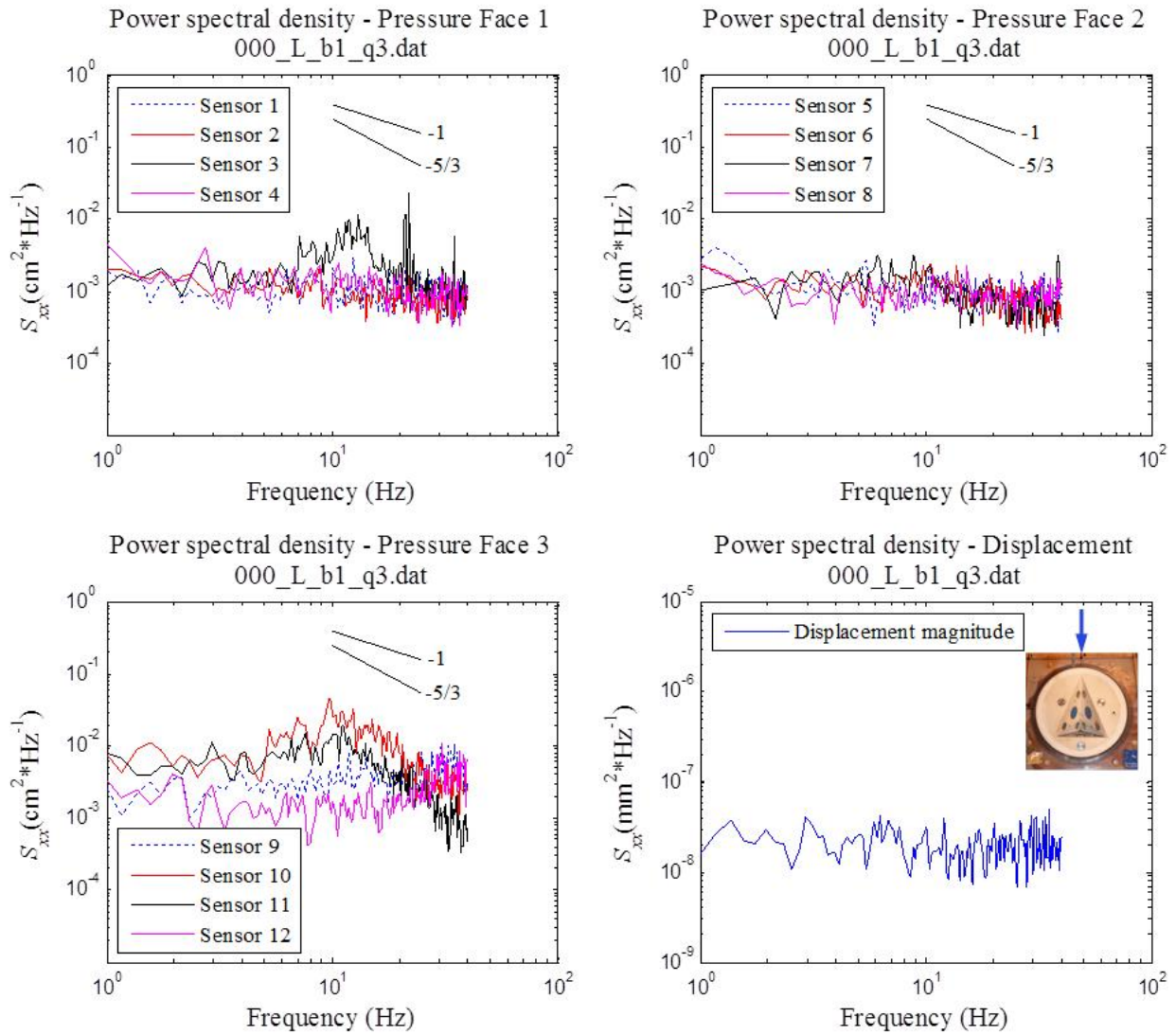
Block response 1, $\psi = 180$ deg., High T_u , Block 2, Q_3



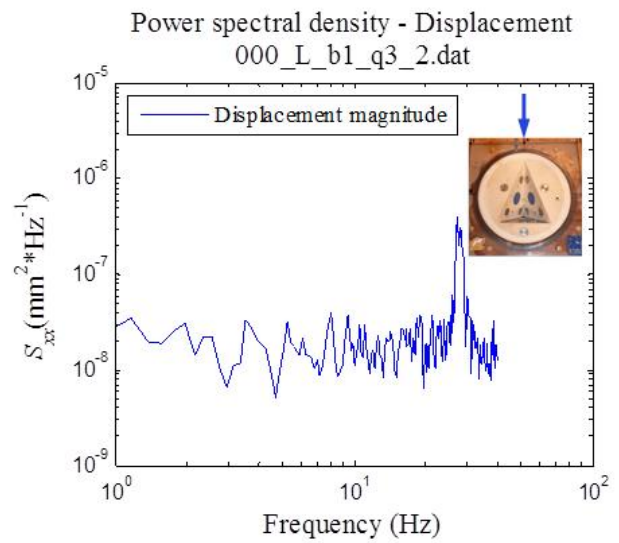
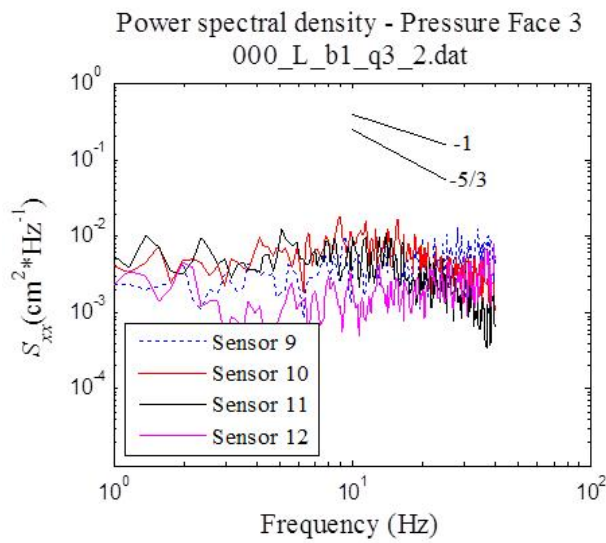
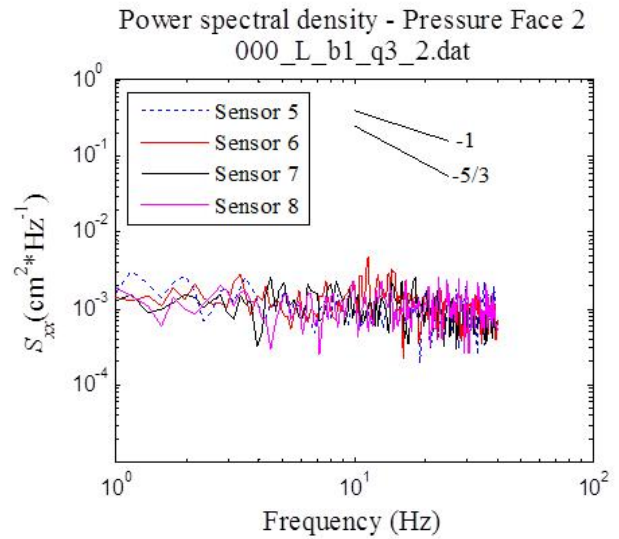
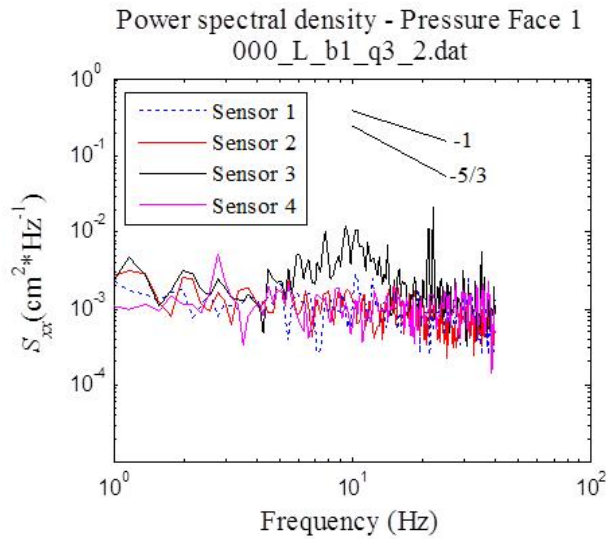
Block response 1, $\psi = 180$ deg., High T_u , Block 2, Q_3



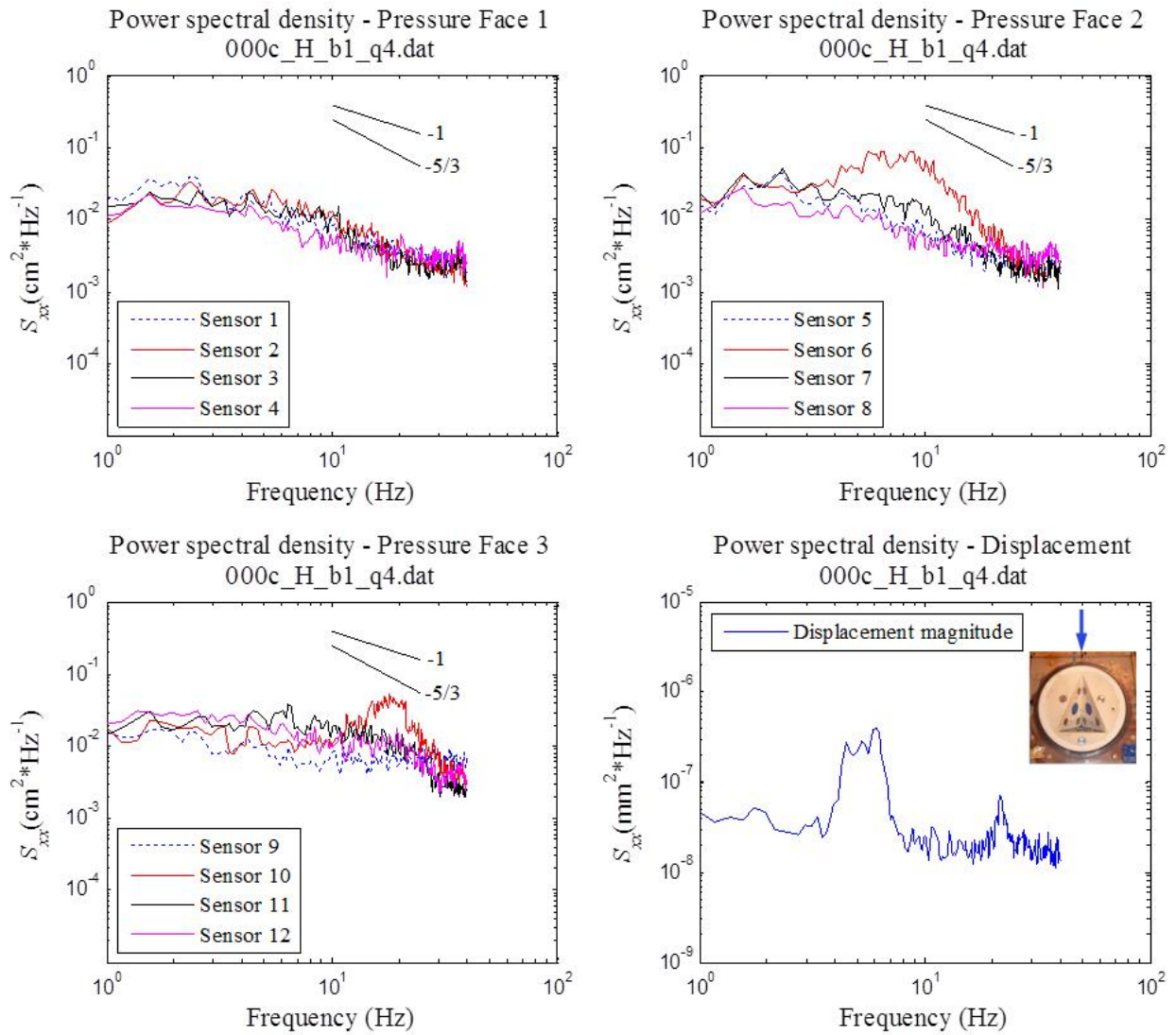
Block response 2, $\psi = 0$ deg., Low T_u , Block 1, Q_3



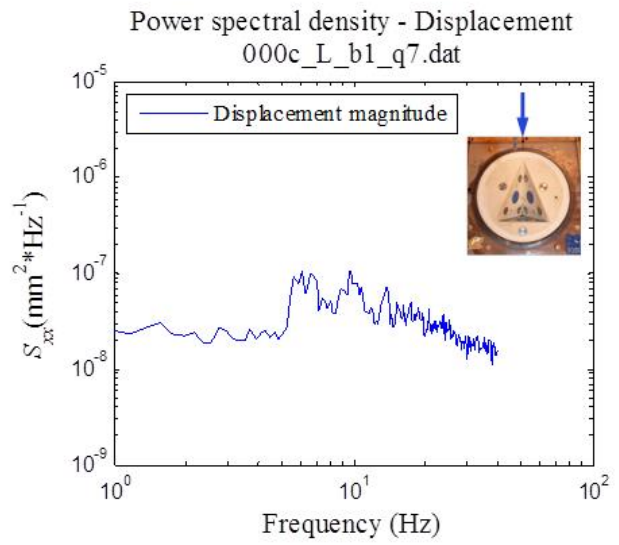
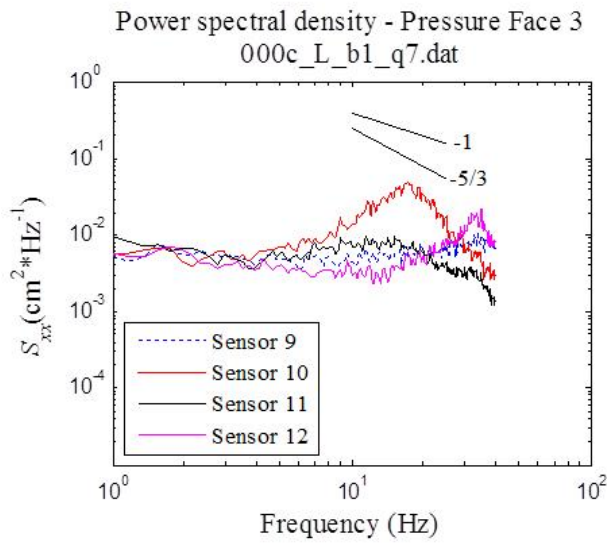
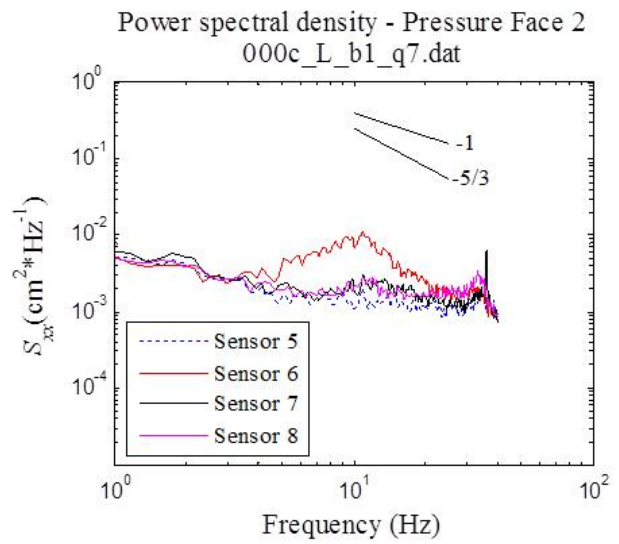
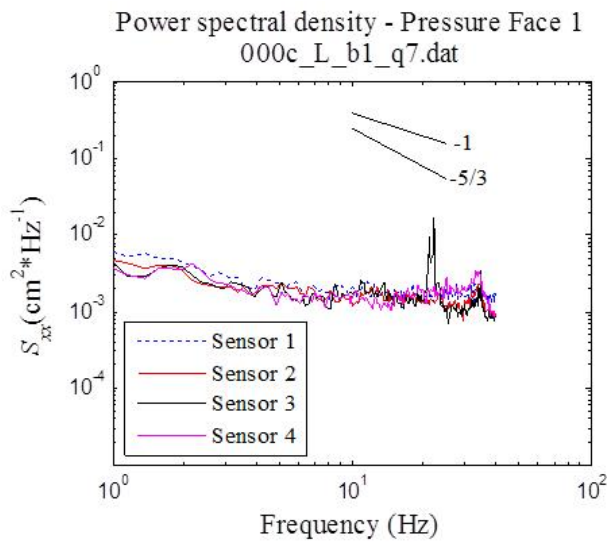
Block response 2, $\psi = 0$ deg., Low T_u , Block 1, Q_3



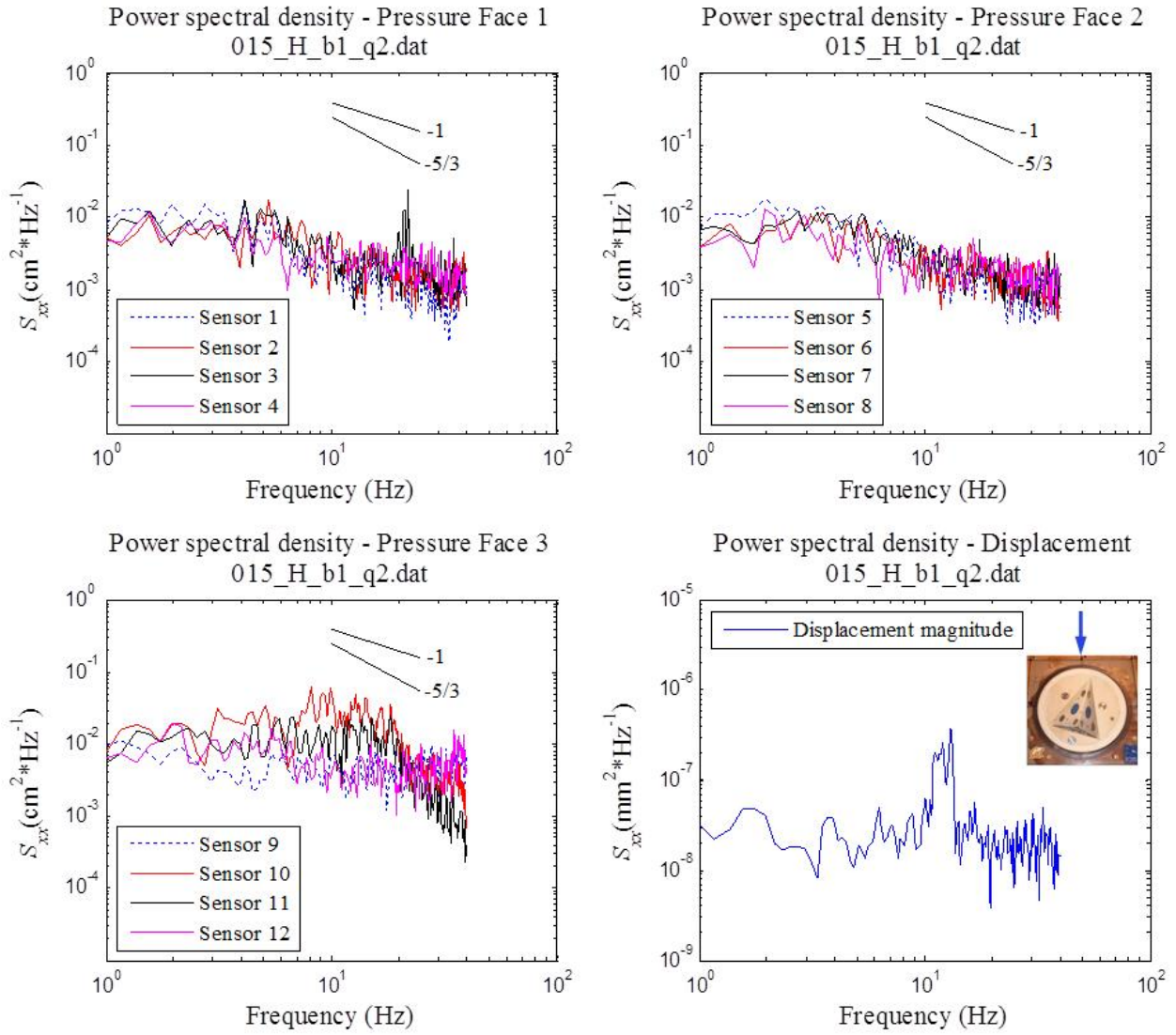
Block response 2, $\psi = 0$ deg., High T_u , Block 1, Q_4



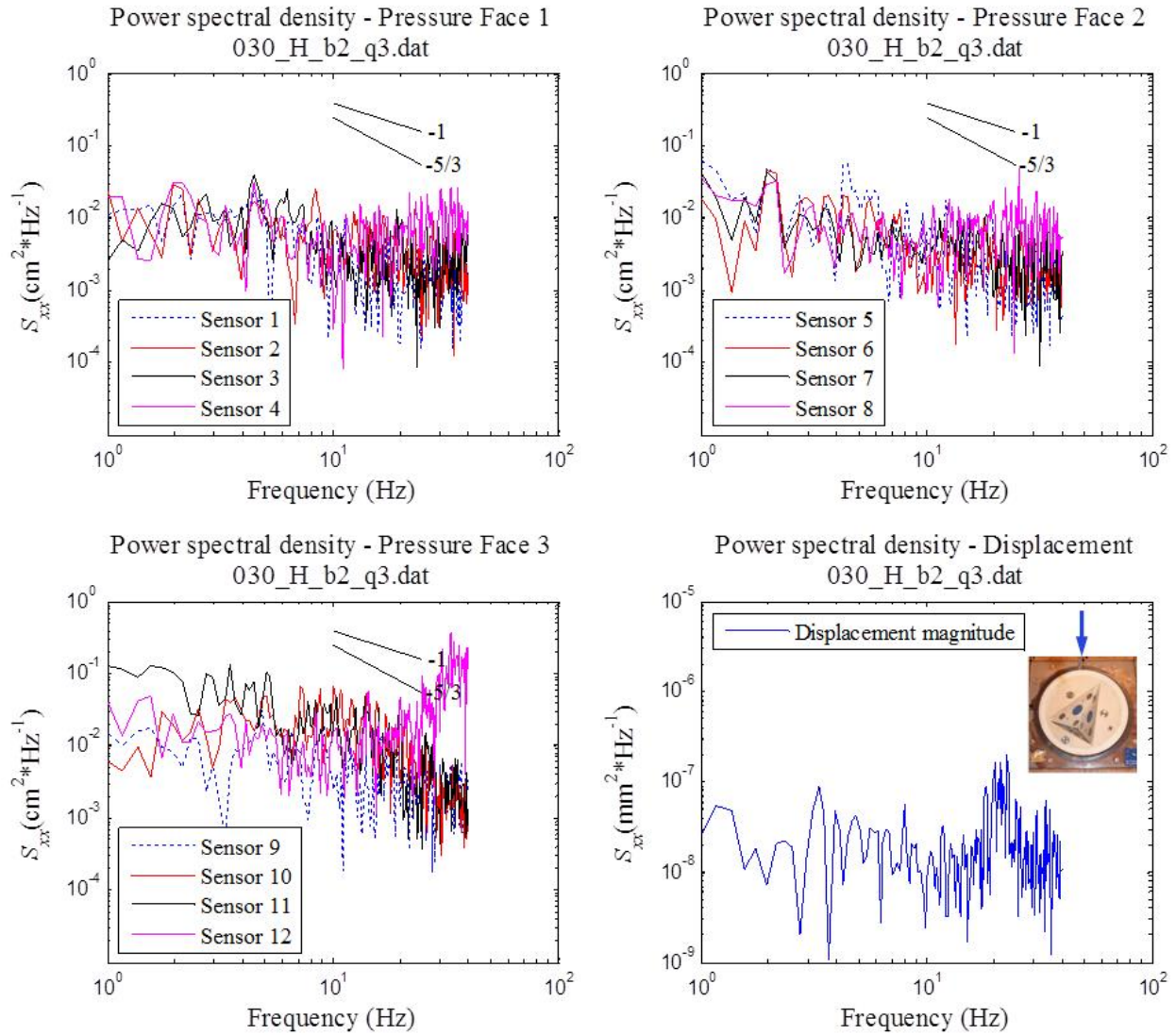
Block response 2, $\psi = 0$ deg., Low T_u , Block 1, Q_7



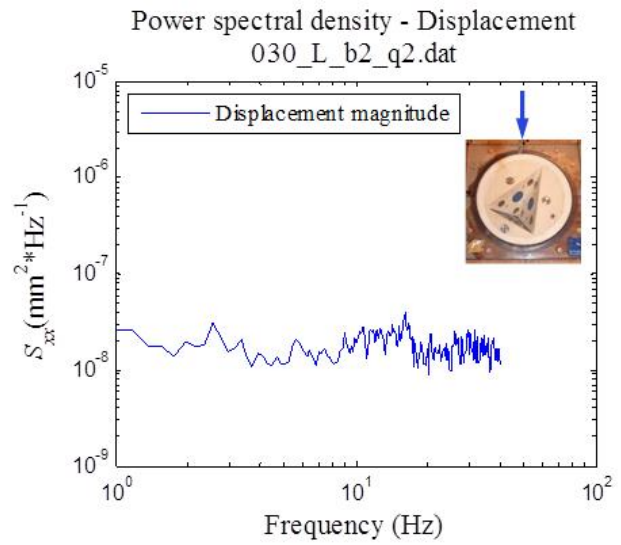
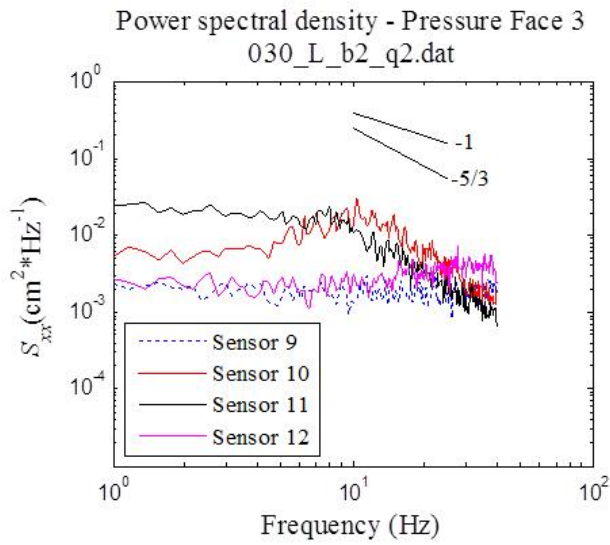
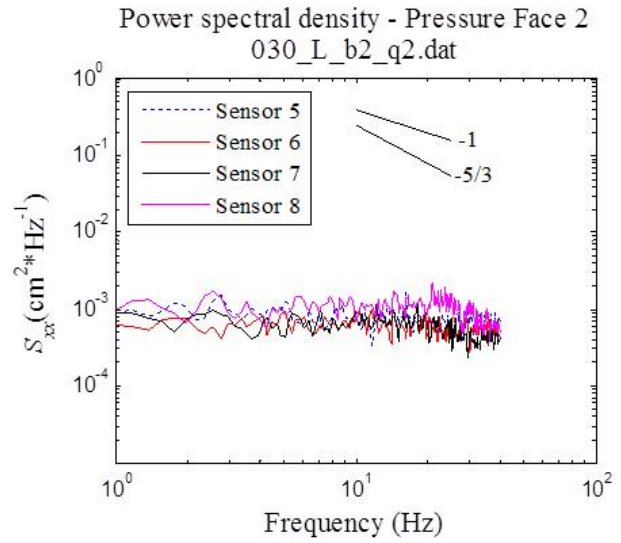
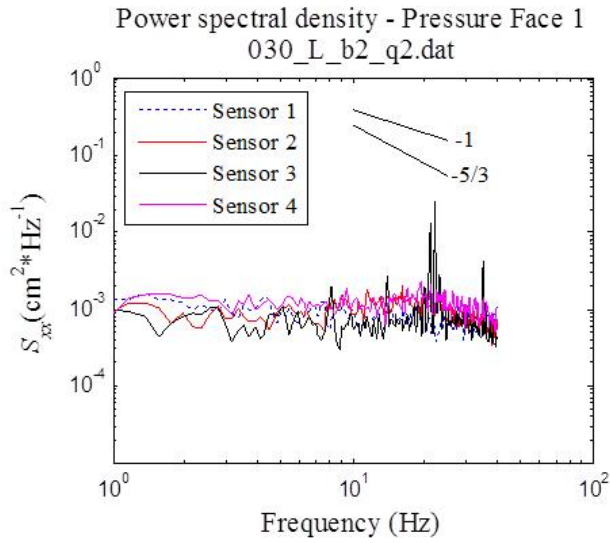
Block response 2, $\psi = 15$ deg., High T_u , Block 1, Q_2



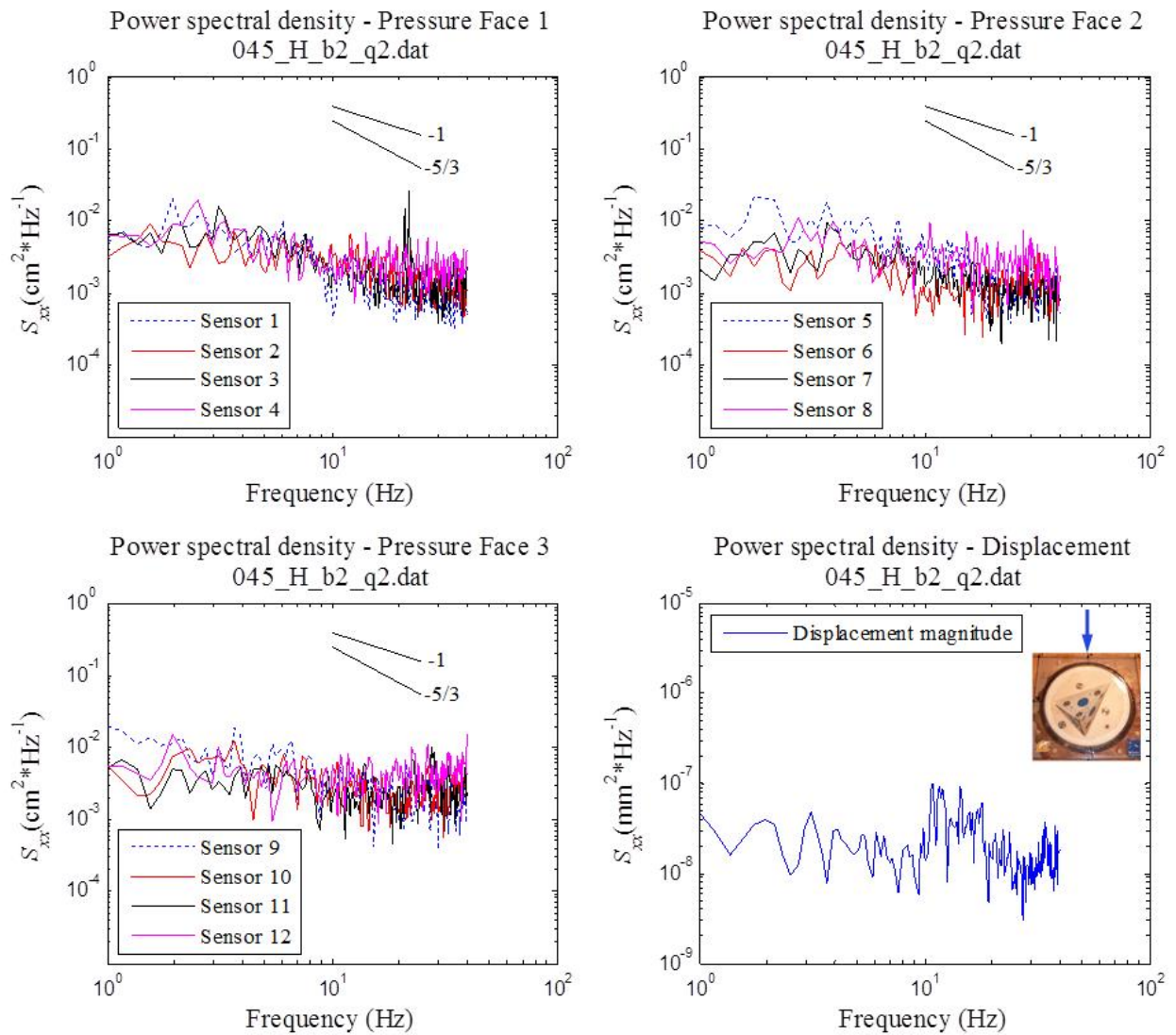
Block response 2, $\psi = 30$ deg., High T_u , Block 2, Q_3



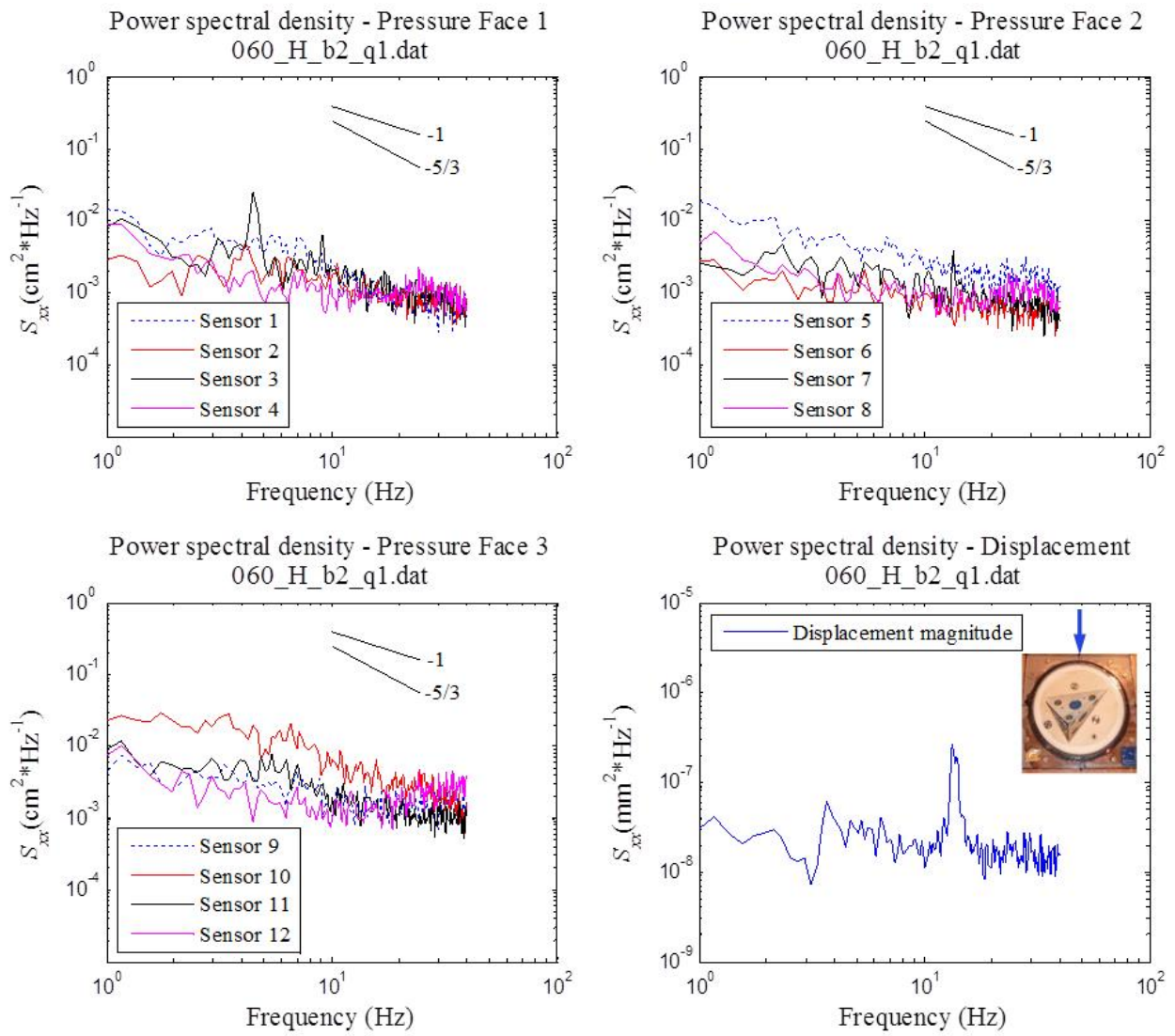
Block response 2, $\psi = 30$ deg., Low T_u , Block 2, Q_2



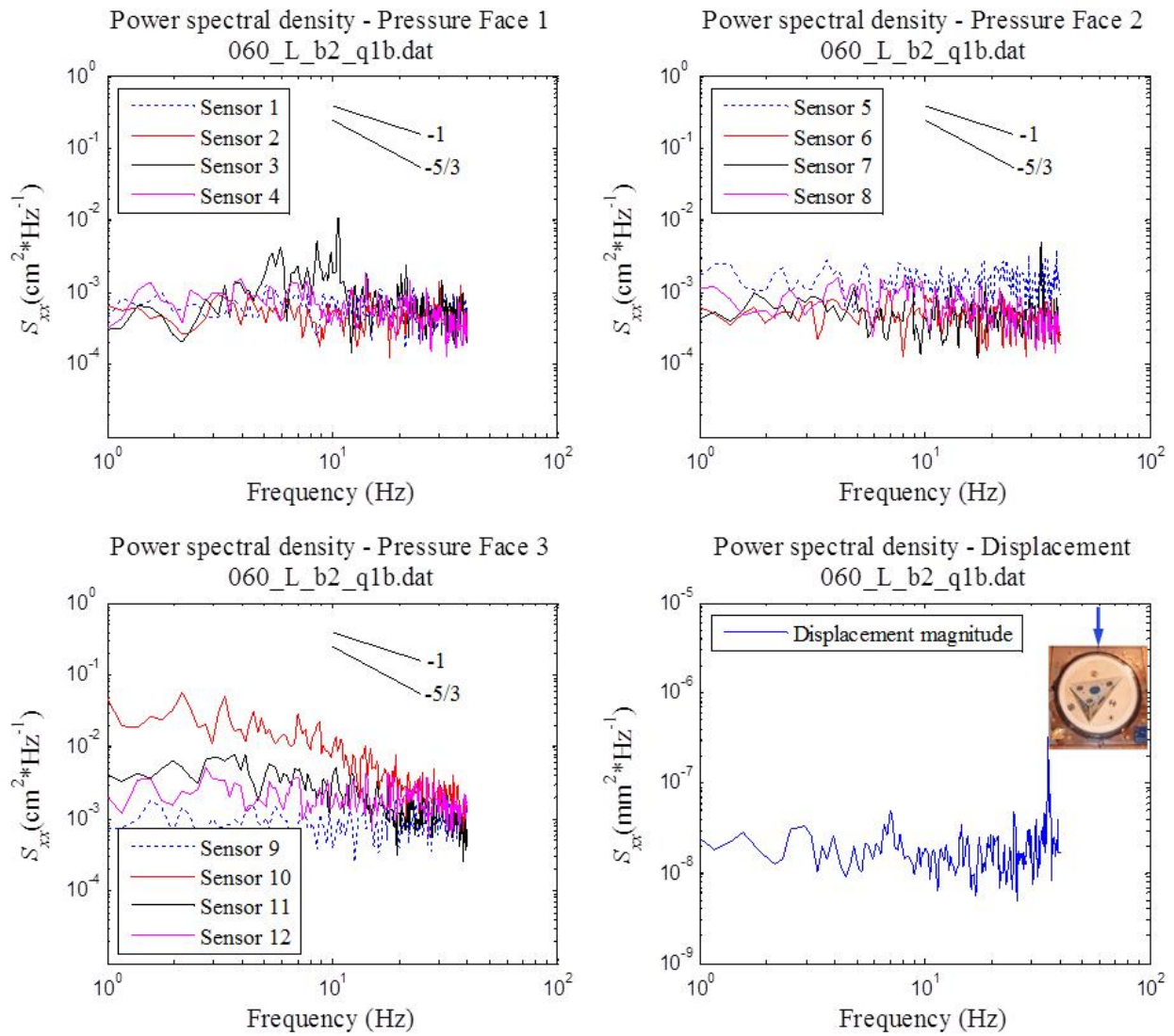
Block response 2, $\psi = 45$ deg., High T_u , Block 2, Q_2



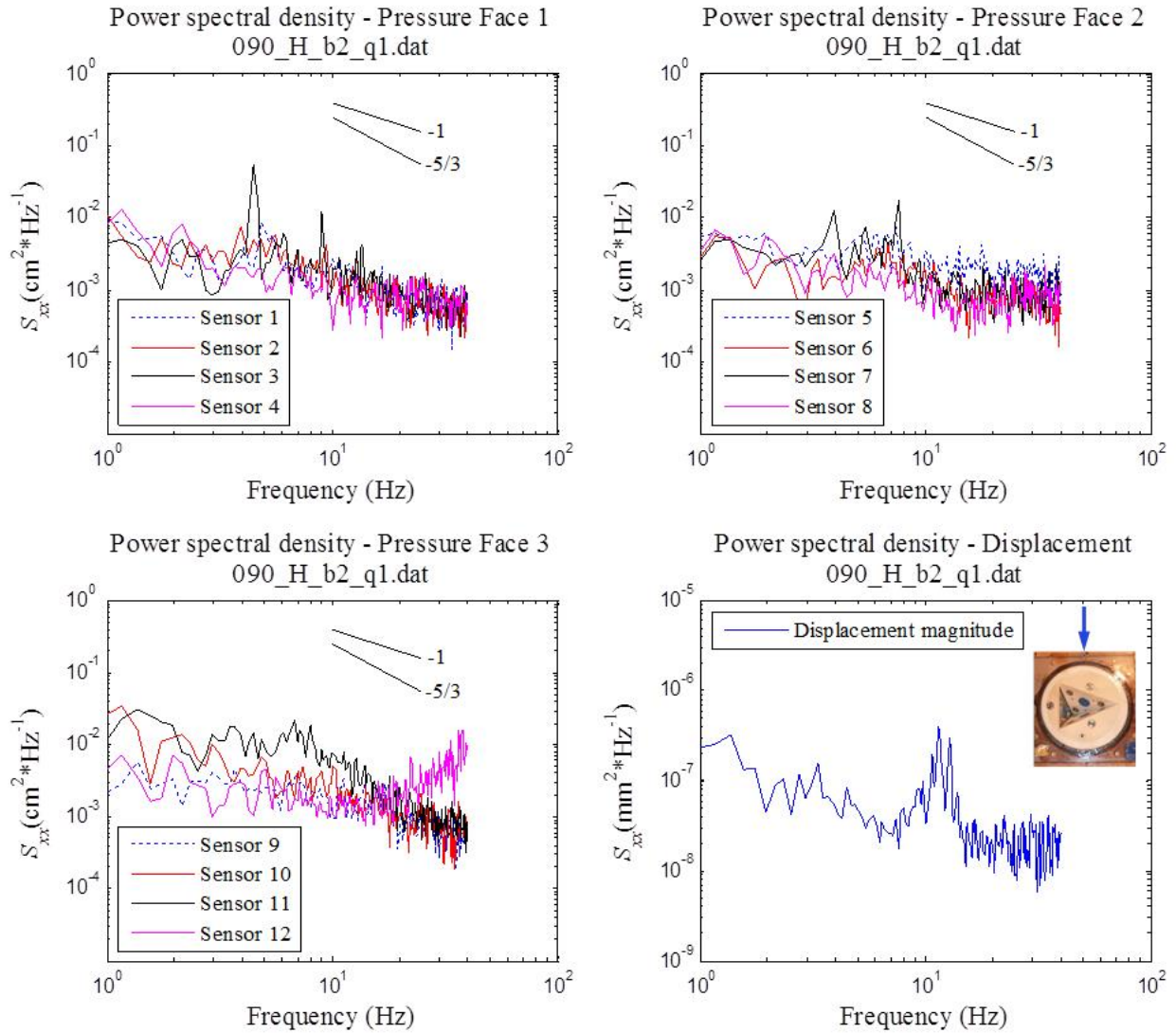
Block response 2, $\psi = 60$ deg., High T_u , Block 2, Q_I



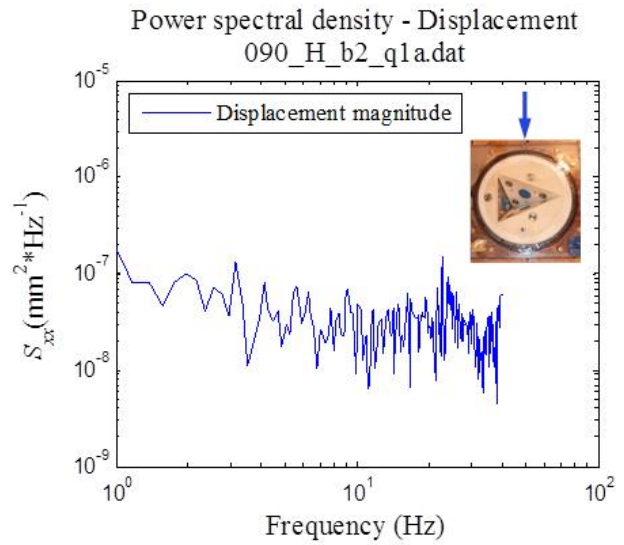
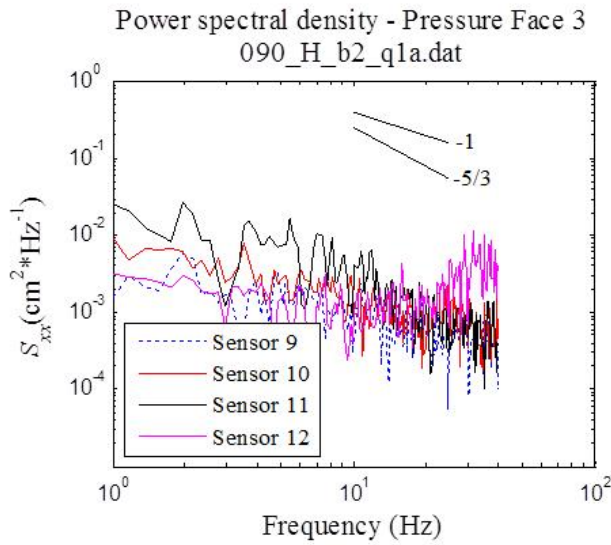
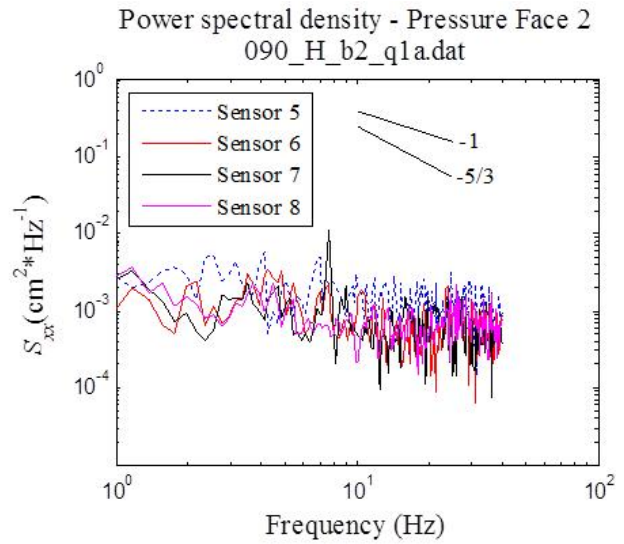
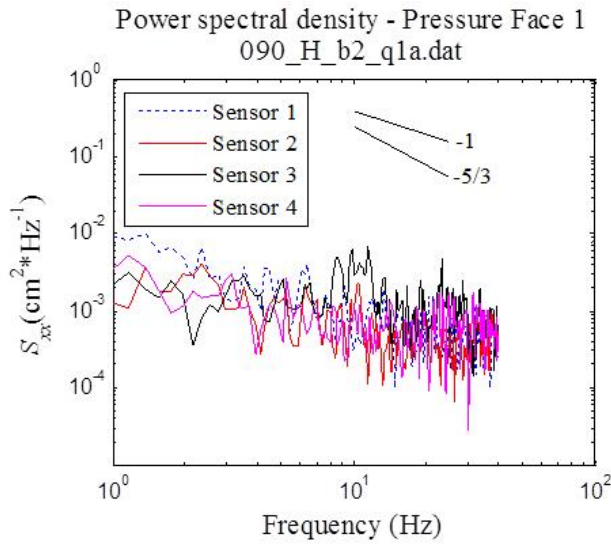
Block response 2, $\psi = 60$ deg., Low T_u , Block 2, Q_I



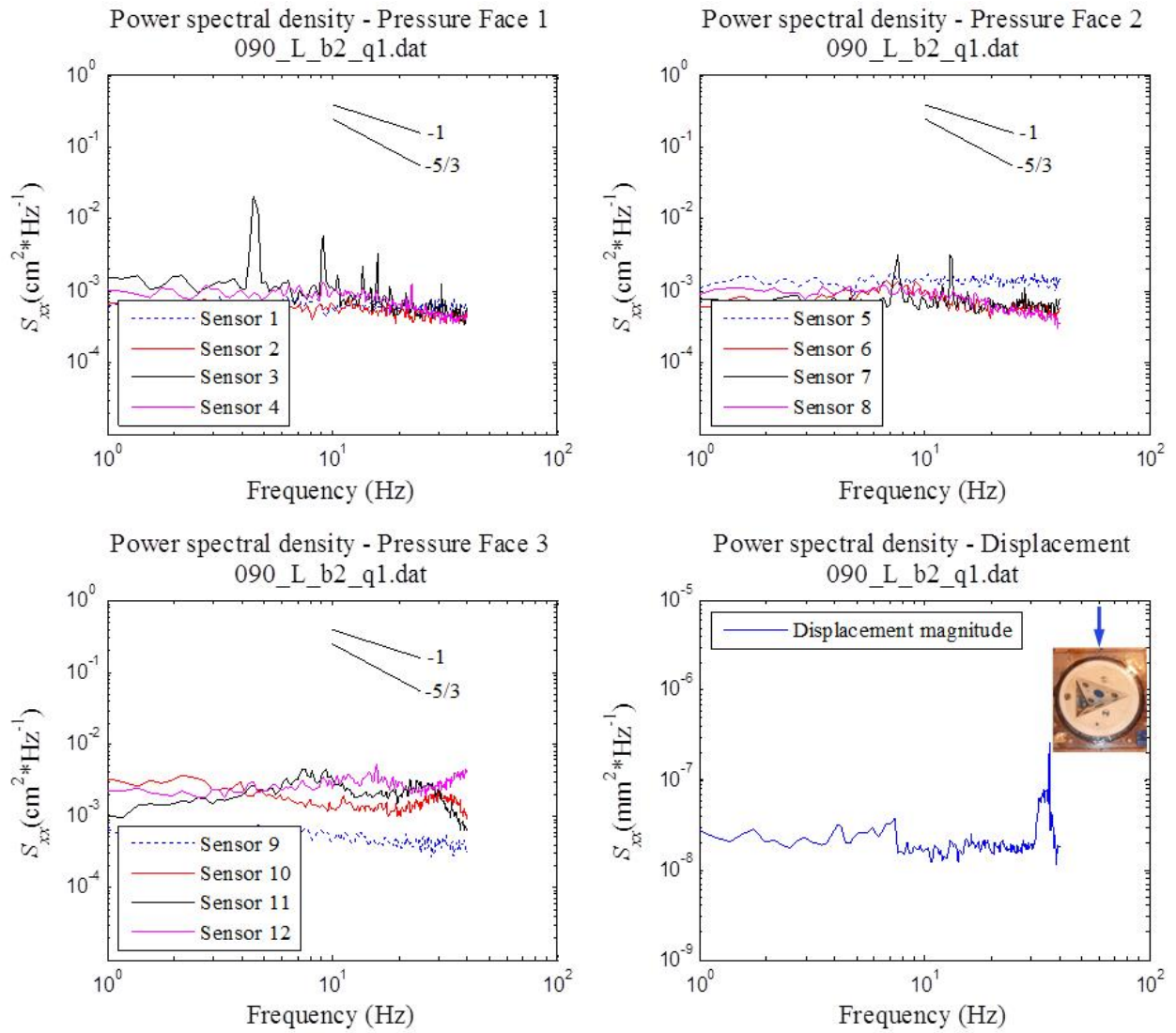
Block response 2, $\psi = 90$ deg., High T_u , Block 2, Q_I



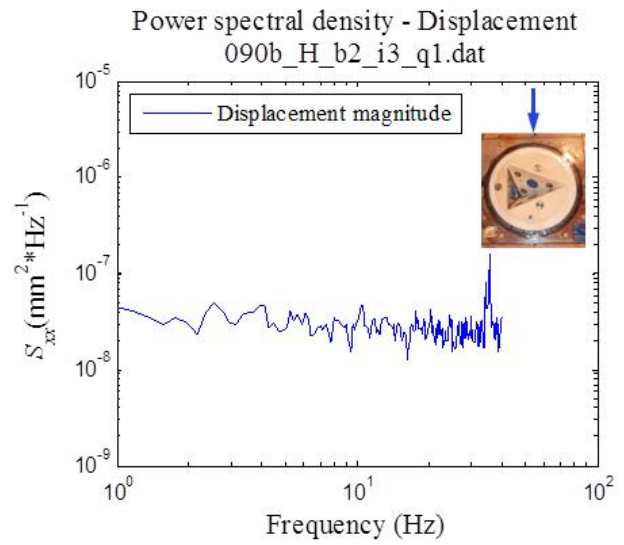
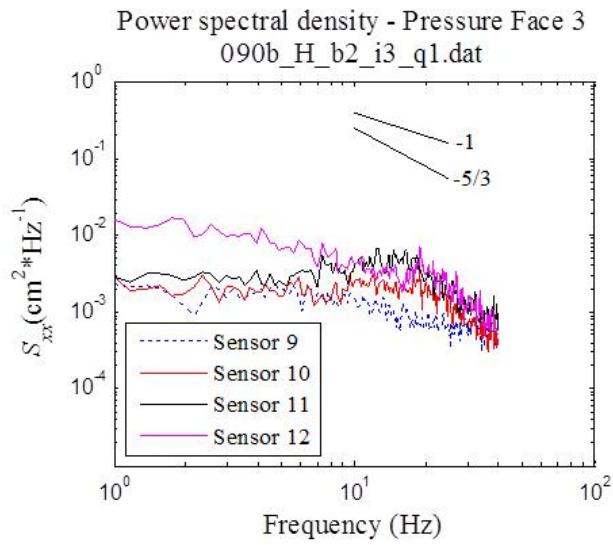
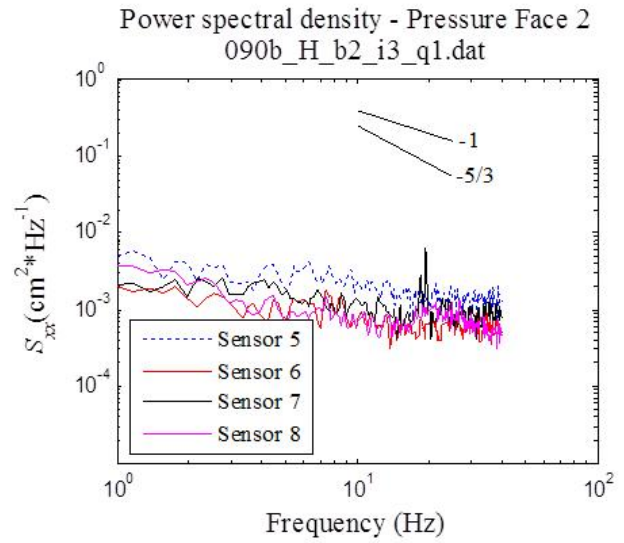
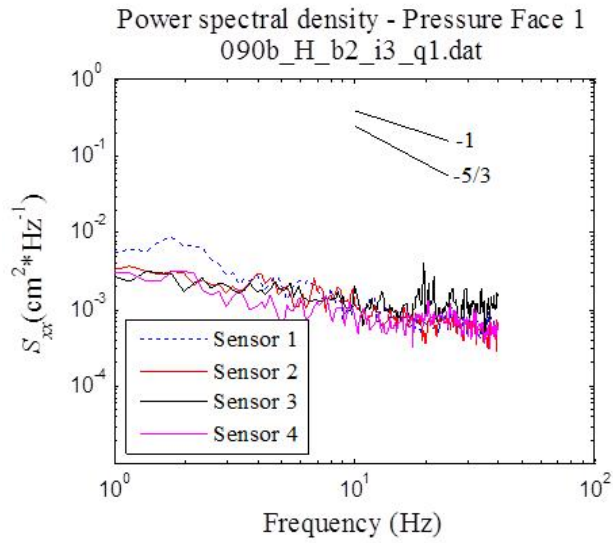
Block response 2, $\psi = 90$ deg., High T_u , Block 2, Q_I



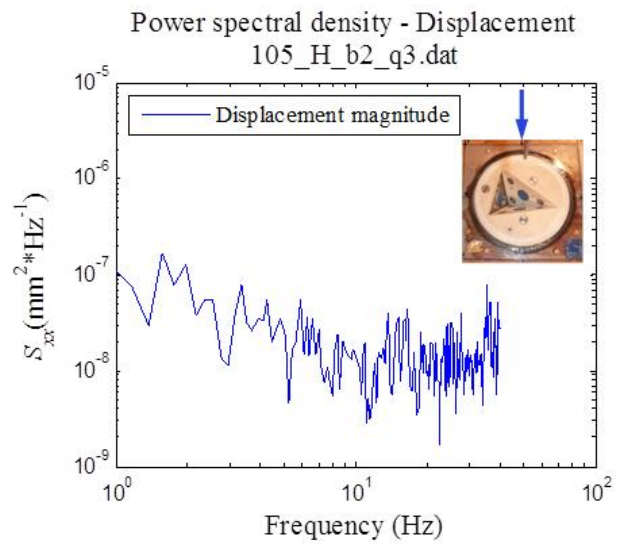
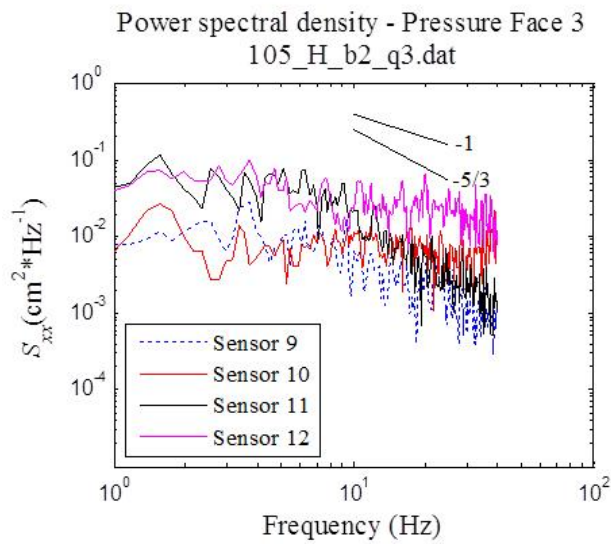
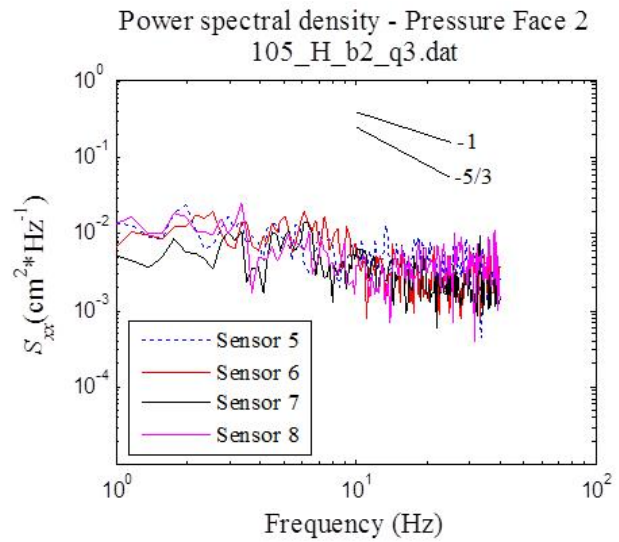
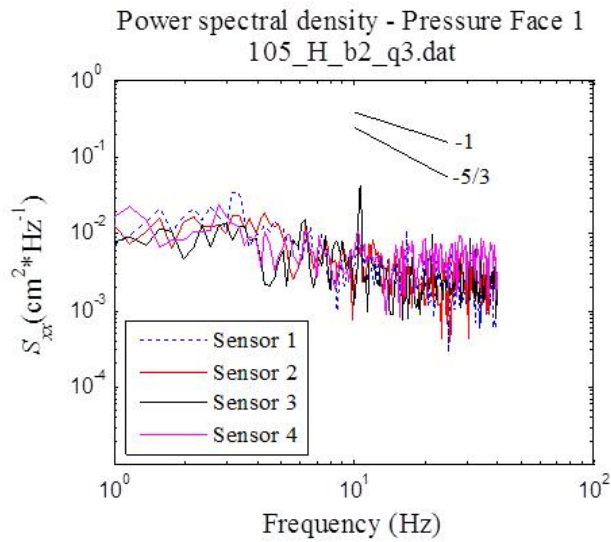
Block response 2, $\psi = 90$ deg., Low T_u , Block 2, Q_I



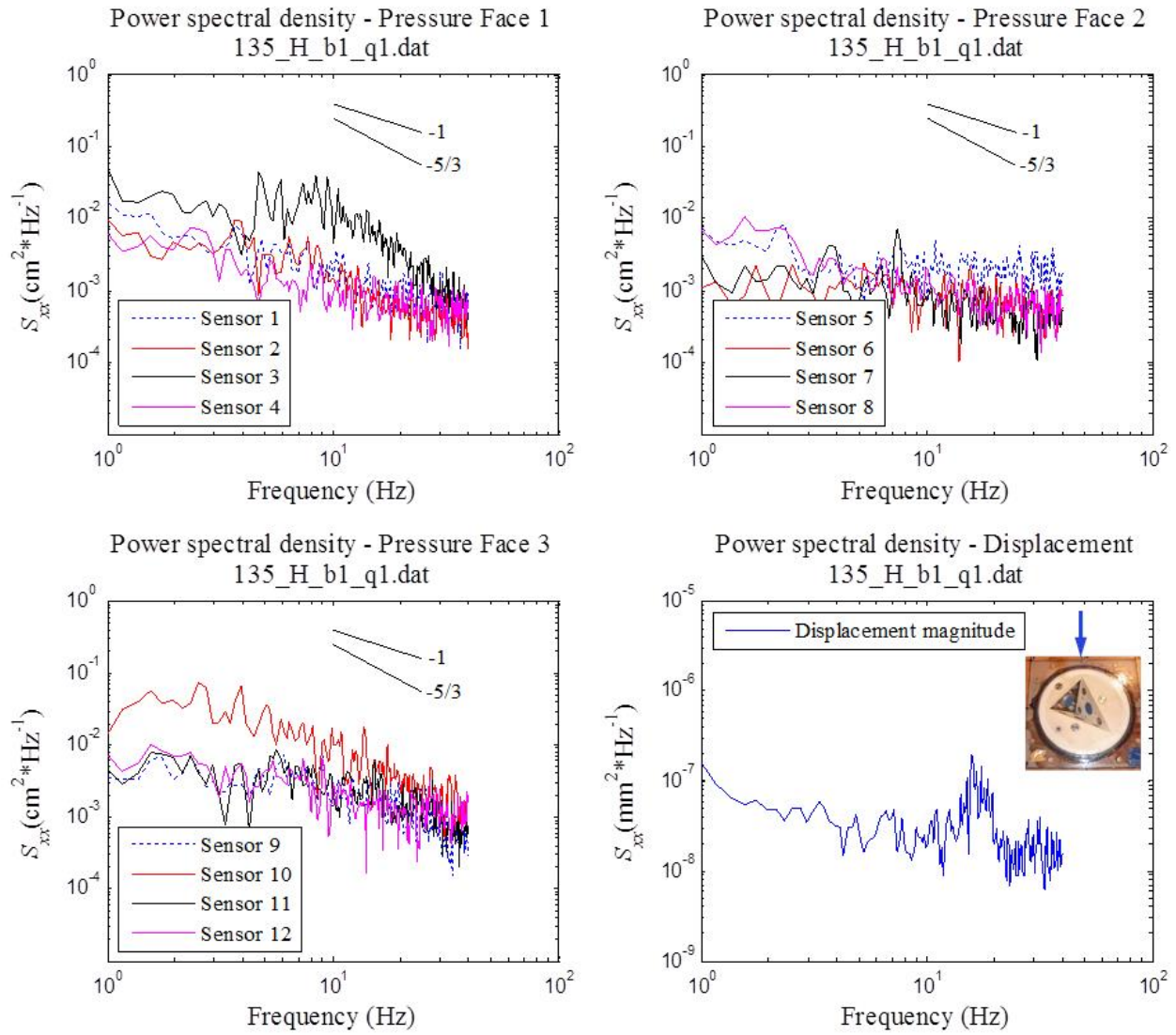
Block response 2, $\psi = 90$ deg., High T_u , Block 2, Q_I



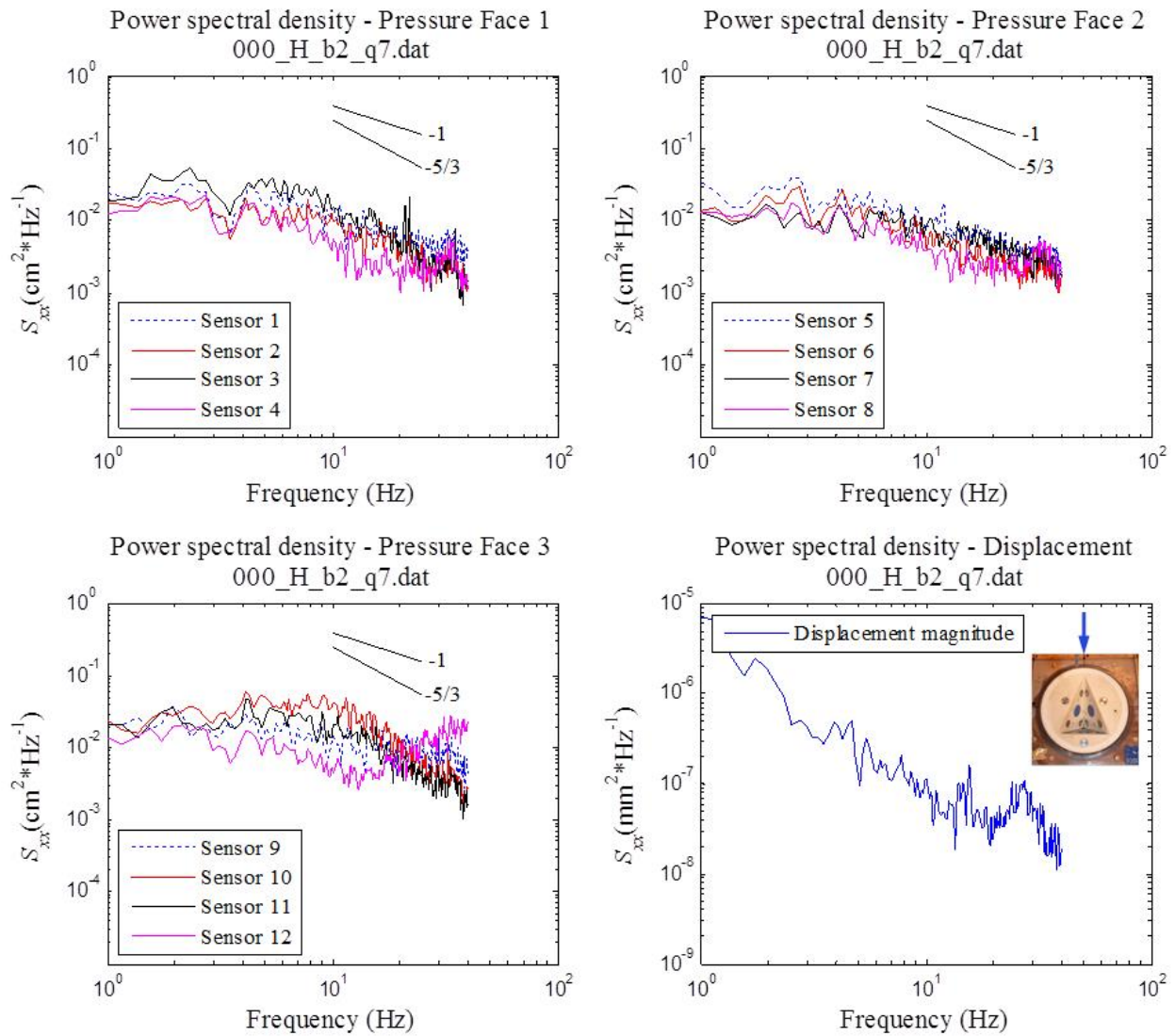
Block response 2, $\psi = 105$ deg., High T_u , Block 2, Q_3



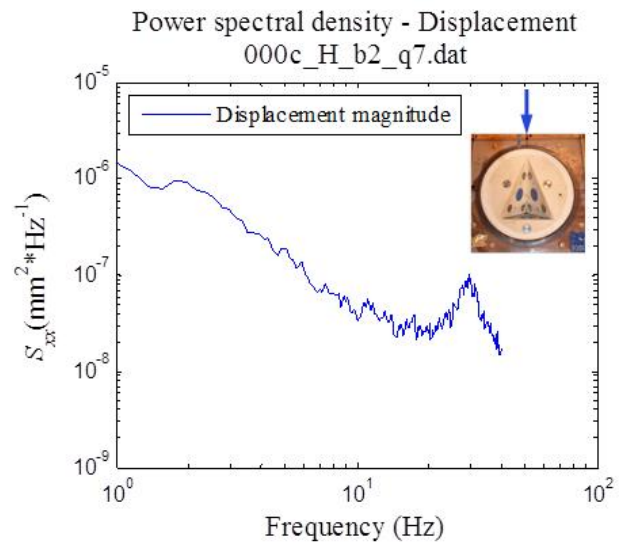
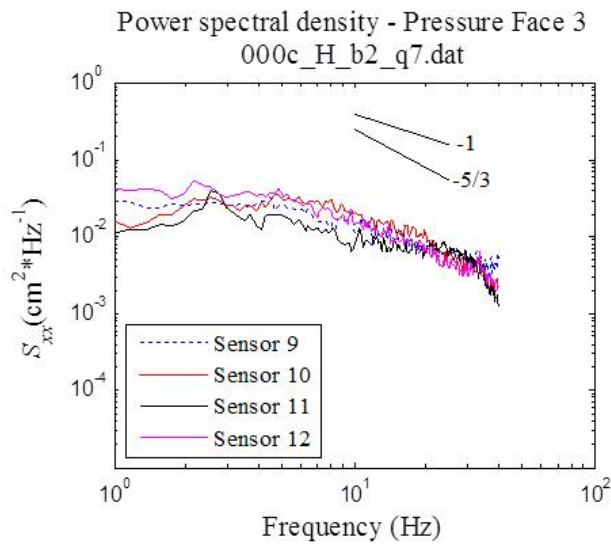
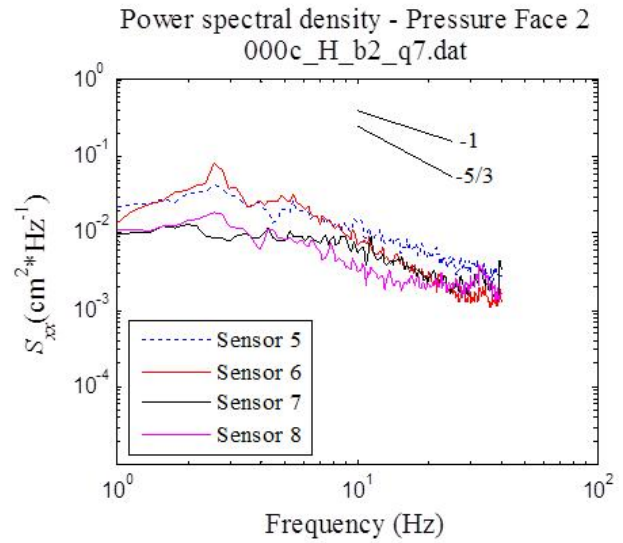
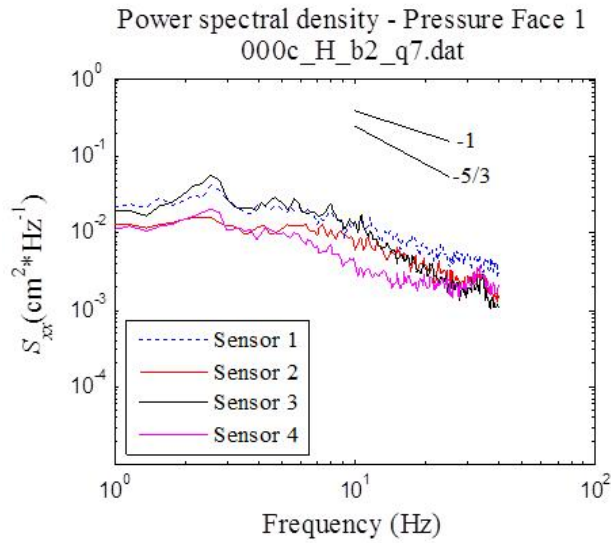
Block response 2, $\psi = 135$ deg., High T_u , Block 1, Q_I



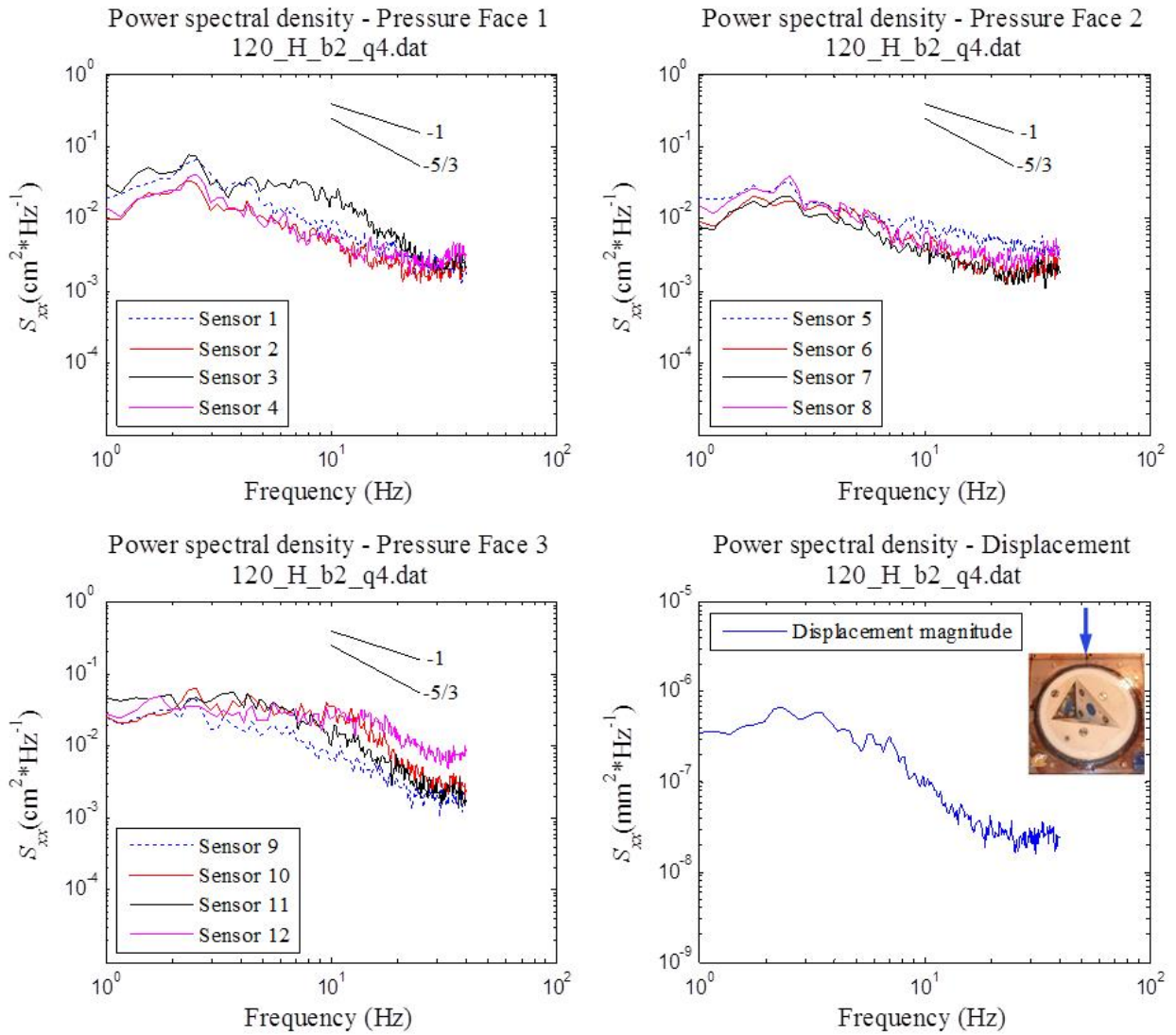
Block response 3, $\psi = 0$ deg., High T_u , Block 2, Q_7



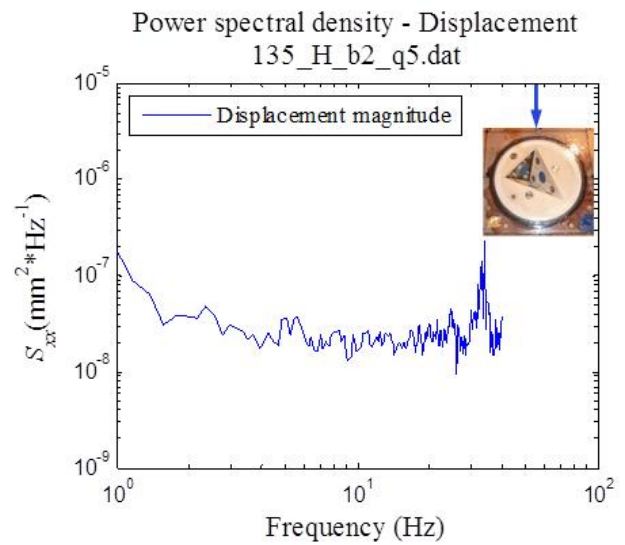
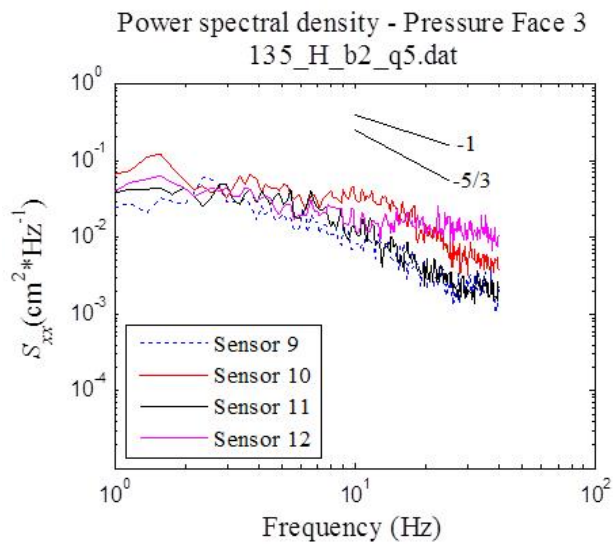
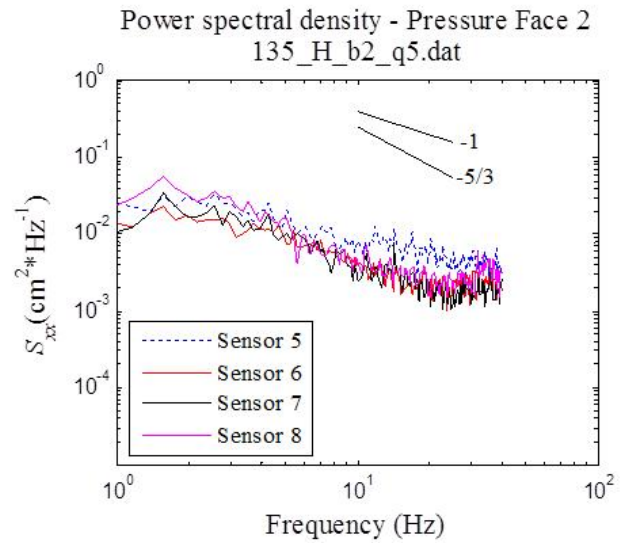
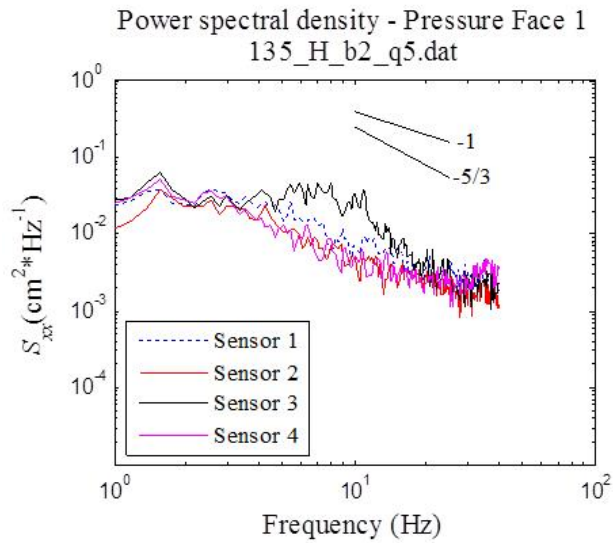
Block response 3, $\psi = 0$ deg., High T_u , Block 2, Q_7



Block response 3, $\psi = 120$ deg., High T_u , Block 2, Q_4



Block response 3, $\psi = 135$ deg., High T_u , Block 2, Q_5



Appendix F – Hydraulic model experiment: Block pressure statistics

Numerical values for C_p , C'_p , C_p^+ and C_p^-

		High T_u											
ψ (deg.)		Block 1				Block 2				Block 3			
		$f1$	$f2$	$f3$	$f4$	$f1$	$f2$	$f3$	$f4$	$f1$	$f2$	$f3$	$f4$
C_p	0	0.145	0.092	0.074	-	0.114	0.096	0.076	-	0.133	0.160	0.130	0.092
	15	0.177	0.121	0.096	-	-	-	-	-	-	-	-	-
	30	0.230	0.159	0.138	-	0.151	0.113	0.107	-	0.099	0.094	0.102	0.098
	45	-	-	-	-	0.141	0.092	0.116	-	0.088	0.085	0.077	0.103
	60	0.319	0.192	0.176	-	0.187	0.118	0.122	-	0.089	0.081	0.070	0.092
	75	0.305	0.177	0.185	-	0.211	0.132	0.132	-	0.098	0.093	0.067	0.080
	90	0.293	0.177	0.175	-	0.188	0.122	0.116	-	0.100	0.091	0.077	0.109
	105	0.270	0.160	0.186	-	0.150	0.093	0.094	-	-	-	-	-
	120	-	-	-	-	-	-	-	-	0.087	0.102	0.063	0.089
	135	0.216	0.168	0.218	-	-	-	-	-	0.094	0.113	0.065	0.093
	150	-	-	-	-	0.105	0.113	0.131	-	0.080	0.096	0.048	0.094
	165	-	-	-	-	0.111	0.117	0.154	-	-	-	-	-
	180	0.165	0.164	0.233	-	0.136	0.129	0.175	-	0.083	0.074	0.060	0.103
	AVG	-	-	-	-	-	-	-	-	0.090			0.095
C'_p	0	0.022	0.023	0.031	-	0.015	0.015	0.019	-	0.018	0.017	0.019	0.018
	15	0.020	0.017	0.029	-	-	-	-	-	-	-	-	-
	30	0.021	0.016	0.029	-	0.020	0.017	0.030	-	0.015	0.015	0.022	0.018
	45	-	-	-	-	0.020	0.016	0.030	-	0.014	0.014	0.022	0.018
	60	-	-	-	-	0.020	0.016	0.029	-	0.013	0.012	0.021	0.017
	75	0.020	0.015	0.027	-	0.016	0.014	0.023	-	0.013	0.013	0.023	0.017
	90	0.022	0.017	0.026	-	0.016	0.014	0.019	-	0.014	0.014	0.021	0.017
	105	0.021	0.015	0.023	-	0.018	0.017	0.027	-	-	-	-	-
	120	-	-	-	-	-	-	-	-	0.016	0.014	0.019	0.017
	135	0.023	0.016	0.030	-	-	-	-	-	0.019	0.014	0.020	0.018
	150	-	-	-	-	0.015	0.014	0.023	-	0.023	0.014	0.019	0.018
	165	-	-	-	-	0.015	0.015	0.024	-	-	-	-	-
	180	0.016	0.016	0.028	-	0.015	0.016	0.022	-	0.014	0.013	0.016	0.018
	AVG		0.022		-		0.019		-		0.017		0.018

		Low T_u											
ψ (deg.)		Block 1				Block 2				Block 3			
		$f1$	$f2$	$f3$	$f4$	$f1$	$f2$	$f3$	$f4$	$f1$	$f2$	$f3$	$f4$
C_p	0	0.092	0.056	0.046	-	0.095	0.083	0.069	-	0.085	0.084	0.081	0.071
	15	0.143	0.095	0.080	-	0.095	0.067	0.072	-	-	-	-	-
	30	-	-	-	-	0.133	0.101	0.098	-	0.107	0.068	0.076	0.097
	45	-	-	-	-	0.140	0.092	0.103	-	-	-	-	-
	60	-	-	-	-	-	-	-	-	0.070	0.063	0.037	0.075
	75	0.239	0.132	0.127	-	0.168	0.098	0.106	-	-	-	-	-
	90	0.234	0.139	0.133	-	0.150	0.098	0.085	-	0.068	0.066	0.054	0.075
	105	0.207	0.116	0.136	-	0.120	0.075	0.082	-	0.058	0.066	0.043	0.069
	120	0.170	0.108	0.140	-	0.097	0.076	0.092	-	0.069	0.082	0.056	0.067
	135	0.164	0.143	0.174	-	-	-	-	-	0.055	0.073	0.040	0.068
	150	0.124	0.126	0.189	-	0.091	0.096	0.114	-	0.063	0.073	0.035	0.074
	165	0.133	0.141	0.180	-	0.097	0.106	0.112	-	0.049	0.060	0.028	0.075
	180	0.135	0.124	0.186	-	0.109	0.095	0.133	-	0.060	0.048	0.040	0.078
		AVG	-	-	-	-	-	-	-	-	0.062		
C'_p	0	0.007	0.008	0.016	-	0.007	0.007	0.015	-	0.009	0.008	0.009	0.007
	15	0.018	0.020	0.020	-	0.007	0.007	0.016	-	-	-	-	-
	30	-	-	-	-	0.017	0.022	0.020	-	0.007	0.006	0.010	0.007
	45	-	-	-	-	0.022	0.014	0.022	-	-	-	-	-
	60	-	-	-	-	-	-	-	-	0.006	0.005	0.009	0.007
	75	0.009	0.009	0.019	-	0.014	0.016	0.021	-	-	-	-	-
	90	0.011	0.010	0.017	-	0.008	0.008	0.011	-	0.006	0.006	0.011	0.007
	105	0.009	0.008	0.013	-	0.011	0.010	0.014	-	0.007	0.006	0.011	0.007
	120	0.010	0.008	0.018	-	0.008	0.007	0.016	-	0.008	0.006	0.009	0.007
	135	0.011	0.008	0.017	-	-	-	-	-	0.008	0.006	0.009	0.007
	150	0.009	0.008	0.016	-	0.007	0.007	0.013	-	0.009	0.006	0.009	0.008
	165	0.009	0.010	0.017	-	0.009	0.010	0.015	-	0.009	0.006	0.008	0.007
	180	0.011	0.012	0.016	-	0.009	0.010	0.013	-	0.006	0.006	0.007	0.007
		AVG		0.012		-		0.012		-		0.008	

		High T_u											
		Block 1				Block 2				Block 3			
ψ (deg.)		$f1$	$f2$	$f3$	$f4$	$f1$	$f2$	$f3$	$f4$	$f1$	$f2$	$f3$	$f4$
C_p^+	0	0.304	0.240	0.355	-	0.215	0.185	0.197	-	0.247	0.287	0.253	0.196
	15	0.321	0.246	0.397	-	-	-	-	-	-	-	-	-
	30	0.389	0.327	0.405	-	0.290	0.245	0.483	-	0.228	0.200	0.250	0.203
	45	-	-	-	-	0.362	0.266	0.445	-	0.210	0.198	0.242	0.200
	60	-	-	-	-	0.378	0.282	0.429	-	0.226	0.164	0.248	0.194
	75	0.441	0.371	0.448	-	0.369	0.298	0.368	-	0.251	0.164	0.221	0.211
	90	0.447	0.388	0.436	-	0.313	0.253	0.301	-	0.210	0.166	0.218	0.217
	105	0.407	0.341	0.457	-	0.268	0.243	0.363	-	-	-	-	-
	120	-	-	-	-	-	-	-	-	0.206	0.182	0.198	0.218
	135	0.419	0.351	0.446	-	-	-	-	-	0.232	0.212	0.183	0.215
	150	-	-	-	-	0.273	0.269	0.397	-	0.207	0.189	0.194	0.218
	165	-	-	-	-	0.342	0.276	0.385	-	-	-	-	-
	180	0.385	0.318	0.407	-	0.334	0.277	0.329	-	0.168	0.163	0.175	0.205
	C_p^+ (% increase from C_p)	0	109%	161%	382%	-	88%	93%	158%	-	86%	79%	94%
15		82%	103%	314%	-	-	-	-	-	-	-	-	-
30		69%	106%	194%	-	92%	117%	351%	-	130%	114%	146%	107%
45		-	-	-	-	157%	190%	284%	-	140%	133%	216%	94%
60		-	-	-	-	102%	140%	251%	-	153%	104%	256%	111%
75		45%	110%	142%	-	75%	126%	179%	-	156%	77%	228%	165%
90		53%	119%	149%	-	67%	108%	161%	-	111%	82%	185%	99%
105		51%	114%	145%	-	78%	162%	287%	-	-	-	-	-
120		-	-	-	-	-	-	-	-	137%	80%	212%	145%
135		94%	109%	104%	-	-	-	-	-	147%	88%	182%	132%
150		-	-	-	-	160%	138%	202%	-	158%	97%	308%	132%
165		-	-	-	-	208%	135%	150%	-	-	-	-	-
180		133%	94%	75%	-	146%	115%	88%	-	104%	121%	190%	98%
MAX			382%		-		351%		-		308%		165%
AVG		127%		-		154%		-		144%		120%	
MIN		45%		-		67%		-		77%		94%	

		Low T_u											
		Block 1				Block 2				Block 3			
ψ (deg.)		<i>f1</i>	<i>f2</i>	<i>f3</i>	<i>f4</i>	<i>f1</i>	<i>f2</i>	<i>f3</i>	<i>f4</i>	<i>f1</i>	<i>f2</i>	<i>f3</i>	<i>f4</i>
C_p^+	0	0.144	0.114	0.157	-	0.152	0.127	0.172	-	0.141	0.125	0.150	0.126
	15	0.235	0.196	0.238	-	0.163	0.125	0.173	-	-	-	-	-
	30	-	-	-	-	0.267	0.205	0.235	-	0.264	0.106	0.139	0.178
	45	-	-	-	-	0.266	0.200	0.261	-	-	-	-	-
	60	-	-	-	-	-	-	-	-	0.15	0.096	0.105	0.121
	75	0.341	0.277	0.330	-	0.285	0.219	0.290	-	-	-	-	-
	90	0.325	0.274	0.302	-	0.225	0.183	0.211	-	0.119	0.098	0.125	0.126
	105	0.289	0.242	0.273	-	0.207	0.175	0.213	-	0.120	0.093	0.116	0.116
	120	0.255	0.203	0.221	-	0.160	0.137	0.179	-	0.142	0.117	0.109	0.121
	135	0.290	0.243	0.270	-	-	-	-	-	0.122	0.117	0.100	0.123
	150	0.241	0.233	0.285	-	0.190	0.172	0.176	-	0.146	0.119	0.092	0.132
	165	0.281	0.251	0.276	-	0.225	0.191	0.226	-	0.108	0.100	0.081	0.131
	180	0.270	0.241	0.290	-	0.228	0.186	0.232	-	0.104	0.090	0.084	0.128
	C_p^+ (% increase from C_p)	0	56%	104%	240%	-	61%	53%	151%	-	65%	48%	85%
15		64%	105%	199%	-	71%	87%	141%	-	-	-	-	-
30		-	-	-	-	100%	103%	140%	-	147%	55%	83%	85%
45		-	-	-	-	90%	118%	152%	-	-	-	-	-
60		-	-	-	-	-	-	-	-	116%	54%	187%	61%
75		43%	111%	159%	-	70%	123%	175%	-	-	-	-	-
90		39%	96%	127%	-	50%	87%	149%	-	75%	48%	130%	69%
105		40%	108%	100%	-	73%	133%	161%	-	107%	40%	170%	68%
120		51%	89%	58%	-	65%	81%	94%	-	107%	43%	96%	80%
135		77%	70%	55%	-	-	-	-	-	121%	60%	151%	82%
150		94%	85%	51%	-	109%	79%	54%	-	132%	62%	162%	78%
165		111%	78%	53%	-	132%	80%	102%	-	120%	69%	193%	75%
180		100%	95%	56%	-	111%	95%	75%	-	73%	87%	113%	63%
MAX			240%		-		175%		-		193%		85%
AVG		90%		-		102%		-		100%		74%	
MIN		39%		-		50%		-		40%		61%	

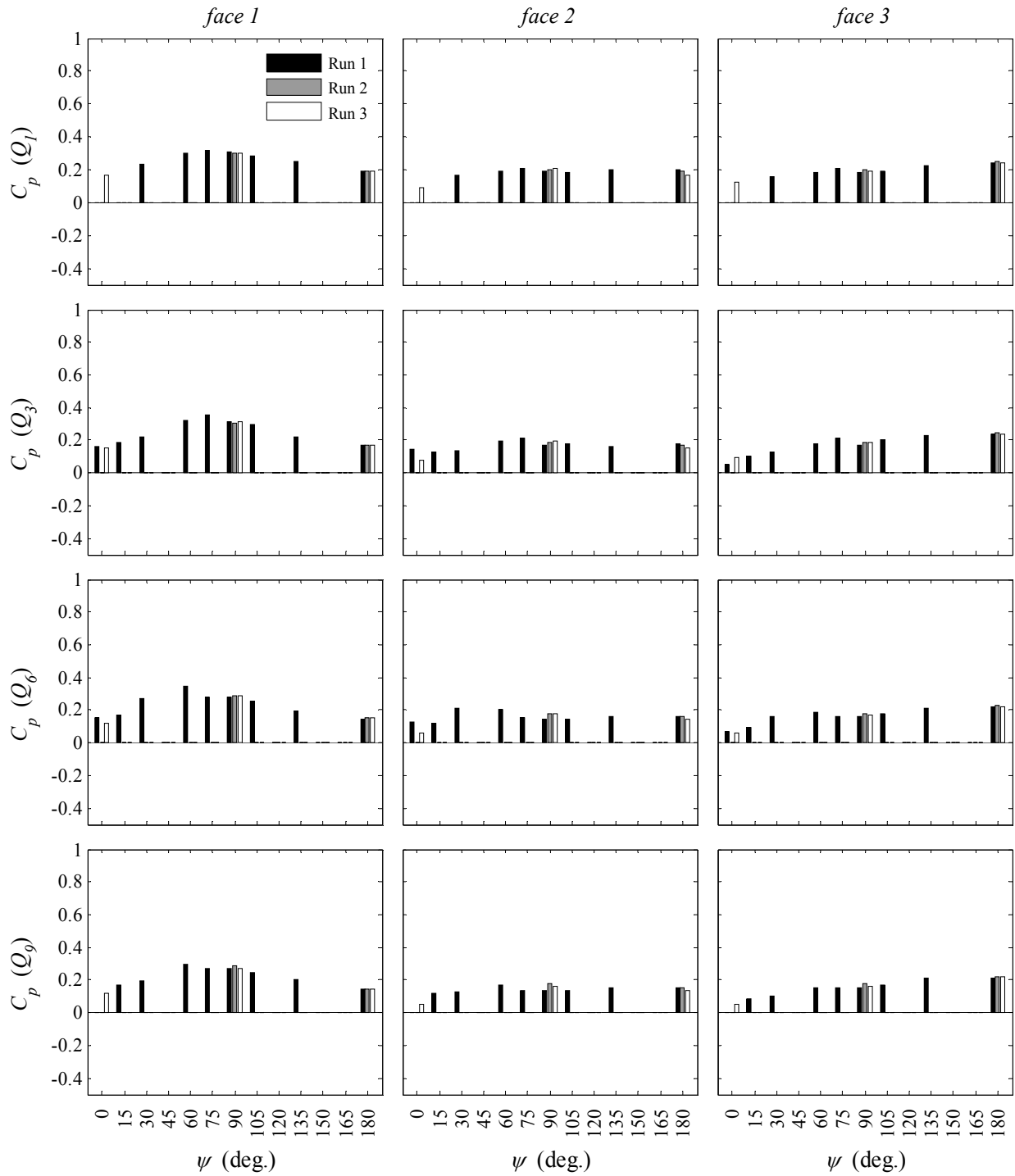
		High T_u											
		Block 1				Block 2				Block 3			
ψ (deg.)		$f1$	$f2$	$f3$	$f4$	$f1$	$f2$	$f3$	$f4$	$f1$	$f2$	$f3$	$f4$
C_p	0	-0.003	-0.080	-0.120	-	0.018	0.010	-0.028	-	-0.012	0.048	0.022	-0.034
	15	0.030	-0.018	-0.072	-	-	-	-	-	-	-	-	-
	30	0.088	0.001	-0.057	-	-0.013	-0.067	-0.166	-	-0.032	-0.004	-0.037	-0.041
	45	-	-	-	-	-0.045	-0.050	-0.105	-	-0.001	0.002	-0.046	-0.060
	60	-	-	-	-	0.01	-0.029	-0.053	-	-0.003	0.01	-0.062	-0.028
	75	0.146	0.035	0.004	-	0.066	0.007	0.001	-	-0.005	0.023	-0.071	-0.079
	90	0.147	0.066	0.012	-	0.072	0.029	-0.008	-	0.014	0.019	-0.048	-0.023
	105	0.113	0.030	0.036	-	0.026	-0.020	-0.070	-	-	-	-	-
	120	-	-	-	-	-	-	-	-	-0.040	0.013	-0.071	-0.045
	135	0.044	0.053	0.031	-	-	-	-	-	-0.039	0.029	-0.086	-0.055
	150	-	-	-	-	-0.004	0.013	-0.101	-	-0.093	0.006	-0.072	-0.101
	165	-	-	-	-	-0.011	0.018	-0.007	-	-	-	-	-
	180	0.041	0.037	0.072	-	0.030	0.015	0.037	-	-0.003	-0.015	-0.055	-0.049
	C_p (% decrease from C_p)	0	-102%	-187%	-262%	-	-84%	-90%	-137%	-	-109%	-70%	-83%
15		-83%	-115%	-175%	-	-	-	-	-	-	-	-	-
30		-62%	-100%	-142%	-	-108%	-159%	-255%	-	-132%	-104%	-137%	-141%
45		-	-	-	-	-132%	-155%	-190%	-	-102%	-98%	-160%	-158%
60		-	-	-	-	-95%	-125%	-143%	-	-103%	-87%	-189%	-130%
75		-52%	-80%	-98%	-	-69%	-95%	-100%	-	-105%	-76%	-206%	-198%
90		-50%	-63%	-93%	-	-62%	-76%	-107%	-	-86%	-80%	-163%	-121%
105		-58%	-81%	-81%	-	-83%	-121%	-175%	-	-	-	-	-
120		-	-	-	-	-	-	-	-	-146%	-87%	-212%	-150%
135		-79%	-68%	-86%	-	-	-	-	-	-141%	-74%	-233%	-159%
150		-	-	-	-	-103%	-88%	-177%	-	-216%	-94%	-252%	-207%
165		-	-	-	-	-110%	-85%	-105%	-	-	-	-	-
180		-75%	-78%	-69%	-	-78%	-89%	-79%	-	-104%	-121%	-192%	-147%
MAX			-50%		-		-62%		-		-70%		-121%
AVG		-98%		-		-116%		-		-132%		-155%	
MIN		-262%		-		-255%		-		-252%		-207%	

		Low T_u											
		Block 1				Block 2				Block 3			
ψ (deg.)		<i>f1</i>	<i>f2</i>	<i>f3</i>	<i>f4</i>	<i>f1</i>	<i>f2</i>	<i>f3</i>	<i>f4</i>	<i>f1</i>	<i>f2</i>	<i>f3</i>	<i>f4</i>
C_p	0	0.050	-0.008	-0.059	-	0.048	0.046	-0.017	-	-0.001	0.026	0.034	0.030
	15	0.060	-0.029	-0.051	-	0.035	0.021	-0.015	-	-	-	-	-
	30	-	-	-	-	0.012	-0.031	-0.026	-	0.013	0.025	0.032	0.033
	45	-	-	-	-	0.012	0.001	-0.006	-	-	-	-	-
	60	-	-	-	-	-	-	-	-	0.021	0.033	-0.011	0.023
	75	0.174	0.048	-0.010	-	0.049	-0.032	-0.004	-	-	-	-	-
	90	0.157	0.049	-0.014	-	0.093	0.037	0.007	-	0.030	0.031	-0.003	0.025
	105	0.150	0.044	0.044	-	0.050	0.005	0.009	-	-0.003	0.033	-0.012	0.008
	120	0.093	0.050	0.016	-	0.044	0.029	0.016	-	-0.001	0.051	-0.002	0.000
	135	0.065	0.060	0.071	-	-	-	-	-	-0.015	0.037	-0.017	-0.004
	150	0.048	0.048	0.093	-	0.038	0.040	0.031	-	-0.012	0.035	-0.034	-0.005
	165	0.044	0.045	0.095	-	0.024	0.026	0.021	-	-0.011	0.021	-0.023	0.007
	180	0.045	0.007	0.105	-	0.040	0.001	0.057	-	0.020	0.009	0.005	0.027
	C_p (% decrease from C_p)	0	-46%	-114%	-227%	-	-49%	-45%	-125%	-	-101%	-70%	-58%
15		-58%	-130%	-164%	-	-63%	-69%	-120%	-	-	-	-	-
30		-	-	-	-	-91%	-131%	-126%	-	-88%	-64%	-58%	-66%
45		-	-	-	-	-92%	-99%	-106%	-	-	-	-	-
60		-	-	-	-	-	-	-	-	-70%	-47%	-130%	-70%
75		-27%	-63%	-108%	-	-71%	-132%	-103%	-	-	-	-	-
90		-33%	-65%	-110%	-	-38%	-62%	-92%	-	-55%	-54%	-106%	-67%
105		-27%	-62%	-68%	-	-58%	-94%	-89%	-	-106%	-50%	-129%	-88%
120		-45%	-54%	-88%	-	-54%	-62%	-83%	-	-102%	-38%	-104%	-100%
135		-61%	-58%	-60%	-	-	-	-	-	-127%	-50%	-143%	-106%
150		-61%	-62%	-51%	-	-59%	-58%	-73%	-	-119%	-52%	-195%	-107%
165		-67%	-68%	-47%	-	-75%	-75%	-81%	-	-123%	-65%	-182%	-90%
180		-67%	-94%	-44%	-	-63%	-99%	-57%	-	-67%	-81%	-88%	-66%
MAX			-27%		-		-38%		-		-38%		-58%
AVG		-74%		-		-82%		-		-91%		-82%	
MIN		-227%		-		-132%		-		-195%		-107%	

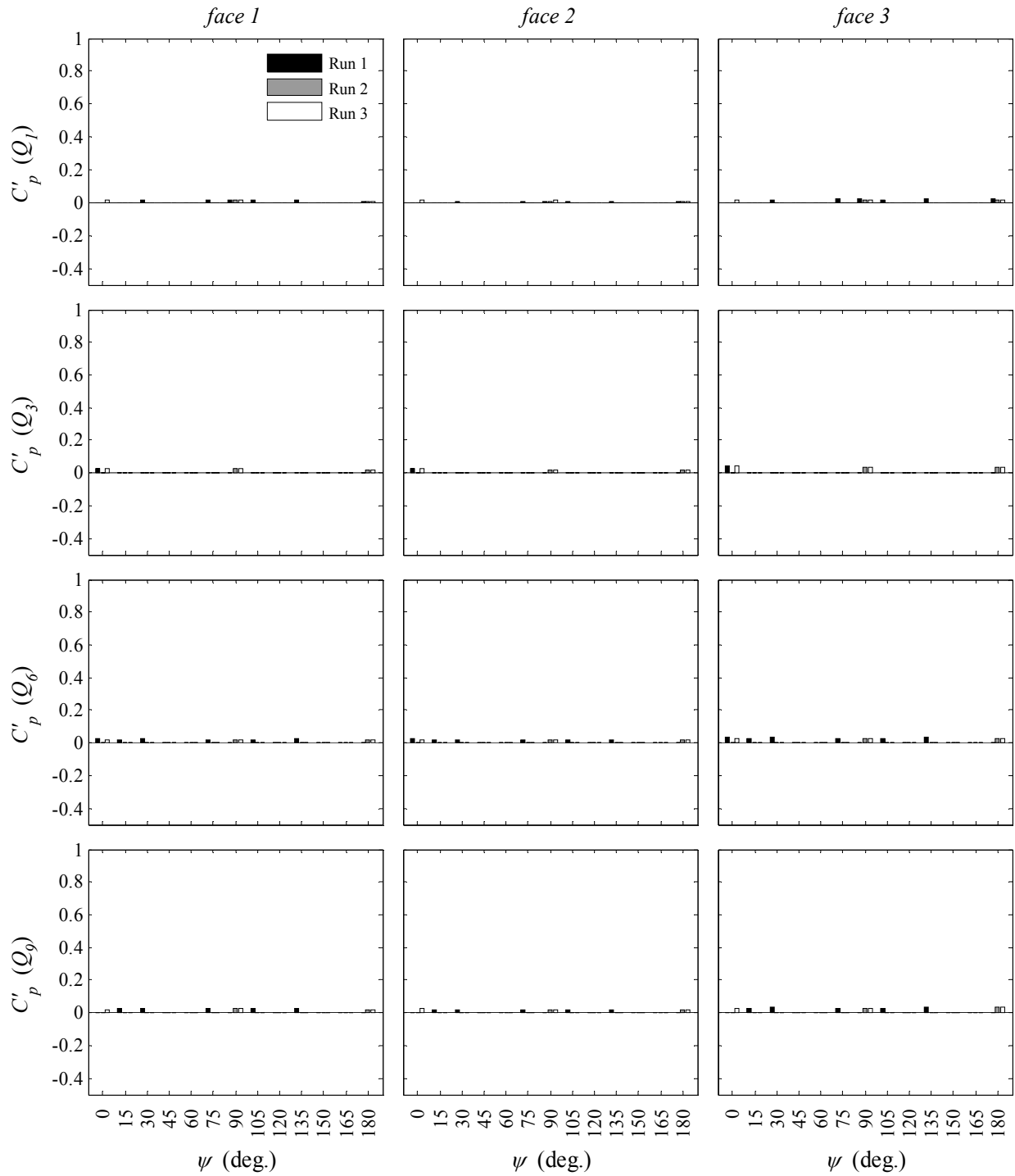
Supplemental figures for C_p , C'_p , C_p^+ and C_p^- for Q_1 , Q_3 , Q_6 and Q_9

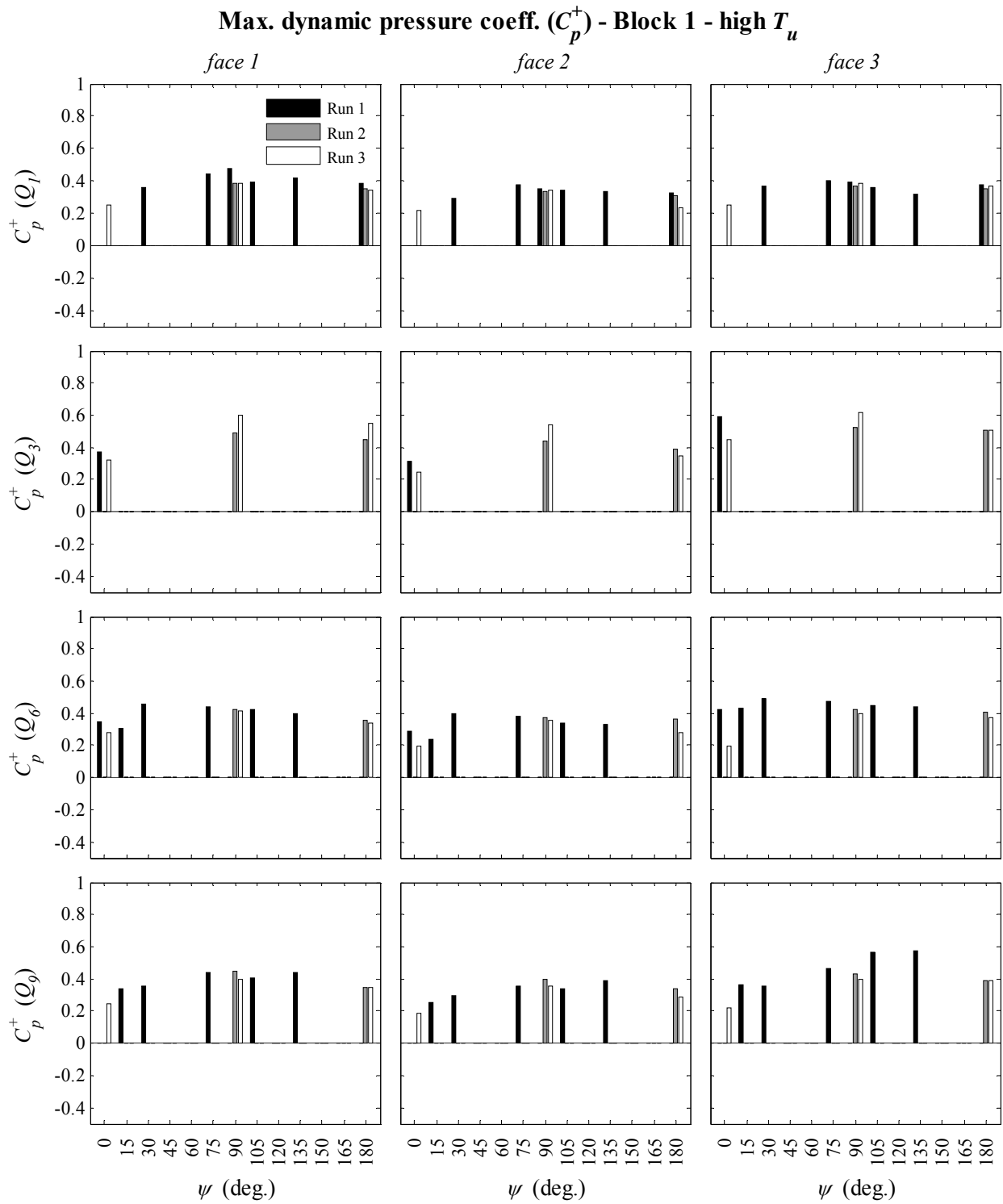
High T_u , Block 1 (faces 1, 2 and 3)

Avg. dynamic pressure coeff. (C_p) - Block 1 - high T_u

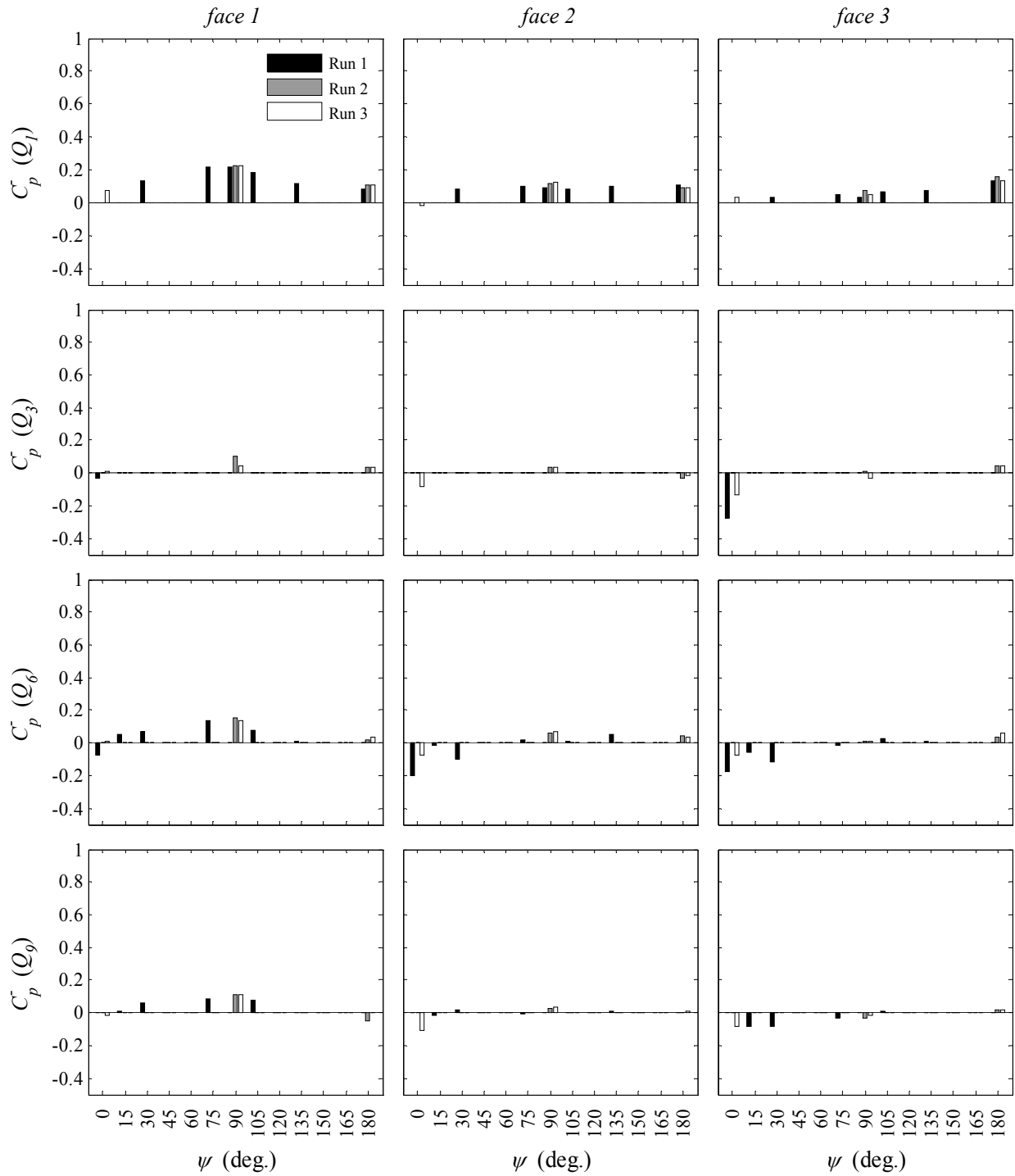


Fluc. dynamic pressure coeff. (C'_p) - Block 1 - high T_u



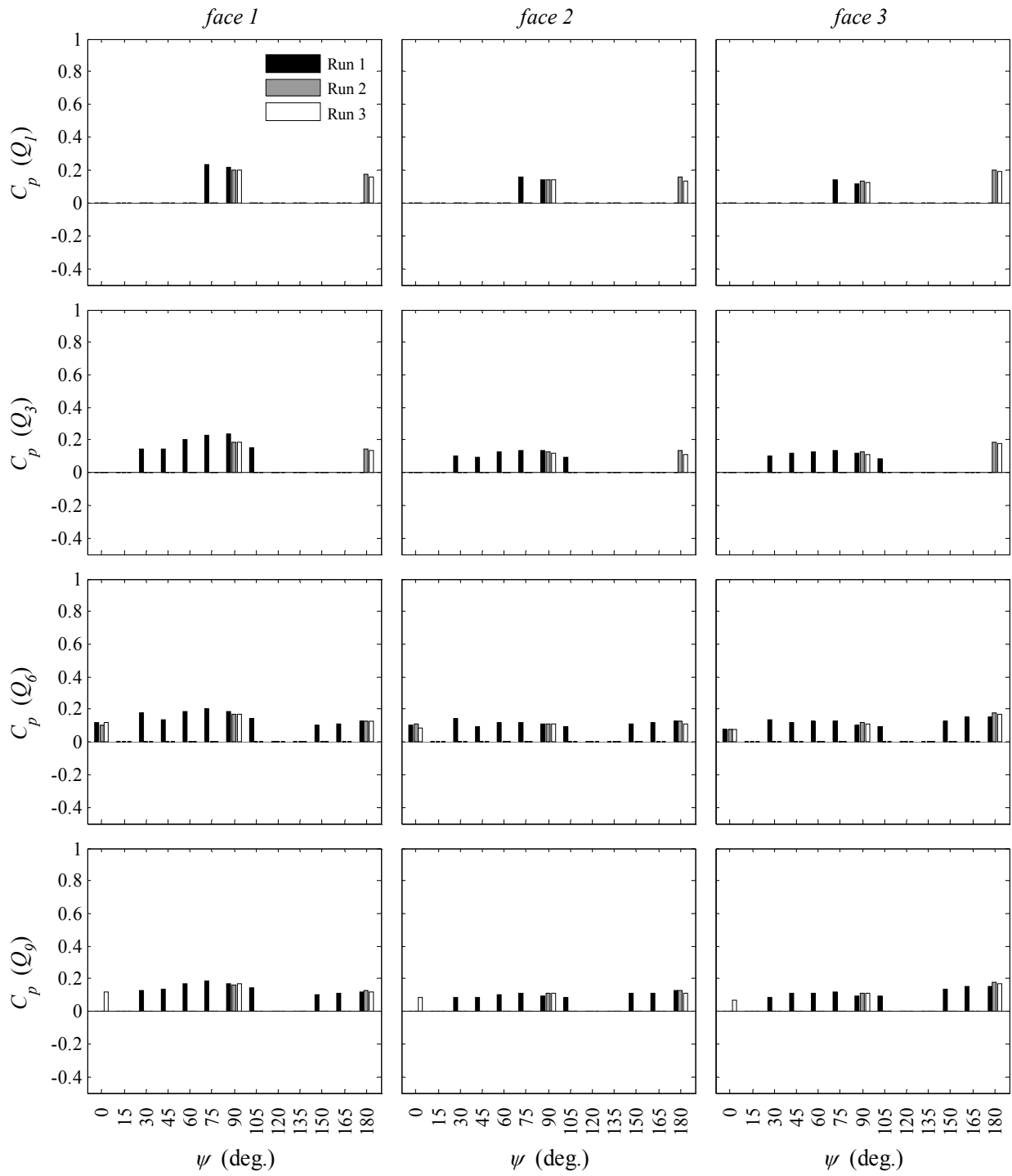


Min. dynamic pressure coeff. (C_p^-) - Block 1 - high T_u

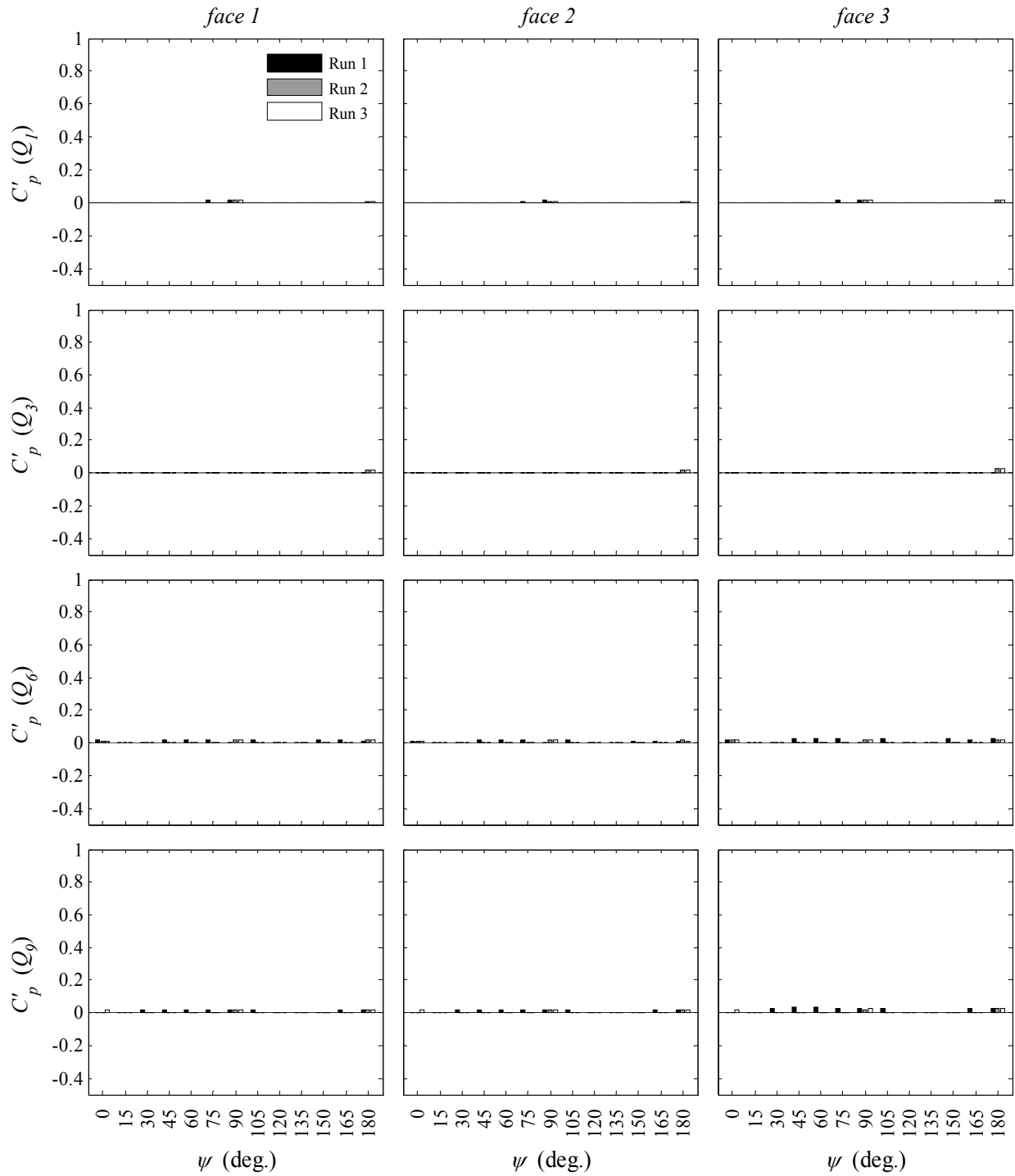


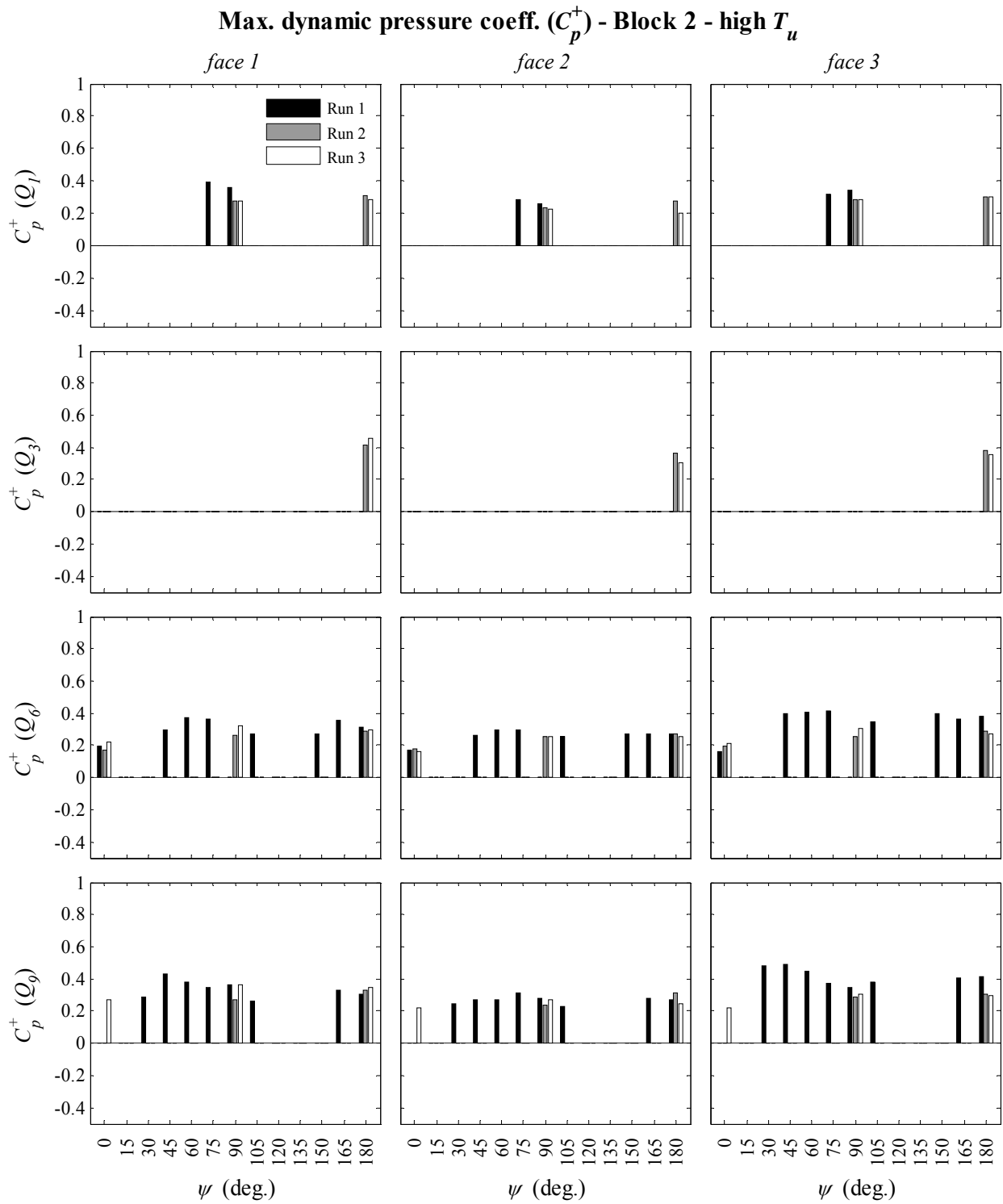
High T_u , Block 2 (faces 1, 2 and 3)

Avg. dynamic pressure coeff. (C_p) - Block 2 - high T_u

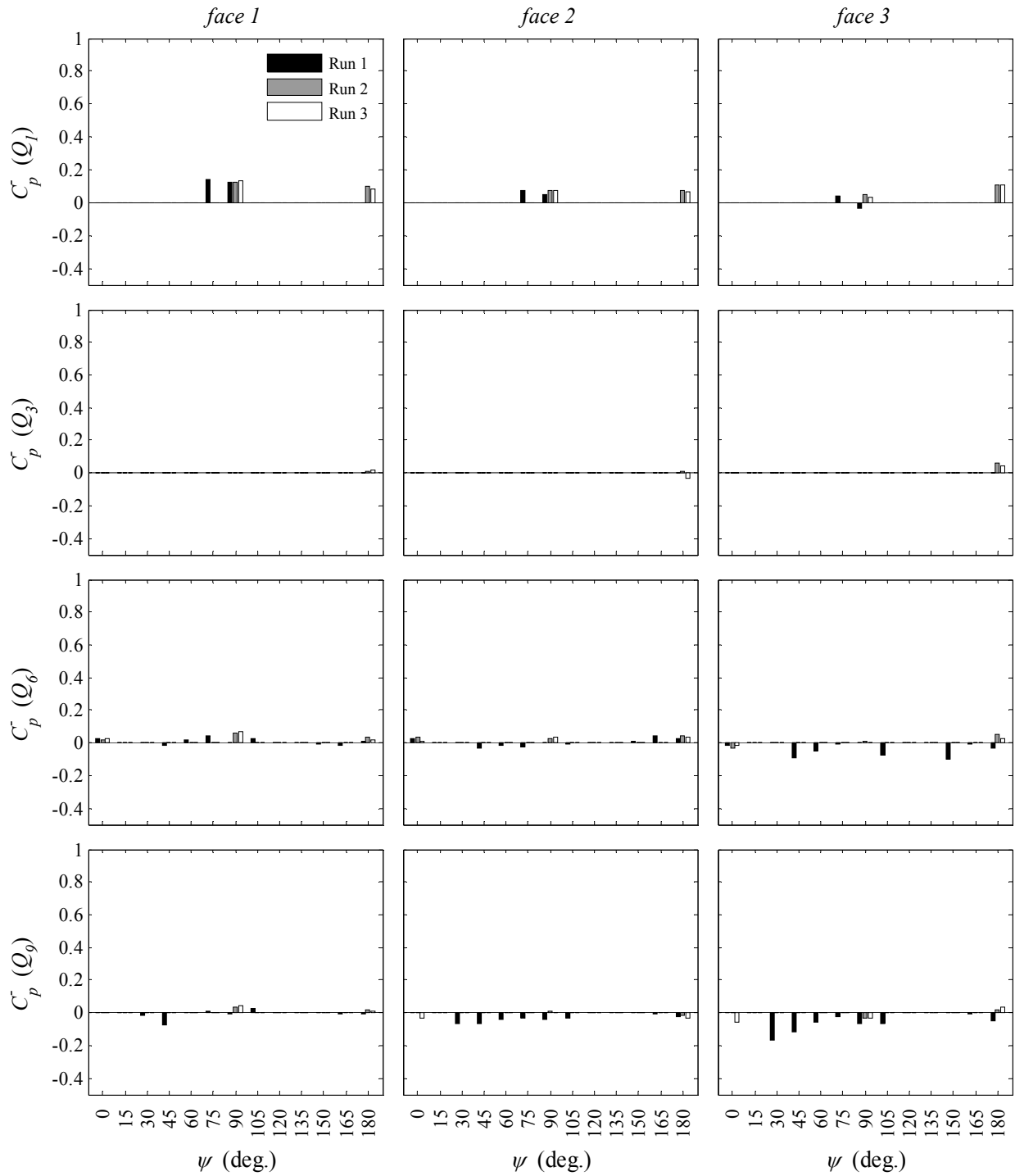


Fluc. dynamic pressure coeff. (C'_p) - Block 2 - high T_u



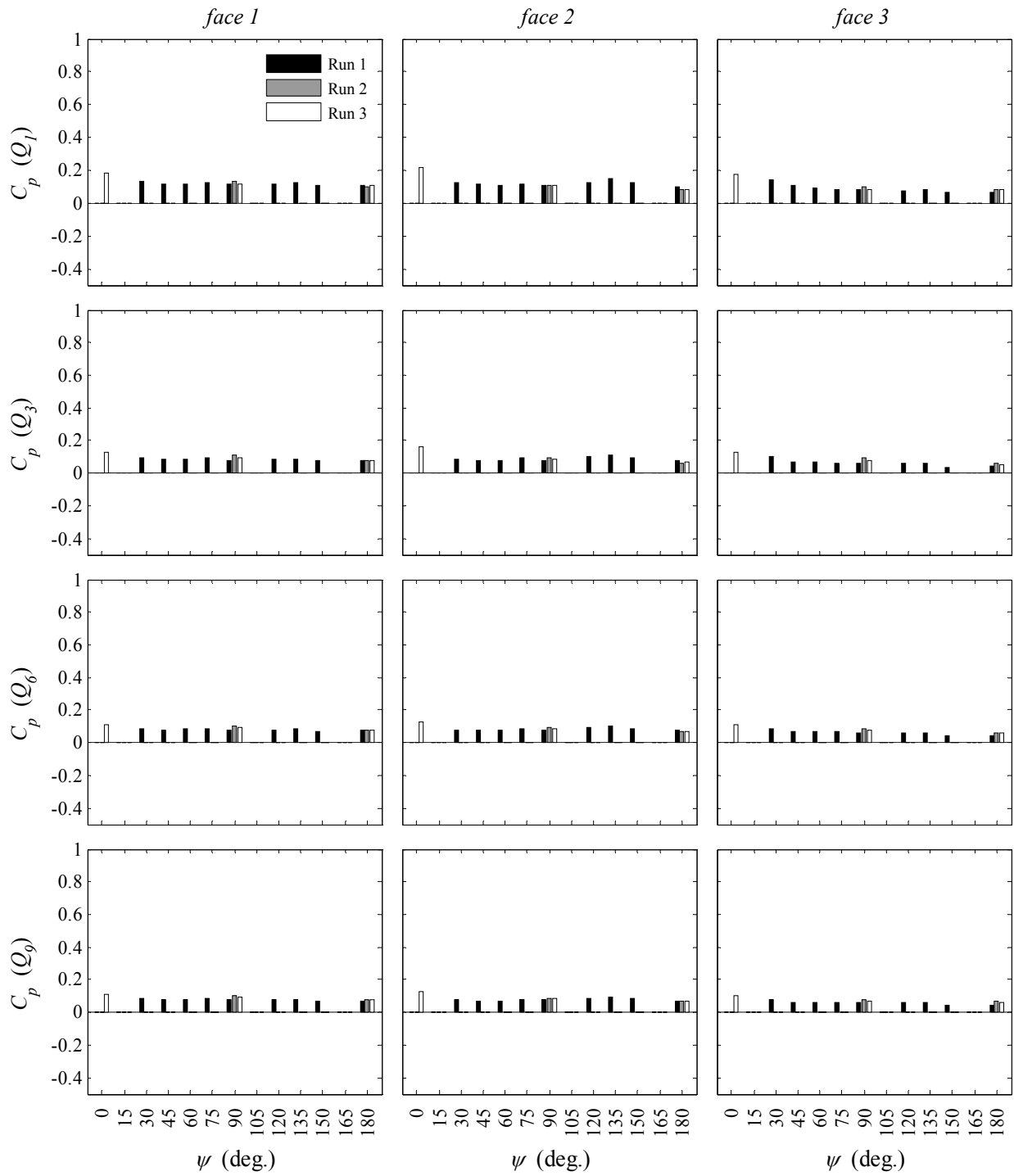


Min. dynamic pressure coeff. (C_p^-) - Block 2 - high T_u

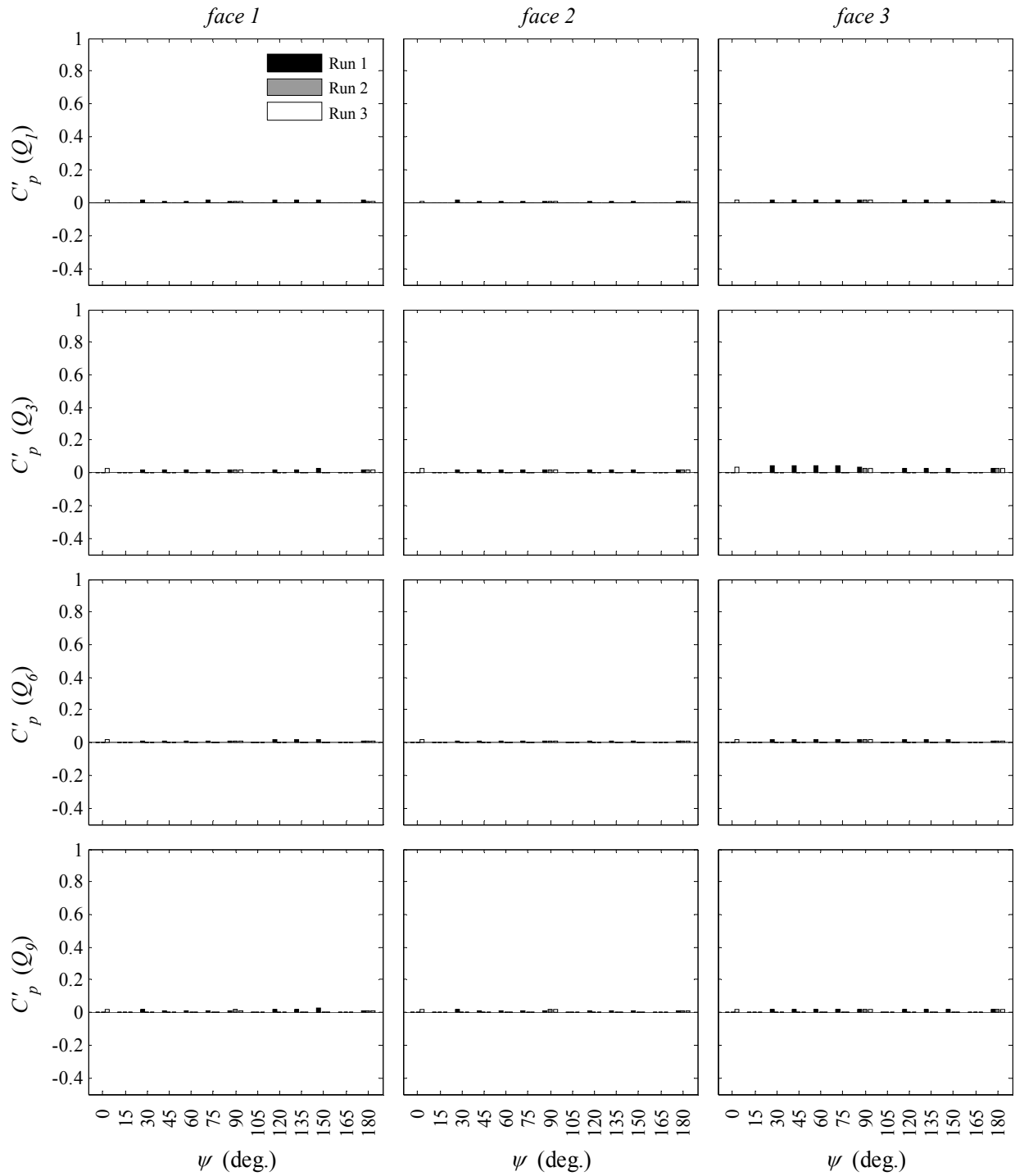


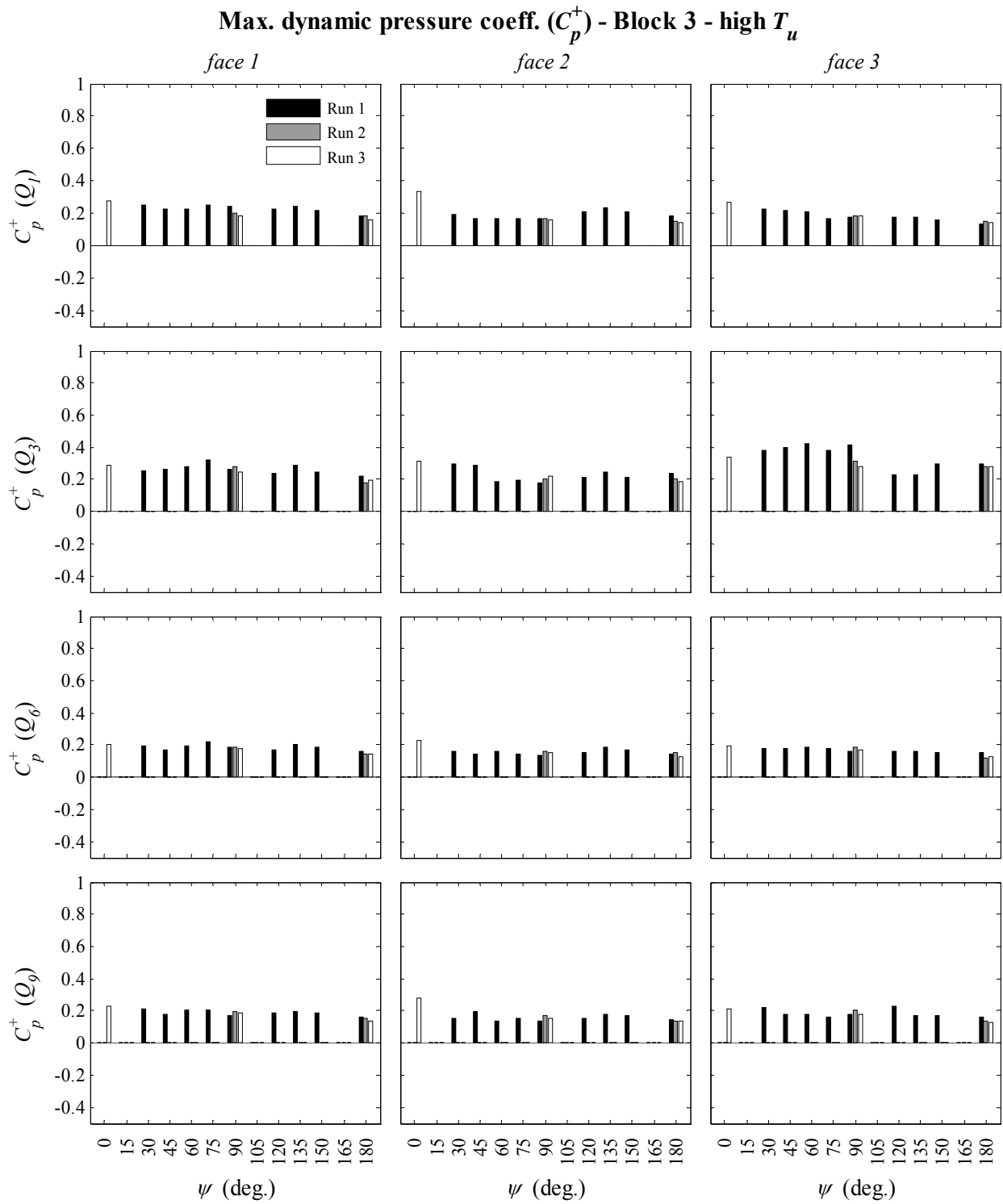
High T_u , Block 3 (faces 1, 2 and 3)

Avg. dynamic pressure coeff. (C_p) - Block 3 - high T_u

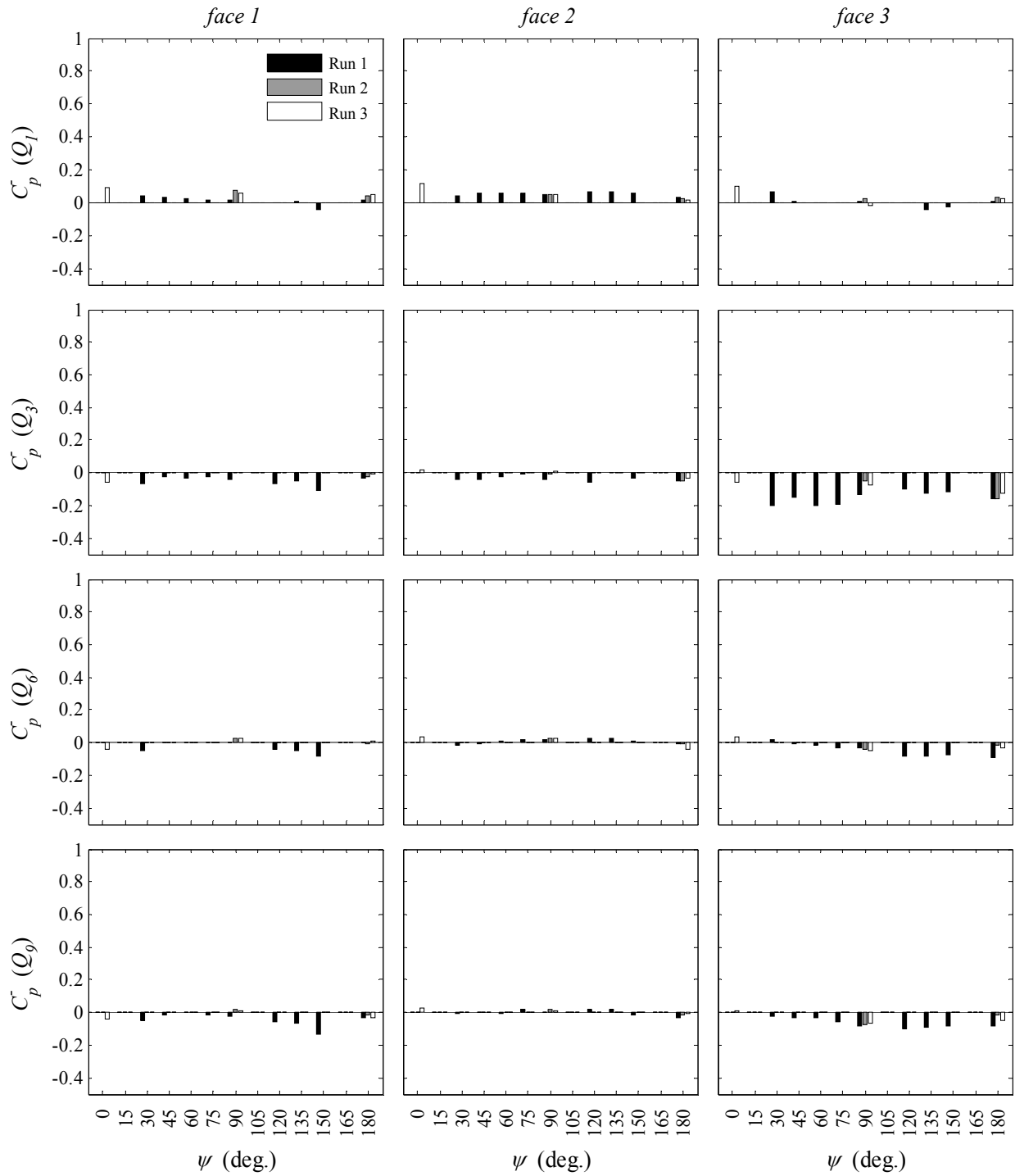


Fluc. dynamic pressure coeff. (C'_p) - Block 3 - high T_u



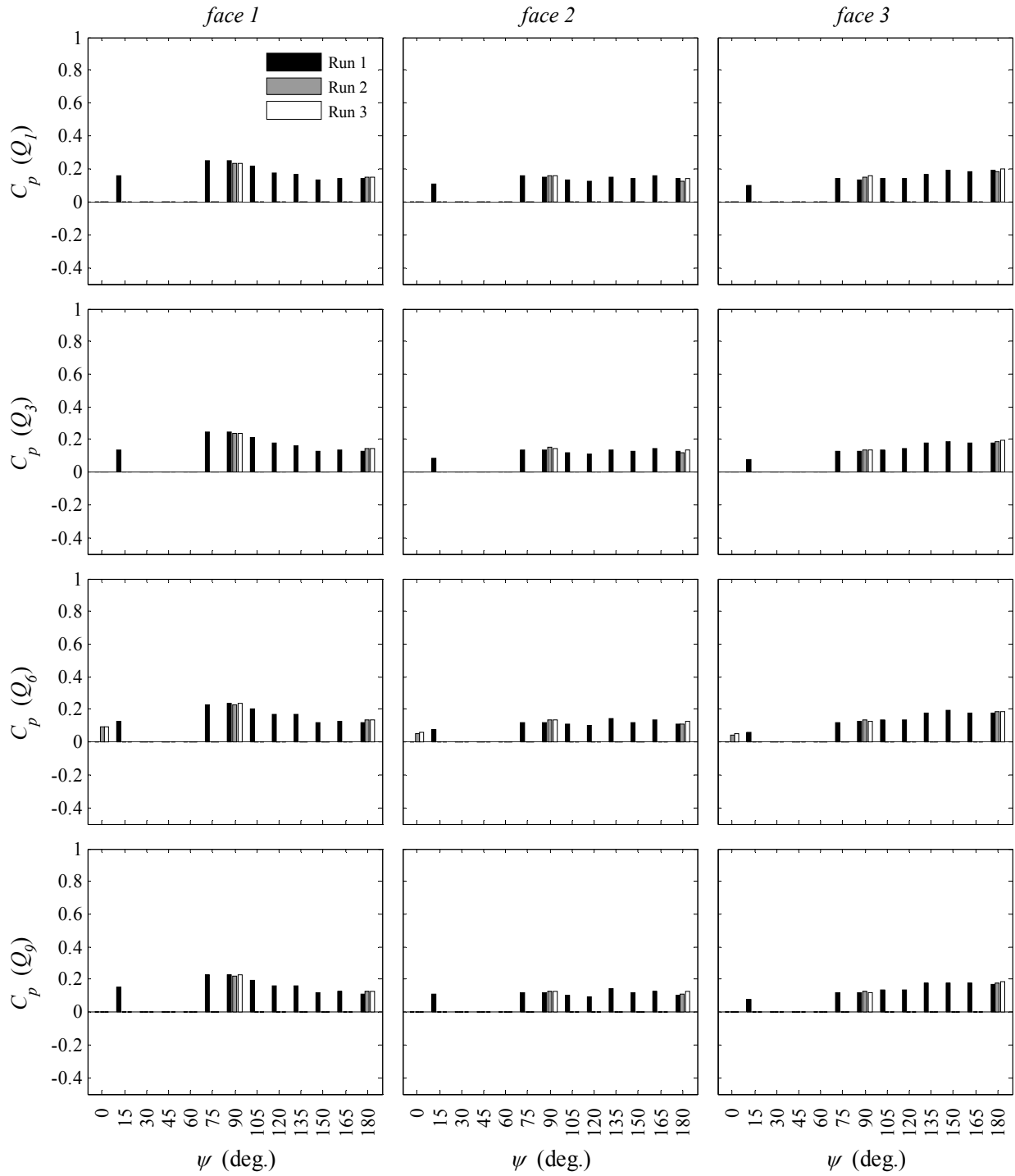


Min. dynamic pressure coeff. (C_p^-) - Block 3 - high T_u

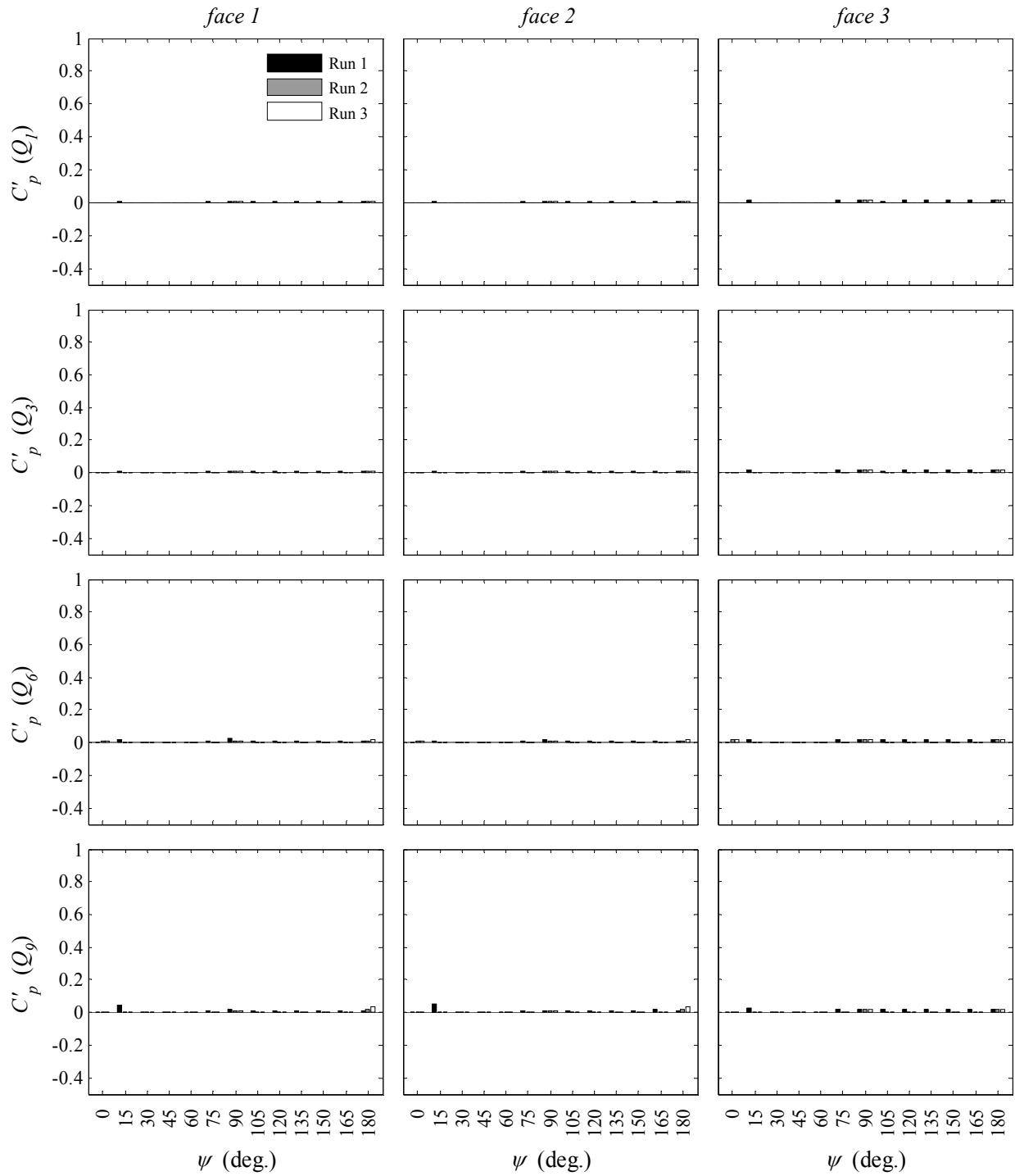


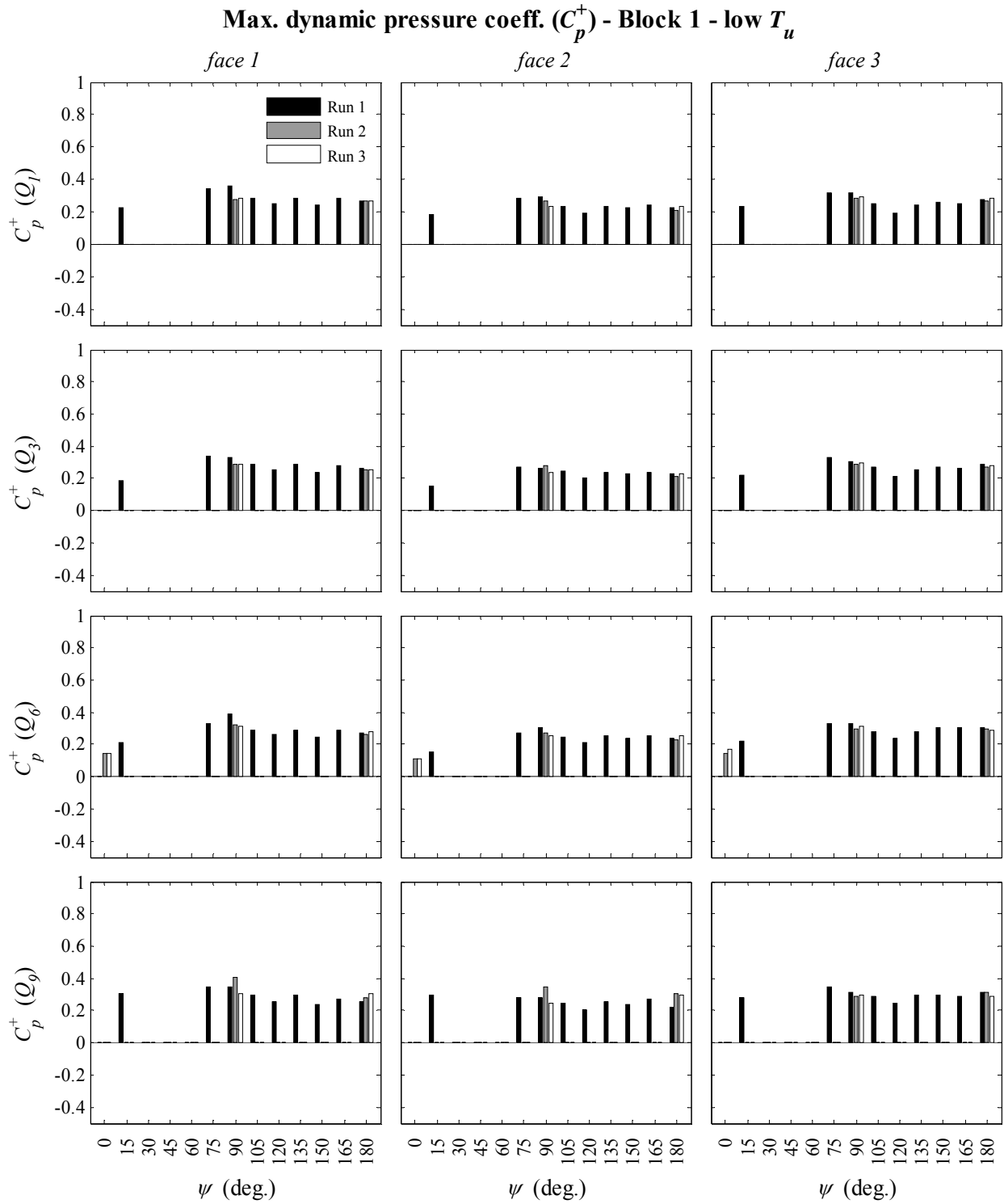
Low T_u , Block 1 (faces 1, 2 and 3)

Avg. dynamic pressure coeff. (C_p) - Block 1 - low T_u

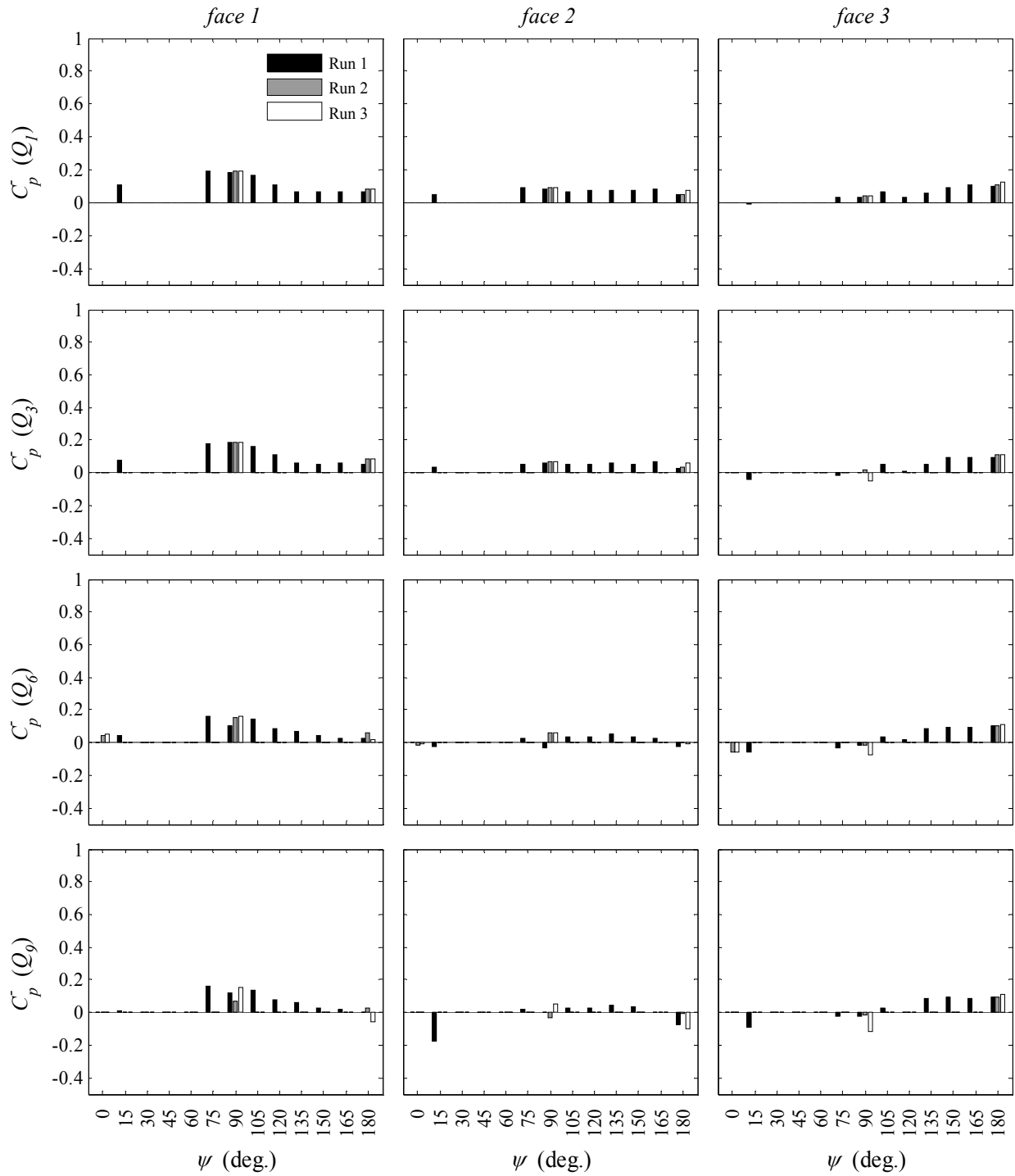


Fluc. dynamic pressure coeff. (C'_p) - Block 1 - low T_u



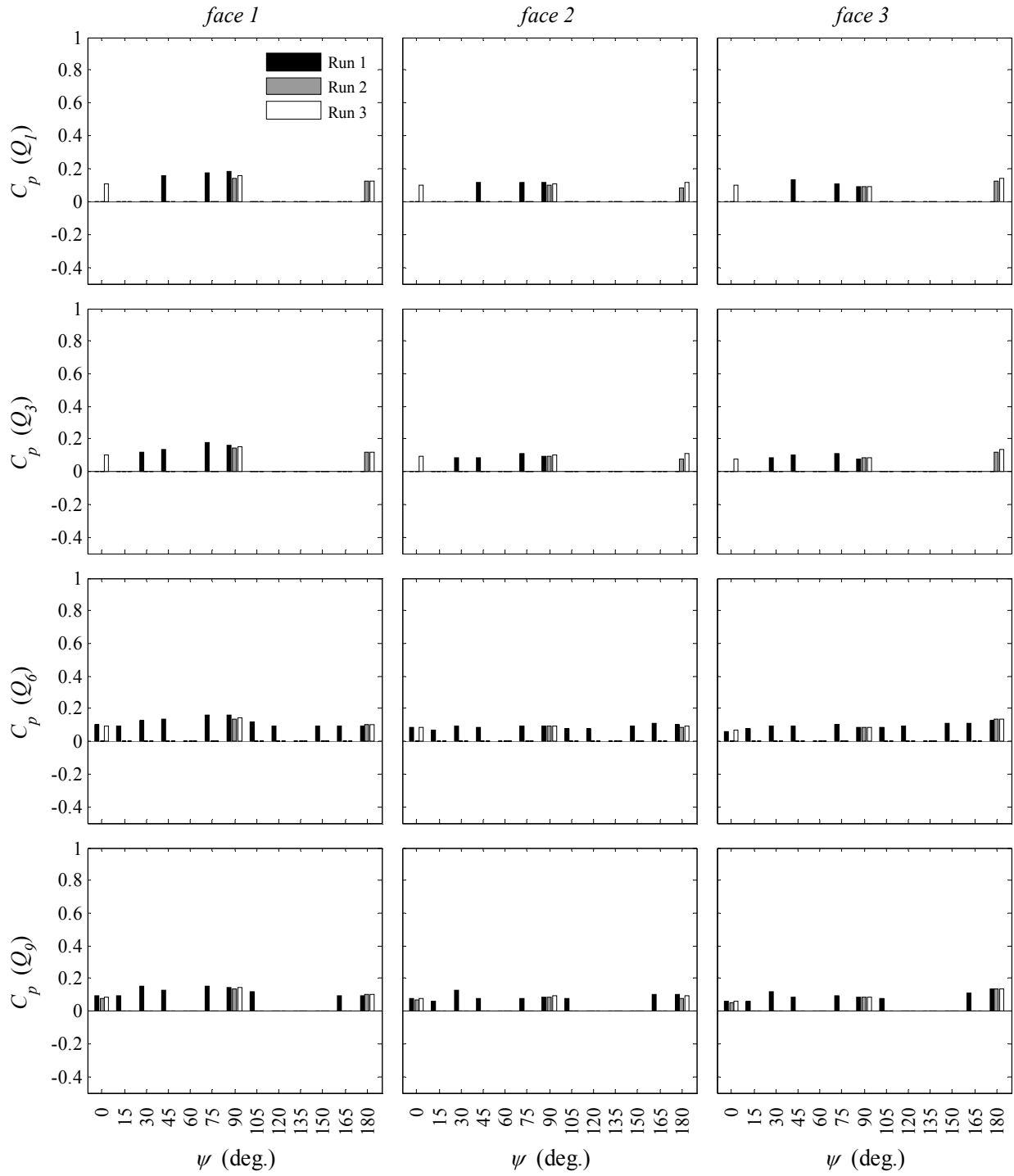


Min. dynamic pressure coeff. (C_p) - Block 1 - low T_u

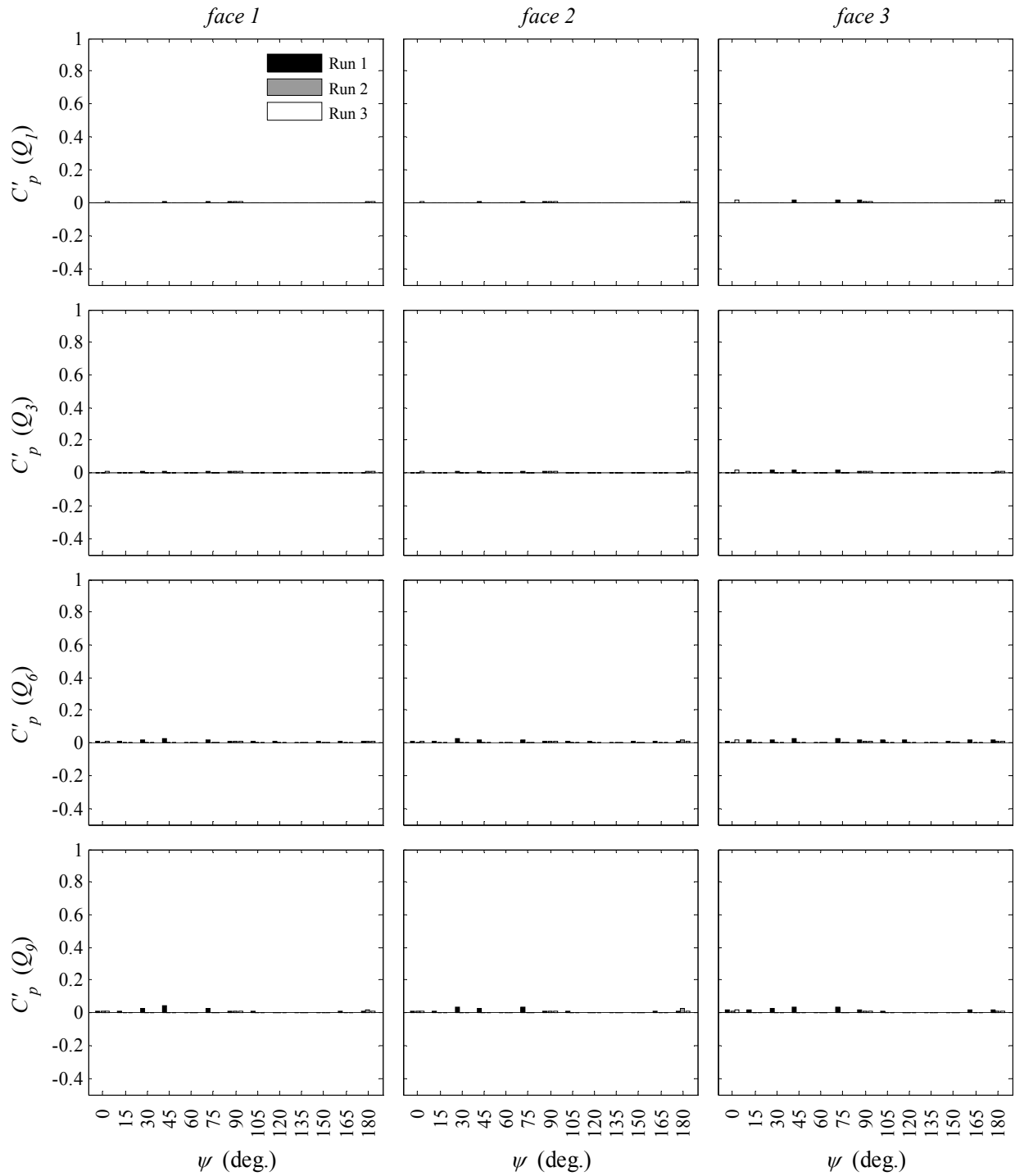


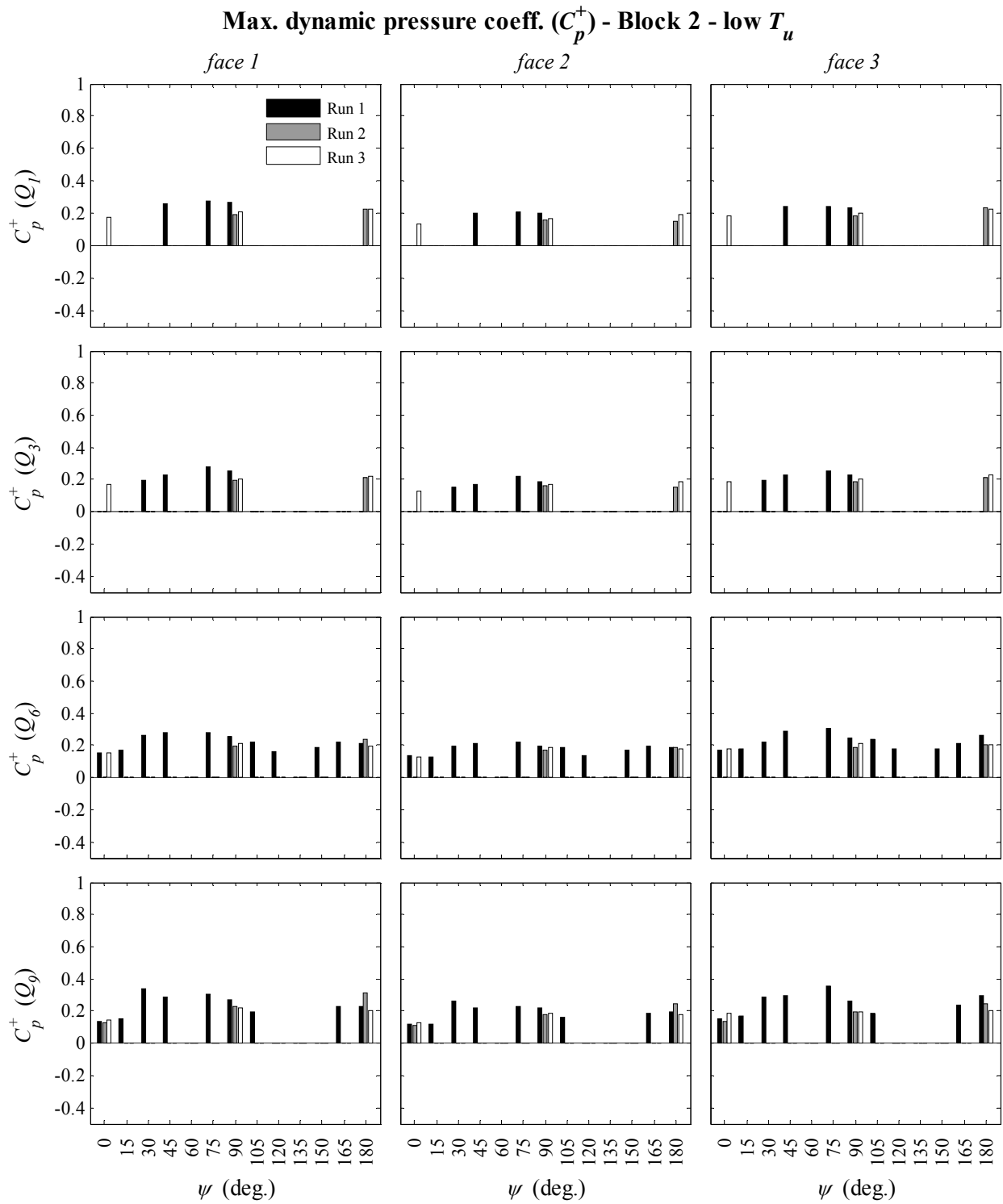
Low T_u , Block 2 (faces 1, 2 and 3)

Avg. dynamic pressure coeff. (C_p) - Block 2 - low T_u

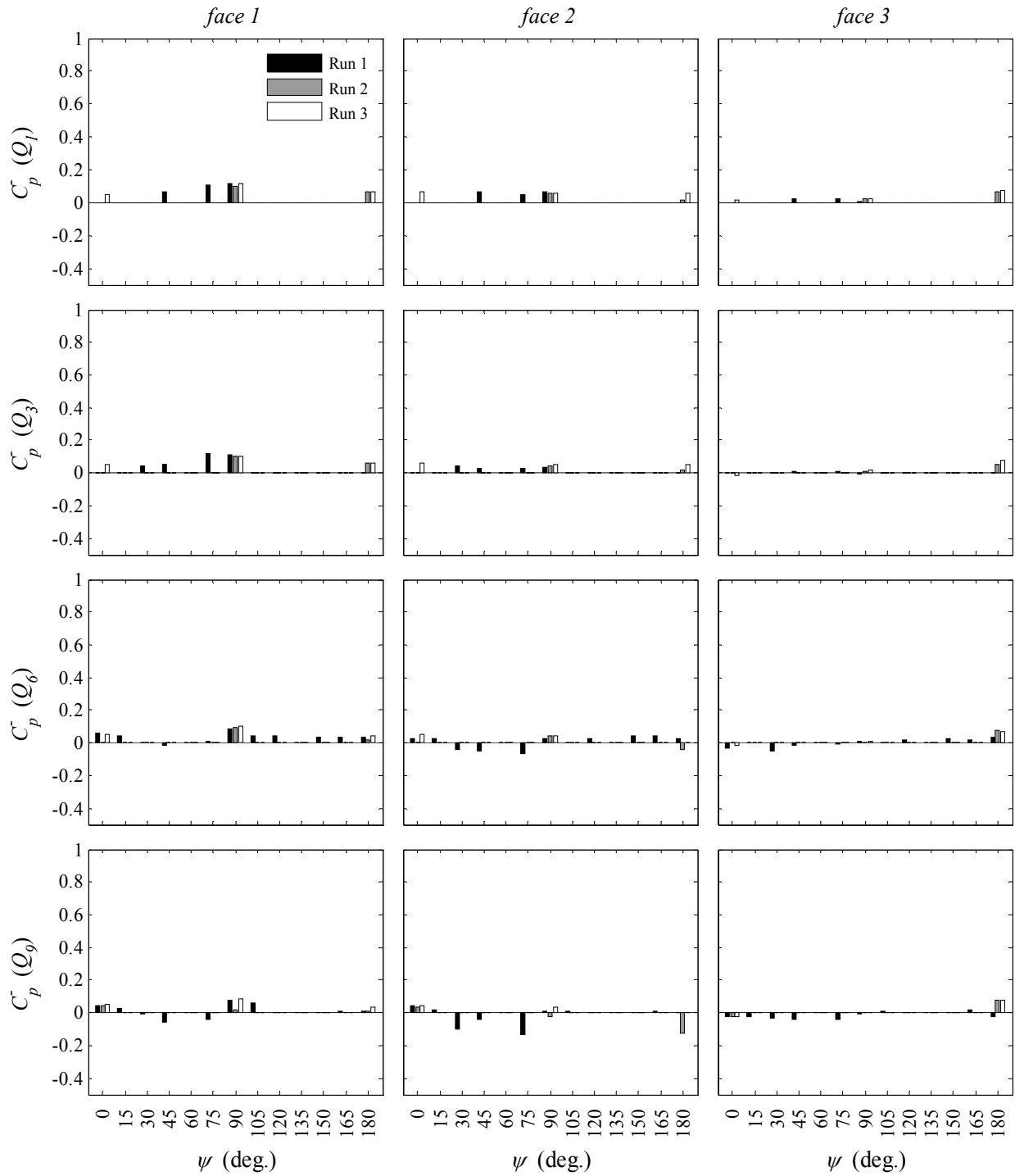


Fluc. dynamic pressure coeff. (C'_p) - Block 2 - low T_u



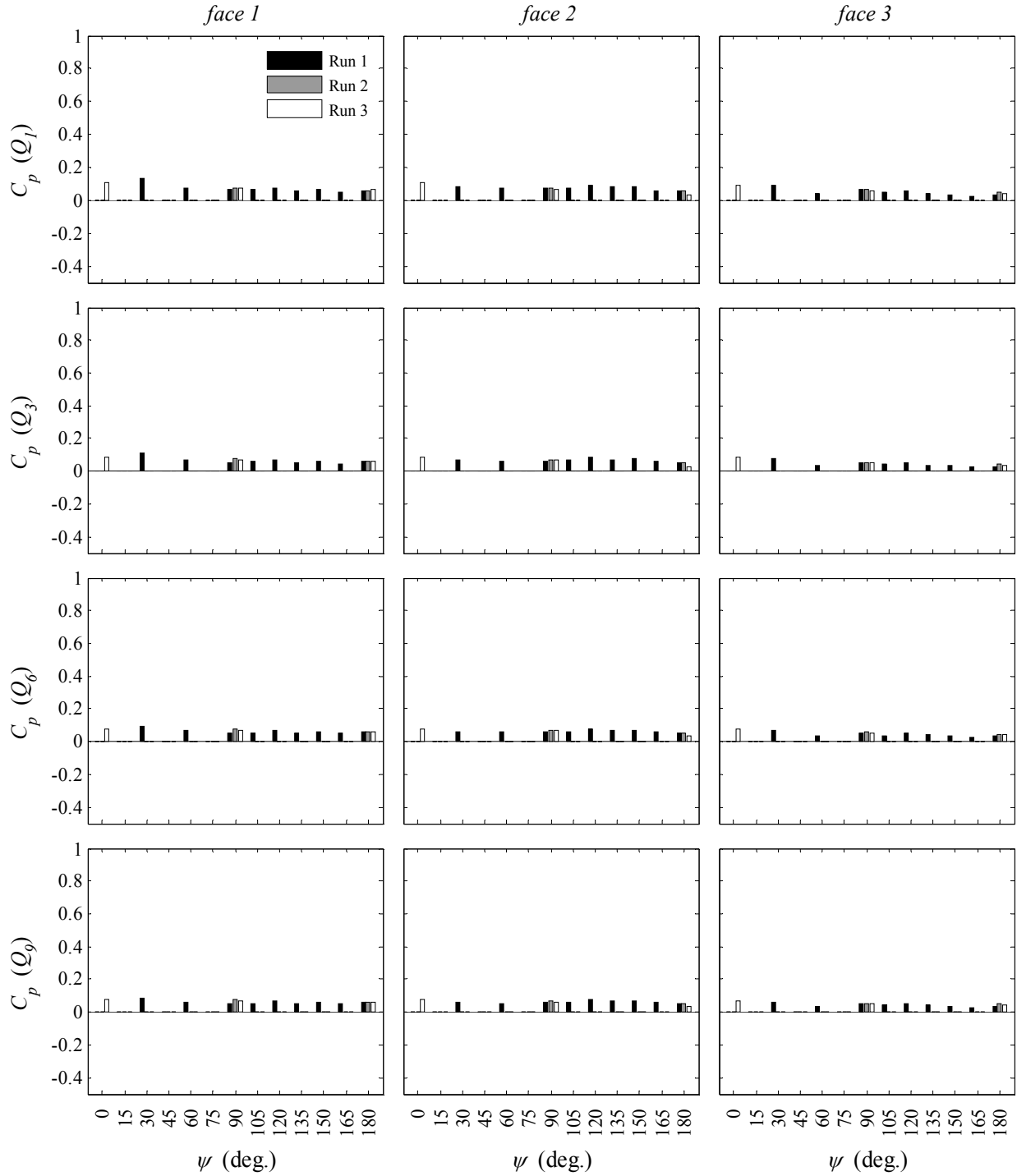


Min. dynamic pressure coeff. (C_p^-) - Block 2 - low T_u

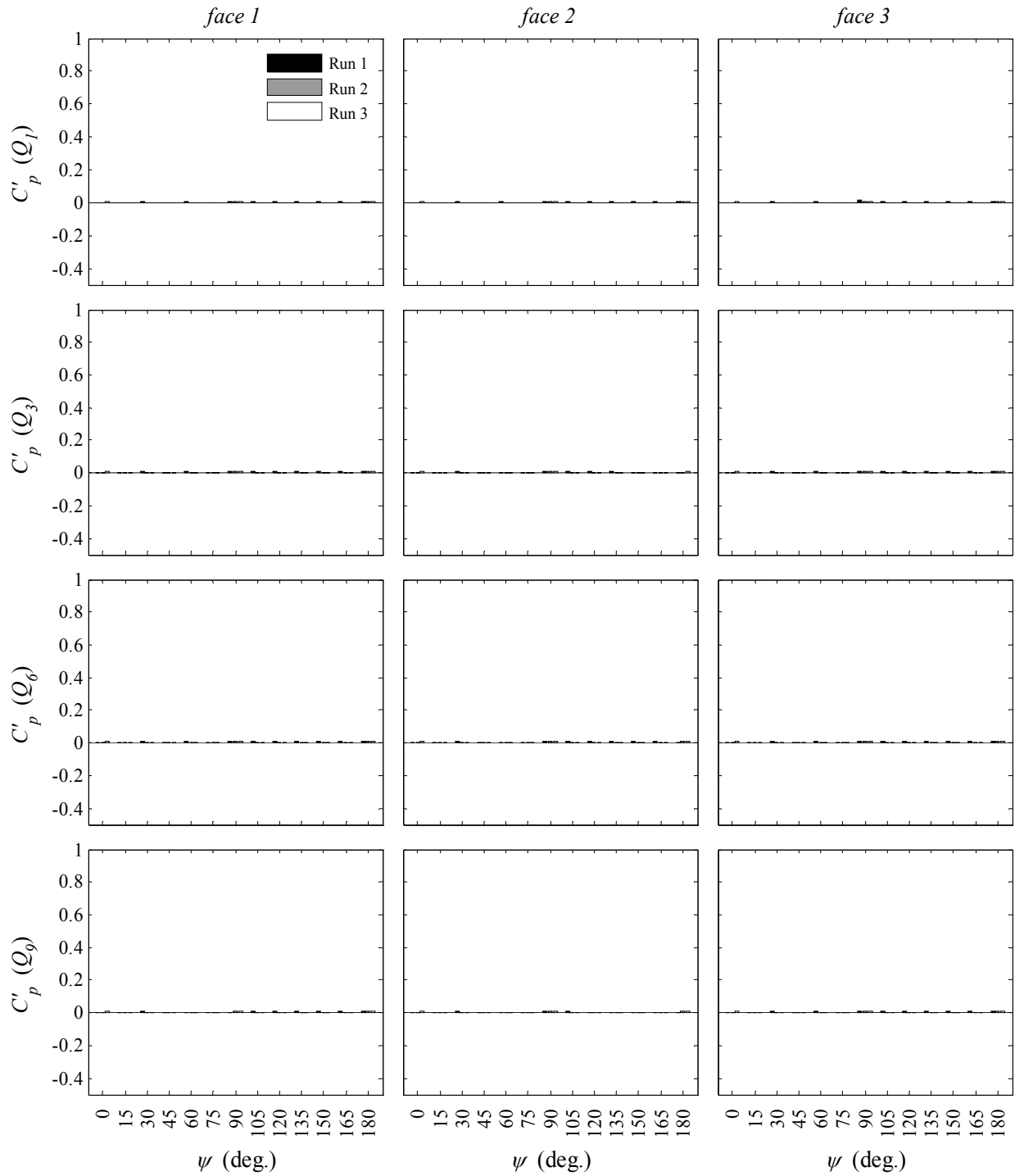


Low T_u , Block 3 (faces 1, 2 and 3)

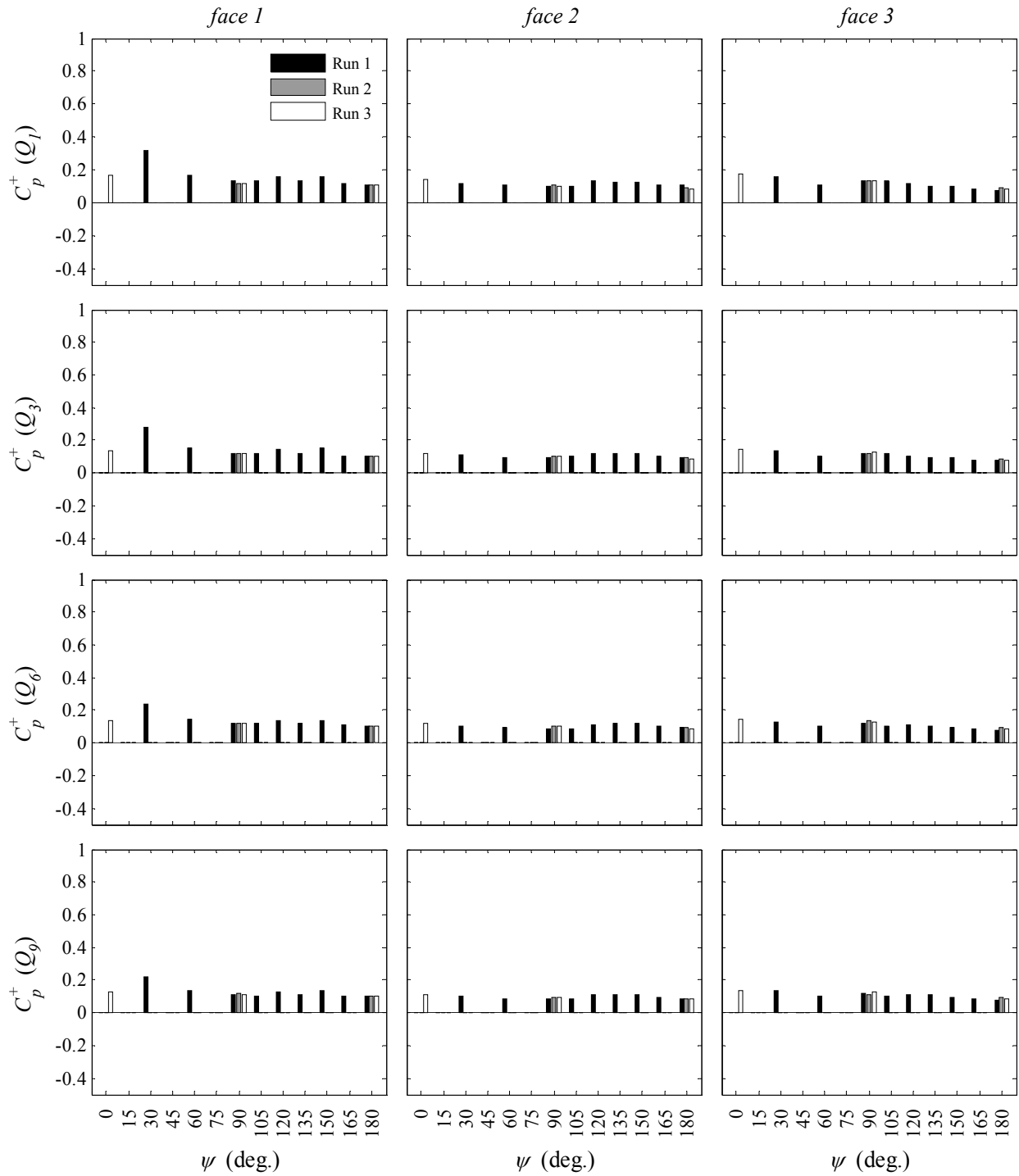
Avg. dynamic pressure coeff. (C_p) - Block 3 - low T_u



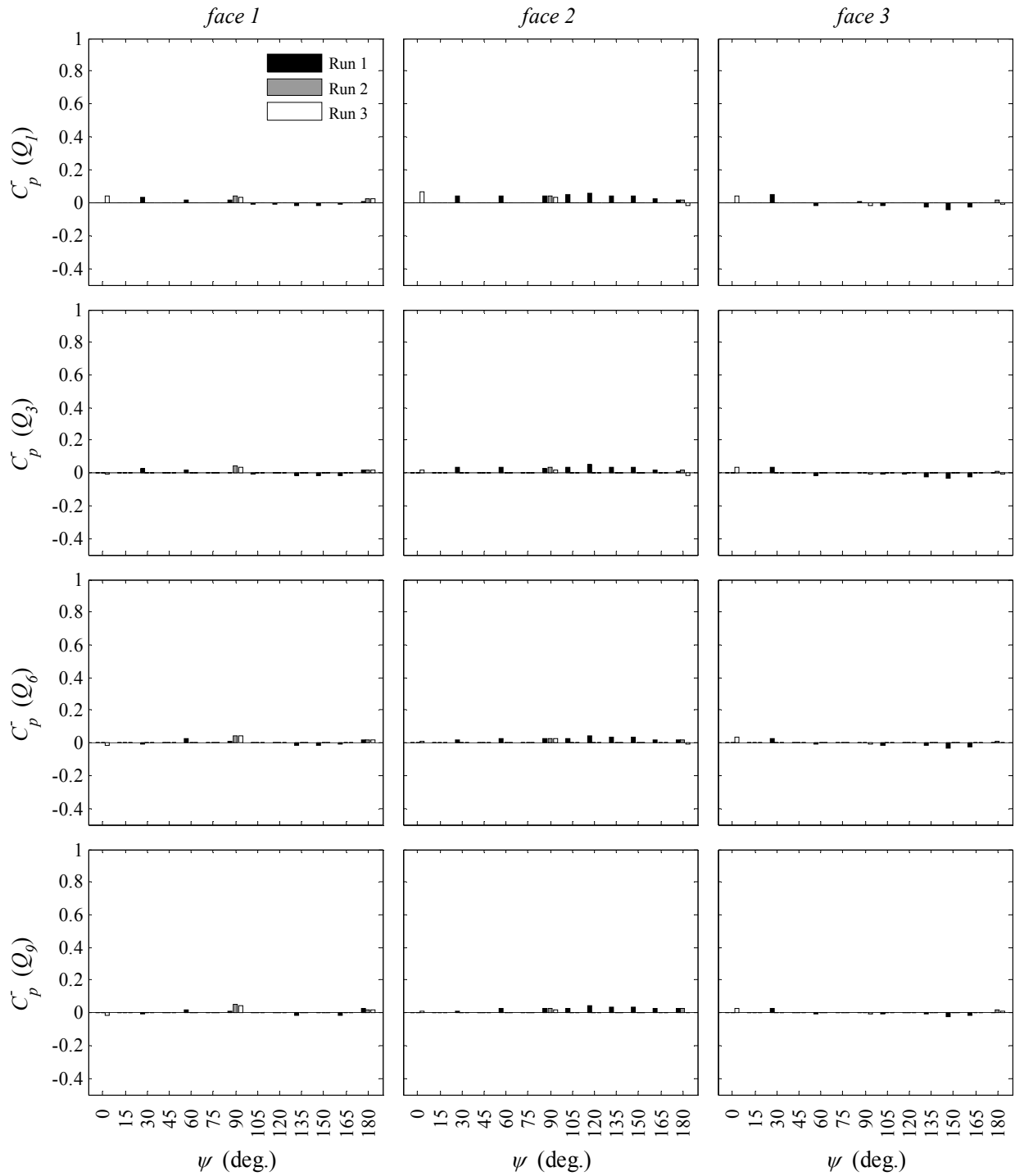
Fluc. dynamic pressure coeff. (C'_p) - Block 3 - low T_u



Max. dynamic pressure coeff. (C_p^+) - Block 3 - low T_u

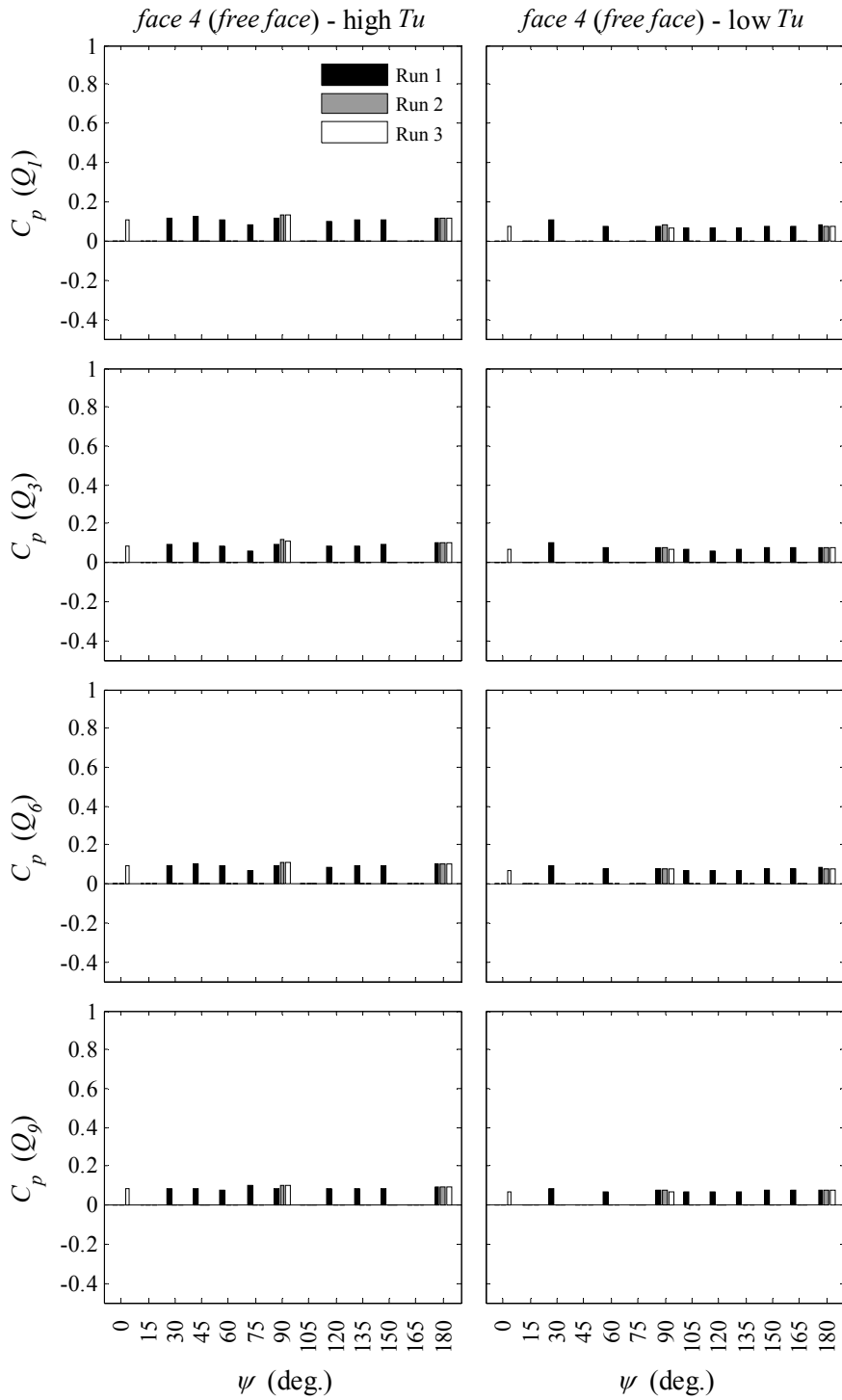


Min. dynamic pressure coeff. (C_p^-) - Block 3 - low T_u

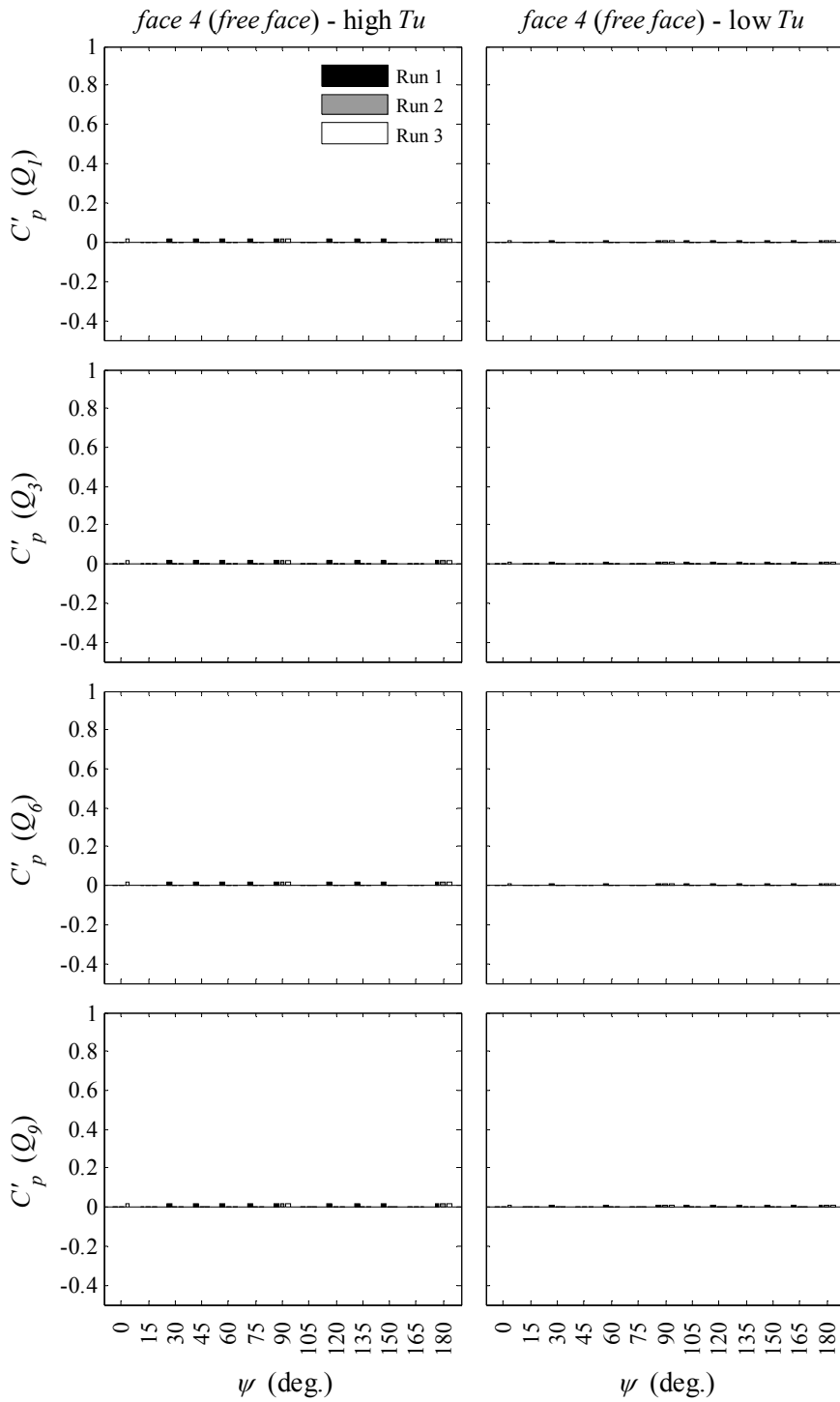


High & Low T_u , Block 3 (face 4)

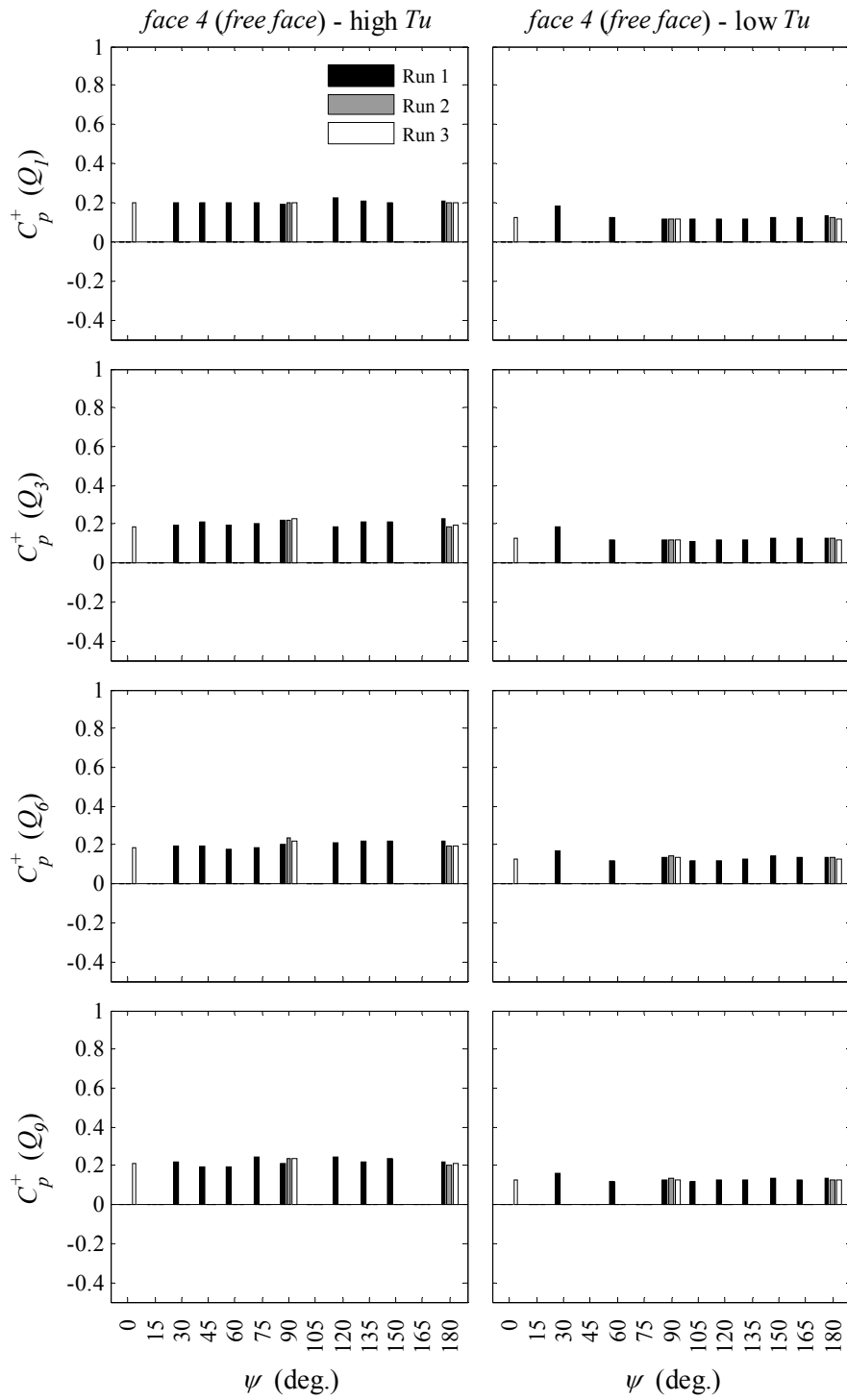
Avg. dynamic pressure coeff. (C_p) - Block 3



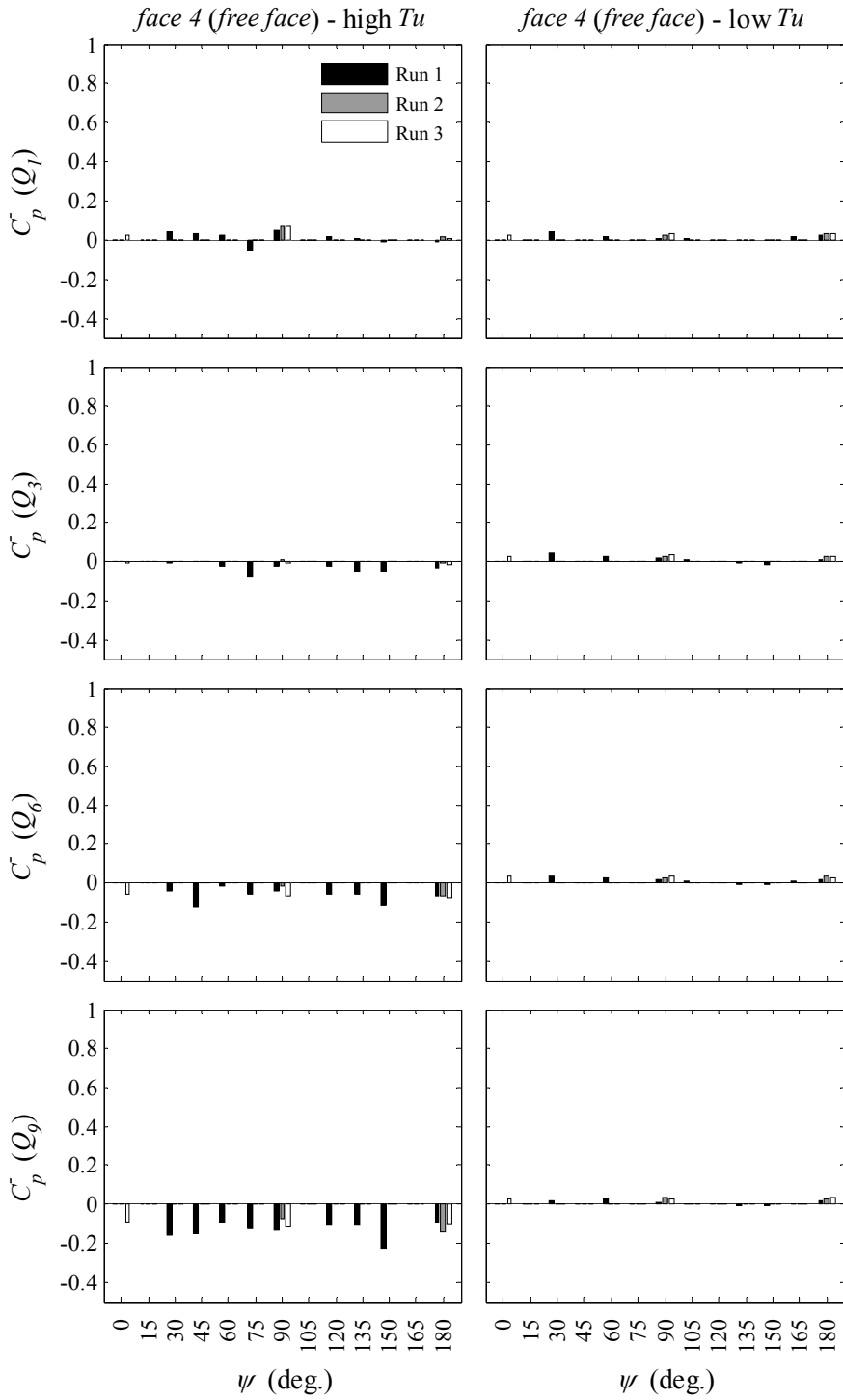
Fluc. dynamic pressure coeff. (C'_p) - Block 3



Max. dynamic pressure coeff. (C_p^+) - Block 3



Min. dynamic pressure coeff. (C_p^-) - Block 3



Least squares regression for C_p data fit

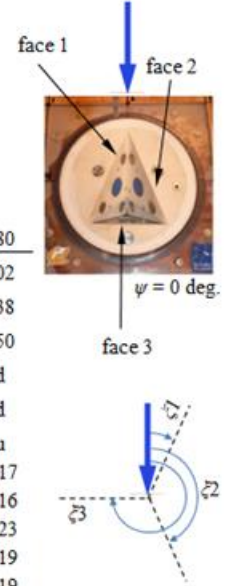
High T_u , Block 1

Least squares regression, X^2

C_p

Block 1, High T_u

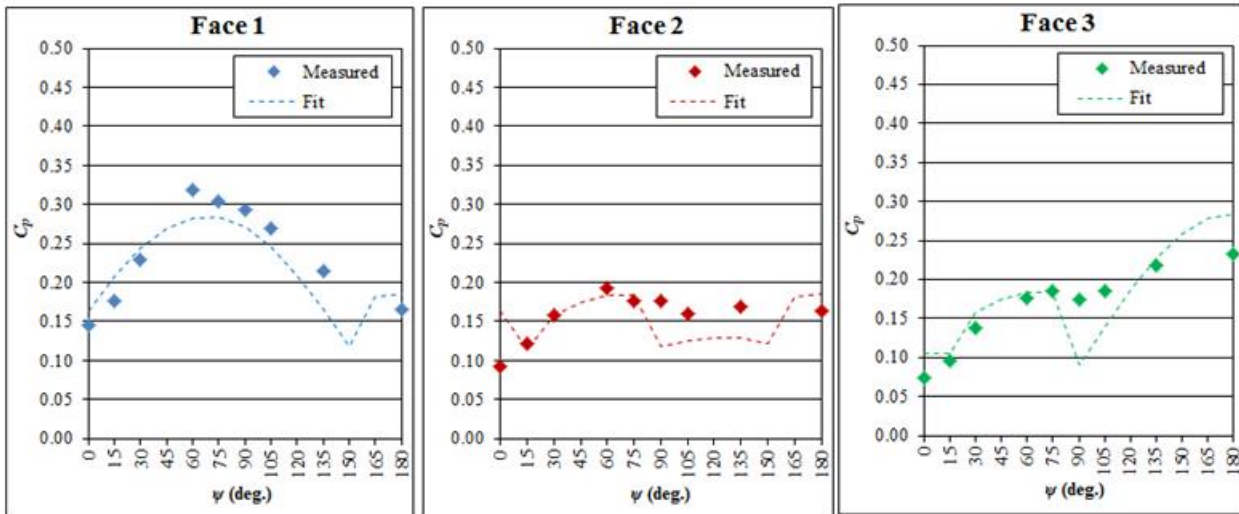
C1	0.19481
C2	0.09 corresponds to Avg. C_p for Block 3 on faces 1,2,3
C3	0.65031



ψ (deg.)	0	15	30	45	60	75	90	105	120	135	150	165	180
ξ_1 (deg.) ^a	22	37	52	67	82	97	112	127	142	157	172	187	202
ξ_2 (deg.) ^a	158	173	188	203	218	233	248	263	278	293	308	323	338
ξ_3 (deg.) ^a	270	285	300	315	330	345	360	375	390	405	420	435	450
Face 1, u/d? ^b	u	u	u	u	u	u	u	u	u	u	u	d	d
Face 2, u/d? ^b	u	u	d	d	d	d	d	d	d	d	d	d	d
Face 3, u/d? ^b	d	d	d	d	d	d	u	u	u	u	u	u	u
CpF1 (measured)	0.15	0.18	0.23		0.32	0.30	0.29	0.27		0.22			0.17
CpF2 (measured)	0.09	0.12	0.16		0.19	0.18	0.18	0.16		0.17			0.16
CpF3 (measured)	0.07	0.10	0.14		0.18	0.19	0.18	0.19		0.22			0.23
CpFIT1	0.16	0.21	0.24	0.27	0.28	0.28	0.27	0.25	0.21	0.17	0.12	0.18	0.19
CpFIT2	0.16	0.11	0.16	0.18	0.18	0.18	0.12	0.13	0.13	0.13	0.12	0.18	0.19
CpFIT3	0.11	0.10	0.16	0.18	0.18	0.18	0.09	0.14	0.19	0.23	0.26	0.28	0.28
(CpFIT1-CpF1) ²	0.0003	0.0009	0.0002		0.0013	0.0005	0.0005	0.0006		0.0024			0.0004
(CpFIT2-CpF2) ²	0.0051	0.0000	0.0000		0.0001	0.0001	0.0036	0.0012		0.0016			0.0004
(CpFIT3-CpF3) ²	0.0010	0.0001	0.0004		0.0001	0.0000	0.0073	0.0021		0.0001			0.0027
(Std. Dev) ²	0.0036 Measured CpF values												
Sum (CpFIT-CpF) ²	0.0330												
X^2	9.1413 Minimize, by changing C1 and C3												

Notes:

^a Angle of block face wrt flow direction, ^b Face is on upstream (u) or downstream (d) side of block



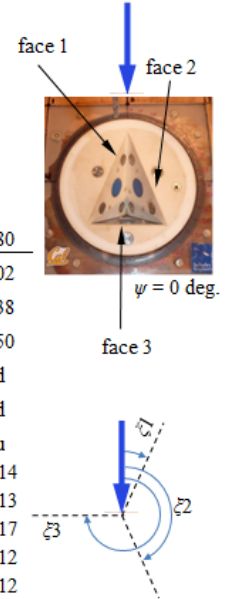
High T_u , Block 2

Least squares regression, X^2

C_p

Block 2, High T_u

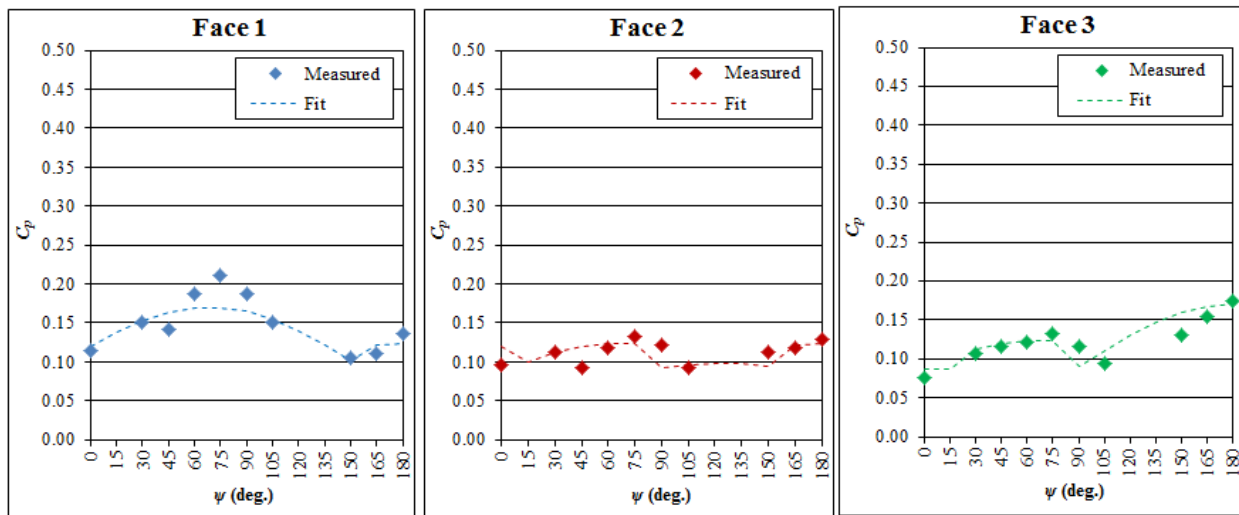
C1	0.08042
C2	0.09 corresponds to Avg. C_p for Block 3 on faces 1,2,3
C3	0.72859



ψ (deg.)	0	15	30	45	60	75	90	105	120	135	150	165	180
ξ_1 (deg.) ^a	22	37	52	67	82	97	112	127	142	157	172	187	202
ξ_2 (deg.) ^a	158	173	188	203	218	233	248	263	278	293	308	323	338
ξ_3 (deg.) ^a	270	285	300	315	330	345	360	375	390	405	420	435	450
Face 1, u/d? ^b	u	u	u	u	u	u	u	u	u	u	u	d	d
Face 2, u/d? ^b	u	u	d	d	d	d	d	d	d	d	d	d	d
Face 3, u/d? ^b	d	d	d	d	d	d	u	u	u	u	u	u	u
CpF1 (measured)	0.11		0.15	0.14	0.19	0.21	0.19	0.15			0.10	0.11	0.14
CpF2 (measured)	0.10		0.11	0.09	0.12	0.13	0.12	0.09			0.11	0.12	0.13
CpF3 (measured)	0.08		0.11	0.12	0.12	0.13	0.12	0.09			0.13	0.15	0.17
CpFIT1	0.12	0.14	0.15	0.16	0.17	0.17	0.16	0.15	0.14	0.12	0.10	0.12	0.12
CpFIT2	0.12	0.10	0.11	0.12	0.12	0.12	0.09	0.10	0.10	0.10	0.10	0.12	0.12
CpFIT3	0.09	0.09	0.11	0.12	0.12	0.12	0.09	0.11	0.13	0.15	0.16	0.17	0.17
(CpFIT1-CpF1) ²	0.0000		0.0000	0.0005	0.0003	0.0017	0.0005	0.0000			0.0000	0.0001	0.0001
(CpFIT2-CpF2) ²	0.0006		0.0000	0.0008	0.0000	0.0001	0.0008	0.0000			0.0003	0.0000	0.0000
(CpFIT3-CpF3) ²	0.0001		0.0000	0.0000	0.0000	0.0001	0.0007	0.0003			0.0008	0.0002	0.0000
(Std. Dev) ²	0.0009 Measured CpF values												
Sum (CpFIT-CpF) ²	0.0083												
X^2	8.83033 Minimize, by changing C1 and C3												

Notes:

^a Angle of block face wrt flow direction, ^b Face is on upstream (u) or downstream (d) side of block



Low T_u , Block 1

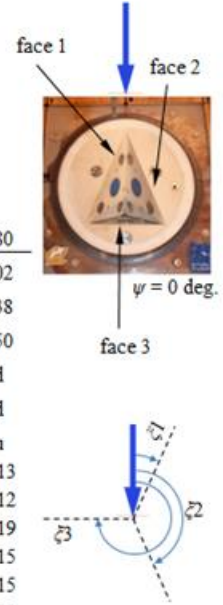
Least squares regression, X^2

C_p

Block 1, Low T_u

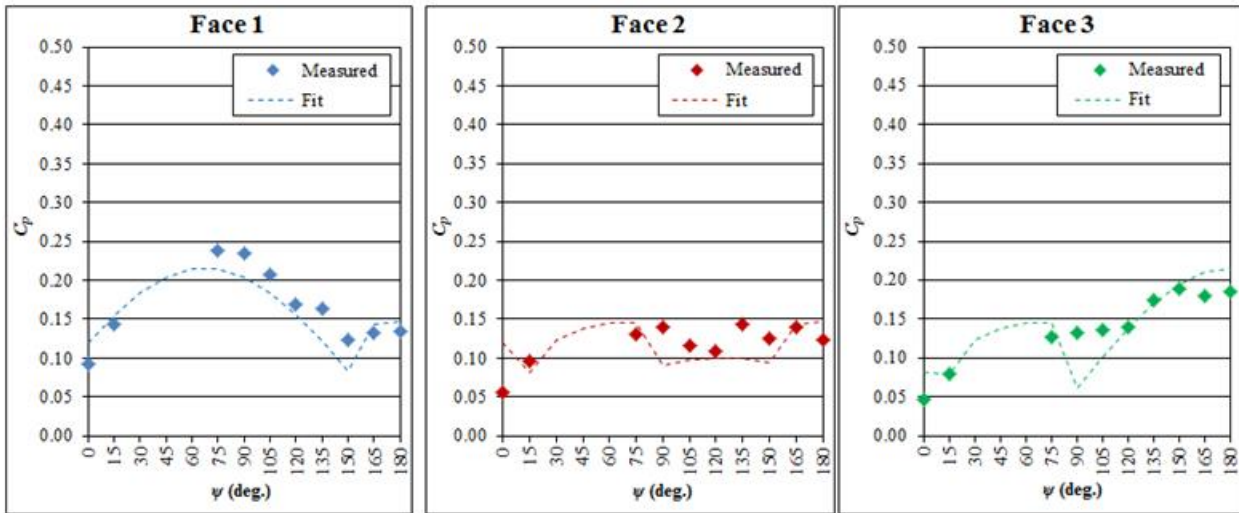
C1	0.15332
C2	0.062 corresponds to Avg. C_p for Block 3 on faces 1,2,3
C3	0.67961

ψ (deg.)	0	15	30	45	60	75	90	105	120	135	150	165	180
ξ_1 (deg.) ^a	22	37	52	67	82	97	112	127	142	157	172	187	202
ξ_2 (deg.) ^a	158	173	188	203	218	233	248	263	278	293	308	323	338
ξ_3 (deg.) ^a	270	285	300	315	330	345	360	375	390	405	420	435	450
Face 1, u/d? ^b	u	u	u	u	u	u	u	u	u	u	u	d	d
Face 2, u/d? ^b	u	u	d	d	d	d	d	d	d	d	d	d	d
Face 3, u/d? ^b	d	d	d	d	d	d	u	u	u	u	u	u	u
CpF1 (measured)	0.09	0.14				0.24	0.23	0.21	0.17	0.16	0.12	0.13	0.13
CpF2 (measured)	0.06	0.10				0.13	0.14	0.12	0.11	0.14	0.13	0.14	0.12
CpF3 (measured)	0.05	0.08				0.13	0.13	0.14	0.14	0.17	0.19	0.18	0.19
CpFIT1	0.12	0.15	0.18	0.20	0.21	0.21	0.20	0.18	0.16	0.12	0.08	0.14	0.15
CpFIT2	0.12	0.08	0.12	0.14	0.15	0.15	0.09	0.10	0.10	0.10	0.09	0.14	0.15
CpFIT3	0.08	0.08	0.12	0.14	0.15	0.15	0.06	0.10	0.14	0.17	0.19	0.21	0.22
(CpFIT1-CpF1) ²	0.0007	0.0001				0.0006	0.0009	0.0005	0.0002	0.0018	0.0017	0.0001	0.0001
(CpFIT2-CpF2) ²	0.0040	0.0002				0.0002	0.0024	0.0004	0.0001	0.0019	0.0010	0.0000	0.0005
(CpFIT3-CpF3) ²	0.0012	0.0000				0.0003	0.0051	0.0012	0.0000	0.0000	0.0000	0.0009	0.0009
(Std. Dev) ²	0.0019 Measured CpF values												
Sum (CpFIT-CpF) ²	0.0270												
X^2	13.8975 Minimize, by changing C1 and C3												



Notes:

^a Angle of block face wrt flow direction, ^b Face is on upstream (u) or downstream (d) side of block



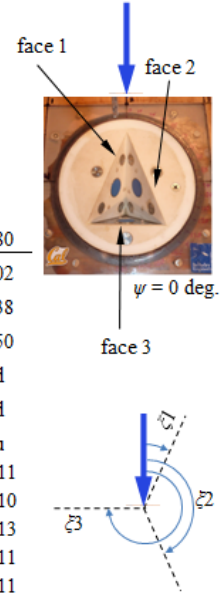
Low T_u , Block 2

Least squares regression, X^2

C_p

Block 2, Low T_u

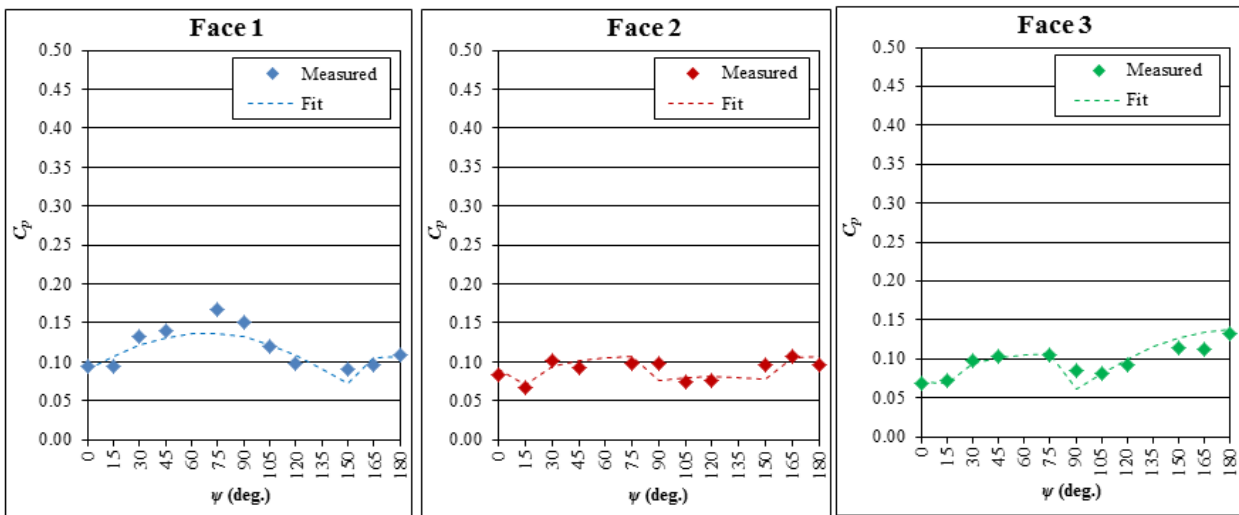
C1	0.0754
C2	0.062 corresponds to Avg. C_p for Block 3 on faces 1,2,3
C3	0.77563



ψ (deg.)	0	15	30	45	60	75	90	105	120	135	150	165	180
ξ_1 (deg.) ^a	22	37	52	67	82	97	112	127	142	157	172	187	202
ξ_2 (deg.) ^a	158	173	188	203	218	233	248	263	278	293	308	323	338
ξ_3 (deg.) ^a	270	285	300	315	330	345	360	375	390	405	420	435	450
Face 1, u/d? ^b	u	u	u	u	u	u	u	u	u	u	u	d	d
Face 2, u/d? ^b	u	u	d	d	d	d	d	d	d	d	d	d	d
Face 3, u/d? ^b	d	d	d	d	d	d	u	u	u	u	u	u	u
CpF1 (measured)	0.09	0.10	0.13	0.14		0.17	0.15	0.12	0.10		0.09	0.10	0.11
CpF2 (measured)	0.08	0.07	0.10	0.09		0.10	0.10	0.07	0.08		0.10	0.11	0.10
CpF3 (measured)	0.07	0.07	0.10	0.10		0.11	0.08	0.08	0.09		0.11	0.11	0.13
CpFIT1	0.09	0.11	0.12	0.13	0.14	0.14	0.13	0.12	0.11	0.09	0.07	0.10	0.11
CpFIT2	0.09	0.07	0.09	0.10	0.11	0.11	0.08	0.08	0.08	0.08	0.08	0.10	0.11
CpFIT3	0.07	0.07	0.09	0.10	0.11	0.11	0.06	0.08	0.10	0.12	0.13	0.13	0.14
(CpFIT1-CpF1) ²	0.0000	0.0002	0.0001	0.0001		0.0009	0.0003	0.0000	0.0001		0.0003	0.0001	0.0000
(CpFIT2-CpF2) ²	0.0001	0.0000	0.0000	0.0001		0.0001	0.0005	0.0000	0.0000		0.0003	0.0000	0.0001
(CpFIT3-CpF3) ²	0.0000	0.0000	0.0000	0.0000		0.0000	0.0005	0.0000	0.0001		0.0002	0.0005	0.0000
(Std. Dev) ²	0.0005 Measured CpF values												
Sum (CpFIT-CpF) ²	0.0048												
X^2	9.38149 Minimize, by changing C1 and C3												

Notes:

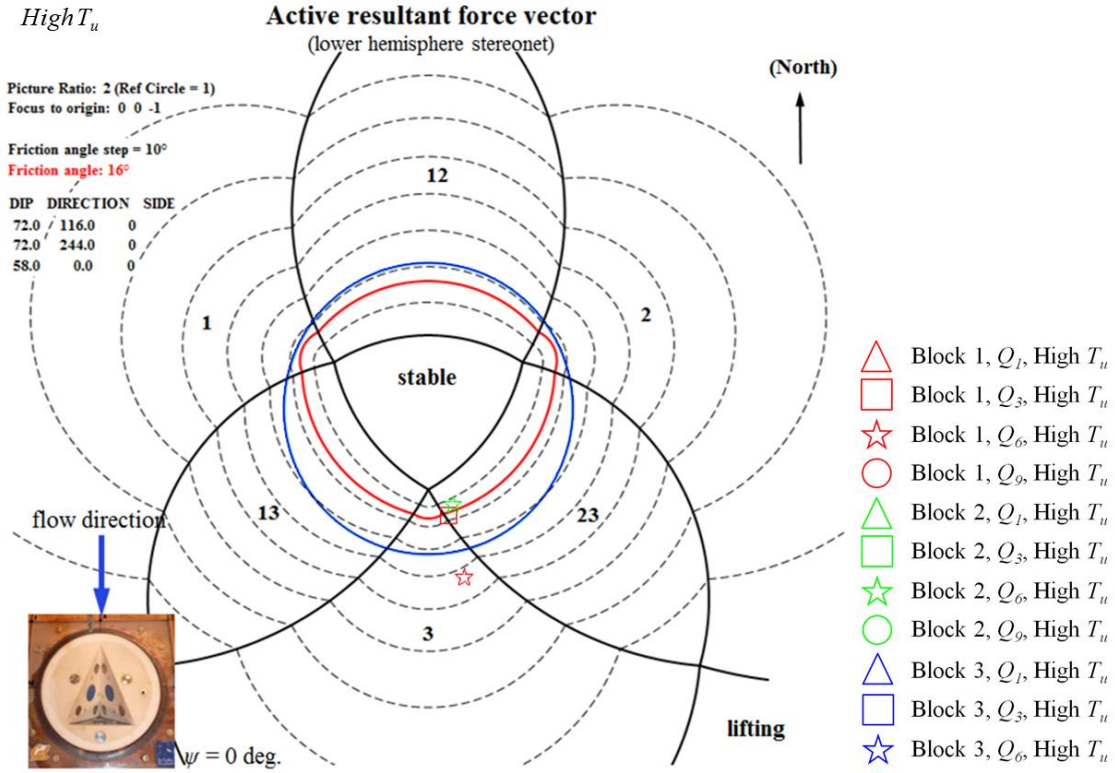
^a Angle of block face wrt flow direction, ^b Face is on upstream (u) or downstream (d) side of block



Limit equilibrium stereonet for calibration of C_p on block face 4

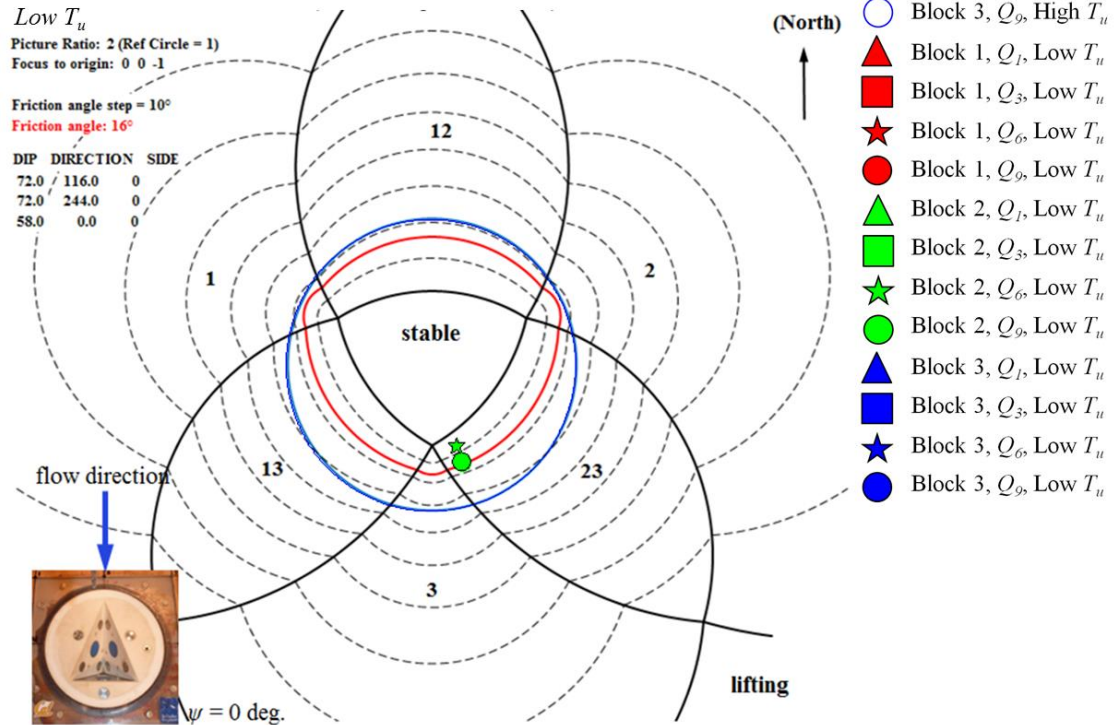
$\psi = 0$ deg.

High T_u



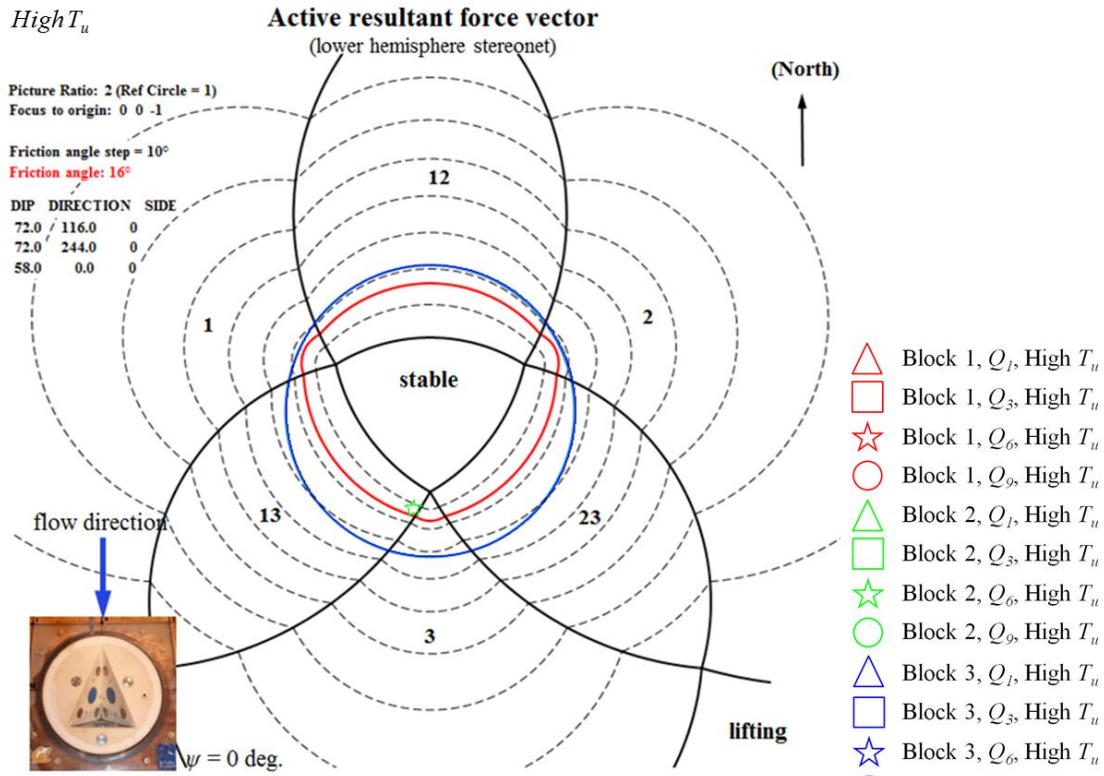
- △ Block 1, Q_1 , High T_u
- Block 1, Q_3 , High T_u
- ☆ Block 1, Q_6 , High T_u
- Block 1, Q_9 , High T_u
- △ Block 2, Q_1 , High T_u
- Block 2, Q_3 , High T_u
- ☆ Block 2, Q_6 , High T_u
- Block 2, Q_9 , High T_u
- △ Block 3, Q_1 , High T_u
- Block 3, Q_3 , High T_u
- ☆ Block 3, Q_6 , High T_u
- Block 3, Q_9 , High T_u
- ▲ Block 1, Q_1 , Low T_u
- Block 1, Q_3 , Low T_u
- ★ Block 1, Q_6 , Low T_u
- Block 1, Q_9 , Low T_u
- ▲ Block 2, Q_1 , Low T_u
- Block 2, Q_3 , Low T_u
- ★ Block 2, Q_6 , Low T_u
- Block 2, Q_9 , Low T_u
- ▲ Block 3, Q_1 , Low T_u
- Block 3, Q_3 , Low T_u
- ★ Block 3, Q_6 , Low T_u
- Block 3, Q_9 , Low T_u

Low T_u

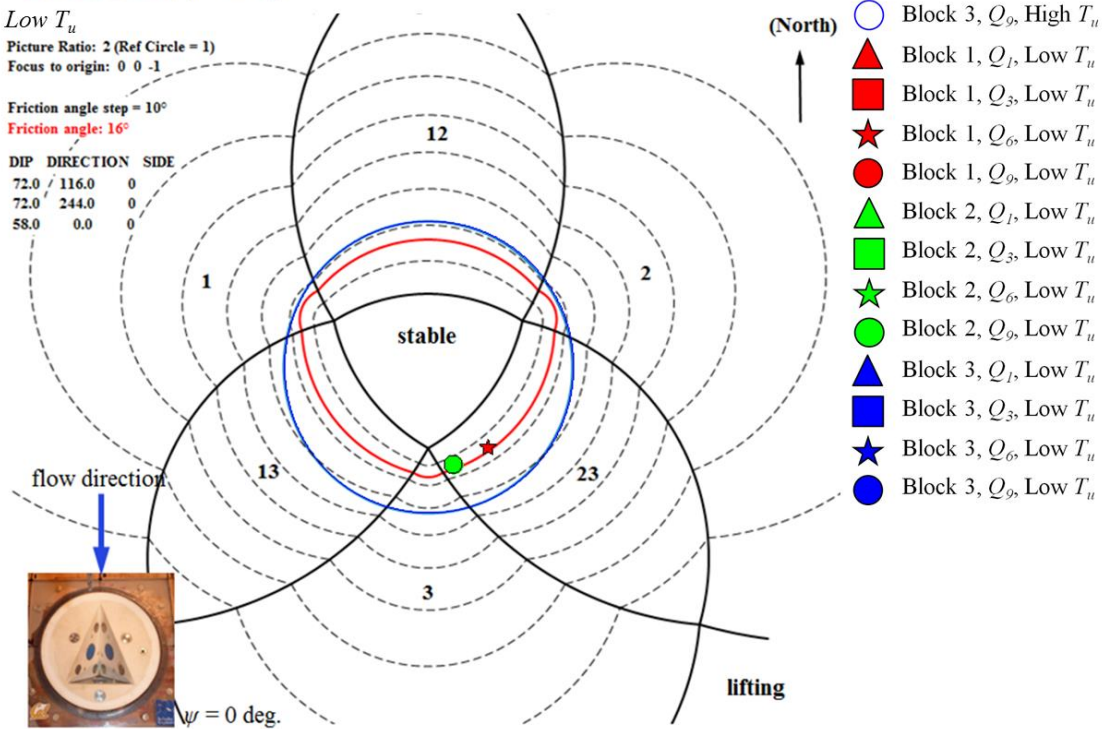


$\psi = 0$ deg.

High T_u

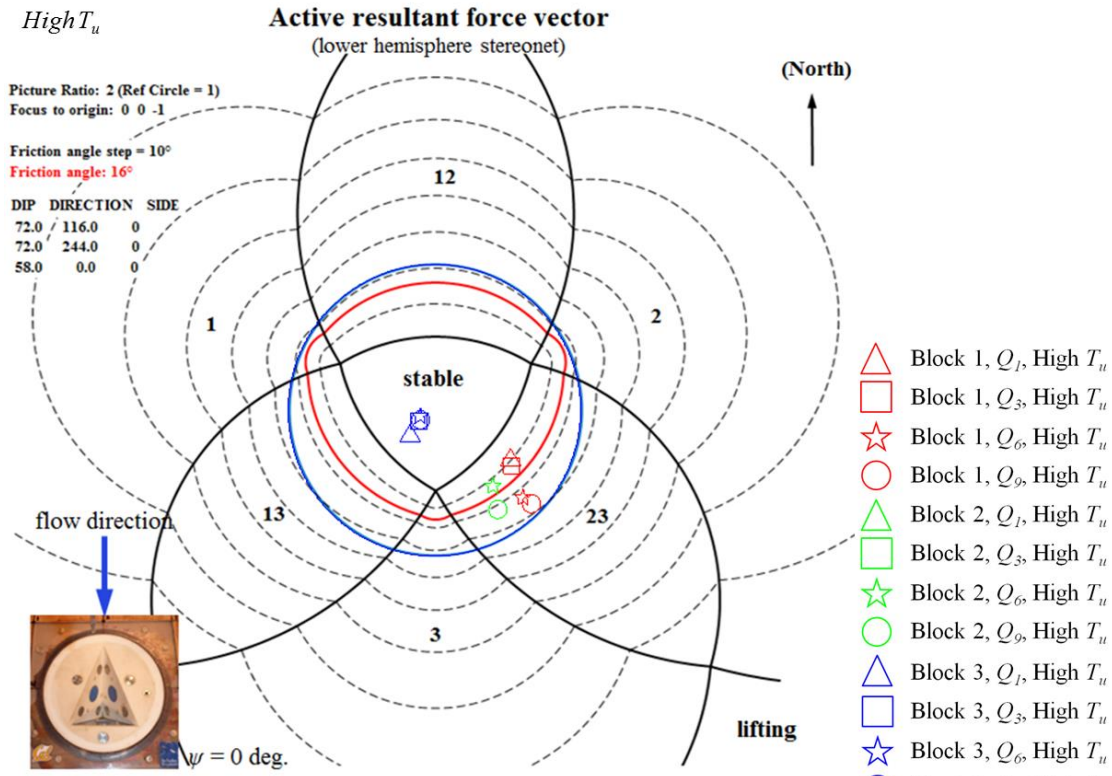


Low T_u

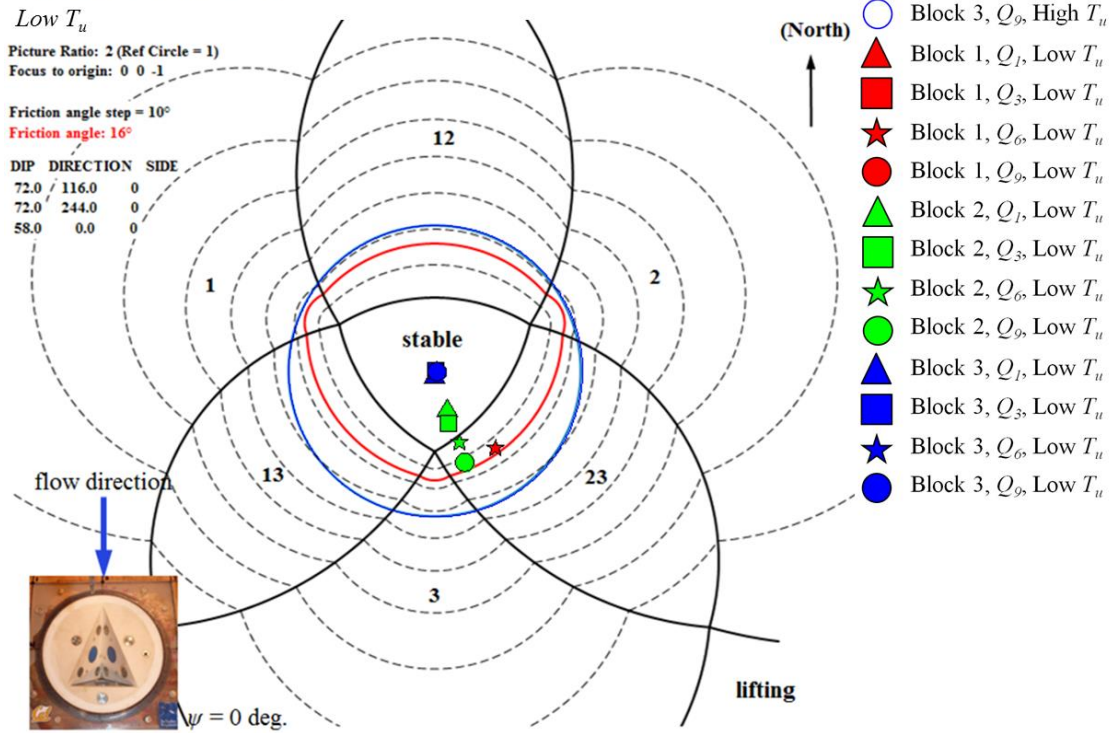


$\psi = 0c \text{ deg.}$

High T_u

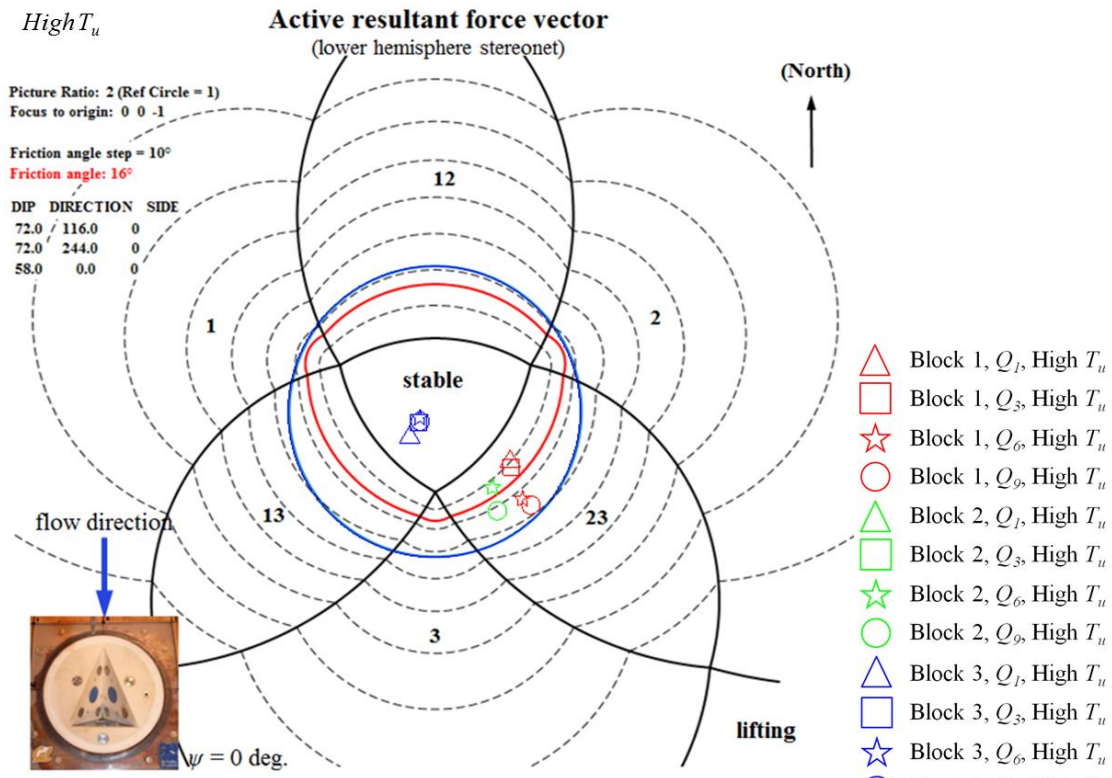


Low T_u

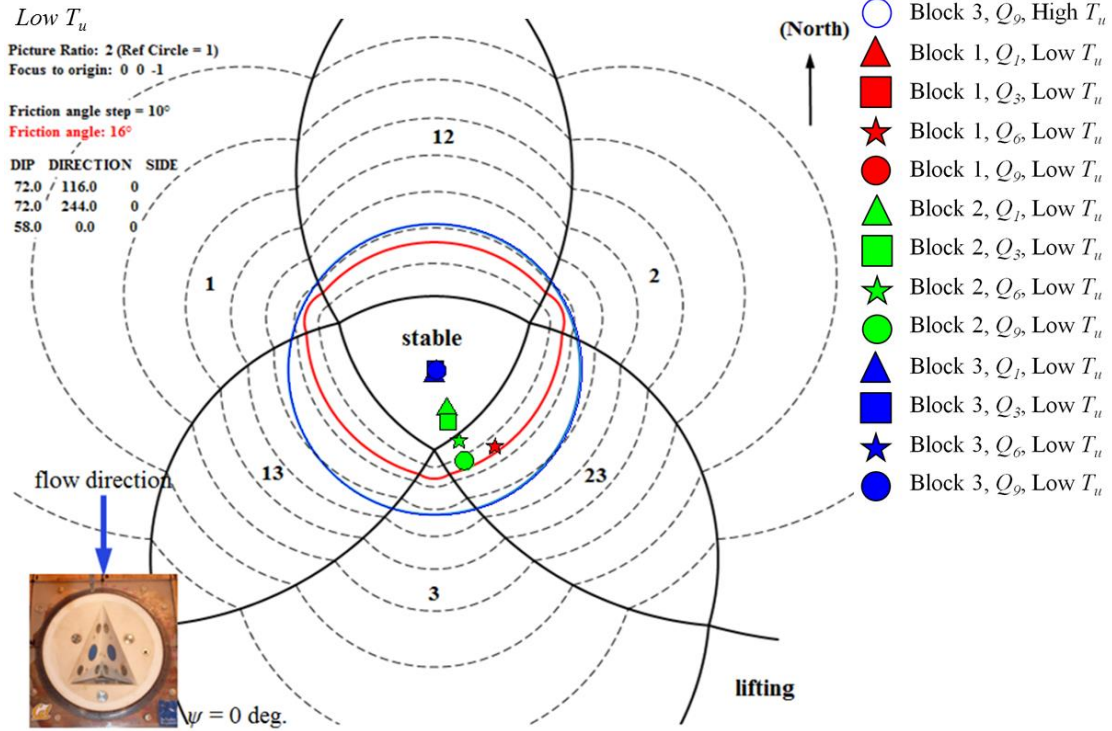


$\psi = 15 \text{ deg.}$

High T_u



Low T_u



$\psi = 30 \text{ deg.}$

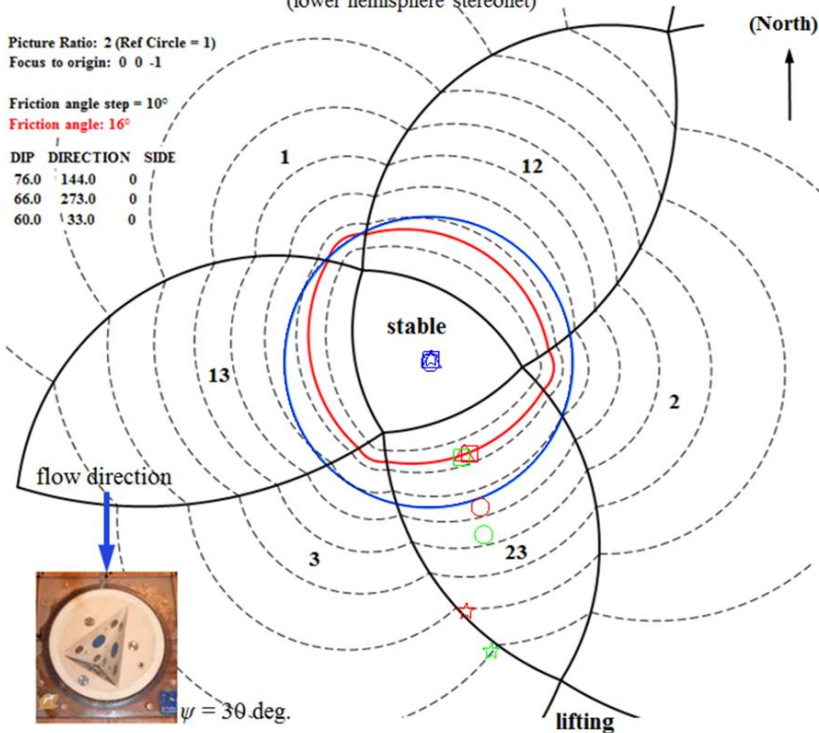
High T_u

Active resultant force vector
(lower hemisphere stereonet)

Picture Ratio: 2 (Ref Circle = 1)
Focus to origin: 0 0 -1

Friction angle step = 10°
Friction angle: 16°

DIP	DIRECTION	SIDE
76.0	144.0	0
66.0	273.0	0
60.0	33.0	0

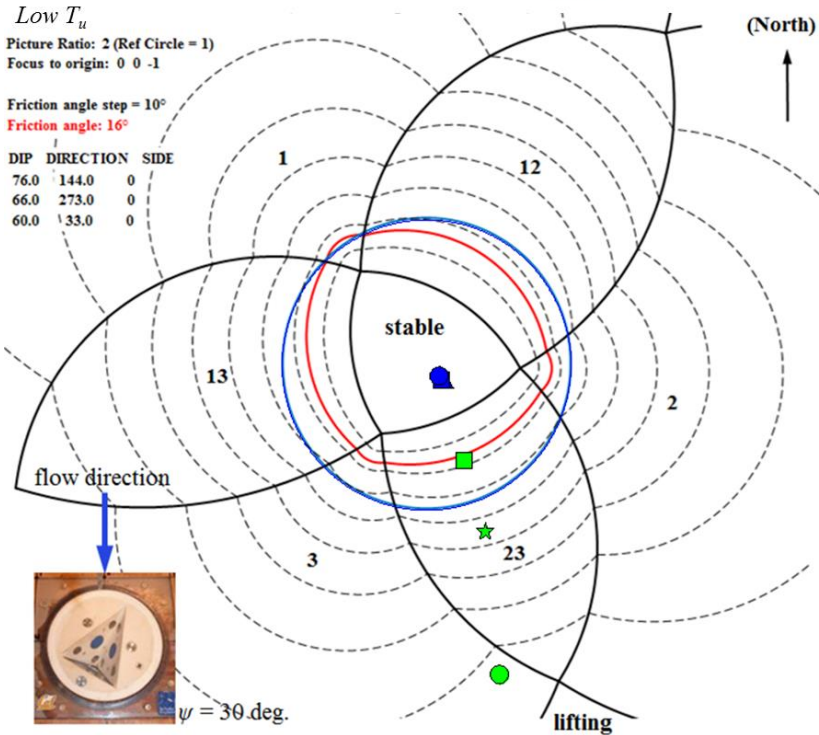


Low T_u

Picture Ratio: 2 (Ref Circle = 1)
Focus to origin: 0 0 -1

Friction angle step = 10°
Friction angle: 16°

DIP	DIRECTION	SIDE
76.0	144.0	0
66.0	273.0	0
60.0	33.0	0



- △ Block 1, Q_1 , High T_u
- Block 1, Q_3 , High T_u
- ☆ Block 1, Q_6 , High T_u
- Block 1, Q_9 , High T_u
- △ Block 2, Q_1 , High T_u
- Block 2, Q_3 , High T_u
- ☆ Block 2, Q_6 , High T_u
- Block 2, Q_9 , High T_u
- △ Block 3, Q_1 , High T_u
- Block 3, Q_3 , High T_u
- ☆ Block 3, Q_6 , High T_u
- Block 3, Q_9 , High T_u
- ▲ Block 1, Q_1 , Low T_u
- Block 1, Q_3 , Low T_u
- ★ Block 1, Q_6 , Low T_u
- Block 1, Q_9 , Low T_u
- ▲ Block 2, Q_1 , Low T_u
- Block 2, Q_3 , Low T_u
- ★ Block 2, Q_6 , Low T_u
- Block 2, Q_9 , Low T_u
- ▲ Block 3, Q_1 , Low T_u
- Block 3, Q_3 , Low T_u
- ★ Block 3, Q_6 , Low T_u
- Block 3, Q_9 , Low T_u

$\psi = 45 \text{ deg.}$

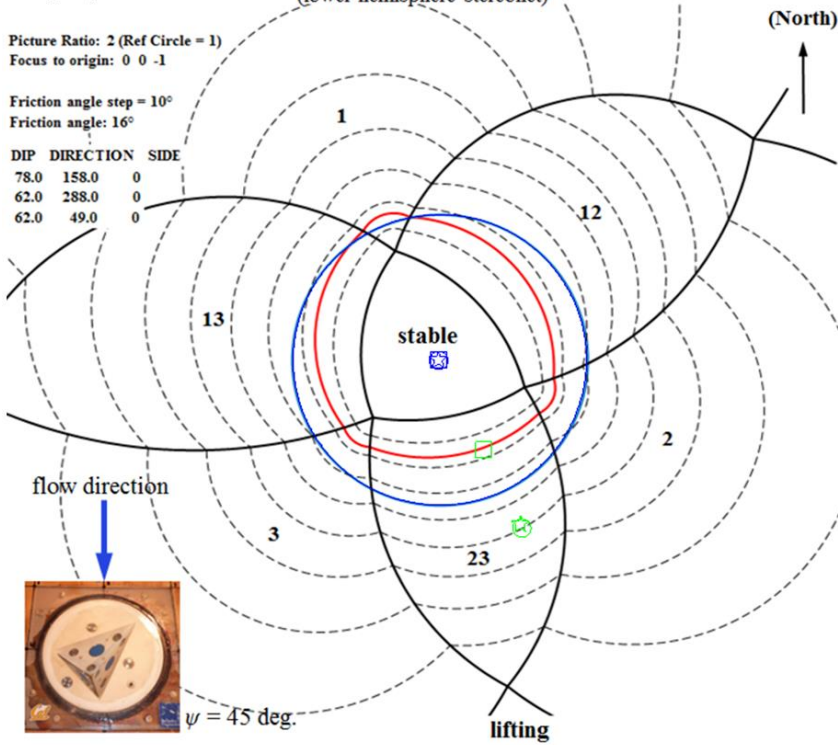
High T_u

Active resultant force vector
(lower hemisphere stereonet)

Picture Ratio: 2 (Ref Circle = 1)
Focus to origin: 0 0 -1

Friction angle step = 10°
Friction angle: 16°

DIP	DIRECTION	SIDE
78.0	158.0	0
62.0	288.0	0
62.0	49.0	0



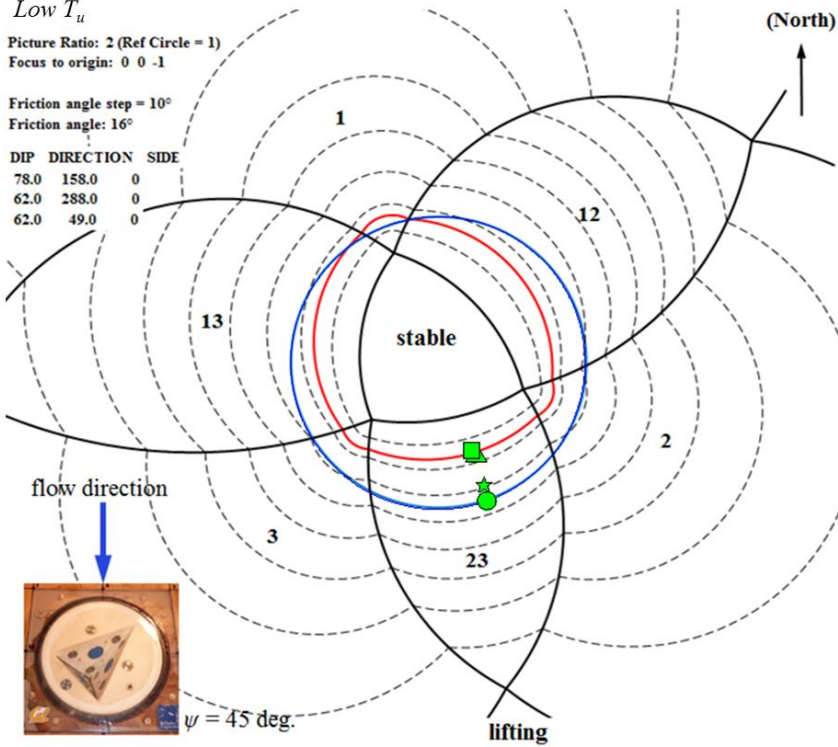
- △ Block 1, Q_1 , High T_u
- Block 1, Q_3 , High T_u
- ☆ Block 1, Q_6 , High T_u
- Block 1, Q_9 , High T_u
- △ Block 2, Q_1 , High T_u
- Block 2, Q_3 , High T_u
- ☆ Block 2, Q_6 , High T_u
- Block 2, Q_9 , High T_u
- △ Block 3, Q_1 , High T_u
- Block 3, Q_3 , High T_u
- ☆ Block 3, Q_6 , High T_u
- Block 3, Q_9 , High T_u
- ▲ Block 1, Q_1 , Low T_u
- Block 1, Q_3 , Low T_u
- ★ Block 1, Q_6 , Low T_u
- Block 1, Q_9 , Low T_u
- ▲ Block 2, Q_1 , Low T_u
- Block 2, Q_3 , Low T_u
- ★ Block 2, Q_6 , Low T_u
- Block 2, Q_9 , Low T_u
- ▲ Block 3, Q_1 , Low T_u
- Block 3, Q_3 , Low T_u
- ★ Block 3, Q_6 , Low T_u
- Block 3, Q_9 , Low T_u

Low T_u

Picture Ratio: 2 (Ref Circle = 1)
Focus to origin: 0 0 -1

Friction angle step = 10°
Friction angle: 16°

DIP	DIRECTION	SIDE
78.0	158.0	0
62.0	288.0	0
62.0	49.0	0



$\psi = 75 \text{ deg.}$

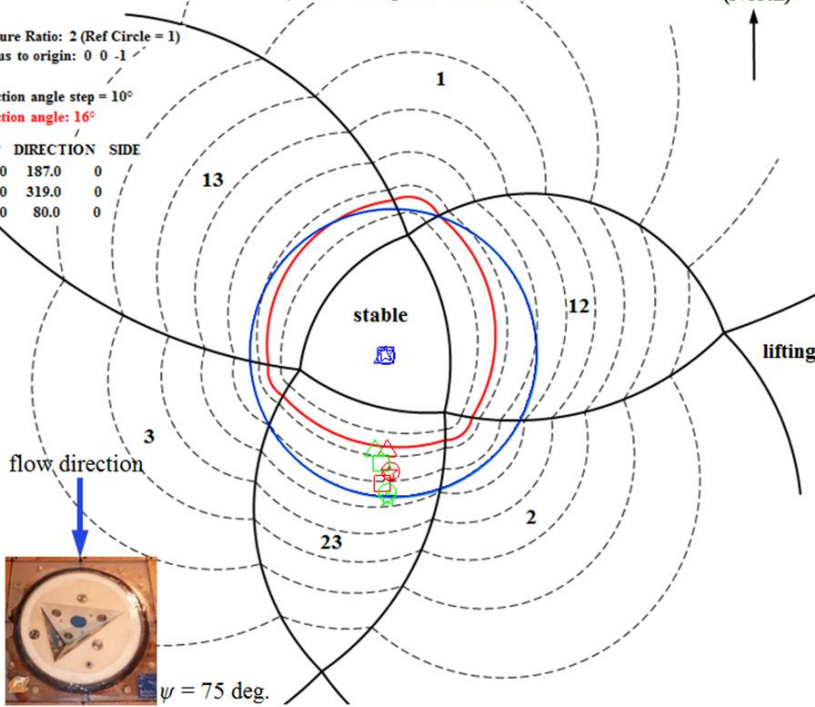
High T_u

Active resultant force vector
(lower hemisphere stereonet)

Picture Ratio: 2 (Ref Circle = 1)
Focus to origin: 0 0 -1

Friction angle step = 10°
Friction angle: 16°

DIP	DIRECTION	SIDE
79.0	187.0	0
57.0	319.0	0
67.0	80.0	0



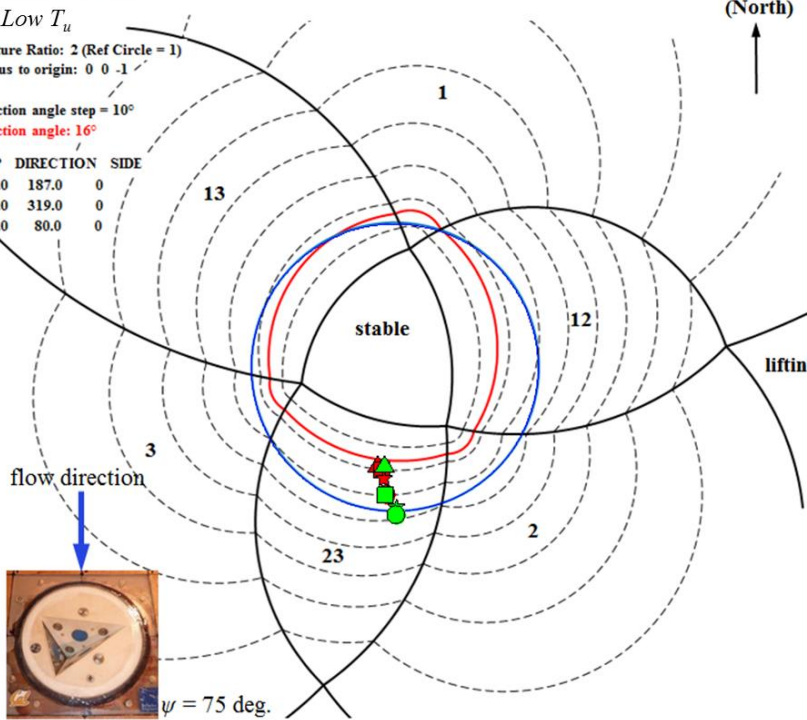
- △ Block 1, Q_1 , High T_u
- Block 1, Q_3 , High T_u
- ☆ Block 1, Q_6 , High T_u
- Block 1, Q_9 , High T_u
- △ Block 2, Q_1 , High T_u
- Block 2, Q_3 , High T_u
- ☆ Block 2, Q_6 , High T_u
- Block 2, Q_9 , High T_u
- △ Block 3, Q_1 , High T_u
- Block 3, Q_3 , High T_u
- ☆ Block 3, Q_6 , High T_u
- Block 3, Q_9 , High T_u
- ▲ Block 1, Q_1 , Low T_u
- Block 1, Q_3 , Low T_u
- ★ Block 1, Q_6 , Low T_u
- Block 1, Q_9 , Low T_u
- ▲ Block 2, Q_1 , Low T_u
- Block 2, Q_3 , Low T_u
- ★ Block 2, Q_6 , Low T_u
- Block 2, Q_9 , Low T_u
- ▲ Block 3, Q_1 , Low T_u
- Block 3, Q_3 , Low T_u
- ★ Block 3, Q_6 , Low T_u
- Block 3, Q_9 , Low T_u

Low T_u

Picture Ratio: 2 (Ref Circle = 1)
Focus to origin: 0 0 -1

Friction angle step = 10°
Friction angle: 16°

DIP	DIRECTION	SIDE
79.0	187.0	0
57.0	319.0	0
67.0	80.0	0

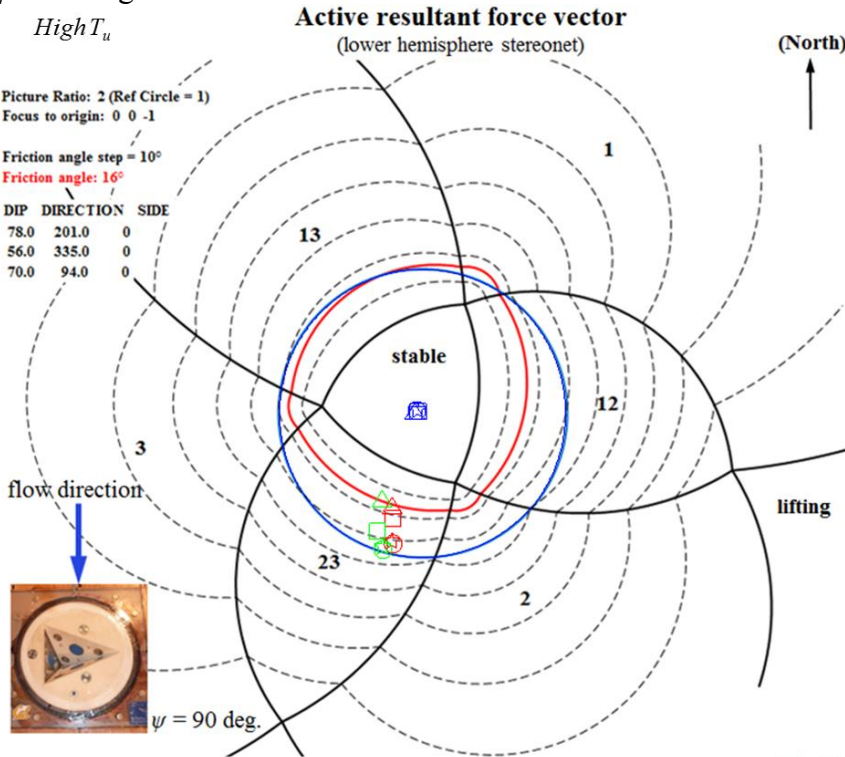


$\psi = 90$ deg.
High T_u

Picture Ratio: 2 (Ref Circle = 1)
 Focus to origin: 0 0 -1

Friction angle step = 10°
 Friction angle: 16°

DIP	DIRECTION	SIDE
78.0	201.0	0
56.0	335.0	0
70.0	94.0	0



(North)

(North)

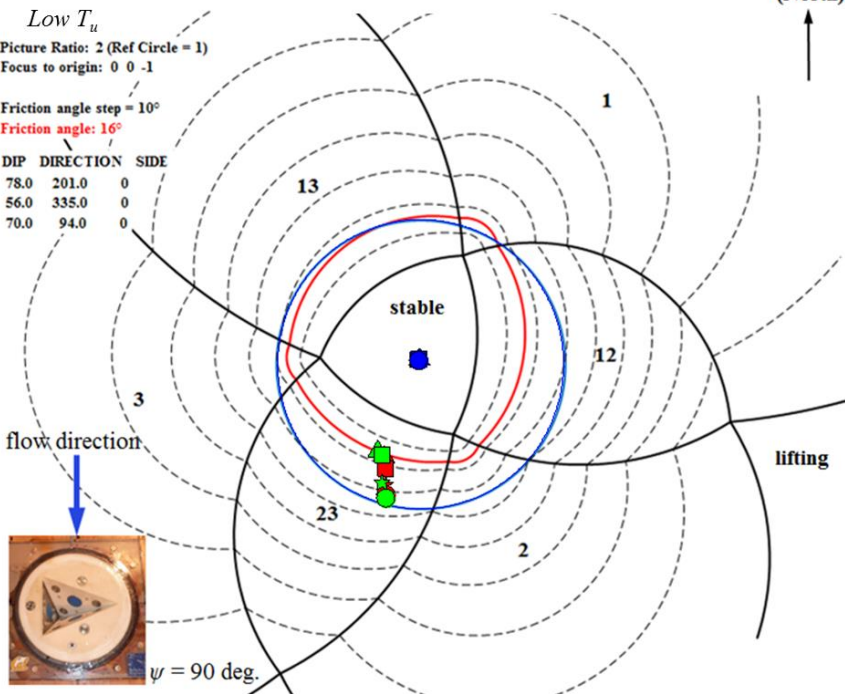
- △ Block 1, Q_1 , High T_u
- Block 1, Q_3 , High T_u
- ☆ Block 1, Q_6 , High T_u
- Block 1, Q_9 , High T_u
- △ Block 2, Q_1 , High T_u
- Block 2, Q_3 , High T_u
- ☆ Block 2, Q_6 , High T_u
- Block 2, Q_9 , High T_u
- △ Block 3, Q_1 , High T_u
- Block 3, Q_3 , High T_u
- ☆ Block 3, Q_6 , High T_u
- Block 3, Q_9 , High T_u
- ▲ Block 1, Q_1 , Low T_u
- Block 1, Q_3 , Low T_u
- ★ Block 1, Q_6 , Low T_u
- Block 1, Q_9 , Low T_u
- ▲ Block 2, Q_1 , Low T_u
- Block 2, Q_3 , Low T_u
- ★ Block 2, Q_6 , Low T_u
- Block 2, Q_9 , Low T_u
- ▲ Block 3, Q_1 , Low T_u
- Block 3, Q_3 , Low T_u
- ★ Block 3, Q_6 , Low T_u
- Block 3, Q_9 , Low T_u

Low T_u

Picture Ratio: 2 (Ref Circle = 1)
 Focus to origin: 0 0 -1

Friction angle step = 10°
 Friction angle: 16°

DIP	DIRECTION	SIDE
78.0	201.0	0
56.0	335.0	0
70.0	94.0	0



(North)

(North)

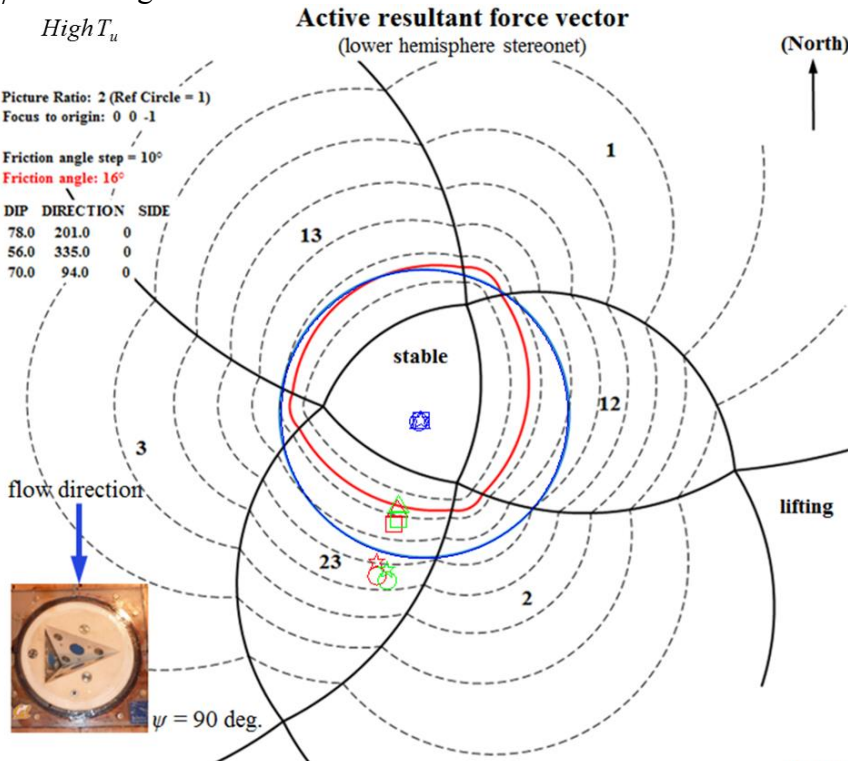
$\psi = 90$ deg.

High T_u

Picture Ratio: 2 (Ref Circle = 1)
Focus to origin: 0 0 -1

Friction angle step = 10°
Friction angle: 16°

DIP	DIRECTION	SIDE
78.0	201.0	0
56.0	335.0	0
70.0	94.0	0

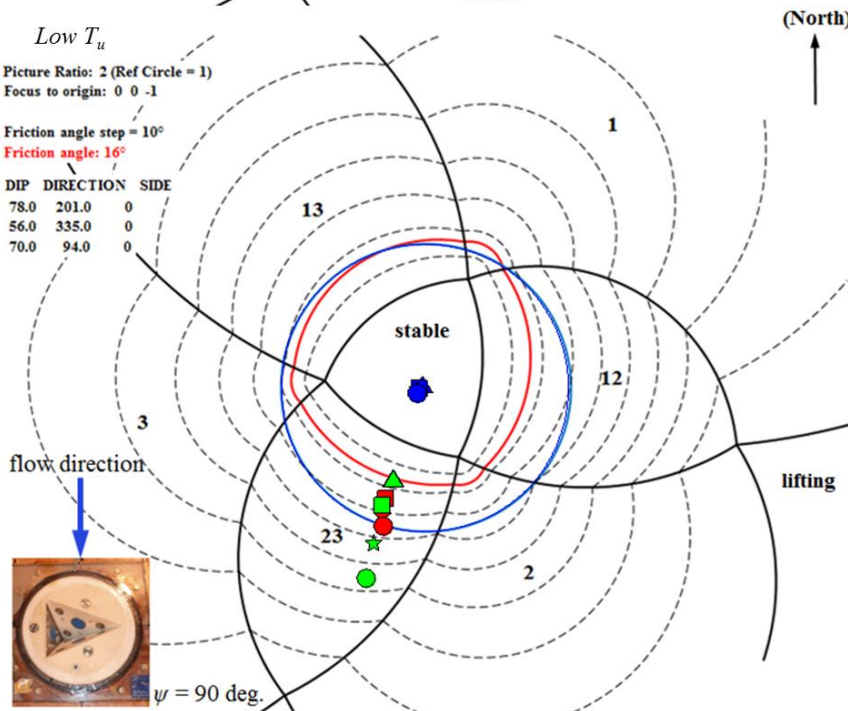


Low T_u

Picture Ratio: 2 (Ref Circle = 1)
Focus to origin: 0 0 -1

Friction angle step = 10°
Friction angle: 16°

DIP	DIRECTION	SIDE
78.0	201.0	0
56.0	335.0	0
70.0	94.0	0

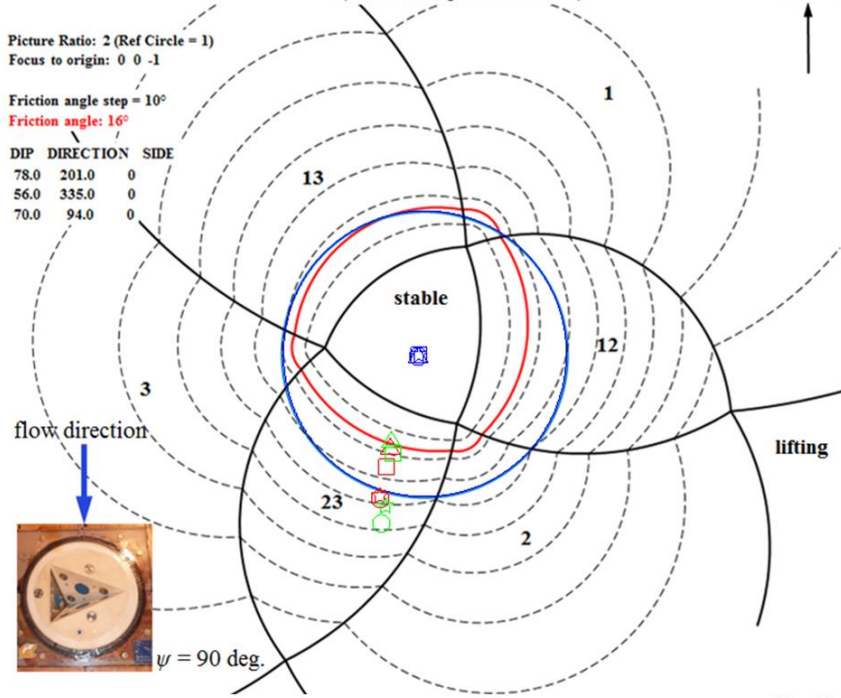


- △ Block 1, Q_1 , High T_u
- Block 1, Q_3 , High T_u
- ☆ Block 1, Q_6 , High T_u
- Block 1, Q_9 , High T_u
- △ Block 2, Q_1 , High T_u
- Block 2, Q_3 , High T_u
- ☆ Block 2, Q_6 , High T_u
- Block 2, Q_9 , High T_u
- △ Block 3, Q_1 , High T_u
- Block 3, Q_3 , High T_u
- ☆ Block 3, Q_6 , High T_u
- Block 3, Q_9 , High T_u
- △ Block 1, Q_1 , Low T_u
- Block 1, Q_3 , Low T_u
- ☆ Block 1, Q_6 , Low T_u
- Block 1, Q_9 , Low T_u
- △ Block 2, Q_1 , Low T_u
- Block 2, Q_3 , Low T_u
- ☆ Block 2, Q_6 , Low T_u
- Block 2, Q_9 , Low T_u
- △ Block 3, Q_1 , Low T_u
- Block 3, Q_3 , Low T_u
- ☆ Block 3, Q_6 , Low T_u
- Block 3, Q_9 , Low T_u

$\psi = 90c$ deg.

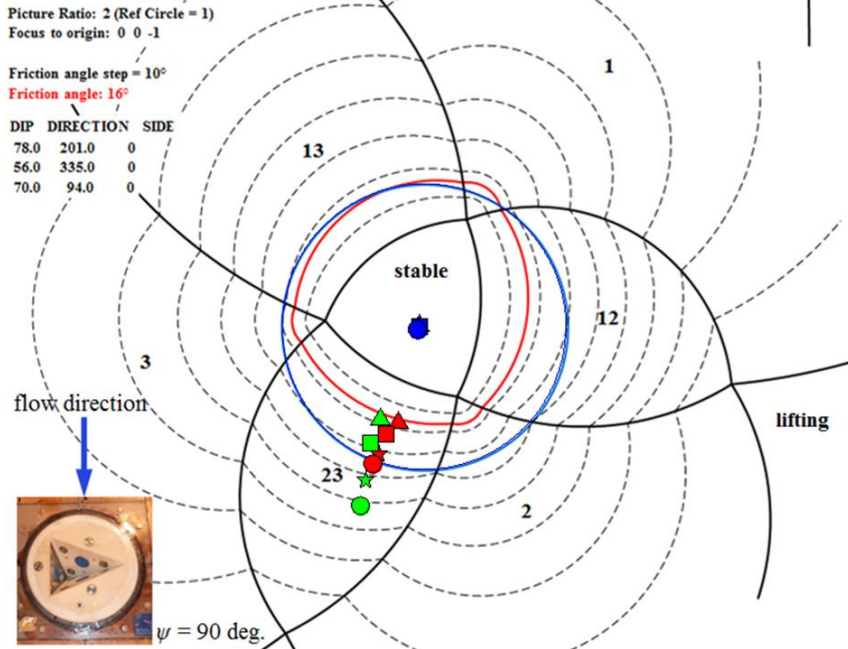
High T_u

Active resultant force vector
(lower hemisphere stereonet)

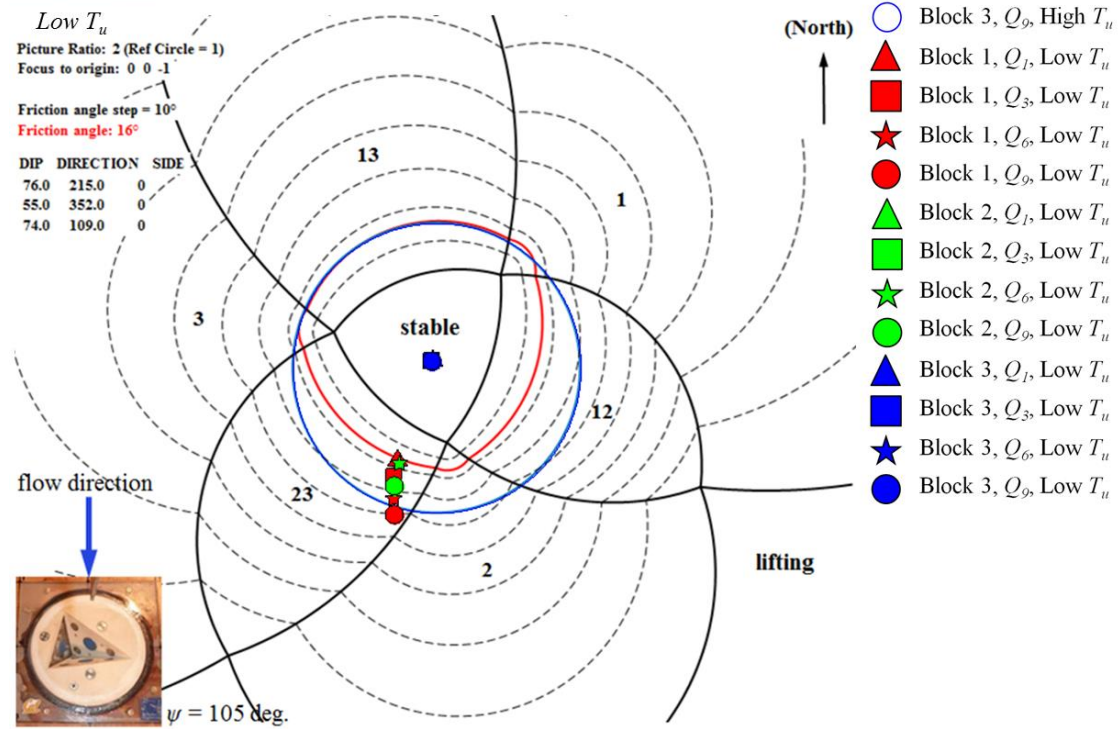
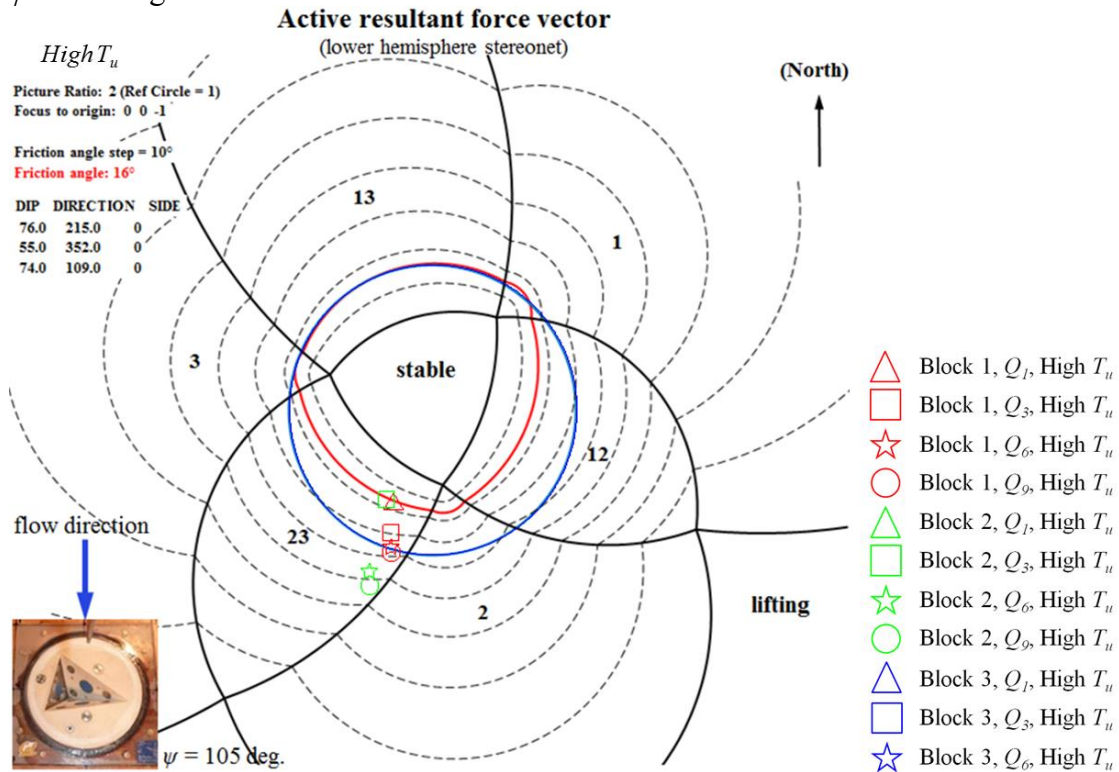


- △ Block 1, Q_1 , High T_u
- Block 1, Q_3 , High T_u
- ☆ Block 1, Q_6 , High T_u
- Block 1, Q_9 , High T_u
- △ Block 2, Q_1 , High T_u
- Block 2, Q_3 , High T_u
- ☆ Block 2, Q_6 , High T_u
- Block 2, Q_9 , High T_u
- △ Block 3, Q_1 , High T_u
- Block 3, Q_3 , High T_u
- ☆ Block 3, Q_6 , High T_u
- Block 3, Q_9 , High T_u
- △ Block 1, Q_1 , Low T_u
- Block 1, Q_3 , Low T_u
- ☆ Block 1, Q_6 , Low T_u
- Block 1, Q_9 , Low T_u
- △ Block 2, Q_1 , Low T_u
- Block 2, Q_3 , Low T_u
- ☆ Block 2, Q_6 , Low T_u
- Block 2, Q_9 , Low T_u
- △ Block 3, Q_1 , Low T_u
- Block 3, Q_3 , Low T_u
- ☆ Block 3, Q_6 , Low T_u
- Block 3, Q_9 , Low T_u

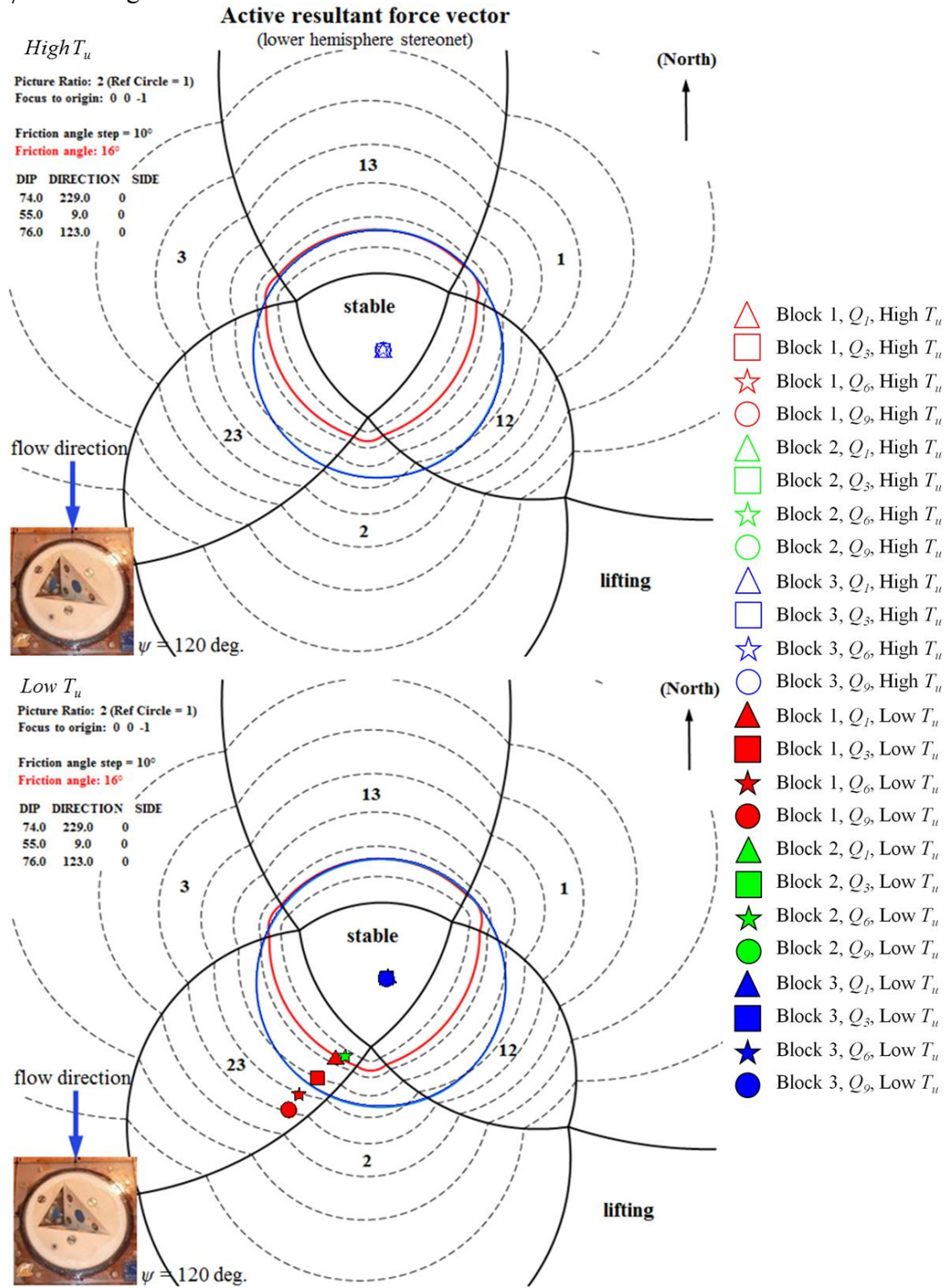
Low T_u



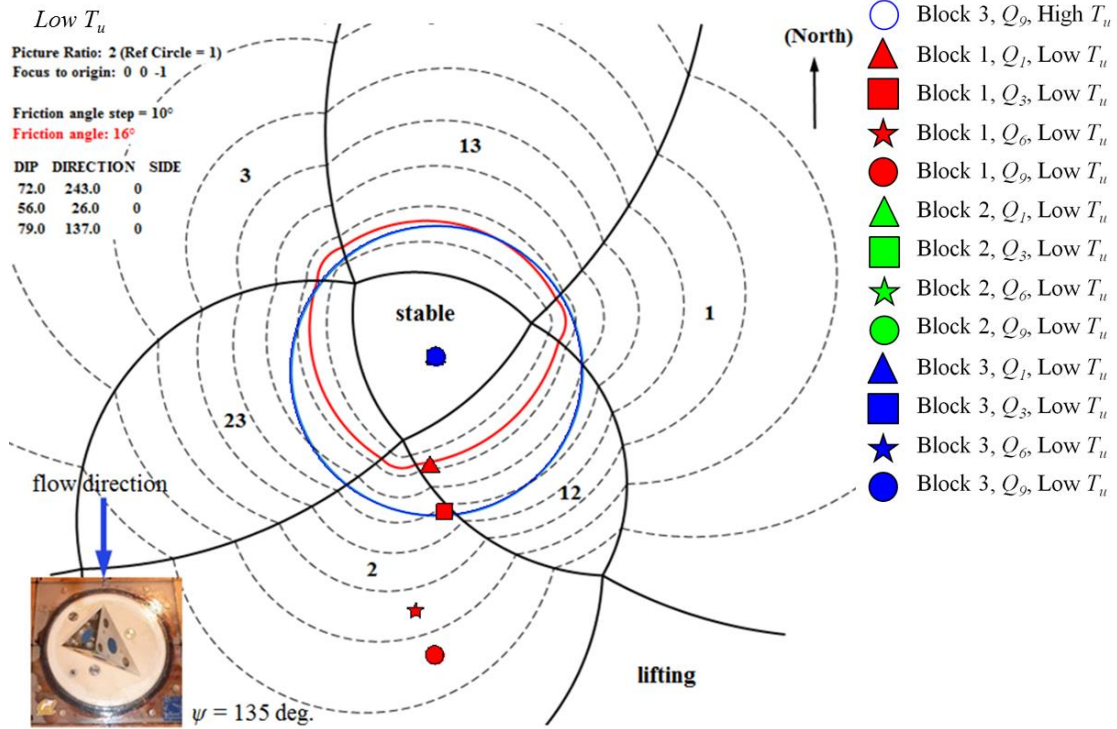
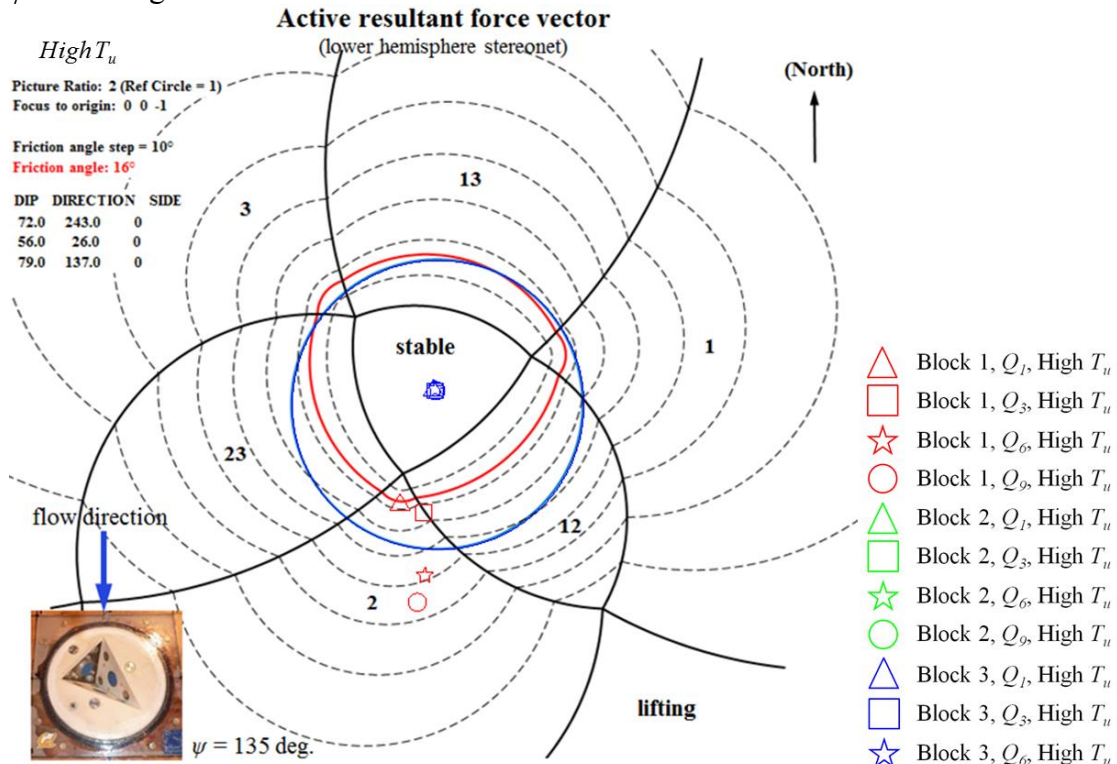
$\psi = 105 \text{ deg.}$



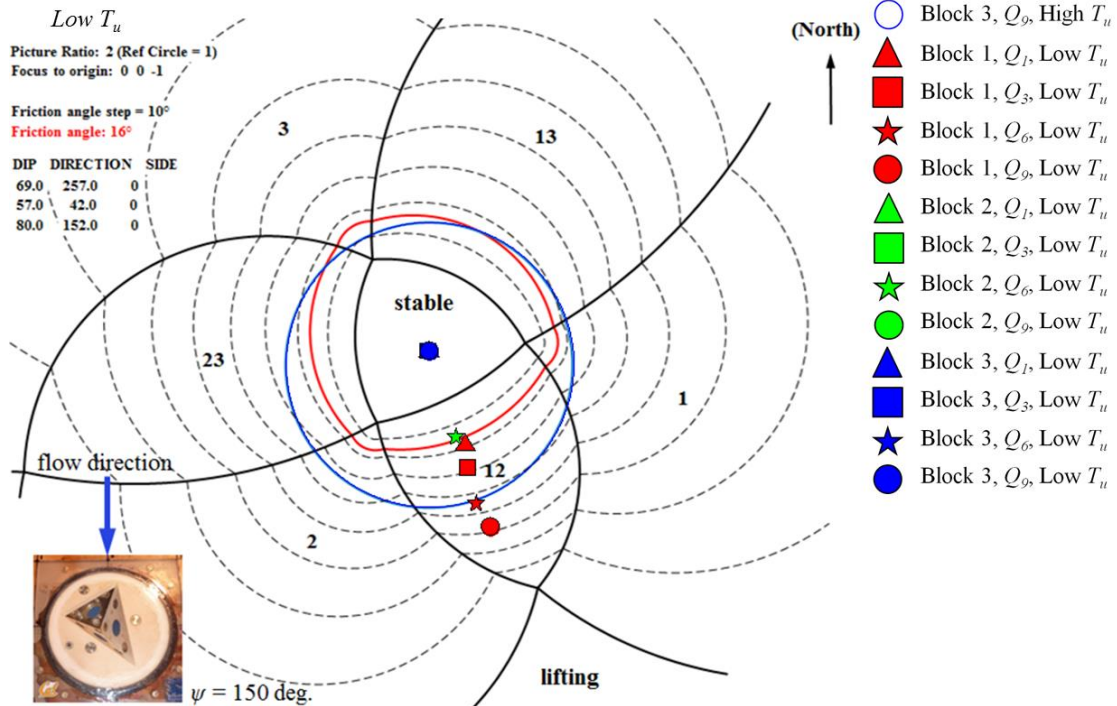
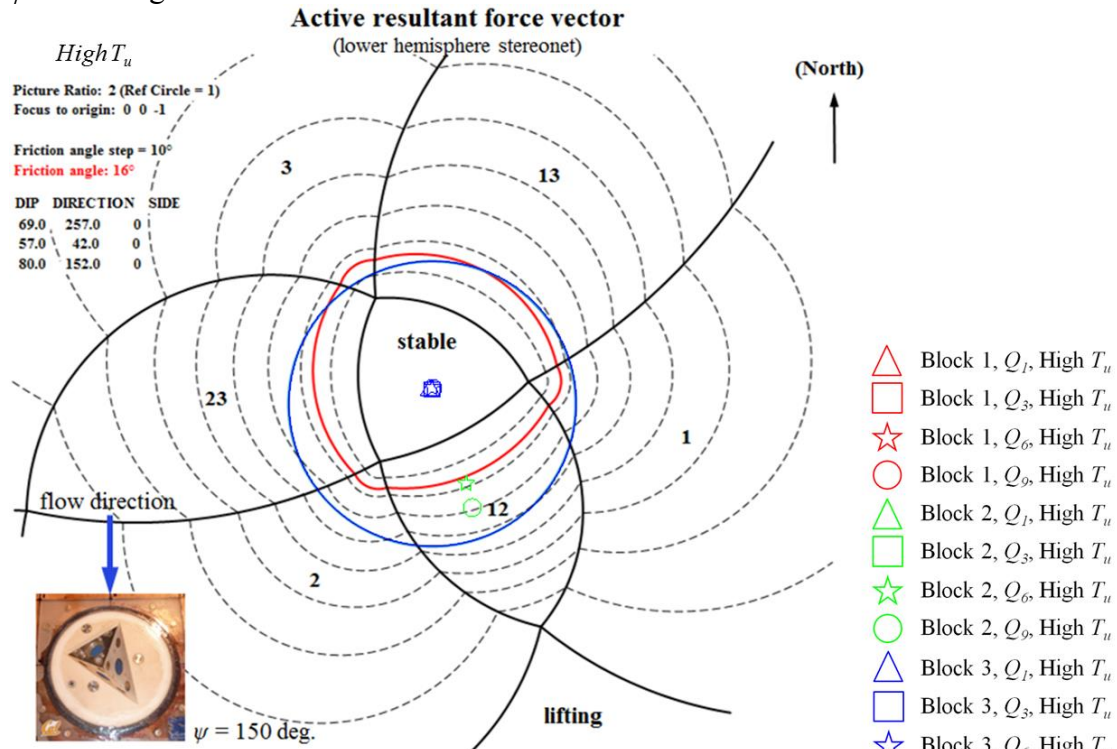
$\psi = 120$ deg.



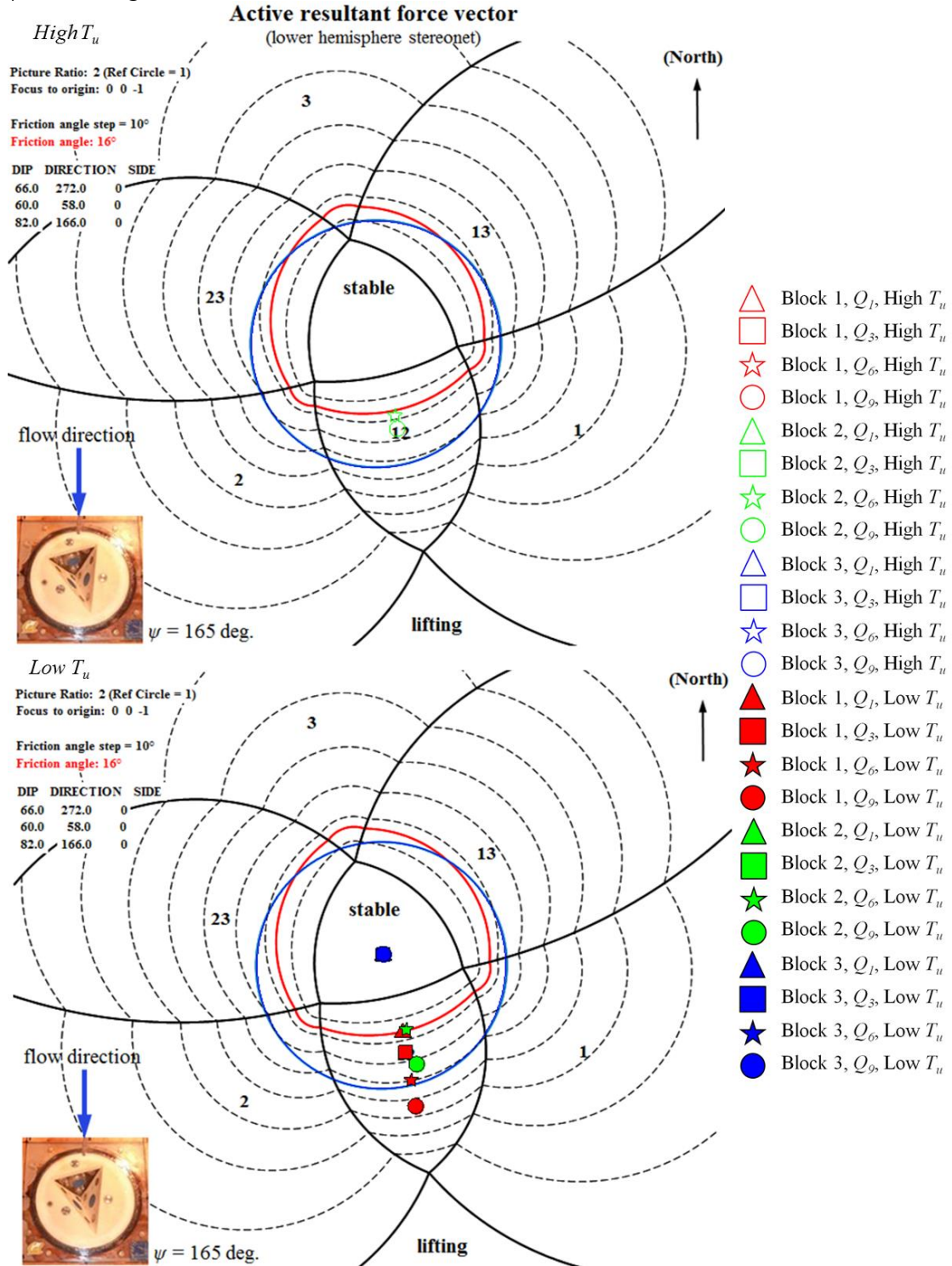
$\psi = 135$ deg.



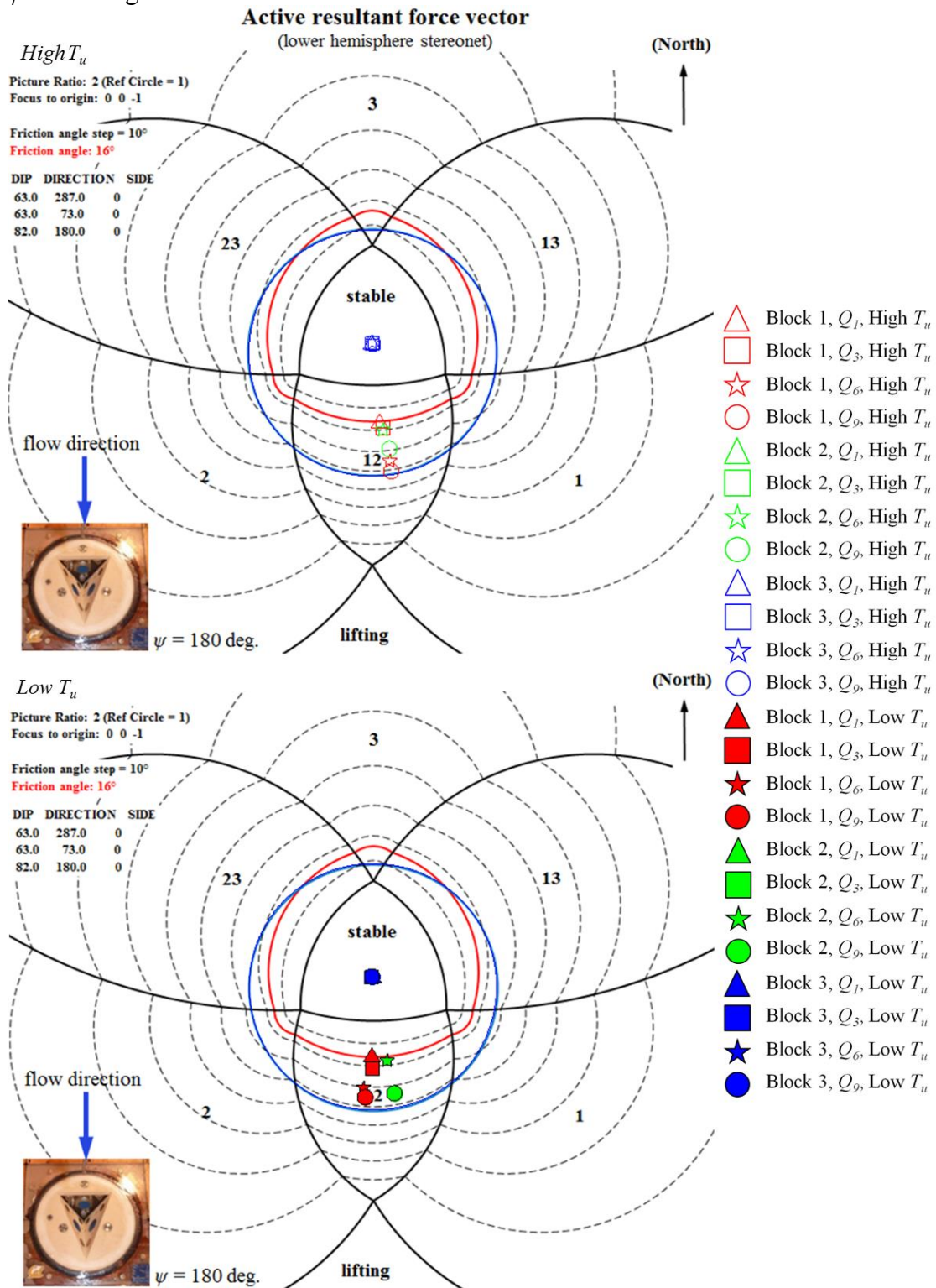
$\psi = 150$ deg.



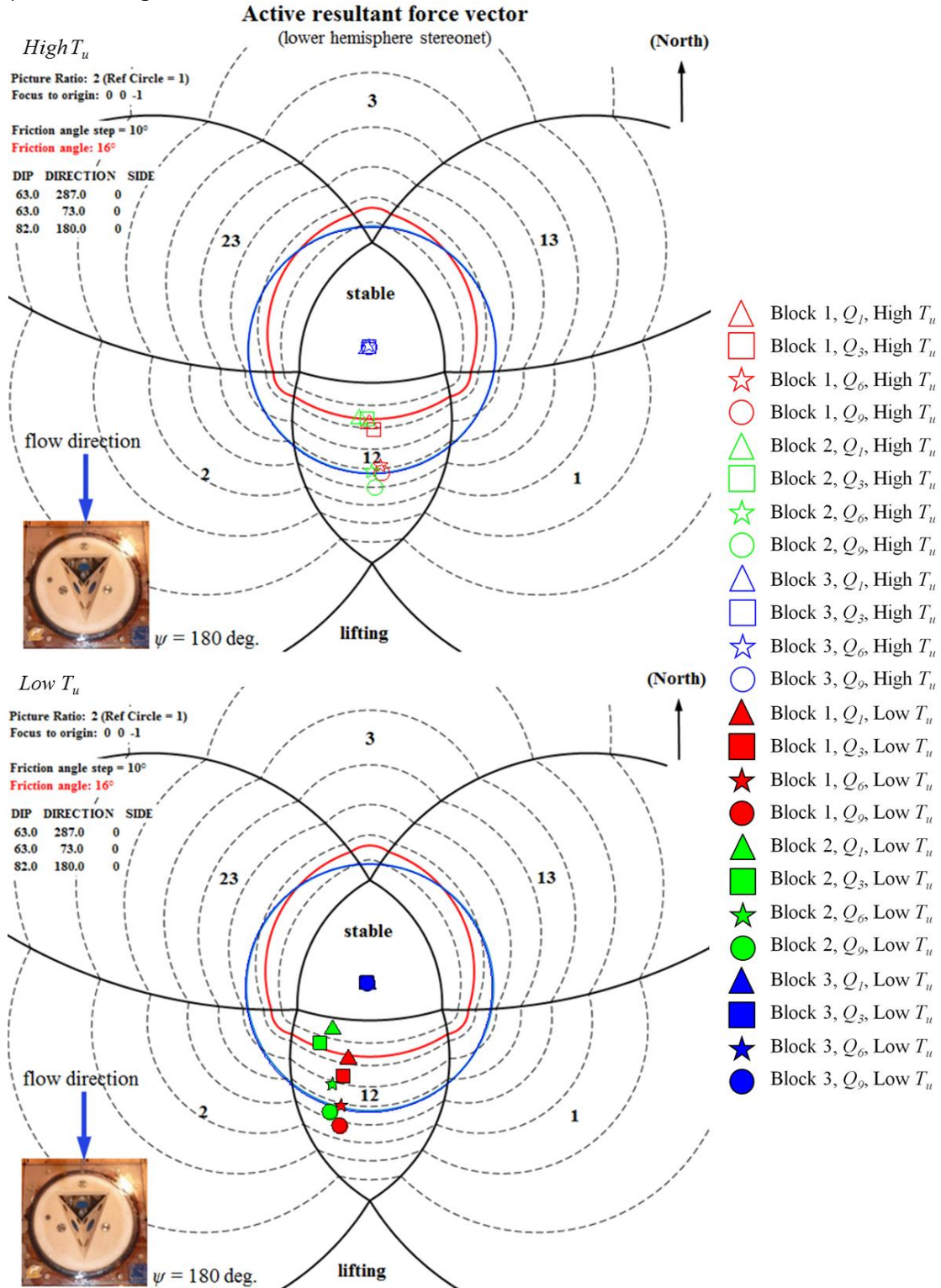
$\psi = 165$ deg.



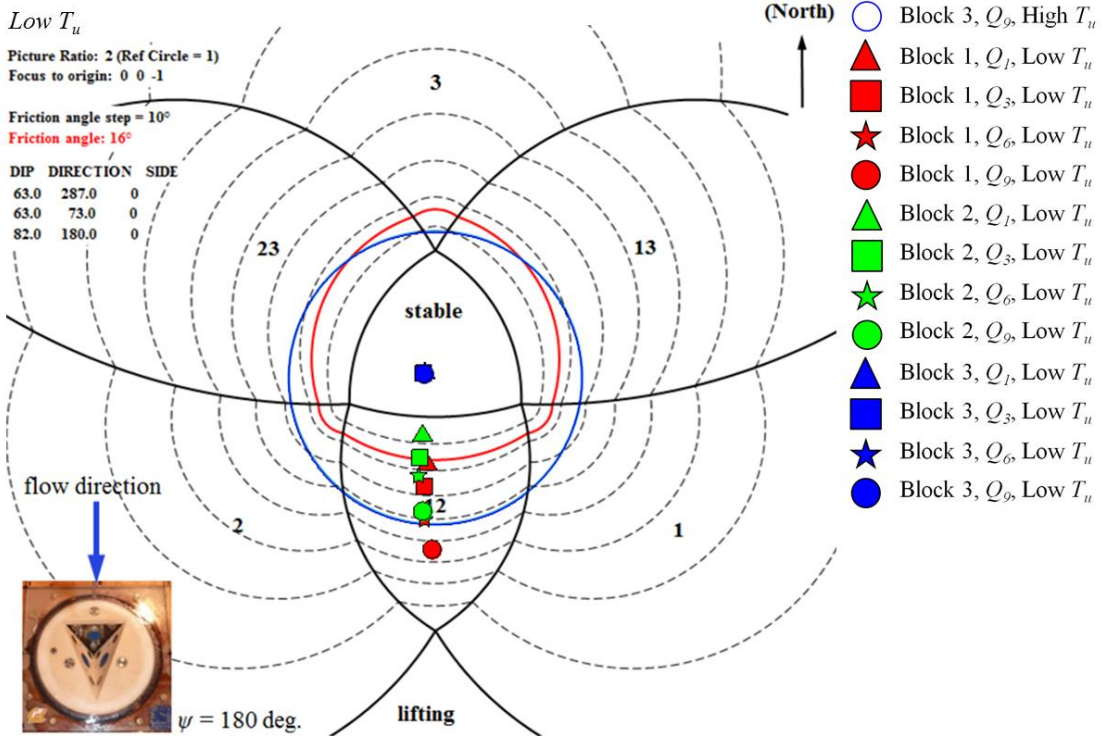
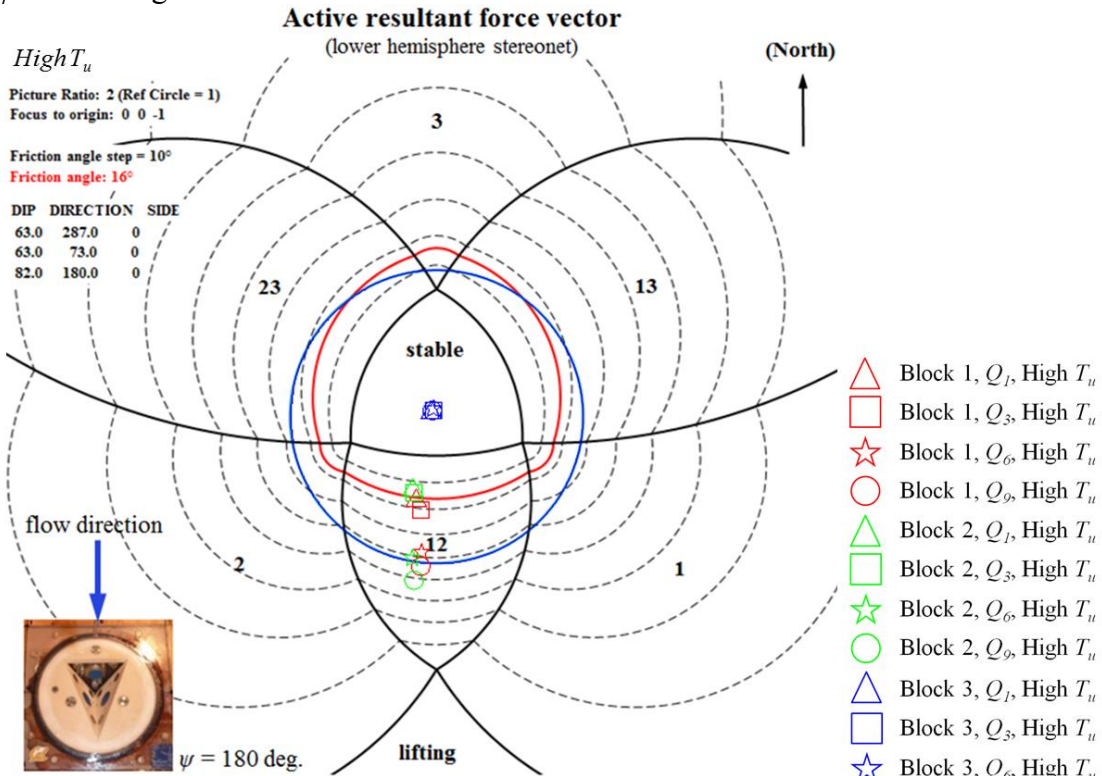
$\psi = 180$ deg.



$\psi = 180$ deg.



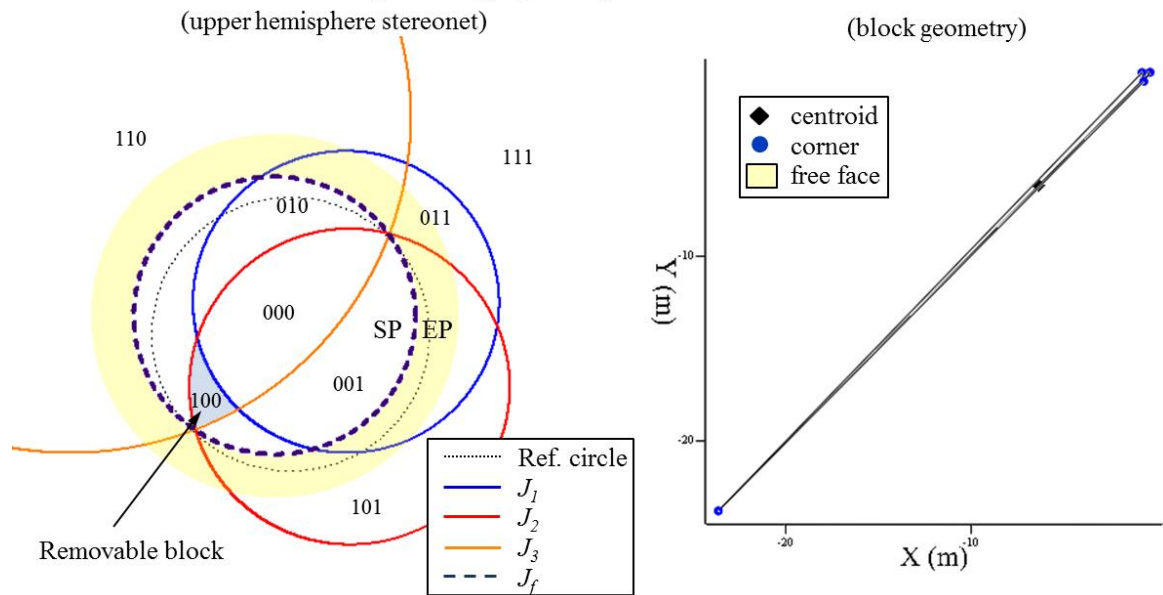
$\psi = 180$ deg.



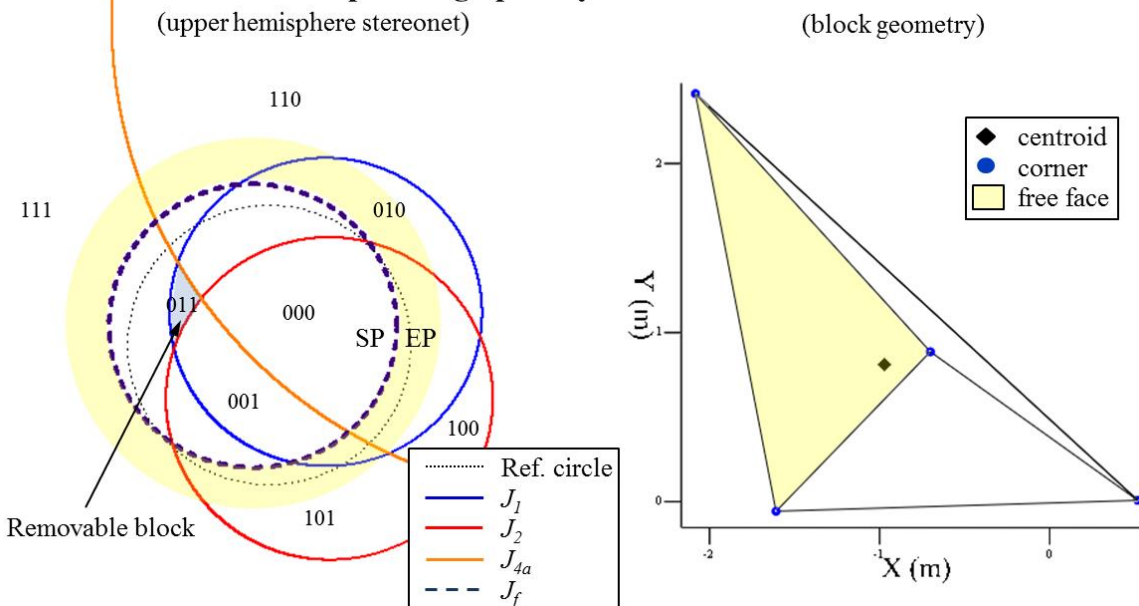
Appendix G – Block theory analysis

Spaulding Dam No. 2 spillway – removable blocks

Spaulding spillway - removable block 1



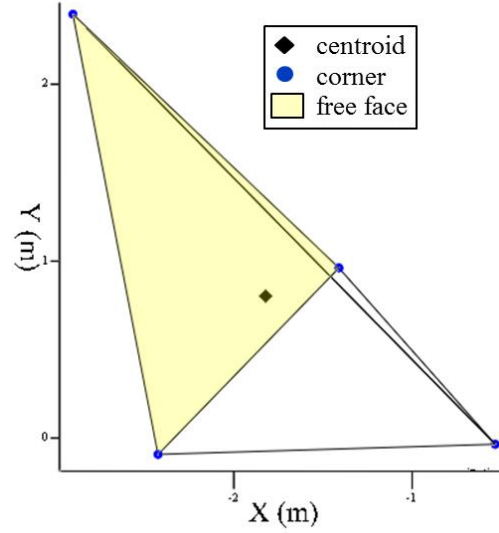
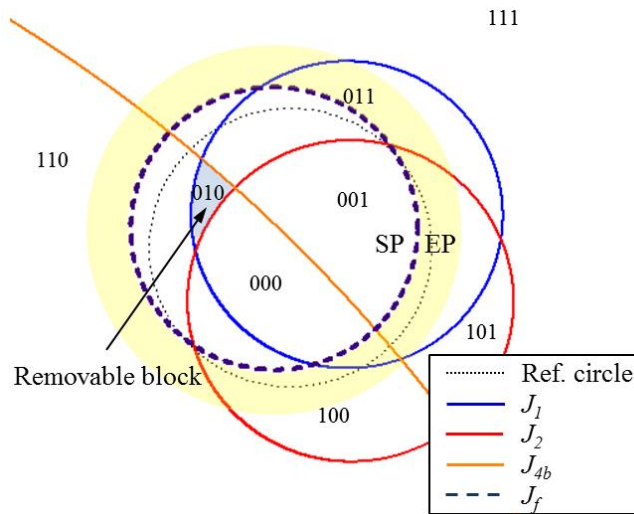
Spaulding spillway - removable block 2



Spaulding spillway - removable block 3

(upper hemisphere stereonet)

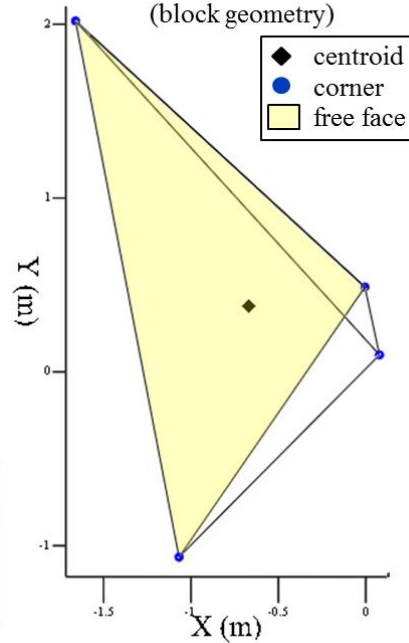
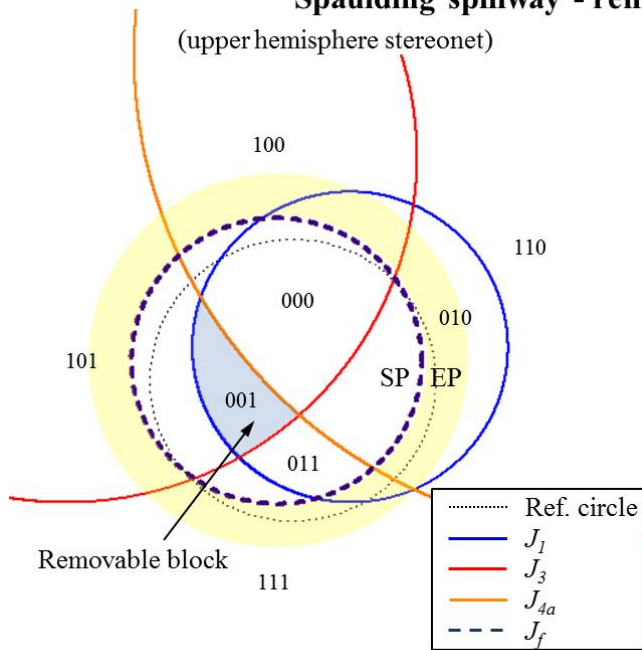
(block geometry)



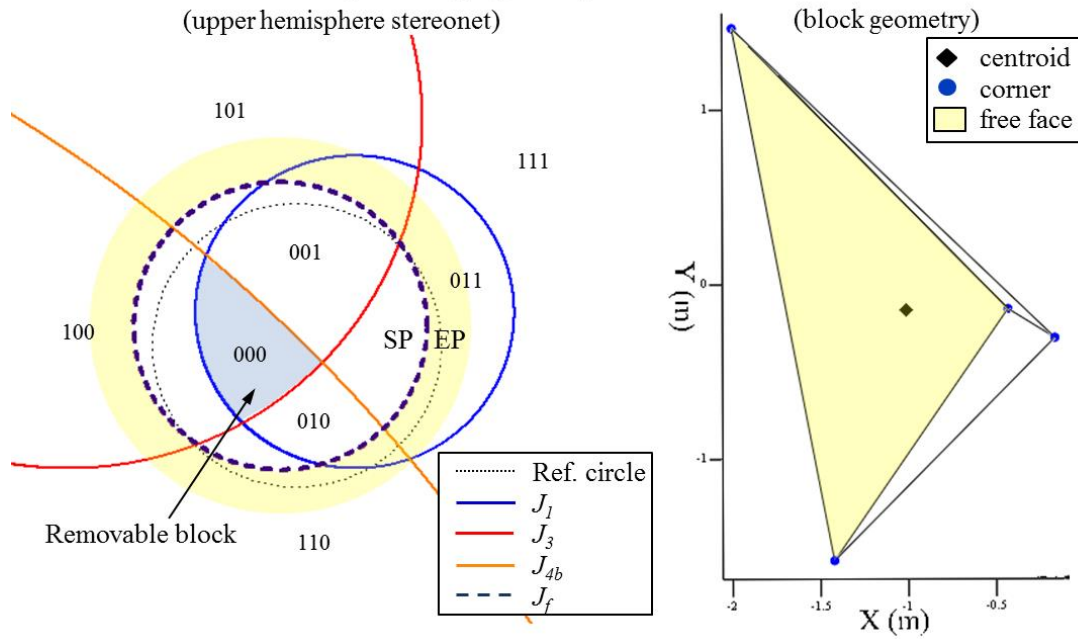
Spaulding spillway - removable block 4

(upper hemisphere stereonet)

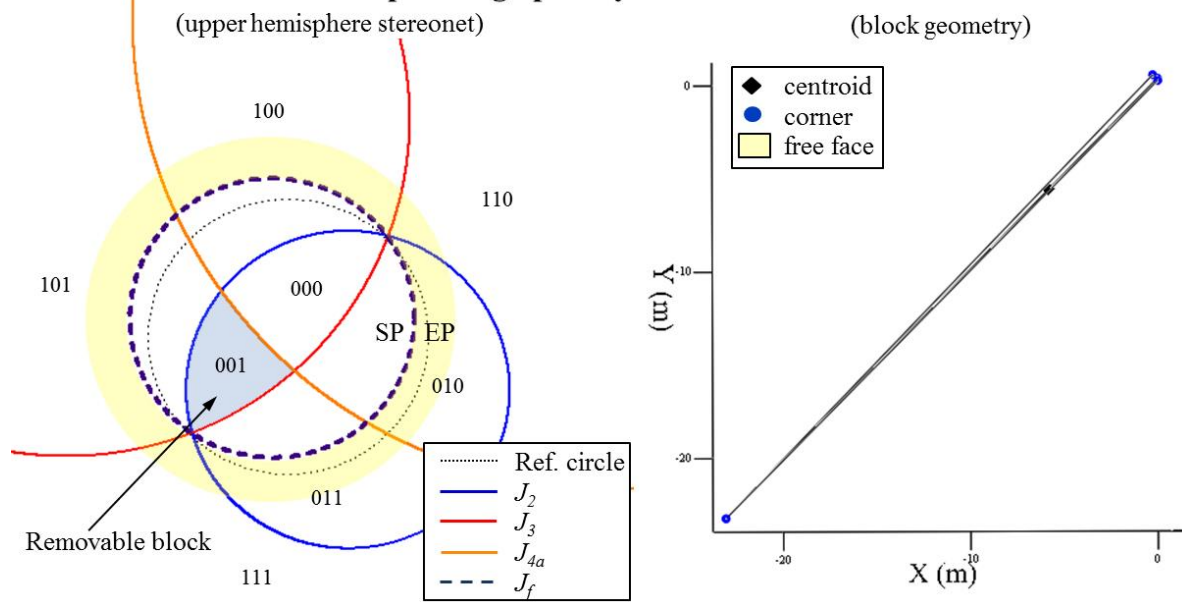
(block geometry)



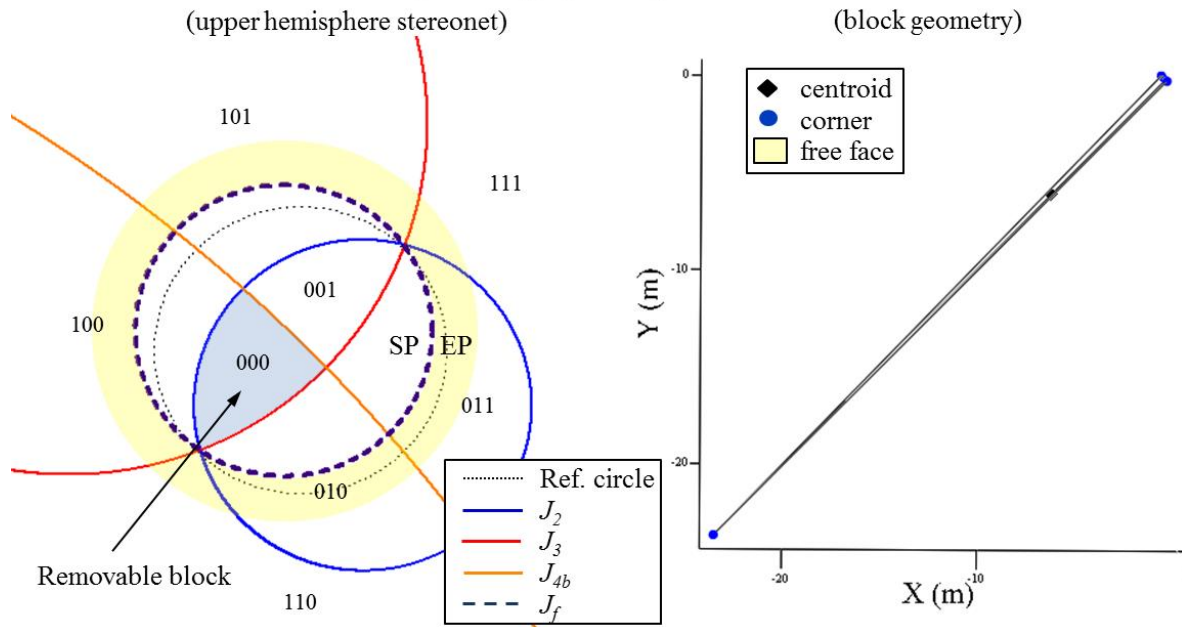
Spaulding spillway - removable block 5



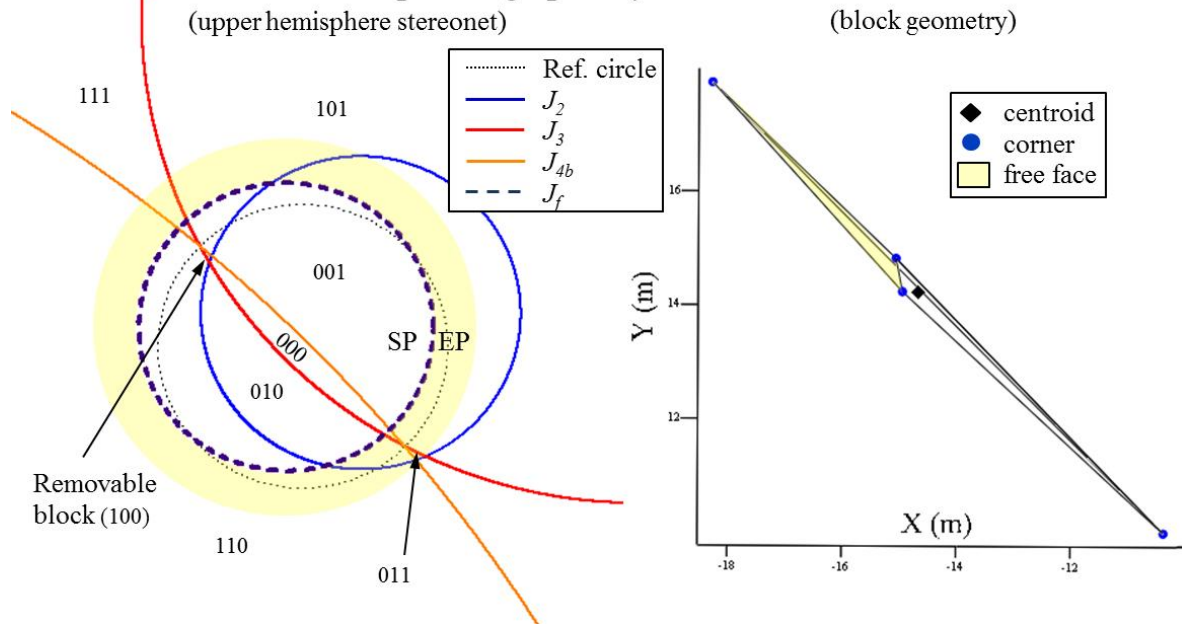
Spaulding spillway - removable block 6



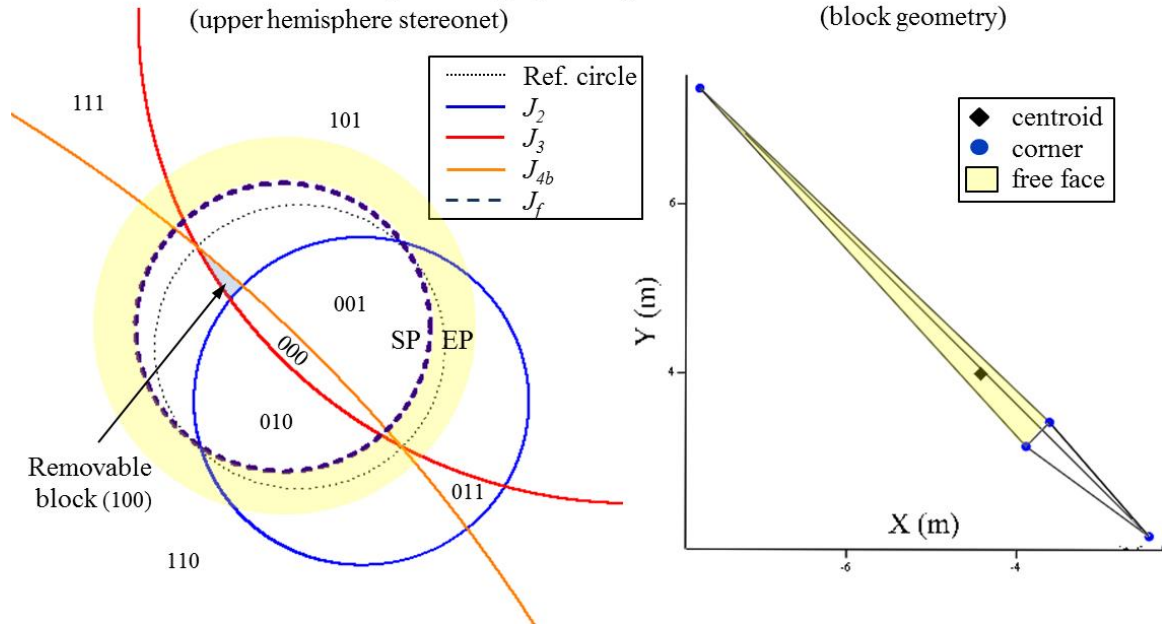
Spaulding spillway - removable block 7



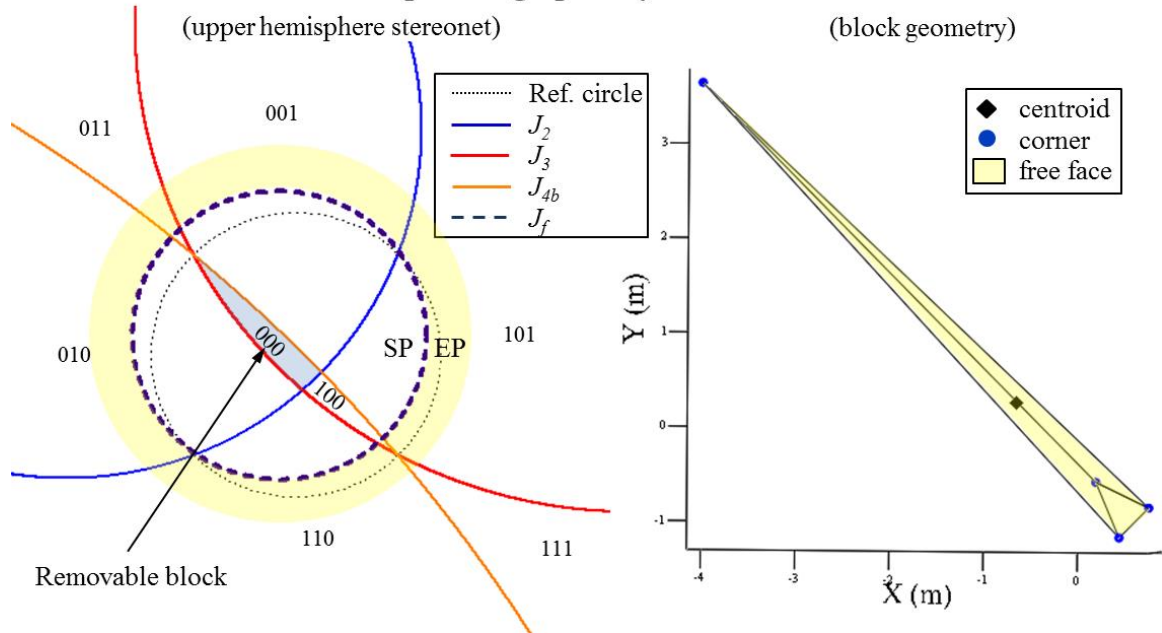
Spaulding spillway - removable block 8



Spaulding spillway - removable block 9

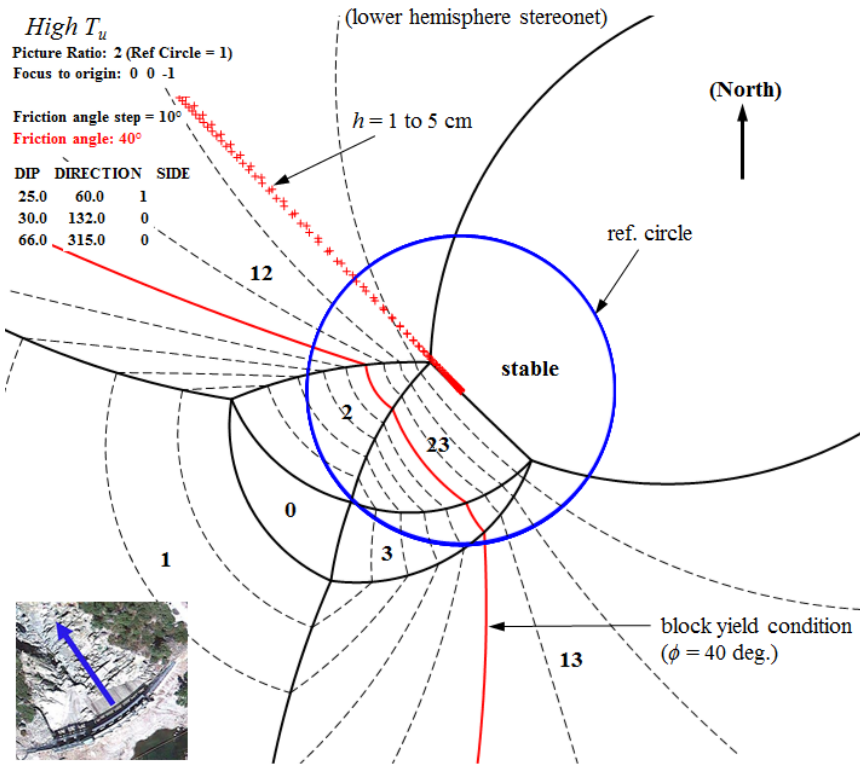


Spaulding spillway - removable block 10

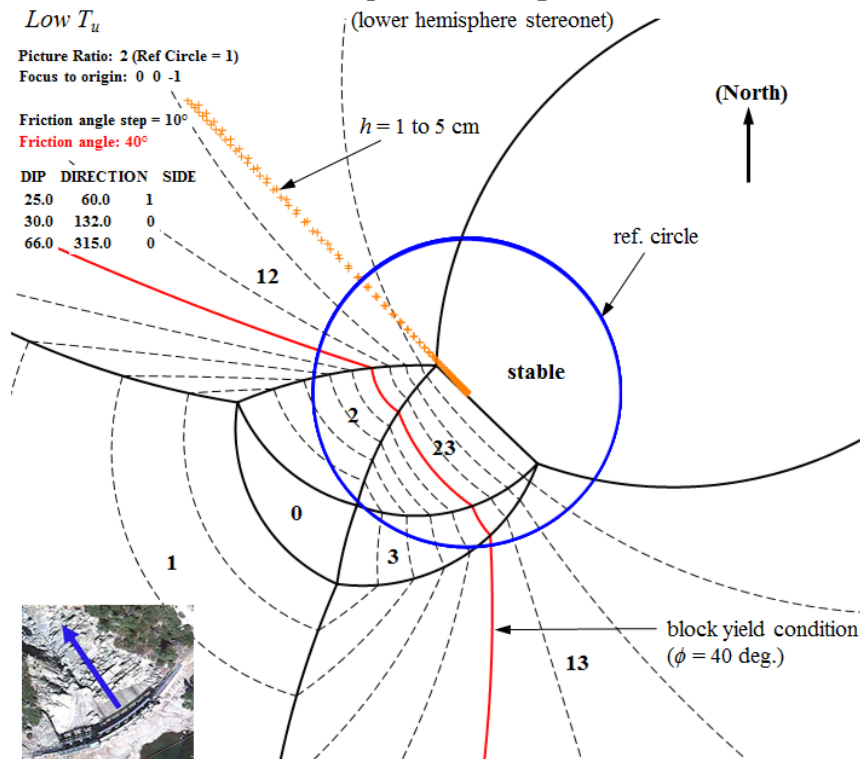


Spaulding Dam No. 2 spillway – limit equilibrium stereonet

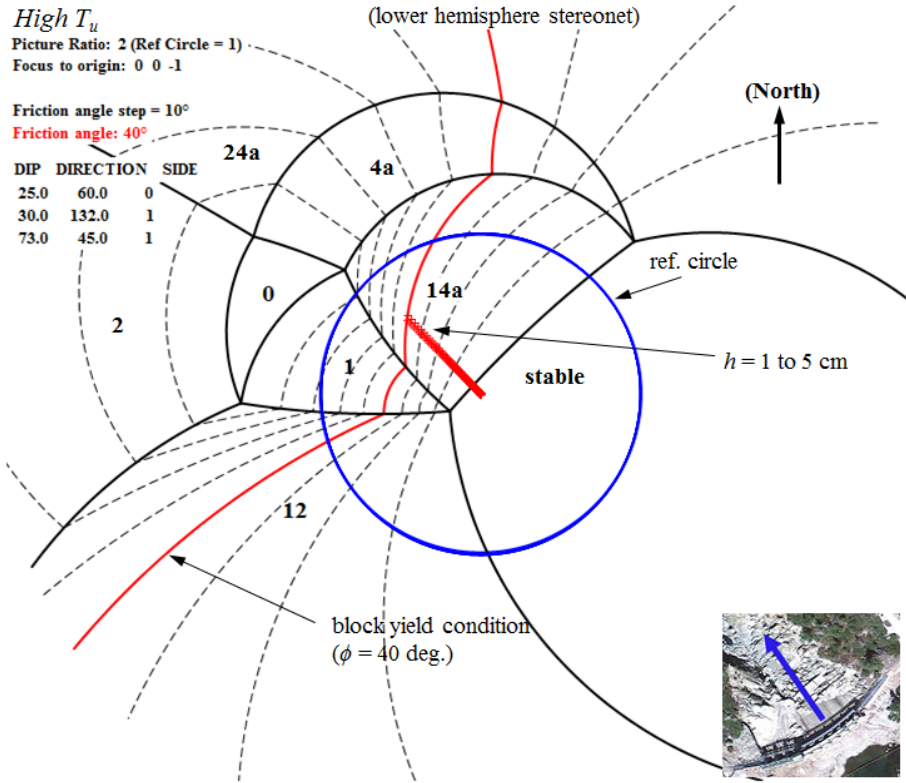
Limit Equilibrium Regions - Block 1



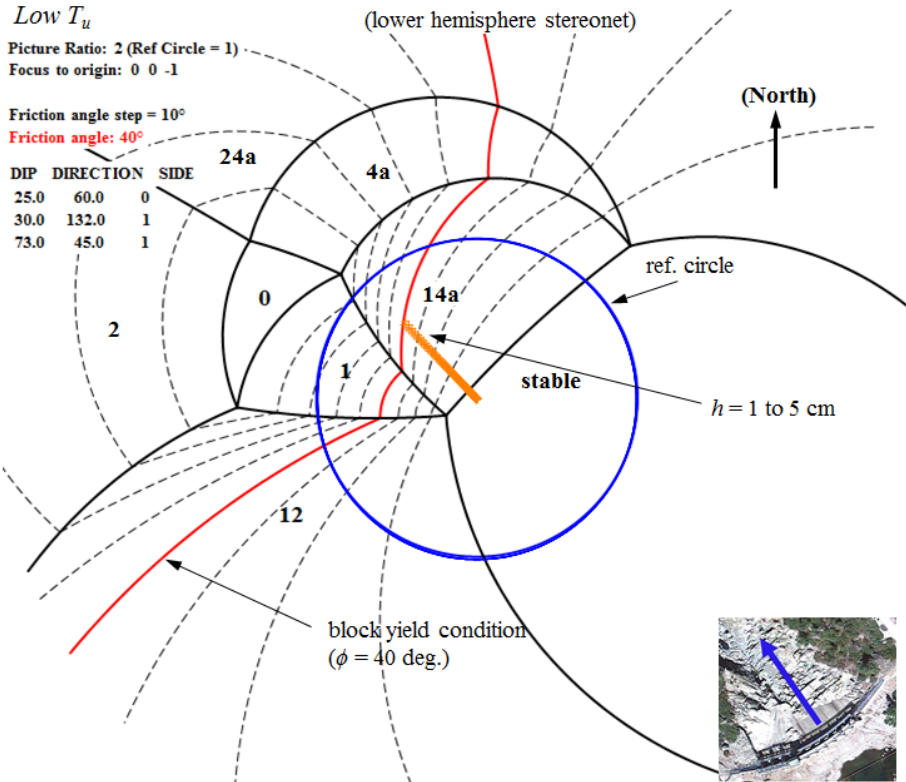
Limit Equilibrium Regions - Block 1



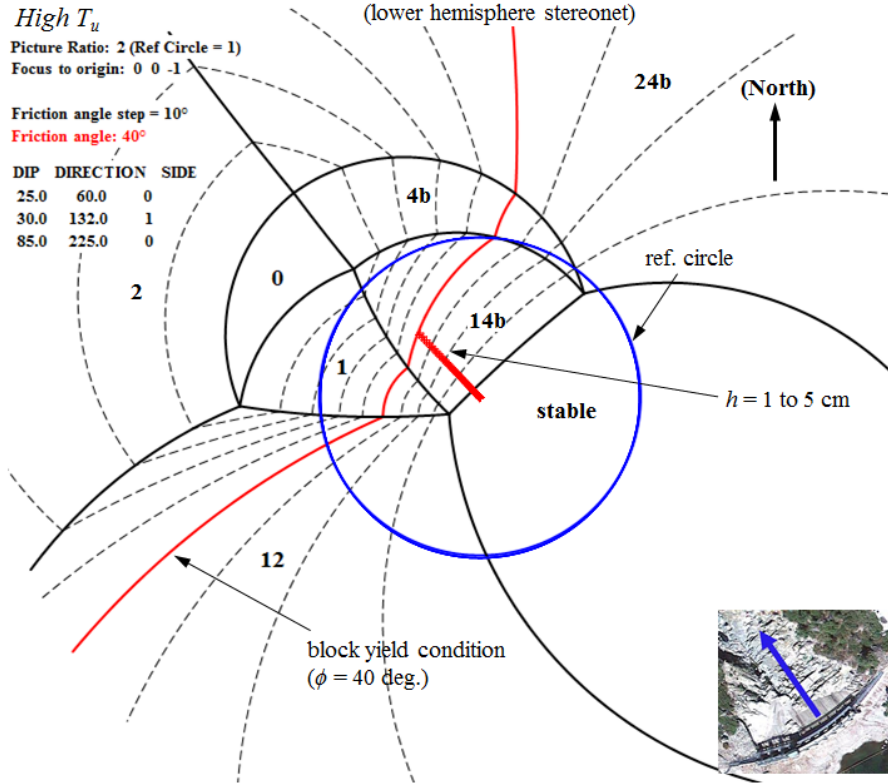
Limit Equilibrium Regions - Block 2



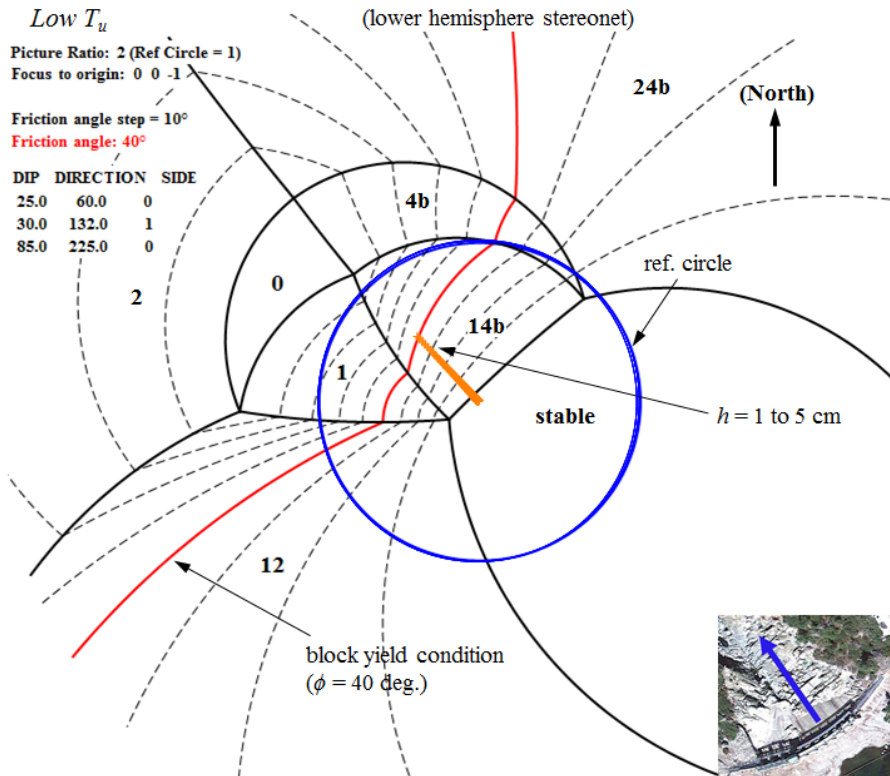
Limit Equilibrium Regions - Block 2



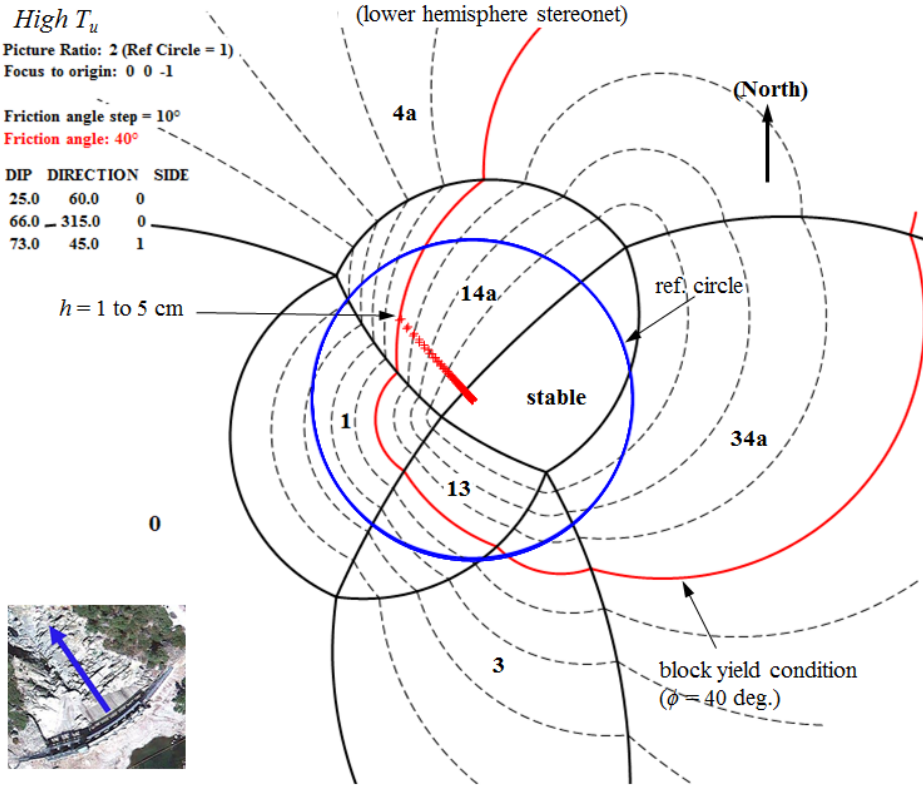
Limit Equilibrium Regions - Block 3



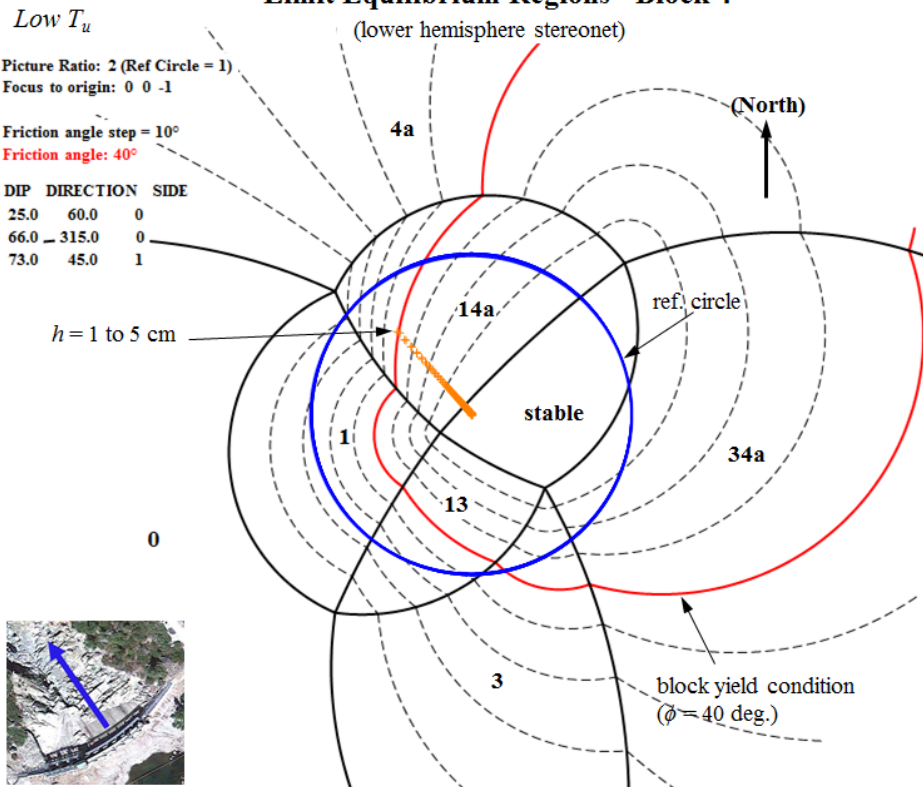
Limit Equilibrium Regions - Block 3

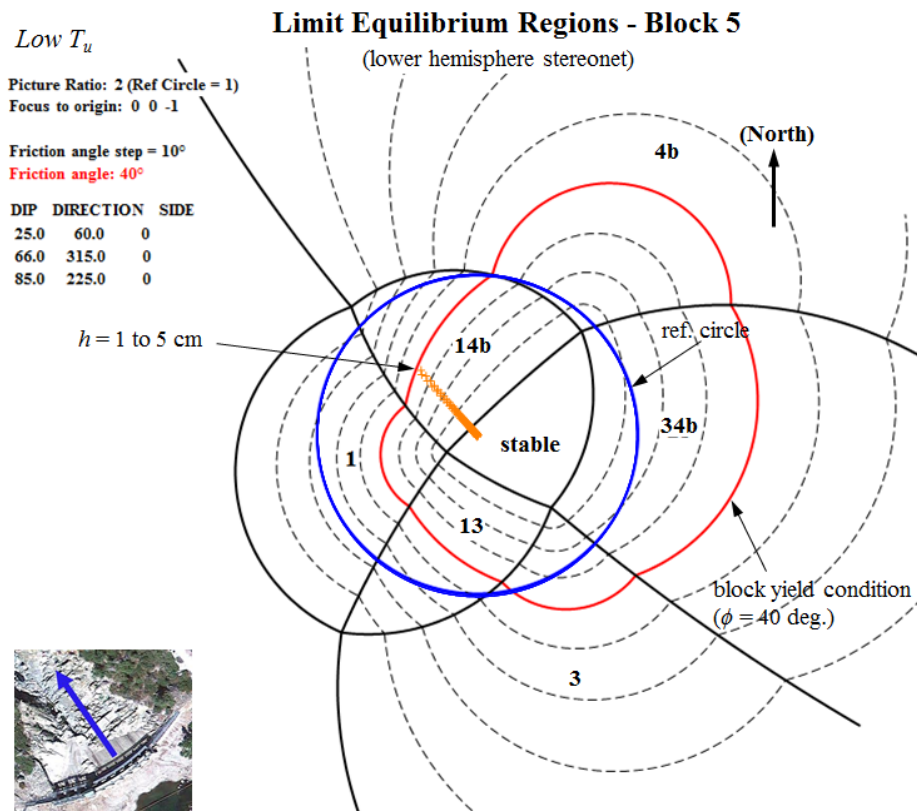
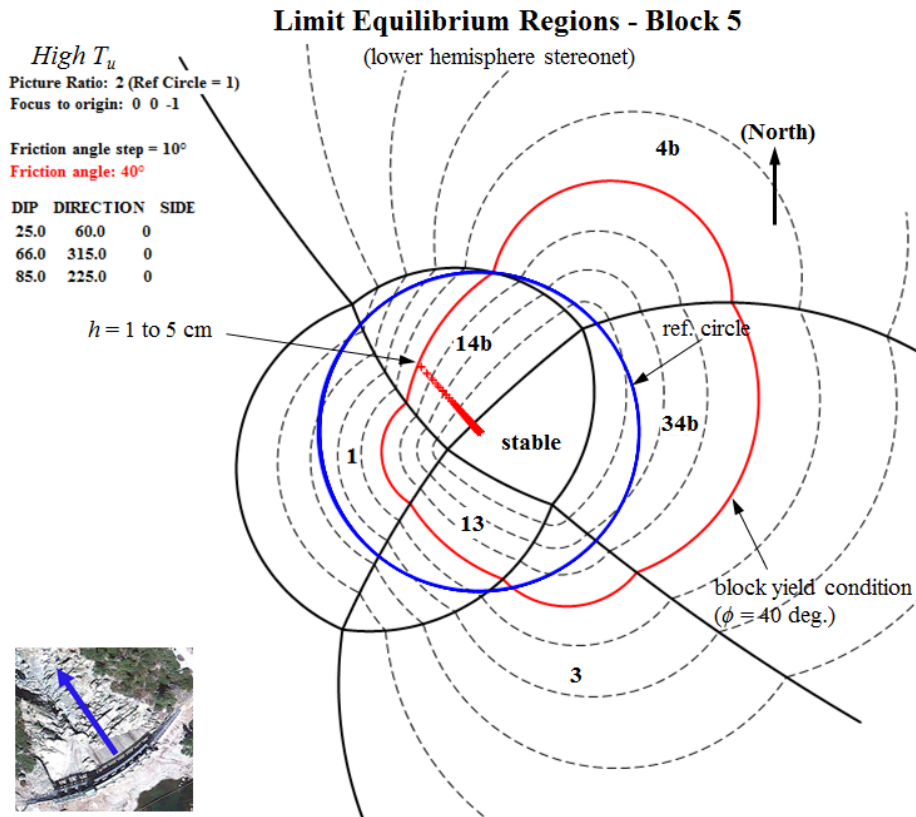


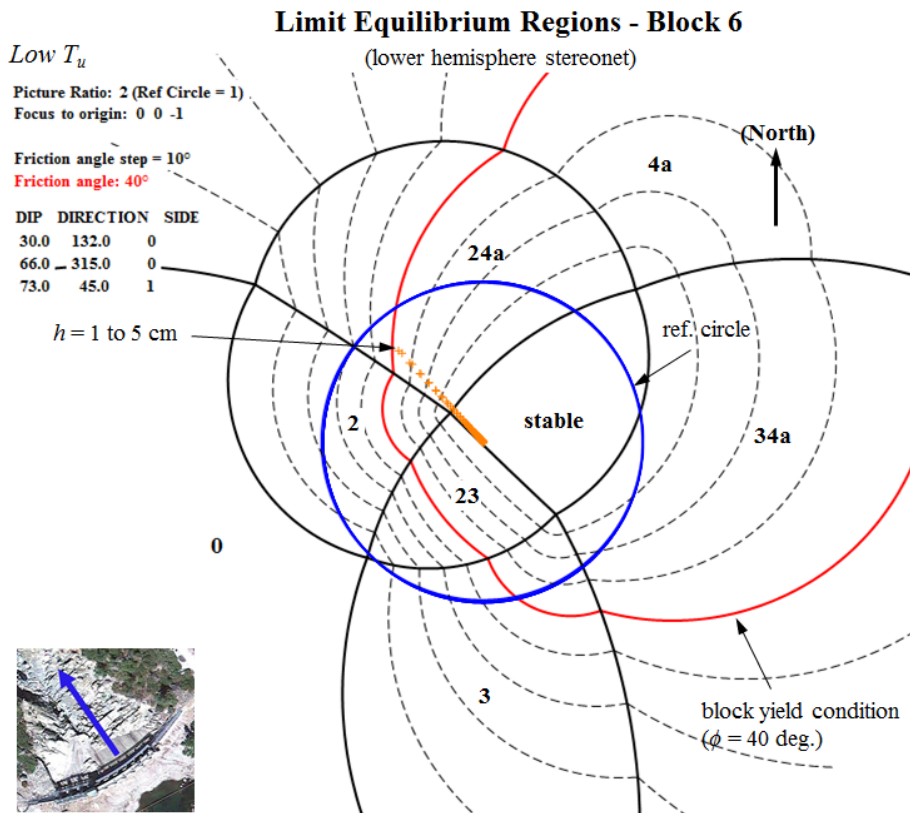
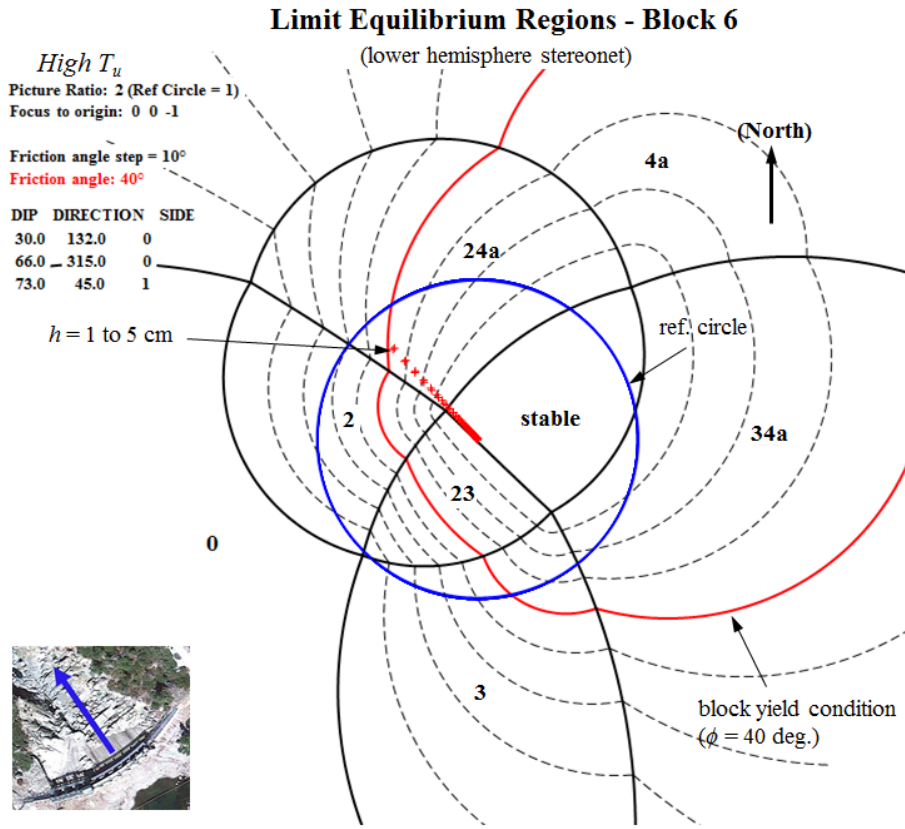
Limit Equilibrium Regions - Block 4

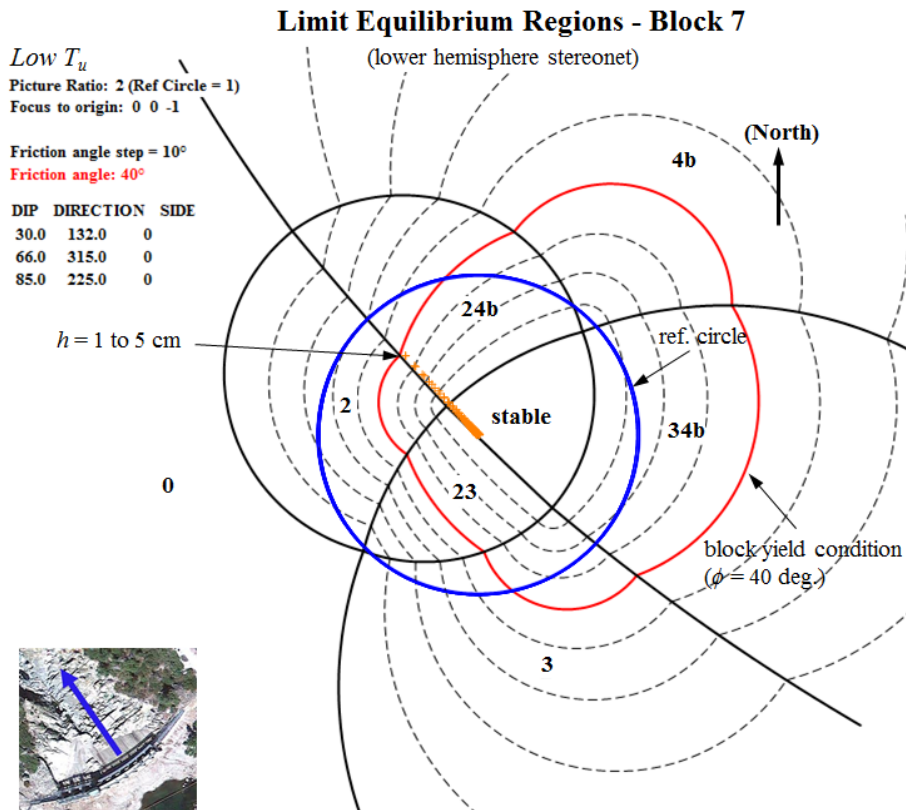
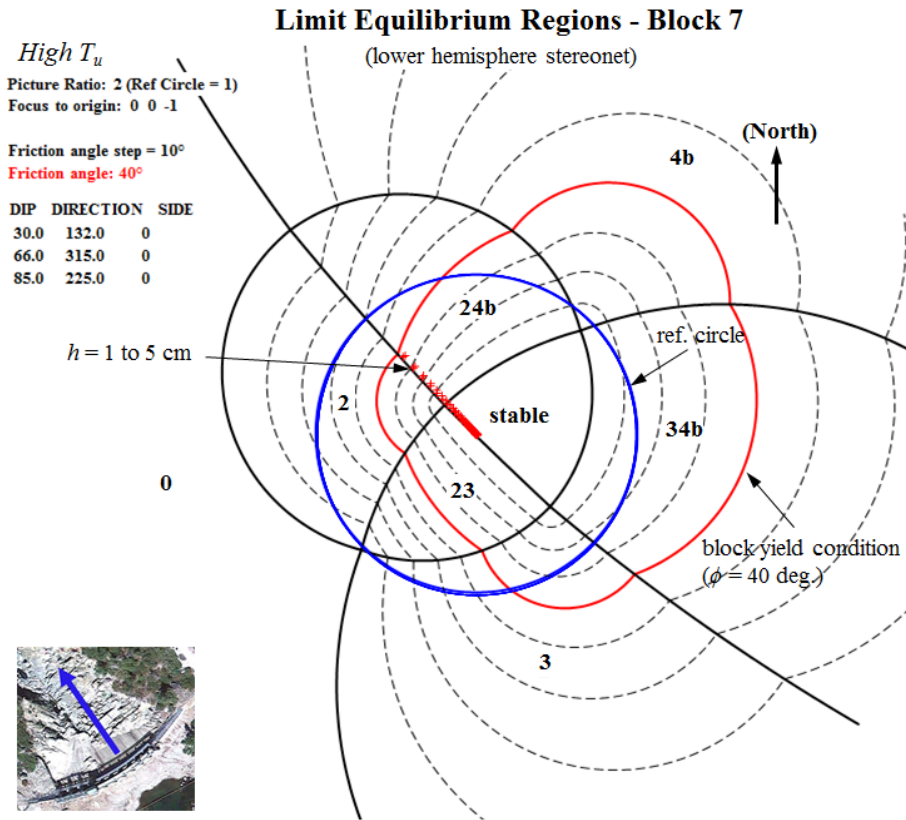


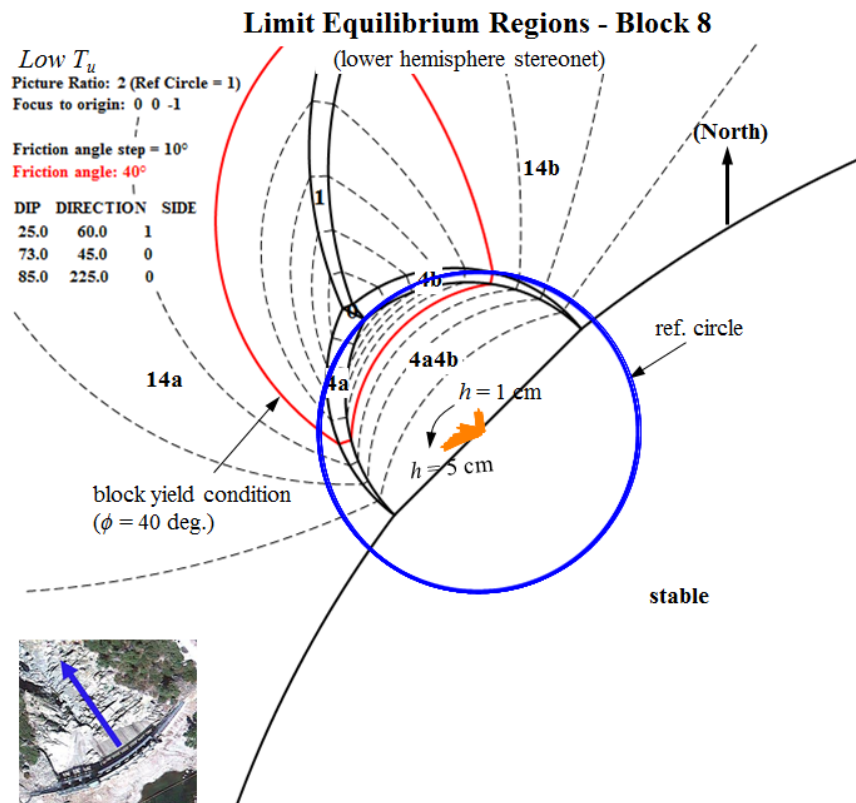
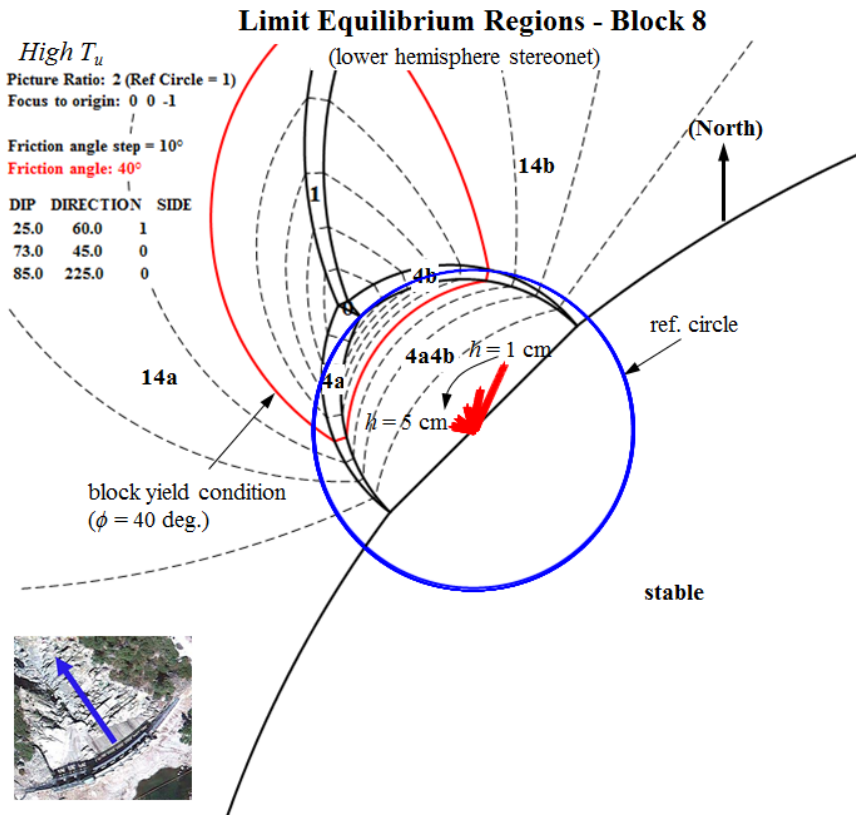
Limit Equilibrium Regions - Block 4



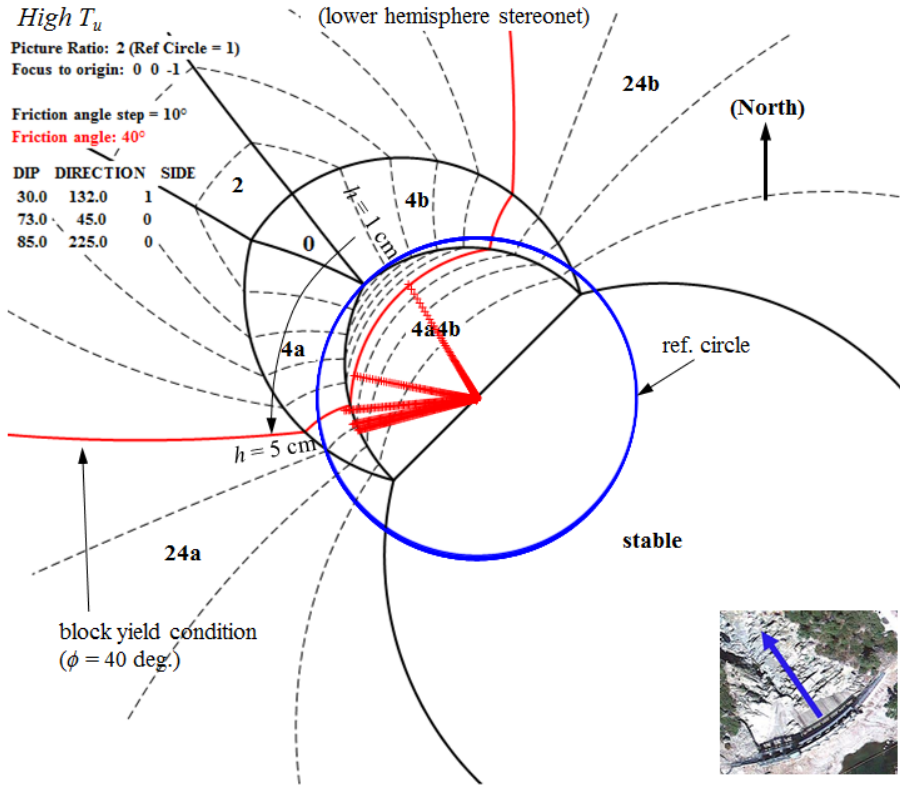








Limit Equilibrium Regions - Block 9



Limit Equilibrium Regions - Block 9

